2017

Constitutive Modeling Of Viscoplastic Porous Single Crystals And Polycrystals: Macroscopic Response And Evolution Of The Microstructure

Dawei Song
University of Pennsylvania, liuyuanjushi@gmail.com

Constitutive Modeling Of Viscoplastic Porous Single Crystals And Polycrystals: Macroscopic Response And Evolution Of The Microstructure

Abstract
\noindent Porosity can have a significant effect on the overall constitutive behavior of many materials, especially when it serves to relax kinematic constraints imposed by the underlying matrix behavior. In this study, we investigate the multiscale, finite-strain response of viscoplastic porous single crystals and porous polycrystals. For these materials, the presence of voids leads to highly nonlinear dilatational behavior for loads with a large hydrostatic component, even though the matrix material itself is essentially incompressible.

\vspace*{15pt}

\noindent In this study, we employ the recently developed ``fully optimized second-order" homogenization approach, along with an iterated homogenization procedure, to obtain accurate estimates for the effective behavior of porous single crystals and porous polycrystals with fixed states of the microstructure. The method makes use of the effective properties of a ``linear comparison composite," whose local properties are chosen according to a suitably designed variational principle, to generate the corresponding estimates for the actual nonlinear porous materials. Additionally, consistent homogenization estimates for the average strain-rate and spin fields in the phases are used to develop approximate evolution equations for the microstructures. The model is quite general, and applies for viscoplastic porous single crystals and polycrystals with general crystallographic texture, general ellipsoidal voids, and general ellipsoidal grains, which are subjected to general loading conditions. The model is used to study both the instantaneous response and the evolution of the microstructure for porous FCC and HCP single crystals and polycrystals. It is found that the intrinsic anisotropy of the matrix phase---either due to the local crystallography in single crystals or to the texture of polycrystals---has significant effects on the porosity evolution, as well as on the overall hardening/softening behavior of the porous materials. In particular, the predictions of the model for porous single crystals are found to be in fairly good agreement with the full-field, numerical results available in the literature. The results for porous polycrystals suggest that the macroscopic behavior is controlled by porosity growth at high stress triaxialities, while it is controlled by texture evolution of the underlying matrix at low triaxialities.

Degree Type
Dissertation

Degree Name
Doctor of Philosophy (PhD)

Graduate Group
Mechanical Engineering & Applied Mechanics

First Advisor
Pedro Ponte Castañeda

Keywords
Crystal Plasticity, Homogenization, Multiscale Modeling, Polycrystals, Porous Materials, Texture

Subject Categories
Mechanical Engineering

CONSTITUTIVE MODELING OF VISCOPLASTIC POROUS SINGLE CRYSTALS AND POLYCRYSTALS: MACROSCOPIC RESPONSE AND EVOLUTION OF THE MICROSTRUCTURE

Dawei Song

A DISSERTATION

in

Mechanical Engineering and Applied Mechanics

Presented to the Faculties of the University of Pennsylvania

in

Partial Fulfillment of the Requirements for the

Degree of Doctor of Philosophy

2017

Supervisor of Dissertation:

Pedro Ponte Castañeda, Raymond S. Markowitz Faculty Fellow and Professor
Department of Mechanical Engineering and Applied Mechanics

Graduate Group Chairperson:

Kevin Turner, Professor and MEAM Associate Chair for Graduate Affairs and Graduate Group Chair
Department of Mechanical Engineering and Applied Mechanics

Dissertation Committee:

John L. Bassani, Richard H. and S. L. Gabel Professor
Department of Mechanical Engineering and Applied Mechanics

Celia Reina, William K. Gemmill Term Assistant Professor
Department of Mechanical Engineering and Applied Mechanics

CONSTITUTIVE MODELING OF VISCOPLASTIC POROUS SINGLE CRYSTALS AND POLYCRYSTALS: MACROSCOPIC RESPONSE AND EVOLUTION OF THE MICROSTRUCTURE

To My Parents and My Wife, Xiyu

Acknowledgments

I am finding it rather difficult to write this part, since I owe thanks to so many people who provided wisdom, encouragement, friendship and patience.

Gratitude and the utmost respect are owed to my advisor Dr. Pedro Ponte Castañeda, who I have had the privilege to work with during the last five years. I would like to thank him for the countless hours he spent on discussing scientific issues with me, both in the office and on the way back home. His immense knowledge, passion and integrity in science have been instrumental in inspiring and encouraging me during my PhD study.

I gratefully thank my thesis committee members Dr. John L. Bassani and Dr. Celia Reina, who have provided tremendous support and advice on my research project. I have benefited a lot from the instructive courses they offered, as well as the helpful discussions we made.

I would like to thank Michalis for his help at the beginning of my PhD. I would also like to thank my colleagues and friends, Morteza, Reza, Sheng, Xiaojun, Chenchen, Xiaoguai, Shuvrangsu, Jaspreet and Josh. Our discussions, which sometimes may be too loud in the lab, have been one of the most joyful parts of my gradute study.

I want to thank my parents for their unconditional love. My mother, a fearless warrior who battles cancer, has inspired me so much when I face various challenges in my life.

Finally, but certainly not least, I would like to thank my best friend and my wife, Xiyu. I truly love her, and it would not be possible for me to go this far without her love, patience, and kind.

ABSTRACT

CONSTITUTIVE MODELING OF VISCOPLASTIC POROUS SINGLE CRYSTALS AND POLYCRYSTALS:
MACROSCOPIC RESPONSE AND EVOLUTION OF THE MICROSTRUCTURE

Dawei Song

Pedro Ponte Castañeda

Porosity can have a significant effect on the overall constitutive behavior of many materials, especially when it serves to relax kinematic constraints imposed by the underlying matrix behavior. In this study, we investigate the multiscale, finite-strain response of viscoplastic porous single crystals and porous polycrystals. For these materials, the presence of voids leads to highly nonlinear dilatational behavior for loads with a large hydrostatic component, even though the matrix material itself is essentially incompressible.

In this study, we employ the recently developed "fully optimized second-order" homogenization approach, along with an iterated homogenization procedure, to obtain accurate estimates for the effective behavior of porous single crystals and porous polycrystals with fixed states of the microstructure. The method makes use of the effective properties of a "linear comparison composite," whose local properties are chosen according to a suitably designed variational principle, to generate the corresponding estimates for the actual nonlinear porous materials. Additionally, consistent homogenization estimates for the average strain-rate and spin fields in the phases are used to develop approximate evolution equations for the microstructures. The model is quite general, and applies for viscoplastic porous single crystals and polycrystals with general crystallographic texture, general ellipsoidal voids, and general ellipsoidal grains, which are subjected to general loading conditions. The model is used to study both the instantaneous response and the evolution of the microstructure for porous FCC

and HCP single crystals and polycrystals. It is found that the intrinsic anisotropy of the matrix phase—either due to the local crystallography in single crystals or to the texture of polycrystals—has significant effects on the porosity evolution, as well as on the overall hardening/softening behavior of the porous materials. In particular, the predictions of the model for porous single crystals are found to be in fairly good agreement with the full-field, numerical results available in the literature. The results for porous polycrystals suggest that the macroscopic behavior is controlled by porosity growth at high stress triaxialities, while it is controlled by texture evolution of the underlying matrix at low triaxialities.

Contents

List of Tables

List of Figures

Chapter 1

Introduction

Many materials—both man-made and natural—are aggregates of a large number of randomly distributed single-crystal grains. More often than not, these materials contain defects such as micro-voids and micro-cracks, or porosities. Porosity can have a dramatic impact on the macroscopic behavior of these materials, especially when it serves to relax kinematic constraints imposed by the underlying matrix behavior. For example, it is well known that plasticity is intrinsically a volume-preserving deformation mechanism. As a consequence, a single-crystal sample cannot accommodate volumetric strains under application of a hydrostatic loading. However, the presence of even a small amount of pores in the single crystal can make macroscopic samples of the nominally incompressible material undergo changes in volume, which can be of significant consequence on the macroscopic response under tensile hydrostatic loadings. Therefore, it is of great technological and scientific importance to be able to characterize the macroscopic behavior of these porous materials.

Modeling of the overall constitutive behavior of porous materials has been of central interest in the solid mechanics community over decades. Much of the motivation for the study of porous materials comes from its fundamental connection to one of the major failure mechanisms in ductile metallic materials, namely, the nucleation, growth and the coalescence of voids and micro-cracks (Tvergaard, 1990; Benzerga and Leblond, 2010; Benzerga et al., 2016). However, there are many areas, both of theoretical and practical interest, where the effect of porosity on the constitutive

response of materials is of critical importance. This is the case, for example, of the development of metal alloys, as well as metal-matrix composites of these materials, which typically exhibit non-negligible amounts of residual porosity and involve forming and processing technologies (Saby et al., 2013). Another particularly important example of the dramatic impacts of porosity is provided by minerals and geologic materials, such as ice, which contain predominantly intra/intergranular voids. Study of the deformation behavior of ice is crucial to further understand many large-scale phenomena such as the flow and dynamics of glaciers and ice sheets (Schulson and Duval, 2009).

Over the years, significant progress has been made to model the overall constitutive behavior of porous materials. Up to now, most studies are carried out in the context of two-phase material systems consisting of voided inclusions and an isotropic (visco)plastic matrix phase, as usually characterized by von Mises yield criterion or flow potential (e.g., Gurson, 1977; Danas and Ponte Castañeda, 2009a; Ponte Castañeda and Zaidman, 1994; Agoras and Ponte Castañeda, 2014). However, for more realistic and general conditions, the material surrounding the voids exhibits *anisotropic* behavior—either due to local crystallography in single crystals, or to the crystallographic texture for polycrystalline aggregates. For example, metallographic observations of Ni-based single-crystal superalloys have shown the presence of microvoids, which can have dramatic impact on the creep deformation and failure of such materials at high operating temperatures in jet engines (Srivastava et al., 2012). On the other hand, there is ample of experimental evidence showing that initial texture and its evolution can induce strong anisotropy in the overall response of polycrystalline aggregates, which can, in turn, affect the way they fail by void growth to coalescence (e.g., Caré and Zaoui, 1996; Lebensohn et al., 1996). Moreover, the voids that are present in polycrystalline solids may have different sizes relative to the size of the single-crystal grains, thus leading to multiple length scales of the microstructure. For instance, the pores can be much larger than the grains, as shown in Fig. 1.1(a) for an optical micrography of a titanium foam. In this case, the porous polycrystal can be treated as a composite of particulate microstrucutre, with a polycrystal matrix

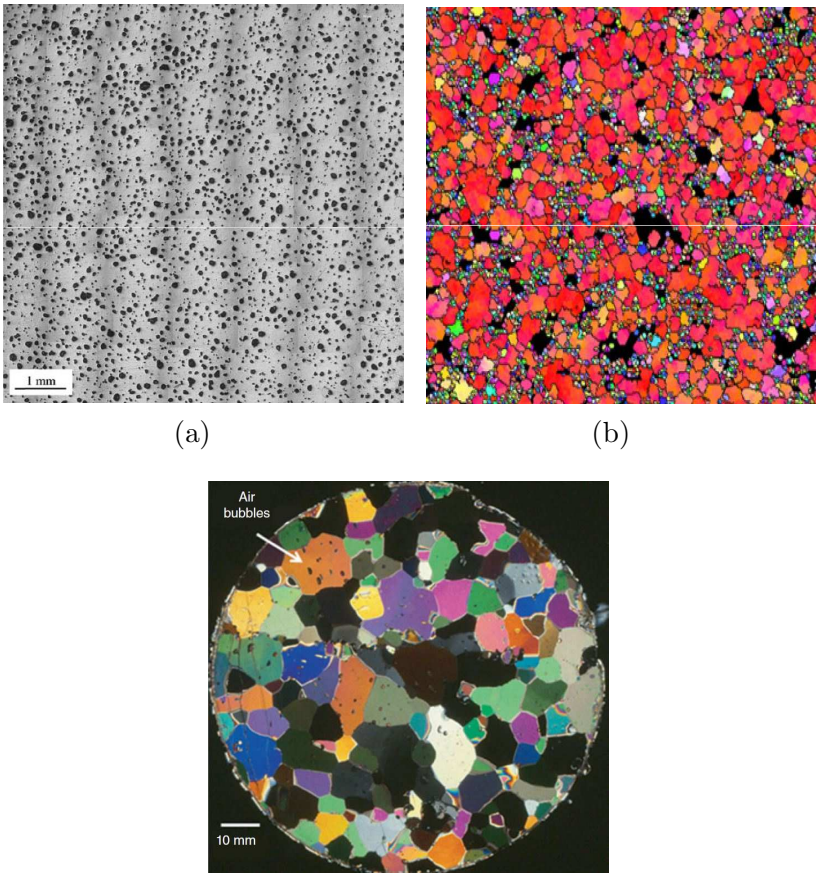

Figure 1.1: Examples of porous polycrystals. (a) Optical micrograph of a titanium foam (Shen et al., 2006), (b) EBSD inverse pole figure of deformed polycrystalline specimen of Mg alloy AZ31 showing in voids in black (Boehlert et al., 2012), and (c) Nearly isotropic granular large-grained sintered snow ice, with elongated voids inside the grains, from Ward Hunt Ice Shelf, Ellesmere Island, Canada (photo by N. K. Sinha, unpublished) (Shokr and Sinha, 2015).

and voided inclusions. In addition, the size of the voids may be comparable to that of the grains, as indicated by Fig. 1.1(b), which shows the microstructure of a deformed polycrystalline specimen containing intergranular voids (in black). The cavities can then be treated as additional "voided" grains in the solid polycrystal (e.g., Boehlert et al., 2012). Furthermore, the voids can be much smaller than the grains (see Fig. 1.1(c)), so that they can easily exist within the grains (Shokr and Sinha, 2015). This is often the case when the grain size is large, or when the particles from which the voids originate are very small.

The modeling of the macroscopic response of porous materials is generally difficult, even in the simplest case of two-phase porous isotropic materials, due to the strong nonlinear features of the problem. The physical source of this nonlinearity is related to the fact that while porosity can accommodate a hydrostatic macroscopic strain, it has to do so by respecting the isochoric deformation constraints everywhere in the matrix. In other words, the porous material accommodates the volumetric strain by means of deviatoric strains everywhere in the matrix phase (which has a nonlinear constitutive response). A simple micro-mechanical model for porous isotropic materials was developed many years ago by Gurson (1977), making use of limit analysis of a cylindrical/spherical shell. The model has been found to be successful in predicting the macroscopic response, as well as ductile failure of metals at moderate to large stress triaxialities (the ratio of the hydrostatic stress to the von Mises equivalent stress). However, it becomes less accurate for low stress triaxialities since the Gurson model neglects the change of the void shape, which is expected to be significant for shear dominated loadings. For this reason, many attempts have been made to extend this model by incorporating void-shape effect, first for spheroidal voids (e.g., Gologanu et al., 1993), and then for more general ellipsoidal voids (Madou and Leblond, 2012a). The literature for the Gurson-type model is huge and we will refer interested readers to the review articles by Benzerga and Leblond (2010) and Benzerga et al. (2016) for more details.

However, it is important to note that there are several important limitations in the Gurson approach. First, to the best knowledge of the author, it has not been possible to extract estimates for the average strain-rate and spin fields in the pore phase using Gurson's approach. For this reason, it has been necessary to complement the limit analysis estimates for the yield surfaces of porous materials with evolution laws for the pore morphology obtained from homogenization approach (heuristically modified according to full-field finite element simulation). Another disadvantage is related to the use of a spherical shell (and its generalizations) as a proxy for a representative volume element (RVE). In fact, both FFT (Bilger et al., 2005) and FEM (Fritzen et al., 2012) simulations of porous ideally plastic solids show deformation patterns involving

shear bands linking up voids, especially at small porosities, and even for hydrostatic loadings. While the predictions of the Gurson-type models for the macroscopic yield surfaces are still fairly accurate, the same is unlikely to be true for corresponding predictions for the phases averages of the strain rate and vorticity in the pores.

Alternative, and more general models have been proposed in the framework of homogenization approach for porous isotropic materials. Ponte Castañeda and Willis (1988) obtained estimates for the dilatant (instantaneous) response of porous viscoplastic materials by means of the nonlinear Hashin-Shtrikman-type variational approach of Talbot and Willis (1985). Ponte Castañeda and Zaidman (1994) made use of the variational homogenization (VH) method of Ponte Castañeda (1991)—based on the notion of a linear comparison composite (LCC)—to develop a finite-strain constitutive model for porous (visco)plastic materials under triaxial loadings, accounting for the evolution of the microstructure (porosity and void shape). The model was progressively generalized to incorporate the void-distribution effect (Kailasam et al., 1997), void rotations under general nonaligned loadings (Kailasam and Ponte Castañeda, 1997), as well as strain hardening and elasticity for the matrix (Kailasam et al., 2000; Aravas and Ponte Castañeda, 2004). Contrary to the classic Gurson model, the predictions of these homogenization models were found to be quite accurate for low stress triaxialities but less so for high stress triaxialities, especially for low porosities and high material nonlinearities. In order to remedy this shortcoming, Danas and Ponte Castañeda (2009a, 2009b) proposed an improved finite-strain constitutive model, utilizing the more sophisticated second-order (SO) linear comparison method of Ponte Castañeda (2002), along with an ad hoc modification enforcing the agreement of the SO model with exact results for spherical/cylindrical shells subjected to purely hydrostatic loadings. The SO model has been found to yield fairly accurate estimates in several comparisons with numerical simulations and other exact results. However, the SO model requires certain fitting parameters and is therefore not fully predictive. Very recently, Agoras and Ponte Castañeda (2014) proposed a novel finite-strain constitutive model for porous materials under triaxial loadings, making exclusively use of the VH method of Ponte Castañeda (1991), albeit in a novel *iterated* fashion (Ponte

Castañeda, 2012; Agoras and Ponte Castañeda, 2013). The iterated variational homogenization (IVH) model has the advantage that it does *not* involve any ad hoc modification, providing estimates that coincide with the exact spherical/cylindrical shell results under purely hydrostatic loadings (when the iteration number $N \to \infty$), and preserving the accuracy of the traditional VH model for low stress triaxialities. In practice, however, a relatively small number of iterations ($N \approx 5 - 10$) has been found to be sufficient to provide accurate results and, therefore, the new IVH model is relatively easy to implement. The model was further generalized by Song et al. (2015) to account for void rotations under general nonaligned loadings.

In comparison with the more empirical Gurson-type models, the IVH method has several distinguishing advantages: (i) it can be generalized in a seamless fashion to deal with multi-phase heterogeneous material systems, such as porous polycrystals, making use of appropriate statistical measures of the microstructure, such as porosity, orientation distribution function (texture), average shape and orientation of the pores and grains, etc., (ii) it naturally accounts for the evolution of the microstructure by means of consistent estimates for the average strain rate and spin fields in the constituent phases (Agoras and Ponte Castañeda, 2014; Song et al., 2015), and (iii) it is based on rigorous mathematical procedures that are entirely predictive and involves no extraneous "fitting" parameters or complicated inter/extrapolations.

By contrast, much less effort has been made to investigate the constitutive behavior of porous single crystals and porous polycrystals. However, constitutive theories are already available to estimate the viscoplastic response of *fully dense* polycrystalline solids in terms of their morphological and crystallographic texture. It is impossible to provide here a complete review of all the work in the area of viscoplastic polycrystals, and so we will restrict ourselves to some key references that are particularly relevant for this work. In particular, a new class of nonlinear self-consistent methods, improving significantly on the "classical" theories (Hill, 1965; Hutchinson, 1976; Molinari et al., 1987; Lebensohn et al., 1993) were developed by Ponte Castañeda and coworkers (deBotton and Ponte Castañeda, 1995; Nebozhyn et al., 2001; Liu and Ponte Castañeda, 2004a). Like the above-mentioned theories for porous

materials, these theories rely on the use of a LCC, consisting of a polycrystal with the same microstructure as the nonlinear polycrystal but whose single-crystal response is identified with a certain linearization of the corresponding nonlinear phase, guided by appropriately designed variational principles. Among these, the most accurate one is the second-order self-consistent theory of Liu and Ponte Castañeda (2004a), which is a generalization of the second-order variational method of Ponte Castañeda (2002). It yields estimates that are exact to second order in the heterogeneity contrast and satisfy all available bounds, including the variational self-consistent bound of Nebozhyn et al. (2001). Comparisons with full-field numerical simulations for cubic and hexagonal polycrystals have shown that the second-order self-consistent theory (Liu and Ponte Castañeda, 2004a) provides the most accurate and reliable estimates among the various nonlinear self-consistent theories available to date (Lebensohn et al., 2004; Lebensohn et al., 2007). The significant improvements of these theories have been identified with the use of the *field fluctuations* in the linearization scheme, in contrast with the classical self-consistent theories, which only utilize the phase averages—in an *ad hoc* fashion—for the linearization scheme. However, the second-order estimates (Liu and Ponte Castañeda, 2004a) have the undesirable feature that they are not fully stationary with respect to the properties of the LCC, which hamper their efficient applications in practice. These include the fact that the macroscopic behavior and field statistics in the nonlinear polycrystals do not coincide with the corresponding estimates in the LCC, and the existence of a duality gap, i.e., the estimates based on the dissipation potential and the dual stress potential are different. In order to remedy this deficiency, Ponte Castañeda (2015) proposed a new second-order approach, making use of a more general variational principle, such that the resulting estimates are guaranteed to be fully stationary with respect to the properties of the LCC, and to be exact to second-order in the heterogeneity contrast. Therefore, the fully-optimized second-order (FOSO) estimates are expected to be more accurate, exhibiting no duality gap, and the field statistics in the LCC can be consistently used to estimate the field statistics in the actual nonlinear composites.

Building on the recent advances in homogenization approaches for viscoplastic

crystalline composites, a few models have been proposed to describe the macroscopic behavior of porous single crystals and porous polycrystals. Idiart and Ponte Castañeda (2007b) obtained estimates for the effective flow stress of a model two-dimensional single crystal containing cylindrical voids with circular cross sections and subjected to anti-plane loadings, making use of a generalization of the variational homogenization approach of deBotton and Ponte Castañeda (1995). Han et al. (2013) developed a yield function for porous single crystals with spherical voids, utilizing the variational homogenization approach of deBotton and Ponte Castañeda (1995), together with an ad hoc modification inspired by Gurson limit analysis approach. Mbiakop et al. (2015a) developed a modified variational (MVAR) homogenization model to obtain effective flow potentials for porous single crystals containing general ellipsoidal voids subjected to general loadings (see also Mbiakop et al., 2015b for the corresponding results for two-dimensional porous single crystals containing cylindrical voids with general elliptical cross sections). The MVAR model has been shown to deliver fairly accurate estimates in comparison with the corresponding FEM results for a wide range of parameters. However, the MVAR model involves certain simplifications designed for single crystals with equal flow stresses for all available slip systems. Therefore, the model is expected to be less accurate for porous single crystals with large slip contrast. More recently, Ling et al. (2016) extended the model of Han et al. (2013) to finite strains, by accounting for the evolution of the porosity and strain hardening of the crystal matrix, although not for possible changes in the lattice orientation and void morphology. In terms of recent progresses on the modeling of porous polycrystals, Lebensohn et al. (2011) made use of a generalization of the second-order approach of Liu and Ponte Castañeda (2004a) to obtain estimates for the yield surfaces of polycrystalline solids containing intergranular voids. However, the corresponding predictions for *high stress triaxialities* exhibit the same shortcoming of the earlier homogenization models for porous materials with isotropic matrix, and are unrealistically stiff, especially at low porosities and high nonlinearities.

For completeness, it should be mentioned that Gurson approach has also been extended to incorporate the plastic anisotropy of matrix by Benzerga and Besson

(2001), and was further generalized by Monchiet et al. (2006), Keralavarma and Benzerga (2010), Morin et al. (2015) and others. These models typically assume that the plastic matrix obeys the phenomenological orthotropic yield criterion of Hill (1948) and, in principle, can not account for the crystallographic details, such as the orientation and constitutive response of the available slip systems. Paux et al. (2015) made use of a regularized Schmid law and Gurson limit-analysis to derive a Gurson-type yield criterion for porous single crystals. However, none of these theories are general enough to handle *finite-strain* constitutive behavior of viscoplastic porous single crystals and porous polycrystals, and to account for the complex coupled effects of porosity, void morphology and crystallographic texture.

Given this background, the objective of this study is to develop general finite-strain constitutive models for the viscoplastic response of porous single crystals and polycrystals, which can account for both the effect of porosity and its anisotropic evolution, as well as for the intrinsic anisotropy of the underlying matrix material. In particular, we will make use of the recently developed fully optimized second-order (FOSO) approach of Ponte Castañeda (2015), together with a generalization of the iterated homogenization approach of Agoras and Ponte Castañeda (2013), to obtain accurate estimates for the instantaneous response of porous single crystals and porous polycrystals. Additionally, consistent homogenization estimates for the average strain rate and spin fields in the phases will be used to develop self-consistent evolution equations for the microstructural variables of the materials. In their final forms, the constitutive models to be developed may be treated as the standard internal-variable viscoplastic models, where the microstructural variables play the role of internal variables.

This dissertation is organized into chapters whose contents correspond to papers that have been published, or are in preparation for publication. For convenience, the list of such papers is provided at the end of this introduction. Next, we briefly introduce the content of each chapter in this dissertation.

In **Chapter 2**, which corresponds to reference 2, we make use of a generalization of the iterated homogenization approach of Agoras and Ponte Castañeda (2013) to

provide *bounds* for the effective flow potential of porous viscoplastic single crystals under general loading conditions. We use the developed method to investigate the instantaneous response of low-symmetry, high-anisotropy porous HCP single crystals, such as porous ice, under axisymmetric loading conditions. Moreover, we compute the average strain rate in the voids to explore its implication for the evolution of the microstructure. Finally, we deduce the intrinsic effect of the crystal anisotropy by comparing with the corresponding results for porous materials with isotropic matrix.

In **Chapter 3**, which corresponds to reference 3, we develop a general *finite-strain* homogenization model for viscoplastic porous single crystals, which is referred to as the Iterated Second-order (ISO) model. The model makes use of the recently developed FOSO method of Ponte Castañeda (2015), along with the iterated homogenization approach of Agoras and Ponte Castañeda (2013), to determine the effective instantaneous response of porous single crystals with fixed states of the microstructure. Then, we make use of the homogenization estimates for the average strain-rate and spin field in the phases, together with the standard kinematical relations, to develop evolution laws for the microstructural variables.

Chapter 4, which corresponds to reference 4, is concerned with the applications of the ISO model developed in chapter 3. In particular, the model is used to investigate both the instantaneous response and the evolution of the microstructure for porous FCC and HCP single crystals. The effects of the loading conditions, including the principal loading directions, stress triaxiality and Lode angle, on the finite-strain behavior of porous single crystals are studied in detail. Moreover, the complex coupled effects of porosity, void morphology and crystal anisotropy on the overall hardening/softening behavior of porous single crystals are analyzed. The predictions of the model are also compared with the corresponding full-field, numerical simulations available in the literature to assess the accuracy of the model.

Before moving on to the constitutive modeling of porous polycrystals, in **Chapter 5**, which corresponds to reference 5, we use the FOSO method of Ponte Castañeda (2015) to generate estimates of the self-consistent type for the macroscopic behavior and field statistics in viscoplastic *solid polycrystals*. Additionally, we develop evolution

laws characterizing the texture evolution of solid polycrystals at finite strains. The model is applied to study the effective flow stress, field fluctuation and finite-strain response of low-symmetry HCP polycrystals, including ice polycrystals. The new FOSO estimates are compared with the earlier homogenization estimates, as well as with the full-field numerical simulations available in the literature, to validate the FOSO model.

In **Chapter 6**, which corresponds to reference 6, we propose a general finite-strain homogenization model for the two-scale, viscoplastic porous polycrystals, consisting of large pores randomly distributed in a fine-scale solid polycrystal matrix (where the size of the pores is much larger than that of the single-crystal grains). The model makes use of the effective property of a suitably chosen two-scale linear comparison composite (LCC)—with sub-structure identical to that of the nonlinear porous polycrystal of interest—to estimate the effective behavior of the nonlinear composite. The effective properties of the LCC are determined by means of a sequential homogenization procedure, involving the self-consistent estimates for the effective behavior of the polycrystal matrix, and the Hashin-Shtrikman type estimates for the effective behavior of the porous composite. In addition, consistent homogenization estimates for the strain-rate and spin fields in the phases are used to develop evolution equations for the microstructure, characterizing the evolution of the size, shape and orientation of the pores, as well as of the morphological and crystallographic textures of the polycrystal matrix.

In **Chapter 7**, which corresponds to reference 7, we consider specific applications of the model for porous FCC and HCP polycrystals. In particular, we examine the instantaneous effective behavior, as well as the finite-strain macroscopic response of porous FCC and HCP polycrystals, for axisymmetric loading conditions with different stress triaxialities and Lode parameters. The effect of the loading conditions on the sub-structure evolution, field fluctuations, and the overall hardening/softening behavior of the porous polycrystals is investigated in detail. In addition, the intrinsic effect of the texture evolution of the polycrystal matrix is deduced by comparing with corresponding results for porous isotropic materials, and found to be quite significant.

Finally, it is remarked that in the course of this dissertation the author has also been involved in a research project—conducted in collaboration with Dr. Michalis Agoras and Dr. Pedro Ponte Castaneda—on the evolution of pore shape and orientation in plastically deforming metals. This work resulted in one publication corresponding to reference 1, which is attached in this thesis as Appendix A.

List of publications that result from this dissertation work

1. Song, D., Agoras, M., Ponte Castañeda, P., 2015. The evolution of pore shape and orientation in plastically deforming metals: Implications for macroscopic response and shear localization. *Mech. Mater.* 90, 47–68.

2. Song, D., Ponte Castañeda, P., 2017a. Macroscopic response of strongly anisotropic porous viscoplastic single crystals and applications to ice. *Extreme Mech. Lett.* 10, 41–49.

3. Song, D., Ponte Castañeda, P., 2017b. A finite-strain homogenization model for viscoplastic porous single crystals: I– Theory. *J. Mech. Phys. Solids* 107, 560–579.

4. Song, D., Ponte Castañeda, P., 2017c. A finite-strain homogenization model for viscoplastic porous single crystals: II– Applications. *J. Mech. Phys. Solids* 107, 580–602.

5. Song, D., Ponte Castañeda, P., 2017d. Fully optimized second-order homogenization estimates for the effective behavior and texture evolution of viscoplastic polycrystals. *In preparation.*

6. Song, D., Ponte Castañeda, P., 2017e. A finite-strain multiscale homogenization model for viscoplastic porous polycrystals with large voids: I– Theory. *In preparation.*

7. Song, D., Ponte Castañeda, P., 2017f. A finite-strain multiscale homogenization model for viscoplastic porous polycrystals with large voids: II– Applications. *In preparation.*

Chapter 2

Iterated variational homogenization model for porous single crystals

A recently developed iterated homogenization procedure is generalized for porous viscoplastic single crystals and applied to characterize the effective behavior of low-symmetry high-anisotropy porous HCP single crystals (e.g., ice), focusing on the complex coupled effects of the porosity, void shape and crystal anisotropy. Consistent estimates for the average strain rate in the voids are also obtained and their implications for the evolution of the microstructure are explored. The intrinsic effect of the strong crystal anisotropy of porous ice is deduced from comparisons with corresponding results for porous isotropic materials, and found to be significant. In particular, as a consequence of the strong crystal anisotropy of ice, the porosity growth is found to be quite fast at low stress triaxiality, while the void distortion rates can be more significant at high stress triaxialities. Finally, the coupling between the "morphological" anisotropy induced by the void shape and the underlying crystalline anisotropy is investigated and found to have significant effects on the void growth and the void distortion, leading to significantly different behaviors for porous ice and porous isotropic materials.

2.1 Introduction

Most metals and minerals—both man-made and natural—appear in the polycrystalline form. Micro-defects, such as intra/inter-granular voids and cracks, which are usually distributed with random positions and orientations in the crystalline material, have significant effects on the macroscopic behavior, as well as on their failure. It is then of great interest to be able to characterize the effective response of such porous crystalline materials in terms of the known properties of their constituents and statistical information about their microstructures. In this work, the focus will be on the case where the voids exist either within a homogeneous single-crystal material, or within single-crystal grains of a polycrystalline material, and the size of the voids is much smaller than that of the single crystal (grains), so that the stress and strain fields around the voids develop as if they were embedded in an infinitely large single-crystal matrix subjected to homogeneous loading conditions. The objective of this chapter is to develop a constitutive model for the macroscopic response of porous viscoplastic single crystals with random microstructures, by means of a generalization of the recently developed iterated nonlinear homogenization method (Ponte Castañeda, 2012; Agoras and Ponte Castañeda, 2013).

A classical subject in mechanics of materials that calls for such constitutive models is the ductile fracture of crystalline metals and alloys, where it has been evidenced both theoretically and experimentally that the nucleation, growth and coalescence of microvoids play a significant role in the creep fracture of such materials (e.g., Crépin et al., 1996; Srivastava et al., 2012). Another particularly important subject is the study of the grain-scale behavior of polycrystalline ice, which is of great scientific and practical values for further understanding the large-scale geophysical phenomena such as the flow of glaciers (Schulson and Duval, 2009). Since microvoids exist predominantly within the ice single-crystal grains, the constitutive model proposed in this work provides a useful tool for investigating the effects of the intra-granular voids on the macroscopic behavior of ice.

Over the years, important progress has been made to characterize the behavior

of porous single crystals. On one hand, the effect of the crystal orientation on the void growth has been studied by means of full-field, unit-cell simulations based on the finite element method (O'regan et al., 1997; Yerra et al., 2010; Ha and Kim, 2010; Srivastava and Needleman, 2015). On the other hand, a few models have been proposed to describe the macroscopic behavior of porous single crystals. Han et al. (2013) developed a yield function for porous single crystals containing spherical voids based on the variational homogenization method developed by deBotton and Ponte Castañeda (1995) and ad hoc modifications inspired by the limit analysis of the Gurson (1977) type model. Paux et al. (2015) proposed a Gurson-type yield criterion by means of a regularized form of the Schmid law and limit-analysis calculations. These approaches all show satisfactory agreements with the corresponding unit-cell calculations for porous FCC single crystals from the work of Han et al. (2013). However, they all involve fitting of parameters to finite element simulations of porous FCC single crystals, which have not been calibrated for other types of single crystals (e.g., BCC, HCP and etc.). In this sense, the homogenization models to be developed in this work are more general since they are entirely predictive, involving no fitting parameters, and are applicable for porous single crystals of general type. Estimates for porous single crystals were developed by Idiart and Ponte Castañeda (2007b), making use of a generalization of the rigorous variational (VAR) homogenization methods of Ponte Castañeda (1991) and deBotton and Ponte Castañeda (1995). In particular, estimates were obtained for the effective flow stress of 2D porous single crystals containing cylindrical voids subjected to anti-plane shear loadings. More recently, Mbiakop et al. (2015b) developed a modified variational (MVAR) homogenization model, and used it to characterize the effective yield potential of 3D porous single crystals containing general ellipsoidal voids under general loading conditions. The model was derived by using the VAR procedure of Ponte Castañeda (1991), together with an ad hoc modification, enforcing the agreement of the MVAR model with the Gurson model for the special case of spherical voids with infinite number of equiangular slip systems subjected to purely hydrostatic loadings. The MVAR model has been found to be in good agreement with the unit-cell calculations for a wide range

of parameters. However, the limiting factor of this approach is the assumption of equal flow stresses for all available slip systems made in its derivation, which makes it unsuitable for porous crystals with large anisotropy, such as porous ice, where the non-basal slip systems are known to have much larger flow stresses than the basal slip systems.

In this work, the homogenization method to be developed is based entirely on the nonlinear variational homogenization method, albeit used in a novel iterated fashion (Ponte Castañeda, 2012; Agoras and Ponte Castañeda, 2013), and has the capability of providing bounds and estimates that remain accurate for porous single crystals with general crystal anisotropy, general ellipsoidal voids, subjected to general loading conditions. Here, for illustrative purposes, the model is applied to porous hexagonal closed-packed (HCP) single crystals, including porous ice, and the effects of the porosity, void shape and crystal anisotropy on the new estimates for the flow potential are investigated in some detail. In addition, the average strain rate in the voids is also computed to explore the implications for the evolution of the microstructure.

2.2 Homogenization framework for porous single crystals

In this work, porous single crystals are idealized as two-phase materials with single-crystal matrix (phase 1) and vacuous inclusions (phase 2). In addition, separation of length scales is assumed implying that the size of the voids is much smaller than the size of the specimen and the scale of variation of the applied loadings. Furthermore, the porous single crystal is assumed to have statistically uniform and ergodic microstructure. As shown in Fig. 2.1, consider porous single crystals containing ellipsoidal voids (phase 2) that are aligned in a certain direction, but distributed randomly in the surrounding crystal matrix with two-point probability functions for their centers characterized by "ellipsoidal symmetry" (Willis, 1977; Ponte Castañeda and Willis, 1995). In general, the shape of the ellipsoid characterizing the distribution can

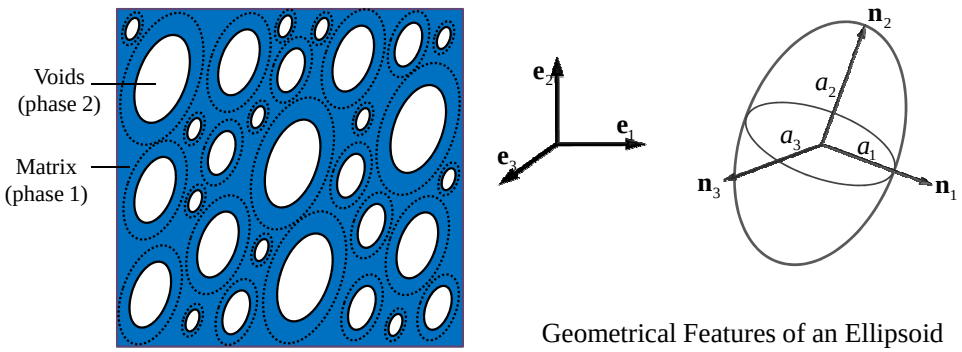

Figure 2.1: Schematic representation of a porous single crystal consisting of aligned, ellipsoidal voids (solid lines) that are distributed with the same ellipsoidal symmetry (dotted lines) in a single-crystal matrix.

be different from the shape of the ellipsoid characterizing the voids (Ponte Castañeda and Willis, 1995; Agoras and Ponte Castañeda, 2013). However, differences between the shape of the voids and that of the distribution are expected to have effects on the macroscopic response that are of second order in the volume fraction and will not be considered here for simplicity (Agoras and Ponte Castañeda, 2014; Song et al., 2015).

According to the above hypothesis, the microstructure of the porous single crystal can be completely characterized by the set of microstructural variables

$$\mathbf{s} \equiv \{f, w_1, w_2, \mathbf{n}_1, \mathbf{n}_2, \mathbf{n}_3\}, \tag{2.1}$$

where f is the volume fraction of the voids (or porosity), $w_1 = a_3/a_1, w_2 = a_3/a_2$ are the two aspect ratios characterizing the shape (and distribution) of the voids (a_1, a_2 and a_3 are respectively the lengths of the three semi-axes of the ellipsoid), and $\mathbf{n}_1$, $\mathbf{n}_2$ and $\mathbf{n}_3$ are unit vectors along the three principal directions of the ellipsoid. It should be mentioned that, in general, the voids (and their distribution) are of arbitrary ellipsoidal shape, where $w_1 \neq w_2 \neq 1$ and $\mathbf{n}_i \neq \mathbf{e}_i$, leading to additional "morphological" anisotropy superimposed on the underlying anisotropy of the single-crystal matrix.

Single crystals are assumed to deform by multi-glide along K slip systems. For simplicity, the constitutive behavior of the single-crystal matrix (phase 1) is taken to be viscoplastic, and the effects of elasticity are neglected. Then, the local constitutive

response of the single crystal can be described by

$$\mathbf{D} = \frac{\partial u^{(1)}(\boldsymbol{\sigma})}{\partial \boldsymbol{\sigma}}, \quad u^{(1)}(\boldsymbol{\sigma}) = \sum_{k=1}^{K} \phi_{(k)}(\tau_{(k)}), \tag{2.2}$$

where $u^{(1)}$ is the stress potential for the crystal matrix, $\boldsymbol{\sigma}$ is the Cauchy stress and $\mathbf{D}$ is the Eulerian strain rate. The convex functions $\phi_{(k)}$ $(k = 1, ..., K)$ characterize the response of the K slip systems, and depend on the resolved shear (or Schmid) stresses

$$\tau_{(k)} = \boldsymbol{\sigma} \cdot \boldsymbol{\mu}_{(k)}, \quad \text{where} \quad \boldsymbol{\mu}_{(k)} = \frac{1}{2}\left(\mathbf{n}_{(k)} \otimes \mathbf{m}_{(k)} + \mathbf{m}_{(k)} \otimes \mathbf{n}_{(k)}\right). \tag{2.3}$$

Here, the $\boldsymbol{\mu}_{(k)}$ are the second order Schmid tensors, with $\mathbf{n}_{(k)}$ and $\mathbf{m}_{(k)}$ denoting respectively the unit vectors normal to the slip plane and along the slip direction of the kth slip system. The slip potentials $\phi_{(k)}$ are given by the common power-law form

$$\phi_{(k)}(\tau) = \frac{\dot{\gamma}_0 (\tau_0)_{(k)}}{n+1} \left| \frac{\tau}{(\tau_0)_{(k)}} \right|^{n+1}, \quad k = 1, ..., K, \tag{2.4}$$

where $\dot{\gamma}_0$ denotes the reference strain rate, $(\tau_0)_{(k)} > 0$ is the reference flow stress of the kth slip system and n is the creep exponent. Note that $(\tau_{(0)})_{(k)}$ can be very different for each slip system, which may lead to extreme anisotropic behavior of the crystal matrix. Also note that the creep exponent n is taken to be the same for all slip systems and, hence, the stress potential $u^{(1)}$ is a homogeneous function of degree $n+1$ in $\boldsymbol{\sigma}$. However, n could in general be different for different slip systems, but here it will be assumed to be the same for simplicity. In particular, two limiting cases as n tends to 1 and ∞ are of special interest, since they correspond to linearly viscous and rigid ideally plastic behavior for the single crystal, respectively. On the other hand, the stress potential of the voids (phase 2) is such that $u^{(2)}(\boldsymbol{\sigma}) = 0$ if $\boldsymbol{\sigma}$ is identically zero, while $u^{(2)}(\boldsymbol{\sigma}) = \infty$ otherwise.

Given the local constitutive behavior of each phase, as well as the prescribed microstructural information (2.1), the effective response of the porous single crystal can be described by the constitutive relation between the macroscopic Eulerian strain

rate $\overline{\mathbf{D}}$ and the macroscopic Cauchy stress $\overline{\boldsymbol{\sigma}}$, as given by

$$\overline{\mathbf{D}} = \frac{\partial \widetilde{u}(\overline{\boldsymbol{\sigma}})}{\partial \overline{\boldsymbol{\sigma}}}, \quad \widetilde{u}(\overline{\boldsymbol{\sigma}}) \equiv \min_{\boldsymbol{\sigma} \in \mathcal{S}(\overline{\boldsymbol{\sigma}})} \langle u(\mathbf{x}, \boldsymbol{\sigma}) \rangle. \tag{2.5}$$

Here $\widetilde{u}$ is the effective stress potential of the porous single crystal, $\mathcal{S}(\overline{\boldsymbol{\sigma}})$ is the associated "statically admissible" set, including all $\boldsymbol{\sigma}$ fields that are divergence free, satisfy the traction continuity condition $\boldsymbol{\sigma}\mathbf{n} = \mathbf{0}$ on the void boundaries, and are such that $\langle \boldsymbol{\sigma} \rangle = \overline{\boldsymbol{\sigma}}$. It should be noted that the symbol $\langle . \rangle$ denotes the volume average over the total volume occupied by a representative volume element of the porous single crystal.

From the homogeneity of the local potential (2.4) in $\boldsymbol{\sigma}$, it follows that the effective potential (2.5) of the porous single crystal is homogeneous of degree $n+1$ in $\overline{\boldsymbol{\sigma}}$. Then, the effective behavior of the porous single crystal can be completely characterized by a single equi-potential surface in $\overline{\boldsymbol{\sigma}}$ space, i.e., $\widetilde{u}(\overline{\boldsymbol{\Sigma}}) = \text{const}$, where any other equi-potential surface is just a homothetic surface (Leblond et al., 1994). In particular, the *gauge surface* of the porous single crystal is defined by

$$\widetilde{u}(\overline{\boldsymbol{\Sigma}}) = \frac{\dot{\gamma}_0 \tau_0^{-n}}{n+1}, \tag{2.6}$$

where τ_0 is a reference flow stress, which can be chosen to be, e.g., one of the reference flow stresses $(\tau_0)_{(k)}$ $(k = 1, ..., K)$. Note that the normal to the gauge surface indicates the direction of the plastic flow. Also, in the limit of ideally plasticity $(n \to \infty)$, the gauge surface tends to the standard yield surface.

Alternatively, the gauge surface can be obtained by introducing a gauge factor Γ, such that the effective stress potential can be written in the form

$$\widetilde{u}(\overline{\boldsymbol{\sigma}}) = \frac{\dot{\gamma}_0 \tau_0}{n+1} \left(\frac{\Gamma(\overline{\boldsymbol{\sigma}})}{\tau_0} \right)^{n+1}, \tag{2.7}$$

where Γ is a homogeneous function of degree 1 in $\overline{\boldsymbol{\sigma}}$, which depends on the creep exponent n, the microstructural variables $\mathbf{s}$ defined in (2.1), and the reference flow stresses $(\tau_0)_{(k)}$, $k = 1, ..., K$. Then, for any prescribed macroscopic stress $\overline{\boldsymbol{\sigma}}$, the

normalized stress tensor

$$\overline{\boldsymbol{\Sigma}} = \frac{\overline{\boldsymbol{\sigma}}}{\Gamma(\overline{\boldsymbol{\sigma}})} \tag{2.8}$$

will always lie on the gauge surface. In other words, the stress tensor $\overline{\boldsymbol{\Sigma}}$ on the gauge surface can be obtained by computing the effective stress potential $\widetilde{u}$ for arbitrary $\overline{\boldsymbol{\sigma}}$, determining the corresponding gauge factor $\Gamma(\overline{\boldsymbol{\sigma}})$ from (2.7), and normalizing $\overline{\boldsymbol{\sigma}}$ according to (2.8). Similarly, it is useful to introduce the corresponding normalized macroscopic strain rate

$$\overline{\mathbf{E}} = \frac{\overline{\mathbf{D}}}{\dot{\gamma}_0(\Gamma(\overline{\boldsymbol{\sigma}})/\tau_0)^n} = \frac{\partial\Gamma(\overline{\boldsymbol{\sigma}})}{\partial\overline{\boldsymbol{\sigma}}}. \tag{2.9}$$

Note that $\overline{\mathbf{E}}$ is independent of the magnitude of $\overline{\boldsymbol{\sigma}}$, and depends only on the direction of $\overline{\boldsymbol{\sigma}}$.

In this work, estimates for the effective stress potential $\widetilde{u}$ are obtained by means of the iterated homogenization approach (Agoras and Ponte Castañeda, 2013) in combination with the nonlinear Variational Homogenization (VH) method developed by deBotton and Ponte Castañeda (1995), and will be referred to here as the Iterated Variational Homogenization (IVH) method. It should be mentioned that the VH method makes use of the effective property of a suitably chosen porous "linear comparison composite" (LCC)—with *uniform* matrix properties and microstructure identical to that of the nonlinear porous single crystal of interest—to estimate the effective behavior of the nonlinear composite. However, while this method is known to yield rigorous bounds, they tend to be overly stiff estimates for the effective behavior of porous single crystals, especially at low porosity, high stress triaxiality and high nonlinearity (Agoras and Ponte Castañeda, 2013). The key idea of IVH is to construct the porous microstructure iteratively in a self-similar fashion (see Fig. 2 and associated discussions in Agoras and Ponte Castañeda, 2013), in such a way that, at each iteration level, the IVH involves an LCC with identical microstructure to the corresponding nonlinear composite and with a linear single-crystal matrix, allowing for a *non-uniform* distribution of the matrix phase in the LCC, thus leading to improved estimates, which retain their bounding character.

In particular, the viscous compliance tensor of the LCC crystal matrix at the ith

level is assumed to be of the form

$$\mathbb{M}^{(1)}_{[i]} = \sum_{k=1}^{K} \alpha^{[i]}_{(k)} \boldsymbol{\mu}_{(k)} \otimes \boldsymbol{\mu}_{(k)}, \quad i = 1, ..., N, \quad k = 1, ..., K, \tag{2.10}$$

where the $\alpha^{[i]}_{(k)}$ are the slip compliances (which will be specified later), and N is the total number of iterations in the IVH procedure. Furthermore, the effective behavior of each level LCC is computed by means of the estimates of Ponte Castañeda and Willis (1995) (to be referred to here as PCW estimates), which are given by expression (2.19) in the Appendix.

In their final form, the IVH estimates for the effective stress potential $\widetilde{u}$ of the nonlinear porous single crystal can be written as

$$\widetilde{u}^{IVH}(\overline{\boldsymbol{\sigma}}) = (1 - f^{\frac{1}{N}}) \sum_{i=1}^{N} f^{\frac{N-i}{N}} \left(\sum_{k=1}^{K} \phi_{(k)}(\hat{\tau}^{[i]}_{(k)}) \right). \tag{2.11}$$

In expression (2.11), the $\hat{\tau}^{[i]}_{(k)}$ are the second moment variables defined by

$$\hat{\tau}^{[i]}_{(k)} = \sqrt{\boldsymbol{\mu}_{(k)} \cdot \langle \boldsymbol{\sigma} \otimes \boldsymbol{\sigma} \rangle^{(1)}_{[i]} \boldsymbol{\mu}_{(k)}}, \quad i = 1, ..., N, \quad k = 1, ..., K, \tag{2.12}$$

where the $\langle \boldsymbol{\sigma} \otimes \boldsymbol{\sigma} \rangle^{(1)}_{[i]}$ $(i = 1, ..., N)$ denote the second moments of the stress fields in the matrix of the LCC at level i, which can be computed by means of (2.22) in the Appendix. In addition, the slip compliances $\alpha^{[i]}_{(k)}$, as determined by the application of VH method in terms of the LCC at each level, are given by the closure conditions

$$\alpha^{[i]}_{(k)} = \frac{\phi'_{(k)}(\hat{\tau}^{[i]}_{(k)})}{\hat{\tau}^{[i]}_{(k)}}, \quad i = 1, ..., N, \quad k = 1, ..., K. \tag{2.13}$$

In fact, $\widetilde{u}^{IVH}$ is known to be a lower bound for the effective potential of the porous single crystals, the accuracy of which improves progressively with increasing N. However, the fast convergence of IVH with increasing values of N (Agoras and Ponte Castañeda, 2013) allows the use of relatively small numbers of iterations N to get accurate results, and thus, $N = 10$ is used in this work, which can be shown to

give sufficiently accurate predictions for porous single crystals.

The macroscopic constitutive behavior, as well as the average strain rate in the voids of the nonlinear porous single crystal can then be obtained directly from those of the LCC (Idiart and Ponte Castañeda, 2007c; Agoras and Ponte Castañeda, 2013). In particular, the IVH estimates for the macroscopic strain rate $\overline{\mathbf{D}}$ of the nonlinear porous single crystal under the applied loading $\overline{\boldsymbol{\sigma}}$ is given by

$$\overline{\mathbf{D}} = \frac{\partial \widetilde{u}^{IVH}}{\partial \overline{\boldsymbol{\sigma}}}(\overline{\boldsymbol{\sigma}}) = \widetilde{\mathbb{M}}\overline{\boldsymbol{\sigma}}, \tag{2.14}$$

where $\widetilde{\mathbb{M}} \equiv \widetilde{\mathbb{M}}_{[N]}$ is the PCW estimate for the effective viscous compliance tensor of the N-level LCC, as given by (2.19). Moreover, the corresponding IVH estimate for the average strain rate in the voids $\overline{\mathbf{D}}^{(2)}$ is determined by

$$\overline{\mathbf{D}}^{(2)} = \mathbb{A}^{(2)}\overline{\mathbf{D}}, \tag{2.15}$$

with $\mathbb{A}^{(2)}$ denoting the PCW strain-rate concentration tensor, which is given by (2.23) together with (2.24) in the Appendix.

Given the normalized macroscopic strain rate $\overline{\mathbf{E}}$, as defined by (2.9), we define correspondingly the normalized average strain rate in the voids by $\overline{\mathbf{E}}^{(2)} = \mathbb{A}^{(2)}\overline{\mathbf{E}}$. Furthermore, by using appropriate evolution laws for the porosity f and the aspect ratios of the voids w_α ($\alpha = 1, 2$) (Gurson, 1977; Ponte Castañeda and Zaidman, 1994), we define the normalized porosity growth rate $\dot{f}$ and the normalized rate of change of the void aspect ratios $\dot{w}_\alpha$ ($\alpha = 1, 2$), which are respectively of the form

$$\dot{f} = (1-f)\overline{E}_{kk}, \qquad \dot{w}_\alpha = w_\alpha\left(\mathbf{n}_3 \otimes \mathbf{n}_3 - \mathbf{n}_\alpha \otimes \mathbf{n}_\alpha\right) \cdot \overline{\mathbf{E}}^{(2)}, \quad \alpha = 1, 2. \tag{2.16}$$

2.3 Application to porous HCP single crystals

In this section, we investigate the predictions of the IVH estimates for the instantaneous macroscopic response of porous HCP single crystals, focusing on the effect of the crystal anisotropy, the porosity and the void shape, with particular emphasis

on porous ice crystals. In addition, consistent IVH estimates for the average strain rate in the voids are computed to explore the implications for the evolution of the microstructure.

Ice single crystals belong to the class of low-symmetry, HCP crystals, with a c/a ratio of 1.629, and a creep exponent n of 3. The relevant slip systems are the three basal slips ($\{0001\}\langle 11\bar{2}0\rangle$), the three prismatic slips ($\{10\bar{1}0\}\langle 11\bar{2}0\rangle$) and the six second-order ($\{11\bar{2}2\}\langle 11\bar{2}3\rangle$) pyramidal-$\langle c+a\rangle$ slips, which will be denoted by labels A, B and C, respectively. In addition, the basal slips are taken to be the "soft" slip systems, with reference flow stress τ_A, while the prismatic and pyramidal slips are taken to be the "hard" slip systems, with the same reference flow stresses $\tau_B = \tau_C = M\tau_A$. For ice, $M = 60$ (Duval et al., 1983), but in this work we will consider values of M such that $1 \leq M \leq 60$ to investigate the effect of the anisotropy of HCP single crystals more generally.

First, we examine the effect of various parameters on the gauge surfaces of porous HCP crystals for loading conditions of the type

$$\overline{\boldsymbol{\Sigma}} = \overline{\Sigma}_m \mathbf{I} + \overline{\Sigma}_a \left(-\frac{1}{3}\mathbf{e}_1 \otimes \mathbf{e}_1 - \frac{1}{3}\mathbf{e}_2 \otimes \mathbf{e}_2 + \frac{2}{3}\mathbf{e}_3 \otimes \mathbf{e}_3 \right), \tag{2.17}$$

combining the hydrostatic stress $\overline{\Sigma}_m$ and the axisymmetric shear stress $\overline{\Sigma}_a = \overline{\Sigma}_{33} - \overline{\Sigma}_{11} = \overline{\Sigma}_{33} - \overline{\Sigma}_{22} = \pm\overline{\Sigma}_e$, where $\overline{\Sigma}_e$ is the macroscopic equivalent stress. For simplicity, it is further assumed that the symmetry axis $\mathbf{e}_3$ of the macroscopic loading (2.17) is aligned with the $\langle c\rangle$-axis of the ice single crystal. At this stage, recall that the gauge surface is defined by (2.6), and τ_0 is chosen to be τ_A for all results shown below. In addition, note that the lower bound $\widetilde{u}^{IVH}$ on the effective stress potential translates into an outer bound on the gauge surface.

Figure 2.2(a) shows gauge surfaces for porous HCP crystals, as predicted by the IVH and Taylor method. In particular, Fig. 2.2(a) depicts the $\overline{\boldsymbol{\Sigma}}_m - \overline{\boldsymbol{\Sigma}}_a$ cross sections of gauge surfaces for porous crystals with porosity $f = 1\%$, void aspect ratios $w_1 = w_2 = 1$ and contrast parameter $M = 1$. Corresponding IVH results are also shown for a viscoplastic porous isotropic material with isotropic matrix characterized by the

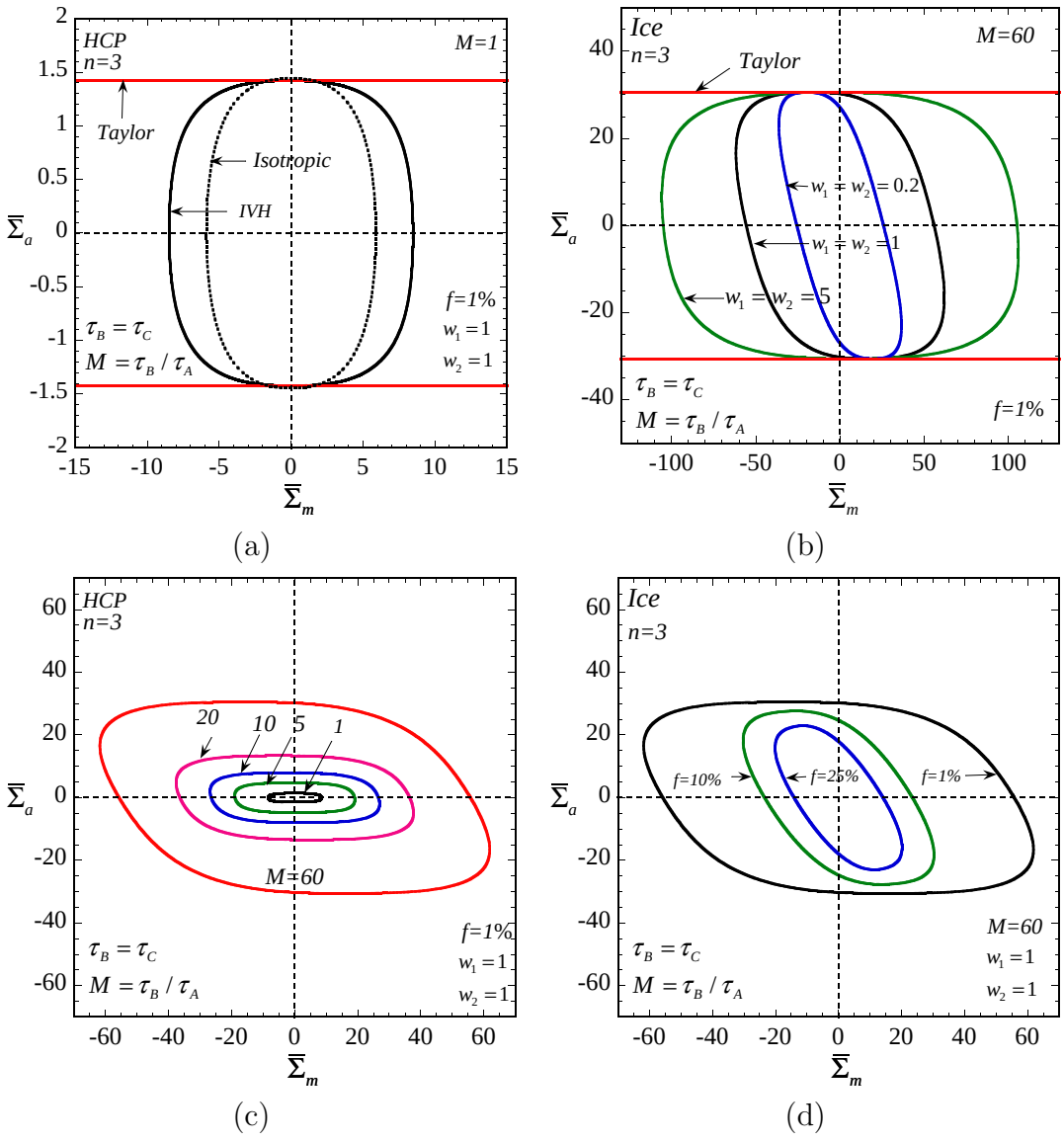

Figure 2.2: IVH results for the $\overline{\boldsymbol{\Sigma}}_a - \overline{\boldsymbol{\Sigma}}_m$ cross sections of the gauge surfaces for porous HCP single crystals subjected to axisymmetric loadings (2.17). (a) Comparisons of the IVH and Taylor gauge surfaces for the porous HCP crystal with porosity $f = 1\%$, void aspect ratios $w_1 = w_2 = 1$ and contrast parameter $M = 1$. Plots are also shown for the effect of the (b) void shape, as defined by the aspect ratios w_1 and w_2, (c) crystal anisotropy, as defined by the contrast parameter M, and (d) porosity f on the gauge surfaces for porous HCP crystals.

power-law stress potential

$$u^{\text{iso}}(\boldsymbol{\sigma}) = \frac{\dot{\gamma}_0 \sigma_0}{n+1} \left(\frac{\sigma_e}{\sigma_0} \right)^{n+1}, \tag{2.18}$$

where $\sigma_0 = 1.657\tau_A$ denotes the reference flow stress, $n = 3$ is the creep exponent, and σ_e is the equivalent stress. Note that σ_0 is chosen such that in the linear case ($n = 1$), the constitutive relation (2.2), together with (2.4), for the isotropic HCP single crystal reduces to the isotropic power-law relation (2.18). We observe from Fig. 2.2(a) that the effective behavior of the porous crystal with $M = 1$ is similar to that of the porous isotropic material: the porous isotropic material exhibits a somewhat softer response at high stress triaxiality $X_\Sigma = \overline{\boldsymbol{\Sigma}}_m / \overline{\boldsymbol{\Sigma}}_e$ and a slightly stiffer response at low stress triaxiality. The Taylor estimate assumes a uniform strain rate in the phases, leading to two straight lines parallel to the horizontal hydrostatic axis, and providing an outer bound for the gauge surface of porous HCP crystals. The corresponding IVH gauge surface lies within the Taylor gauge surface for all ranges of stress state, leading to a tighter outer bound that is finite for all stress states. It should be mentioned that similar results for the gauge surface of the porous crystal with $M = 1$ can be obtained by means of the MVAR method developed by Mbiakop et al. (2015b). However, we should emphasize that the MVAR method was designed for crystals with values of $M \sim 1$ and becomes progressively less accurate with increasing crystal anisotropy (values of M), while the IVH method has the advantage of providing estimates that are valid and should remain accurate for arbitrary crystal anisotropy.

Figure 2.2(b) shows the effect of the void shape on the IVH gauge surfaces for porous ice ($M = 60$) with fixed porosity $f = 1\%$. In particular, three different void shapes are considered: a spherical void shape with aspect ratios $w_1 = w_2 = 1$, a prolate void shape with $w_1 = w_2 = 5$, and an oblate void shape with $w_1 = w_2 = 0.2$. Note that the symmetry axes of the spheroidal voids are assumed to be aligned with the direction of the unit vector $\mathbf{e}_3$ and, hence, also aligned with the direction of the $\langle c \rangle$-axis of the ice single crystal. First, it is observed that the gauge surface of porous ice with $w_1 = w_2 = 1$ and $M = 60$ becomes much larger and tilted with respect to the

vertical deviatoric axis, when compared with the corresponding result for $M = 1$ in Fig. 2.2(a). In addition, we observe from Fig. 2.2(b) that changing the void shape changes both the size and shape of the gauge surface, suggesting that changes in void shape should have strong *anisotropic* hardening or softening effects. Furthermore, we found that the effect of the void shape exhibits a strong dependence on the crystal anisotropy. For instance, when subjected to purely hydrostatic loadings, porous ice ($M = 60$) with prolate voids ($w_1 = w_2 = 5$) is stiffer than that with spherical voids ($w_1 = w_2 = 1$), while it is the other way around for $M = 1$ (the corresponding results are not shown due to limitations of space). As expected, the IVH results corresponding to three different void shapes all lie within the Taylor outer bound (two straight lines parallel to the horizontal hydrostatic axis), which is independent of the void shape.

Figure 2.2(c) displays the effect of the crystal anisotropy on the IVH gauge surfaces for porous HCP crystals with porosity $f = 1\%$, void aspect ratios $w_1 = w_2 = 1$ and different values of the contrast parameter ($M = 1, 5, 10, 20, 60$). The main observation from Fig. 2.2(c) is that increasing M leads to the expansion of the gauge surface and, hence, to stronger behavior for the porous crystals, as expected. However, the gauge surface changes its shape and rotates counterclockwise as M increases, implying a strong distortional hardening effect with increasing values of M. The above observation has important implications on the plastic anisotropy of the porous single crystal. For instance, when the porous crystal is subjected to purely hydrostatic loading, the direction of the induced plastic flow, as determined by the normal to the gauge surface, changes significantly with increasing values of M. It should also be mentioned that when $M \to \infty$, the corresponding gauge surface tends to infinity, suggesting that non-basal slip is required for the overall plastic response of porous HCP crystals, under loading condition (2.17).

Figure 2.2(d) shows the effect of the porosity on the gauge surfaces for porous ice ($M = 60$) with void aspect ratios $w_1 = w_2 = 1$, where three values of porosity ($f = 1\%, 10\%$ and 25%) are considered. As expected, increasing f leads to the contraction of the gauge surface for all loading directions and, thus, to softer behavior. However, the reduction of the gauge surface with increasing values of f is more significant at

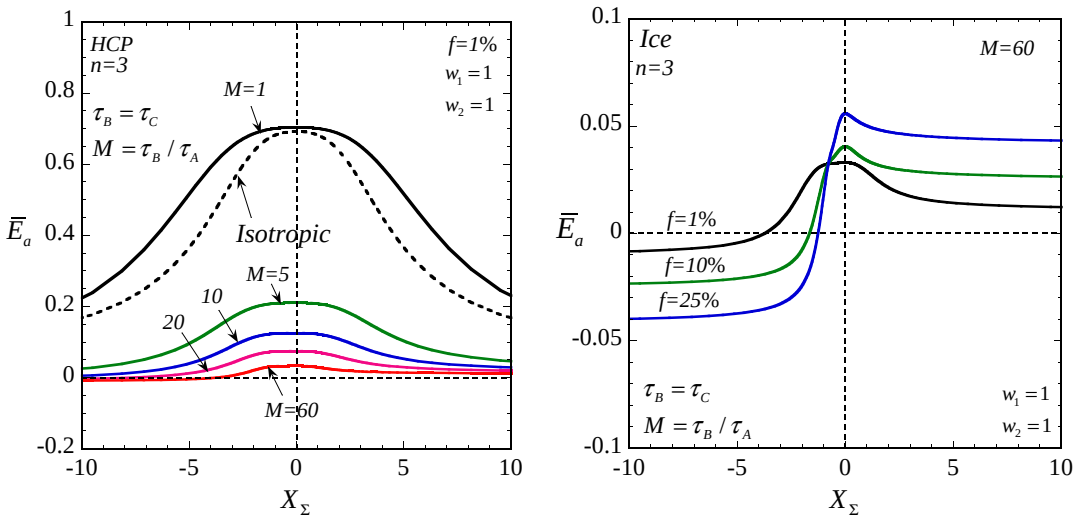

Figure 2.3: IVH results for the normalized macroscopic strain rate $\overline{E}_a$ (defined by (2.9)), as functions of the stress triaxiality X_Σ, for porous HCP crystals subjected to axisymmetric loadings (2.17). Plots are shown for different values of the (a) contrast parameter M and (b) porosity f.

high stress triaxialities, inducing a dramatic change in the shape of the gauge surface. In particular, for high porosity (e.g., $f = 25\%$), the shape of the gauge surface is nearly elliptical, whereas for low porosity (e.g., $f = 1\%$), the gauge surface tends to become flat near the vertical deviatoric axis and develops a markedly non-elliptical shape.

For completeness, results for the normalized macroscopic strain rate $\overline{E}_a = \frac{2}{3}(\overline{E}_{33} - \overline{E}_{11}) = \frac{2}{3}(\overline{E}_{33} - \overline{E}_{22}) = \pm\overline{E}_e$, as determined by expression (2.9), are presented in Figs. 2.3(a) and 2.3(b), corresponding to the cases considered in Figs. 2.2(c) and 2.2(d), respectively. In particular, Fig. 2.3(a) depicts plots of $\overline{E}_a$ as a function of the stress triaxiality X_Σ and the contrast parameter M, for porous crystals with porosity $f = 1\%$ and aspect ratios $w_1 = w_2 = 1$. For comparison purposes, the corresponding result for a porous isotropic material is also presented in Fig. 2.3(a). In this context, it should be mentioned that, for all values of X_Σ considered in the following, $\overline{\Sigma}_a \geq 0$ is assumed, so that $X_\Sigma = \overline{\Sigma}_m/\overline{\Sigma}_e = \overline{\Sigma}_m/\overline{\Sigma}_a$. The corresponding results for $\overline{\Sigma}_a < 0$ can be easily obtained by symmetry considerations. It can be seen that the IVH estimate of $\overline{E}_a$ for $M = 1$ is similar to that for the porous isotropic material, in agreement with

the similarity of the corresponding gauge surfaces observed in Fig. 2.2(a). On the other hand, $\overline{E}_a$ decreases with increasing values of M, indicating a strong effect of increasing crystal anisotropy, as already observed in Fig. 2.2(c). In addition, $\overline{E}_a$ reaches its maximum value at $X_\Sigma = 0$ for all values of M, implying that the porous HCP crystal with $M = 1$ undergoes the largest amount of shear deformation under purely deviatoric loadings, as expected on physical grounds. On the other hand, Fig. 2.3(b) shows plots of $\overline{E}_a$ as a function of the stress triaxiality X_Σ and the porosity f, for porous ice ($M = 60$) with void aspect ratios $w_1 = w_2 = 1$, where various porosities ($f = 1\%, 10\%$ and 25%) are considered. Similar to the findings in Fig. 2.3(a), E_a reaches its maximum value under purely deviatoric loadings, independent of the porosity f. However, as f increases, the curve for E_a becomes progressively more asymmetric with respect to the vertical deviatoric axis $X_\Sigma = 0$, consistent with the developing asymmetry of the corresponding gauge surfaces with respect to the vertical axis $\overline{\Sigma}_m = 0$ ($X_\Sigma = 0$) in Fig. 2.2(d), and indicating a strong anisotropic effect induced by the porosity change.

Next, we present results for the porosity growth rate $\dot{f}$ and the rate of change of the void shape $\dot{w}$, as defined by the normalization (2.16), and explore their implications for the evolution of the microstructure. For simplicity, we will only consider the case of initially spheroidal voids ($w_1 = w_2$) here, and the symmetry axes of the voids are assumed to be aligned with those of the applied loading (2.17), leaving the cases of more general orientations for future consideration. Due to the symmetry of the problem considered, $\dot{w}_1 = \dot{w}_2 = \dot{w}$, indicating that the initially spheroidal voids will remain spheroidal in shape under loading condition (2.17), but will, in general, change their size and aspect ratios. It should be mentioned that the normalized results shown for $\dot{f}$ and $\dot{w}$ depend only on the direction of the applied stress $\overline{\boldsymbol{\sigma}}$, so that multiplication of $\overline{\boldsymbol{\sigma}}$ by a scalar will not change the results. In addition, larger values of $\dot{f}$ imply a faster growth of the porosity and, in particular, $\dot{f} > 0$ indicates that the porosity increases and $\dot{f} < 0$ indicates that the porosity decreases. On the other hand, larger magnitudes of $\dot{w}$ indicate more significant void distortion rates and, in particular, $\dot{w} > 0$ means that the voids are becoming more prolate, while $\dot{w} < 0$ means that the

voids are becoming more oblate.

Figures 2.4(a) and 2.4(b) show respectively the effect of the crystal anisotropy on $\dot{f}$ and $\dot{w}$ for porous HCP crystals with porosity $f = 1\%$, void aspect ratios $w_1 = w_2 = 1$ and different values of the contrast parameter ($M = 1, 5, 10, 20, 60$). For comparison purposes, corresponding results for porous isotropic materials are also incorporated in the figures. It can be seen from Fig. 2.4(a) that, for all cases considered, the porosity grows faster at high stress triaxiality, as expected. The $\dot{f}$ curve for the porous HCP crystal with $M = 1$ is similar to that for the porous isotropic material, consistent with the previous observations from Figs. 2.2(a) and 2.3(a). However, as M increases, $\dot{f}$ tends to increase at small values of stress triaxiality, and to decrease at large (positive and negative) values of stress triaxiality, indicating that increasing crystal anisotropy facilitates the void growth at low stress triaxiality, while it suppresses it at high stress triaxiality. On the other hand, we observe from Fig. 2.4(b) that while $\dot{w}$ is symmetric with respect to the vertical axis ($X_\Sigma = 0$) for the porous isotropic material, the corresponding curves for the porous HCP crystals become progressively more asymmetric with increasing values of M, due to the correspondingly increasing crystal anisotropy. In particular, for the porous isotropic material $\dot{w}$ tends to zero as $X_\Sigma \to \infty$, suggesting that the void distortion rate becomes insignificant at high stress triaxiality, whereas the magnitude of $\dot{w}$ for porous ice ($M = 60$) can be quite large, indicating significant void distortion rates, even at high stress triaxiality.

Figures 2.4(c) and 2.4(d) demonstrate the effect of the initial porosity f on $\dot{f}$ and $\dot{w}$, respectively, for porous ice ($M = 60$) with void aspect ratios $w_1 = w_2 = 1$. Three values of the initial porosity ($f = 1\%, 10\%$ and 25%) are considered in each figure. We observe from Fig. 2.4(c) that for a given fixed value of X_Σ, the dependence of $\dot{f}$ on the initial porosity f is qualitatively the same for porous ice as for the porous isotropic materials (which is not shown here, for brevity). However, due to the strong anisotropy of the ice single crystal, the corresponding results for $\dot{f}$ lose their symmetry with respect to the origin. In particular, the porosity growth for porous ice can be quite significant even at low stress triaxiality. In fact, the value of $\dot{f}$ at $X_\Sigma = 0$ is comparable to that at high stress triaxiality. This behavior of porous

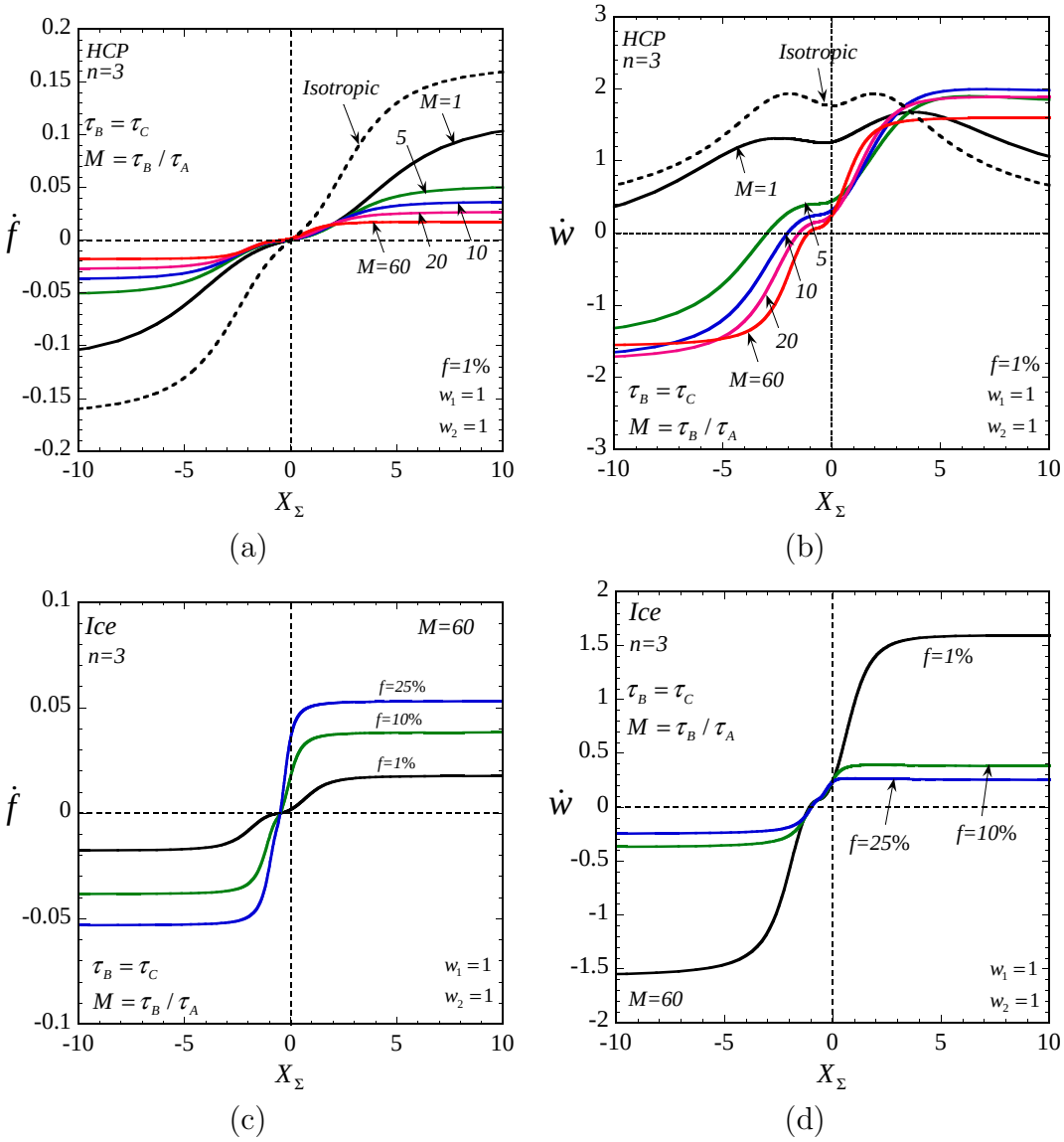

Figure 2.4: IVH results for the normalized growth rates of the porosity $\dot{f}$ and the aspect ratios $\dot{w}$ (as defined by (2.16)), as functions of X_Σ, for porous HCP single crystals subjected to axisymmetric loadings (2.17). Plots are shown for (a) $\dot{f}$ and (b) $\dot{w}$ for different values of the contrast parameter M, as well as for (c) $\dot{f}$ and (d) $\dot{w}$ for different values of the initial porosity f.

ice is significantly different from that of the porous isotropic material, since the void growth rate for the latter case is always zero at $X_\Sigma = 0$. On the other hand, Fig. 2.4(d) shows that, for all values of f, the void distortion rates, as described by $\dot{w}$, are more significant at high stress triaxiality than at low stress triaxiality. In particular, note that the value of $\dot{w}$ at $X_\Sigma = 10$ is several times greater than that at $X_\Sigma = 0$ for $f = 1\%$. This is unlike the case of porous isotropic materials, where $\dot{w}$ tends to become relatively small at high stress triaxiality. Furthermore, we observe that the effect of the initial porosity f on $\dot{w}$ is significant at high stress triaxiality, where it is observed that the void distortion is much faster for lower initial porosity, while the effect of f on $\dot{w}$ is negligible at low stress triaxiality.

Finally, Figs. 2.5(a) and 2.5(b) show respectively the effect of the initial void shape on $\dot{f}$ and $\dot{w}$, for porous ice ($M = 60$) with initial porosity $f = 1\%$. For comparison purposes, corresponding results for porous isotropic materials are also shown in Fig. 2.5(c) and Fig. 2.5(d), respectively. First, we observe from Fig. 2.5(c) that the results for $\dot{f}$ for porous isotropic materials with non-spherical voids are asymmetric with respect to the origin, due to the "morphological" anisotropy induced by the void shape. In addition, the $\dot{f}$ curve for porous isotropic materials with prolate voids ($w_1 = w_2 = 5$) approximately lies between that with oblate voids ($w_1 = w_2 = 0.2$) and spherical voids ($w_1 = w_2 = 1$). However, this is not the case for porous ice, where the order of the corresponding results for $w_1 = w_2 = 5$ and $w_1 = w_2 = 1$ are interchanged (see Fig. 2.5(a)). The above facts strongly suggest that the effect of the void shape on the porosity growth depends crucially on the crystal anisotropy, indicating a strong coupling between the "morphological" anisotropy and the crystal anisotropy. Similarly, it can be seen from Fig. 2.5(d) that the $\dot{w}$ curves for porous isotropic materials with non-spherical voids are asymmetric with respect to $X_\Sigma = 0$ due to the above-mentioned "morphological" anisotropy. In particular, for porous isotropic materials with $w_1 = w_2 = 5$, $\dot{w}$ decreases monotonically with increasing values of X_Σ, becoming negative for $X_\Sigma > 1.25$, while the opposite is true for $w_1 = w_2 = 0.2$. However, Fig. 2.5(b) shows that all of the three $\dot{w}$ curves for porous ice with different void shapes exhibit qualitatively similar behaviors, indicating that the

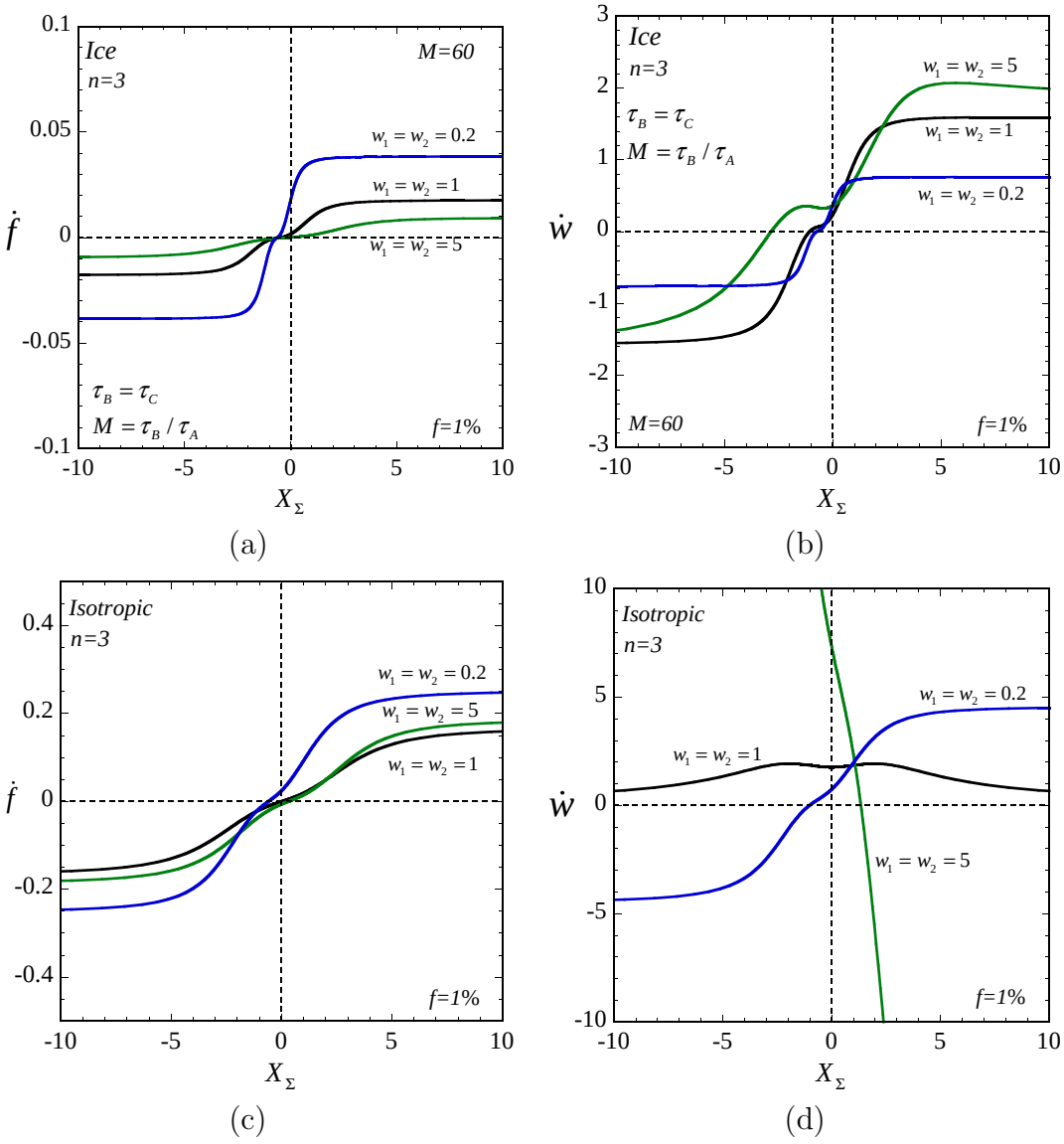

Figure 2.5: IVH results for the normalized growth rates of the porosity $\dot{f}$ and the aspect ratios $\dot{w}$ (as defined by (2.16)), as functions of X_Σ, for porous HCP single crystals subjected to axisymmetric loadings (2.17). Plots are shown for (a) $\dot{f}$ and (b) $\dot{w}$ for different initial void shapes. For comparison purposes, corresponding results are also shown for the porous isotropic materials for (c) $\dot{f}$ and (d) $\dot{w}$ for different initial void shapes.

extreme anisotropy induced by the crystal matrix prevails over the "morphological" anisotropy induced by the void shape, so that the dependence of $\dot{w}$ on the stress triaxiality X_Σ for ice is qualitatively unaffected by the void shape.

2.4 Concluding remarks

In this chapter, a generalization of a recently developed iterated variational homogenization (IVH) method (Agoras and Ponte Castañeda, 2013) has been developed to generate bounds for the effective flow potential of porous viscoplastic single crystals. The method was then implemented for low-symmetry, high-anisotropy porous HCP single crystals, such as porous ice, to investigate the macroscopic response of these materials under axisymmetric loadings. In general, it was found that the overall size, shape and orientation of the macroscopic gauge surfaces depends sensitively on the instantaneous values of the porosity, void shape and crystal anisotropy, suggesting strong distortional hardening/softening effects in the macroscopic response of these materials under finite-strain loading conditions (leading to evolution of the microstructure). In particular, it was observed that strong crystal anisotropy could significantly affect the dependence of the gauge surfaces on the porosity and void-shape parameters. For example, it was found that while changing the void shape from spherical to prolate has a softening effect on the effective behavior for porous crystals with low anisotropy ($M = 1$)—in agreement with earlier results (Agoras and Ponte Castañeda, 2013; Mbiakop et al., 2015b)—the opposite is true for porous crystals with high anisotropy, such as ice ($M = 60$), with prolate voids leading to a stronger response than spherical voids. In addition, consistent IVH estimates for the average strain rate in the voids were computed to explore their implications for the evolution of the microstructure. Thus, it was found that strong crystal anisotropy may lead to fast porosity growth at low stress triaxiality and to significant void distortion rates at high stress triaxiality, which is in contrast to the corresponding results for porous isotropic materials. Furthermore, it was found that the dependence of the porosity growth and void distortion on the initial void shape is also strongly affected

by the crystal anisotropy. In fact, the crystal anisotropy largely dominates over the effect of the void shape, leading to significantly different behaviors for porous ice and porous isotropic materials. The fact that the IVH model predicts a complex coupled effect of the "morphological" anisotropy and crystal anisotropy provides strong encouragement for its further development into the finite-strain regime, thus accounting for evolving microstructures by incorporating the effects of the lattice rotation, void growth as well as the matrix hardening, building on the earlier models of Agoras and Ponte Castañeda (2014) and Song et al. (2015) for porous isotropic materials. These developments will be considered in future publications. Finally, it is noted that the IVH method can also be used for high-symmetry crystals. Indeed, preliminary results for porous FCC crystals indicate fairly good agreement with FEM results based on unit cell calculations (Srivastava and Needleman, 2015). These results will be shown in the following chapters.

2.5 Appendix: Expressions for the IVH method

In this Appendix, detailed expressions for the IVH method are provided, which are generalizations of the corresponding expressions in the work of Agoras and Ponte Castañeda Agoras and Ponte Castañeda (2013). In this context, it is important to mention that these expressions are obtained by means of the PCW estimates of Ponte Castañeda and Willis Ponte Castañeda and Willis (1995) for the LCC at each iteration step. In addition, it is assumed for simplicity that the shape and orientation of the voids are identical to those of their distribution. However, more general cases with different shapes and orientations of the voids and their distribution can be accounted for, as was done, for example, by Agoras and Ponte Castañeda Agoras and Ponte Castañeda (2013).

We begin by recalling that the viscous compliance tensor $\mathbb{M}^{(1)}_{[i]}$ of the matrix of the i-level LCC is given by (2.10), while the effective compliance tensor $\widetilde{\mathbb{M}}_{[i]}$ of the

i-level LCC is given by

$$\widetilde{\mathbb{M}}_{[i]} = \mathbb{M}^{(1)}_{[i]} + c^{(2)}_{[i]} \left[\left(\widetilde{\mathbb{M}}_{[i-1]} - \mathbb{M}^{(1)}_{[i]} \right)^{-1} + (1 - c^{(2)}_{[i]}) \mathbb{Q}_{[i]} \right]^{-1}, \qquad i = 1, ..., N, \tag{2.19}$$

where the $c^{(2)}_{[i]}$ $(i = 1, ..., N)$ are the incremental volume fractions required to satisfy the condition $f = \prod_{i=1}^{N} c^{(2)}_{[i]}$, which will be simply chosen as $c^{(2)}_{[i]} = f^{1/N}$ $(i = 1, .., N)$, and the $\mathbb{Q}_{[i]}$ $(i = 1, ..., N)$ are fourth-order microstructural tensors, depending on the matrix property $\mathbb{M}^{(1)}_{[i]}$ and the shape and orientation of the voids (see Nebozhyn et al. (2001) for their corresponding expressions). It should be mentioned that $\widetilde{\mathbb{M}}_{[0]} \to \infty$ in (2.19), representing the compliance tensor of the vacuous inclusion in the first level LCC.

Following the work of Agoras and Ponte Castañeda Agoras and Ponte Castañeda (2013), the macroscopic stress $\overline{\boldsymbol{\sigma}}_{[i]}$ of the i-level LCC can be written in the form

$$\overline{\boldsymbol{\sigma}}_{[i]} = \left[\prod_{j=i+1}^{N} \mathbb{B}^{(2)}_{[j]} \right] \overline{\boldsymbol{\sigma}}, \quad i = 1, ..., N-1, \quad \text{and} \quad \overline{\boldsymbol{\sigma}}_{[\mathrm{N}]} = \overline{\boldsymbol{\sigma}}, \tag{2.20}$$

where the corresponding stress concentration tensors are provided by

$$\mathbb{B}^{(2)}_{[i]} = \left[\mathbb{I} + (1 - c^{(2)}_{[i]}) \mathbb{Q}_{[i]} \left(\widetilde{\mathbb{M}}_{[i-1]} - \mathbb{M}^{(1)}_{[i]} \right) \right]^{-1}, \quad i = 2, ..., N, \tag{2.21}$$

with $\mathbb{I}$ denoting the fully symmetric fourth-order identity tensor. Given expressions (2.19), (2.20) and (2.21), the second moment of the stress field in the matrix of the i-level LCC can be computed via

$$\langle \boldsymbol{\sigma} \otimes \boldsymbol{\sigma} \rangle^{(1)}_{[i]} = \frac{1}{1 - c^{(2)}_{[i]}} \overline{\boldsymbol{\sigma}}_{[i]} \cdot \frac{\partial \widetilde{\mathbb{M}}_{[i]}}{\partial \mathbb{M}^{(1)}_{[i]}} \overline{\boldsymbol{\sigma}}_{[i]}, \quad i = 1, ..., N. \tag{2.22}$$

On the other hand, the iterated PCW estimates for the average strain-rate field in the voids can also be obtained, following the work of Agoras and Ponte Castañeda Agoras and Ponte Castañeda (2013), and is given by $\overline{\mathbf{D}}^{(2)} = \mathbb{A}^{(2)} \overline{\mathbf{D}}$, where $\mathbb{A}^{(2)}$ is the

associated strain-rate concentration tensor, determined by

$$\mathbb{A}^{(2)} = \prod_{i=1}^{N} \mathbb{A}_{[i]}^{(2)}, \tag{2.23}$$

with

$$\mathbb{A}_{[i]}^{(2)} = \left[c_{[i]}^{(2)} \mathbb{I} + \left(1 - c_{[i]}^{(2)}\right) \left[\left(\mathbb{M}_{[i]}^{(1)} - \mathbb{M}_{[i]}^{(1)} \mathbb{Q}_{[i]} \mathbb{M}_{[i]}^{(1)} \right) \left(\widetilde{\mathbb{M}}_{[i-1]} \right)^{-1} + \mathbb{M}_{[i]}^{(1)} \mathbb{Q}_{[i]} \right] \right]^{-1},$$
$$i = 1, ..., N. \tag{2.24}$$

Chapter 3

Iterated second-order homogenization model for viscoplastic porous single crystals: Theory

This chapter presents a homogenization-based constitutive model for the finite-strain, macroscopic response of porous viscoplastic single crystals. The model accounts explicitly for the evolution of the average lattice orientation, as well as the porosity, average shape and orientation of the voids (and their distribution), by means of appropriate microstructural variables playing the role of internal variables and serving to characterize the evolution of both the "crystallographic" and "morphological" anisotropy of the porous single crystals. The model makes use of the fully optimized second-order variational method of Ponte Castañeda (2015), together with the iterated homogenization approach of Agoras and Ponte Castañeda (2013), to characterize the instantaneous effective response of the porous single crystals with fixed values of the microstructural variables. Consistent homogenization estimates for the average strain rate and vorticity fields in the phases are then used to derive evolution equations for the associated microstructural variables. The model is 100% predictive,

requiring no fitting parameters, and applies for porous viscoplastic single crystals with general crystal anisotropy and average void shape and orientation, which are subjected to general loading conditions. In the next chapter, results for both the instantaneous response and the evolution of the microstructure will be presented for porous FCC and HCP single crystals under a wide range of loading conditions, and good agreement with available FEM results will be shown.

3.1 Introduction

The presence of microscopic voids and cracks has important effects on the constitutive response of ductile solids. In particular, voids can give rise to significant dilatational macroscopic strains under hydrostatic loading conditions in nominally incompressible plastic or viscoplastic materials. Moreover, failure in ductile solids is known to take place by the nucleation, growth and coalescence of voids. For these reasons, the investigation of the effect of porosity and its evolution on the constitutive response of ductile solids has been a problem of central importance in solid mechanics for many years (see Tvergaard, 1990). While most of the work has made the simplifying assumption of isotropy for the solid material (e.g., Gurson, 1977), it should be recalled that metals and many other materials consist of aggregates of single-crystal grains, and that the voids are often at scales that are small compared to the size of the grains, in such a way that the microstructures could be idealized as aggregates of porous single-crystal grains. In addition, there are engineering applications where the effect of void growth in single crystals is important, including lifetime prediction of Ni-based single-crystal superalloys for jet engine turbine applications (Srivastava et al., 2012). For these reasons, there have already been several efforts to investigate porous single crystals via numerical simulations (e.g., O'regan et al., 1997; Schacht et al., 2003; Yerra et al., 2010; Han et al., 2013; Srivastava and Needleman, 2012; 2013; 2015). These studies have shown that crystallographic anisotropy can have a significant effect on the growth and coalescence of the voids, as well as on the macroscopic response of porous single crystals.

Motivated by these works, our objective here is to develop constitutive models for porous single crystals. For this purpose, we will make use of recent advances in nonlinear homogenization. We begin with a brief review of especially relevant literature in the application of homogenization methods for porous solids with *isotropic* viscoplastic matrix phases. Bounds of the Hashin-Shtrikman type for porous isotropic viscoplastic materials were given by Ponte Castañeda (1991) by means of a variational homogenization (VH) method making use of a linear comparison composite (LCC). Equivalent bounds were derived by Willis (1991) by means of a nonlinear generalization of the Hashin-Shtrikman variational principles (Willis, 1983), and by Suquet (1992) for the special case of power-law media by means of Hölder's inequality. Making use of the VH method to obtain estimates for the macroscopic response, as well as for the average strain rate in the pores, Ponte Castañeda and Zaidman (1994) advanced a finite-strain constitutive model for porous (visco)plastic materials under general triaxial loadings, accounting for the evolution of the microstructure (porosity and void shape). The model was later generalized to include the effect of independent changes in the void distribution, as measured by the "shape" and "orientation" of the two-point correlation functions (Kailasam et al., 1997). The important effect of void rotations under general shear loadings (with non-vanishing macroscopic vorticity) was added in the works of Kailasam and Ponte Castañeda (1997; 1998). In addition, strain hardening and elasticity for the matrix was considered by Kailasam et al. (2000) and Aravas and Ponte Castañeda (2004).

While the VH bounds were found to improve on the Gurson estimate for purely deviatoric loadings, they were also found to be overly stiff for hydrostatic loadings, especially for low porosities and high nonlinearities. In order to remedy this shortcoming, Danas and Ponte Castañeda (2009a, 2009b) proposed an improved finite-strain constitutive model, utilizing the more sophisticated second-order (SO) linear comparison method (Ponte Castañeda, 2002), along with an *ad hoc* modification to bring the predictions of the model for hydrostatic loadings into agreement with exact results for spherical/cylindrical shells subjected to purely hydrostatic loadings (see also Danas and Aravas, 2012, for a similar ad hoc modification of the VH model). The

SO model has been found to yield fairly good estimates for the macroscopic response in several comparisons with numerical simulations and other exact results, and to account for a strong dependence on the Lode angle (Danas and Ponte Castañeda, 2012), but its implementation required certain fitting parameters and was therefore not fully predictive. More recently, Agoras and Ponte Castañeda (2014) proposed a general finite-strain constitutive model for porous materials under triaxial loadings, making exclusive use of the VH method of Ponte Castañeda (1991), albeit in a novel *iterated* fashion (Agoras and Ponte Castañeda, 2013). The iterated variational homogenization model has the advantage that it does *not* involve any ad hoc modification, providing estimates that, in particular, recover the exact results for spherical/cylindrical shells under purely hydrostatic loadings (as the number of iterations $N \to \infty$), while preserving the accuracy of the traditional VH model for low stress triaxialities. In practice, however, a relatively small number of iterations ($N \approx 5-10$) has been found to be sufficient to provide accurate results and, therefore, the new model is relatively easy to implement. The model was further generalized by Song et al. (2015) to account for void rotations under general shear loadings, including simple shear loading conditions. In agreement with earlier versions of the model (Kailasam et al., 1997) and unit-cell calculations (Tvergaard, 2015), the model was found to give different predictions for shear localization under simple shear and pure shear loading conditions, highlighting the importance of void rotations.

At this point, it should also be noted that the Gurson approach has also been used to account for void shape effects. This work has been thoroughly reviewed recently by Benzerga and Leblond (2010) and Benzerga et al. (2016), and for this reason we will not provide further details here, except to note that there are several important limitations in the Gurson approach compared with the homogenization approach. First, it should be recalled that it has not been possible to extract estimates for the average strain-rate and vorticity fields in the void phase using Gurson's approach—and for this reason it has been necessary to complement the limit analysis estimates for the yield surfaces of porous ideally plastic materials with evolution laws for the pore shape and orientation obtained from the above-mentioned homogenization methods

(appropriately modified by parameters fitted to numerical simulations of the shell problems). A second disadvantage is related to the use of a spherical shell (and generalizations thereof) as a proxy for a representative volume element (RVE). Indeed, full-field numerical simulations of appropriately defined RVEs show deformation patterns that have little in common with the radially symmetric deformation patterns implicitly assumed in spherical shell models. For example, both FFT (Bilger et al., 2005) and FEM (Fritzen et al., 2012) simulations of porous ideally plastic solids depict deformation patterns involving shear bands linking up voids, especially at small porosities, and even for hydrostatic loadings. While the predictions of the Gurson-type models for the macroscopic yield surfaces are still fairly accurate, the same is unlikely to be the case for corresponding predictions for the phases averages of the strain rate and vorticity in the pores.

Next, moving on to homogenization approaches for anisotropic materials, including heterogeneous materials with crystalline viscoplastic phases, we should mention the work of deBotton and Ponte Castañeda (1995), which provided an extension of the VH method of Ponte Castañeda (1991) by considering more general LCCs with anisotropic phases mimicking the symmetries of the crystalline viscoplastic phases. An alternative generalization of the VH method was given by Idiart and Ponte Castañeda (2007a) for more general types of anisotropies and shown to have the capability of producing tighter bounds than the method of deBotton and Ponte Castañeda (1995), when specialized to composites with crystalline phases. However, this second method is significantly harder to implement, and for this reason the first method has been generally preferred for composites with crystalline phases. In particular, Idiart and Ponte Castañeda (2007b) considered a model two-dimensional porous single crystal consisting of aligned cylindrical voids with circular cross-section subjected to anti-plane strain loadings. More recently, Han et al. (2013) made use of the VH method, together with an ad hoc modification inspired by the Gurson model, to obtain yield functions for porous FCC single crystals with spherical voids. In addition, Mbiakop et al. (2015b) proposed an alternative ad hoc modification (MVAR) of the VH approach of deBotton and Ponte Castañeda (1995) to obtain

effective flow potentials for porous single crystals containing general ellipsoidal voids and subjected to general loadings (see also Mbiakop et al. (2015a) for corresponding results for two-dimensional single crystals containing cylindrical voids with general elliptical cross-sections). The MVAR model made use of the assumption that all the slip systems have nearly identical flow stresses and enforced agreement with the exact result of a spherical/cylindrical shell for the special case of spherical/cylindrical voids with an infinite number of equi-angular slip systems subjected to purely hydrostatic loadings. The model of Han et al. (2013) was also further extended recently for finite strains by Ling et al. (2016), by accounting for the evolution of the porosity and strain hardening of the crystal matrix, although not for possible changes in void shape and orientation. A more general implementation of the VH method of deBotton and Ponte Castañeda (1995) for porous single crystals with large anisotropy was made by Song and Ponte Castañeda (2017a). To improve the accuracy of the predictions of the VH model for small porosities and hydrostatic loading conditions, Song and Ponte Castañeda (2017a) made use of the iterated approach of Agoras and Ponte Castañeda (2013) to "discretize" the matrix phase, thereby generating tighter bounds for the effective flow potential of porous single crystals, such as porous HCP crystals. (Strictly, the bounds apply for special classes of microstructures with hierarchical microstructures; however, these authors provided arguments suggesting that the bounds should hold under more general conditions.) Retaining the distinguishing advantages of the iterated approach for porous isotropic materials, the iterated variational homogenization (IVH) model is entirely predictive, requiring no ad hoc modifications, and is expected to remain accurate for porous single crystals with general crystallographic anisotropy and general ellipsoidal voids, subjected to general loadings.

For completeness, it should be mentioned that early results for the growth and collapse of isolated spherical voids in elasto-viscoplastic single crystals subjected to far-field, axisymmetric loadings were obtained by Hori and Nasser (1988) by means of the Eshelby method used in incremental fashion. The Gurson approach was also extended to incorporate the plastic anisotropy of matrix by Benzerga and Besson (2001), and was further generalized by Monchiet et al. (2006), Keralavarma and Ben-

zerga (2010) and others. These models typically assume that the plastic matrix obeys the phenomenological Hill-type orthotropic yield criterion and, in principle, cannot account for the crystallographic details, such as the orientation and constitutive properties of the active slip systems. Kysar et al. (2005) made use of anisotropic slip line theory to derive analytic solutions for the stress and deformation fields around cylindrical voids in FCC single crystals, and their results were in good agreement with the FEM and experimental results of Gan et al. (2006). However, these results are rigorously valid for dilute values of the porosity, where void-interaction effects are relatively small. In addition, Paux et al. (2015) made use of a regularized Schmid law and Gurson limit analysis to derive a Gurson-type yield criterion for porous single crystals.

Given this background, the objective of this work is to develop a *general finite-strain* constitutive model for porous viscoplastic single crystals, which not only provides the instantaneous response of the porous medium for a given state of the microstructure, but which can also account for the evolution of the "crystallographic" anisotropy induced by lattice rotation, as well as the corresponding evolution of the "morphological" anisotropy induced by changes in the porosity, and average shape and orientation of the voids. In this part of the work, we present the theoretical development of the proposed model. Specifically, we make use of the recently developed fully optimized second-order (FOSO) variational approach of Ponte Castañeda (2015), in combination with a generalization of the iterated variational homogenization procedure of Agoras and Ponte Castañeda (2013), to characterize the instantaneous macroscopic behavior of porous single crystals. In addition, consistent homogenization estimates for the average strain rate and spin fields in the phases are, in turn, used to develop self-consistent evolution equations for the lattice orientation, porosity, void shape and void orientation. In this context, it should be recalled that the FOSO estimates for the the average strain rate and spin fields in the phases of the viscoplastic porous single crystal may be obtained directly from the corresponding average fields in the phases of the LCC. However, we expect such estimates to be able to account—at least approximately—for strong interactions (leading to localization of

the deformation) between the voids in the ideally plastic limit (see Ponte Castañeda, 2016). In chapter 4, we consider applications of the model for porous FCC and HCP single crystals. We will also make use of the unit-cell FEM results of Srivastava and Needleman (2012, 2015) to assess the predictive capability of the proposed model.

3.2 Background and formulation

In this work, porous single crystals are idealized as two-phase materials with vacuous inclusions (phase 2) embedded in the single-crystal matrix (phase 1). The single-crystal matrix is assumed to have a crystal lattice defined by means of three *linearly independent* crystallographic axes $\mathbf{l}_1$, $\mathbf{l}_2$ and $\mathbf{l}_3$ (see Fig. 3.1). The lattice can be completely general, so that $\mathbf{l}_1$, $\mathbf{l}_2$ and $\mathbf{l}_3$ are not necessarily mutually orthogonal or have the same length. There are two main deformation mechanisms for the single-crystal matrix: (i) the elastic distortion of the atomic lattice and (ii) the plastic deformation through the motion of dislocations. In this work, however, we mainly focus on the response of porous single crystals under large plastic deformations and, for this reason, the elastic strains, which are typically very small (of the order 10^{-3}), will be neglected. However, lattice rotation will be accounted for. Thus, the crystal matrix is assumed to deform by dislocation glide along K well-defined crystallographic slip systems, and the local constitutive behavior of the single crystal is taken to be viscoplastic, and can be characterized by

$$\mathbf{D} = \frac{\partial u^{(1)}(\boldsymbol{\sigma})}{\partial \boldsymbol{\sigma}}, \quad u^{(1)}(\boldsymbol{\sigma}) = \sum_{k=1}^{K} \phi_{(k)}(\tau_{(k)}), \tag{3.1}$$

where $u^{(1)}$ denotes the stress potential for the crystal matrix, $\boldsymbol{\sigma}$ is the Cauchy stress and $\mathbf{D}$ is the Eulerian strain rate. The convex functions $\phi_{(k)}$ $(k = 1, ..., K)$ are the slip potentials characterizing the response of the K slip systems, and depend on the resolved shear (or Schmid) stresses

$$\tau_{(k)} = \boldsymbol{\sigma} \cdot \boldsymbol{\mu}_{(k)}, \quad \text{where} \quad \boldsymbol{\mu}_{(k)} = \frac{1}{2}\left(\mathbf{n}_{(k)} \otimes \mathbf{m}_{(k)} + \mathbf{m}_{(k)} \otimes \mathbf{n}_{(k)}\right). \tag{3.2}$$

Here the $\boldsymbol{\mu}_{(k)}$ are the second-order Schmid tensors obtained from the symmetrized dyadic product of $\mathbf{n}_{(k)}$ and $\mathbf{m}_{(k)}$, with $\mathbf{n}_{(k)}$ and $\mathbf{m}_{(k)}$ denoting the unit vectors normal to the slip plane and along the slip direction of the kth slip system, respectively. Although more general constitutive response could be considered for the crystal matrix, for simplicity, the slip potentials $\phi_{(k)}$ are assumed to be of the usual power-law form

$$\phi_{(k)}(\tau) = \frac{\dot{\gamma_0}(\tau_0)_{(k)}}{n+1}\left|\frac{\tau}{(\tau_0)_{(k)}}\right|^{n+1}, \quad k = 1, ..., K, \tag{3.3}$$

where $\dot{\gamma_0}$ denotes the reference strain rate, $(\tau_0)_{(k)} > 0$ is the reference flow stress of the kth slip system and n is the creep exponent (the inverse of the strain rate sensitivity $m = 1/n$). This class of slip potentials is known to be particularly appropriate for exploring the effect of nonlinearity and crystallographic anisotropy for a wide range of material behaviors. Note that the $(\tau_0)_{(k)}$ can be very different for different slip systems, which may lead to strongly anisotropic behavior for the single crystal. Also note that the creep exponent n could be taken to be different for different slip systems, but here, for simplicity, it will be taken to be identical for all slip systems, such that the stress potential $u^{(1)}$ for the crystal matrix is a homogeneous function of degree $n+1$ in $\boldsymbol{\sigma}$. In particular, the two limiting cases as n tends to 1 and ∞ are of special interest, since they respectively describe linearly viscous and rigid ideally plastic behavior for the single crystal.

As shown in Fig. 3.1, the voids are assumed—on average—to be ellipsoidal in shape, and to be aligned in a given direction, but distributed with *random* positions in the surrounding single-crystal matrix, as described by two-point probability functions (for their centers) with "ellipsoidal symmetry" (Willis, 1977; Ponte Castañeda and Willis, 1995). In general, the ellipsoid characterizing the void distribution can be different from the ellipsoid characterizing the voids (Ponte Castañeda and Willis, 1995; Agoras and Ponte Castañeda, 2013). However, the effect of the void distribution on the macroscopic behavior of the porous single crystals is only of second order in the volume fraction of the voids (porosity) and becomes less important at low to moderate porosities. For this reason, it is further assumed that the ellipsoidal shape

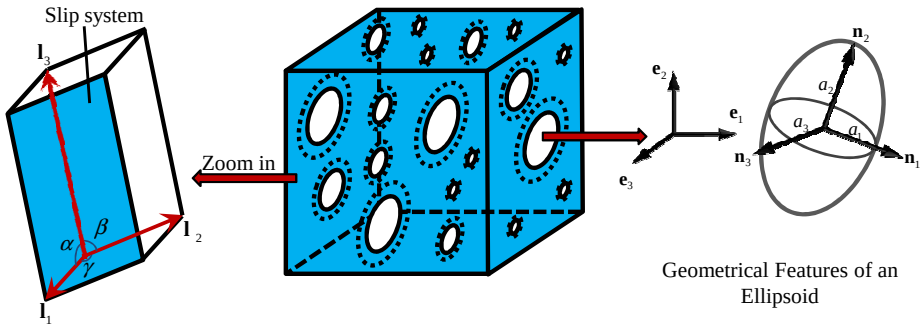

Figure 3.1: Schematic representation of a porous single crystal consisting of aligned, ellipsoidal voids (solid lines) that are distributed with the same ellipsoidal symmetry (dotted lines) in a single-crystal matrix.

and orientation of the distribution function are identical to the ellipsoidal shape and orientation of the voids (Agoras and Ponte Castañeda, 2014; Song et al., 2015). In view of these hypotheses, the microstructure of the porous single crystal under consideration can be completely described by the set of microstructural variables

$$\mathbf{s} \equiv \{\mathbf{l}_1, \mathbf{l}_2, \mathbf{l}_3, f, w_1, w_2, \mathbf{n}_1, \mathbf{n}_2, \mathbf{n}_3\}, \tag{3.4}$$

where $\mathbf{l}_1$, $\mathbf{l}_2$ and $\mathbf{l}_3$ characterize the lattice vectors of the crystal matrix, f denotes the volume fraction of the voids (or porosity), $w_1 = a_3/a_1, w_2 = a_3/a_2$ are the two aspect ratios of the representative ellipsoids characterizing the shape and distribution of the voids (a_1, a_2 and a_3 are the lengths of the three semi-axes of the ellipsoid), and $\mathbf{n}_1$, $\mathbf{n}_2$ and $\mathbf{n}_3$ are unit vectors along the three principal directions of the representative ellipsoid (see Fig. 3.1). It is remarked that, among the above-defined microstructural variables (3.4), $\mathbf{l}_1$, $\mathbf{l}_2$ and $\mathbf{l}_3$ describe the underlying anisotropy of the crystal matrix, or the "crystallographic" anisotropy, while the others $(f, w_1, w_2, \mathbf{n}_1, \mathbf{n}_2, \mathbf{n}_3)$ characterize the "morphological" anisotropy of the porous single crystal.

For a given fixed state of the microstructure, as described by the microstructural variables (3.4), the instantaneous effective viscoplastic response of the porous single crystal, characterizing the relation between the average strain rate $\langle \mathbf{D} \rangle = \overline{\mathbf{D}}$ and the average stress $\langle \boldsymbol{\sigma} \rangle = \overline{\boldsymbol{\sigma}}$, may be written in the form (e.g., Ponte Castañeda and Suquet,

1998)

$$\overline{\mathbf{D}} = \frac{\partial \widetilde{u}(\overline{\boldsymbol{\sigma}})}{\partial \overline{\boldsymbol{\sigma}}}, \quad \widetilde{u}(\overline{\boldsymbol{\sigma}}) = (1-f) \min_{\boldsymbol{\sigma} \in \mathcal{S}(\overline{\boldsymbol{\sigma}})} \langle u(\mathbf{x}, \boldsymbol{\sigma}) \rangle^{(1)}. \tag{3.5}$$

Here $\widetilde{u}$ is the effective stress potential for the porous single crystal, $\mathcal{S}(\overline{\boldsymbol{\sigma}})$ is the set of statically admissible stress fields, including all $\boldsymbol{\sigma}$ fields that are divergence free, lead to zero traction on the void surfaces, and satisfy the condition $\langle \boldsymbol{\sigma} \rangle = \overline{\boldsymbol{\sigma}}$. The triangular brackets $\langle \cdot \rangle$ denote volume averages over a representative volume element (RVE) of the porous material, while $\langle \cdot \rangle^{(r)}$ denotes volume averages over phase r in the RVE.

In summary, the instantaneous macroscopic response of the porous single crystals considered in this work can be completely determined by the effective stress potential $\widetilde{u}$ defined in (3.5). However, given the nonlinear constitutive relations of the crystal matrix and the complexity of the random microstructure, the determination of the exact values of $\widetilde{u}$ is impossible in practice, since it requires solving sets of nonlinear partial differential equations with randomly oscillating coefficients. In this work, approximate estimates for the effective potential will be obtained by means of a novel iterative homogenization scheme, making use of the recently developed fully optimized second-order (FOSO) variational homogenization method (Ponte Castañeda, 2015). In the next section, for completeness, we first recall the main features of the FOSO method in some detail. The FOSO method is then used in an iterative fashion, following the work of Agoras and Ponte Castañeda (2013), to obtain new estimates for the instantaneous effective behavior of porous single crystals. Finally, consistent homogenization estimates for the average strain-rate and vorticity fields in the phases of porous single crystals are used to develop complementary evolution laws for the microstructural variables (3.4), characterizing the evolution of both the "crystallographic" and "morphological" anisotropy of the porous single crystals at finite deformations.

3.3 Fully optimized second-order variational estimates

The FOSO variational method of Ponte Castañeda (2015) makes use of the effective behavior of an appropriately chosen porous "linear comparison composite" (LCC)—with *uniform* matrix properties and microstructure identical to that of the nonlinear porous single crystal of interest—to estimate the effective behavior of the nonlinear composite. To set the stage for the FOSO estimates, we first describe the porous LCC involved in the FOSO procedure.

For the class of porous single crystals defined in section 6.2, consider a porous LCC with the same microstructure as the nonlinear porous single crystal (described by the microstructural variables (3.4)), but with a crystal matrix (phase 1) characterized by the quadratic stress potential

$$u_L^{(1)}(\boldsymbol{\sigma}) = \frac{1}{2}\boldsymbol{\sigma}\cdot\mathbb{M}^{(1)}\boldsymbol{\sigma} + \boldsymbol{\eta}^{(1)}\cdot\boldsymbol{\sigma}, \tag{3.6}$$

where $\mathbb{M}^{(1)}$ and $\boldsymbol{\eta}^{(1)}$ are uniform, anisotropic fourth- and second-order tensors, respectively, corresponding to the viscous compliance tensor and eigenstrain-rate tensor of the crystal matrix, which are defined by

$$\mathbb{M}^{(1)} = \sum_{k=1}^{K} \frac{1}{2\mu_{(k)}} \boldsymbol{\mu}_{(k)} \otimes \boldsymbol{\mu}_{(k)}, \quad \text{and} \quad \boldsymbol{\eta}^{(1)} = \sum_{k=1}^{K} \eta_{(k)}\ \boldsymbol{\mu}_{(k)}. \tag{3.7}$$

Here the scalars $\mu_{(k)}$ and $\eta_{(k)}$ $(k = 1, ..., K)$ are respectively the positive slip viscosities and slip eigenstrain rates, which are unknown a priori but will be specified later. Differentiation of the stress potential (3.6) with respect to $\boldsymbol{\sigma}$ shows that the constitutive relation of the LCC matrix is linear, i.e.,

$$\mathbf{D} = \mathbb{M}^{(1)}\boldsymbol{\sigma} + \boldsymbol{\eta}^{(1)}. \tag{3.8}$$

Note that the constitutive relation (3.8) for the matrix of the LCC, corresponding to a linearly viscous material with prescribed eigenstrain rates, is mathematically

analogous to that for a 'thermoelastic' material. On the other hand, the stress potential for the vacuous inclusion (phase 2) is also assumed to be of the form (3.6), but with a viscous compliance tensor $\mathbb{M}^{(2)} \to \infty$ and an eigenstrain-rate tensor $\boldsymbol{\eta}^{(2)} = \mathbf{0}$. Then, for any prescribed macroscopic stress $\overline{\boldsymbol{\sigma}}$, the effective stress potential $\widetilde{u}_L$ for the porous LCC may be estimated by means of the estimates of Ponte Castañeda and Willis (1995) (to be referred to here as PCW estimates), and is given by

$$\widetilde{u}_L\left(\overline{\boldsymbol{\sigma}}\right) = \frac{1}{2}\overline{\boldsymbol{\sigma}} \cdot \widetilde{\mathbb{M}}\overline{\boldsymbol{\sigma}} + \widetilde{\boldsymbol{\eta}} \cdot \overline{\boldsymbol{\sigma}}. \tag{3.9}$$

In the above expression, $\widetilde{\mathbb{M}}$ and $\widetilde{\boldsymbol{\eta}}$ are the effective compliance tensor and the effective eigenstrain-rate tensor of the porous LCC, respectively. They are given by

$$\widetilde{\mathbb{M}} = \mathbb{M}^{(1)} + \frac{f}{1-f}\mathbb{Q}^{-1}, \quad \text{and} \quad \widetilde{\boldsymbol{\eta}} = \boldsymbol{\eta}^{(1)}. \tag{3.10}$$

Here $\mathbb{Q}$ is a fourth-order microstructural tensor related to the Eshelby tensor, depending on the matrix property $\mathbb{M}^{(1)}$ and the shape and orientation of the voids, and is given by

$$\mathbb{Q} = \frac{1}{4\pi w_1 w_2} \int\limits_{|\boldsymbol{\zeta}|=1} \frac{\left(\mathbb{M}^{(1)}\right)^{-1} - \left(\mathbb{M}^{(1)}\right)^{-1} \mathbb{H}(\boldsymbol{\zeta}) \left(\mathbb{M}^{(1)}\right)^{-1}}{|\boldsymbol{Z}^{-1}\boldsymbol{\zeta}|^3} dS, \tag{3.11}$$

where $\boldsymbol{\zeta}$ is a unit vector and $H_{ijkl} = K^{-1}_{ik}\zeta_j\zeta_l|_{(ij)(kl)}$ (the parentheses denote symmetrization with respect to the corresponding indices), with $K_{ik} = \left(M^{(1)}\right)^{-1}_{imkn}\zeta_m\zeta_n$ denoting the acoustic tensor. The symmetric second-order tensor $\boldsymbol{Z}$ serves to characterize the shape and orientation of the voids (and their distribution), and can be written in the form

$$\boldsymbol{Z} = w_1\mathbf{n}_1 \otimes \mathbf{n}_1 + w_2\mathbf{n}_2 \otimes \mathbf{n}_2 + \mathbf{n}_3 \otimes \mathbf{n}_3. \tag{3.12}$$

Correspondingly, the first and second moments of the stress field over the matrix of the porous LCC, which are required by the FOSO method, are determined by

$$\overline{\boldsymbol{\sigma}}^{(1)} = \frac{1}{1-f}\overline{\boldsymbol{\sigma}}, \quad \text{and} \quad \langle\boldsymbol{\sigma} \otimes \boldsymbol{\sigma}\rangle^{(1)} = \frac{2}{1-f}\frac{\partial\widetilde{u}_L}{\partial\mathbb{M}^{(1)}}. \tag{3.13}$$

Following the work of Ponte Castañeda (2015), the FOSO estimates for the effective stress potential $\tilde{u}$ (as defined by (3.5)) of the nonlinear porous single crystals are given by

$$\widetilde{u}^{\mathrm{SO}}(\overline{\boldsymbol{\sigma}}) = (1-f)\sum_{k=1}^{K}\left[\alpha\phi_{(k)}(\check{\tau}_{(k)}) + (1-\alpha)\,\phi_{(k)}(\hat{\tau}_{(k)})\right], \tag{3.14}$$

where α is an appropriately chosen constant weight factor between 0 and 1, the $\check{\tau}_{(k)}$ and $\hat{\tau}_{(k)}$ $(k = 1, ..., K)$ are stress variables depending on both the first and second moments of the stress field over the matrix of the porous LCC (see expression (3.13)). They satisfy the relations (Ponte Castañeda, 2015)

$$\alpha\check{\tau}_{(k)} + (1-\alpha)\,\hat{\tau}_{(k)} = \overline{\boldsymbol{\sigma}}^{(1)} \cdot \boldsymbol{\mu}_{(k)} = \overline{\tau}_{(k)}, \tag{3.15}$$

and

$$\alpha\left(\check{\tau}_{(k)}\right)^2 + (1-\alpha)\left(\hat{\tau}_{(k)}\right)^2 = \boldsymbol{\mu}_{(k)} \cdot \langle\boldsymbol{\sigma}\otimes\boldsymbol{\sigma}\rangle^{(1)}\boldsymbol{\mu}_{(k)} = \overline{\overline{\tau}}_{(k)}, \tag{3.16}$$

where $\overline{\tau}_{(k)}$ and $\overline{\overline{\tau}}_{(k)}$ correspond to the first and second moments of the resolved shear stresses over the kth slip system of the LCC matrix. More specifically, $\check{\tau}_{(k)}$ and $\hat{\tau}_{(k)}$ are chosen to be such that $\check{\tau}_{(k)} \le \hat{\tau}_{(k)}$ and can be easily obtained by solving the set of quadratic equations (3.15) and (3.16), so that

$$\check{\tau}_{(k)} = \overline{\tau}_{(k)} - \sqrt{\frac{1-\alpha}{\alpha}}\sqrt{\overline{\overline{\tau}}_{(k)} - \overline{\tau}^2_{(k)}} = \overline{\tau}_{(k)} - \sqrt{\frac{1-\alpha}{\alpha}}\mathrm{SD}^{(1)}\left(\tau_{(k)}\right) \tag{3.17}$$

and

$$\hat{\tau}_{(k)} = \overline{\tau}_{(k)} + \sqrt{\frac{\alpha}{1-\alpha}}\sqrt{\overline{\overline{\tau}}_{(k)} - \overline{\tau}^2_{(k)}} = \overline{\tau}_{(k)} + \sqrt{\frac{\alpha}{1-\alpha}}\mathrm{SD}^{(1)}\left(\tau_{(k)}\right), \tag{3.18}$$

with $\mathrm{SD}^{(1)}\left(\tau_{(k)}\right) = \sqrt{\overline{\overline{\tau}}_{(k)} - \overline{\tau}^2_{(k)}}$ denoting the standard deviation of the resolved shear stresses over slip system k in the LCC matrix. In this connection, it should be emphasized that the quantities $\check{\tau}_{(k)}$ and $\hat{\tau}_{(k)}$—depending on both the first and second moments of the stress field over the LCC matrix—are functions of the properties of the LCC, as determined by the variables $\mu_{(k)}$ and $\eta_{(k)}$ in (3.7).

In turn, the properties of the porous LCC have to be specified such that the slip

viscosities $\mu_{(k)}$ and the slip eigenstrain rates $\eta_{(k)}$ satisfy the linearization conditions

$$\phi'_{(k)}(\hat{\tau}_{(k)}) - \frac{1}{2\mu_{(k)}}\hat{\tau}_{(k)} = \eta_{(k)} = \phi'_{(k)}(\check{\tau}_{(k)}) - \frac{1}{2\mu_{(k)}}\check{\tau}_{(k)}. \tag{3.19}$$

Note that these two conditions imply that

$$\frac{1}{2\mu_{(k)}} = \frac{\phi'_{(k)}(\hat{\tau}_{(k)}) - \phi'_{(k)}(\check{\tau}_{(k)})}{\hat{\tau}_{(k)} - \check{\tau}_{(k)}}, \tag{3.20}$$

which identifies the slip viscosities $\mu_{(k)}$ of the LCC matrix with 'generalized secant' linearizations of the nonlinear slip potentials for the viscoplastic single-crystal matrix, accounting for both the first and second moments of the stress field in the crystal matrix. (Note further that this expression reduces to the 'tangent' linearization when there are no field fluctuations in the phase and the $\hat{\tau}_{(k)} \to \check{\tau}_{(k)}$.) Expressions (3.17)-(3.19) provide a system of $4K$ nonlinear algebraic equations for the variables $\check{\tau}_{(k)}$, $\hat{\tau}_{(k)}$, $\mu_{(k)}$ and $\eta_{(k)}$ $(k = 1, .., K)$, which can be easily solved numerically.

As already mentioned, the macroscopic constitutive behavior and the corresponding field statistics (e.g., the first and second moments of the stress and strain rate fields) of the nonlinear porous single crystals can be obtained directly from those of the porous LCC (Ponte Castañeda, 2015). (This follows from the full stationarity of the FOSO estimates in the properties of the LCC, together with the results of Idiart and Ponte Castañeda (2007c), and is independent of the choice of the weights α.) In particular, the FOSO estimate for the macroscopic strain rate $\overline{\mathbf{D}}$ of the nonlinear porous single crystal under the applied loading $\overline{\boldsymbol{\sigma}}$ is given by

$$\overline{\mathbf{D}} = \frac{\partial \widetilde{u}^{\mathrm{SO}}}{\partial \overline{\boldsymbol{\sigma}}}(\overline{\boldsymbol{\sigma}}) = \frac{\partial \widetilde{u}_L}{\partial \overline{\boldsymbol{\sigma}}}(\overline{\boldsymbol{\sigma}}) = \widetilde{\mathbb{M}}\overline{\boldsymbol{\sigma}} + \widetilde{\boldsymbol{\eta}}, \tag{3.21}$$

where it is recalled that $\widetilde{\mathbb{M}}$ and $\widetilde{\boldsymbol{\eta}}$ are the effective compliance tensor and the effective eigenstrain-rate tensor of the porous LCC, respectively, which are given by (3.10). We should emphasize that $\widetilde{\mathbb{M}}$ and $\widetilde{\boldsymbol{\eta}}$ depend nonlinearly on $\overline{\boldsymbol{\sigma}}$ and, therefore, the macroscopic constitutive relation (3.21) is also nonlinear, as expected.

At this point, it should be recalled (Ponte Castañeda, 2015) that the results

discussed in this section are valid for any choice of the weights α. Unfortunately, at the present time there is no mathematically or physically motivated prescription available to select these weights in 'optimal' fashion. One alternative possibility would be to use these weights to try to fit our theoretical predictions to the results of numerical simulations or experimental results, but—in this first application of the method for porous single crystals—we choose not to pursue this option, preferring instead to make use of the simplest choice $\alpha = 1/2$ (see below).

On the other hand, the average strain rate and spin fields in the voids, which are useful for establishing the complementary equations for the evolution of the microstructure, can be consistently obtained from the PCW estimates for the corresponding fields in the LCC. In particular, the average strain rate in the voids $\overline{\mathbf{D}}^{(2)}$ may be expressed in terms of the macroscopic strain rate $\overline{\mathbf{D}}$ as

$$\overline{\mathbf{D}}^{(2)} = \mathbb{A}^{(2)}\overline{\mathbf{D}} + \mathbf{a}^{(2)}, \tag{3.22}$$

where $\mathbb{A}^{(2)}$ and $\mathbf{a}^{(2)}$ are the associated strain-rate concentration tensors given by

$$\mathbb{A}^{(2)} = \left[f\mathbb{I} + (1-f)\,\mathbb{M}^{(1)}\mathbb{Q}\right]^{-1}, \tag{3.23}$$

and

$$\mathbf{a}^{(2)} = -(1-f)\,\mathbb{A}^{(2)}\left(\mathbb{I} - \mathbb{M}^{(1)}\mathbb{Q}\right)\boldsymbol{\eta}^{(1)}, \tag{3.24}$$

with $\mathbb{I}$ denoting the fully symmetric fourth-order identity tensor. Similarly, the average spin in the voids can be written in terms of the macroscopic strain rate $\overline{\mathbf{D}}$ and the macroscopic spin $\overline{\mathbf{W}}$ as

$$\overline{\mathbf{W}}^{(2)} = \overline{\mathbf{W}} - \mathbb{C}^{(2)}\overline{\mathbf{D}} - \boldsymbol{\beta}^{(2)}, \tag{3.25}$$

where $\mathbb{C}^{(2)}$ and $\boldsymbol{\beta}^{(2)}$ are the associated spin-concentration tensors provided by

$$\mathbb{C}^{(2)} = -(1-f)\boldsymbol{\Pi}\mathbb{A}^{(2)}, \tag{3.26}$$

and

$$\boldsymbol{\beta}^{(2)} = -(1-f)\boldsymbol{\Pi}(\mathbf{a}^{(2)} - \boldsymbol{\eta}^{(1)}). \tag{3.27}$$

Here $\boldsymbol{\Pi}$ is the fourth-order Eshelby rotation tensor determining the spin of an isolated void in an infinite linearly viscous matrix, and is given by

$$\boldsymbol{\Pi} = \frac{1}{4\pi w_1 w_2} \int\limits_{|\boldsymbol{\zeta}|=1} \frac{\hat{\mathbb{H}}(\boldsymbol{\zeta})\,(\mathbb{M}^{(1)})^{-1}}{|\boldsymbol{Z}^{-1}\boldsymbol{\zeta}|^3} dS, \tag{3.28}$$

with $\hat{H}_{ijkl} = K_{ik}^{-1}\zeta_j\zeta_l|_{[ij](kl)}$ (the square bracket denotes the skew symmetric part of the first two indices, while the round bracket denotes the symmetric part of the last two indices). We recall that $K_{ik} = (M^{(1)})^{-1}_{imkn}\,\zeta_m\zeta_n$ is the acoustic tensor, and $\boldsymbol{Z}$ as given by (3.12) is a symmetric second-order tensor describing the instantaneous shape and orientation of the voids (and their distribution).

Next, it is necessary to determine the average slip rates $\overline{\gamma}_{(k)}$ $(k = 1, ..., K)$ over different slip systems in the single-crystal matrix. Letting $\overline{\mathbf{D}}^{(1)}$ denote the average strain rate in the crystal matrix, they will be required here to satisfy the relation

$$\overline{\mathbf{D}}^{(1)} = \sum_{k=1}^{K} \overline{\gamma}_{(k)} \boldsymbol{\mu}_{(k)}. \tag{3.29}$$

Note that $\overline{\mathbf{D}}^{(1)}$ can be directly estimated from the constitutive relation (3.8) for the LCC matrix, i.e.,

$$\overline{\mathbf{D}}^{(1)} = \mathbb{M}^{(1)}\overline{\boldsymbol{\sigma}}^{(1)} + \boldsymbol{\eta}^{(1)} = \sum_{k=1}^{K} \left(\frac{1}{2\mu_{(k)}} \overline{\tau}_{(k)} + \eta_{(k)} \right) \boldsymbol{\mu}_{(k)}, \tag{3.30}$$

or, using (3.7), (3.15) and (3.19), from the expression

$$\overline{\mathbf{D}}^{(1)} = \sum_{k=1}^{K} \Big[\alpha\phi'_{(k)}(\check{\tau}_{(k)}) + (1-\alpha)\phi'_{(k)}(\hat{\tau}_{(k)}) \Big] \boldsymbol{\mu}_{(k)}. \tag{3.31}$$

It then follows from (3.29), (3.30) and (3.31) that the average slip rates $\overline{\gamma}_{(k)}$ can be

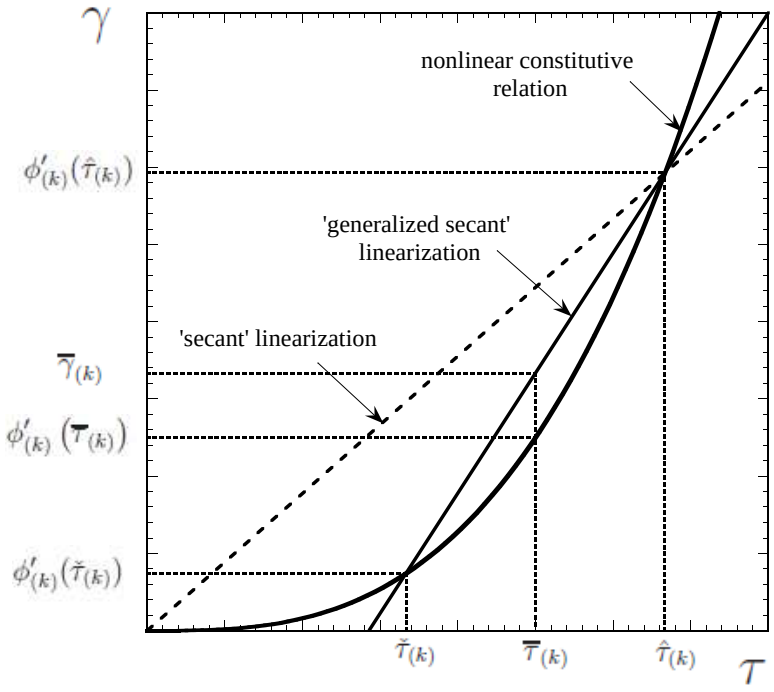

Figure 3.2: The 'generalized secant' linearization (3.20) and the 'secant' linearization (3.36) of the nonlinear constitutive response of the viscoplastic single crystals. The evaluation of the corresponding average slip rate $\overline{\gamma}_{(k)}$ is also shown in the figure.

expressed in the equivalent forms

$$\overline{\gamma}_{(k)} = \frac{1}{2\mu_{(k)}}\overline{\tau}_{(k)} + \eta_{(k)} = \alpha\phi'_{(k)}(\check{\tau}_{(k)}) + (1-\alpha)\phi'_{(k)}(\hat{\tau}_{(k)}). \tag{3.32}$$

Note that $\overline{\gamma}_{(k)} \neq 2\overline{\mathbf{D}}^{(1)} \cdot \boldsymbol{\mu}_{(k)}$, except when the Schmid tensors $\boldsymbol{\mu}_{(k)}$ are orthogonal to each other for the crystal matrix. Thus, the $\overline{\gamma}_{(k)}$ $(k = 1, ..., K)$ can be estimated directly from the LCC, whose properties are determined by (3.19) (or, equivalently, the 'generalized secant' condition (3.20)). For visualization purposes, the 'generalized secant' condition (3.20) and the evaluation of the corresponding $\overline{\gamma}_{(k)}$ from expression (3.32) is depicted graphically in Fig. 3.2. In particular, it can be seen that the 'generalized secant' condition provides a linear interpolation between the slip rates $\check{\gamma}_{(k)} = \phi'_{(k)}\left(\check{\tau}_{(k)}\right)$ and $\hat{\gamma}_{(k)} = \phi'_{(k)}\left(\hat{\tau}_{(k)}\right)$, associated with the resolved shear stresses $\check{\tau}_{(k)}$ and $\hat{\tau}_{(k)}$, respectively. More importantly, the average slip rates $\overline{\gamma}_{(k)}$ are seen in Fig. 3.2 to be related to the average resolved shear stresses $\overline{\tau}_{(k)}$—lying between $\check{\tau}_{(k)}$ and $\hat{\tau}_{(k)}$—by the linearized constitutive relation (3.32)–and not by the nonlinear

constitutive relation, i.e.,

$$\overline{\gamma}_{(k)} \neq \phi'_{(k)}\left(\overline{\tau}_{(k)}\right). \tag{3.33}$$

Note further that, due to the nonlinear stress-strain rate response of the single-crystal matrix, the inequality (3.33) is to be expected. This is because the average of a nonlinear function is generally different from the function of the average. For this reason, the fact that the FOSO estimates (3.32) for $\overline{\gamma}_{(k)}$ are entirely consistent with (3.33) is a distinguishing feature of the FOSO method in comparison to the earlier second-order estimates of Liu and Ponte Castañeda (2004a), which involves the use of an "affine" approximation of the average slip rates, i.e., $\overline{\gamma}_{(k)} = \phi'_{(k)}\left(\overline{\tau}_{(k)}\right)$, violating the general expectation of relation (3.33). Finally, note that the weight factor α will be chosen to be 1/2, which is the most symmetric choice, although there may be other better choices for the value of α. This is a point that will require further investigation in future works.

In this context, we should mention that the FOSO estimate (3.14) for $\widetilde{u}$ is a generalization of the variational homogenization (VH) estimate of deBotton and Ponte Castañeda (1995), which may be recovered from the FOSO estimate (3.14) by formally setting the eigenstrain-rate tensor $\boldsymbol{\eta}^{(1)} = \mathbf{0}$. In its final form, the VH estimate for the effective stress potential $\widetilde{u}$ of the nonlinear porous single crystal can be written as

$$\widetilde{u}^{\mathrm{VH}}(\overline{\boldsymbol{\sigma}}) = (1-f)\sum_{k=1}^{K}\phi_{(k)}(\hat{\tau}_{(k)}). \tag{3.34}$$

Here the stress variables $\hat{\tau}_{(k)}$ depend only on the second moments of the resolved shear stresses over the LCC matrix, which are given by

$$\hat{\tau}_{(k)} = \sqrt{\overline{\tau}_{(k)}} = \sqrt{\boldsymbol{\mu}_{(k)} \cdot \langle \boldsymbol{\sigma} \otimes \boldsymbol{\sigma} \rangle^{(1)} \boldsymbol{\mu}_{(k)}}, \tag{3.35}$$

where the second moment $\langle \boldsymbol{\sigma} \otimes \boldsymbol{\sigma} \rangle^{(1)}$ may be obtained from the PCW estimates $(3.13)_2$ with the $\boldsymbol{\eta}^{(1)} = \mathbf{0}$. In turn, the slip viscosities $\mu_{(k)}$ in the porous LCC are given by the conditions

$$\frac{1}{2\mu_{(k)}} = \frac{\phi'_{(k)}(\hat{\tau}_{(k)})}{\hat{\tau}_{(k)}}. \tag{3.36}$$

Note that (3.36) identifies the slip viscosities $\mu_{(k)}$ of the LCC matrix with 'secant' linearizations of the nonlinear constitutive response for the corresponding slip systems in the viscoplastic single-crystal matrix (see the dashed straight line in Fig. 3.2), accounting for the second moment of the stress field in the crystal matrix. Also note that the VH estimates for the average slip rates $\overline{\gamma}_{(k)}$ over different slip systems can be obtained directly from the LCC, i.e., $\overline{\gamma}_{(k)} = \overline{\tau}_{(k)}/\left(2\mu_{(k)}\right) \neq \phi'_{(k)}(\overline{\tau}_{(k)})$.

The FOSO estimates (3.14) are known to be exact to second order in the heterogeneity contrast (Ponte Castañeda, 2015), when used in combination with estimates for the LCC that are exact to second order in the heterogeneity contrast (e.g., the PCW estimates used in this work). For this reason, they are more accurate then the VH estimates (3.34), which are only exact to first order in the heterogeneity contrast. In fact, the VH estimate can be shown to be a rigorous lower bound for all other estimates for the effective stress potential $\widetilde{u}$ of the porous single crystals (deBotton and Ponte Castañeda, 1995). Although the FOSO estimates (3.14) provide fairly accurate estimates in most cases, they become less accurate for low porosity and high nonlinearity, especially at high stress triaxialities. As already noted in the context of the VH method (Agoras and Ponte Castañeda, 2013), this drawback is attributed to the assumption, employed in their derivation, that the matrix property in the LCC is uniform. For this reason, in the next section we develop improved estimates by incorporating *non-uniform* properties of the matrix phase in the LCC.

3.4 Iterated second-order estimates

In this section, we make use of the iterative homogenization approach of Agoras and Ponte Castañeda (2013) in combination with the FOSO method—as discussed in section 3.3—to obtain further improved estimates for the effective stress potential $\widetilde{u}$ of the nonlinear porous single crystals, which will be referred to here as the Iterated Second-Order (ISO) homogenization estimates. Following the work of Agoras and Ponte Castañeda (2013) and as illustrated in Fig. 3.3, the key idea of the ISO method is to construct the porous microstructure iteratively in a self-similar fashion. In the

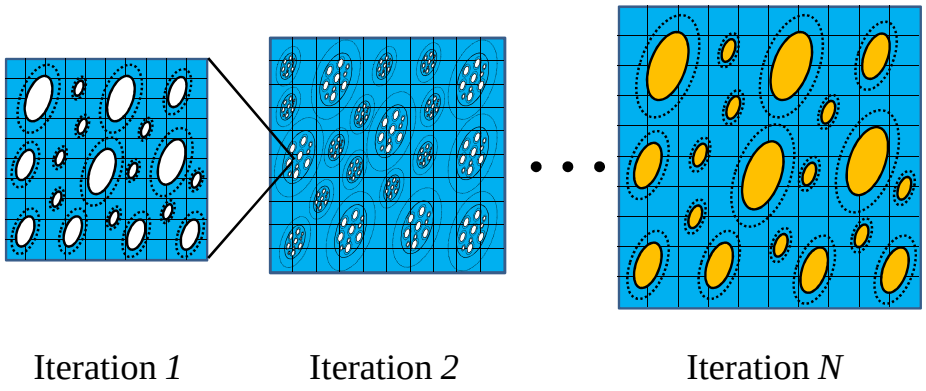

Figure 3.3: Schematic representation of the iterated homogenization procedure for a porous single crystal consisting of aligned, ellipsoidal voids (solid lines) that are distributed with the same ellipsoidal symmetry (dotted lines) in a single-crystal matrix.

first iteration ($i = 1$), the voids are distributed in the matrix with volume fraction $c^{(2)}_{[1]} > f$ and given (generally different) shapes for the voids and the distribution ellipsoid. In the second iteration ($i = 2$), "composite inclusions" of the porous material from the first iteration are distributed in the same matrix phase (including same orientation) with volume fraction $c^{(2)}_{[2]}$ and with inclusion and distribution shapes that are identical to the distribution shape of the voids in the first iteration. At iteration 3 ($i = 3$), "composite inclusions" of the porous material from iteration 2 are distributed in the same matrix phase with volume fraction $c^{(2)}_{[3]}$ and with inclusion and distribution shapes identical to the distribution shape of the voids in the first iteration. The procedure is continued N times in such a way that the final composite ($i = N$) consists of a porous single crystal with the desired porosity f, such that

$$f = \prod_{i=1}^{N} c^{(2)}_{[i]}, \tag{3.37}$$

where $c^{(2)}_{[i]}$ $(i = 2, ..., N)$ represents the volume fraction of the "composite inclusion" in the level-i composite. Note that the voids in the final, level-N microstructure have the given shape (from the first iteration) and are distributed in "hierarchical clusters," but still possessing ellipsoidal distribution of a given (possibily different) shape. With the above construction procedure, it can be shown (Agoras and Ponte Castañeda, 2013) that the resulting level-N composite still belongs to the class of

random porous materials defined in section 6.2, and is characterized by the same set of microstructural variables (3.4). Moreover, while the hierarchical nature of the microstructure in the iterated procedure may be expected to have an effect on the effective properties relative to those of the original (non-iterated) microstructure, it is known (Ponte Castañeda, 2012; Agoras and Ponte Castañeda, 2013) that the PCW estimates for the effective properties of porous linear-elastic materials are insensitive to the hierarchical nature of the microstructure. In other words, the PCW estimates for the effective properties of porous linear-elastic materials with iterated and non-iterated (single-scale) microstructures are identical and given by expressions (3.10), provided that they both have the same porosity and void and distribution shapes and orientations. Because of this, the assumption will be made here that the same is true of the corresponding FOSO "linear comparison" estimates of the PCW type for the nonlinear porous materials, keeping in mind that the reason for introducing this iterated procedure is that it allows for the use of more general (non-uniform) "trial fields" for the moduli of the LCC in the matrix—in a way that is consistent with the given statistics of the random microstructures.

Estimates for the effective behavior of the porous single crystals of interest in this work may then be obtained by applying the FOSO method iteratively to the above-described level-N composite. Thus, the ISO procedure involves, at each iteration, an LCC with microstructure identical to that of the corresponding nonlinear composite, but with a linear single-crystal matrix and a linear (compressible) inclusion phase. Specifically, the stress potential of the LCC crystal matrix (phase 1) at the ith iteration is assumed to be of the form (3.6), but with the viscous compliance and eigenstrain-rate tensors given by

$$\mathbb{M}^{(1)}_{[i]} = \sum_{k=1}^{K} \frac{1}{2\mu^{[i]}_{(k)}} \boldsymbol{\mu}_{(k)} \otimes \boldsymbol{\mu}_{(k)}, \quad \text{and} \quad \boldsymbol{\eta}^{(1)}_{[i]} = \sum_{k=1}^{K} \eta^{[i]}_{(k)} \boldsymbol{\mu}_{(k)}, \tag{3.38}$$

respectively. Here the label $[i]$ is used to denote the appropriate quantities of the LCC at level i, so that the $\mu^{[i]}_{(k)}$ and $\eta^{[i]}_{(k)}$ are respectively the slip viscosities and slip eigenstrain rates (to be specified later), and N is the total number of iterations in the

ISO procedure. On the other hand, the stress potential of the inclusion phase in the LCC at level i is also assumed to be of the form (3.6), but with a viscous compliance tensor $\mathbb{M}^{(2)}_{[i]}$ and eigenstrain-rate tensor $\boldsymbol{\eta}^{(2)}_{[i]}$ $(i = 1, ..., N)$. In particular, for the LCC at the lowest iteration $i = 1$, $\mathbb{M}^{(2)}_{[1]} \to \infty$ and $\boldsymbol{\eta}^{(2)}_{[1]} = \mathbf{0}$ correspond respectively to the viscous compliance tensor and eigenstrain-rate tensor of the vacuous inclusion, while, at each subsequent iterations $i = 2, ..., N$, $\mathbb{M}^{(2)}_{[i]}$ and $\boldsymbol{\eta}^{(2)}_{[i]}$ correspond respectively to the linearized compliance tensor and eigenstrain-rate tensor of the (compressible) composite inclusion. Furthermore, the effective behavior of the LCC at each level, and the corresponding field statistics, can be estimated by means of the PCW estimates, which are given in detail in Appendix I.

Next, we provide the ISO estimates for the effective stress potential $\widetilde{u}$ of the porous single crystals in a little more detail. For later use, define $\overline{\boldsymbol{\sigma}}_{[i]} = \langle \boldsymbol{\sigma} \rangle_{[i]}$ $(i = 1, ..., N)$ to be the average stress field over the level-i composite, and define $\widetilde{u}_{[i]}$ accordingly to be the effective stress potential for the level-i composite. At the lowest iteration, the effective behavior of the level-1 porous single crystal can be obtained by means of expression (3.14), such that

$$\widetilde{u}^{\mathrm{ISO}}_{[1]}(\overline{\boldsymbol{\sigma}}_{[1]}) = \left(1 - c^{(2)}_{[1]}\right) \sum_{k=1}^{K} \left[\alpha \phi_{(k)}(\check{\tau}^{[1]}_{(k)}) + (1 - \alpha)\, \phi_{(k)}(\hat{\tau}^{[1]}_{(k)})\right], \tag{3.39}$$

where the stress variables $\check{\tau}^{[1]}_{(k)}$ and $\hat{\tau}^{[1]}_{(k)}$ $(\check{\tau}^{[1]}_{(k)} \le \hat{\tau}^{[1]}_{(k)})$ are determined by expressions (3.17) and (3.18), specialized to the first iteration. They are given by setting the superscript $i = 1$ in the following expressions

$$\check{\tau}^{[i]}_{(k)} = \overline{\tau}^{[i]}_{(k)} - \sqrt{\frac{1-\alpha}{\alpha}} \sqrt{\overline{\overline{\tau}}^{[i]}_{(k)} - \left(\overline{\tau}^{[i]}_{(k)}\right)^2} = \overline{\tau}^{[i]}_{(k)} - \sqrt{\frac{1-\alpha}{\alpha}} \mathrm{SD}^{(1)}_{[i]}\left(\tau^{[i]}_{(k)}\right) \tag{3.40}$$

and

$$\hat{\tau}^{[i]}_{(k)} = \overline{\tau}^{[i]}_{(k)} + \sqrt{\frac{\alpha}{1-\alpha}} \sqrt{\overline{\overline{\tau}}^{[i]}_{(k)} - \left(\overline{\tau}^{[i]}_{(k)}\right)^2} = \overline{\tau}^{[i]}_{(k)} + \sqrt{\frac{\alpha}{1-\alpha}} \mathrm{SD}^{(1)}_{[i]}\left(\tau^{[i]}_{(k)}\right), \tag{3.41}$$

where $0 < \alpha < 1$ is a weight factor, which will be chosen here to be $1/2$ for simplicity,

while $\overline{\tau}^{[i]}_{(k)} = \overline{\boldsymbol{\sigma}}^{(1)}_{[i]} \cdot \boldsymbol{\mu}_{(k)}$, $\overline{\overline{\tau}}^{[i]}_{(k)} = \boldsymbol{\mu}_{(k)} \cdot \langle \boldsymbol{\sigma} \otimes \boldsymbol{\sigma} \rangle^{(1)}_{[i]} \boldsymbol{\mu}_{(k)}$, and $\mathrm{SD}^{(1)}_{[i]}\left(\tau^{[i]}_{(k)}\right) = \sqrt{\overline{\overline{\tau}}^{[i]}_{(k)} - \left(\overline{\tau}^{[i]}_{(k)}\right)^2}$ denote, respectively, the first moment, the second moment, and the standard deviation of the resolved shear stress over slip system k in the level-i LCC matrix. In these expressions, $\overline{\boldsymbol{\sigma}}^{(1)}_{[i]}$ and $\langle \boldsymbol{\sigma} \otimes \boldsymbol{\sigma} \rangle^{(1)}_{[i]}$ $(i = 1, ..., N)$ denote, respectively, the first and second moments of the stress field in the level-i LCC matrix, as given by $(3.84)_1$, together with (3.72), (3.73), and (3.88) in Appendix I.

In turn, the corresponding slip viscosities $\mu^{[1]}_{(k)}$ and slip eigenstrain rates $\eta^{[1]}_{(k)}$ of the LCC matrix at level 1 are obtained by setting the superscript $i = 1$ in the following expressions

$$\frac{1}{2\mu^{[i]}_{(k)}} = \frac{\phi'_{(k)}(\hat{\tau}^{[i]}_{(k)}) - \phi'_{(k)}(\check{\tau}^{[i]}_{(k)})}{\hat{\tau}^{[i]}_{(k)} - \check{\tau}^{[i]}_{(k)}}, \quad \text{and} \quad \eta^{[i]}_{(k)} = \phi'_{(k)}(\check{\tau}^{[i]}_{(k)}) - \frac{1}{2\mu^{[i]}_{(k)}} \check{\tau}^{[i]}_{(k)}. \tag{3.42}$$

Next, consider the level-2 porous single crystal, where the above homogenized level-1 composite—with the effective stress potential $\widetilde{u}^{\mathrm{ISO}}_{[1]}$ given by (3.39)—is distributed in the form of "composite inclusion" in the single-crystal matrix. Making use of the fact that the PCW estimate for the stress field within the inclusion phase is *uniform*, the ISO estimates for the effective response of the level-2 composite may be written in the form (Ponte Castañeda, 2015)

$$\widetilde{u}^{\mathrm{ISO}}_{[2]}(\overline{\boldsymbol{\sigma}}_{[2]}) = \left(1 - c^{(2)}_{[2]}\right) \sum_{k=1}^{K} \left[\alpha \phi_{(k)}(\check{\tau}^{[2]}_{(k)}) + (1 - \alpha)\, \phi_{(k)}(\hat{\tau}^{[2]}_{(k)})\right] + c^{(2)}_{[2]} \widetilde{u}^{\mathrm{ISO}}_{[1]}\left(\overline{\boldsymbol{\sigma}}^{(2)}_{[2]}\right). \tag{3.43}$$

Here $\overline{\boldsymbol{\sigma}}^{(2)}_{[2]}$ denotes the average stress field over the inclusion phase of the level-2 LCC, as given by (3.73) in Appendix I, while the stress variables $\check{\tau}^{[2]}_{(k)}$ and $\hat{\tau}^{[2]}_{(k)}$ $(\check{\tau}^{[2]}_{(k)} \leq \hat{\tau}^{[2]}_{(k)})$, as well as the slip viscosities $\mu^{[2]}_{(k)}$ and slip eigenstrain rates $\eta^{[2]}_{(k)}$ of the LCC matrix at level 2, are given by setting $i = 2$ in expressions (3.40) to (3.42). On the other hand, the compliance tensor $\mathbb{M}^{(2)}_{[2]}$ and eigenstrain-rate tensor $\boldsymbol{\eta}^{(2)}_{[2]}$ of the inclusion phase of the LCC at level 2 have to satisfy the consistency condition

$$\frac{\partial \widetilde{u}^{\mathrm{ISO}}_{[1]}}{\partial \boldsymbol{\sigma}}\left(\overline{\boldsymbol{\sigma}}^{(2)}_{[2]}\right) = \mathbb{M}^{(2)}_{[2]} \overline{\boldsymbol{\sigma}}^{(2)}_{[2]} + \boldsymbol{\eta}^{(2)}_{[2]}. \tag{3.44}$$

Making use of equation (3.21), along with the relation $\overline{\boldsymbol{\sigma}}^{(2)}_{[2]} = \overline{\boldsymbol{\sigma}}_{[1]}$, we have that equation (3.44) implies that

$$\mathbb{M}^{(2)}_{[2]} = \widetilde{\mathbb{M}}_{[1]} \quad \text{and} \quad \boldsymbol{\eta}^{(2)}_{[2]} = \widetilde{\boldsymbol{\eta}}_{[1]}, \tag{3.45}$$

where $\widetilde{\mathbb{M}}_{[1]}$ and $\widetilde{\boldsymbol{\eta}}_{[1]}$ are the PCW estimates for the effective compliance tensor and effective eigenstrain-rate tensor of the level-1 LCC, respectively.

Next, making use of expression (3.39) for $\widetilde{u}^{\text{ISO}}_{[1]}$ in (3.43), the ISO estimates for the effective stress potential of the level-2 composite may be rewritten as

$$\begin{aligned}\widetilde{u}^{\text{ISO}}_{[2]}(\overline{\boldsymbol{\sigma}}_{[2]}) =& c^{(2)}_{[2]}\left(1 - c^{(2)}_{[1]}\right)\sum_{k=1}^{K}\left[\alpha\phi_{(k)}(\check{\tau}^{[1]}_{(k)}) + (1-\alpha)\,\phi_{(k)}(\hat{\tau}^{[1]}_{(k)})\right] \\ &+ \left(1 - c^{(2)}_{[2]}\right)\sum_{k=1}^{K}\left[\alpha\phi_{(k)}(\check{\tau}^{[2]}_{(k)}) + (1-\alpha)\,\phi_{(k)}(\hat{\tau}^{[2]}_{(k)})\right].\end{aligned} \tag{3.46}$$

The ISO estimates for the effective stress potential of the porous single crystal at each subsequent iterations $i = 3, ..., N$ can be obtained by means of a procedure completely analogous to the one adopted above for the derivation of (3.46). Then, it follows that the resulting estimates at a general iteration i ($i = 2, ..., N$) may be written in a form similar to (3.43), namely

$$\widetilde{u}^{\text{ISO}}_{[i]}(\overline{\boldsymbol{\sigma}}_{[i]}) = \left(1 - c^{(2)}_{[i]}\right)\sum_{k=1}^{K}\left[\alpha\phi_{(k)}(\check{\tau}^{[i]}_{(k)}) + (1-\alpha)\,\phi_{(k)}(\hat{\tau}^{[i]}_{(k)})\right] + c^{(2)}_{[i]}\widetilde{u}^{\text{ISO}}_{[i-1]}(\overline{\boldsymbol{\sigma}}^{(2)}_{[i]}). \tag{3.47}$$

Starting with $\widetilde{u}^{\text{ISO}}_{[1]}$ in (3.39), and making use of expression (3.47) recursively for $i = 2, ..., N$ to estimate $\widetilde{u}_{[i]}$ in terms of $\widetilde{u}_{[i-1]}$, we obtain the following ISO estimates for the final, level-N porous single crystal:

$$\widetilde{u}^{\text{ISO}}(\overline{\boldsymbol{\sigma}}) = \sum_{i=1}^{N}\left(1 - c^{(2)}_{[i]}\right)\left(\prod_{j=i+1}^{N} c^{(2)}_{[j]}\right)\left[\sum_{k=1}^{K}\left(\alpha\phi_{(k)}(\check{\tau}^{[i]}_{(k)}) + (1-\alpha)\,\phi_{(k)}(\hat{\tau}^{[i]}_{(k)})\right)\right], \tag{3.48}$$

where we have made use of the fact that $\overline{\boldsymbol{\sigma}}_{[N]} \equiv \overline{\boldsymbol{\sigma}}$ for the level-N composite. In expression (3.48), the stress variables $\check{\tau}^{[i]}_{(k)}$ and $\hat{\tau}^{[i]}_{(k)}$ ($\check{\tau}^{[i]}_{(k)} < \hat{\tau}^{[i]}_{(k)}$), with $i = 1, ..., N$, are given by expressions (3.40) and (3.41), respectively. In turn, the properties of the

LCC must be specified such that the slip viscosities $\mu_{(k)}^{[i]}$ and slip eigenstrain rates $\eta_{(k)}^{[i]}$ of the LCC matrix at level i satisfy the conditions (3.42). It should be emphasized here that the stress variables $\check{\tau}_{(k)}^{[i]}$ and $\hat{\tau}_{(k)}^{[i]}$ $(i = 1, ..., N;\ k = 1, ..., K)$ are functions of the properties of the LCC, as determined by the variables $\mu_{(k)}^{[i]}$ and $\eta_{(k)}^{[i]}$ $(i = 1, ..., N,\ k = 1, ..., K)$ in (3.38).

On the other hand, the viscous compliance tensor $\mathbb{M}_{[i]}^{(2)}$ and eigenstrain-rate tensor $\boldsymbol{\eta}_{[i]}^{(2)}$ of the inclusion phase in the level-i LCC are specified to be

$$\mathbb{M}_{[1]}^{(2)} \to \infty, \quad \boldsymbol{\eta}_{[1]}^{(2)} = \mathbf{0} \quad \text{and} \quad \mathbb{M}_{[i]}^{(2)} = \widetilde{\mathbb{M}}_{[i-1]}, \quad \boldsymbol{\eta}_{[i]}^{(2)} = \widetilde{\boldsymbol{\eta}}_{[i-1]}, \quad i = 2, ..., N, \tag{3.49}$$

where $\widetilde{\mathbb{M}}_{[i]}$ and $\widetilde{\boldsymbol{\eta}}_{[i]}$ are the PCW estimates for the effective compliance tensor and the effective eigenstrain-rate tensor of the level-i LCC, respectively, as given by (3.67) and (3.68) in Appendix I.

In summary, the computation of the ISO estimates (3.48) requires the solution of $4K \times N$ nonlinear algebraic equations, as given by (3.40), (3.41) and (3.42), where the unknowns are the stress variables $\check{\tau}_{(k)}^{[i]}$ $(K \times N)$ and $\hat{\tau}_{(k)}^{[i]}$ $(K \times N)$, as well as the slip viscosities $\mu_{(k)}^{[i]}$ $(K \times N)$ and slip eigenstrain rates $\eta_{(k)}^{[i]}$ $(K \times N)$ for the LCC matrix at each iteration $(i = 1, ..., N;\ k = 1, ..., K)$. In general, this set of nonlinear algebraic equations has to be solved numerically by means of an appropriate method, e.g., Newton-Raphson method. Further details on the implementation are provided in Appendix II.

Retaining the distinctive advantages of the FOSO estimates (3.14), the ISO estimates (3.48) are exact to second order in the heterogeneity contrast. (This is because for weakly inhomogeneous materials, field fluctuations in the constituent phases are rather small and the ISO estimates are expected to be very similar to the corresponding FOSO estimates.) Moreover, the macroscopic behavior and field statistics of the nonlinear porous single crystal can be estimated directly from the suitably optimized LCC (Ponte Castañeda, 2015; Agoras and Ponte Castañeda, 2013). However, as will be seen in the next chapter, the ISO estimates (3.48) improve significantly over the FOSO estimates for small porosity and large nonlinearity, especially at large stress

triaxiality. In general, the accuracy of (3.48) improves progressively with increasing N. However, the fast convergence of ISO with increasing values of N allows the use of relatively small number of iterations N to obtain accurate results and, hence, $N = 10$ is used in this work, which can be shown to provide sufficiently accurate estimates (error within 1%) of the $N \to \infty$ ISO limits for the effective behavior of porous single crystals. On the other hand, for sufficiently large N, the specific values of the inclusion volume fractions $c_{[i]}^{(2)}$ $(i = 1, ..., N)$ will not significantly affect the accuracy of (3.48) and they can be simply chosen to be given by $c_{[i]}^{(2)} = f^{1/N}$ $(i = 1, ..., N)$ (Agoras and Ponte Castañeda, 2013). Finally, it is noted that the ISO estimates (3.48) reduce to the FOSO estimates (3.14) for $N = 1$, as they should.

Given that the macroscopic constitutive relation can be conveniently extracted from that of the LCC, the ISO estimates for the macroscopic strain rate $\overline{\mathbf{D}}$ of the nonlinear porous single crystal under the applied loading $\overline{\boldsymbol{\sigma}}$ can be obtained via

$$\overline{\mathbf{D}} = \frac{\partial \widetilde{u}^{\mathrm{ISO}}}{\partial \overline{\boldsymbol{\sigma}}}(\overline{\boldsymbol{\sigma}}) = \widetilde{\mathbb{M}}_{[N]}\overline{\boldsymbol{\sigma}} + \widetilde{\boldsymbol{\eta}}_{[N]}, \tag{3.50}$$

where we recall that $\widetilde{\mathbb{M}}_{[N]}$ and $\widetilde{\boldsymbol{\eta}}_{[N]}$ are the PCW estimates for the effective viscous compliance tensor and effective eigenstrain-rate tensor of the level-N LCC, as given by expressions (3.67) and (3.68) in Appendix I, respectively. Similar to (3.21), the macroscopic constitutive relation (3.50) is also nonlinear, due to the nonlinear dependence of $\widetilde{\mathbb{M}}_{[N]}$ and $\widetilde{\boldsymbol{\eta}}_{[N]}$ on $\overline{\boldsymbol{\sigma}}$. Moreover, the average strain rate $\overline{\mathbf{D}}^{(2)}$ and the average spin $\overline{\mathbf{W}}^{(2)}$ in the voids may also be determined consistently from those of the LCC, and their corresponding expressions are given by (3.78) and (3.83) in Appendix I, with $i = 1$ (i.e., $\overline{\mathbf{D}}^{(2)} = \overline{\mathbf{D}}_{[1]}^{(2)}$ and $\overline{\mathbf{W}}^{(2)} = \overline{\mathbf{W}}_{[1]}^{(2)}$).

Next, we compute the ISO estimates for the average slip rates $\overline{\gamma}_{(k)}$ $(k = 1, ..., K)$, as defined by (3.29), over different slip systems of the crystal matrix. Similar to the FOSO method, the $\overline{\gamma}_{(k)}$ can be estimated directly from those of the LCC, whose properties must be specified according to (3.42) and (3.49). However, due to the *non-uniform* distribution of the matrix phase in the LCC, we first compute the average slip rates over the crystal matrix at each iteration separately, and then compute their

appropriate weighted averages to obtain the corresponding average slip rates over the total crystal matrix. Similar to (3.29), define the average slip rates $\overline{\gamma}^{[i]}_{(k)}$ $(i = 1, ..., N,$ $k = 1, ..., K)$ over the level-i crystal matrix via

$$\overline{\mathbf{D}}^{(1)}_{[i]} = \sum_{k=1}^{K} \overline{\gamma}^{[i]}_{(k)} \boldsymbol{\mu}_{(k)}, \tag{3.51}$$

where $\overline{\mathbf{D}}^{(1)}_{[i]}$ denotes the average strain rate over the crystal matrix at level i. Following a procedure similar to that used for the derivation of (3.32), we have that

$$\overline{\gamma}^{[i]}_{(k)} = \frac{1}{2\mu^{[i]}_{(k)}} \overline{\tau}^{[i]}_{(k)} + \eta^{[i]}_{(k)} = \alpha \phi'_{(k)}(\check{\tau}^{[i]}_{(k)}) + (1-\alpha)\phi'_{(k)}(\hat{\tau}^{[i]}_{(k)}). \tag{3.52}$$

Again, we should emphasize that the $\overline{\gamma}^{[i]}_{(k)}$ are related to the average resolved shear stresses $\overline{\tau}^{[i]}_{(k)}$ through the linearized constitutive relations instead of the nonlinear ones, i.e., $\overline{\gamma}^{[i]}_{(k)} \neq \phi'_{(k)}(\overline{\tau}^{[i]}_{(k)})$.

Noting that the total volume fraction of the level-i crystal matrix (over the entire level-N composite) is given by

$$c^{M}_{[i]} = \left(\prod_{j=i+1}^{N} c^{(2)}_{[j]} \right) \left(1 - c^{(2)}_{[i]} \right), \tag{3.53}$$

and that the total volume fraction of the solid crystal matrix is simply given by $1 - f$, the average slip rates $\overline{\gamma}_{(k)}$ $(k = 1, ..., K)$ over the entire crystal matrix can be straightforwardly obtained from the weighted averages of $\overline{\gamma}^{[i]}_{(k)}$, namely

$$\overline{\gamma}_{(k)} = \sum_{i=1}^{N} \frac{c^{M}_{[i]}}{1-f} \overline{\gamma}^{[i]}_{(k)}. \tag{3.54}$$

After some manipulation, the $\overline{\gamma}_{(k)}$ $(k = 1, ..., K)$ may also be written as

$$\overline{\gamma}_{(k)} = \frac{1}{1-f} \left[\alpha \sum_{i=1}^{N} \left(c^{M}_{[i]} \phi'_{(k)}(\check{\tau}^{[i]}_{(k)}) \right) + (1-\alpha) \sum_{i=1}^{N} \left(c^{M}_{[i]} \phi'_{(k)}(\hat{\tau}^{[i]}_{(k)}) \right) \right], \tag{3.55}$$

with the $c^{M}_{[i]}$ given by (3.53), and the stress variables $\check{\tau}^{[i]}_{(k)}$ and $\hat{\tau}^{[i]}_{(k)}$—depending on

both the first and second moments of the stress field in the LCC—given by (3.40) and (3.41), respectively.

Finally, we should note that the ISO estimate (3.48) for $\widetilde{u}$ is also a generalization of the iterated variational homogenization (IVH) estimate of Song and Ponte Castañeda (2017a), which is related to the ISO estimate in the same fashion as the VH estimate (3.34) is related to the FOSO estimate (3.14). Similarly, the IVH estimate may be recovered from the ISO estimate by setting formally the eigenstrain-rate tensors $\boldsymbol{\eta}_{[i]}^{(1)} = \mathbf{0}$. In its final form, the IVH estimate for $\widetilde{u}$ can be written as

$$\widetilde{u}^{\mathrm{IVH}}(\overline{\boldsymbol{\sigma}}) = \sum_{i=1}^{N}\left(1 - c_{[i]}^{(2)}\right)\left(\prod_{j=i+1}^{N} c_{[j]}^{(2)}\right)\sum_{k=1}^{K}\phi_{(k)}(\hat{\tau}_{(k)}^{[i]}). \tag{3.56}$$

Here the stress variables $\hat{\tau}_{(k)}^{[i]}$ depend only on the second moments of the resolved shear stresses over the LCC matrix, and are given by

$$\hat{\tau}_{(k)}^{[i]} = \sqrt{\overline{\overline{\tau}}_{(k)}^{[i]}} = \sqrt{\boldsymbol{\mu}_{(k)} \cdot \langle \boldsymbol{\sigma} \otimes \boldsymbol{\sigma} \rangle_{[i]}^{(1)} \boldsymbol{\mu}_{(k)}}, \tag{3.57}$$

where the second moments $\langle \boldsymbol{\sigma} \otimes \boldsymbol{\sigma} \rangle_{[i]}^{(1)}$ may be computed by means of the PCW estimates (3.88) in Appendix I, with the $\boldsymbol{\eta}_{[i]}^{(1)} = \mathbf{0}$. In turn, the slip viscosities $\mu_{(k)}^{[i]}$ in the porous LCC are given by the "modified secant" conditions (Ponte Castañeda and Suquet, 1998)

$$\frac{1}{2\mu_{(k)}^{[i]}} = \frac{\phi'_{(k)}(\hat{\tau}_{(k)}^{[i]})}{\hat{\tau}_{(k)}^{[i]}}. \tag{3.58}$$

Similar to the VH estimate (3.34), the IVH estimate (3.56) is also known to be a rigorous lower bound for the effective potential $\widetilde{u}$. However, the IVH bound (3.56) is much tighter than the VH bound (3.34), especially at low porosity, high nonlinearity and high stress triaxiality (Song and Ponte Castañeda, 2017a).

3.5 Evolution equations for the microstructural variables

When the porous single crystal undergoes finite-strain deformation, the microstructural variables defined in (3.4) evolve with the deformation, thereby affecting the instantaneous macroscopic response of the porous single crystal. In this section, we develop the corresponding evolution laws for the microstructural variables (3.4)—characterizing both the "crystallographic" and "morphological" anisotropy of the porous single crystal.

Due to the presence of voids in the single-crystal matrix, the deformation fields in the matrix become highly inhomogeneous, leading to variations in the crystallographic orientation of the crystal lattice in the matrix phase. However, for the purposes of homogenization, it is sufficient to keep track of the *average* crystallographic orientation of the lattice during the deformation. Thus, the lattice will be assumed to rotate *rigidly* (on average) with the average "microstructural" (or "elastic") spin $\overline{\boldsymbol{\omega}}_e^{(1)}$ in the crystal matrix, leading to the following evolution laws for the associated crystallographic axes $\mathbf{l}_1$, $\mathbf{l}_2$ and $\mathbf{l}_3$

$$\dot{\mathbf{l}}_1 = \overline{\boldsymbol{\omega}}_e^{(1)}\mathbf{l}_1, \quad \dot{\mathbf{l}}_2 = \overline{\boldsymbol{\omega}}_e^{(1)}\mathbf{l}_2, \quad \dot{\mathbf{l}}_3 = \overline{\boldsymbol{\omega}}_e^{(1)}\mathbf{l}_3, \tag{3.59}$$

where $\overline{\boldsymbol{\omega}}_e^{(1)}$ is defined as the difference between the average "continuum" spin $\overline{\mathbf{W}}^{(1)}$ and the average "plastic" spin $\overline{\mathbf{W}}_p^{(1)}$ in the crystal matrix (Mandel, 1972), i.e.,

$$\overline{\boldsymbol{\omega}}_e^{(1)} = \overline{\mathbf{W}}^{(1)} - \overline{\mathbf{W}}_p^{(1)}. \tag{3.60}$$

In the above equation, $\overline{\mathbf{W}}^{(1)}$ may be simply obtained from the global average condition

$$\overline{\mathbf{W}}^{(1)} = \frac{1}{1-f}\left(\overline{\mathbf{W}} - f\overline{\mathbf{W}}^{(2)}\right), \tag{3.61}$$

where it is recalled that $\overline{\mathbf{W}}^{(2)}$ is the average spin tensor in the voids, which can be obtained consistently from the ISO procedure by means of expression (3.83) with

$i = 1$ (i.e., $\overline{\mathbf{W}}^{(2)} = \overline{\mathbf{W}}^{(2)}_{[1]}$). On the other hand, $\overline{\mathbf{W}}^{(1)}_p$ can be expressed in terms of the average slip rates $\overline{\gamma}_{(k)}$ (see equation (3.55)) in the crystal matrix:

$$\overline{\mathbf{W}}^{(1)}_p = \frac{1}{2}\sum_{k=1}^{K} \overline{\gamma}_{(k)} \left(\mathbf{m}_{(k)} \otimes \mathbf{n}_{(k)} - \mathbf{n}_{(k)} \otimes \mathbf{m}_{(k)} \right). \tag{3.62}$$

It should be emphasized here that while we are using only phase averages to describe the average evolution of the lattice vectors, the second moments have been used in the characterization of the LCC determining the quantities $\overline{\mathbf{W}}^{(1)}$ and $\overline{\mathbf{W}}^{(1)}_p$.

Considering the incompressibility of the crystal matrix, the volume change of the porous single crystal equals the volume change of the void phase. Therefore, the evolution of the porosity f is governed by (Gurson, 1977)

$$\dot{f} = (1 - f)\overline{D}_{kk}, \tag{3.63}$$

where we recall that $\overline{\mathbf{D}}$ is the macroscopic strain rate. Note that the void nucleation is not considered in the above equation, but can be readily incorporated by appropriate modifications of (3.63) (Tvergaard, 1990).

The evolution of the shape and orientation of the voids (and their distribution) depends on the local deformation field in a complicated fashion and is, in practice, impossible to determine exactly. However, for the purposes of a homogenization procedure, it is again sufficient to determine how the *average* shape and orientation of the voids (and their distribution) evolve. Following the work of Ponte Castañeda and Zaidman (1994), Kailasam and Ponte Castañeda (1998) and Aravas and Ponte Castañeda (2004), we assume that the evolution of the average shape and orientation of the voids (and their distribution) is determined by the average strain rate $\overline{\mathbf{D}}^{(2)}$ and the average spin $\overline{\mathbf{W}}^{(2)}$ in the void phase, such that the average shape of the voids (and their distribution) remains ellipsoidal, but can change its aspect ratios and orientation during the deformation process. With the above hypothesis, the evolution of the aspect ratios w_1 and w_2 are governed by the standard kinematical

relations

$$\dot{w}_1 = w_1\left(\overline{D}_{33}^{(2)'} - \overline{D}_{11}^{(2)'}\right), \quad \text{and} \quad \dot{w}_2 = w_2\left(\overline{D}_{33}^{(2)'} - \overline{D}_{22}^{(2)'}\right), \tag{3.64}$$

where $\overline{\mathbf{D}}^{(2)}$ can be consistently estimated from the ISO procedure by means of expression (3.78) with $i = 1$ (i.e., $\overline{\mathbf{D}}^{(2)} = \overline{\mathbf{D}}_{[1]}^{(2)}$), and primes in this section are used to denote tensor components relative to axes instantaneously coinciding with the principal directions $\mathbf{n}_1$, $\mathbf{n}_2$ and $\mathbf{n}_3$ of the ellipsoidal voids.

On the other hand, the evolution of the orientation vectors $\mathbf{n}_l$ ($l = 1, 2, 3$) along the three principal directions of the ellipsoidal voids (and their distribution) is governed by

$$\dot{\mathbf{n}}_1 = \overline{\boldsymbol{\omega}}^{(2)}\mathbf{n}_1, \quad \dot{\mathbf{n}}_2 = \overline{\boldsymbol{\omega}}^{(2)}\mathbf{n}_2, \quad \dot{\mathbf{n}}_3 = \overline{\boldsymbol{\omega}}^{(2)}\mathbf{n}_3. \tag{3.65}$$

Here $\overline{\boldsymbol{\omega}}^{(2)}$ is the spin of the Eulerian axes of the average deformation gradient of the voids (Aravas and Ponte Castañeda, 2004); its *non-zero* components are given by (Ogden, 1984)

$$\left(1 - \frac{w_q^2}{w_p^2}\right)\overline{\omega}_{pq}^{(2)'} = \left(1 - \frac{w_q^2}{w_p^2}\right)\overline{W}_{pq}^{(2)'} + \left(1 + \frac{w_q^2}{w_p^2}\right)\overline{D}_{pq}^{(2)'}, \quad p, q = 1, 2, 3, \quad p \neq q, \tag{3.66}$$

with $w_3 = a_3/a_3 = 1$. Note that for the special cases in which at least two of the aspect ratios are equal, e.g., $w_p = w_q$ ($p \neq q$), (3.66) has a clear interpretation, i.e., the principal directions of the voids should be chosen such that $\overline{D}_{pq}^{(2)'} = 0$ and $\overline{\omega}_{pq}^{(2)'} = \overline{W}_{pq}^{(2)'}$.

At this point, it is important to emphasize that separate evolution laws for the shape and orientation of the voids and their distribution could be taken into account, for example, by assuming that the shape and orientation of the void distribution evolve with the macroscopic strain rate $\overline{\mathbf{D}}$ and the macroscopic spin $\overline{\mathbf{W}}$ (Kailasam et al., 1997). However, for simplicity, this will not be pursued here, since we mainly focus on porous single crystals with low to moderate porosities prior to void coalescence, where the effect of the void distribution on the macroscopic behavior of the porous single crystal is not expected to be significant. Finally, it is remarked that strain hardening of the single-crystal matrix will be neglected in this work, again for simplicity, so that the reference flow stresses $(\tau_0)_{(k)}$ of all slip systems remain fixed

during the entire deformation process. However, the effect of matrix hardening can be easily incorporated by employing an appropriate hardening law for the crystal matrix, e.g., the phenomenological Voce-type hardening law (Balasubramanian and Anand, 2002).

In summary, the instantaneous effective constitutive relation (3.50), along with the evolution laws (3.59) and (3.63) to (3.65) for the microstructural variables (3.4), provide a complete viscoplastic model for the macroscopic response and field statistics of porous single crystals with general crystallographic anisotropy, general ellipsoidal voids, subjected to general, finite-strain loading conditions. In particular, the ISO model incorporates the effect of the lattice rotation, as well as the changing size, shape and orientation of the voids, capturing the complex coupled effect of the "crystallographic" and "morphological" anisotropy of the porous single crystals. The model requires only the initial lattice orientation, as well as the initial porosity and average shape and orientation of the voids, and can predict the evolution of these variables for prescribed loading conditions by straightforward numerical integration of the above-mentioned microstructural evolution laws. The integration of the ISO constitutive model can be effectively carried out by means of an explicit, forward-Euler integration scheme, as adopted in the work of Liu (2003). Finally, it should be emphasized that the ISO model is entirely predictive, since it does not make use of parameters to be fitted to finite element simulations or experimental results.

3.6 Concluding remarks

In this chapter, we have developed a finite-strain constitutive model for the macroscopic response of porous viscoplastic single crystals subjected to general three-dimensional loading conditions. The model makes use of the fully optimized second-order (FOSO) variational method of Ponte Castañeda (2015), in combination with an appropriate generalization of the iterated homogenization procedure of Agoras and Ponte Castañeda (2013), to determine the instantaneous effective response of porous single crystals, accounting for microstructural variables such as the average crystallo-

graphic orientation of the matrix, the porosity, and the average shape and orientation of the voids. In addition, consistent homogenization estimates for the average strain rate and spin in the matrix and void phases were used to derive the evolution laws for these microstructural variables. In its final form, the iterated second-order (ISO) homogenization model can be treated as a standard internal-variable viscoplastic model with the aforementioned microstructural variables playing the role of internal variables.

The new ISO model has several distinguishing advantages in comparison to other models that have been proposed in the literature for porous single crystals. First, the ISO model is the first model to consistently account for the evolution of both the "crystallographic" anisotropy induced by lattice rotation, as well as the "morphological" anisotropy induced by changes in size, shape and orientation of the voids. These distinctive features are crucial for the frame indifference of the resulting constitutive models. Second, the ISO methodology provides estimates that are exact to second order in the heterogeneity contrast for the instantaneous response of two-phase composite materials, and therefore improves on the recently developed iterated variational homogenization (IVH) model of Song and Ponte Castañeda (2017a), which provides bounds that are only exact to first order in the heterogeneity contrast. Correspondingly, the ISO model also provides improved estimates for the average strain rate and spin fields in the phases, thus leading to more accurate predictions for the evolution of the microstructure. As will be seen in chapter 4, the predictions of the ISO model for the special case of porous FCC single crystals are in fairly good agreement with the FEM results of Srivastava and Needleman (2012, 2015) for a wide range of loading conditions. Third, the ISO model applies for porous single crystals with general crystallographic anisotropy (e.g., cubic, hexagonal), general material nonlinearity and general ellipsoidal voids. Importantly, the ISO can be used for porous single crystals with large crystal anisotropy, where the flow stresses of different slip systems can be very different. For this reason, the ISO will be seen in chapter 4 to improve on the MVAR model of Mbiakop et al. (2015b), which made certain simplifications designed for porous single crystals with nearly equal flow stresses for all slip systems and is

expected to become less accurate for large crystal anisotropy (Mbiakop et al., 2015b). Fourth, with the choice made for the weight parameters α, the ISO model is 'predictive' in the sense that it does not require calibration by fitting of parameters to either numerical or experimental results. In other words, given the constitutive properties of the single-crystal matrix and the initial state of the microstructure, the ISO model can provide estimates for the time-dependent macroscopic response of the porous single crystals under general loading conditions. This is a major advantage relative to other more macroscopic models requiring recalibration/redevelopment for porous material with different matrix crystallography or void morphology, not to mention different constitutive properties (e.g., strain-rate sensitivity, etc) of the matrix phase. Having said this, the method is still subject to potential improvements by means of other, yet-to-be-developed choices of the weights α (that could be determined by either mathematically or physically motivated prescriptions). At the very least, the weights α could be used as fitting parameters, in particular, to improve the results for hydrostatic loadings. However, for simplicity, we have chosen not to pursue this strategy in this first application of the method for porous single crystals. Finally, it should be mentioned that the effects of elastic strains and matrix hardening that were neglected for simplicity in this work can be incorporated—at least approximately—into the ISO method in a relatively straightforward manner. This would allow the model to be implemented into constitutive subroutines for standard finite element codes (e.g., ABAQUS), as has already been done for porous materials with isotropic matrix phases (Aravas and Ponte Castañeda, 2004; Danas and Aravas, 2012).

3.7 Appendix I: Detailed expressions for the LCC in the ISO method

In this Appendix, explicit expressions for the macroscopic constitutive relation and field statistics of the LCC are provided. These expressions are needed for the ISO method and provide generalizations of corresponding expressions in the work of Ago-

ras and Ponte Castañeda (2013) and Song and Ponte Castañeda (2017a) for the simpler iterated variational homogenization (IVH) procedure. Different from the linearly viscous LCC that was used in the previous IVH approach, the LCC utilized in the new ISO method is linearly viscous with a general non-zero eigenstrain rate, being mathematically analogous to a linear thermoelastic material. In this context, it is important to mention that the expressions provided in this Appendix are obtained by means of the estimates of PCW type (Ponte Castañeda and Willis, 1995) for the LCC at each iteration step. In addition, the first and second moments of the fields in the matrix and inclusion phases of the LCC can be used directly to estimate the corresponding quantities in the actual nonlinear composite (Ponte Castañeda, 2015). Furthermore, as already mentioned, the shape and orientation of the voids are assumed to be identical to those of their distribution, for simplicity. However, more general expressions with different shapes and orientations of the voids and their distribution can be derived building on the work of Agoras and Ponte Castañeda (2013) for the IVH model.

We begin by recalling that the viscous compliance tensor $\mathbb{M}^{(1)}_{[i]}$ and the eigenstrain-rate tensor $\boldsymbol{\eta}^{(1)}_{[i]}$ of the matrix of the level-i LCC are given by (3.38). Then, the effective compliance tensor $\widetilde{\mathbb{M}}_{[i]}$ of the level-i LCC is given by

$$\widetilde{\mathbb{M}}_{[i]} = \mathbb{M}^{(1)}_{[i]} + c^{(2)}_{[i]} \left[\left(\widetilde{\mathbb{M}}_{[i-1]} - \mathbb{M}^{(1)}_{[i]} \right)^{-1} + (1 - c^{(2)}_{[i]}) \mathbb{Q}_{[i]} \right]^{-1}, \qquad i = 1, ..., N, \tag{3.67}$$

where it is recalled that the $c^{(2)}_{[i]}$ $(i = 1, ..., N)$ are the volume fractions of the inclusion phase in the level-i LCC, which can be simply chosen as $c^{(2)}_{[i]} = f^{1/N}$ $(i = 1, .., N)$, and the $\mathbb{Q}_{[i]}$ $(i = 1, ..., N)$ are fourth-order microstructural tensors, depending on the matrix compliance tensor $\mathbb{M}^{(1)}_{[i]}$ and the shape and orientation of the voids, which may be computed via equation (3.11) (with $\mathbb{M}^{(1)}$ in (3.11) replaced by $\mathbb{M}^{(1)}_{[i]}$). Note that $\widetilde{\mathbb{M}}_{[0]} \to \infty$ in (3.67), representing the compliance tensor of the voided inclusion in the first level LCC. Note further that the matrix compliance tensor $\mathbb{M}^{(1)}_{[i]}$ is singular due to the incompressibility of the single-crystal matrix. Therefore, it is necessary to add a "fictitious" compressible term $1/(3\kappa)\mathbb{J}$ ($\mathbb{J}$ is the standard fourth-order spherical pro-

jection tensor) to $\mathbb{M}_{[i]}^{(1)}$ and take the appropriate incompressibility limit (i.e., $\kappa \to \infty$) when evaluating the kernel of the integral (3.11). However, the resulting expressions are too complicated and will not be reported here for brevity.

On the other hand, the effective eigenstrain-rate tensor $\widetilde{\boldsymbol{\eta}}_{[i]}$ of the level-i LCC is given by

$$\widetilde{\boldsymbol{\eta}}_{[i]} = \boldsymbol{\eta}_{[i]}^{(1)} + c_{[i]}^{(2)} \left(\mathbb{B}_{[i]}^{(2)}\right)^T \left(\widetilde{\boldsymbol{\eta}}_{[i-1]} - \boldsymbol{\eta}_{[i]}^{(1)}\right), \qquad i = 1, ..., N, \tag{3.68}$$

where the $\mathbb{B}_{[i]}^{(2)}$ are the corresponding stress-concentration tensors provided by

$$\mathbb{B}_{[i]}^{(2)} = \left[\mathbb{I} + (1 - c_{[i]}^{(2)})\mathbb{Q}_{[i]} \left(\widetilde{\mathbb{M}}_{[i-1]} - \mathbb{M}_{[i]}^{(1)}\right)\right]^{-1}, \quad i = 1, ..., N, \tag{3.69}$$

with $\mathbb{I}$ denoting the fully symmetric fourth-order identity tensor. Note that $\widetilde{\boldsymbol{\eta}}_{[0]} = \mathbf{0}$ in (3.68), denoting the eigenstrain-rate tensor of the voided inclusion in the first level LCC.

The associated PCW estimates for the volume averages of the stress and strain-rate fields over the phases of each level LCC may also be determined iteratively following the work of Agoras and Ponte Castañeda (2013). In particular, letting $\overline{\boldsymbol{\sigma}}_{[i]}^{(2)} = \langle \boldsymbol{\sigma} \rangle_{[i]}^{(2)}$ $(i = 1, ..., N)$ denote the average stress field over the inclusion phase in the level-i LCC, it follows that $\overline{\boldsymbol{\sigma}}_{[i]}^{(2)}$ is determined by

$$\overline{\boldsymbol{\sigma}}_{[i]}^{(2)} = \mathbb{B}_{[i]}^{(2)} \overline{\boldsymbol{\sigma}}_{[i]} + \mathbf{b}_{[i]}^{(2)}, \quad i = 1, ..., N. \tag{3.70}$$

Here we recall that $\overline{\boldsymbol{\sigma}}_{[i]}$ is the average stress field over the level-i LCC, and the $\mathbb{B}_{[i]}^{(2)}$ and $\mathbf{b}_{[i]}^{(2)}$ $(i = 1, ..., N)$ are the associated stress-concentration tensors, with $\mathbb{B}_{[i]}^{(2)}$ provided by (3.69) and $\mathbf{b}_{[i]}^{(2)}$ given by

$$\mathbf{b}_{[i]}^{(2)} = \left(1 - c_{[i]}^{(2)}\right) \mathbb{B}_{[i]}^{(2)} \mathbb{Q}_{[i]} \left(\boldsymbol{\eta}_{[i]}^{(1)} - \widetilde{\boldsymbol{\eta}}_{[i-1]}\right), \quad i = 1, ..., N. \tag{3.71}$$

Next, making use of (3.70) recursively for $i = N, ..., 1$, together with the facts that

$$\overline{\boldsymbol{\sigma}}_{[N]} = \overline{\boldsymbol{\sigma}} \quad \text{and} \quad \overline{\boldsymbol{\sigma}}_{[i-1]} = \overline{\boldsymbol{\sigma}}_{[i]}^{(2)}, \quad i = N, ..., 2, \tag{3.72}$$

it can be shown that $\overline{\boldsymbol{\sigma}}_{[i]}^{(2)}$ may be written in terms of the macroscopic stress $\overline{\boldsymbol{\sigma}}$ and the associated stress-concentration tensors $\mathbb{B}_{[i]}^{(2)}$ and $\mathbf{b}_{[i]}^{(2)}$ as

$$\overline{\boldsymbol{\sigma}}_{[i]}^{(2)} = \left[\prod_{j=i}^{N} \mathbb{B}_{[j]}^{(2)}\right]\overline{\boldsymbol{\sigma}} + \sum_{j=i+1}^{N}\left(\prod_{k=i}^{j-1} \mathbb{B}_{[k]}^{(2)}\right)\mathbf{b}_{[j]}^{(2)} + \mathbf{b}_{[i]}^{(2)}, \quad i = 1, ..., N. \tag{3.73}$$

Similarly, the average strain rate $\overline{\mathbf{D}}_{[i]}^{(2)}$ over the inclusion phase of the level-i LCC is given by

$$\overline{\mathbf{D}}_{[i]}^{(2)} = \mathbb{A}_{[i]}^{(2)}\overline{\mathbf{D}}_{[i]} + \mathbf{a}_{[i]}^{(2)}, \quad i = 1, ..., N, \tag{3.74}$$

where $\overline{\mathbf{D}}_{[i]} = \langle \mathbf{D} \rangle_{[i]}$ $(i = 1, ..., N)$ denotes the average strain-rate field over the level-i LCC, and the $\mathbb{A}_{[i]}^{(2)}$ and $\mathbf{a}_{[i]}^{(2)}$ $(i = 1, ..., N)$ are the associated strain-rate concentration tensors given by

$$\mathbb{A}_{[i]}^{(2)} = \left\{c_{[i]}^{(2)}\mathbb{I} + (1 - c_{[i]}^{(2)})\left[\left(\mathbb{M}_{[i]}^{(1)} - \mathbb{M}_{[i]}^{(1)}\mathbb{Q}_{[i]}\mathbb{M}_{[i]}^{(1)}\right)\left(\widetilde{\mathbb{M}}_{[i-1]}\right)^{-1} + \mathbb{M}_{[i]}^{(1)}\mathbb{Q}_{[i]}\right]\right\}^{-1}, \quad i = 1, ..., N, \tag{3.75}$$

and

$$\mathbf{a}_{[i]}^{(2)} = -\left(1 - c_{[i]}^{(2)}\right)\mathbb{A}_{[i]}^{(2)}\left(\mathbb{I} - \mathbb{M}_{[i]}^{(1)}\mathbb{Q}_{[i]}\right)\left(\boldsymbol{\eta}_{[i]}^{(1)} - \mathbb{M}_{[i]}^{(1)}\widetilde{\mathbb{M}}_{[i-1]}^{-1}\widetilde{\boldsymbol{\eta}}_{[i-1]}\right), \quad i = 1, ..., N. \tag{3.76}$$

Following a development completely analogous to that used above for the derivation of (3.73), and accounting for the relations

$$\overline{\mathbf{D}}_{[N]} = \overline{\mathbf{D}} \quad \text{and} \quad \overline{\mathbf{D}}_{[i-1]} = \overline{\mathbf{D}}_{[i]}^{(2)}, \quad i = N, ..., 2, \tag{3.77}$$

$\overline{\mathbf{D}}_{[i]}^{(2)}$ may be written in terms of the macroscopic strain rate $\overline{\mathbf{D}}$ and the associated strain-rate concentration tensors $\mathbb{A}_{[i]}^{(2)}$ and $\mathbf{a}_{[i]}^{(2)}$ as

$$\overline{\mathbf{D}}_{[i]}^{(2)} = \left[\prod_{j=i}^{N} \mathbb{A}_{[j]}^{(2)}\right]\overline{\mathbf{D}} + \sum_{j=i+1}^{N}\left(\prod_{k=i}^{j-1} \mathbb{A}_{[k]}^{(2)}\right)\mathbf{a}_{[j]}^{(2)} + \mathbf{a}_{[i]}^{(2)}, \quad i = 1, ..., N. \tag{3.78}$$

Correspondingly, the average spin field over the inclusion phase of the level-i LCC

can also be obtained by means of the PCW estimate

$$\overline{\mathbf{W}}^{(2)}_{[i]} = \overline{\mathbf{W}}_{[i]} - \mathbb{C}^{(2)}_{[i]}\overline{\mathbf{D}}_{[i]} - \boldsymbol{\beta}^{(2)}_{[i]}, \quad i = 1, ..., N, \tag{3.79}$$

where the $\overline{\mathbf{W}}_{[i]} = \langle \mathbf{W} \rangle_{[i]}$ $(i = 1, ..., N)$ are the average spin field over the level-i LCC, and the $\mathbb{C}^{(2)}_{[i]}$ and $\boldsymbol{\beta}^{(2)}_{[i]}$ $(i = 1, ..., N)$ are the associated spin-concentration tensors determined by

$$\mathbb{C}^{(2)}_{[i]} = \left(1 - c^{(2)}_{[i]}\right) \boldsymbol{\Pi}_{[i]} \left(\mathbb{M}^{(1)}_{[i]} \widetilde{\mathbb{M}}^{-1}_{[i-1]} - \mathbb{I}\right) \mathbb{A}^{(2)}_{[i]}, \quad i = 1, ..., N, \tag{3.80}$$

and

$$\boldsymbol{\beta}^{(2)}_{[i]} = \left(1 - c^{(2)}_{[i]}\right) \boldsymbol{\Pi}_{[i]} \left[\left(\mathbb{M}^{(1)}_{[i]} \widetilde{\mathbb{M}}^{-1}_{[i-1]} - \mathbb{I}\right) \mathbf{a}^{(2)}_{[i]} + \boldsymbol{\eta}^{(1)}_{[i]} - \mathbb{M}^{(1)}_{[i]} \left(\widetilde{\mathbb{M}}_{[i-1]}\right)^{-1} \widetilde{\boldsymbol{\eta}}_{[i-1]}\right], \quad i = 1, ..., N. \tag{3.81}$$

Here the $\boldsymbol{\Pi}_{[i]}$ $(i = 1, ..., N)$ are fourth-order Eshelby rotation tensors depending on the matrix compliance tensor $\mathbb{M}^{(1)}_{[i]}$ and the shape and orientation of the voids, which can be computed via (3.28) (with $\mathbb{M}^{(1)}$ replaced by $\mathbb{M}^{(1)}_{[i]}$). Making use of (3.79) recursively for $i = N, ..., 1$, and accounting for the relations

$$\overline{\mathbf{W}}_{[N]} = \overline{\mathbf{W}} \quad \text{and} \quad \overline{\mathbf{W}}_{[i-1]} = \overline{\mathbf{W}}^{(2)}_{[i]}, \quad i = N, ..., 2, \tag{3.82}$$

$\overline{\mathbf{W}}^{(2)}_{[i]}$ may be written in the form

$$\overline{\mathbf{W}}^{(2)}_{[i]} = \overline{\mathbf{W}} - \left(\sum_{j=i}^{N} \mathbb{C}^{(2)}_{[j]} \overline{\mathbf{D}}_{[j]}\right) - \sum_{j=i}^{N} \boldsymbol{\beta}^{(2)}_{[j]}, \quad i = 1, ..., N, \tag{3.83}$$

where we recall that the $\overline{\mathbf{D}}_{[i]}$ $(i = 1, ..., N)$ are determined by (3.77) and (3.78). In this connection, it should be mentioned that the corresponding average fields over the vacuous inclusion of the porous LCC can be obtained from equation (3.73), (3.78) and (3.83), respectively, with $i = 1$ (i.e., $\overline{\boldsymbol{\sigma}}^{(2)} = \overline{\boldsymbol{\sigma}}^{(2)}_{[1]}$, $\overline{\mathbf{D}}^{(2)} = \overline{\mathbf{D}}^{(2)}_{[1]}$ and $\overline{\mathbf{W}}^{(2)} = \overline{\mathbf{W}}^{(2)}_{[1]}$).

The average stress and strain rate fields over the matrix phase of the level-i LCC

can be easily obtained from the global average conditions, that is,

$$\overline{\boldsymbol{\sigma}}_{[i]}^{(1)} = \frac{1}{1-c_{[i]}^{(2)}}\left(\overline{\boldsymbol{\sigma}}_{[i]} - c_{[i]}^{(2)}\overline{\boldsymbol{\sigma}}_{[i]}^{(2)}\right) \quad \text{and} \quad \overline{\mathbf{D}}_{[i]}^{(1)} = \frac{1}{1-c_{[i]}^{(2)}}\left(\overline{\mathbf{D}}_{[i]} - c_{[i]}^{(2)}\overline{\mathbf{D}}_{[i]}^{(2)}\right), \quad i = 1, ..., N. \tag{3.84}$$

Finally, the effective stress potential of the level-i LCC may be written in the form

$$\widetilde{u}_{L[i]}\left(\overline{\boldsymbol{\sigma}}_{[i]}\right) = \frac{1}{2}\overline{\boldsymbol{\sigma}}_{[i]} \cdot \widetilde{\mathbb{M}}_{[i]}\overline{\boldsymbol{\sigma}}_{[i]} + \widetilde{\boldsymbol{\eta}}_{[i]} \cdot \overline{\boldsymbol{\sigma}}_{[i]} + \frac{1}{2}\widetilde{g}_{[i]}, \quad i = 1, ..., N, \tag{3.85}$$

where the $\widetilde{\mathbb{M}}_{[i]}$ and $\widetilde{\boldsymbol{\eta}}_{[i]}$ $(i = 1, ..., N)$ are determined by expressions (3.67)-(3.73), and the $\widetilde{g}_{[i]}$ $(i = 1, ..., N)$ denote the corresponding effective energy under zero applied stress, and are given by

$$\widetilde{g}_{[i]} = c_{[i]}^{(2)}\left[\left(\widetilde{\boldsymbol{\eta}}_{[i-1]} - \boldsymbol{\eta}_{[i]}^{(1)}\right) \cdot \mathbf{b}_{[i]}^{(2)} + \widetilde{g}_{[i-1]}\right], \quad i = 1, ..., N, \tag{3.86}$$

with $\widetilde{g}_{[0]} = 0$ representing the energy at zero stress of the voided inclusion in the first level LCC. Then, the second moment of the stress field in the matrix of the level-i LCC can be computed by differentiation of expression (3.85) with respect to $\mathbb{M}_{[i]}^{(1)}$ to obtain the result that

$$\langle \boldsymbol{\sigma} \otimes \boldsymbol{\sigma} \rangle_{[i]}^{(1)} = \frac{1}{1-c_{[i]}^{(2)}}\left(\overline{\boldsymbol{\sigma}}_{[i]} \cdot \frac{\partial \widetilde{\mathbb{M}}_{[i]}}{\partial \mathbb{M}_{[i]}^{(1)}}\overline{\boldsymbol{\sigma}}_{[i]} + 2\frac{\partial \widetilde{\boldsymbol{\eta}}_{[i]}}{\partial \mathbb{M}_{[i]}^{(1)}} \cdot \overline{\boldsymbol{\sigma}}_{[i]} + \frac{\partial \widetilde{g}_{[i]}}{\partial \mathbb{M}_{[i]}^{(1)}}\right), \quad i = 1, ..., N, \tag{3.87}$$

where $\partial\widetilde{\mathbb{M}}_{[i]}/\partial\mathbb{M}_{[i]}^{(1)}$, $\partial\widetilde{\boldsymbol{\eta}}_{[i]}/\partial\mathbb{M}_{[i]}^{(1)}$ and $\partial\widetilde{g}_{[i]}/\partial\mathbb{M}_{[i]}^{(1)}$ are eighth-, sixth- and fourth-order tensors, respectively. Note that the first and second terms on the right-hand side of (3.87) involve the summation over indices corresponding to the numerators of the eighth- and sixth-order tensors, respectively. After some calculations, expression (3.87) can be further rewritten as

$$\begin{aligned}\langle \boldsymbol{\sigma} \otimes \boldsymbol{\sigma} \rangle_{[i]}^{(1)} = {} & \overline{\boldsymbol{\sigma}}_{[i]}^{(1)} \otimes \overline{\boldsymbol{\sigma}}_{[i]}^{(1)} - \frac{1}{c_{[i]}^{(2)}}\left(\overline{\boldsymbol{\sigma}}_{[i]}^{(1)} - \overline{\boldsymbol{\sigma}}_{[i]}\right) \otimes \left(\overline{\boldsymbol{\sigma}}_{[i]}^{(1)} - \overline{\boldsymbol{\sigma}}_{[i]}\right) - \\ & \frac{1}{c_{[i]}^{(2)}}\left[\mathbb{Q}_{[i]}^{-1}\left(\overline{\boldsymbol{\sigma}}_{[i]}^{(1)} - \overline{\boldsymbol{\sigma}}_{[i]}\right)\right] \cdot \frac{\partial \mathbb{Q}_{[i]}}{\partial \mathbb{M}_{[i]}^{(1)}}\left[\mathbb{Q}_{[i]}^{-1}\left(\overline{\boldsymbol{\sigma}}_{[i]}^{(1)} - \overline{\boldsymbol{\sigma}}_{[i]}\right)\right], \quad i = 1, ..., N,\end{aligned} \tag{3.88}$$

where $\partial\mathbb{Q}_{[i]}/\partial\mathbb{M}^{(1)}_{[i]}$ is an eighth-order tensor that can be computed via equation (3.11), with the kernel of the integral (3.11) replaced by its derivative with respect to the matrix compliance tensor. Note that the last term of (3.88) also involves the summation over indices corresponding to the numerator of $\partial\mathbb{Q}_{[i]}/\partial\mathbb{M}^{(1)}_{[i]}$.

3.8 Appendix II: Numerical aspects of the ISO model

In this Appendix, we briefly summarize the procedure for computing the ISO estimates (3.48) in Section 6.3.2, characterizing the instantaneous response of the porous single crystal with a fixed state of the microstructure (as described by the microstructural variables (3.4)). For finite-strain deformation, the microstructural variables (3.4) are updated by integrating the evolution laws (3.59) and (3.63)-(3.65) provided in Section 3.5 using an explicit forward-Euler scheme. The numerical integration of the evolution laws has been discussed in detail for porous isotropic materials by Aravas and Ponte Castañeda (2004) (see also Danas and Ponte Castañeda, 2009a), and will not be repeated here for brevity.

As already discussed in Section 6.3.2, the determination of the ISO estimates (3.48) requires the solution of $4N\times K$ nonlinear algebraic equations (3.40), (3.41) and (3.42) for the unknown variables $\check{\tau}^{[i]}_{(k)}$, $\hat{\tau}^{[i]}_{(k)}$, $\mu^{[i]}_{(k)}$ and $\eta^{[i]}_{(k)}$ $(i = 1,...,N;\ k = 1,...,K)$. Here the stress variables $\check{\tau}^{[i]}_{(k)}$ and $\hat{\tau}^{[i]}_{(k)}$ are chosen to be the *primary* unknowns, while the slip viscosities $\mu^{[i]}_{(k)}$ and slip eigenstrain rates $\eta^{[i]}_{(k)}$ are taken to be functions of the primary unknowns, as given by (3.42). The original problem is then reduced to the solution of $2N\times K$ nonlinear equations, as given by (3.40) and (3.41), for the primary unknowns $\check{\tau}^{[i]}_{(k)}$ and $\hat{\tau}^{[i]}_{(k)}$ $(i = 1,...,N;\ k = 1,...,K)$. The above set of $2N\times K$ nonlinear equations can be efficiently solved by means of Newton-Raphson method as follows.

1. For a prescribed macroscopic stress $\overline{\boldsymbol{\sigma}}$, initial guesses for the primary unknowns $\check{\tau}^{[i]}_{(k)}$ and $\hat{\tau}^{[i]}_{(k)}$ $(i = 1,...,N;\ k = 1,...,K)$ are assumed.

2. With current guesses of $\check{\tau}^{[i]}_{(k)}$ and $\hat{\tau}^{[i]}_{(k)}$, the slip viscosities $\mu^{[i]}_{(k)}$ and eigenstrain

rates $\eta_{(k)}^{[i]}$ $(i = 1, ..., N;\ k = 1, ..., K)$ are computed by means of (3.42), and the viscous compliance tensor $\mathbb{M}_{[i]}^{(1)}$ and eigenstrain rate tensor $\boldsymbol{\eta}_{[i]}^{(1)}$ $(i = 1, ..., N)$ are computed by means of (3.38) for the LCC matrix at each iteration.

3. The effective compliance tensor $\widetilde{\mathbb{M}}_{[i]}$, the effective eigenstrain rate tensor $\widetilde{\boldsymbol{\eta}}_{[i]}$, as well as the corresponding stress concentration tensors $\mathbb{B}_{[i]}^{(2)}$ and $\mathbf{b}_{[i]}^{(2)}$ $(i = 1, ..., N)$, for the LCC at each iteration are computed by means of equations (3.67)-(3.69) and (3.71). Note that this step requires the computation of the fourth-order tensors $\mathbb{Q}_{[i]}$ $(i = 1, ..., N)$, whose components are two-dimensional integrals (see (3.11)) that need to be evaluated numerically in general (see below).

4. The first and second moments of the stress field over the LCC matrix at each iteration, $\overline{\boldsymbol{\sigma}}_{[i]}^{(1)}$ and $\langle \boldsymbol{\sigma} \otimes \boldsymbol{\sigma} \rangle_{[i]}^{(1)}$ $(i = 1, ..., N)$, are computed via equations (3.72), (3.73), $(3.84)_1$ and (3.88). Then, the first and second moments of the resolved shear stresses $\overline{\tau}_{(k)}^{[i]}$ and $\overline{\overline{\tau}}_{(k)}^{[i]}$ $(i = 1, ..., N;\ k = 1, ..., K)$ are computed by projecting the corresponding stress moments on the Schimid tensor $\boldsymbol{\mu}_{(k)}$ for each slip system in the LCC matrix (see their detailed expressions in the paragraph after equation (3.41)). Note that the computation of the second moment by (3.88) requires the evaluation of the eighth-order tensors $\partial \mathbb{Q}_{[i]} / \partial \mathbb{M}_{[i]}^{(1)}$ $(i = 1, ..., N)$, whose components are also two-dimensional integrals that need to be evaluated numerically in general, constituting the most sensitive and time-consuming part for the implementation of the ISO model (see below).

5. The residues are computed for equations (3.40) and (3.41). If the sum of the magnitudes of the residues is smaller than a prescribed tolerance (typically 10^{-8}), convergence is reached. If not, the Jacobian is computed to update the solutions for $\check{\tau}_{(k)}^{[i]}$ and $\hat{\tau}_{(k)}^{[i]}$. Then, steps 2-5 are repeated until convergence is reached.

As a final remark, the integrals required in the computation of $\mathbb{Q}_{[i]}$ and $\partial \mathbb{Q}_{[i]} / \partial \mathbb{M}_{[i]}^{(1)}$ $(i = 1, ..., N)$ are evaluated by means of a two-dimensional Gaussian quadrature integration scheme. Details for the calculation of these integrals have been discussed

thoroughly in Appendix 2 of Liu et al. (2003) and will not be repeated here for brevity. However, we should emphasize that these integrals depend on the matrix compliance tensor $\mathbb{M}_{[i]}^{(1)}$ as well as the shape and orientation of the voids. In particular, when the compliance tensor $\mathbb{M}_{[i]}^{(1)}$ is strongly anisotropic, or when the shape of the voids is significantly distorted (i.e., the aspect ratios of the voids are very different from unity), a relatively large number of Gaussian integration points are needed to guarantee the accuracy of these integrals. The number of Gaussian points considered in the application of the ISO model is provided in chapter 4 of this work.

Chapter 4

Iterated second-order homogenization model for viscoplastic porous single crystals: Applications

In chapter 3, a new homogenization-based constitutive model was developed for the finite-strain, macroscopic response of porous viscoplastic single crystals. In this chapter, the new model is first used to investigate the instantaneous response and the evolution of the microstructure for porous FCC single crystals for a wide range of loading conditions. The loading orientation, Lode angle and stress triaxiality are found to have significant effects on the evolution of porosity and average void shape, which play crucial roles in determining the overall hardening/softening behavior of porous single crystals. The predictions of the model are found to be in fairly good agreement with numerical simulations available from the literature for all loadings considered, especially for low triaxiality conditions. The model is then used to investigate the strong effect of crystal anisotropy on the instantaneous response and the evolution of the microstructure for porous HCP single crystals. For uniaxial tension and compression, the overall hardening/softening behavior of porous HCP crystals is

found to be controlled mostly by the evolution of void shape, and not so much by the evolution of porosity. In particular, porous HCP crystals exhibit overall hardening behavior with increasing porosity, while they exhibit overall softening behavior with decreasing porosity. This interesting behavior is consistent with corresponding results for porous FCC crystals, but is found to be more significant for porous HCP crystals with large anisotropy, such as porous ice, where the non-basal slip systems are much harder than the basal systems.

4.1 Introduction

In chapter 3, we have developed a homogenization-based constitutive model for the characterization of both the instantaneous macroscopic response, as well as the evolution of the microstructure, for porous viscoplastic single crystals subjected to general three-dimensional loading conditions. The model is based on the fully-optimized second-order variational approach of Ponte Castañeda (2015) used in iterated fashion (Agoras and Ponte Castañeda, 2013), and is referred to as the Iterated Second-Order (ISO) homogenization model. The ISO model is capable of accounting for the evolution of the "crystallographic" anisotropy induced by lattice rotation, as well as that of the "morphological" anisotropy due to changes in size, shape and orientation of the voids. In particular, the internal variables serving to characterize the underlying microstructure of porous single crystals have been defined by the set

$$\mathbf{s} \equiv \{\mathbf{l}_1, \mathbf{l}_2, \mathbf{l}_3, f, w_1, w_2, \mathbf{n}_1, \mathbf{n}_2, \mathbf{n}_3\}, \tag{4.1}$$

where $\mathbf{l}_1$, $\mathbf{l}_2$ and $\mathbf{l}_3$ are the three linearly independent crystallographic axes of the lattice, f is the porosity, $w_1 = a_3/a_1, w_2 = a_3/a_2$ are the two aspect ratios characterizing the *average* shape (and distribution) of the ellipsoidal voids (a_1, a_2 and a_3 are the lengths of the three semi-axes of the ellipsoidal voids), and $\mathbf{n}_1$, $\mathbf{n}_2$ and $\mathbf{n}_3$ are unit vectors along the three principal directions of the ellipsoidal voids (see Fig. 3.1).

This chapter is concerned with the applications of the ISO model for two different

types of porous single crystals: (*i*) porous (high-symmetry) FCC single crystals and (*ii*) porous (low-symmetry) HCP single crystals. Specifically, we will first investigate the instantaneous response (section 4.2) and the evolution of the microstructure (section 4.3) for porous FCC single crystals subjected to triaxial loadings with different stress triaxialities, Lode angles and loading orientations (relative to the crystal lattice axes). The complex, coupled effect of the intrinsic crystallographic anisotropy and the deformation-induced morphological anisotropy will be explored. The predictions of the ISO model will also be compared with those of earlier models and numerical results available from the literature in order to validate the model. We will also make use of the ISO model to predict the instantaneous response, as well as the evolution of the microstructure (section 4.4), for porous HCP single crystals, such as porous ice, under axisymmetric loadings. In particular, the effect of the crystal anisotropy on the macroscopic response of the porous HCP crystals will be investigated in some detail. Finally, we summarize our findings and provide some concluding remarks in section 4.5.

4.2 Porous FCC single crystals: Instantaneous macroscopic response

In this section, we consider the application of the ISO model to generate estimates for the instantaneous macroscopic response of porous FCC single crystals. The high-symmetry, FCC single crystals are assumed to deform by dislocation glide on a set of four slip planes of the type $\{111\}$, along three slip directions (per plane) of the type $\langle 110 \rangle$, which constitute the set of twelve primary octahedral slip systems with appropriately defined Schmid tensor $\boldsymbol{\mu}_{(k)}$ (see equation (3.2) for its definition). Among these, five are linearly independent, thus allowing arbitrary (isochoric) plastic deformation for the single crystal. For simplicity, all slip systems are assumed to have the same reference flow stresses, i.e., $(\tau_0)_{(k)} = \tau_0$ $(k = 1, ..., 12)$, and hardening is neglected. In addition, the reference strain rate $\dot{\gamma}_0$ and the creep exponent n are also assumed

to be identical for all slip systems (see equation (3.3)). Following the work of Srivastava and Needleman (2015), these material parameters are taken to be $\tau_0 = 245\text{MPa}$, $\dot{\gamma}_0 = 1.53 \times 10^{-9}\text{s}^{-1}$ and $n = 5$, corresponding to Ni-based single-crystal superalloys.

In general, the effective behavior of porous FCC single crystals depends on the applied stress $\overline{\boldsymbol{\sigma}}$ and the microstructure, as characterized by the set of microstructural variables $\mathbf{s}$ defined in (4.1). For simplicity, we consider a *fixed* crystal orientation with the [100], [010] and [001] crystallographic orientations aligned with the laboratory frame axes $\mathbf{e}_1$, $\mathbf{e}_2$ and $\mathbf{e}_3$, respectively. (Note that $\mathbf{l}_1$, $\mathbf{l}_2$ and $\mathbf{l}_3$ in (4.1) can be simply chosen to be the [100], [010] and [001] crystallographic axes, respectively.) However, we allow the principal directions of the applied stress $\overline{\boldsymbol{\sigma}}$ to be aligned with possibily different crystallographic orientations. For simplicity, we further assume that the principal axes of the ellipsoidal voids $\mathbf{n}_1$, $\mathbf{n}_2$ and $\mathbf{n}_3$ are aligned with the principal loading directions, and we will confine our attention to the effects of the loading orientation, porosity and void shape on the instantaneous response of porous FCC crystals, leaving consideration of void orientations for future work.

Next, we briefly recall the definition for the *gauge surface*. From the homogeneity of the local potential $u^{(1)}$ in $\boldsymbol{\sigma}$, it follows that the effective potential $\widetilde{u}(\overline{\boldsymbol{\sigma}})$ of the porous single crystal is a positively homogeneous function of degree $n+1$ in $\overline{\boldsymbol{\sigma}}$. Then, the effective behavior of the porous single crystal may be conveniently described by means of the gauge surface, generalizing the notion of the yield surface from standard plasticity to viscoplasticity (Leblond et al., 1994). Thus, the effective stress potential $\widetilde{u}(\overline{\boldsymbol{\sigma}})$ can be expressed in the form

$$\widetilde{u}(\overline{\boldsymbol{\sigma}}) = \frac{\dot{\gamma}_0 \tilde{\tau}_0}{n+1} \left(\frac{\Gamma(\overline{\boldsymbol{\sigma}})}{\tilde{\tau}_0} \right)^{n+1}, \tag{4.2}$$

where $\tilde{\tau}_0$ is a reference flow stress, which can be chosen to be, e.g., one of the reference flow stresses $(\tau_0)_{(k)}$ $(k = 1, ..., K)$, and $\Gamma(\overline{\boldsymbol{\sigma}})$ is the gauge factor, depending on the creep exponent n, the microstructural variables $\mathbf{s}$ defined in (4.1), and the reference flow stresses $(\tau_0)_{(k)}$, $k = 1, ..., K$. As already mentioned, for the porous FCC single crystals of interest in this section, all the reference flow stresses are identical and $\tilde{\tau}_0$

will be set equal to τ_0. Then, noting that $\Gamma(\overline{\boldsymbol{\sigma}})$ is homogeneous of degree 1 in $\overline{\boldsymbol{\sigma}}$, it follows that the normalized stress tensor

$$\overline{\boldsymbol{\Sigma}}(\overline{\boldsymbol{\sigma}}) = \frac{\overline{\boldsymbol{\sigma}}}{\Gamma(\overline{\boldsymbol{\sigma}})} \tag{4.3}$$

is homogeneous of degree 0 in $\overline{\boldsymbol{\sigma}}$. Making use of the relation (4.2), along with the fact that $\Gamma(\overline{\boldsymbol{\sigma}})$ is homogeneous of degree 1 in $\overline{\boldsymbol{\sigma}}$, we can easily see that $\overline{\boldsymbol{\Sigma}}(\overline{\boldsymbol{\sigma}})$ will always lie on an equi-potential surface

$$\widetilde{u}(\overline{\boldsymbol{\Sigma}}) = \frac{\dot{\gamma}_0 \tilde{\tau}_0^{-n}}{n+1}, \tag{4.4}$$

which is defined to be the *gauge surface*. Therefore, the stress tensor $\overline{\boldsymbol{\Sigma}}$ on the gauge surface may be conveniently obtained by computing the stress potential $\widetilde{u}$ for $\overline{\boldsymbol{\sigma}}$ of arbitrary magnitude, determining the corresponding gauge factor $\Gamma(\overline{\boldsymbol{\sigma}})$ from (4.2), and then normalizing $\overline{\boldsymbol{\sigma}}$ according to (4.3). It should be recalled here that the normal to the gauge surface indicates the direction of the macroscopic plastic flow. Moreover, the gauge surface tends to the standard yield surface in the ideally plastic limit $n \to \infty$. Finally, it is also noted that a *lower bound* for the effective stress potential $\widetilde{u}$ translates into an *outer bound* for the gauge surface (4.4).

Next, we describe the various loading conditions considered in this work. We consider *triaxial* states of stress, such that the macroscopic stress tensor is given by $\overline{\boldsymbol{\sigma}} = \overline{\sigma}_{11}\mathbf{x}_1 \otimes \mathbf{x}_1 + \overline{\sigma}_{22}\mathbf{x}_2 \otimes \mathbf{x}_2 + \overline{\sigma}_{33}\mathbf{x}_3 \otimes \mathbf{x}_3$, where $\mathbf{x}_1$, $\mathbf{x}_2$ and $\mathbf{x}_3$ is a set of orthonormal vectors (not necessarily aligned with the laboratory axes). However, it is convenient to introduce the hydrostatic stress $\overline{\sigma}_m$, the von Mises equivalent stress $\overline{\sigma}_e$, and the third invariant of the deviatoric stress J_3, which are defined by

$$\overline{\sigma}_m = \frac{\mathrm{tr}\,(\overline{\boldsymbol{\sigma}})}{3}, \quad \overline{\sigma}_e = \sqrt{\frac{3}{2}\overline{\boldsymbol{\sigma}}' \cdot \overline{\boldsymbol{\sigma}}'}, \quad J_3 = \det\left(\overline{\boldsymbol{\sigma}}'\right), \tag{4.5}$$

where $\overline{\boldsymbol{\sigma}}' = \overline{\boldsymbol{\sigma}} - \overline{\sigma}_m \mathbf{I}$ denotes the deviatoric stress tensor, and $\mathbf{I}$ is the second-order identity tensor. We then define the stress triaxiality X_σ ($-\infty \leq X_\sigma \leq \infty$), the Lode

angle θ ($0 \le \theta < 2\pi$) and the Lode parameter L ($-1 \le L \le 1$) via the relations

$$X_\sigma = \frac{\overline{\sigma}_m}{\overline{\sigma}_e}, \quad \cos(3\theta) = \frac{27}{2}\frac{J_3}{\overline{\sigma}_e^3}, \quad L = \frac{2\overline{\sigma}_{II} - \overline{\sigma}_I - \overline{\sigma}_{III}}{\overline{\sigma}_I - \overline{\sigma}_{III}}, \tag{4.6}$$

where $\overline{\sigma}_I \ge \overline{\sigma}_{II} \ge \overline{\sigma}_{III}$ are the (ordered) principal stresses. Note that $\overline{\boldsymbol{\sigma}}$ can be written in the alternative form

$$\overline{\boldsymbol{\sigma}} = \overline{\sigma}_m \mathbf{I} + \frac{2}{3}\overline{\sigma}_e \left[-\cos\left(\theta + \frac{\pi}{3}\right) \mathbf{x}_1 \otimes \mathbf{x}_1 - \cos\left(\theta - \frac{\pi}{3}\right) \mathbf{x}_2 \otimes \mathbf{x}_2 + \cos(\theta)\, \mathbf{x}_3 \otimes \mathbf{x}_3 \right]. \tag{4.7}$$

Thus, our state of stress can be described by the hydrostatic stress $\overline{\sigma}_m$ (or stress triaxiality X_σ), together with a *loading configuration*, which is defined by the loading directions $\mathbf{x}_l$ ($l = 1, 2, 3$) and the Lode angle θ (or parameter L). Here, we consider two different loading orientations characterized by the orientation of the principal loading axes $\mathbf{x}_1$-$\mathbf{x}_2$-$\mathbf{x}_3$ relative to the crystallographic orientations: (*i*) [100]-[010]-[001] and (*ii*) [110]-[$\overline{1}$10]-[001]. For the first loading orientation, the principal loading axes are aligned with the laboratory frame axes, i.e., $\mathbf{x}_l = \mathbf{e}_l$ ($l = 1, 2, 3$), while for the second loading orientation, the principal loading axes are given by $\mathbf{x}_1 = (\mathbf{e}_1 + \mathbf{e}_2)/\sqrt{2}$, $\mathbf{x}_2 = (-\mathbf{e}_1 + \mathbf{e}_2)/\sqrt{2}$ and $\mathbf{x}_3 = \mathbf{e}_3$. For each loading orientation, we consider all possible states of axisymmetric tension (AXT), axisymmetric compression (AXC) and pure shear (PS). While, in principle, there are 24 such loading configurations, because of the symmetry of the FCC single crystal, only 8 of them are independent, and they are listed in Table 4.1. For example, the label AXT[001] (AXC[001]) denotes axisymmetric tension (compression) with the symmetry axis aligned with the [001] crystallographic orientation, while the label PS[001]-[100] stands for pure shear with an equal amount of tension and compression along the [001] and [100] crystallographic orientations, respectively. Note that cases I-III correspond to the [100]-[010]-[001] loading orientation, whereas cases IV-VIII correspond to the [110]-[$\overline{1}$10]-[001] loading orientation. The corresponding normalized macroscopic stress tensor $\overline{\boldsymbol{\Sigma}}$ in (4.3)—having the same "shape" as $\overline{\boldsymbol{\sigma}}$ but with a different magnitude—can be defined similarly by means of equation (4.7) along with Table 4.1, with $\overline{\sigma}_m$ and $\overline{\sigma}_e$ in (4.7) replaced by $\overline{\Sigma}_m$ and $\overline{\Sigma}_e$, respectively. Note that $X_\Sigma = \overline{\Sigma}_m/\overline{\Sigma}_e = X_\sigma = \overline{\sigma}_m/\overline{\sigma}_e$.

Cases	Loading configuration	θ	L	Loading orientation
I	$AXT[001]$	0	-1	
II	$AXC[001]$	π	1	[100]-[010]-[001]
III	$PS[001]$-$[100]$	$11\pi/6$	0	
IV	$PS[110]$-$[\overline{1}10]$	$\pi/2$	0	
V	$AXT[110]$	$2\pi/3$	-1	
VI	$PS[110]$-$[001]$	$5\pi/6$	0	[110]-[$\overline{1}$10]-[001]
VII	$AXC[110]$	$5\pi/3$	1	
VIII	$PS[001]$-$[110]$	$11\pi/6$	0	

Table 4.1: Different loading configurations corresponding to axisymmetric and pure shear stress states (assuming that $\overline{\sigma}_m = 0$), with two different loading orientations relative to the crystallographic orientations: (*i*) [100]-[010]-[001] and (*ii*) [110]-[$\overline{1}$10]-[001].

Figures 4.1 show the $\overline{\Sigma}_m$-$\overline{\Sigma}_e$ cross sections of the ISO gauge surfaces for porous FCC crystals with porosity $f = 1\%$ and void aspect ratios $w_1 = w_2 = 1$, for loading conditions of type I (refer to Table 4.1). Figure 4.1(a) shows the effect of the iteration number N on the ISO gauge surfaces, where different values of N are considered ($N = 1, 2, 5, 10$). The corresponding Iterated Variational Homogenization (IVH) gauge surfaces of Song and Ponte Castañeda (2017a), which are known to be outer bounds, are also included for comparison (dashed lines). We observe from Fig. 4.1(a) that the ISO gauge surfaces become gradually tighter with increasing values of N for large stress triaxialities, converging to a certain limit for large values of N (the ISO result for $N = 20$ is practically indistinguishable to that for $N = 10$ and is not shown). In particular, the hydrostatic point for the ISO gauge surface with $N = 10$ is nearly half of that for the SO gauge surface (corresponding to the ISO gauge surface with $N = 1$), indicating a significant improvement of the ISO estimates over the SO estimates, which are known to be too stiff at large stress triaxialities. On the other hand, increasing N has *no* significant effect on the ISO gauge surfaces for small triaxialities (e.g., $X_\Sigma < 1$), consistent with the fact that the SO estimates (corresponding to the ISO estimates with $N = 1$) are already fairly accurate in this case. The above observations also hold for the associated IVH gauge surfaces. However, for a given value of N, the ISO gauge surface lies well below the corresponding IVH outer bound

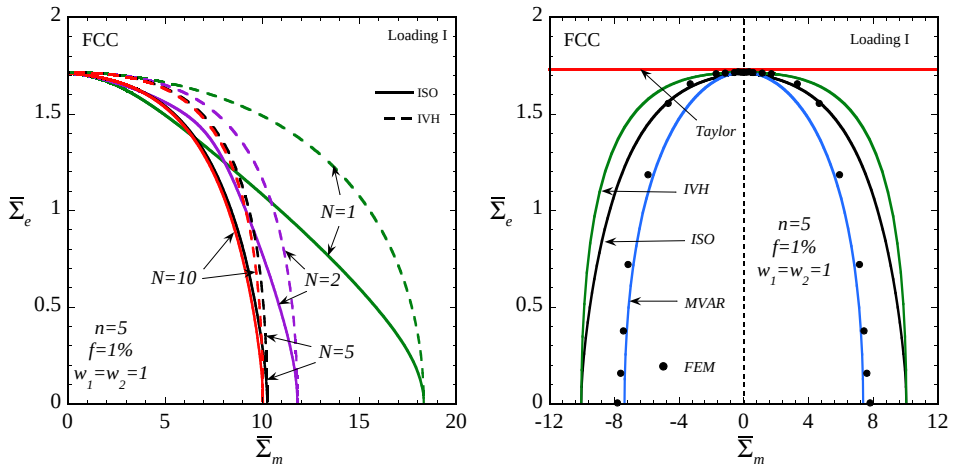

(a) (b)

Figure 4.1: The $\overline{\Sigma}_m$-$\overline{\Sigma}_e$ cross sections of gauge surfaces for porous viscoplastic (n = 5) FCC single crystals with porosity f = 1% and void aspect ratios w_1 = w_2 = 1, subjected to loading conditions of type I (refer to Table 4.1). (a) The effect of the iteration number N on the ISO gauge surfaces (solid lines), where different values of N are considered ($N = 1, 2, 5, 10$). The corresponding IVH gauge surfaces of Song and Ponte Castañeda (2017a) are also shown (in dashed lines) for comparison. (b) Comparison of the ISO gauge surface with the corresponding Taylor, IVH (Song and Ponte Castañeda, 2017a) and MVAR (Mbiakop et al., 2015b) gauge surfaces. The FEM results in the work of Mbiakop et al. (2015b) are also shown.

for all stress triaxialities, except in the purely hydrostatic limit ($X_\Sigma \to \infty$), when the ISO gauge surface coincides with the IVH bound. Finally, we emphasize that the ISO and IVH gauge surfaces converge very rapidly with increasing values of N. In fact, numerical studies show that a relatively small number of iterations (e.g., N = 10) can provide quite accurate estimates (with error less than 1%) for the corresponding $N \to \infty$ limits of the ISO and IVH results. Hence, *all the ISO and IVH results to be shown in the following will be computed for* N = 10.

Figure 4.1(b) shows a comparison of the ISO gauge surface with the corresponding gauge surfaces obtained by the Taylor, IVH (Song and Ponte Castañeda, 2017a) and MVAR (Mbiakop et al., 2015b) models, as well as with the FEM results of Mbiakop et al. (2015b). The following observations can be made from this figure. The Taylor gauge surface, which is obtained by assuming a uniform strain rate in the material, is a straight line parallel to the horizontal hydrostatic axis (and hence unbounded for

hydrostatic loadings), providing an outer bound for the gauge surfaces of the porous FCC crystals. By contrast, the IVH gauge surface exhibits a finite hydrostatic limit and lies within the Taylor gauge surface for all stress triaxialities, thus leading to an outer bound that is much more restrictive than the Taylor bound. Consistent with their bound status, both the Taylor and IVH gauge surfaces tend to overestimate the FEM result especially at large stress triaxialities (of course, the IVH estimate is in much better agreement with the FEM result than the Taylor estimate). On the other hand, both the ISO and MVAR gauge surfaces (which are *not* bounds) lie within the IVH and Taylor gauge surfaces for all stress triaxialities. Moreover, for $0 \leq |X_\Sigma| \leq 3$ (note the difference in the horizontal and vertical scales), the ISO result is in excellent agreement with the corresponding FEM result, while the MVAR result underestimates the FEM result. Note that for this range of the stress triaxiality, the normal to the gauge surface—dictating the direction of the induced plastic flow—is significantly different for the ISO and MVAR estimates. On the other hand, for very large stress triaxialities ($|X_\Sigma| \gtrsim 3$), the ISO estimate is somewhat stiffer than the FEM result and tends to the IVH outer bound in the purely hydrostatic limit ($|X_\Sigma| \to \infty$), while the MVAR estimate slightly underestimates the FEM result and shows better agreement with the FEM. In particular, the ISO prediction for the hydrostatic point is about 25% larger than the corresponding FEM result in this particular case. Improved homogenization results for large stress triaxialities may be possible by means of the more general FOSO method of Ponte Castañeda (2016), used in combination with the iterated approach. As shown in section 5 of this reference, this more general method involves one less approximation than the method of Ponte Castañeda (2015) for crystalline materials and may lead to improved results, but is more difficult to implement. A similar situation has already been noted in the context of the variational method of deBotton and Ponte Castañeda (1995) by Idiart and Ponte Castañeda (2007b), where it was shown that the bounds of deBotton and Ponte Castañeda (1995) could be obtained by a "relaxation" procedure from the more general method of Idiart and Ponte Castañeda (2007a), and that they provide strictly weaker (relaxed) bounds.

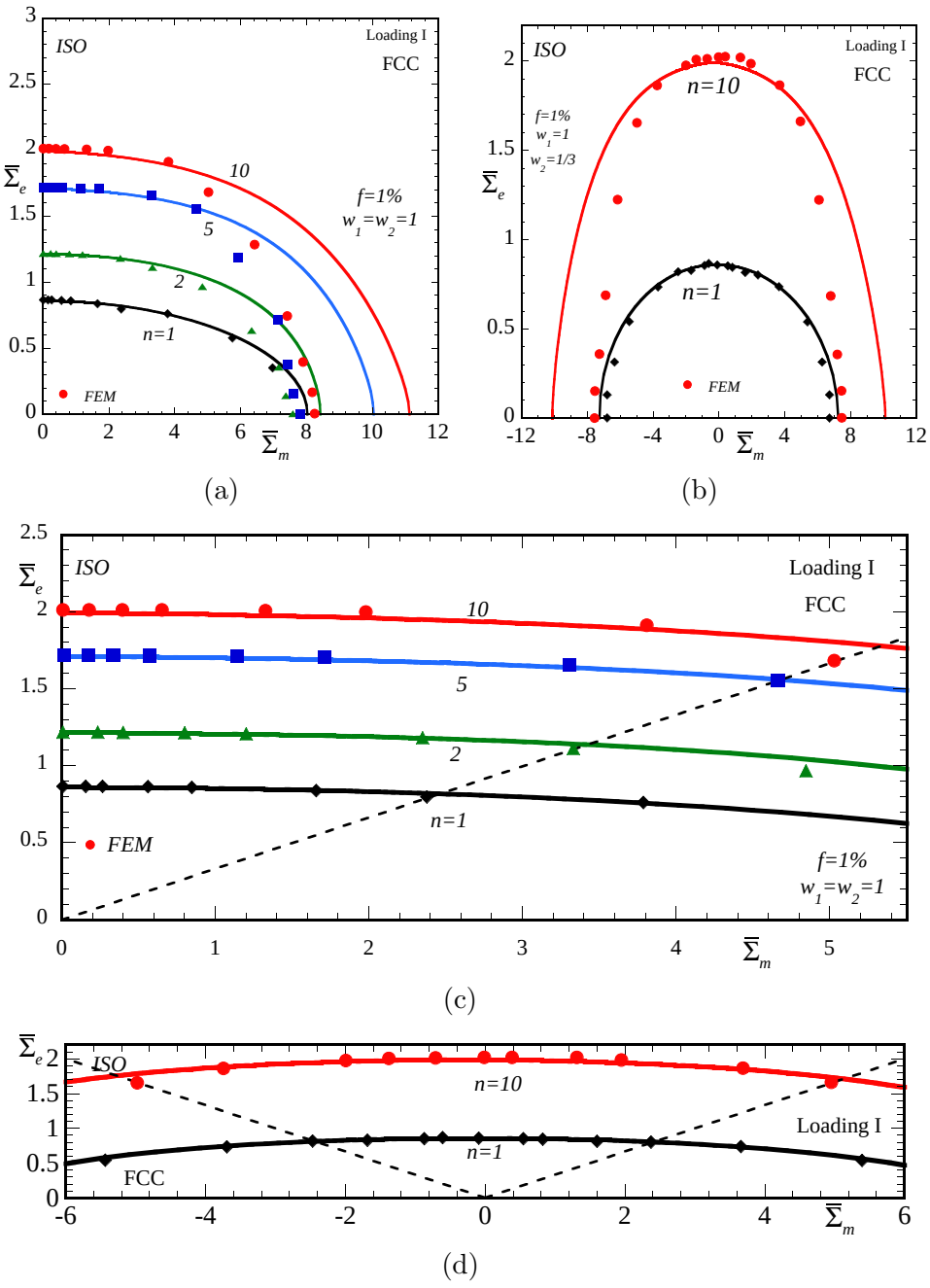

Figure 4.2: $\overline{\Sigma}_m$-$\overline{\Sigma}_e$ cross sections of the gauge surfaces for porous viscoplastic FCC single crystals with porosity $f = 1\%$, subjected to loading conditions of type I (refer to Table 4.1). Comparisons of the ISO gauge surfaces with the corresponding FEM results of Mbiakop et al. (2015b) are shown for (a) void aspect ratios $w_1 = w_2 = 1$ and different creep exponents ($n = 1, 2, 5, 10$), and (b) void aspect ratios $w_1 = 1$, $w_2 = 1/3$ and two different creep exponents ($n = 1$ and 10). (c) Zoomed-in view of (a) for the range of stress triaxiality $0 \leq X_\Sigma \leq 3$, where the dashed line indicates the direction of $X_\Sigma = 3$. (d) Zoomed-in view of (b) for the range of stress triaxiality $-3 \leq X_\Sigma \leq 3$, where the dashed lines indicate the directions of $X_\Sigma = -3$ and 3.

Figure 4.2 shows additional comparisons for the $\overline{\Sigma}_m$-$\overline{\Sigma}_e$ cross sections of the ISO gauge surfaces with the corresponding FEM results of Mbiakop et al. (2015b) for porous FCC single crystals subjected to loading conditions of type I (refer to Table 4.1). Figure 4.2(a) displays the ISO gauge surfaces for porous FCC crystals with porosity $f = 1\%$, void aspect ratios $w_1 = w_2 = 1$ and different creep exponents ($n = 1, 2, 5, 10$). In addition, a zoomed-in view of Fig. 4.2(a) for the range of stress triaxiality $0 \leq X_\Sigma \leq 3$ is shown in Fig. 4.2(c), where the dashed line indicates the direction of a constant stress triaxiality $X_\Sigma = 3$. We can see from Figs. 4.2(a) and 4.2(c) that, for $0 \leq X_\Sigma \leq 3$, the ISO gauge surfaces are in good agreement with the corresponding FEM results for all creep exponents, except for $n = 10$, where the ISO slightly overestimates the FEM result for $X_\Sigma = 3$ (see Fig. 4.2(c)). On the other hand, for very large stress triaxialities, while the ISO gauge surface for $n = 1$ remains in fairly good agreement with the FEM results, the ISO gauge surfaces for higher creep exponents ($n = 2, 5, 10$) are "stiffer" than the FEM results, with the largest difference at the hydrostatic point. Fig. 4.2(b) shows the corresponding ISO gauge surfaces for porous FCC crystals with porosity $f = 1\%$, void aspect ratios $w_1 = 1$, $w_2 = 1/3$, and for two different creep exponents ($n = 1$ and 10). Fig. 4.2(d) provides a zoomed-in view of Fig. 4.2(b) for the range of stress triaxiality $|X_\Sigma| \leq 3$, where the dashed lines indicate the directions of constant triaxialities $X_\Sigma = -3$ and 3. Similar to the observations made in the context of Figs. 4.2(a) and 4.2(c), the ISO gauge surface for $n = 1$ is in good agreement with the FEM results for all triaxialities (see Fig. 4.2(b)), while the ISO gauge surface for $n = 10$ agrees fairly well with the FEM results for $|X_\Sigma| \leq 3$ (see Fig. 4.2(d)) but overestimates the FEM results for larger magnitudes of the stress triaxiality (see Fig. 4.2(b)).

In Fig. 4.3, we investigate the effect of the loading configuration (as defined by the loading orientation as well as the Lode angle), porosity and average void shape on the ISO gauge surfaces for porous FCC single crystals. In particular, Fig. 4.3(a) shows the effect of the loading configuration on the ISO gauge surfaces for porous FCC crystals with porosity $f = 1\%$ and aspect ratios $w_1 = w_2 = 1$, for different loadings of type I, III, IV and V. Recall that loadings I and III refer to the [100]-[010]-[001] loading

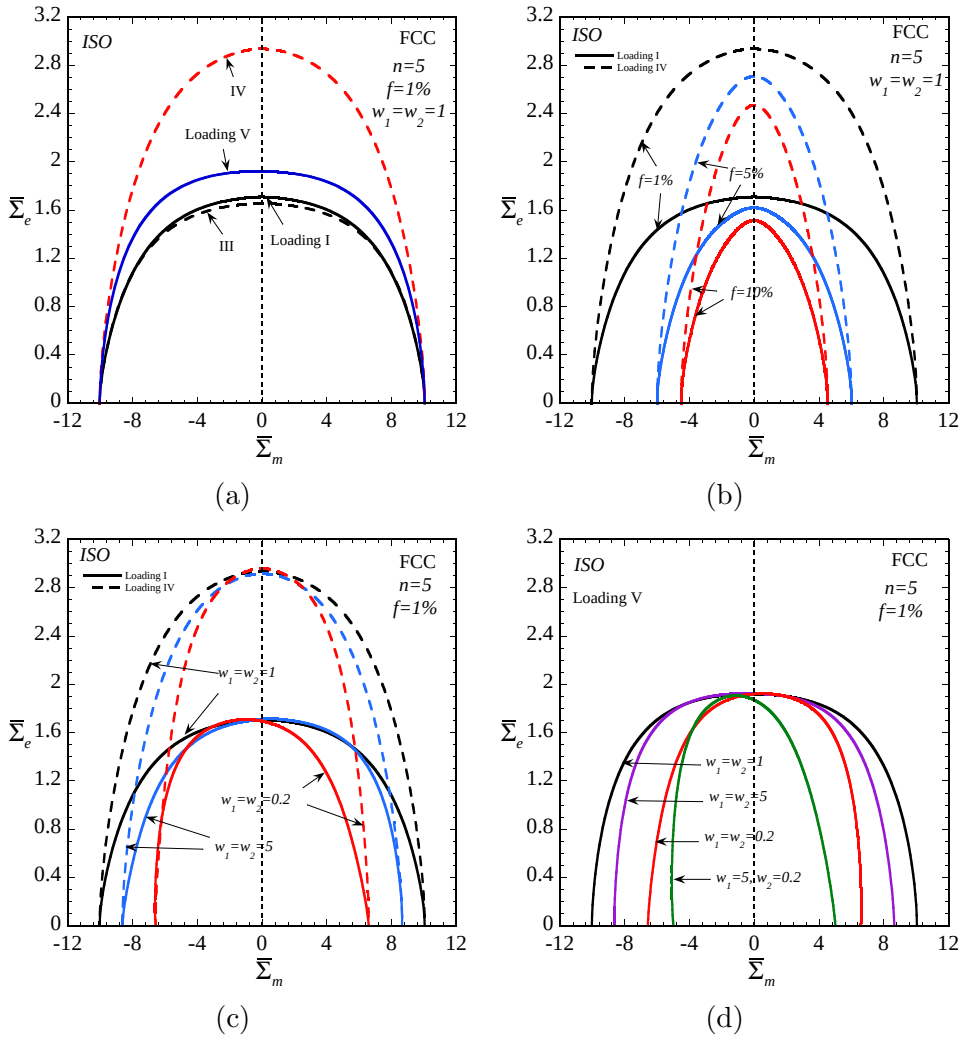

Figure 4.3: The effect of the (a) loading configuration (defined by the loading orientation relative to the crystallographic axes and the Lode angle as shown in Table 4.1), (b) porosity f, (c) and (d) average void shape, as characterized by the two aspect ratios w_1 and w_2, on the $\overline{\Sigma}_m$-$\overline{\Sigma}_e$ cross sections of the ISO gauge surfaces for porous viscoplastic ($n = 5$) FCC single crystals subjected to different types of loadings (refer to Table 4.1). In (b) and (c), results are shown for both loading I (solid lines) and loading IV (dashed lines), while in (d) results are shown for loading V.

orientation, while loadings IV and V refer to the [110]-[$\overline{1}$10]-[001] loading orientation. In addition, loadings I and V correspond to axisymmetric loadings with Lode parameter $L = -1$, whereas loadings III and IV correspond to pure shear loadings with superimposed hydrostatic pressures and Lode parameter $L = 0$. The main observation from Fig. 4.3(a) is that the loading configuration has a significant effect on the macroscopic behavior of porous FCC single crystals, especially for small magnitudes of the stress triaxiality. In particular, the gauge surfaces for loadings IV and V are much larger than those for loadings I and III, indicating that the macroscopic response of porous FCC crystals for the [110]-[$\overline{1}$10]-[001] loading orientation is much stronger than that for the [100]-[010]-[001] loading orientation. In addition, it is found that the effect of the Lode parameter L on the macroscopic response of the porous crystals depends on the specific loading orientation. For instance, for the [100]-[010]-[001] loading orientation, changing the Lode parameter from $L = -1$ (loading I) to $L = 0$ (loading III) leads to slightly softer behavior for the porous crystal under purely deviatoric loadings. However, the opposite is true for the [110]-[$\overline{1}$10]-[001] loading orientation, where changing the Lode parameter from $L = -1$ (loading V) to $L = 0$ (loading IV) leads to significantly stronger behavior for the material under purely deviatoric loadings. In this context, it is remarked that the differences between gauge surfaces for different loading configurations are of the same order as those between the corresponding gauge surfaces for fully dense FCC single crystals (which are not shown here for brevity), suggesting that the dependence of the effective behavior of the porous crystal on the loading configuration is a direct consequence of the intrinsic anisotropy of the crystal matrix. Furthermore, we observe that the gauge surfaces for loadings III and IV exhibit perfect symmetries with respect to the deviatoric axis ($\overline{\boldsymbol{\Sigma}}_m = 0$), in contrast with the cases for loadings I and V, where the corresponding gauge surfaces are slightly *asymmetric* with respect to the deviatoric axis. In fact, by flipping the gauge surfaces for loadings I and V with respect to the deviatoric axis, we obtain the corresponding gauge surfaces for loadings II and VII (refer to Table 4.1), respectively, due to the corresponding symmetries of the loadings (these results are not shown in the figure again for brevity). Finally, note that the gauge surfaces

for different loading configurations coincide in the hydrostatic limit ($|X_\Sigma| \to \infty$), as they should.

Figure 4.3(b) shows the effect of the porosity on the ISO gauge surfaces for porous FCC crystals with void aspect ratios $w_1 = w_2 = 1$ for loading conditions of type I (solid lines) and type IV (dashed lines), and different values of the porosity ($f = 1\%$, 5% and 10%) are considered. We observe from Fig. 4.3(b) that, for both loading configurations (I and IV), increasing porosity leads to the reduction of the gauge surface for all stress triaxialities and, hence, to softer behavior for the material, as expected on physical grounds. In addition, changing porosity also induces changes in the shape of the gauge surfaces for both loading configurations. For instance, for larger porosity ($f = 10\%$), the curvature of the gauge surfaces is quite sharp near the deviatoric axis, while for smaller porosity ($f = 1\%$) the corresponding gauge surfaces become relatively flat near the deviatoric axis. Furthermore, the effect of the porosity is found to be sensitive to the loading configuration, especially for small magnitudes of the stress triaxiality. For instance, for purely deviatoric loadings ($X_\Sigma = 0$), the reduction of the gauge surface with increasing porosity is more significant for loading IV than for loading I. However, such differences tend to disappear for large triaxialities ($|X_\Sigma| \to \infty$).

Figures 4.3(c) and 4.3(d) show the effect of the void shape on the ISO gauge surfaces for porous FCC crystals with a fixed porosity $f = 1\%$ for loading conditions of type I (solid lines in Fig. 4.3(c)), IV (dashed lines in Fig. 4.3(c)) and V (Fig. 4.3(d)). In Fig. 4.3(c), we consider three different void shapes: (*i*) spherical ($w_1 = w_2 = 1$), (*ii*) prolate spheroidal ($w_1 = w_2 = 5$) and (*iii*) oblate spheroidal ($w_1 = w_2 = 0.2$). In addition, the symmetry axis $\mathbf{n}_3$ of the spheroidal voids is assumed to be aligned with the direction of the laboratory axis $\mathbf{e}_3$ and, thus, also with the [001] crystallographic orientation of the FCC single crystal. We can see from Fig. 4.3(c) that, for both loading configurations (I and IV), changes in the void shape lead to changes in both the size and shape of the gauge surfaces, suggesting that evolution of the void shape should have strong *distortional* hardening or softening effects, depending on the stress triaxiality. For instance, changing the void shape from spherical ($w_1 = w_2 = 1$) to

prolate ($w_1 = w_2 = 5$) has a softening effect for purely hydrostatic loadings, while it has a slightly hardening effect for uniaxial tension (loading I with $X_\sigma = 1/3$). Furthermore, we observe from Fig. 4.3(c) that, for loading I, changing the void shape from spherical to spheroidal induces significant changes in the orientation of the gauge surfaces: the gauge surfaces corresponding to spheroidal voids are dramatically *asymmetric* with respect to the vertical deviatoric axis. This is in contrast with the results for loading IV, where the gauge surfaces for different void shapes remain perfectly symmetric with respect to the deviatoric axis.

Figure 4.3(d) displays the corresponding gauge surfaces for loading V, where results for a general ellipsoidal void shape ($w_1 = 5$, $w_2 = 0.2$) are also included, in addition to the three different void shapes ($w_1 = w_2 = 1$, 5 and 0.2) considered in Fig. 4.3(c). It can be seen that, for a given spheroidal void shape (e.g., $w_1 = w_2 = 0.2$), the gauge surface for loading V (Fig. 4.3(d)) is substantially different from those for loadings I and IV (Fig. 4.3(c)), which confirms the findings in the context of Fig. 4.3(a) that the loading configuration has a significant effect on the macroscopic behavior of porous crystals. In addition, we observe from Fig. 4.3(d) that the gauge surface for ellipsoidal voids is markedly different from those for spherical and spheroidal voids: the porous crystal with ellipsoidal voids ($w_1 = 5$, $w_2 = 0.2$) exhibits a softer behavior than that with oblate voids ($w_1 = w_2 = 0.2$) for positive stress triaxialities ($X_\Sigma > 0$), while it exhibits a dramatically softer behavior than those with spherical ($w_1 = w_2 = 1$) and prolate ($w_1 = w_2 = 5$) voids for all stress triaxialities, especially for moderate to large magnitudes of the stress triaxiality. In particular, note that the hydrostatic strength for porous crystals with ellipsoidal voids ($w_1 = 5$, $w_2 = 0.2$) is less than half of that for porous crystals with spherical voids ($w_1 = w_2 = 1$).

In conclusion, we have found that the effect of the porosity and average void shape on the instantaneous macroscopic response of porous FCC crystals exhibits a strong dependence on the loading configuration (as defined by the loading orientation and Lode angle), suggesting a complex coupled effect of the intrinsic crystallographic anisotropy with the morphological anisotropy.

At this point, it should be recalled that the implementation of the ISO model

requires the computation of the fourth-order tensors $\mathbb{Q}_{[i]}$ and their derivatives, whose components are two-dimensional Eshelby integrals (over the unit sphere) that need to be evaluated numerically in general. In this work, a two-dimensional Gaussian quadrature integration scheme is used to evaluate these integrals in spherical coordinates. Note that when the crystal matrix is strongly anisotropic, or when the aspect ratios w_1 and w_2 are very different from unity, a relatively large number of Gaussian points is required to guarantee the accuracy of these integrals. In particular, for the ISO gauge surfaces presented in this section for porous FCC crystals, 50 Gaussian points in each direction are used. Further increasing the number of Gaussian points will not significantly affect the results for the gauge surfaces and, therefore, the above choice is thought to be sufficient to obtain fairly accurate results. While this rather large number of Gaussian points can significantly slow down the computations, improvements in the computational algorithms of these integrals are certainly possible and will be attempted in future works.

4.3 Porous FCC crystals: Microstructure evolution and finite-strain response

In this section, we make use of the ISO model to investigate the finite-strain response of porous FCC single crystals, including the associated evolution of the microstructure, for a wide range of loading conditions. In addition, we compare the ISO results with the corresponding unit-cell, finite-element simulations (FEM) of Srivastava and Needleman (2012, 2015) in order to assess the predictive capability of the ISO model. In this context, it is important to emphasize that the ISO model does *not* contain any fitting parameters.

We consider a porous FCC single crystal containing initially spherical voids distributed randomly and isotropically ($w_1 = w_2 = 1$) in the crystal matrix, with an initial porosity $f_0 = 1\%$. As already discussed at the beginning of section 4.2, the [100], [010] and [001] crystallographic orientations of the FCC-crystal matrix are

initially parallel to the fixed laboratory frame axes $\mathbf{e}_1$, $\mathbf{e}_2$ and $\mathbf{e}_3$, respectively. In addition, hardening of the crystal matrix is neglected, so that $(\tau_0)_{(k)} = \tau_0 = 245\text{MPa}$ $(k = 1, ..., 12)$, $\dot{\gamma}_0 = 1.53 \times 10^{-9}\text{s}^{-1}$ and $n = 5$. In this section, we consider loading conditions that belong to the 8 types of loading configuration defined in Table 4.1, where the applied loading $\overline{\boldsymbol{\sigma}}$ may be written in the form (4.7), and the Lode angle θ as well as the loading orientation are provided in Table 4.1. Furthermore, the applied stress $\overline{\boldsymbol{\sigma}}$ is assumed to be *fixed* in time, which automatically guarantees a loading history with a constant stress triaxiality X_σ. In particular, we set $\overline{\sigma}_e = 750\text{MPa}$, and prescribe the stress triaxiality X_σ by setting $\overline{\sigma}_m = X_\sigma \overline{\sigma}_e$.

The porous FCC single crystal initially exhibits mirror symmetry with respect to the planes normal to the (two sets of) principal loading axes $\mathbf{x}_1$, $\mathbf{x}_2$ and $\mathbf{x}_3$. Consequently, it can be shown that the average "elastic" spin in the crystal matrix (see equation (3.60) in chapter 3) is zero, given that both the average "continuum" spin and the average "plastic" spin in the crystal matrix are zero, leading to *no* lattice rotation *on average* throughout the deformation (although the crystal lattice is expected to rotate locally in the matrix due to the heterogeneity in the deformation fields induced by the voids). On the other hand, during the deformation, the average shape of the voids evolves from the initial spherical shape into a general ellipsoidal shape, while its orientation vectors *remain aligned with the principal loading axes*, i.e., $\mathbf{n}_l = \mathbf{x}_l$ $(l = 1, 2, 3)$. Thus, the loading conditions considered in this work affect the porosity f and the average void shape, as characterized by the aspect ratios w_1 and w_2, but *not* the average lattice and void orientation. We should emphasize, however, that the ISO model is capable of handling more general loading conditions leading to the rotation of both the crystal lattice and the voids, but such more complex loading conditions will be pursued in future work.

Due to the symmetry of the applied loading $\overline{\boldsymbol{\sigma}}$, the principal directions of the resulting macroscopic strain rate $\overline{\mathbf{D}}$ are also aligned with the principal loading axes, such that $\overline{\mathbf{D}} = \overline{D}_{11}\mathbf{x}_1 \otimes \mathbf{x}_1 + \overline{D}_{22}\mathbf{x}_2 \otimes \mathbf{x}_2 + \overline{D}_{33}\mathbf{x}_3 \otimes \mathbf{x}_3$, and the macroscopic equivalent

strain rate is given by

$$\overline{D}_e = \sqrt{\frac{2}{3}\overline{\mathbf{D}}' \cdot \overline{\mathbf{D}}'} = \frac{\sqrt{2}}{3}\sqrt{\left(\overline{D}_{11} - \overline{D}_{22}\right)^2 + \left(\overline{D}_{22} - \overline{D}_{33}\right)^2 + \left(\overline{D}_{33} - \overline{D}_{11}\right)^2}, \tag{4.8}$$

with $\overline{\mathbf{D}}'$ denoting the macroscopic deviatoric strain rate tensor. Then, it follows that the macroscopic logarithmic strain tensor $\overline{\mathbf{E}}$ is given by

$$\overline{\mathbf{E}} = \overline{E}_{11}\mathbf{x}_1 \otimes \mathbf{x}_1 + \overline{E}_{22}\mathbf{x}_2 \otimes \mathbf{x}_2 + \overline{E}_{33}\mathbf{x}_3 \otimes \mathbf{x}_3, \tag{4.9}$$

where $\overline{E}_{11} = \int_0^t \overline{D}_{11} dt$, $\overline{E}_{22} = \int_0^t \overline{D}_{22} dt$ and $\overline{E}_{33} = \int_0^t \overline{D}_{33} dt$ are the three principal values of $\overline{\mathbf{E}}$, and t denotes time. The corresponding macroscopic equivalent strain is given by an expression completely analogous to expression (4.8) for $\overline{D}_e$.

In this context, it is useful to also define the corresponding (uniform) strain rate for a homogeneous fully dense single crystal, i.e.,

$$\mathbf{D}^{\infty} = \sum_{k=1}^{K} \dot{\gamma}_0 \left| \frac{\overline{\tau}_{(k)}}{(\tau_0)_{(k)}} \right|^n \operatorname{sgn}\left(\overline{\tau}_{(k)}\right) \boldsymbol{\mu}_{(k)}, \tag{4.10}$$

where the $\overline{\tau}_{(k)} = \overline{\boldsymbol{\sigma}} \cdot \boldsymbol{\mu}_{(k)}$ $(k = 1, ..., K)$ are the resolved shear stresses. Given that $\mathbf{D}^{\infty}$ is purely deviatoric ($D^{\infty}_{kk} = 0$) for a fully dense crystal, the associated equivalent strain rate is simply given by $D^{\infty}_e = \sqrt{\frac{2}{3}\mathbf{D}^{\infty} \cdot \mathbf{D}^{\infty}}$.

The finite-strain macroscopic response of the porous crystal exhibits a strong dependence on the specific loading conditions, as characterized by the stress triaxiality and the loading configuration (defined by the orientation of the loading axes relative to the crystal axes and the Lode angle). We will explore separately the effect of the stress triaxiality and the loading configuration on the evolution of the microstructure, as well as on the macroscopic behavior of the porous FCC crystals. We first consider loading conditions with the same stress triaxiality ($X_\sigma = 1/3$), but for seven different loading configurations (I-VII) provided in Table 4.1. We will then consider loading conditions with several values of the stress triaxiality for three representative loading configurations (I, II and IV), and the effect of the triaxiality will be investigated separately for each loading configuration. We will also make comparisons with the

corresponding FEM results of Srivastava and Needleman (2012; 2015). However, we should emphasize that the ISO results pertain to porous crystals with random microstructures, while the FEM results (Srivastava and Needleman, 2012; 2015) involve single-void, unit-cell calculations for porous crystals with periodic microstructures. For this reason, great care should be exercised when comparing the ISO and FEM results due to the possible sensitivity of the effective behavior of the porous medium to the void distribution (random vs. periodic). In fact, experimental results show that the plastic flow tends to localize along bands seeking the voids. Moreover, it should be kept in mind that the constitutive behavior for the single-crystal matrix is assumed to be elasto-viscoplastic for the FEM, while it is assumed to be purely viscoplastic for the ISO. However, the effect of elasticity is expected to be relatively small, provided that no unloading takes place. Furthermore, all the FEM results to be shown below are from the work of Srivastava and Needleman (2015), where the single crystals undergo only steady creep (as is the case for the ISO), with two exceptions where results will also be taken from the work of Srivastava and Needleman (2012) for single crystals undergoing both primary and steady creep. As pointed out by Srivastava and Needleman (2015), primary creep has very small influence on the results (when plotted against the macroscopic strain) and, therefore, the comparisons between the FEM and the ISO (which incorporates only steady creep) for the porosity and void shape evolution should still be meaningful. The first exception is concerned with the evolution of the void aspect ratios, because the work of Srivastava and Needleman (2015) did not include results for the aspect ratios. The second exception is concerned with high-triaxiality conditions. In fact, the works of Srivastava and Needleman (2012) and Srivastava and Needleman (2015) make use of different measures of macroscopic strain, and while the different measures seem to give consistent results for low-triaxiality conditions, some appreciable differences are observed for high-triaxiality conditions. Finally, we should note that the FEM results are for two different unit cells, characterized by the orientation of the edges of the unit cell (determining the symmetry axes for the periodic distribution of the voids) relative to the crystal axes: [100]-[010]-[001] and [110]-[$\overline{1}$10]-[001]. For this reason,

these two cases correspond to two different periodic distributions of the voids and, in particular, the FEM results for the first orientation are depicted with *solid symbols*, while those for the second orientation, with *empty symbols*.

Under certain loading conditions leading to void collapse, the voids can become considerably distorted and the use of an average ellipsoidal void shape becomes insufficient, since the surfaces of the voids may come into contact prior to the complete closure of the voids (Hutchinson and Tvergaard, 2012). Hence, we define the aspect ratio w to be the ratio of the length of the minor semi-axis a_{min} to that of the major semi-axis a_{max} of the voids, i.e., $w = a_{min}/a_{max}$, so that w describes the largest amount of void distortion. However, the directions of the major and minor axes of the voids depend on the applied loading and, thus, the aspect ratio w may have different functional forms in terms of the two voids aspect ratios w_1 and w_2 (e.g., $w = w_1$, $w = 1/w_1$, $w = w_1/w_2$, etc.) for different loading conditions. The condition for a *severely distorted* void shape will be taken to correspond to the (arbitrarily chosen) aspect ratio $w = 0.1$. This point will be indicated in the figures with *open triangles*; results beyond this point (shown in dotted lines) may not be physically relevant and may need to be modified, due to the possible contact of the void faces. In this context, it should be mentioned that, for the evolution results to be shown below for porous FCC crystals, at most 64 Gaussian points are used in each direction for the numerical quadratures of the two-dimensional Eshelby integrals, and this choice has been found to be enough to obtain sufficiently accurate results, at least prior to the possible contact of the void surfaces (indicated by open triangles). For the evolution results beyond those open triangles (shown in dotted lines), it is possible that an even larger number of Gaussian points are required to obtain accurate results, due to the extremely distorted void shape. However, this is not pursued in this work, since those results are not expected to be physically relevant anyway.

4.3.1 The effect of the loading configuration.

Figure 4.4 shows the strong effect of the loading configuration on the microstructure evolution and on the macroscopic response of porous FCC single crystals, for applied

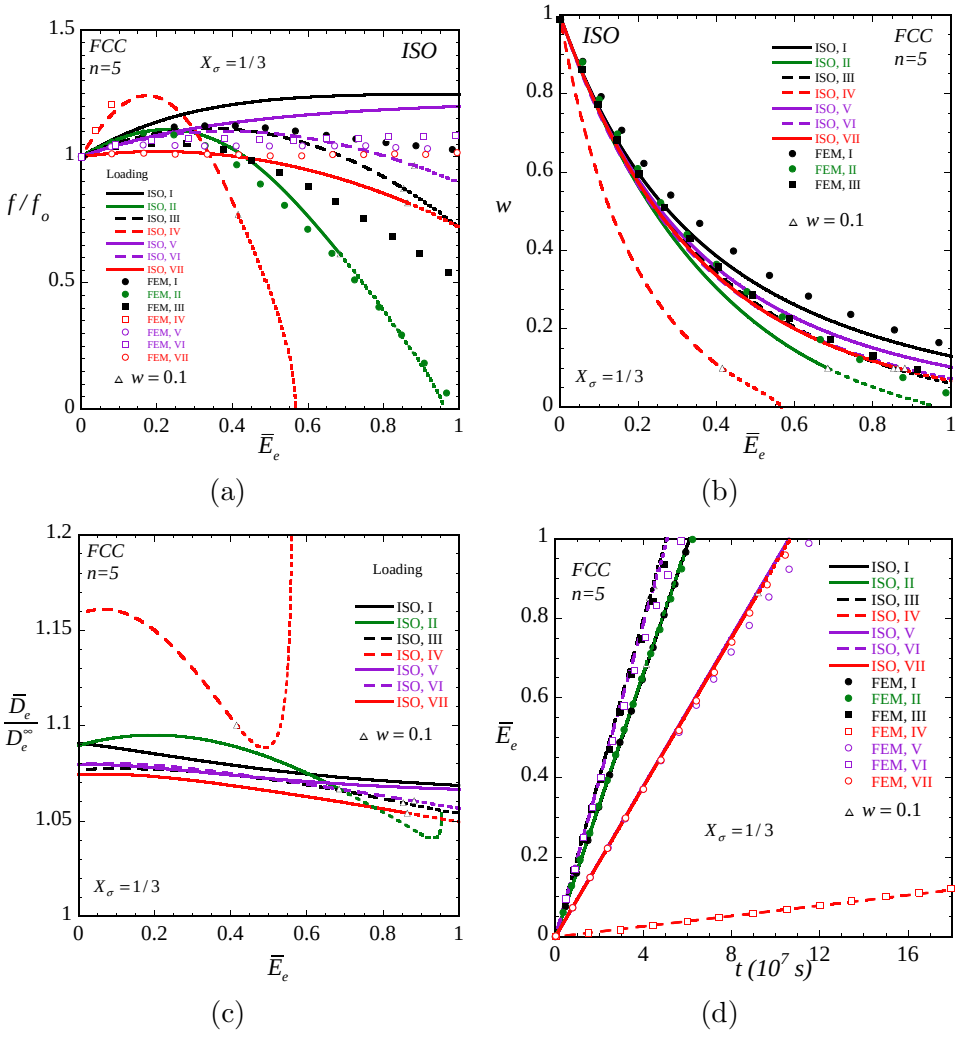

Figure 4.4: ISO results for porous FCC single crystals with an initially isotropic distribution of spherical voids ($w_1 = w_2 = 1$) in $f_0 = 1\%$ initial porosity, subjected to different loading conditions I-VII defined in Table 4.1 with the same stress triaxiality $X_\sigma = 1/3$. Plots are shown for the evolution of the (a) normalized porosity f/f_0, (b) aspect ratios $w = a_{min}/a_{max}$, where $w = a_1/a_3 = 1/w_1$ for loadings I, III and VII, $w = a_3/a_1 = w_1$ for loadings II, V and VI, while $w = a_2/a_1 = w_1/w_2$ for loading IV (a_1, a_2 and a_3 are the lengths of the three semi-axes of the voids along the void principal axes $\mathbf{n}_1$, $\mathbf{n}_2$ and $\mathbf{n}_3$, respectively, and $\mathbf{n}_l = \mathbf{x}_l$ $(l = 1, 2, 3)$), (c) normalized macroscopic equivalent strain rate $\overline{D}_e/D_e^\infty$, as functions of the macroscopic equivalent logarithmic strain $\overline{E}_e$. Plots are also shown for (d) the evolution of the macroscopic equivalent logarithmic strain $\overline{E}_e$ as a function of time t. The corresponding FEM results available in the work of Srivastava and Needleman (2012, 2015) are also included for comparison.

loadings with the same stress triaxiality $X_\sigma = 1/3$, but with different loading configurations (I-VII in Table 4.1). For comparison purposes, the FEM results of Srivastava and Needleman (2012; 2015) are also included. The results for loading VIII are very similar to those for loading VI and are not included for brevity. The ISO results for axisymmetric loadings ($L = \pm 1$) are shown in solid lines and the corresponding FEM results are denoted by circles, while the ISO results for pure shear loadings ($L = 0$) with superimposed hydrostatic pressure are shown in dashed lines and the corresponding FEM results are denoted by squares. Figure 4.4(a) presents plots for the normalized porosity f/f_0 as a function of the macroscopic equivalent strain $\overline{E}_e$. We observe that f/f_0 may increase slightly, remain nearly a constant, or even decrease with $\overline{E}_e$, depending on the specific loading configuration. Moreover, the ISO model can be seen to capture quite well the main features of the corresponding FEM results. In particular, for loadings I and V, f/f_0 slightly increases with $\overline{E}_e$ and saturates at a finite value, while for loadings II and IV, f/f_0 first increases with $\overline{E}_e$ and then decreases continuously to zero, leading to void collapse.

Figure 4.4(b) shows the corresponding plots for the (smallest) aspect ratio w versus the macroscopic equivalent strain $\overline{E}_e$. We can see that w decreases monotonically with $\overline{E}_e$ for all loading configurations. However, it is important to emphasize that the aspect ratios displayed in Fig. 4.4(b) for different loading configurations have different functional forms in terms of w_1 and w_2, i.e., $w = a_1/a_3 = 1/w_1$ for loadings I, III and VII, $w = a_3/a_1 = w_1$ for loadings II, V and VI, while $w = a_2/a_1 = w_1/w_2$ for loading IV, indicating that the initially spherical void shape evolves into different ellipsoidal shapes, depending on the loading configuration. Specifically, the average void shape becomes prolate spheroidal for loading I, while it becomes oblate spheroidal for loading II, with the symmetry axes of the spheroidal voids aligned with the [001] crystallographic orientation. However, for other loading configurations (III to VII), the average void shape evolves into a general ellipsoidal shape with its principal axes aligned with the principal loading directions (e.g., an ellipsoidal void shape with its major and minor axes aligned with the [001] and [100] crystallographic orientations, respectively, for loading III, while with its major and minor axes aligned with the [110]

and $[\overline{1}10]$ crystallographic orientations, respectively, for loading IV). Interestingly, the ISO predictions are found to agree fairly well with the corresponding FEM results for loadings I, II and III (no FEM results are available for loadings IV-VII).

Figure 4.4(c) presents plots for the normalized macroscopic equivalent strain rate $\overline{D}_e/D_e^\infty$ as a function of $\overline{E}_e$. We note that $\overline{D}_e/D_e^\infty$ is a measure of the normalized effective (nonlinear) viscous compliance for the porous crystals and, therefore, increasing $\overline{D}_e/D_e^\infty$ implies softening, while decreasing $\overline{D}_e/D_e^\infty$ implies hardening. In addition, $\overline{D}_e/D_e^\infty \geq 1$ at any stage of the deformation, since the effective behavior for a porous crystal is always softer than that for a fully dense crystal. We observe from Fig. 4.4(c) that $\overline{D}_e/D_e^\infty$ depends strongly on the loading configuration, due to the fact that the evolution of porosity and void shape—acting as hardening or softening mechanisms for the macroscopic behavior of the porous crystals (see Figs. 4.3(b)-4.3(d))—differ significantly between the various loading configurations (Figs. 4.4(a) and 4.4(b)). In particular, the $\overline{D}_e/D_e^\infty$ plots for loadings I and V (uniaxial tensions along the [100] and [110] crystallographic orientations, respectively) decrease slightly with $\overline{E}_e$, indicating (weak) hardening for the porous crystal, even though the corresponding porosities increase (slightly) with $\overline{E}_e$ (Fig. 4.4(a)) suggesting a softening effect. This can be explained by the fact that changes in the void shape (Fig. 4.4(b)) has a hardening effect that dominates the softening arising from porosity growth, thus leading to overall hardening of the material. On the other hand, the $\overline{D}_e/D_e^\infty$ plots for the rest of the loading configurations exhibit behaviors that are consistent with the behaviors of the corresponding f/f_0 plots (Fig. 4.4(a)), indicating that the overall hardening or softening of the material is controlled by the porosity evolution. Note that the $\overline{D}_e/D_e^\infty$ curves for loadings II and IV exhibit abrupt upturns at the very end of the deformation (in dotted lines), suggesting dramatic softening behavior for the porous crystals. This is induced by the sharp drop of the aspect ratio w prior to void collapse (see Fig. 4.4(b)), which has a strong softening effect that dominates the hardening due to porosity reduction (Fig. 4.4(a)). However, as already mentioned, the above predictions may not be physically relevant since the softening occurs at fairly small aspect ratios ($w < 0.1$), where void surface contact may already have taken place, thus

completely shutting down the void collapse mechanism responsible for such softening behavior (Hutchinson and Tvergaard, 2012). It would be interesting to explore this effect further either experimentally or numerically.

Figure 4.4(d) displays plots for the macroscopic equivalent strain $\overline{E}_e$. We observe that the macroscopic strain $\overline{E}_e$ increases almost linearly with time for all loading configurations. This is due to the fact that, throughout the deformation, the porosity remains small ($f < 1.3\%$) for all loading configurations (see Fig. 4.4(a)) and, thus, the $\overline{E}_e$ plots for the porous crystals are nearly identical to those for the fully dense crystals. However, the slopes of the $\overline{E}_e$ curves exhibit a strong dependence on the loading configuration. In particular, the time evolution of $\overline{E}_e$ is the slowest for loading IV, while the fastest for loading III, consistent with the fact that for $X_\sigma = 1/3$ the porous FCC crystal exhibits the strongest behavior for loading IV while the softest behavior for loading III (see Fig. 4.3(a)). In addition, the ISO predictions for $\overline{E}_e$ are in quite good agreement with the corresponding FEM results and capture very well the hierarchy of the time evolution of $\overline{E}_e$ with respect to the loading configuration.

4.3.2 The effect of the stress triaxiality.

In Fig. 4.5, we investigate the effect of the stress triaxiality on the evolution of the porosity and average void shape, as well as on the macroscopic response of porous FCC single crystals, for loadings of type I ($L = -1$) *always leading to prolate spheroidal void shapes*. Different values of the stress triaxiality X_σ ranging from −3 to 3 are considered, with results for positive triaxialities ($X_\sigma > 0$) shown in red, and for negative triaxialities ($X_\sigma < 0$) in blue. Figure 4.5(a) shows the evolution of the normalized porosity f/f_0 with the macroscopic equivalent strain $\overline{E}_e$. For comparison purposes, the corresponding FEM results for positive triaxialities ($X_\sigma = 3$, 2/3 and 1/3) are also included (negative triaxialities were not considered in the works of Srivastava and Needleman (2012; 2015)). We observe from Fig. 4.5(a) that, for large values of the triaxiality ($X_\sigma = 3$ and 2/3), the normalized porosity f/f_0 increases continuously with $\overline{E}_e$, whereas for negative triaxialities ($X_\sigma < 0$), f/f_0 decreases with $\overline{E}_e$ until the porosity goes to zero. (As already seen, for $X_\sigma = 1/3$, f/f_0 increases initially with

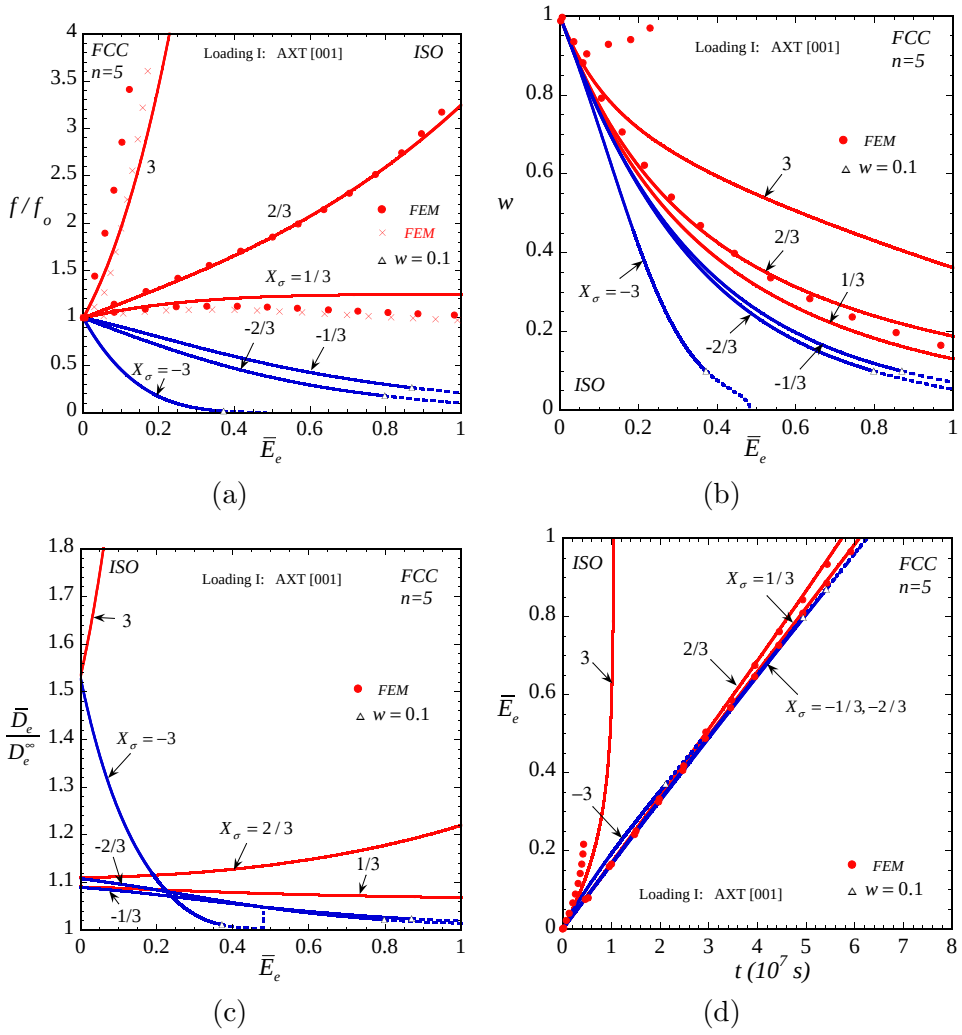

Figure 4.5: ISO results for porous FCC single crystals with an initially isotropic distribution of spherical voids ($w_1 = w_2 = 1$) in $f_0 = 1\%$ initial porosity, subjected to loading conditions of type I (defined in Table 4.1) always leading to prolate spheroidal voids, for different values of the stress triaxiality X_σ. Plots are shown for the evolution of the (a) normalized porosity f/f_0, (b) aspect ratio $w = a_{min}/a_{max} = a_1/a_3 = a_2/a_3 = 1/w_1 = 1/w_2$, (c) normalized macroscopic equivalent strain rate $\overline{D}_e/D_e^\infty$, as functions of the macroscopic equivalent logarithmic strain $\overline{E}_e$. Plots are also shown for (d) the evolution of the macroscopic equivalent logarithmic strain $\overline{E}_e$ as a function of time t. The corresponding FEM results available in the work of Srivastava and Needleman (2012, 2015) are also included for comparison.

$\overline{E}_e$ and approaches an asymptote.) In addition, we can see that f/f_0 grows faster for larger values of X_σ in the range $X_\sigma > 0$, while f/f_0 decreases faster for smaller values of X_σ in the range $X_\sigma < 0$, as expected. Furthermore, the ISO results for f/f_0 are in good qualitative agreement with the corresponding FEM results for $X_\sigma > 0$. In this context, it should be noted that, in addition to the FEM results of Srivastava and Needleman (2015) (depicted with solid circles), the corresponding FEM results of Srivastava and Needleman (2012) are also shown in Fig. 4.5(a) (with cross symbols) for $X_\sigma = 3$ and $1/3$ ($X_\sigma = 2/3$ was not considered by Srivastava and Needleman (2012)). It can be seen that, while for $X_\sigma = 1/3$ the two sets of FEM results are rather similar, for $X_\sigma = 3$ they are somewhat different. Those differences would appear to be due to the different definitions for the overall effective creep strain (against which the normalized porosity f/f_0 is plotted) for the two sets of FEM results (see the corresponding references for details). In this context, it should be noted that the overall effective creep strain defined by Srivastava and Needleman (2012) is more consistent with the effective equivalent logarithmic strain $\overline{E}_e$ defined in the present work. This observation may help explain the better quantitative agreement of the ISO estimates with the FEM results of Srivastava and Needleman (2012). However, because a more complete set of loading conditions was considered by Srivastava and Needleman (2015), and because the two sets of FEM results are not expected to be very different (especially for low stress triaxiality such as $X_\sigma = 1/3$), from now on, all the comparisons for the porosity evolution will be made with the FEM results of Srivastava and Needleman (2015). In summary, the ISO gives excellent quantitative agreement for $X_\sigma = 1/3$, but the agreement deteriorates somewhat for large triaxiality ($X_\sigma = 3$). This is consistent with earlier observations for the corresponding gauge surfaces. However, it should also be kept in mind that, while the FEM results for the gauge surfaces were obtained for unit cells with a random distribution of voids, the FEM results in this figure are for cubic (periodic) distributions of voids. For the higher triaxiality ($X_\sigma = 3$), the porosity increases and the results can be strongly affected by the periodicity of the microstructure (e.g., stronger directional interactions between the voids for the FEM results that would not be expected for the random mi-

crostructures considered for the ISO estimates). In addition, the differences between the FEM results for $X_\sigma = 3$ are of the same order of magnitude as the differences between the ISO estimates and FEM results.

Figure 4.5(b) displays plots for the aspect ratio $w = a_1/a_3 = a_2/a_3 = 1/w_1 = 1/w_2$ (the ratio of the length of the void semi-axis in the transverse direction to that in the axial direction) as a function of the macroscopic equivalent strain $\overline{E}_e$. The main observation from Fig. 4.5(b) is that the aspect ratio w starts from one and decreases monotonically with $\overline{E}_e$ for all values of X_σ, suggesting that the average shape of the voids deforms continuously from spherical to prolate spheroidal. However, the drop of w is faster for smaller values of X_σ. In particular, for $X_\sigma = 1/3$ the aspect ratio w decreases rather slowly and tends to zero as $\overline{E}_e \to \infty$ (as already discussed in Fig. 4.4(b)). For $X_\sigma > 1/3$, the decreasing rate of w is even slower than for $X_\sigma = 1/3$, while for $X_\sigma < 1/3$, w decreases with a faster rate and tends to zero at the same (finite) strain that f/f_0 tends to zero, indicating that the voids collapse into infinitely thin needles. For $X_\sigma = 1/3$, the ISO result for w compares qualitatively well with the corresponding FEM result, but slightly overestimates the drop in w. On the other hand, for $X_\sigma = 3$, the ISO and FEM results for w are in good agreement up to a small amount of strain ($\overline{E}_e \approx 0.1$), but the two results deviate from each other at larger strains: the ISO result decreases continuously with $\overline{E}_e$ while the FEM result starts to increase with $\overline{E}_e$. This discrepancy is likely due, at least in part, to the different void distributions for the ISO and the FEM (random vs. periodic). In particular, for $X_\sigma = 3$, the porosities for both the ISO and FEM increase rapidly with strain (see Fig. 4.5(a)) and, hence, the effect of the void distribution becomes progressively more significant. As pointed out by Srivastava and Needleman (2012), the increase of w at larger strains in the FEM simulation is induced by the necking of the inter-void ligament in the $\mathbf{x}_1$ and $\mathbf{x}_2$ directions (simultaneously), leading to rapid increases of the void radii in these directions. However, there is no well-defined inter-void ligaments for random microstructures and such "local" effects can not be captured by the ISO homogenization model.

Figure 4.5(c) shows plots for the normalized macroscopic equivalent strain rate

$\overline{D}_e/D_e^\infty$ versus the macroscopic equivalent strain $\overline{E}_e$. We observe that for large positive triaxialities (X_σ = 3 and 2/3), $\overline{D}_e/D_e^\infty$ increases monotonically with $\overline{E}_e$ indicating softening of the material with the deformation. However, for negative triaxialities ($X_\sigma < 0$), $\overline{D}_e/D_e^\infty$ decreases with $\overline{E}_e$ indicating hardening. This correlates with Fig. 4.5(a), which shows that the porosity grows towards one for X_σ = 3 and 2/3 and decreases to zero for $X_\sigma < 0$, acting as a softening and hardening mechanism, respectively. As discussed earlier, for X_σ = 1/3 (uniaxial tension), $\overline{D}_e/D_e^\infty$ decreases with strain, indicating overall hardening (although the porosity increases with strain (Fig. 4.5(a)) inducing a softening effect). Furthermore, it can be seen from Fig. 4.5(c) that the variation of $\overline{D}_e/D_e^\infty$ with $\overline{E}_e$ is more significant for X_σ = ±3 than for other values of X_σ. This is consistent with the fact that the porosity exhibits the fastest growth (or reduction) for X_σ = 3 (or −3), thus leading to the strongest softening (or hardening) behavior for the material.

Next, Fig. 4.5(d) presents results for the macroscopic equivalent strain $\overline{E}_e$ as a function of time. The corresponding FEM results for X_σ = 3, 2/3 and 1/3 are also included. We can see that for X_σ = 3, the macroscopic strain $\overline{E}_e$ increases very rapidly in time with a progressively faster rate, as a consequence of the rapid growth of the macroscopic strain rate observed in Fig. 4.5(c). As already mentioned, this strong softening behavior is induced by the significant porosity growth (Fig. 4.5(a)), which is expected to lead to final failure of the material by void coalescence. By contrast, for other values of X_σ, the macroscopic strains $\overline{E}_e$ increase almost linearly with time and are very similar to each other. This is because for $X_\sigma \leq 2/3$ the porosity remains fairly small ($f < 3.5\%$) throughout the deformation and, therefore, the corresponding $\overline{E}_e$ curves for porous crystals are almost identical to that for a fully dense crystal (which is not shown here for simplicity). Furthermore, the ISO results for $\overline{E}_e$ are found to be in fairly good agreement with the corresponding FEM results. This is true even for X_σ = 3, in spite of the fact that the corresponding predictions for the evolution of the aspect ratio were not in agreement, suggesting that at these large triaxialities the evolution of the aspect ratio is not very important.

Figure 4.6 shows the effect of the stress triaxiality on the evolution of the porosity

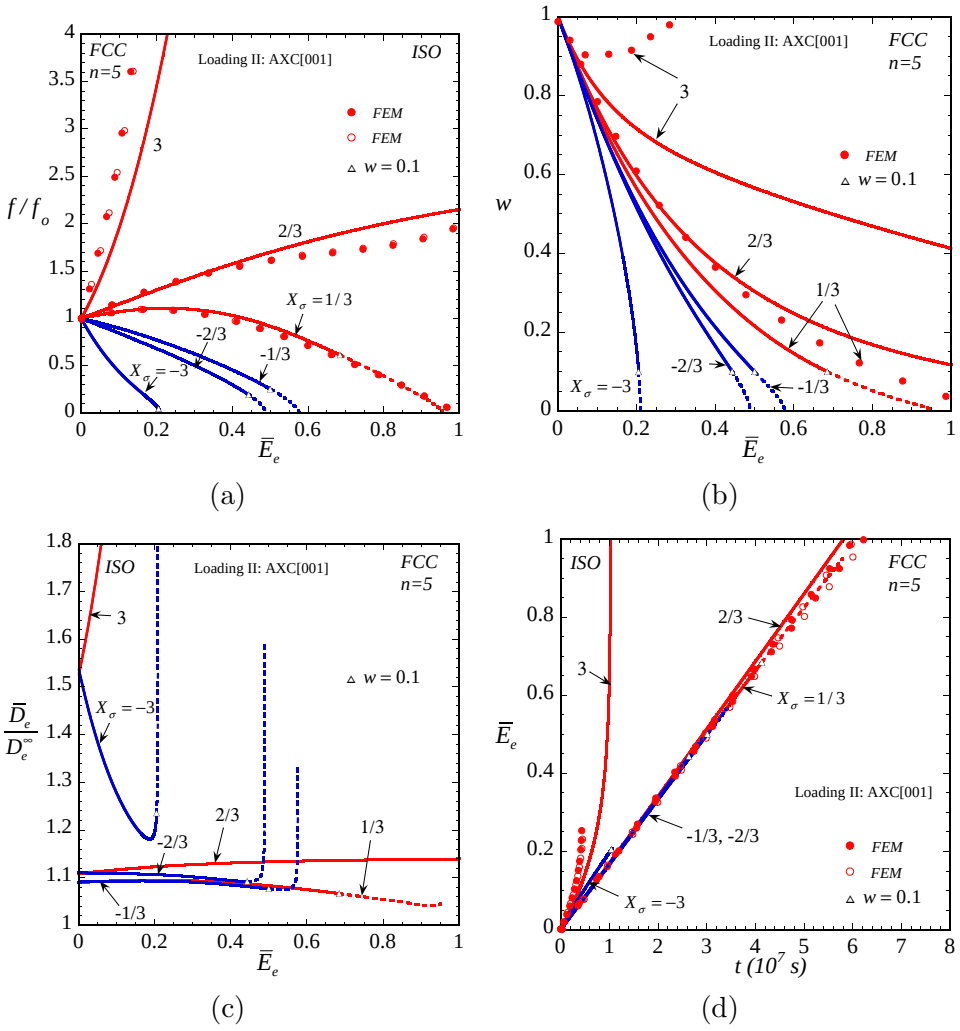

Figure 4.6: ISO results for porous FCC single crystals with an initially isotropic distribution of spherical voids ($w_1 = w_2 = 1$) in $f_0 = 1\%$ initial porosity, subjected to loading conditions of type II (defined in Table 4.1) always leading to oblate spheroidal voids, for different values of the stress triaxiality X_σ. Plots are shown for the evolution of the (a) normalized porosity f/f_0, (b) aspect ratio $w = a_{min}/a_{max} = a_3/a_1 = a_3/a_2 = w_1 = w_2$, (c) normalized macroscopic equivalent strain rate $\overline{D}_e/D_e^\infty$, as functions of the macroscopic equivalent logarithmic strain $\overline{E}_e$. Plots are also shown for (d) the evolution of the macroscopic equivalent logarithmic strain $\overline{E}_e$ as a function of time t. The corresponding FEM results available in the work of Srivastava and Needleman (2012, 2015) are also included for comparison.

and void shape and on the effective behavior of the porous FCC single crystals for loadings of type II (L = 1) *always leading to oblate spheroidal void shapes*. The corresponding FEM results for positive stress triaxialities (X_σ = 3, 2/3 and 1/3) are also included for comparison. In particular, in Figs. 4.6(a) and 4.6(d), two sets of the FEM results corresponding to two different unit-cell orientations ([100]-[010]-[001] and [110]-[$\overline{1}$10]-[001]) are shown for each positive X_σ, while in Fig. 4.6(b), only the FEM results corresponding to the [100]-[010]-[001] unit-cell orientation are shown. Figs. 4.6(a) and 4.6(b) present plots for the normalized porosity f/f_0 and the aspect ratio $w = a_3/a_1 = a_3/a_2 = w_1 = w_2$ (the ratio of the length of the void semi-axis in the axial direction to that in the transverse direction), respectively, versus the macroscopic equivalent strain $\overline{E}_e$, for different values of the stress triaxiality. We can see by comparing these figures to the corresponding figures for loading I (Figs. 4.5(a) and 4.5(b)) that the general trends for loading II are similar to those for loading I, but there are some differences. Most importantly, for loading II the porosity and aspect ratio tend to zero for triaxialities $X_\sigma \leq 1/3$, while for loading I this clearly happens only for $X_\sigma = -3$. This suggests that void collapse to penny-shaped cracks (lying in the $\mathbf{x}_1$-$\mathbf{x}_2$ ([100]-[010]) plane) will be more likely for loading II than void collapse to needles for loading I. In addition, the ISO results for f/f_0 are seen to be in fairly good agreement with the corresponding FEM results for positive triaxialities. (Note that for each positive X_σ, the two sets of FEM results corresponding to different unit-cell orientations are very similar and stay on top of each other, except for $X_\sigma = 3$ where there are some noticeable differences.) Although there are no FEM results to compare with for negative stress triaxialities, the predictions of the ISO model for $X_\sigma < 0$ that the initially spherical voids collapse into infinitely thin needles under loadings of type I while into penny-shaped micro-cracks under loadings of type II are qualitatively consistent with the results of Hori and Nasser (1988) for the behavior of an isolated spherical void in an elasto-viscoplastic FCC single crystal subjected to remote, incremental, axisymmetric loadings.

Figure 4.6(c) presents plots for the normalized macroscopic equivalent strain rate $\overline{D}_e/D_e^\infty$ versus the macroscopic equivalent strain $\overline{E}_e$ for loadings of type II at dif-

ferent values of the stress triaxiality. We observe that for the larger positive stress triaxialities ($X_\sigma \geq 2/3$), $\overline{D}_e/D_e^\infty$ exhibits a behavior that is largely consistent with the corresponding f/f_0 plot (Fig. 4.6(a)), indicating that the overall softening of the material is dominated by the porosity evolution. On the other hand, for $X_\sigma \leq -1/3$, the behavior is much more complex, exhibiting regimes of both hardening and softening. In particular, for large negative values of the stress triaxiality ($X_\sigma = -2/3$ and -3), $\overline{D}_e/D_e^\infty$ first decreases with $\overline{E}_e$ (hardening) and then increases abruptly (strong softening) prior to void collapse. Referring to the corresponding plots for the porosity and aspect ratio, it is deduced that the initial hardening is associated with the reduction in the porosity, while the softening for larger strains is explained by the sudden shape changes associated with void collapse. Note that for $X_\sigma = -2/3$ (and also for $-1/3$), the abrupt upturn of $\overline{D}_e/D_e^\infty$ (strong softening) occurs when the aspect ratio w is very small ($w < 0.1$). As already mentioned, such results could be questioned on physical grounds because void surface contact may have already taken place, thus arresting the softening effect induced by void collapse (Hutchinson and Tvergaard, 2012). However, it is interesting to note that, for $X_\sigma = -3$, the softening induced by the change of the void shape takes place before void surface contact is expected to occur—and could, therefore, be physically relevant. In fact, the numerical simulations of Srivastava and Needleman (2015) have shown that an overall enhanced creep rate may occur during void collapse, albeit for a different loading condition.

Figure 4.6(d) shows the corresponding plots for the macroscopic equivalent strain $\overline{E}_e$ as a function of time. It can be seen that for all values of X_σ considered, the $\overline{E}_e$ curves for loading II (Fig. 4.6(d)) are very similar to the corresponding curves for loading I (Fig. 4.5(d)). However, it should be emphasized that, the evolution of the macroscopic logarithmic strain tensor $\overline{\mathbf{E}}$ is quite different for loadings I and II, due to the different loading types (different Lode parameters). Furthermore, the ISO predictions are found to agree quite well with the corresponding FEM results for positive stress triaxialities. (For each positive X_σ, the two sets of the FEM results for different unit-cell orientations are nearly identical.)

In Fig. 4.7, we explore the effect of the stress triaxiality on the evolution of

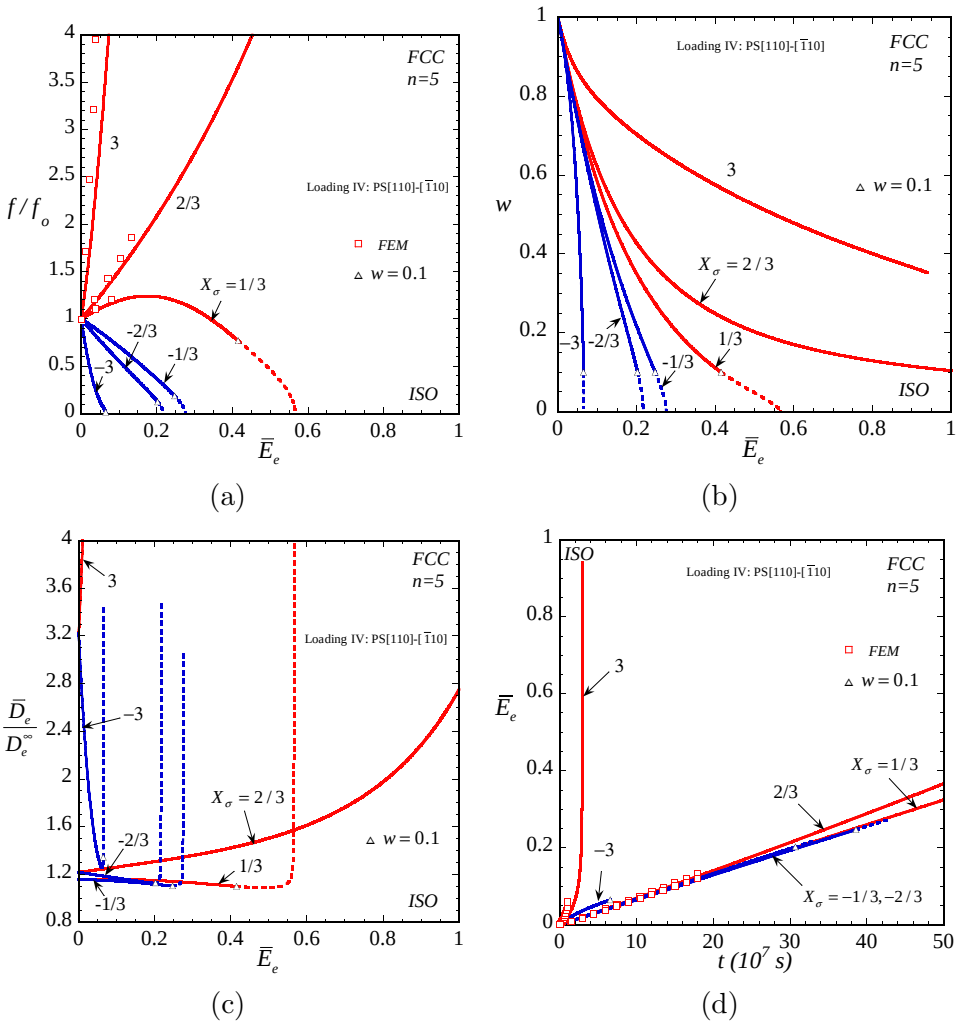

Figure 4.7: ISO results for porous FCC single crystals with an initially isotropic distribution of spherical voids ($w_1 = w_2 = 1$) in $f_0 = 1\%$ initial porosity, subjected to loading conditions of type IV (defined in Table 4.1) leading to voids of general ellipsoidal shape, for different values of the stress triaxiality X_σ. Plots are shown for the evolution of the (a) normalized porosity f/f_0, (b) aspect ratio $w = a_{min}/a_{max} = a_2/a_1 = w_1/w_2$, (c) normalized macroscopic equivalent strain rate $\overline{D}_e/D_e^\infty$, as functions of the macroscopic equivalent logarithmic strain $\overline{E}_e$. Plots are also shown for (d) the evolution of the macroscopic equivalent logarithmic strain $\overline{E}_e$ as a function of time t. The corresponding FEM results available in the work of Srivastava and Needleman (2012, 2015) are also included for comparison.

the microstructure and on the effective behavior of the porous FCC single crystals for loading conditions of type IV ($L = 0$) *leading to voids of general ellipsoidal shape*. It is important to note that loading IV refers to the [110]-[$\overline{1}$10]-[001] loading orientation, which is different from the [100]-[010]-[001] loading orientation for loadings I and II considered above. Figs. 4.7(a) and 4.7(b) show plots for the normalized porosity f/f_0 and the aspect ratio $w = a_2/a_1 = w_1/w_2$ (in the $\mathbf{x}_1$-$\mathbf{x}_2$ ([110]-[$\overline{1}$10]) plane), respectively, versus the macroscopic equivalent strain $\overline{E}_e$, for different values of X_σ. The corresponding FEM results for positive stress triaxialities ($X_\sigma = 3$, 2/3 and 1/3) are also included in Fig. 4.7(a) (no FEM results are available for the aspect ratio w). We observe from Figs. 4.7(a) and 4.7(b) that the plots for the normalized porosity f/f_0 and the aspect ratio w for loading IV are qualitatively similar to those for loading II in Figs. 4.6(a) and 4.6(b), indicating that the effect of the stress triaxiality on the microstructure evolution is qualitatively similar for the above two different loading configurations. However, for given values of X_σ, both f/f_0 and w evolve much more rapidly with $\overline{E}_e$ for loading IV than for loading II. Our interpretation of this result is as follows. The FCC crystal matrix exhibits stronger behavior and is much more resistant to finite-strain plastic deformation for loading IV than for loading II. As a consequence, larger fractions of the macroscopic deformation are accommodated by the voids, leading to faster evolution of porosity and void shape with increasing macroscopic strain. In addition, we can see from Fig. 4.7(a) that the ISO results for f/f_0 agree very well with the corresponding FEM results. Note that for $X_\sigma = 2/3$ and 1/3, the FEM simulations of Srivastava and Needleman (2015) terminate at $t = 18 \times 10^7 s$, where the corresponding values of the macroscopic strain $\overline{E}_e$ are still relatively small (this explains the abrupt ends of the FEM results for $X_\sigma = 2/3$ and 1/3).

Figure 4.7(c) shows the corresponding results for the normalized macroscopic equivalent strain rate $\overline{D}_e/D_e^\infty$ versus the macroscopic equivalent strain $\overline{E}_e$, for loadings of type IV. We can see that while the $\overline{D}_e/D_e^\infty$ plots for loading IV (Fig. 4.7(c)) are qualitatively similar to those for loading II (Fig. 4.6(c)), they evolve much more rapidly with $\overline{E}_e$ in quantitative terms. This is consistent with the observation made

in Figs. 4.7(a) and 4.7(b) for the evolution of porosity and void shape, which play the role of hardening or softening mechanisms for the macroscopic behavior of porous crystals. On the other hand, we can see from Fig. 4.7(d) that the effect of the stress triaxiality on the time evolution of $\overline{E}_e$ for loading IV is qualitatively similar to those for loadings I and II: for large triaxiality (X_σ = 3) $\overline{E}_e$ increases very rapidly in time with an increasing rate, while for other values of the triaxiality $\overline{E}_e$ increases almost linearly in time with a much slower rate. However, for given values of X_σ, the time evolution of $\overline{E}_e$ is significantly slower for loading IV than for loadings I and II (note that the time scale in Fig. 4.7(d) is much larger than those in Figs. 4.5(d) and 4.6(d)). This is in accordance with the fact that, for the range of the stress triaxiality considered, the macroscopic behavior for the porous FCC crystal is much stronger (leading to much slower creep rate) for loading IV than for loadings I and II (see Fig. 4.3(a)). Furthermore, we observe from Fig. 4.7(d) that the ISO results are in very good agreement with the corresponding FEM results for $X_\sigma > 0$.

At this point, it should be remarked that the evolution of the microstructure and the macroscopic response of porous FCC crystals subjected to loadings I-III with the [100]-[010]-[001] loading orientation are quite similar to the corresponding results for porous isotropic materials (e.g., Ponte Castañeda and Zaidman, 1994; Danas and Ponte Castañeda, 2009b), indicating that the finite-strain macroscopic behavior of porous FCC crystals for this loading orientation is rather "isotropic". However, this is not true for the corresponding results for loadings IV-VII with the [110]-[$\overline{1}$10]-[001] loading orientation, which are actually quite different from the corresponding isotropic results. This observation provides justification for the need of homogenization-based constitutive models, such as the ISO model, that can account more accurately for the coupled effect of crystallographic anisotropy and deformation-induced morphological anisotropy. Next, we consider porous single crystals with stronger crystal anisotropies.

4.4 Porous HCP single crystals

In this section, we make use of the ISO model to explore both the instantaneous and finite-strain response for porous, low-symmetry, HCP single crystals. The corresponding results obtained with the IVH model (Song and Ponte Castañeda, 2017a) will also be included for comparison purposes (unfortunately, no FEM results are available to compare with).

We consider HCP single crystals with a c/a ratio of 1.629, and a creep exponent n of 3, which are known to be appropriate for ice. The principal slip systems are the three basal slips ($\{0001\}\langle 11\bar{2}0\rangle$), the three prismatic slips ($\left\{10\bar{1}0\right\}\langle 11\bar{2}0\rangle$) and the six second-order ($\left\{11\bar{2}2\right\}\langle 11\bar{2}3\rangle$) pyramidal-$\langle c+a\rangle$ slips, which will be denoted by labels A, B and C, respectively. Note that the three basal slips together with the three prismatic slips provide only four (two each) linearly independent slip systems, allowing no straining along the $\langle c\rangle$-axis. However, the six second-order pyramidal-$\langle c+a\rangle$ slips contain sets of five linearly independent slip systems, thus allowing arbitrary (isochoric) plastic deformation. The reference flow stresses $(\tau_0)_{(k)}$ in expression (3.3) are taken to be identical for each family of slip systems, but generally different for different families of slip systems. The basal slips are taken to be the "soft" slip systems, with a reference flow stress τ_A, while the prismatic and pyramidal slips are taken to be the "hard" slip systems, with the same reference flow stresses $\tau_B = \tau_C$. For later use, we define $M = \tau_B/\tau_A = \tau_C/\tau_A$ to be the contrast parameter, characterizing the anisotropy of HCP crystals. Note that $M \approx 60$ for ice (Duval et al., 1983), but here we will consider more general values of M ($1 \le M \le 60$) to investigate the effect of the anisotropy of HCP crystals (as a case study for the highly anisotropic material systems).

4.4.1 Instantaneous macroscopic response

In this subsection, we examine the instantaneous macroscopic response of porous HCP crystals for given fixed states of the microstructure, by means of the gauge surface defined by (4.4), focusing on the effect of the crystal anisotropy (values of

M), porosity and void shape. The new ISO results will be compared with the IVH results of Song and Ponte Castañeda (2017a), which provide *outer bounds* for the gauge surfaces.

We consider porous HCP crystals subjected to axisymmetric loadings of the type

$$\overline{\mathbf{\Sigma}} = \overline{\Sigma}_m \mathbf{I} + \overline{\Sigma}_a \left(-\frac{1}{3}\mathbf{e}_1 \otimes \mathbf{e}_1 - \frac{1}{3}\mathbf{e}_2 \otimes \mathbf{e}_2 + \frac{2}{3}\mathbf{e}_3 \otimes \mathbf{e}_3 \right), \tag{4.11}$$

combining the hydrostatic stress $\overline{\Sigma}_m$ and the axisymmetric shear stress $\overline{\Sigma}_a = \pm\overline{\Sigma}_e$, where it is recalled that $\overline{\Sigma}_e$ is the macroscopic equivalent stress. Note that loading (4.11) with $\overline{\Sigma}_a > 0$ is identical to loading I ($L = -1$) in Table 4.1 for porous FCC crystals, while loading (4.11) with $\overline{\Sigma}_a < 0$ is identical to loading II ($L = 1$) in Table 4.1. For simplicity, we further assume that the $\langle c \rangle$-axis of the HCP-crystal matrix is aligned with the symmetry axis $\mathbf{e}_3$ of the applied loading (4.11). (Note that $\mathbf{l}_1$ and $\mathbf{l}_2$ in (4.1) may be chosen to be any two linearly independent crystallographic axes lying in the basal plane, and $\mathbf{l}_3$ is aligned with the $\langle c \rangle$-axis.) In addition, we choose $\tilde{\tau}_0 = \tau_A$ in (4.4), so that all results for the gauge surfaces of porous HCP crystals shown below are normalized by τ_A.

Figure 4.8 shows $\overline{\Sigma}_m$-$\overline{\Sigma}_a$ cross sections of the gauge surfaces for the porous HCP crystals. In Fig. 4.8(a), we investigate the effect of the crystal anisotropy ($M = 1, 5, 10, 20, 60$) on the ISO gauge surfaces for porous HCP crystals with porosity $f = 1\%$, void aspect ratios $w_1 = w_2 = 1$. For comparison purposes, the corresponding IVH gauge surfaces (Song and Ponte Castañeda, 2017a) are also shown in Fig. 4.8(a) in dashed lines, while the corresponding MVAR gauge surfaces (Mbiakop et al., 2015b) are shown in Fig. 4.8(b). We can see from Fig. 4.8(a) that increasing M leads to the expansion of the ISO gauge surface for all stress triaxialities and, thus, to stronger effective behavior for the porous HCP crystal. Nonetheless, both the shape and orientation of the ISO gauge surfaces change significantly as M increases, indicating a strong *distortional* hardening effect. In addition, the ISO results are found to be very similar to the corresponding IVH outer bounds, except for the "corner" regions, where the slopes of the ISO and IVH surfaces are rather different (indicating that the

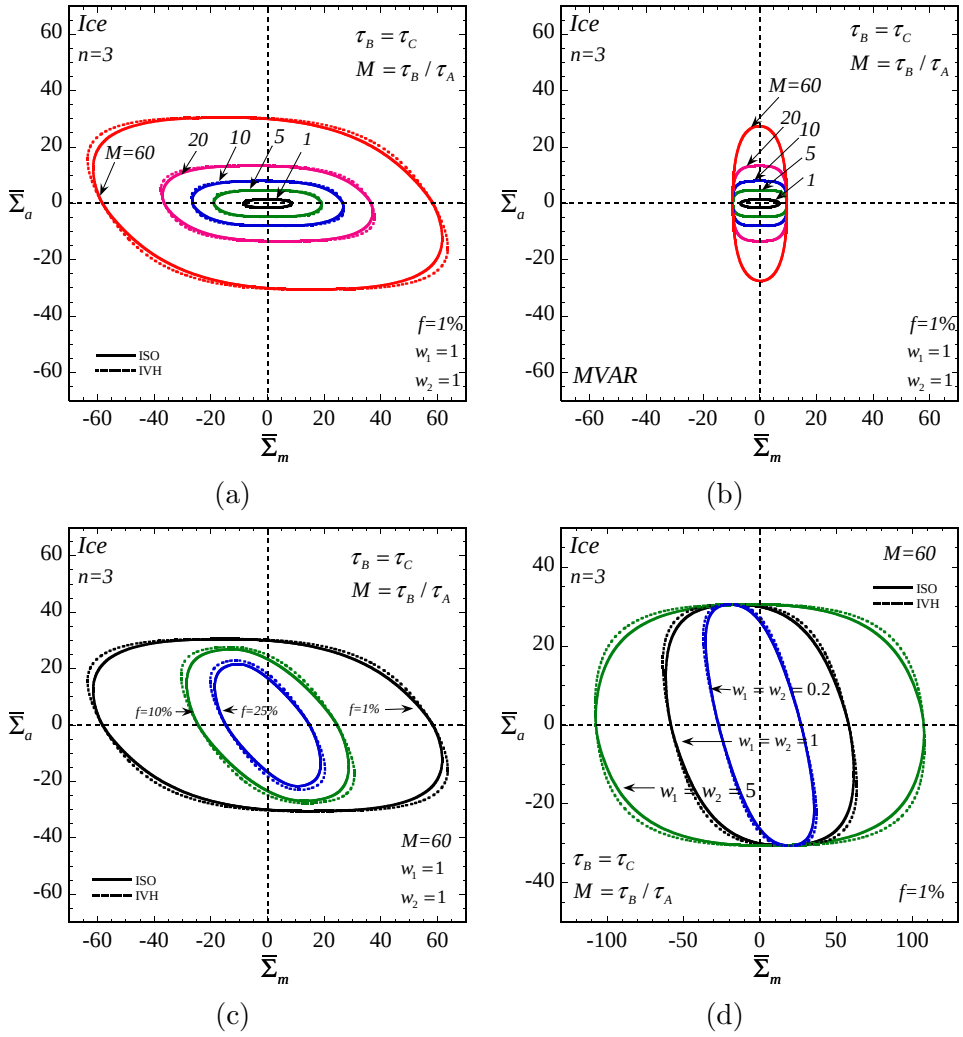

Figure 4.8: The $\overline{\Sigma}_m$-$\overline{\Sigma}_a$ cross sections of the gauge surfaces for porous viscoplastic (n = 3) HCP crystals subjected to axisymmetric loadings (4.11). Results are shown for the effect of the crystal anisotropy, as defined by the contrast parameter M, on the (a) ISO gauge surfaces (solid lines), IVH gauge surfaces of Song and Ponte Castañeda (2017a) (dashed lines), and (b) MVAR gauge surfaces of Mbiakop et al. (2015b), for porous HCP crystals. Results are also shown for the effect of the (c) porosity f, and (d) average void shape, as characterized by the aspect ratios w_1 and w_2, on the ISO (solid lines) and IVH (dashed lines) gauge surfaces for porous ice (M = 60).

direction of the induced plastic flow can also be quite different for the ISO and IVH).

On the other hand, we observe from Fig. 4.8(b) that, while the MVAR gauge surface for $M = 1$ is very similar to the corresponding ISO and IVH gauge surfaces (as expected from the results for porous FCC crystals), the MVAR gauge surfaces for $M \geq 5$ are much smaller than the corresponding ISO and IVH surfaces, indicating a dramatically softer response, especially for moderate to large magnitudes of the stress triaxiality. In this context, we should recall that the MVAR model was based on certain simplifying assumptions designed for porous crystals with equal (or similar) reference flow stresses for all available slip systems ($M \sim 1$). In this regard, it is interesting to note that both the ISO and IVH gauge surfaces tend to infinity as $M \to \infty$, indicating that non-basal slip is necessary for non-vanishing overall plastic deformation of the porous HCP crystals (under loading condition (4.11)). However, this is not the case for the MVAR gauge surface, which—contrary to expectations—tends to a finite limit for all stress triaxialities. In fact, the full-field, unit-cell simulations of Mbiakop et al. (2015b) have shown that, when only three basal slips are available, the porous HCP crystal cannot undergo macroscopic plastic deformation (under loading (4.11))—which is consistent with the ISO and IVH predictions, but not with the MVAR results. In addition, as already noted by Mbiakop et al. (2015b), the MVAR model does predict a rigid overall response if it is assumed (from the start) that there are only three basal slips (with equal flow stresses), instead of twelve slips, where the flow stresses of the non-basal systems are allowed to tend to infinity, as mentioned above. Clearly, this is an inconsistency with the MVAR method, which suggests that the results of Fig. 4.8(b) cannot be accurate for large values of M.

Figure 4.8(c) shows the effect of the porosity on the ISO gauge surfaces for porous ice ($M = 60$) with spherical voids ($w_1 = w_2 = 1$) and different values of the porosity ($f = 1\%$, 10% and 25%). We also include, for comparison, the corresponding IVH gauge surfaces (in dashed lines) of Song and Ponte Castañeda (2017a). We observe that, for given values of f, the gauge surfaces for porous ice are much larger and less symmetric with respect to the vertical deviatoric axis ($\overline{\Sigma}_m = 0$) than the corresponding results for porous FCC crystals (solid curves in Fig. 4.3(b)), indicating a strong effect

of the crystallographic anisotropy (HCP vs. FCC) on the effective behavior of porous crystals. In addition, we can see from Fig. 4.8(c) that increasing porosity has a definite softening effect on porous ice for all stress triaxialities, similar to the findings in Fig. 4.3(b) for porous FCC crystals. However, for porous ice the contraction of the gauge surface with increasing values of f exhibits a much stronger dependence on X_Σ, thus leading to substantial changes in the shape of the gauge surfaces. The ISO results are quite similar to the corresponding IVH outer bounds. Nonetheless, the maximum relative difference between the ISO and IVH results is found to be larger for high porosities (e.g., approximately 8% at $X_\Sigma \approx -0.9$ for $f = 25\%$) than for low porosities (e.g., approximately 5% at $X_\Sigma \approx -2.8$ for $f = 1\%$).

Figure 4.8(d) shows the effect of the void shape on the ISO gauge surfaces for porous ice ($M = 60$) with the same porosity $f = 1\%$, but with three different void shapes: (*i*) spherical ($w_1 = w_2 = 1$), (*ii*) prolate spheroidal ($w_1 = w_2 = 5$) and (*iii*) oblate spheroidal ($w_1 = w_2 = 0.2$). It is further assumed that the symmetry axis $\mathbf{n}_3$ of the voids is aligned with the loading axis $\mathbf{e}_3$ and, thus, also aligned with the $\langle c \rangle$-axis of the crystal matrix. The corresponding IVH gauge surfaces are also included for comparison. First, we observe that the porous ice gauge surface for a given void shape is substantially different from that for porous FCC crystals (solid curves in Fig. 4.3(c)), demonstrating a significant effect of the crystallographic anisotropy (HCP vs. FCC) on the macroscopic behavior of porous crystals. In addition, it can be seen from Fig. 4.8(d) that the change of the void shape has strong *distortional* hardening or softening effects on the macroscopic behavior of porous ice, in agreement with the observations made for porous FCC crystals in Figs. 4.3(c) and 4.3(d). However, the effect of the void shape exhibits a strong dependence on the crystallographic anisotropy. For instance, while the hydrostatic strength for porous ice with prolate spheroidal voids ($w_1 = w_2 = 5$) is much larger than that with spherical voids ($w_1 = w_2 = 1$), the opposite is true for porous FCC crystals (see solid curves in Fig. 4.3(c)). This observation reveals a complex, coupled effect of the morphological anisotropy induced by the void shape and the crystallographic anisotropy. The ISO results are, again, rather similar to the corresponding IVH outer bounds, except for the "corner"

regions of the gauge surfaces.

At this point, we should remark that for axisymmetric loadings (4.11) that are aligned with the $\langle c \rangle$-axis of the crystal matrix, as well as with the symmetry axis of the spheroidal voids ($w_1 = w_2$), the two-dimensional Eshelby integrals involved in the calculation can be reduced to one dimension, so that a one-dimensional Gaussian quadrature integration scheme can be used to improve the numerical efficiency. In particular, 120 Gaussian points are used for the cases with $M \leq 20$, while 240 Gaussian points are used for $M = 60$ corresponding to the most sensitive cases.

4.4.2 Microstructure evolution and finite-strain response

In this subsection, we investigate the microstructure evolution and the finite-strain response for porous HCP crystals under *uniaxial loading conditions*, also focusing on the effect of the crystal anisotropy (values of M). Thus, we consider porous HCP crystals with initially random, isotropic distributions of spherical voids ($w_1 = w_2 = 1$) and porosity $f_0 = 1\%$, subjected to uniaxial loadings of the type $\overline{\boldsymbol{\sigma}} = \overline{\sigma}_{33}\mathbf{e}_3 \otimes \mathbf{e}_3$. We investigate two cases: (i) uniaxial tension with $\overline{\sigma}_{33} > 0$ ($X_\sigma = 1/3$, $L = -1$), and uniaxial compression with $\overline{\sigma}_{33} < 0$ ($X_\sigma = -1/3$, $L = 1$). Given that the $\langle c \rangle$-axis of the crystal matrix is initially aligned with the loading direction $\mathbf{e}_3$, it can be shown that the average "elastic" spin in the crystal matrix (see equation (3.60) in chapter 3) is zero, as a consequence of the fact that both the average "continuum" spin and the average "plastic" spin in the crystal matrix are identically zero. Therefore, the *average* lattice orientation remains fixed throughout the deformation. In addition, it can be shown that the average void shape deforms from initially spherical to spheroidal ($w_1 = w_2$), with the symmetry axis $\mathbf{n}_3$ of the voids always parallel to the loading axis $\mathbf{e}_3$ (also parallel to the $\langle c \rangle$-axis of the crystal matrix). Furthermore, the resulting macroscopic logarithmic strain $\overline{\mathbf{E}}$ (and macroscopic strain rate $\overline{\mathbf{D}}$) can be shown to be axisymmetric of the form (4.9) with $\overline{E}_{11} = \overline{E}_{22}$ (or $\overline{D}_{11} = \overline{D}_{22}$), and $\mathbf{x}_l = \mathbf{e}_l$ ($l = 1, 2, 3$). For simplicity, it is further assumed that all slip systems are *non-hardening*, so that the reference flow stresses τ_A, τ_B, τ_C and the contrast parameter M remain fixed throughout the deformation.

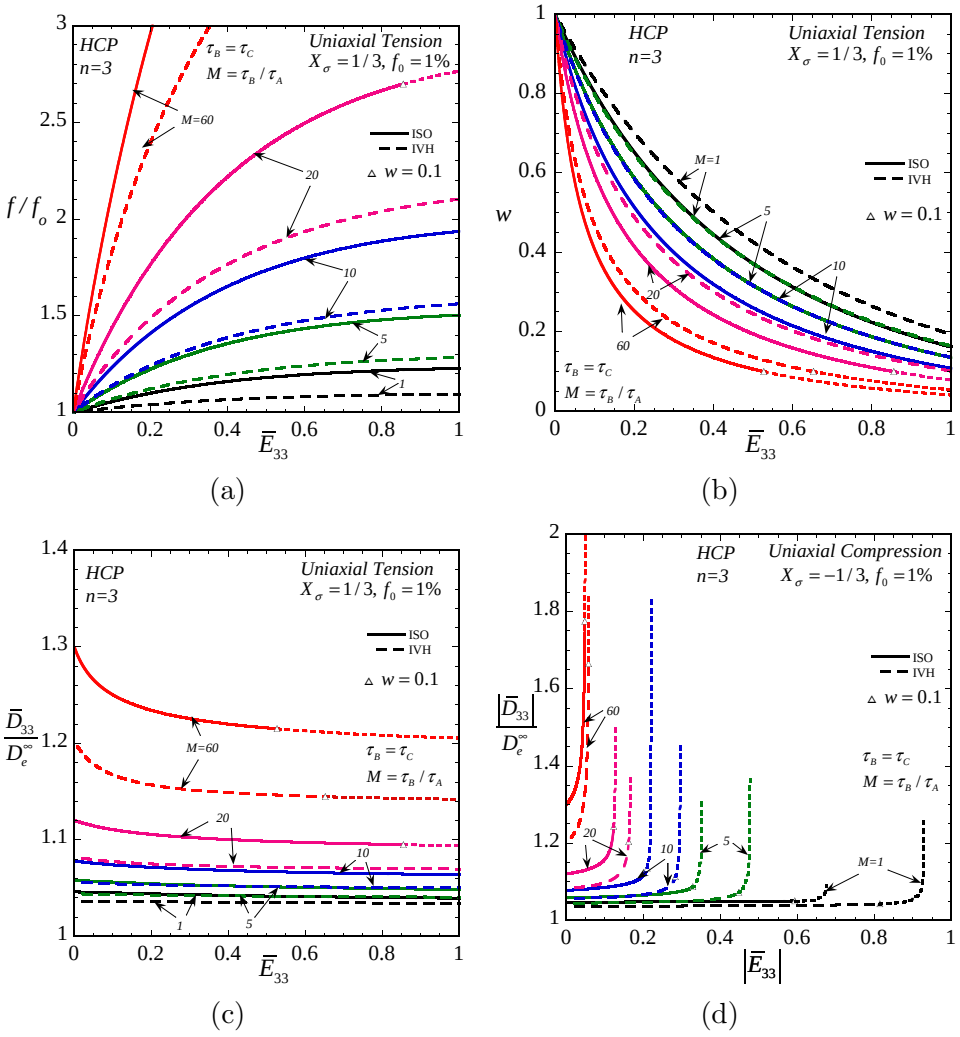

Figure 4.9: ISO results for porous HCP single crystals with an initially isotropic distribution of spherical voids ($w_1 = w_2 = 1$) in $f_0 = 1\%$ initial porosity, subjected to uniaxial tensions ($X_\sigma = 1/3$ and $L = -1$) aligned with the $\langle c \rangle$-axis of the crystal, where different values of the contrast parameter M are considered ($M = 1$, 5, 10, 20 and 60). Plots are shown for the evolution of the (a) normalized porosity f/f_0, (b) aspect ratio $w = a_{min}/a_{max} = a_1/a_3 = a_2/a_3 = 1/w_1 = 1/w_2$, and (c) normalized macroscopic axial strain rate $\overline{D}_{33}/D_e^\infty$, as functions of the macroscopic axial logarithmic strain $\overline{E}_{33}$. The corresponding IVH results are also shown for comparison. Fig. 4.9(d) shows the magnitude of the normalized macroscopic axial strain rate $|\overline{D}_{33}|/D_e^\infty$ as a function of the magnitude of the macroscopic axial logarithmic strain $|\overline{E}_{33}|$ for uniaxial compressions ($X_\sigma = -1/3$ and $L = 1$), and will be discussed in the context of Fig. 4.10.

Uniaxial tension. Figures 4.9(a)-4.9(c) present ISO and IVH results for the evolution of the microstructure and for the macroscopic response of porous HCP single crystals subjected to uniaxial tension for different values of the contrast parameter ($M = 1, 5, 10, 20, 60$). Figure 4.9(a) depicts the normalized porosity f/f_0 versus the macroscopic axial strain $\overline{E}_{33}$. We observe that the ISO estimate for f/f_0 initially increases with $\overline{E}_{33}$ and saturates at a finite value at large enough strains for all values of M. However, as M increases, the ISO estimate for f/f_0 grows more rapidly with $\overline{E}_{33}$ and approaches a larger asymptote, indicating that porosity growth can be quite significant at low stress triaxiality ($X_\sigma = 1/3$) for porous HCP crystals with large crystal anisotropy. Note that the porosity evolution for porous HCP crystals with $M = 1$ is rather similar to that for porous FCC single crystals in Fig. 4.5(a) with $X_\sigma = 1/3$ (uniaxial tension), while the corresponding plot for porous ice with $M = 60$ initially grows with a rate that is roughly 20 times larger than that for $M = 1$, and tends to a significantly larger asymptote around 6 (not shown in the figure). The above observations also hold for the IVH results. However, for given values of M, the porosity growth predicted by the IVH is much weaker than for the ISO.

Figure 4.9(b) gives the corresponding results for the aspect ratio $w = a_1/a_3 = a_2/a_3 = 1/w_1 = 1/w_2$ (the ratio of the length of the void semi-axis in the transverse direction to that in the axial direction). It can be seen that the ISO results for w start from one and decrease continuously to zero as $\overline{E}_{33} \to \infty$ for all values of M, indicating that the initially spherical void shape becomes progressively more prolate tending to a cylindrical void shape as the deformation continues to increase. Moreover, we observe that increasing M has the effect of accelerating the change in shape of the voids towards their limiting values. The IVH results for w are found to be qualitatively similar, although the evolution is a bit slower. Thus, our results show that the evolution of the porosity and void shape with the macroscopic axial strain is faster for porous HCP crystals with larger crystal anisotropies. Given that the capacity of the crystal to accommodate axial extension is progressively reduced with increasing values of M, a larger proportion of the macroscopic axial extension must be accommodated by the voids, thus leading to faster porosity growth and axial void

elongation.

Figure 4.9(c) presents the corresponding results for the normalized macroscopic axial strain rate $\overline{D}_{33}/D_e^\infty$ as a function of $\overline{E}_{33}$ for uniaxial tension. It can be seen that the ISO results for $\overline{D}_{33}/D_e^\infty$ decreases monotonically with $\overline{E}_{33}$ for all values of M, indicating overall hardening for the porous HCP crystals (even though the corresponding porosity grows with $\overline{E}_{33}$ suggests softening). This overall hardening behavior is induced by the change of the void shape from spherical to prolate spheroidal (Fig. 4.9(b)), which, as shown in Fig. 4.8(d), has a hardening effect that can dominate the softening due to porosity growth (Fig. 4.9(a)). In addition, we can see from Fig. 4.9(c) that the drop in $\overline{D}_{33}/D_e^\infty$ becomes progressively sharper with increasing values of M, indicating stronger hardening for porous HCP crystals with larger crystal anisotropy. The above observation also holds for the IVH results. However, for given values of M, the IVH estimates for $\overline{D}_{33}/D_e^\infty$ are considerably lower than the corresponding ISO estimates, consistent with the fact that the IVH estimates for the effective behavior of porous crystals are stiffer than the corresponding ISO estimates.

Uniaxial compression. Figures 4.10 and 4.9(d) show the effect of the crystal anisotropy (values of M) on the microstructure evolution and on the macroscopic response of porous HCP crystals subjected to uniaxial compression. First, we note that the corresponding results for uniaxial compression are significantly different from those for uniaxial tension, as expected on physical grounds. Next, Figs. 4.10(a) and 4.10(b) present results for the normalized porosity f/f_0 and the aspect ratio $w = a_3/a_1 = a_3/a_2 = w_1 = w_2$, respectively, as functions of the magnitude of the macroscopic axial strain $|\overline{E}_{33}|$. We can see that for all values of M, the ISO estimates for both f/f_0 and w decrease monotonically with $|\overline{E}_{33}|$ and tend to zero simultaneously at sufficiently large strains, indicating that the initially spherical voids collapse into penny-shaped cracks lying on the $\mathbf{e}_1$-$\mathbf{e}_2$ plane. In addition, we observe from Figs. 4.10(a) and 4.10(b) that increasing M leads to a faster reduction of both the normalized porosity f/f_0 and the aspect ratio w and, therefore, to faster collapse of the voids. In particular, the ISO plots for f/f_0 and w for porous HCP crystals with $M = 1$ are similar to those for porous FCC crystals in Figs. 4.6(a) and 4.6(b) for $X_\sigma = -1/3$ (uniaxial compression),

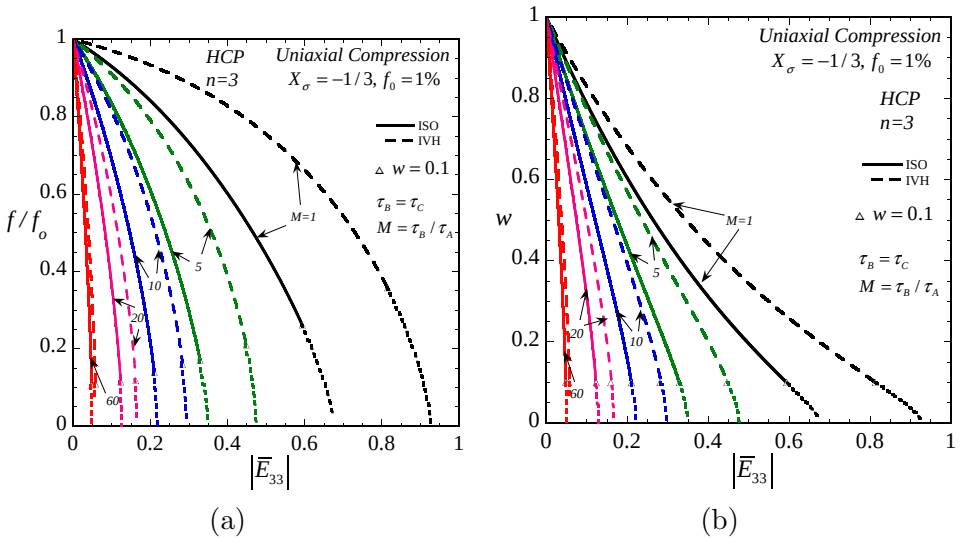

Figure 4.10: ISO results for porous HCP single crystals with an initially isotropic distribution of spherical voids ($w_1 = w_2 = 1$) in $f_0 = 1\%$ initial porosity, subjected to uniaxial compressions ($X_\sigma = -1/3$ and $L = 1$) aligned with the $\langle c \rangle$-axis of the crystal, where different values of the contrast parameter M are considered ($M = 1$, 5, 10, 20 and 60). Plots are shown for the evolution of the (a) normalized porosity f/f_0, and (b) aspect ratio $w = a_{min}/a_{max} = a_3/a_1 = a_3/a_2 = w_1 = w_2$ as functions of the magnitude of the macroscopic axial logarithmic strain $\overline{E}_{33}$. The corresponding IVH results are also shown for comparison.

while the corresponding results for porous ice with $M = 60$ exhibit much faster drops with $|\overline{E}_{33}|$, tending to zero at an axial strain that is more than 10 times smaller than that for $M = 1$. The physical explanation for this result is that, as M increases, the capability of the crystal matrix to accommodate axial contraction is progressively reduced and, therefore, larger fractions of the macroscopic axial contraction must be accommodated by the voids. The IVH estimates for f/f_0 and w are qualitatively similar to the corresponding ISO estimates, but again underestimate the evolution of both variables, especially for smaller values of M (the relative differences between the ISO and IVH results can be more than 50%).

Figure 4.9(d) provides the corresponding results for the magnitude of the normalized macroscopic axial strain rate $|\overline{D}_{33}|/D_e^\infty$ versus the magnitude of the axial strain $|\overline{E}_{33}|$. We can see that for all values of M, the ISO estimates for $|\overline{D}_{33}|/D_e^\infty$ increase monotonically with $|\overline{E}_{33}|$, indicating overall softening for the material (even though the corresponding porosities decrease with $|\overline{E}_{33}|$ inducing a hardening effect). This

counterintuitive overall softening behavior is found to be a consequence of the rapid change of the void shape from spherical to oblate spheroidal (void collapse), which prevails over the hardening expected from porosity reduction. Furthermore, we observe that increasing M results in faster growth in $|\overline{D}_{33}|/D_e^{\infty}$, indicating stronger softening for porous HCP crystals with larger anisotropy (values of M). In this connection, it should be emphasized that the softening behavior for porous HCP crystals is fairly smooth and can occur quite early in the deformation—well before any possible void surface contact. The above observation is also true for the IVH estimates with the only difference that the IVH estimates are somewhat lower than the corresponding ISO estimates. As already mentioned earlier, this is expected since the IVH leads to stiffer estimates for the effective behavior of porous crystals when compared with the ISO.

In conclusion, it has been found that, for both uniaxial tension and compression, the overall hardening or softening of porous HCP crystals is largely controlled by the evolution of the void shape (with the porosity playing a smaller role). This is especially the case for porous HCP crystals with large crystal anisotropies, such as porous ice, where the hardening or softening induced by the void shape changes can be quite significant.

4.5 Concluding remarks

In this chapter, the Iterated Second-Order (ISO) homogenization model, developed in chapter 3 of this work, was used to generate estimates for both the instantaneous response and the evolution of the microstructure for porous viscoplastic FCC and HCP single crystals. The resulting estimates were found to be in quite good agreement with FEM results available from the literature (Srivastava and Needleman, 2012; 2015; Mbiakop et al., 2015b), demonstrating a remarkable predictive capability for the ISO model. Specifically, it was found that the effective instantaneous response of porous single crystals exhibits a strong dependence on the "crystallographic" anisotropy induced by the preferred orientation and constitutive properties

of the active slip systems, as well as on the "morphological" anisotropy determined by the instantaneous values of the porosity and void shape. In addition, the intrinsic crystallographic anisotropy was found to have a significant effect on the dependence of the macroscopic response of the porous single crystals on the porosity and void morphology, indicating a complex, coupled interaction between the two different types of anisotropies. Furthermore, the evolution of the microstructure and the finite-strain response of porous crystals were found to be quite sensitive to the specific loading conditions, as characterized by the loading orientation, Lode angle and stress triaxiality. In particular, the ISO model revealed a significant effect of the crystallographic anisotropy on the evolution of the microstructure, which in turn has implications for the overall hardening (or softening)—and therefore also for shear localization—in these materials.

The ISO model is based on the recently developed fully optimized second-order method (Ponte Castañeda, 2015), and uses this homogenization procedure in an iterated fashion (Agoras and Ponte Castañeda, 2013) to "discretize" the properties of the matrix and thereby generate significantly improved estimates, especially for high triaxiality conditions and small porosities. Earlier homogenization models based on the variational (VAR) linear comparison approach (deBotton and Ponte Castañeda, 1995) provide rigorous bounds for porous single crystals, but they are too "stiff" for large triaxialities and small porosities. For this reason, Mbiakop et al. (2015b) proposed an *ad hoc* modification of the VAR approach (called MVAR), which was designed to give accurate results for the gauge surfaces of porous crystals with nearly equal flow stresses for all active slip systems. In addition, Song and Ponte Castañeda (2017a) proposed an alternative modification (IVH) that was also based on the iterated approach of Agoras and Ponte Castañeda (2013). Compared to these earlier approaches, the new ISO method was found to give somewhat improved predictions relative to the IVH method, and to give similarly accurate predictions to the MVAR method, for the instantaneous response of porous single crystals with small crystal anisotropy (e.g., porous FCC crystals). On the other hand, the ISO and IVH models were found to give significantly improved estimates for the instantaneous response of

porous single crystals with large anisotropy (e.g., porous ice). However, the main advantage of the ISO model lies in its ability to predict rather well the evolution of the microstructure and associated macroscopic response for large-deformation processes, which is something that no other method can do presently.

Thus, the results of this chapter helped confirm the important effect of crystallographic anisotropy on the overall constitutive response of porous single crystals, suggesting an additional level of complexity in the modeling of such materials. Due to its ability to deal with broad classes of materials with different crystallographic anisotropies, material nonlinearities, porosities and void morphologies—without the need for fitting parameters requiring recalibration for different material systems—the ISO homogenization model provides a powerful tool for effectively handling the effect of porosity in single crystals. Having said this, the ISO model is still amenable to potential improvements, especially for hydrostatic loadings. In addition, the effects of elastic strains and matrix hardening that were neglected in the present work can also be accounted for—at least approximately—in a straightforward fashion. As a final remark, we note that the ISO model developed in this work can be generalized in seamless fashion for porous polycrystals, thus accounting for the coupled effects of morphological and crystallographic textures, whose evolution is crucial for modeling the macroscopic behavior of porous low-symmetry materials, such as porous Ti and ice polycrystals. A first step in this direction was provided in the work of Lebensohn et al. (2011), where a less accurate homogenization approach was used to examine the instantaneous response of polycrystalline solids containing intergranular voids, but much remains to be done in this area, in particular, to be able to handle morphological and crystallographic texture evolution in finite-strain processes. This will be pursued in the following chapters.

Chapter 5

Fully optimized second-order homogenization model of viscoplastic polycrystals

In this chapter, we present a fully optimized second-order (FOSO) homogenization model for the finite-strain response of viscoplastic polycrystals. The model makes use of a recently developed variational homogenization method, together with the self-consistent estimates for the instantaneous response of an optimally selected linear comparison composite (LCC), to generate the corresponding estimates for a nonlinear polycrystal. The estimates are guaranteed to be exact to second order in the heterogeneity contrast, and to satisfy all known bounds. Unlike the earlier second-order estimates, the FOSO estimate has the advantage that the macroscopic behavior and field statistics in the nonlinear composite can be conveniently extracted from those in the LCC. Moreover, consistent homogenization estimates for the average strain-rate and spin fields are used to derive the evolution equations for the morphological and crystallographic textures of the polycrystals at finite strains. In particular, the FOSO model is applied to investigate the effective behavior and field statistics of untextured HCP polycrystals, and the effects of the rate sensitivity and grain anisotropy are studied in detail. It is found that the new FOSO estimates are in the best agreement with available numerical results. Finally, the FOSO model is used to predict the

texture evolution for HCP polycrystals under uniaxial compression at finite strains. It is found that a strong basal texture develops as a consequence of the predominant basal slips, and the material exhibits an interesting softening-hardening behavior due to texture evolution.

5.1 Introduction

Many minerals and industrial materials are aggregates of randomly orientated and distributed single-crystal grains. One example is ice, which is a common mineral on the earth's surface. The study on the grain-scale rheology of ice has received much attention especially at a time of climate change, due to its crucial importance for understanding a wide variety of large-scale geophysical phenomena such as the flow and dynamics of glaciers and ice sheets. Another example is the metal alloys (titanium, magnesium and etc.), which exhibit excellent mechanical and biological properties and are thus widely used for transportation, defense and biomedical applications. For these reasons, it is of great scientific and technological value to be able to characterize the *effective* behavior of polycrystalline samples, from the known properties of their constituents and given statistical information of their microstructures. In addition, when the polycrystalline samples are subjected to finite-strain deformations, their microstructures—such as the grain shape and the distribution of the crystallographic orientations—evolve as the deformation progresses, which can in turn affect the effective response of the polycrystals. Thus, the objective of the present work is to develop homogenization models to characterize the effective response, as well as the evolution of the microstructure for viscoplastic polycrystals at finite strains.

Several constitutive models are already available in the literature to estimate the viscoplastic response of polycrystalline solids. Among these, the simplest and most commonly used is the uniform strain rate approximation of Taylor (1938). There is also the complementary uniform stress approximation of Reuss (1929). These estimates are known to provide the upper and lower bounds, respectively, for the effective flow stress of the polycrystals. However, because of their uniform field assumptions,

the Taylor and Reuss estimates are not expected to be very accurate, especially when the single-crystal behavior becomes highly nonlinear and anisotropic. For example, while the Taylor model yields fairly good estimates for the macroscopic constitutive response and texture evolution of certain highly symmetric polycrystals (e.g., Kocks et al., 1998), they may predict overly stiff material properties and qualitatively incorrect texture evolutions for polycrystals with highly anisotropic grains (e.g., Siemes, 1974).

Improved estimates were developed by means of various nonlinear generalizations of the self-consistent estimates (Hershey, 1954; Kröner, 1958; Willis, 1977), which are known to be very accurate for linearly viscous polycrystals. The central idea of these nonlinear self-consistent methods is to suitably linearize the constitutive relation, and to use the self-consistent estimates for a linear polycrystal to obtain the corresponding estimates for a nonlinear polycrystal. However, the main difficulty consists of finding the 'right' linearization scheme to select the linear polycrystal in an 'optimal' fashion. The earlier nonlinear self-consistent methods utilize only *first-moment* information of the stress fields, together with various *ad hoc* linearization schemes, to approximate the grain interactions. Among these, perhaps the most popular are the incremental method of Hill (1965) and Hutchinson (1976), and the tangent method of Molinari et al. (1987) and Lebensohn et al. (1993). In particular, the tangent, or the viscoplastic self-consistent (VPSC), model was widely used to predict the texture evolution in viscoplastic polycrystals, see, for example, Castelnau et al. (1996, 1997). While the incremental and tangent methods provide estimates that are quite similar for polycrystals with weak nonlinearity, they yield significantly different estimates for strongly nonlinear polycrystals. For instance, for polycrystals with isotropic textures, the incremental estimates for the effective flow stress tend to the Taylor upper bound, while the corresponding tangent estimates tend to the Reuss lower bound. The discrepancy among these estimates is particularly dramatic for materials with high grain anisotropy, including minerals such as ice and olivine, and industrial alloys such as titanium and zirconium, where the Taylor upper bound can be several times the Reuss lower bound.

Significantly improved nonlinear self-consistent methods were developed by Ponte Castañeda and coworkers, making use of linearization schemes depending not only on the first moment, but also on the *second moment* of the stress field. These methods are derived from rigorous variational principles, which express the potential of a nonlinear polycrystal in terms of that of a linear comparison composite (LCC), whose properties play the role of trial fields in the variational principles. Thus, the linearization condition can be identified as the stationary condition associated with the variational principle. Along these lines, Nebozhyn et al. (2001) proposed a variational self-consistent method employing the variational principle of deBotton and Ponte Castañeda (1995), and building on the earlier work of Ponte Castañeda (1991) for isotropic materials. This method involves a 'secant' linearization of the nonlinear response evaluated at the second moments of the stresses in the grains. Due to their extremal character, the variational estimates for the effective flow stress provide rigorous upper bounds for all other self-consistent estimates. The latter fact is used to demonstrate the inconsistency of the incremental estimates, which are often found to violate the rigorous bounds. Moreover, the stationary character of the variational estimates allows the use of the macroscopic behavior and field statistics in the LCC to estimate the corresponding quantities in the nonlinear polycrystal. The variational method was later used by Liu et al. (2003) to predict the texture evolution in titanium polycrystals. Compared with the earlier homogenization estimates, the variational results are found to be in much better agreement with the experimental and numerical results. However, precisely because of their bounding properties, the variational predictions are expected to be overestimates for the effective behavior.

More accurate estimates of the self-consistent type were developed by Liu and Ponte Castañeda (2004a), making use of a generalization of the second-order variational method of Ponte Castañeda (2002). This method involves a 'generalized secant' linearization of the nonlinear response, incorporating dependence on both the first and second moments of the stress field, and yields estimates that are *exact to second order* in the heterogeneity contrast. The method was then employed to predict the texture evolution of viscoplastic polycrystals by Liu et al. (2005) and Lebensohn

et al. (2007), and was found to yield the most accurate estimates among the various self-consistent theories available to date. However, the second-order estimates have the undesirable feature that the macroscopic behavior and field statistics in the nonlinear polycrystals do not coincide with the corresponding quantities in the LCC, due to the lack of full stationarity of the estimates with respect to the properties of the LCC. In fact, Idiart and Ponte Castañeda (2007a) have shown that additional terms involving difficult-to-compute derivatives are required to obtain consistent estimates for the above quantities in the nonlinear polycrystals, hindering the efficient implementation of the second-order method. In order to remedy this deficiency, Ponte Castañeda (2015) proposed a new 'generalized secant' second-order approach, making use of a more general variational principle, such that the estimates are *fully stationary* with respect to the properties of the LCC, and are still exact to second order in the heterogeneity contrast. This new method requires the same amount of information on the field statistics (i.e., the first and second moments of the stress field), but has all the advantages of the earlier variational estimates in that the macroscopic constitutive relation and field statistics in the LCC can be directly used to estimate the corresponding quantities in the nonlinear polycrystals.

In this work, the fully optimized second-order (FOSO) method will be used for the first time to generate estimates of the self-consistent type for the macroscopic behavior and field statistics (e.g., phase averages and field fluctuations) for viscoplastic polycrystals with given fixed states of the microstructure. In addition, consistent homogenization estimates for the average strain rate and spin fields will be used to account for the evolution of the microstructure at finite strains. Furthermore, applications of the FOSO model for HCP polycrystals will be considered, and the new FOSO estimates will be compared with the earlier nonlinear homogenization estimates, as well as with the full-field, Fast Fourier Transform (FFT) results of Lebensohn et al. (2004, 2007). The effect of the nonlinearity and anisotropy of the single-crystal grains on the macroscopic behavior and field statistics in the polycrystals will be investigated separately in detail. Finally, the finite-strain response and texture evolution of the HCP polycrystals under uniaxial compression will be considered.

5.2 Background and formulation

In this work, polycrystals are taken to be aggregates of randomly distributed, perfectly bonded (anisotropic) single-crystal grains with varying orientations. Separation of length scales is assumed so that the size of the grains is much smaller than the size of the specimen and the scale of variation of the loading conditions. Furthermore, the polycrystal is assumed to have statistically uniform and ergodic microstructure.

Here we confine our attention to monolithic polycrystals, so that the single-crystal grains differ from each other only in terms of crystallographic orientation, but not in crystallographic structure or composition. For simplicity, it is further assumed that the crystal orientations take on a set of discrete values, characterized by (orthogonal) rotation tensors $\mathbf{Q}^{(r)}$ $(r = 1, ..., N)$, so that the lattice vectors $\mathbf{l}_i^{(r)}$ $(i = 1, 2, 3)$ for a given crystal orientation are related to the corresponding lattice vectors $\mathbf{l}_i$ $(i = 1, 2, 3)$ for a 'reference' single-crystal via $\mathbf{l}_i^{(r)} = (\mathbf{Q}^{(r)})^T \mathbf{l}_i$ $(i = 1, 2, 3)$. The polycrystal is assumed to occupy a region of space Ω, while all the grains with a given orientation $\mathbf{Q}^{(r)}$ occupy (disconnected) subregions $\Omega^{(r)}$ $(r = 1, ..., N)$ and will be collectively referred to as 'phase r'. Let the symbols $\langle\cdot\rangle$ and $\langle\cdot\rangle^{(r)}$ denote volume averages over the polycrystal (Ω) and phase r $(\Omega^{(r)})$, respectively. The distribution of various phases can be described by the indicator functions $\chi^{(r)}(\mathbf{x})$, which are defined to be equal to 1 if the position vector $\mathbf{x}$ is in $\Omega^{(r)}$ and 0 otherwise. In the random context, it is necessary to consider the ensemble averages of the indicator functions $\chi^{(r)}(\mathbf{x})$. In particular, the ensemble average of $\chi^{(r)}(\mathbf{x})$ defines the one-point probability $p^{(r)}(\mathbf{x})$ of finding phase r at point $\mathbf{x}$, while the ensemble average of $\chi^{(r)}(\mathbf{x})\chi^{(s)}(\mathbf{x'})$ defines the two-point probability $p^{(rs)}(\mathbf{x}, \mathbf{x'})$ of finding simultaneously phase r at $\mathbf{x}$ and phase s at $\mathbf{x'}$. Due to the ergodic hypothesis, it is possible to replace the ensemble averages by the volume averages, so that the one-point probability $p^{(r)}(\mathbf{x})$ can be identified with the volume fraction of phase r, as given by $c^{(r)} = \langle\chi^{(r)}(\mathbf{x})\rangle$, while the two-point probability $p^{(rs)}(\mathbf{x}, \mathbf{x'})$ can be identified with the volume average $\langle\chi^{(r)}(\mathbf{x})\chi^{(s)}(\mathbf{x'})\rangle$. Note that the volume fractions $c^{(r)}$ $(r = 1, ..., N)$ and the rotation tensors $\mathbf{Q}^{(r)}$ $(r = 1, ..., N)$ determine the orientation distribution function (ODF) of the polycrystals,

characterizing the *crystallographic* texture, while the two-point statistics $p^{(rs)}(\mathbf{x}, \mathbf{x}')$ $(r, s = 1, ..., N)$ serve to describe the distribution of the grains in space, characterizing (in an approximate way) the *morphological* texture.

In particular, we assume that the two-point probabilities $p^{(rs)}(\mathbf{x}, \mathbf{x}')$ exhibit "ellipsoidal" symmetry (Willis, 1977), as can be characterized by a symmetric second-order tensor $\boldsymbol{Z}$, so that $p^{(rs)}(\mathbf{x}, \mathbf{x}') = p^{(rs)}(|\boldsymbol{Z}(\mathbf{x} - \mathbf{x}')|)$. In this case, the tensor $\boldsymbol{Z}$ correlates with the ellipsoidal average grain shape, and is defined by

$$\boldsymbol{Z} = w_1 \mathbf{n}_1 \otimes \mathbf{n}_1 + w_2 \mathbf{n}_2 \otimes \mathbf{n}_2 + \mathbf{n}_3 \otimes \mathbf{n}_3, \tag{5.1}$$

where $w_1 = a_3/a_1$, $w_2 = a_3/a_2$ are the two aspect ratios characterizing the average shape of the ellipsoidal grains (a_1, a_2 and a_3 are respectively the length of the three semi-axes of the grain), and $\mathbf{n}_i$ $(i = 1, 2, 3)$ are unit vectors along the three principal directions of the ellipsoidal grains. For later use, we define a rotation tensor $\mathbf{G}^{(g)}$ that relates the grain axes $\mathbf{n}_i$ $(i = 1, 2, 3)$ to the sample axes $\mathbf{e}_i$ $(i = 1, 2, 3)$, such that $\mathbf{n}_i = \left(\mathbf{G}^{(g)}\right)^{\mathrm{T}} \mathbf{e}_i$ $(i = 1, 2, 3)$. Then, the microstructure of the polycrystal can be described by the set of microstructural variables

$$\{\mathbf{Q}^{(r)}, w_1, w_2, \mathbf{G}^{(g)}\}, \tag{5.2}$$

with $r = 1, ..., N$. Note that with the above choice of the microstructural variables, the evolution of the ODF in large deformations is characterized by the rotation of the tensors $\mathbf{Q}^{(r)}$ $(r = 1, ..., N)$, while the corresponding volume fractions $c^{(r)}$ $(r = 1, ..., N)$ of the single-crystal phases are taken to be fixed, due to the incompressibility of the single-crystal grains (this is why we do not include $c^{(r)}$ in the microstructural variables (5.2)). However, it should be mentioned that there are other ways to describe the evolution of the ODF (see, e.g., Dawson and Marin, 1997). Note further that the microstructural variables (5.2) include only up to two-point statistics and, thus, do not suffice to determine exactly the properties of the polycrystals. However, the objective of this work is to obtain estimates of the self-consistent type for the macroscopic response of the polycrystals, and it is well known that these estimates depend only

on the one- and two-point statistics.

In this work, the single-crystal grains are assumed to deform by dislocation glide along K well-defined crystallographic slip systems. In addition, the constitutive behavior of the single-crystal phases is taken to be viscoplastic (elasticity is neglected for simplicity), so that the *local* constitutive response of the polycrystal is given by

$$\mathbf{D} = \frac{\partial u^{(r)}}{\partial \boldsymbol{\sigma}}, \quad u(\mathbf{x}, \boldsymbol{\sigma}) = \sum_{r=1}^{N} \chi^{(r)}(\mathbf{x}) u^{(r)}(\boldsymbol{\sigma}), \quad u^{(r)}(\boldsymbol{\sigma}) = \sum_{k=1}^{K} \phi_{(k)}^{(r)}(\tau_{(k)}^{(r)}), \tag{5.3}$$

where $\mathbf{D}$ is the Eulerian strain rate, $\boldsymbol{\sigma}$ is the Cauchy stress, and u and $u^{(r)}$ are the *convex* stress potentials for the polycrystal and single-crystal phase with orientation $\mathbf{Q}^{(r)}$, respectively. The functions $\phi_{(k)}^{(r)}$ $(k = 1, ..., K)$ are the slip potentials characterizing the response of the K slip systems in a crystal with orientation $\mathbf{Q}^{(r)}$, and depend on the resolved shear (or Schmid) stresses

$$\tau_{(k)}^{(r)} = \boldsymbol{\sigma} \cdot \boldsymbol{\mu}_{(k)}^{(r)}, \quad \text{where} \quad \boldsymbol{\mu}_{(k)}^{(r)} = \frac{1}{2}\left(\mathbf{n}_{(k)}^{(r)} \otimes \mathbf{m}_{(k)}^{(r)} + \mathbf{m}_{(k)}^{(r)} \otimes \mathbf{n}_{(k)}^{(r)}\right). \tag{5.4}$$

Here the $\boldsymbol{\mu}_{(k)}^{(r)}$ are the second-order Schmid tensors with $\mathbf{n}_{(k)}^{(r)}$ and $\mathbf{m}_{(k)}^{(r)}$ denoting, respectively, the unit vectors normal to the slip plane and along the slip direction of the kth slip system, for a crystal with orientation $\mathbf{Q}^{(r)}$. Note that the Schmid tensors $\boldsymbol{\mu}_{(k)}^{(r)}$ for the polycrystal are related to the corresponding Schmid tensors $\boldsymbol{\mu}_{(k)}$ for a 'reference' single crystal via $\boldsymbol{\mu}_{(k)}^{(r)} = {\mathbf{Q}^{(r)}}^T \boldsymbol{\mu}_{(k)} \mathbf{Q}^{(r)}$. For simplicity, the slip potentials of all grains are assumed to be of the power-law form

$$\phi_{(k)}(\tau) = \frac{\dot{\gamma}_0 (\tau_0)_{(k)}}{n+1} \left| \frac{\tau}{(\tau_0)_{(k)}} \right|^{n+1}, \tag{5.5}$$

where $\dot{\gamma}_0$ denotes the reference strain rate, $(\tau_0)_{(k)} > 0$ is the reference flow stress of the kth slip system, and $m = 1/n$ is the strain rate sensitivity (n is the viscous exponent). Note that the two limiting cases as n tends to 1 and ∞ are of special interest, as they describe linearly viscous and rigid ideally plastic behavior, respectively.

The effective viscoplastic response of the polycrystals may be written in the form

(e.g., Hutchinson, 1976; Ponte Castañeda and Suquet, 1998)

$$\overline{\mathbf{D}} = \frac{\partial \widetilde{u}(\overline{\boldsymbol{\sigma}})}{\partial \overline{\boldsymbol{\sigma}}}, \quad \widetilde{u}(\overline{\boldsymbol{\sigma}}) = \min_{\boldsymbol{\sigma} \in \mathcal{S}(\overline{\boldsymbol{\sigma}})} \langle u(\mathbf{x}, \boldsymbol{\sigma}) \rangle = \min_{\boldsymbol{\sigma} \in \mathcal{S}(\overline{\boldsymbol{\sigma}})} \sum_{r=1}^{K} c^{(r)} \langle u^{(r)}(\boldsymbol{\sigma}) \rangle^{(r)}, \tag{5.6}$$

where $\widetilde{u}$ is the effective stress potential for the polycrystal, $\overline{\mathbf{D}} = \langle \mathbf{D} \rangle$ and $\overline{\boldsymbol{\sigma}} = \langle \boldsymbol{\sigma} \rangle$ are the macroscopic strain rate and Cauchy stress, and $\mathcal{S}(\overline{\boldsymbol{\sigma}}) = \{\boldsymbol{\sigma}, \text{div } \boldsymbol{\sigma} = \mathbf{0} \text{ in } \Omega, \text{ and } \langle \boldsymbol{\sigma} \rangle = \overline{\boldsymbol{\sigma}}\}$ is the set of statically admissible stress fields.

A dual formulation of the problem may be given in terms of the dissipation potentials $w^{(r)}$ of the phases, which are defined by the Legendre transform

$$w^{(r)}(\mathbf{D}) = (u^{(r)})^*(\mathbf{D}) = \max_{\boldsymbol{\sigma}} \{\boldsymbol{\sigma} \cdot \mathbf{D} - u^{(r)}(\boldsymbol{\sigma})\}. \tag{5.7}$$

Then, the local constitutive relation of the polycrystal can be characterized by

$$\boldsymbol{\sigma} = \frac{\partial w}{\partial \mathbf{D}}, \quad w(\mathbf{x}, \mathbf{D}) = \sum_{r=1}^{N} \chi^{(r)}(\mathbf{x}) w^{(r)}(\mathbf{D}), \tag{5.8}$$

while its effective response is given by

$$\overline{\boldsymbol{\sigma}} = \frac{\partial \widetilde{w}(\overline{\mathbf{D}})}{\partial \overline{\mathbf{D}}}, \quad \widetilde{w}(\overline{\mathbf{D}}) = \min_{\mathbf{D} \in \mathcal{K}(\overline{\mathbf{D}})} \langle w(\mathbf{x}, \mathbf{D}) \rangle = \min_{\mathbf{D} \in \mathcal{K}(\overline{\mathbf{D}})} \sum_{r=1}^{K} c^{(r)} \langle w^{(r)}(\mathbf{D}) \rangle^{(r)}. \tag{5.9}$$

Here $\widetilde{w}$ is the effective dissipation potential, and $\mathcal{K}(\overline{\mathbf{D}})$ is the set of kinematically admissible strain-rate fields $\mathbf{D}$, such that there exists a continuous velocity field $\mathbf{v}$ satisfying $\mathbf{D} = (\nabla \mathbf{v} + \nabla \mathbf{v}^T)/2$ in Ω and $\mathbf{v} = \overline{\mathbf{D}}\mathbf{x}$ on $\partial\Omega$. Furthermore, it can be shown that the above two formulations in terms of stress and dissipation potentials are exactly equivalent to each other in the sense of Legendre duality, i.e., $\widetilde{w} = \widetilde{u}^*$. In general, the effective potentials $\widetilde{u}$ and $\widetilde{w}$ for nonlinear polycrystals cannot be computed exactly, except for certain special cases where both the microstructure and the response of the slip systems are very simple. In this work, approximate estimates for these potentials will be computed by means of the recently developed fully optimized second-order (FOSO) method of Ponte Castañeda (2015), as will be seen in Section 5.3.

For later use, here we define the relevant field statistics in the polycrystals. The first moments of the stress, strain-rate and spin fields over phase r are defined via $\overline{\boldsymbol{\sigma}}^{(r)} = \langle \boldsymbol{\sigma} \rangle^{(r)}$, $\overline{\mathbf{D}}^{(r)} = \langle \mathbf{D} \rangle^{(r)}$, and $\overline{\mathbf{W}}^{(r)} = \langle \mathbf{W} \rangle^{(r)}$, which are required to satisfy the global average conditions $\overline{\boldsymbol{\sigma}} = \sum_{r=1}^{N} c^{(r)} \overline{\boldsymbol{\sigma}}^{(r)}$, $\overline{\mathbf{D}} = \sum_{r=1}^{N} c^{(r)} \overline{\mathbf{D}}^{(r)}$, and $\overline{\mathbf{W}} = \sum_{r=1}^{N} c^{(r)} \overline{\mathbf{W}}^{(r)}$, with $\overline{\mathbf{W}}$ denoting the macroscopic spin. The von Mises equivalent measures for $\overline{\boldsymbol{\sigma}}^{(r)}$ and $\overline{\mathbf{D}}^{(r)}$ are defined by $\overline{\sigma}_e^{(r)} = \sqrt{\frac{3}{2} \overline{\boldsymbol{\sigma}}^{(r)\prime} \cdot \overline{\boldsymbol{\sigma}}^{(r)\prime}}$, where $\overline{\boldsymbol{\sigma}}^{(r)\prime}$ denotes the average stress deviator in phase r, and $\overline{D}_e^{(r)} = \sqrt{\frac{2}{3} \overline{\mathbf{D}}^{(r)} \cdot \overline{\mathbf{D}}^{(r)}}$ ($\overline{\mathbf{D}}^{(r)}$ is purely deviatoric due to the incompressibility of the single-crystal phases). Furthermore, the second moments of the stress and strain-rate fields over phase r are defined via $\langle \boldsymbol{\sigma} \otimes \boldsymbol{\sigma} \rangle^{(r)}$ and $\langle \mathbf{D} \otimes \mathbf{D} \rangle^{(r)}$, while the corresponding phase fluctuation covariance tensors are given by

$$\mathbb{C}_{\boldsymbol{\sigma}}^{(r)} \doteq \langle (\boldsymbol{\sigma} - \overline{\boldsymbol{\sigma}}^{(r)}) \otimes (\boldsymbol{\sigma} - \overline{\boldsymbol{\sigma}}^{(r)}) \rangle^{(r)} = \langle \boldsymbol{\sigma} \otimes \boldsymbol{\sigma} \rangle^{(r)} - \overline{\boldsymbol{\sigma}}^{(r)} \otimes \overline{\boldsymbol{\sigma}}^{(r)}, \tag{5.10}$$

and similarly for $\mathbb{C}_{\mathbf{D}}^{(r)}$. In particular, we will make use of the statistical quantities

$$\overline{\tau}_{(k)}^{(r)} = \overline{\boldsymbol{\sigma}}^{(r)} \cdot \boldsymbol{\mu}_{(k)}^{(r)}, \quad \overline{\overline{\tau}}_{(k)}^{(r)} = \boldsymbol{\mu}_{(k)}^{(r)} \cdot \langle \boldsymbol{\sigma} \otimes \boldsymbol{\sigma} \rangle^{(r)} \boldsymbol{\mu}_{(k)}^{(r)}, \quad \text{and} \quad \mathrm{SD}^{(r)}(\tau_{(k)}^{(r)}) = \sqrt{\overline{\overline{\tau}}_{(k)}^{(r)} - \left(\overline{\tau}_{(k)}^{(r)} \right)^2} \tag{5.11}$$

to denote the first moment, the second moment and the standard deviation of the resolved shear stress $\tau_{(k)}^{(r)}$ over slip system k in phase r. We will also make use of the standard deviations for the equivalent stress and strain rate over phase r:

$$\mathrm{SD}^{(r)}(\sigma_e) = \sqrt{\langle \sigma_e^2 - \left(\overline{\sigma}_e^{(r)} \right)^2 \rangle^{(r)}}, \quad \mathrm{SD}^{(r)}(D_e) = \sqrt{\langle D_e^2 - \left(\overline{D}_e^{(r)} \right)^2 \rangle^{(r)}}. \tag{5.12}$$

Completely analogous expressions can be obtained for the overall fluctuation covariance tensors $\mathbb{C}_{\boldsymbol{\sigma}}$ and $\mathbb{C}_{\mathbf{D}}$, as well as for the corresponding overall standard deviations $\mathrm{SD}(\sigma_e)$ and $\mathrm{SD}(D_e)$. For example, $\mathbb{C}_{\boldsymbol{\sigma}} = \langle \boldsymbol{\sigma} \otimes \boldsymbol{\sigma} \rangle - \overline{\boldsymbol{\sigma}} \otimes \overline{\boldsymbol{\sigma}}$, and $\mathrm{SD}(\sigma_e) = \sqrt{\langle \sigma_e^2 - \overline{\sigma}_e^2 \rangle}$.

5.3 Fully optimized second-order homogenization approach

In this section, we make use of the fully optimized second-order (FOSO) variational method of Ponte Castañeda (2015) to obtain estimates for the effective potential $(5.6)_2$, or equivalently $(5.9)_2$, for the viscoplastic polycrystals. The central idea of the FOSO method is to make use of the effective behavior of a linear comparison composite (LCC)—with the same microstructure as the nonlinear polycrystal of interest and with local properties determined by a suitably designed variational principle—to determine the effective behavior of the actual nonlinear composite. In particular, the local stress potentials for the LCC are given by the (quadratic) functions

$$u_L(\mathbf{x},\boldsymbol{\sigma}) = \sum_{r=1}^{N} \chi^{(r)}(\mathbf{x}) u_L^{(r)}(\boldsymbol{\sigma}), \quad u_L^{(r)}(\boldsymbol{\sigma}) = \frac{1}{2}\boldsymbol{\sigma}\cdot\mathbb{M}^{(r)}\boldsymbol{\sigma} + \boldsymbol{\eta}^{(r)}\cdot\boldsymbol{\sigma}, \tag{5.13}$$

where

$$\mathbb{M}^{(r)} = \sum_{k=1}^{K} \frac{1}{2\mu_{(k)}^{(r)}} \boldsymbol{\mu}_{(k)}^{(r)} \otimes \boldsymbol{\mu}_{(k)}^{(r)}, \quad \text{and} \quad \boldsymbol{\eta}^{(r)} = \sum_{k=1}^{K} \eta_{(k)}^{(r)}\, \boldsymbol{\mu}_{(k)}^{(r)} \tag{5.14}$$

are the uniform viscous compliance tensor and uniform eigenstrain-rate tensor, respectively, for phase r of the LCC, and the scalars $\mu_{(k)}^{(r)}$ and $\eta_{(k)}^{(r)}$ are the slip viscosities and slip eigenstrain rates, respectively. Differentiation of the stress potential $(5.13)_2$ with respect to $\boldsymbol{\sigma}$ shows that the constitutive relation for the phases in the LCC is mathematically analogous to that for a linear thermoelastic material, i.e., $\mathbf{D} = \mathbb{M}^{(r)}\boldsymbol{\sigma} + \boldsymbol{\eta}^{(r)}$.

Making use of $(5.6)_2$, we have that the effective response of the LCC can be characterized by the effective stress potential

$$\widetilde{u}_L(\overline{\boldsymbol{\sigma}}) = \min_{\boldsymbol{\sigma}\in\mathcal{S}(\overline{\boldsymbol{\sigma}})} \langle u_L(\mathbf{x},\boldsymbol{\sigma})\rangle = \min_{\boldsymbol{\sigma}\in\mathcal{S}(\overline{\boldsymbol{\sigma}})} \sum_{r=1}^{K} c^{(r)} \langle \frac{1}{2}\boldsymbol{\sigma}\cdot\mathbb{M}^{(r)}\boldsymbol{\sigma} + \boldsymbol{\eta}^{(r)}\cdot\boldsymbol{\sigma}\rangle^{(r)}. \tag{5.15}$$

In this work, $\widetilde{u}_L$ is computed by means of the estimates of the self-consistent (SC) type (Hershey, 1954; Willis, 1977), which depend on the microstructural variables (5.2) and are known to be very accurate for linear polycrystals (e.g., Lebensohn et al., 2004). The corresponding expressions for the SC estimates are briefly recalled in

Appendix I.

Following Ponte Castañeda (2015), the effective stress potential $\widetilde{u}$ in (5.6) for the nonlinear polycrystal can be written in the form

$$\widetilde{u}(\overline{\boldsymbol{\sigma}}) = \sum_{r=1}^{N} c^{(r)} \sum_{k=1}^{K} \left[\alpha_{(k)}^{(r)} \phi_{(k)}^{(r)}(\check{\tau}_{(k)}^{(r)}) + \left(1 - \alpha_{(k)}^{(r)}\right) \phi_{(k)}^{(r)}(\hat{\tau}_{(k)}^{(r)}) \right], \tag{5.16}$$

where $\alpha_{(k)}^{(r)}$ is an appropriately chosen 'weight factor' between 0 and 1 (see further discussions on choosing $\alpha_{(k)}^{(r)}$ below), and $\check{\tau}_{(k)}^{(r)}$ and $\hat{\tau}_{(k)}^{(r)}$ are stress variables given by

$$\check{\tau}_{(k)}^{(r)} = \overline{\tau}_{(k)}^{(r)} - \sqrt{\frac{1-\alpha_{(k)}^{(r)}}{\alpha_{(k)}^{(r)}}} \sqrt{\overline{\overline{\tau}}_{(k)}^{(r)} - \left(\overline{\tau}_{(k)}^{(r)}\right)^2} = \overline{\tau}_{(k)}^{(r)} - \sqrt{\frac{1-\alpha_{(k)}^{(r)}}{\alpha_{(k)}^{(r)}}} \mathrm{SD}^{(r)}\left(\tau_{(k)}^{(r)}\right), \tag{5.17}$$

and

$$\hat{\tau}_{(k)}^{(r)} = \overline{\tau}_{(k)}^{(r)} + \sqrt{\frac{\alpha_{(k)}^{(r)}}{1-\alpha_{(k)}^{(r)}}} \sqrt{\overline{\overline{\tau}}_{(k)}^{(r)} - \left(\overline{\tau}_{(k)}^{(r)}\right)^2} = \overline{\tau}_{(k)}^{(r)} + \sqrt{\frac{\alpha_{(k)}^{(r)}}{1-\alpha_{(k)}^{(r)}}} \mathrm{SD}^{(r)}\left(\tau_{(k)}^{(r)}\right). \tag{5.18}$$

Here we recall that $\overline{\tau}_{(k)}^{(r)}$, $\overline{\overline{\tau}}_{(k)}^{(r)}$ and $\mathrm{SD}^{(r)}\left(\tau_{(k)}^{(r)}\right)$, as defined by (5.11), are the first moment, the second moment, as well as the standard deviation, respectively, of the resolved shear stress over slip system k in phase r of the homogenization problem for the LCC defined by expression (5.15), while the explicit expressions of the SC type for $\overline{\boldsymbol{\sigma}}^{(r)}$ and $\langle \boldsymbol{\sigma} \otimes \boldsymbol{\sigma} \rangle^{(r)}$ in the LCC are provided by equation (5.41) and (5.42), respectively, in Appendix I.

In turn, the properties of the LCC, as determined by the slip viscosities $\mu_{(k)}^{(r)}$ and slip eigenstrain rates $\eta_{(k)}^{(r)}$ in (5.14), are required to satisfy the optimality conditions

$$\frac{1}{2\mu_{(k)}^{(r)}} = \frac{\phi_{(k)}^{(r)\prime}(\hat{\tau}_{(k)}^{(r)}) - \phi_{(k)}^{(r)\prime}(\check{\tau}_{(k)}^{(r)})}{\hat{\tau}_{(k)}^{(r)} - \check{\tau}_{(k)}^{(r)}}, \quad \text{and} \quad \eta_{(k)}^{(r)} = \phi_{(k)}^{(r)\prime}(\check{\tau}_{(k)}^{(r)}) - \frac{1}{2\mu_{(k)}^{(r)}} \check{\tau}_{(k)}^{(r)}. \tag{5.19}$$

Note that $(5.19)_1$ identifies the slip viscosities $\mu_{(k)}^{(r)}$ of the LCC with 'generalized secant' linearizations for the corresponding slip potentials of the viscoplastic poly-

crystals, accounting for both the first and second moments of the stress field for a given grain orientation. Expression (5.17)-(5.19) provide a set of $4N \times K$ nonlinear algebraic equations for the variables $\hat{\tau}_{(k)}^{(r)}$, $\check{\tau}_{(k)}^{(r)}$, $\mu_{(k)}^{(r)}$ and $\eta_{(k)}^{(r)}$ ($r = 1, ..., N$, $k = 1, ..., K$), which need to be solved numerically in general. In this work, a simple fixed-point method is used to solve these equations, and is found to be numerically efficient.

It is known (Idiart and Ponte Castañeda, 2007c; Ponte Castañeda, 2015) that the macroscopic constitutive relation, as well as the first and second moments of the stress and strain-rate fields in the nonlinear polycrystals can be estimated directly from the LCC, whose properties are given by the optimality conditions (5.19). In particular, the FOSO estimates for the macroscopic constitutive relation is given by

$$\overline{\mathbf{D}} = \frac{\partial \widetilde{u}}{\partial \overline{\boldsymbol{\sigma}}}(\overline{\boldsymbol{\sigma}}) = \frac{\partial \widetilde{u}_L}{\partial \overline{\boldsymbol{\sigma}}}(\overline{\boldsymbol{\sigma}}) = \widetilde{\mathbb{M}}\overline{\boldsymbol{\sigma}} + \widetilde{\boldsymbol{\eta}}, \tag{5.20}$$

where $\widetilde{\mathbb{M}}$ and $\widetilde{\boldsymbol{\eta}}$ are the effective viscous compliance tensor and the effective eigenstrain rate tensor of the LCC, as given by $(5.40)_1$ and $(5.40)_2$, respectively, in Appendix I. Note that $\widetilde{\mathbb{M}}$ and $\widetilde{\boldsymbol{\eta}}$ depend nonlinearly on the applied loading $\overline{\boldsymbol{\sigma}}$ and, thus, the relation (5.20) is nonlinear, as expected. Moreover, the first and second moments of the stress and strain-rate fields $\overline{\boldsymbol{\sigma}}^{(r)}$, $\langle \boldsymbol{\sigma} \otimes \boldsymbol{\sigma} \rangle^{(r)}$, $\overline{\mathbf{D}}^{(r)}$ and $\langle \mathbf{D} \otimes \mathbf{D} \rangle^{(r)}$ in the nonlinear polycrystals are given by expression (5.41), (5.42), (5.46) and (5.47), respectively, in Appendix I. Furthermore, we can similarly show that the first and second moments of the spin field $\overline{\mathbf{W}}^{(r)}$ and $\langle \mathbf{W} \otimes \mathbf{W} \rangle^{(r)}$ in the nonlinear polycrystals can also be directly obtained from the corresponding quantities in the 'optimized' LCC, by means of an appropriate generalization of the results of Idiart and Ponte Castañeda (2007c) (see Appendix II for details).

At this point, it should be remarked that the results discussed in this section are valid for any choice of the weights $\alpha_{(k)}^{(r)}$ appearing in (5.16). Unfortunately, we do not yet have any mathematically or physically based prescription to select $\alpha_{(k)}^{(r)}$ in an optimal fashion, although the recent work of Michel and Suquet (2017) suggests that $\alpha_{(k)}^{(r)}$ could be related to higher moments of the stress field. For simplicity, we choose $\alpha_{(k)}^{(r)} = 1/2$ ($r = 1, ..., N$; $k = 1, ..., K$), which is the most symmetric choice. There may

be other better choices for the values of $\alpha_{(k)}^{(r)}$, and this will be investigated in future work. However, as will be seen in section 5.5, the above choice of $\alpha_{(k)}^{(r)}$ can provide reasonably accurate results.

The average slip rates $\overline{\gamma}_{(k)}^{(r)}$ over slip system k in phase r of the polycrystal, which are required to satisfy the condition

$$\overline{\mathbf{D}}^{(r)} = \sum_{k=1}^{K} \overline{\gamma}_{(k)}^{(r)} \boldsymbol{\mu}_{(k)}^{(r)}, \tag{5.21}$$

can be once again estimated from the LCC, and are given by (Song and Ponte Castañeda, 2017b)

$$\overline{\gamma}_{(k)}^{(r)} = \frac{1}{2\mu_{(k)}^{(r)}} \overline{\tau}_{(k)}^{(r)} + \eta_{(k)}^{(r)} = \alpha_{(k)}^{(r)} \phi_{(k)}^{(r)\prime}(\check{\tau}_{(k)}^{(r)}) + (1 - \alpha_{(k)}^{(r)}) \phi_{(k)}^{(r)\prime}(\hat{\tau}_{(k)}^{(r)}). \tag{5.22}$$

Recall that

$$\overline{\gamma}_{(k)}^{(r)} \neq \phi_{(k)}^{(r)\prime}(\overline{\tau}_{(k)}^{(r)}), \tag{5.23}$$

consistent with the fact that the average of a nonlinear function is generally different from the function of the average. Similar results have been given in the context of porous single crystals in chapter 3, as shown schematically in Fig. 3.2.

In this context, note that the FOSO estimate (5.16) is exact to second order in the heterogeneity contrast, and provides a generalization of the partially optimized second-order (POSO) estimate of Liu and Ponte Castañeda (2004a), which is also exact to second order in the heterogeneity contrast, but is *not* fully stationary with respect to the properties of the LCC. In particular, the variables $\mu_{(k)}^{(r)}$ and $\eta_{(k)}^{(r)}$ for the POSO method are still given by (5.19), but with $\check{\tau}_{(k)}^{(r)} = \overline{\tau}_{(k)}^{(r)}$ and $\hat{\tau}_{(k)}^{(r)} = \overline{\tau}_{(k)}^{(r)} \pm \mathrm{SD}^{(r)}(\tau_{(k)}^{(r)})$, where the plus sign has to be taken when $\overline{\tau}_{(k)}^{(r)} \geq 0$, and the minus sign when $\overline{\tau}_{(k)}^{(r)} < 0$. As shown by Liu and Ponte Castañeda (2004a), the above choice of $\check{\tau}_{(k)}^{(r)}$ and $\hat{\tau}_{(k)}^{(r)}$ leads to estimates that are stationary with respect to $\mu_{(k)}^{(r)}$, but *not* with respect to $\eta_{(k)}^{(r)}$, and that

$$\widetilde{u}(\overline{\boldsymbol{\sigma}}) = \sum_{r=1}^{N} c^{(r)} \sum_{k=1}^{K} \left[\phi_{(k)}^{(r)}(\hat{\tau}_{(k)}^{(r)}) + \phi_{(k)}^{(r)\prime}(\overline{\tau}_{(k)}^{(r)})(\overline{\tau}_{(k)}^{(r)} - \hat{\tau}_{(k)}^{(r)}) \right] \quad \text{(Energy)}. \tag{5.24}$$

Due to the lack of fully stationarity of the POSO estimate, the macroscopic response and field statistics in the nonlinear polycrystals do *not* coincide with the corresponding quantities in the LCC, and additional terms involving difficult-to-compute numerical derivatives are required in general (Idiart and Ponte Castañeda, 2007c). For the sake of simplicity, an alternate version of the POSO estimate may be generated by directly using the effective constitutive relation of the LCC (Liu and Ponte Castañeda, 2004a), as given by (5.21) with

$$\overline{\gamma}_{(k)}^{(r)} = \phi_{(k)}^{(r)\prime}(\overline{\tau}_{(k)}^{(r)}) \quad \text{(Constitutive relation)}. \tag{5.25}$$

However, the estimate (5.25) does *not* possess an associated stress potential $\widetilde{u}$, and is *not* exact to second-order in the heterogeneity contrast. In addition, it is found that (5.25) contradicts with the general expectation of relation (5.23).

The FOSO estimate (5.16) also provides a generalization of the variational (VAR) estimate of deBotton and Ponte Castañeda (1995), which is only exact to first order in the heterogeneity contrast. The VAR estimate may be recovered from the FOSO estimate (5.16) by formally setting the slip eigenstrain rates $\eta_{(k)}^{(r)} = 0$, and by identifying the slip viscosities $\mu_{(k)}^{(r)}$ with 'modified secant' linearizations of the nonlinear slip potentials evaluated at the second moments of the resolved shear stress, i.e., $1/(2\mu_{(k)}^{(r)}) = \phi_{(k)}^{(r)\prime}(\hat{\tau}_{(k)}^{(r)})/\hat{\tau}_{(k)}^{(r)}$ with $\hat{\tau}_{(k)}^{(r)} = \sqrt{\overline{\tau}_{(k)}^{(r)}}$. The final result has been shown to be a rigorous lower bound for all other SC estimates for $\widetilde{u}$, such that

$$\widetilde{u}(\overline{\boldsymbol{\sigma}}) \geq \sum_{r=1}^{N} c^{(r)} \sum_{k=1}^{K} \phi_{(k)}^{(r)}(\hat{\tau}_{(k)}^{(r)}). \tag{5.26}$$

Note that the VAR estimate (5.26) is also fully stationary, so that the macroscopic behavior and field statistics in the LCC can be used directly to estimate the corresponding quantities in the actual nonlinear polycrystals. In particular, the macroscopic strain rate $\overline{\mathbf{D}}$ is given by (5.21) with

$$\overline{\gamma}_{(k)}^{(r)} = \frac{\phi_{(k)}^{(r)\prime}(\hat{\tau}_{(k)}^{(r)})}{\hat{\tau}_{(k)}^{(r)}} \overline{\tau}_{(k)}^{(r)}. \tag{5.27}$$

In summary, the FOSO estimate (5.16) combines the advantages of the earlier estimates, being exact to second-order in the heterogeneity contrast, as well as being fully stationary with respect to the properties of the LCC. It should be remarked that the FOSO estimate requires the same level of statistical information as that needed for the POSO and VAR estimates (i.e., the first and second moments of the stress field in the LCC), without extra computational complexity.

5.4 Microstructure evolution

In this section, we make use of consistent homogenization estimates for the average strain rate and spin fields, together with standard kinematical arguments, to determine the microstructure evolution for viscoplastic polycrystals under finite-strain deformations.

Following Ponte Castañeda (1999) and Liu et al. (2005), the evolution of the granular microstructures of polycrystals is assumed to be governed by the macroscopic flow. More specifically, the *average* shape and orientation of the grains (or more accurately, of the two-point probability functions) are assumed to be controlled by the macroscopic strain rate $\overline{\mathbf{D}}$ and the macroscopic spin $\overline{\mathbf{W}}$. This is the simplest assumption consistent with preservation of the polycrystal integrity, i.e., the aggregate of different grains is required to fill the whole space. With the above hypotheses, the average grain shape remains ellipsoidal, but can change its aspect ratios and principal directions during the deformation. Thus, the evolution of the aspect ratios w_1 and w_2 for the ellipsoidal grains is governed by the kinematical relations

$$\dot{w}_1 = w_1\left(\overline{D}'_{33} - \overline{D}'_{11}\right), \quad \text{and} \quad \dot{w}_2 = w_2\left(\overline{D}'_{33} - \overline{D}'_{22}\right), \tag{5.28}$$

where $\overline{\mathbf{D}}$ is the macroscopic strain rate given by (5.20), and the primes in this section denote tensor components relative to axes instantaneously coinciding with the principal directions of the ellipsoidal grains.

On the other hand, the principal directions of the ellipsoidal grains can be charac-

terized by a rotation tensor $\mathbf{G}^{(g)}$, which can be written in terms of three Euler angles $\varphi_1^{(g)}$, $\psi^{(g)}$ and $\varphi_2^{(g)}$ by means of Bunge's notation (Bunge and Esling, 1982)

$$\mathbf{G}^{(g)} = \begin{pmatrix} C_1C_2 - S_1S_2C & S_1C_2 + C_1S_2C & S_2S \\ -C_1S_2 - S_1C_2C & -S_1S_2 + C_1C_2C & C_2S \\ S_1S & -C_1S & C \end{pmatrix}, \tag{5.29}$$

where $C_1 = \cos\varphi_1^{(g)}$, $C = \cos\psi^{(g)}$, $C_2 = \cos\varphi_2^{(g)}$, $S_1 = \sin\varphi_1^{(g)}$, $S = \sin\psi^{(g)}$ and $S_2 = \sin\varphi_2^{(g)}$. Then, the change of the grain orientation can be completely determined by the evolution of the rotation tensor $\mathbf{G}^{(g)}$:

$$\dot{\mathbf{G}}^{(g)} = -\mathbf{G}^{(g)}\overline{\boldsymbol{\omega}}^{(g)}, \tag{5.30}$$

where $\overline{\boldsymbol{\omega}}^{(g)}$ is the spin of the Eulerian axes of the macroscopic deformation gradient, with its non-zero components given by (Ogden, 1984)

$$\left(1 - \frac{w_q^2}{w_p^2}\right)\overline{\omega}_{pq}^{(g)\prime} = \left(1 - \frac{w_q^2}{w_p^2}\right)\overline{W}'_{pq} + \left(1 + \frac{w_q^2}{w_p^2}\right)\overline{D}'_{pq}, \quad p,q = 1,2,3, \quad p \neq q, \tag{5.31}$$

with $w_3 \equiv 1$. Note that if any two of the aspect ratios w_p and w_q for $p \neq q$ are equal, equation (5.31) implies that the principal directions of the grains should be chosen in such a way that $\overline{D}'_{pq} = 0$, and $\overline{\omega}_{pq}^{(g)\prime} = \overline{W}'_{pq}$.

Next, it is necessary to determine the lattice orientation of the single-crystal phase within each grain. Due to the intragranular heterogeneity in the deformation fields, local lattice reorientation is expected to occur within each grain. However, in the context of a homogenization procedure, it is sufficient to consider the evolution of the *average* lattice orientation for each grain, as characterized by the rotation tensor $\mathbf{Q}^{(r)}$. Note that $\mathbf{Q}^{(r)}$ can be written in a form completely analogous to that of $\mathbf{G}^{(g)}$ in (5.29), with the set of three Euler angles $\varphi_1^{(g)}$, $\psi^{(g)}$ and $\varphi_2^{(g)}$ replaced by $\varphi_1^{(r)}$, $\psi^{(r)}$ and $\varphi_2^{(r)}$, respectively. The evolution of $\mathbf{Q}^{(r)}$ is assumed (Ponte Castañeda, 1999; Liu et al., 2003; 2005) to be governed by the "microstructural" (or "elastic") spin $\overline{\boldsymbol{\omega}}_e^{(r)}$,

and is given by

$$\dot{\mathbf{Q}}^{(r)} = -\mathbf{Q}^{(r)}\overline{\boldsymbol{\omega}}_e^{(r)}, \tag{5.32}$$

where $\overline{\boldsymbol{\omega}}_e^{(r)}$ is given by the difference between the average continuum spin $\overline{\mathbf{W}}^{(r)}$ in phase r and the average plastic spin $\overline{\mathbf{W}}_p^{(r)}$ in phase r (Mandel, 1972), i.e.,

$$\overline{\boldsymbol{\omega}}_e^{(r)} = \overline{\mathbf{W}}^{(r)} - \overline{\mathbf{W}}_p^{(r)}. \tag{5.33}$$

Expressions for $\overline{\mathbf{W}}^{(r)}$ are provided by (5.48) in Appendix I, while $\overline{\mathbf{W}}_p^{(r)}$ can be obtained via

$$\overline{\mathbf{W}}_p^{(r)} = \frac{1}{2}\sum_{k=1}^{K}\overline{\gamma}_{(k)}^{(r)}\left(\mathbf{m}_{(k)}^{(r)}\otimes\mathbf{n}_{(k)}^{(r)} - \mathbf{n}_{(k)}^{(r)}\otimes\mathbf{m}_{(k)}^{(r)}\right), \tag{5.34}$$

in terms of expression (5.22) for the average slip rates $\overline{\gamma}_{(k)}^{(r)}$.

It should be remarked that equation (5.28) and (5.30) characterize the evolution of the morphological texture, while (5.32) characterizes the evolution of the crystallographic texture of the polycrystal. The above differential equations can be effectively integrated by means of an explicit forward Euler integration scheme, as adopted by Liu (2003). Strain hardening for the single-crystal phases will be neglected here, so that the reference flow stresses for all slip systems remain fixed throughout the deformation. However, strain hardening can be easily accounted for by utilizing an appropriate hardening law, e.g., the Voce-type hardening law (Balasubramanian and Anand, 2002), as employed by Liu et al. (2005) in the context of the earlier POSO method.

5.5 Instantaneous response for hexagonal polycrystals

In this section, the FOSO method is used to generate estimates for the macroscopic response and field statistics of hexagonal-close-packed (HCP) polycrystals for given fixed states of the microstructure. The results are compared with the predictions of earlier nonlinear homogenization methods, and with the full field, numerical results

available in the literature.

Here we consider HCP polycrystals with a prescribed c/a ratio, and with three families of principal slip systems: basal slip ($\{0001\}\langle 11\bar{2}0\rangle$), prismatic slip ($\{10\bar{1}0\}\langle 11\bar{2}0\rangle$), and second-order ($\{11\bar{2}2\}\langle 11\bar{2}3\rangle$) pyramidal-$\langle c+a\rangle$ slip, which will be denoted by labels A, B and C, respectively. Note that the three basal slips plus the three prismatic slips provide only four (two each) linearly independent slip systems, allowing no straining along the $\langle c\rangle$-axis. However, the six second-order pyramidal-$\langle c+a\rangle$ slips contain sets of five linearly independent slip systems, thus allowing arbitrary plastic deformation. The reference flow stresses $(\tau_0)_{(k)}$ in expression (5.5) are assumed to be identical for each family of slip systems, but generally different for different families of slip systems, so that the slip families A, B and C are taken to have reference flow stresses τ_A, τ_B and τ_C, respectively. For later use, we define $M_1 = \tau_B/\tau_A$ and $M_2 = \tau_C/\tau_A$ to be the contrast parameters, characterizing the grain anisotropy of the HCP crystals.

In this section, the HCP polycrystals are assumed to be *untextured*, with isotropic two-point statistics ($w_1 = w_2 = 1$), and to be loaded in uniaxial tension. Since the FOSO method requires solving a large set of nonlinear equations with a number of unknowns proportional to the total number of available slip systems, it is of interest to use as few crystallographic orientations as possible. Taking advantage of the crystal and loading symmetry (Van Houtte and Aernoudt, 1976; Kocks et al., 1998), it is possible to consider a reduced set of orientations on an appropriate spherical triangle (see, e.g., Nebozhyn, 2000). In this work, 45 *equispaced* orientations are used, which have been found to be sufficient to obtain accurate results for the effective behavior and field statistics in untextured polycrystals (Liu and Ponte Castañeda, 2004a).

Due to the fact that the viscous exponent n is identical for all the slip systems, the effective stress potential $\widetilde{u}$ of the polycrystal is a homogeneous function of degree $n+1$ in the macroscopic stress $\overline{\boldsymbol{\sigma}}$. Moreover, due to the incompressibility of the polycrystal, $\widetilde{u}$ depends on $\overline{\boldsymbol{\sigma}}$ only through its deviatoric part $\overline{\boldsymbol{\sigma}}'$, such that

$$\widetilde{u}(\overline{\boldsymbol{\sigma}}) = \frac{\dot{\gamma}_0\widetilde{\sigma}_0}{n+1}\left(\frac{\overline{\sigma}_e}{\widetilde{\sigma}_0}\right)^{n+1}. \tag{5.35}$$

Here $\overline{\sigma}_e = \sqrt{\frac{3}{2}\overline{\boldsymbol{\sigma}}' \cdot \overline{\boldsymbol{\sigma}}'}$ is the macroscopic equivalent stress, and $\widetilde{\sigma}_0$ is the *effective flow stress* of the polycrystal, which depends on the loading condition and microstructure of the polycrystal. For untextured polycrystals with isotropic crystallographic and morphological textures, $\widetilde{\sigma}_0$ can be shown (Dendievel et al., 1991) to be a function only of the Lode angle θ, as defined by $\cos(3\theta) = (27/2)\det(\overline{\boldsymbol{\sigma}}'/\overline{\sigma}_e)$. Note that θ is a dimensionless quantity related to the third invariant of the macroscopic stress tensor, and characterizes the type of shear in the deviatoric space. In particular, $\theta = 0$ for uniaxial tension considered in this work, corresponding to axisymmetric shear.

5.5.1 The effect of the rate sensitivity

In this subsection, we present results for HCP polycrystals with a fixed value of the grain anisotropy, $M_1 = 10$ and $M_2 \to \infty$, but with different rate sensitivities $m = 1/n$. Moreover, the c/a ratio of the HCP crystal is taken to be 1.633. Due to the absence of the pyramidal slips ($\tau_C \to \infty$), only four linearly independent slip systems are available for each grain. Thus, strong interactions between grains with different orientations are expected to occur in order to accommodate general plastic deformations. Predicting accurately the macroscopic response of these materials is a challenging problem that may serve to discriminate among different nonlinear homogenization approaches. Fig. 5.1(a) shows plots for the FOSO estimates of the effective flow stress $\widetilde{\sigma}_0$, normalized by the reference flow stress τ_B, as a function of the rate sensitivity $m = 1/n$. The corresponding VAR upper bounds of the SC type (Nebozhyn et al., 2001), POSO estimates of the SC type (Liu and Ponte Castañeda, 2004b), tangent estimates (Lebensohn et al., 1993), as well as the Reuss lower bounds are also included for comparison. Note that the Taylor upper bounds tend to infinity in this case, due to the lack of five linearly independent slip systems. Note further that two different versions of the POSO estimates are presented: (i) the energy (E) version derived from expression (5.24) in solid lines, and (ii) the constitutive (C) version derived from expression (5.25) in dashed lines. We observe from Fig. 5.1(a) that, while the FOSO, POSO, VAR and tangent estimates coincide in the linear case

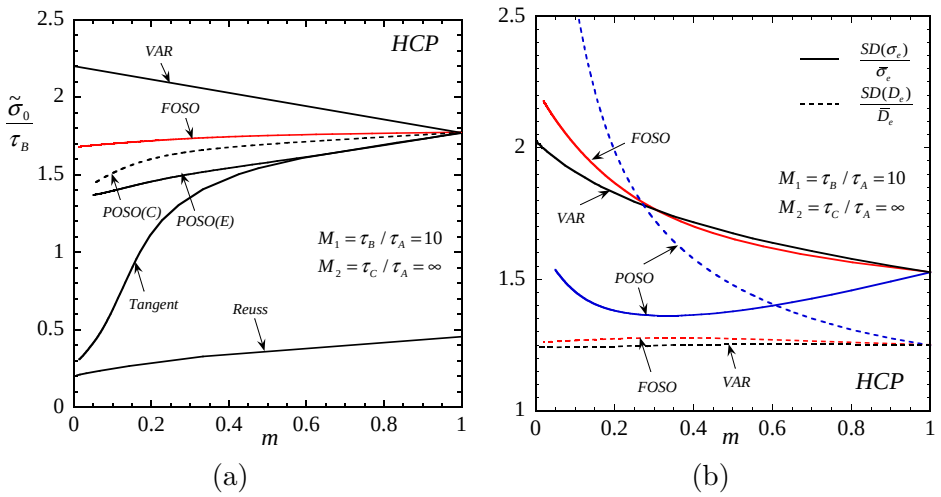

Figure 5.1: The effective flow stress and field fluctuations for untextured, HCP polycrystals with isotropic two-point statistics ($w_1 = w_2 = 1$), and with contrast parameters $M_1 = \tau_B/\tau_A = 10$ and $M_2 = \tau_C/\tau_A \to \infty$, for uniaxial tension, as functions of the rate sensitivity $m = 1/n$. Plots are shown for (a) the effective flow stress normalized by the reference flow stress τ_B, and (b) the overall standard deviations of the equivalent stress $\mathrm{SD}(\sigma_e)$, and of the equivalent strain rate $\mathrm{SD}(D_e)$, normalized by the macroscopic equivalent stress $\overline{\sigma}_e$, and the macroscopic equivalent strain rate $\overline{D}_e$, respectively.

($m = 1$), they deviate from each other for smaller values of m, with the tangent estimates tending to the Reuss lower bounds as $m \to 0$. On the other hand, the FOSO estimates, as well as both versions of the POSO estimates, lie within the VAR upper bounds and Reuss lower bounds for all values of m. In particular, both the FOSO and POSO estimates decrease monotonically with decreasing values of m, with the FOSO results lying somewhat above the POSO results, while the opposite is true for the VAR bounds, which increase monotonically with decreasing values of m.

Figure 5.1(b) displays the corresponding plots for the FOSO estimates of the overall standard deviations of the equivalent stress and equivalent strain rate, $\mathrm{SD}(\sigma_e)$ and $\mathrm{SD}(D_e)$, normalized by the macroscopic equivalent stress $\overline{\sigma}_e$ and strain rate $\overline{D}_e$, respectively. The corresponding VAR and POSO results are also shown for comparison. It can be seen from this figure that, for both the stress and strain rate fluctuations, the FOSO and VAR estimates stay fairly close to each other for all values of m, where the stress fluctuations increase monotonically with decreasing values of m,

while the corresponding strain rate fluctuations remain almost a constant. (Note that the similarity of the FOSO and VAR estimates for the overall field fluctuations is coincidental and *not* a general result, as will be seen below.) By contrast, the corresponding POSO estimates exhibit a qualitatively different behavior, where as m decreases the stress fluctuation varies non-monotonically, while the corresponding strain rate fluctuation increases significantly, exceeding the stress fluctuations for $m \lesssim 0.6$. The above observation would first appear to be in contradiction with the observations made in Fig. 5.1(a), where the FOSO estimates stay closer to the POSO estimates than to the VAR estimates. This may be explained in terms of the fact that the POSO estimates shown in Fig. 5.1(b) (and all the POSO estimates below) make direct use of the field fluctuations in the LCC to estimate the corresponding quantities in the actual nonlinear polycrystals, although the field fluctuations in the nonlinear composite and in the LCC are known (Idiart and Ponte Castañeda, 2007c) to be different for the POSO estimates, due to the lack of full stationarity. In fact, this reference suggests that additional terms involving difficult-to-compute numerical derivatives are required—in addition to the field fluctuations in the LCC—to recover the field fluctuations in the actual nonlinear composite. However, this requires rather heavy numerical computations and is not pursued here for simplicity. On the other hand, both the FOSO and VAR estimates are fully stationary, so that the field fluctuations in the LCC are entirely consistent with those in the nonlinear polycrystals. As already mentioned, this is a remarkable advantage of the new FOSO estimates, which can yield as byproducts estimates of the field fluctuations in the actual nonlinear composites, without additional computational cost.

5.5.2 The effect of the grain anisotropy

In this subsection, we consider HCP polycrystals with a c/a ratio of 1.629, and a fixed value of the creep exponent $n = 3$, which are known to be appropriate for ice at -10°. In addition, the basal slips are taken to be the "soft" slip systems, while the prismatic and pyramidal slips are taken to be the "hard" slip systems with identical flow stresses, such that $M_1 = M_2 = M \geq 1$. As a case study, we will consider different

values of M to explore the effect of the grain anisotropy of HCP crystals.

Fig. 5.2 presents results for the effective flow stress and the overall fluctuations of the stress and strain rate fields, as functions of the grain anisotropy M. In particular, Fig. 5.2(a) shows plots for the FOSO estimates of the effective flow stress $\widetilde{\sigma}_0$, normalized by the reference flow stress τ_A, in linear scales. For comparison purposes, plots are also included for the corresponding Taylor upper bounds, Reuss lower bounds, VAR upper bounds of the self-consistent type, POSO estimates (two different versions), tangent estimates, as well as the full-field FFT results of Lebensohn et al. (2007). Fig. 5.2(b) shows the same set of plots in logarithmic scales. We can see that all estimates grow linearly with M and tend to infinity as M increases, except for the tangent estimates and Reuss lower bounds, which saturate at a finite value leading to overly soft response. Thus, the behavior of the new FOSO estimates is consistent with the scaling law obtained by Nebozhyn et al. (2001) based on the VAR bounds, suggesting that non-basal slips are required to accommodate arbitrary plastic deformations. In addition, we observe that for all values of M considered, the FOSO estimates lie between the two different versions of the POSO estimates, and lie somewhat below the VAR upper bounds. (Note that the VAR upper bounds are much tighter than the Taylor upper bounds, especially for large grain anisotropy.) Finally, the new FOSO estimates are seen to be in excellent agreement with the corresponding FFT results.

Figure 5.2(c) shows the corresponding plots for the overall stress fluctuations $\mathrm{SD}(\sigma_e)$, normalized by the macroscopic equivalent stress $\overline{\sigma}_e$, as a function of the grain anisotropy M. The corresponding FFT results of Lebensohn et al. (2004) are also included for comparison. (Note that FFT results for the field fluctuations are not provided in the work of Lebensohn et al. (2007).) The main observation from this figure is that, the FOSO estimates are rather similar to the corresponding POSO and VAR estimates, where the overall stress fluctuation increases with M in the beginning and approaches an asymptote at large values of M. Furthermore, the above estimates are found to be in fairly good agreement with the corresponding FFT results. On the other hand, the tangent, Taylor and Reuss estimates are seen

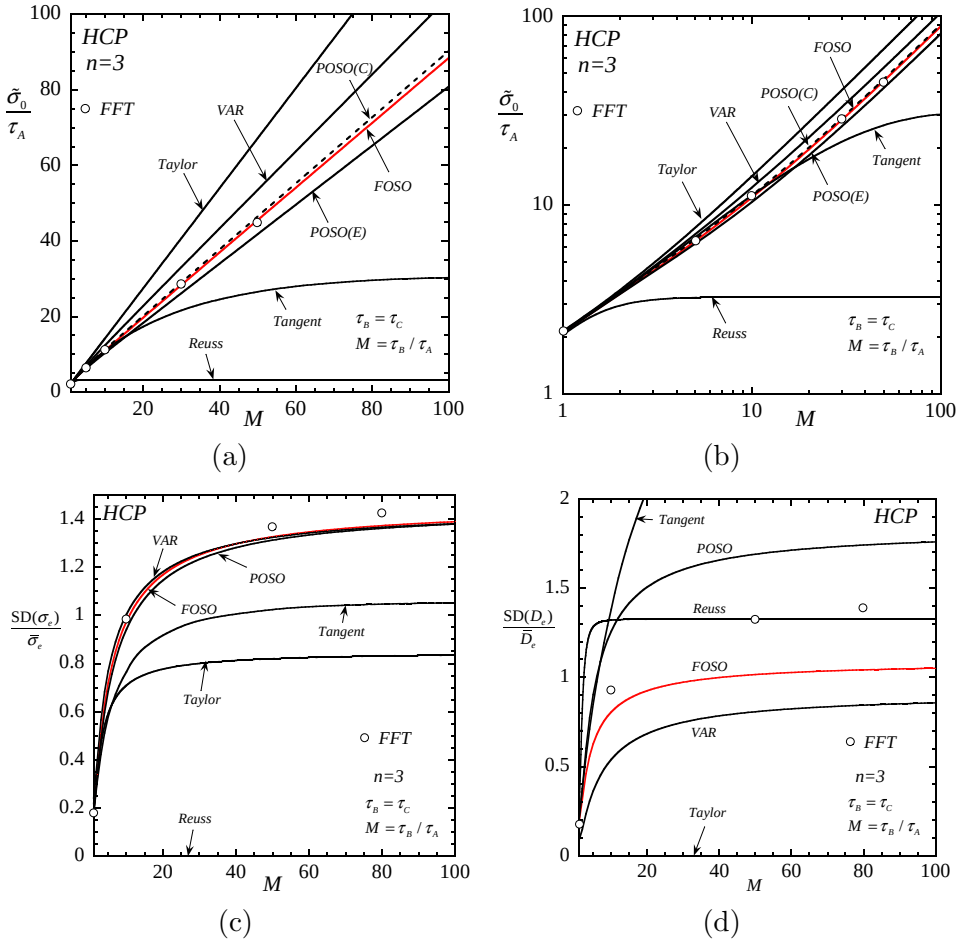

Figure 5.2: The effective flow stress and field fluctuations for untextured, HCP polycrystals with isotropic two-point statistics ($w_1 = w_2 = 1$) and $n = 3$, loaded in uniaxial tension, as functions of the grain anisotropy $M = \tau_B/\tau_A = \tau_C/\tau_A$. Plots are shown for the effective flow stress $\widetilde{\sigma}_0$, normalized by the reference flow stress τ_A, in (a) linear scales, as well as in (b) logarithmic scales. Plots are also shown for the overall standard deviations of (c) the equivalent stress $\mathrm{SD}(\sigma_e)$, and of (d) the equivalent strain rate $\mathrm{SD}(D_e)$, normalized by the macroscopic equivalent stress $\overline{\sigma}_e$, and the macroscopic strain rate $\overline{D}_e$, respectively.

to significantly underestimate the stress fluctuations, with the Reuss estimates giving identically zero values, due to the uniform stress assumption.

Figure 5.2(d) gives the corresponding results for the overall strain rate fluctuations SD(D_e), normalized by the macroscopic strain rate $\overline{D}_e$, as a function of the grain anisotropy M. (Note that the POSO results shown in this figure are computed by means of the constitutive version (5.25).) For comparison purposes, the corresponding FFT results of Lebensohn et al. (2004) are also included. It is observed that, while the FOSO, POSO and VAR estimates exhibit qualitatively similar behaviors, predicting saturation of the strain rate fluctuations, they are quite different in quantitative terms. In particular, the new FOSO estimates lie between the POSO and VAR estimates, yielding the best agreement with the corresponding FFT results. However, the FOSO still underestimates somewhat the FFT results, especially at large values of M, with the largest error being around 25%. However, it should be noted that, as mentioned by Lebensohn et al. (2004), the FFT results for the strain rate fluctuations may not be very accurate, especially for the case of large grain anisotropy. Therefore, improved FFT results should be used to assess the new FOSO estimates, and this will be pursued in future work. On the other hand, the tangent and Taylor estimates severely overestimate and underestimate, respectively, the FFT results, with the Taylor estimates being of course identically zero. Finally, we observe that the corresponding Reuss estimates are qualitatively different from the FFT results, predicting a sharp transition to the saturating value at rather small values of M. However, it is interesting to note that the Reuss estimates capture roughly the magnitudes of the FFT results in this particular case.

Next, we investigate the orientation dependence of the per-phase averages and fluctuations of the stress and strain-rate fields. Given the crystal and loading symmetry already alluded to, it is sufficient to restrict our attention to an appropriate spherical triangle, as shown, for example, in Fig. 5.3, with its left, right and top vertices $\{0001\}$, $\{\overline{1}2\overline{1}0\}$ and $\{1\overline{1}00\}$, respectively. Note that the standard *inverse pole figure* is used to represent crystal orientations in Fig. 5.3, where the uniaxial loading axis is plotted in terms of the local crystal axes of different crystal grains in

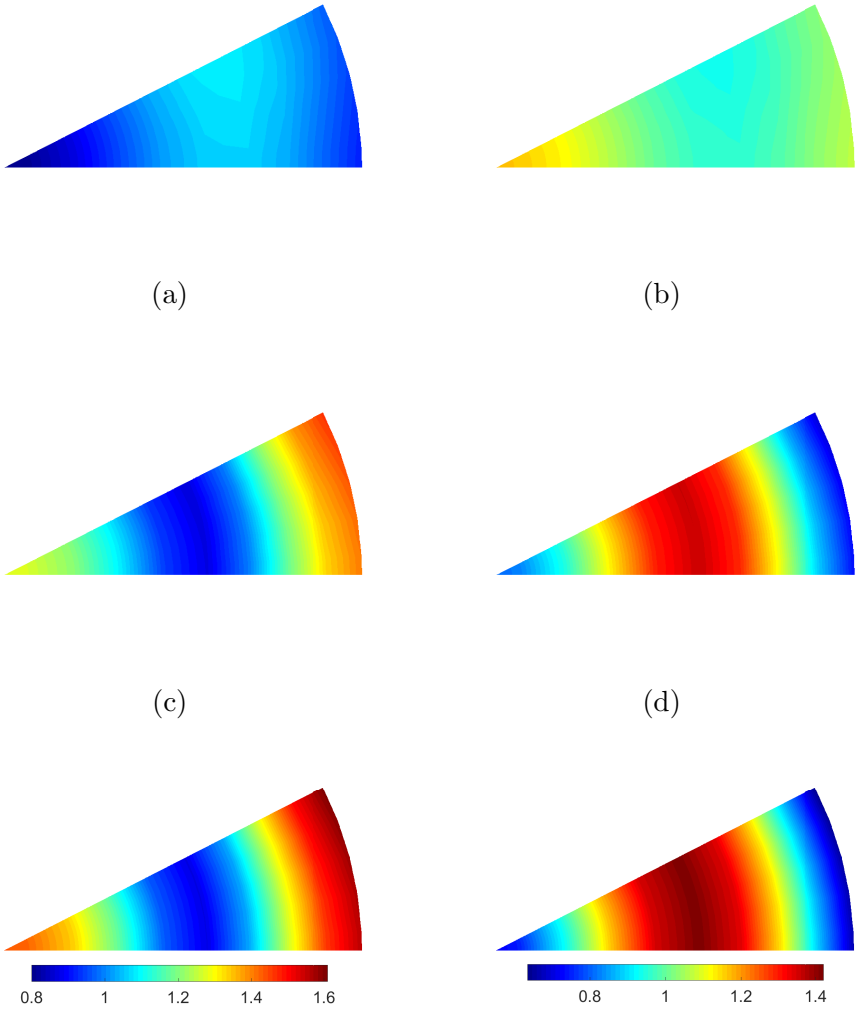

Figure 5.3: Plots for the FOSO estimates of the per-phase averages of the equivalent stress $\overline{\sigma}_e^{(r)}$, and the equivalent strain rate $\overline{D}_e^{(r)}$ are shown on the left- and right-hand sides, respectively, as functions of orientation in the spherical triangle, for isotropic HCP polycrystals with $n = 3$, and grain anisotropy $M = \tau_B/\tau_A = \tau_C/\tau_A$. Parts (a) and (b), (c) and (d), (e) and (f) correspond to the following values of M: 1, 10 and 60.

the polycrystal. Thus, a given point in the spherical triangle corresponds to a grain that is orientated such that the loading axis is aligned with such a direction in the grain. Note further that equal-area projection is used throughout this chapter.

Figure 5.3 displays plots for the FOSO estimates of the averages over grains with a given orientation r of the equivalent stress $\overline{\sigma}_e^{(r)}$, and the equivalent strain rate $\overline{D}_e^{(r)}$, normalized by the macroscopic equivalent stress $\overline{\sigma}_e$ and strain rate $\overline{D}_e$, respectively, for different values of the grain anisotropy (M = 1, 10 and 60). We can see from Fig. 5.3 that, as M increases, both the average stress and strain rate become less uniform over the polycrystal, indicating the development of significant intergranular field fluctuations. In addition, the average strain rate reaches its maximum for a band intermediate between the $\{0001\}$ and $\{\overline{1}2\overline{1}0\}$ directions, except for $M = 1$, where the average strain rate is the largest for the $\{0001\}$ orientation. Note that the average strain rate for this orientation decreases significantly with increasing values of M, consistent with the fact that the pyramidal slips become stronger leading to more viscous behavior of the grains along the $\langle c\rangle$-axis. Note further that the corresponding phase averages of the stress exhibit roughly the opposite behavior. This suggests that for the "soft" grain orientations, relatively small magnitude of stress can induce fairly large strain rate, while the opposite is true for the "hard" grain orientations. Finally, it should be mentioned that the FOSO estimates are qualitatively consistent with the corresponding POSO and VAR estimates (not shown), while there are some quantitative differences, especially for the average strain-rate field. For instance, the POSO estimates for the average strain rate are less uniform than the corresponding FOSO estimates, suggesting larger intergranular fluctuations, while the opposite is true for the VAR estimates. This trend would appear to be consistent with the overall strain-rate fluctuations shown in Fig. 5.2(d).

Figure 5.4 presents results for the FOSO estimates of the corresponding standard deviations over grains with a given orientation r (intragranular fluctuations) of the equivalent stress $\mathrm{SD}^{(r)}(\sigma_e)$, and the equivalent strain rate $\mathrm{SD}^{(r)}(D_e)$, normalized by the macroscopic equivalent stress $\overline{\sigma}_e$ and strain rate $\overline{D}_e$, respectively. It can be observed that, while the stress and strain rate fluctuations are rather small over all

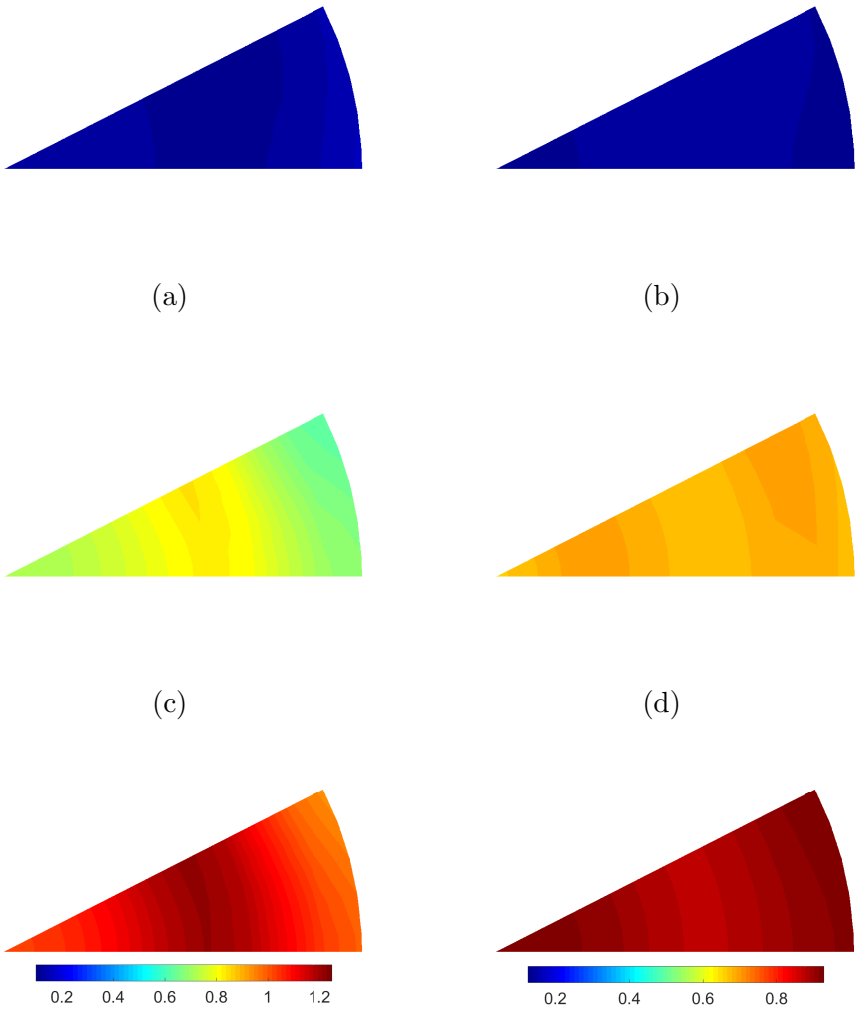

(a) (b) (c) (d) (e) (f)

Figure 5.4: Plots of the per-phase standard deviation of the equivalent stress SD(σ_e), and the equivalent strain rate SD(D_e) are shown on the left- and right-hand sides, respectively, as functions of orientation in the spherical triangle, for isotropic HCP polycrystals with $n = 3$, and grain anisotropy $M = \tau_B/\tau_A = \tau_C/\tau_A$. They are normalized by $\overline{\sigma}_e$ and $\overline{D}_e$, respectively. Parts (a) and (b), (c) and (d), (e) and (f) correspond to the following values of M: 1, 10 and 60.

grain orientations for $M = 1$, they increase significantly with increasing values of M. For instance, for $M = 60$, the largest stress fluctuation, occurring at a thin band lying halfway between the $\{0001\}$ and $\{\bar{1}2\bar{1}0\}$ orientations, can be more than 10 times larger than that for $M = 1$. Moreover, it is found that the phase fluctuations for both the stress and strain rate become less uniform as M increases. For example, in contrast to the almost uniform stress fluctuation for $M = 1$, the corresponding stress fluctuation for $M = 60$ develops a pattern where it gradually decreases from its maximum at the intermediate thin band, to its minimum at the corners of the spherical triangle. The fluctuations for the strain rate are found to have roughly the opposite patterns. Again, the FOSO estimates are found to be qualitatively similar to the corresponding POSO and VAR estimates (not shown). In quantitative terms, while the stress fluctuations predicted by these estimates are quite similar, the corresponding strain rate fluctuations are somewhat different. For instance, the POSO estimates for the strain rate fluctuations could be 50% larger than the corresponding FOSO estimates.

In summary, among the different nonlinear homogenization estimates considered above, the new FOSO estimates are found to be the most accurate ones when compared with available full-field numerical results. In particular, the FOSO estimates for the effective flow stress, as well as for the corresponding stress fluctuations are in excellent agreement with the numerical results. The corresponding strain rate fluctuations, however, underestimate somewhat the numerical results. As already mentioned, this discrepancy could be, at least partially, due to the probable inaccuracy of the numerical results (Lebensohn et al., 2004). Further assessment of the FOSO estimates by using improved numerical results should be considered, and this will be pursued in future work.

5.6 Finite-strain macroscopic response for polycrystalline ice

In this section, we make use of the new FOSO model to obtain estimates for the finite-strain macroscopic response, as well as for the evolution of the microstructure, for polycrystalline ice under uniaxial compression. A better understanding of the deformation process of ice under compressive loadings is of crucial significance in glaciology, since compression (together with shear) is one of the main deformation modes of glaciers and ice sheets. Furthermore, the corresponding POSO and VAR estimates will also be included for comparison purposes, while the corresponding Taylor, Reuss and tangent estimates, which have been found to be less accurate in section 5.5, will not be shown for conciseness.

As already discussed in section 5.5.2, polycrystalline ice is taken to be made of aggregates of HCP single crystals with a c/a ratio of 1.629, and a creep exponent of $n = 3$. The non-basal slips for ice are known to be much harder than the basal slips (Duval et al., 1983), so that the contrast parameter $M = \tau_B/\tau_A = \tau_C/\tau_A \gg 1$. In this context, it should be mentioned that, the grain anisotropies of ice measured from experimental results for single-crystal (Castelnau et al., 1996) and (strongly textured) polycrystalline ice (Castelnau et al., 1997) can be quite different, where $M \approx 20$ for the former case while $M \approx 70$ for the latter. In this work, a relatively large contrast $M = 60$ is used, as a case study to discriminate among the different homogenization estimates. Recall that strain hardening is neglected for all the available slip systems, so that the grain anisotropy remains a constant throughout the deformation process.

We consider an initially (approximately) isotropic polycrystalline aggregate of ice, consisting of $N = 500$ randomly orientated single-crystal grains with equal volume fractions $c^{(r)} = 1/N$ $(r = 1, ..., N)$. In addition, the grains are assumed to be equiaxed with $w_1 = w_2 = 1$. The initial crystallographic texture, as represented by the equal-area projection of the basal poles ((0001)-poles), is shown in Fig. 5.5. (Note that the basal poles correspond to the $\langle c \rangle$-axes of the HCP-crystal grains.) In particular, we consider uniaxial compression loading conditions $\overline{\boldsymbol{\sigma}} = \overline{\sigma}_{33}\mathbf{e}_3 \otimes \mathbf{e}_3$ $(\overline{\sigma}_{33} < 0)$, with $\mathbf{e}_3$

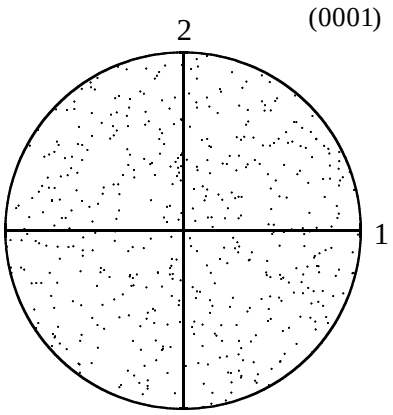

Figure 5.5: The initial crystallographic texture represented by the equal-area projection of the (0001)-poles (with a total of 500 grains)

denoting the loading axis. For later use, we define the quantities

$$\overline{D}_e = \sqrt{\frac{2}{3}\overline{\mathbf{D}} \cdot \overline{\mathbf{D}}}, \quad \text{and} \quad \overline{E}_e = \sqrt{\frac{2}{3}\overline{\mathbf{E}} \cdot \overline{\mathbf{E}}}, \tag{5.36}$$

where $\overline{D}_e$ and $\overline{E}_e$ denote, respectively, the macroscopic equivalent strain rate and macroscopic equivalent logarithmic strain ($\overline{\mathbf{E}}$ is the macroscopic logarithmic strain).

Fig. 5.6 presents results for the equal-area projections of the basal poles at different strain levels, as predicted by the FOSO, POSO and VAR model. The main observation from Fig. 5.6 is that all three models give qualitatively similar results for the texture evolution, where the basal poles rotate gradually towards the loading direction $\mathbf{e}_3$ with increasing strains. (The above observation is also qualitatively consistent with the corresponding Taylor, Reuss, and tangent estimates of Castelnau et al., 1996, although they used different contrast parameters.) In particular, at the strain level $\overline{E}_e = 0.3$, the basal poles are found to have rotated only through a small amount towards the loading axis $\mathbf{e}_3$ (when compared with the initial pole figure in Fig. 5.5). The rotation of the basal poles is then intensified for the moderate strain levels $0.3 < \overline{E}_e < 0.9$, and a clear concentration of the basal poles near the loading axis is observed at $\overline{E}_e = 0.9$. For $\overline{E}_e = 1.5$, the basal poles are almost perfectly aligned with the loading axis, indicating a strong basal texture of the polycrystalline ice. On the other hand, there are some quantitative differences between the FOSO, POSO

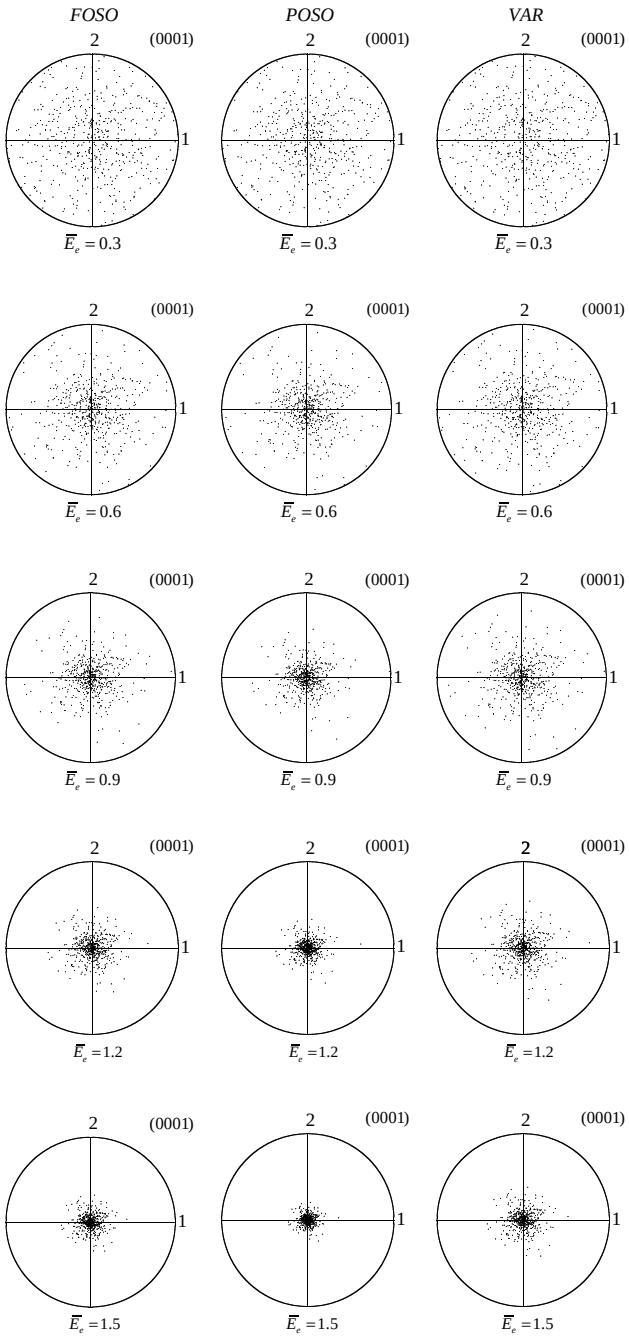

Figure 5.6: Texture evolution of polycrystalline ice under uniaxial compression shown by the (0001)-pole figures. The corresponding FOSO (left), POSO (center) and VAR (right) estimates are shown at the macroscopic strain levels $\overline{E}_e$ = 0.3, 0.6, 0.9, 1.2 and 1.5.

and VAR estimates, where the POSO (center column) yields the most rapid texture development, while the VAR (right column) the slowest, and the new FOSO estimates (left column) lie between them. It should be noted that the rotation of the basal poles is induced by the predominant basal dislocations, which have the smallest reference shear stress and are thus much easier to activate.

Fig. 5.7(a) shows the relevant activities (RA) of different modes of slip systems, as predicted by the FOSO, POSO and VAR model. Note that the relative activity for a given slip mode (e.g., basal or pyramidal) is defined to be

$$RA_{mode} = \frac{\sum_{r=1}^{N} c^{(r)} \sum_{\text{mode}} |\overline{\gamma}_{(k)}^{(r)}|}{\sum_{r=1}^{N} c^{(r)} \sum_{k=1}^{K} |\overline{\gamma}_{(k)}^{(r)}|}, \tag{5.37}$$

where the numerator denotes the sum of the magnitudes of the slip rates on all the slip systems that belong to a given slip mode, while the denominator denotes the sum over all the available slip systems. We can see from Fig. 5.7(a) that the basal activity predicted by the FOSO model increases with $\overline{E}_e$, being much larger than the corresponding pyramidal activity, as expected from the fact that the basal slips are much softer than the pyramidal slips. In addition, the FOSO estimates for the pyramidal activity are found to non-negligible (around 20%), indicating that the strain accommodation requires the activation of the 60 times harder pyramidal slips. In this connection, it should be remarked that significant contributions of non-basal slips involving the $\langle c \rangle$-component dislocations for ice flow have been recently evidenced by Chauve et al. (2017). Thus, the predictions of the above models would appear to be qualitatively consistent with the experimental results. Furthermore, the FOSO results are found to lie between the corresponding POSO and VAR results, similar to the observation made in the context of Fig. 5.6.

Fig. 5.7(b) shows the overall stress and strain rate standard deviations $\text{SD}(\sigma_e)$ and $\text{SD}(D_e)$, normalized by the macroscopic equivalent stress $\overline{\sigma}_e$ and strain rate $\overline{D}_e$, respectively, as functions of the equivalent strain $\overline{E}_e$. It can be seen from Fig. 5.7(b) that the FOSO estimates for the stress fluctuation increase slightly with strain at the beginning, and then decrease monotonically afterwards. On the other hand,

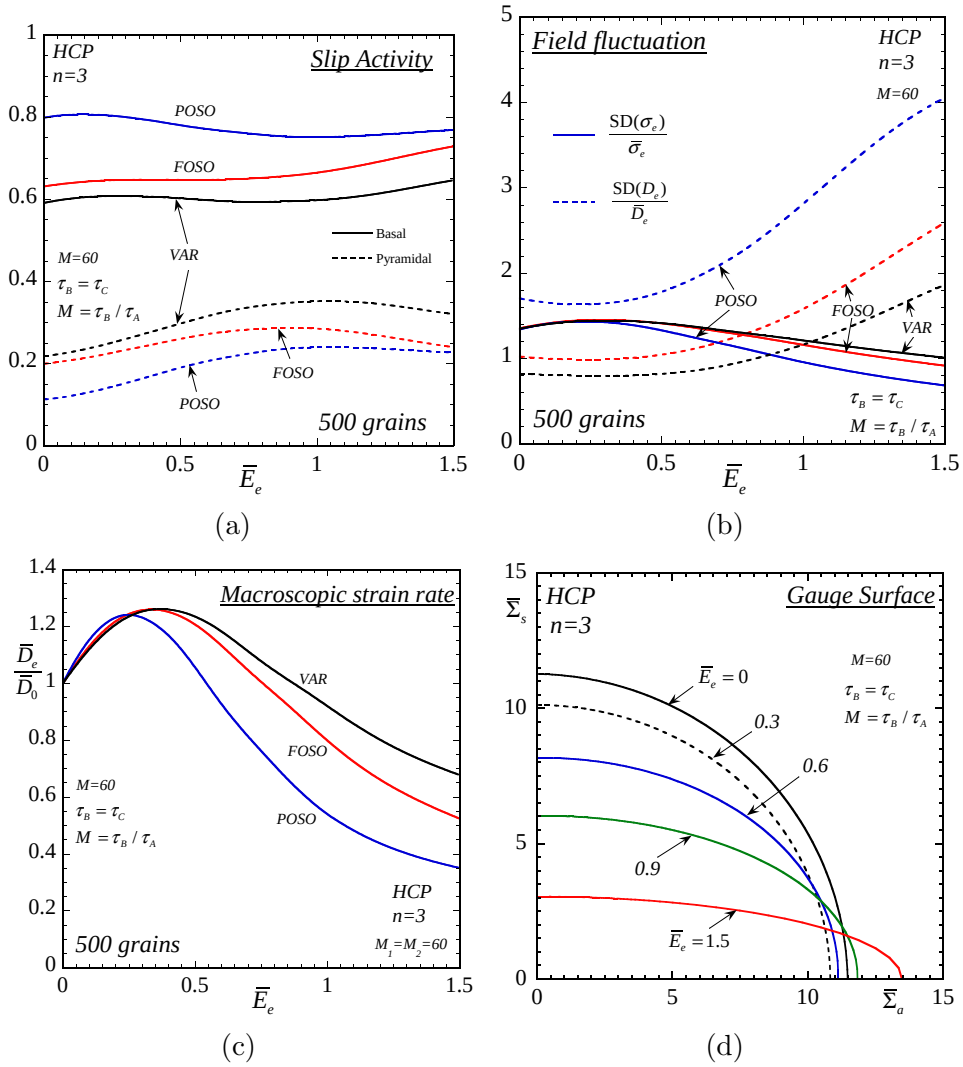

Figure 5.7: FOSO, POSO and VAR results for an initially untextured polylcrystal ice subjected to uniaxial compression loading conditions. Plots are shown for the (a) relative activities for the basal and pyramidal slip systems, (b) overall stress and strain rate fluctuations, and (c) normalized macroscopic strain rate. (d) The FOSO estimates for the $\overline{\Sigma}_a$-$\overline{\Sigma}_s$ cross sections of the gauge surfaces for ice polycrystals, at the strain level $\overline{E}_e$ = 0, 0.3, 0.6, 0.9 and 1.5.

the FOSO estimates for the strain rate fluctuations increase monotonically with $\overline{E}_e$, indicating stronger localizations of the deformation in the polycrystals. In addition, we can see that while the POSO and VAR results are fairly similar to the FOSO results for the stress fluctuations, they are rather different for the strain-rate fluctuations. In particular, the POSO estimates for the strain-rate fluctuations are much larger than the corresponding FOSO and VAR estimates. (This trend is consistent with the observations made in the context of Fig. 5.1(b) and 5.2(d).) It should be recalled that all three models make direct use of the quantities in the LCC to estimate the corresponding ones in the actual nonlinear polycrystal. Although the above usage has been justified for the new FOSO and VAR estimates, it is no so for the POSO estimates, where extra terms are needed to reproduce the actual quantities in the nonlinear composites, as already mentioned. For this reason, the POSO estimates shown here may introduce some errors as a result of the approximation used.

Fig. 5.7(c) presents plots for the macroscopic equivalent strain rate $\overline{D}_e$, normalized by its initial value $\overline{D}_0$ at the beginning of the deformation, as a function of the macroscopic strain $\overline{E}_e$. Note that the quantity $\overline{D}_e/\overline{D}_0$ is a measure of the normalized effective viscous compliance of ice polycrystals. Hence, increasing $\overline{D}_e/\overline{D}_0$ implies softening, while decreasing $\overline{D}_e/\overline{D}_0$ implies hardening of the materials. We observe from Fig. 5.7(c) that the FOSO estimates for $\overline{D}_e/\overline{D}_0$ first increase up to a certain amount of strain (softening), and then decrease continuously with strain (hardening). Since we have neglected strain hardening for all the slip systems, the above softening/hardening behavior of the polycrystal can only be induced by texture evolution, as observed in Fig. 5.6. Moreover, the corresponding POSO and VAR results are found to be qualitatively similar to the FOSO results, but with some quantitative differences. In particular, while the FOSO, POSO and VAR estimates are fairly close for small strains, they deviate from each other at larger strain levels, with the FOSO estimates lying between the POSO and VAR estimates.

For a better understanding of the overall softening/hardening response of polycrystalline ice, we consider below the evolution of the *gauge surfaces* (Leblond et al., 1994) of ice polycrystals. Recall that the gauge surface is defined to be the equi-

potential surface given by

$$\widetilde{u}(\overline{\mathbf{\Sigma}}) = \frac{\dot{\gamma}_0 \widetilde{\tau}_0^{-n}}{n+1}, \tag{5.38}$$

where $\overline{\mathbf{\Sigma}}$ is the *normalized* stress lying on the gauge surface, and $\widetilde{\tau}_0$ is a reference flow stress, which can be chosen to be one of the reference flow stresses $(\tau_0)_{(k)}$ $(k = 1, ..., K)$. In this work, $\widetilde{\tau}_0 = \tau_A$ is used, so that the results are normalized by τ_A. It should be remarked that the gauge surface (5.38) tends to the standard yield surface in the ideally plastic limit $n \to \infty$. For details on how to compute the gauge surfaces, readers are referred to the recent work of Song and Ponte Castañeda (2017a, 2017c).

Fig. 5.7(d) displays the FOSO estimates for the evolution of the $\overline{\Sigma}_a$-$\overline{\Sigma}_s$ cross section of the gauge surface for polycrystalline ice. Note that $\overline{\Sigma}_s = \sqrt{\overline{\Sigma}_{13}^2 + \overline{\Sigma}_{23}^2}$, and $\overline{\Sigma}_a = \left|(\overline{\Sigma}_{11} + \overline{\Sigma}_{22})/2 - \overline{\Sigma}_{33}\right|/\sqrt{3}$ are the two incompressible, transversely isotropic invariants of the stress tensor, corresponding to the longitudinal and axisymmetric shear, respectively. It can be seen from Fig. 5.7(d) that the gauge surface at $\overline{E}_e = 0$ is almost circular, indicating that the initial response of the untextured polycrystalline ice is rather isotropic. (Note that the gauge surface also depends on the third invariant of the applied stress and, thus, it is *not* perfectly circular.) However, the gauge surface is strongly distorted with increasing values of strain, indicating the development of strong anisotropy, as expected. In particular, for $0 \leq \overline{E}_e \lesssim 0.3$, the gauge surface contracts along the $\overline{\Sigma}_a$ (axisymmetric shear) axis suggesting a softening behavior, while for $\overline{E}_e \geq 0.3$ it expands along the $\overline{\Sigma}_a$ axis suggesting a hardening behavior. This result is consistent with the non-monotonic macroscopic strain rate observed in Fig. 5.7(c). Interestingly, the gauge surface always contracts along the $\overline{\Sigma}_s$ (longitudinal shear) axis with increasing strain, indicating a continuous softening behavior for this loading direction.

5.7 Concluding remarks

In this work, the recently developed fully optimized second-order (FOSO) homogenization method (Ponte Castañeda, 2015) was used, for the first time, to obtain estimates of the self-consistent type for the finite-strain response and texture evo-

lution of viscoplastic polycrystals. The central idea is the use of the classic self-consistent estimates for linear thermoelastic polycrystals (or more rigorously, linearly viscous polycrystals with eigenstrain rates) to generate the corresponding estimates for nonlinear viscoplastic polycrystals. The method involves a 'generalized secant' linearization of the nonlinear constitutive response, incorporating dependence on both the first and second moments of the stress fields, and gives estimates that are exact to second-order in the heterogeneity contrast. Moreover, consistent homogenization estimates for the average strain rate and spin fields in the polycrystals were used to develop evolution laws for both the morphological and crystallographic textures at finite-strain deformations.

Compared with the earlier partially optimized second-order (POSO) estimates of Liu and Ponte Castañeda (2004a), the new FOSO estimates have several distinguishing advantages. First, the FOSO estimates are fully optimized with respect to the properties of the LCC, so that the macroscopic constitutive behavior and field statistics of the nonlinear polycrystals can be directly extracted from those of the LCC. Second, the FOSO estimates exhibit *no* duality gap, so that their formulations in terms of the stress or dissipation potential are entirely equivalent, resulting in more accurate predictions. Note that these features were already present in the earlier variational (VAR) estimates of deBotton and Ponte Castañeda (1995), which are nonetheless only exact to first order in the heterogeneity contrast and thus less accurate. Therefore, the FOSO method effectively combines the advantages of the earlier VAR and POSO methods, while at the same time requires no extra computational cost.

The FOSO method was first used to investigate the effective flow stress and field statistics of untextured HCP polycrystals with varying degree of rate sensitivity and grain anisotropy. It was found that the FOSO estimates for the effective flow stress satisfy all known bounds, and show excellent agreement with the available FFT results. In particular, while the improvements over the earlier POSO estimates are only moderate for the effective flow stresses, they are rather significant for the field statistics, especially for low rate sensitivity and high grain anisotropy.

The FOSO model was then employed to study the finite-strain response and texture evolution for initially isotropic ice-like HCP polycrystals, subjected to uniaxial compression. It was found that a strong basal texture develops as a result of the dominant basal slips, being in qualitative agreement with the earlier results of Castelnau et al. (1996) and Lebensohn et al. (2007). In addition, the HCP polycrystal was found to develop a strong anisotropy as the deformation progresses, and to exhibit an overall softening-hardening behavior. Furthermore, it was found that the FOSO estimates for the texture evolution, macroscopic behavior and field fluctuations lie roughly between the corresponding VAR and POSO estimates. Among these, the FOSO model is expected to provide the most accurate estimates, due to its excellent performance in predicting the instantaneous response and field fluctuations for untextured polycrystals. Further assessment of the FOSO model by means of full-field, numerical simulations should be pursued, and this will be considered in future work.

5.8 Appendix I: Detailed expressions for the LCC

In this Appendix, we provide expressions for the macroscopic behavior and field statistics in the LCC, which in turn can be used to estimate the corresponding quantities in the actual nonlinear polycrystals (Idiart and Ponte Castañeda, 2007c; Ponte Castañeda, 2015).

As already mentioned, the LCC is mathematically analogous to a thermoelastic composite. Thus, the associated effective stress potential (5.15) can be written in the form

$$\widetilde{u}_L\left(\overline{\boldsymbol{\sigma}}\right) = \frac{1}{2}\overline{\boldsymbol{\sigma}} \cdot \widetilde{\mathbb{M}}\overline{\boldsymbol{\sigma}} + \widetilde{\boldsymbol{\eta}} \cdot \overline{\boldsymbol{\sigma}} + \frac{1}{2}\widetilde{g}, \tag{5.39}$$

where $\widetilde{\mathbb{M}}$, $\widetilde{\boldsymbol{\eta}}$ and $\widetilde{g}$ are the effective viscous compliance, effective eigenstrain rate and effective potential at zero stress, respectively, and are given by

$$\widetilde{\mathbb{M}} = \sum_{r=1}^{N} c^{(r)} \mathbb{M}^{(r)} \mathbb{B}^{(r)}, \quad \widetilde{\boldsymbol{\eta}} = \sum_{r=1}^{N} c^{(r)} \left(\mathbb{B}^{(r)}\right)^T \boldsymbol{\eta}^{(r)}, \quad \text{and} \quad \widetilde{g} = \sum_{r=1}^{N} c^{(r)} \boldsymbol{\eta}^{(r)} \cdot \mathbf{b}^{(r)}. \tag{5.40}$$

Here $\mathbb{B}^{(r)}$ and $\mathbf{b}^{(r)}$ are the stress concentration tensors, which relate the average stress

$\overline{\boldsymbol{\sigma}}^{(r)}$ over phase r of the LCC and the macroscopic stress $\overline{\boldsymbol{\sigma}}$ via the relation (Laws, 1973; Willis, 1981)

$$\overline{\boldsymbol{\sigma}}^{(r)} = \mathbb{B}^{(r)}\overline{\boldsymbol{\sigma}} + \mathbf{b}^{(r)}. \tag{5.41}$$

Note that $\mathbb{B}^{(r)}$ and $\mathbf{b}^{(r)}$ depend on the specific homogenization method utilized, and the estimates of the self-consistent (SC) type will be used in this work (see below). Moreover, the second moment of the stress field $\langle \boldsymbol{\sigma} \otimes \boldsymbol{\sigma} \rangle^{(r)}$ over phase r of the LCC may be obtained by differentiation of expression (5.39) with respect to $\mathbb{M}^{(r)}$, i.e.,

$$\langle \boldsymbol{\sigma} \otimes \boldsymbol{\sigma} \rangle^{(r)} = \frac{2}{c^{(r)}} \frac{\partial \widetilde{u}_L}{\partial \mathbb{M}^{(r)}}. \tag{5.42}$$

Further details for the numerical implementation of (5.42) have been discussed thoroughly in Appendix 3 of Liu (2003) (see also Lebensohn et al., 2007), and will not be included here for brevity.

Next, we provide expressions for the SC estimates of the above defined quantities in the LCC (Laws, 1973; Willis, 1981). In particular, the effective viscous compliance tensor $\widetilde{\mathbb{M}}$ is given by the solution of the implicit equation

$$\widetilde{\mathbb{M}} = \left\{ \sum_{r=1}^{N} c^{(r)} \left[\mathbb{M}^{(r)} + \widetilde{\mathbb{M}}^{*} \right]^{-1} \right\}^{-1} - \widetilde{\mathbb{M}}^{*}, \tag{5.43}$$

where $\widetilde{\mathbb{M}}^{*} = \widetilde{\mathbb{Q}}^{-1} - \widetilde{\mathbb{M}}$, and $\widetilde{\mathbb{Q}}$ is a fourth-order microstructural tensor given by

$$\begin{aligned} &\widetilde{\mathbb{Q}} = \widetilde{\mathbb{L}} - \widetilde{\mathbb{L}}\widetilde{\mathbb{P}}\widetilde{\mathbb{L}}, \quad \widetilde{\mathbb{P}} = \frac{1}{4\pi \det(\boldsymbol{Z})} \int\limits_{|\boldsymbol{\zeta}|=1} \widetilde{\mathbb{H}} |\boldsymbol{Z}^{-1}\boldsymbol{\zeta}|^{-3} dS, \\ &\widetilde{H}_{ijkl} = \left(\widetilde{\boldsymbol{K}}^{-1} \right)_{ik} \zeta_j \zeta_l |_{(ij)(kl)}, \quad \widetilde{K}_{ik} = \widetilde{L}_{ijkl} \zeta_j \zeta_l, \end{aligned} \tag{5.44}$$

with $\widetilde{\mathbb{L}} = \widetilde{\mathbb{M}}^{-1}$. As already discussed in section 6.2, the second-order tensor $\boldsymbol{Z}$ in $(5.44)_2$ characterizes the "shape" of the angular dependence of the two-point probability, which correlates with the average shape of the grains, while the parentheses in the subscripts of $(5.44)_3$ indicate symmetrization with respect to the corresponding indices.

Furthermore, the SC estimates for the associated stress concentration tensors are given by

$$\mathbb{B}^{(r)} = \left[\mathbb{M}^{(r)} + \widetilde{\mathbb{M}}^{*}\right]^{-1} \widetilde{\mathbb{Q}}^{-1}, \quad \text{and} \quad \mathbf{b}^{(r)} = \left[\mathbb{M}^{(r)} + \widetilde{\mathbb{M}}^{*}\right]^{-1} \left[\widetilde{\boldsymbol{\eta}} - \boldsymbol{\eta}^{(r)}\right]. \tag{5.45}$$

Making use of the local (linear) constitutive relation of the LCC, the first and second moments of the strain rate over phase r of the LCC can be expressed in terms of the corresponding moments of the stress:

$$\overline{\mathbf{D}}^{(r)} = \mathbb{M}^{(r)} \overline{\boldsymbol{\sigma}}^{(r)} + \boldsymbol{\eta}^{(r)}, \quad \text{and} \tag{5.46}$$

$$\langle \mathbf{D} \otimes \mathbf{D} \rangle^{(r)} = \mathbb{M}^{(r)} \langle \boldsymbol{\sigma} \otimes \boldsymbol{\sigma} \rangle^{(r)} \mathbb{M}^{(r)} + \left(\mathbb{M}^{(r)} \overline{\boldsymbol{\sigma}}^{(r)}\right) \otimes \boldsymbol{\eta}^{(r)} + \boldsymbol{\eta}^{(r)} \otimes \left(\mathbb{M}^{(r)} \overline{\boldsymbol{\sigma}}^{(r)}\right) + \boldsymbol{\eta}^{(r)} \otimes \boldsymbol{\eta}^{(r)}. \tag{5.47}$$

Note that (5.46) and (5.47) may be written in a form completely analogous to (5.41) and (5.42), respectively, in terms of the associated strain-rate concentration tensors and the effective dissipation potentials. Such expressions are also available in the work of Laws (1973) and Willis (1981), and will not be shown here for brevity. Finally, the average spin $\overline{\mathbf{W}}^{(r)}$ in phase r of the LCC is related to the macroscopic spin $\overline{\mathbf{W}}$ and the macroscopic strain rate $\overline{\mathbf{D}}$ through

$$\overline{\mathbf{W}}^{(r)} = \overline{\mathbf{W}} - \mathbb{R}\mathbb{P}^{-1} \left(\overline{\mathbf{D}} - \overline{\mathbf{D}}^{(r)}\right), \tag{5.48}$$

where $\mathbb{R}$ is a fourth-order microstructural tensor given by an expression similar to $(5.44)_2$, except that the symmetric parts in $\widetilde{\mathbb{H}}$ with respect to the indices i and j must be replaced by the corresponding anti-symmetric parts.

5.9 Appendix II: Statistic moments of the spin field in the nonlinear polycrystals

In this Appendix, we make use of the procedure developed by Idiart and Ponte Castañeda (2007c) to compute the moments of the spin field in the phases of the nonlinear polycrystals. The key idea is to introduce a perturbing parameter in the local potentials, such that differentiation of the corresponding effective potential with respect to the parameter yields the volume average of the desired quantity.

For our purposes, it is more convenient to work with the dissipation potential. In particular, we consider a nonlinear polycrystal with local potential defined by (5.8). Then, the FOSO estimates for the effective dissipation potential $\widetilde{w}$ of the nonlinear polycrystal is given by (Ponte Castañeda, 2015)

$$\widetilde{w}(\overline{\mathbf{D}}) = \underset{\mu_{(k)}^{(r)},\eta_{(k)}^{(r)}}{\text{stat}} \left\{ \widetilde{w}_L(\overline{\mathbf{D}}) + \sum_{r=1}^{N} c^{(r)} \sum_{k=1}^{K} V_{(k)}^{(r)}(\mu_{(k)}^{(r)}, \eta_{(k)}^{(r)}) \right\}. \tag{5.49}$$

Here the 'stat' denotes a stationary operation, the $V_{(k)}^{(r)}(\mu_{(k)}^{(r)}, \eta_{(k)}^{(r)})$ ($r = 1, ..., N$, $k = 1, ..., K$) are the error functions given by equation (3.26) together with (3.24) in the work of Ponte Castañeda (2015), and will not be repeated here for brevity. Moreover, $\widetilde{w}_L = \widetilde{u}_L^*$ is the corresponding effective dissipation potential of the LCC with local potential

$$\begin{aligned} w_L(\mathbf{x}, \mathbf{D}) &= \sum_{r=1}^{N} \chi^{(r)}(\mathbf{x}) w_L^{(r)}(\mathbf{D}), \\ w_L^{(r)}(\mathbf{D}) &= \left(u_L^{(r)}\right)^*(\mathbf{D}) = \frac{1}{2}\mathbf{D} \cdot \mathbb{L}^{(r)}\mathbf{D} + \boldsymbol{\tau}^{(r)} \cdot \mathbf{D} + f^{(r)}, \end{aligned} \tag{5.50}$$

where $\mathbb{L}^{(r)}$, $\boldsymbol{\tau}^{(r)}$ and $f^{(r)}$ are, respectively, the viscosity, eigenstress and energy at zero strain rate for phase r of the LCC, and are related to the corresponding viscous compliance $\mathbb{M}^{(r)}$ and eigenstrain rate $\boldsymbol{\eta}^{(r)}$ in (5.14) via the relations

$$\mathbb{L}^{(r)} = \left(\mathbb{M}^{(r)}\right)^{-1}, \quad \boldsymbol{\tau}^{(r)} = -\left(\mathbb{M}^{(r)}\right)^{-1} \boldsymbol{\eta}^{(r)}, \quad \text{and} \quad f^{(r)} = \frac{1}{2}\boldsymbol{\eta}^{(r)} \cdot \left(\mathbb{M}^{(r)}\right)^{-1} \boldsymbol{\eta}^{(r)}. \tag{5.51}$$

Note that the estimates (5.49) and (5.16) are completely equivalent to each other (no duality gap) involving precisely the same LCC (Ponte Castañeda, 2015).

Following the idea of Proposition 3.1 of Idiart and Ponte Castañeda (2007c), the first moment of the spin field in phase r of the nonlinear polycrystal is given by

$$\overline{\mathbf{W}}^{(r)} = \frac{1}{c^{(r)}} \frac{\partial \widetilde{w}_s}{\partial \mathbf{s}^{(r)}}(\overline{\mathbf{D}}, \overline{\mathbf{W}})\bigg|_{\mathbf{s}^{(r)}=\mathbf{0}}, \tag{5.52}$$

where $\mathbf{s}^{(r)}$ is a constant, *antisymmetric*, second-order tensor, and $\widetilde{w}_s$ denotes the effective potential of a polycrystal with (perturbed) local potential

$$w_s(\mathbf{x}, \mathbf{D}, \mathbf{W}) = \sum_{s=1}^{N} \chi^{(s)}(\mathbf{x}) w^{(s)}(\mathbf{D}) + \chi^{(r)}(\mathbf{x}) \mathbf{s}^{(r)} \cdot \mathbf{W}. \tag{5.53}$$

When the above results (5.52) and (5.53) are applied to the LCC with local potential (5.50), we have that

$$\overline{\mathbf{W}}_L^{(r)} = \frac{1}{c^{(r)}} \frac{\partial \widetilde{w}_{Ls}}{\partial \mathbf{s}^{(r)}}(\overline{\mathbf{D}}, \overline{\mathbf{W}})\bigg|_{\mathbf{s}^{(r)}=\mathbf{0}}, \tag{5.54}$$

where we have used the subscript L to denote the appropriate quantities in the LCC, and $\widetilde{w}_{Ls}$ denotes the effective potential of a composite with (perturbed) local potential

$$w_{Ls}(\mathbf{x}, \mathbf{D}, \mathbf{W}) = \sum_{s=1}^{N} \chi^{(s)}(\mathbf{x}) w_L^{(s)}(\mathbf{D}) + \chi^{(r)}(\mathbf{x}) \mathbf{s}^{(r)} \cdot \mathbf{W}. \tag{5.55}$$

Then, it follows from (5.49) that the effective dissipation potential of the perturbed nonlinear polycrystals can be written as

$$\widetilde{w}_s(\overline{\mathbf{D}}, \overline{\mathbf{W}}) = \underset{\mu_{(k)}^{(r)}, \eta_{(k)}^{(r)}}{\operatorname{stat}} \left\{ \widetilde{w}_{Ls}(\overline{\mathbf{D}}, \overline{\mathbf{W}}) + \sum_{r=1}^{N} c^{(r)} \sum_{k=1}^{K} V_{(k)}^{(r)}(\mu_{(k)}^{(r)}, \eta_{(k)}^{(r)}) \right\}. \tag{5.56}$$

Noting that the functions $V_{(k)}^{(r)}$ are independent of the perturbation parameter $\mathbf{s}^{(r)}$, and using the chain rule and the stationarity of (5.56) with respect to the variables $\mu_{(k)}^{(r)}$ and $\eta_{(k)}^{(r)}$, it is easy to see that the quantities $\partial \widetilde{w}_s / \partial \mathbf{s}^{(r)}$ and $\partial \widetilde{w}_{Ls} / \partial \mathbf{s}^{(r)}$ (evaluated

at the optimal values of $\mu_{(k)}^{(r)}$ and $\eta_{(k)}^{(r)}$) are identical. By setting $\mathbf{s}^{(r)} = \mathbf{0}$, we have that

$$\overline{\mathbf{W}}^{(r)} = \overline{\mathbf{W}}_L^{(r)}, \tag{5.57}$$

which suggests that the phase averages of the spin field in the nonlinear polycrystals can be estimated consistently from those in the 'optimized' LCC.

Similarly, it is also possible to show by means of an appropriate generalization of Corollaries 3.3 of Idiart and Ponte Castañeda (2007c) that the second moments of the spin field in the nonlinear polycrystals can be directly estimated from the 'optimized' LCC, i.e.,

$$\langle \mathbf{W} \otimes \mathbf{W} \rangle^{(r)} = \langle \mathbf{W} \otimes \mathbf{W} \rangle_L^{(r)}. \tag{5.58}$$

Chapter 6

Iterated second-order homogenization model for viscoplastic porous polycrystals with large voids: Theory

In this chapter, we propose a finite-strain homogenization model for the macroscopic response of viscoplastic porous polycrystals consisting of large pores embedded in a fine-scale polycrystalline matrix. Specifically, the porous polycrystal is modeled as a two-scale composite, which has a porous meso-structure at the larger length scale, and a granular structure for the underlying matrix at the smaller length scale. The instantaneous response of the porous polycrystal for a fixed state of the sub-structure is determined by means of a generalization of the recently developed iterated second-order homogenization method. The method makes use of a linear comparison composite (LCC) with the same sub-structure as the actual nonlinear composite, but whose local properties are chosen optimally via a suitably designed variational principle. The effective properties of the resulting two-scale LCC are determined by means of a sequential homogenization procedure, involving the self-consistent estimates for the effective behavior of the polycrystalline matrix, and the Hashin-Shtrikman type

estimates for the effective behavior of the porous composite. In addition, the iterated homogenization procedure is used to "discretize" the properties of the matrix in the LCC to obtain improved results, especially for low porosities and high triaxialities. Furthermore, consistent homogenization estimates for the average strain rate and spin fields in the phases are used to develop evolution laws for the sub-structural variables, accounting for the evolution of porosity, pore morphology, as well as the texture of the underlying matrix. The model is quite general, and applies to two-scale porous polycrystals with general ellipsoidal pores and grains, and general crystallographic anisotropy, which are subjected to general three-dimensional loading conditions.

6.1 Introduction

Most ductile metals are polycrystalline aggregates consisting of large numbers of randomly distributed single-crystal grains. These materials usually also contain random distributions of micro-voids and micro-cracks, which are generated either from the manufacturing process (e.g., powder metallurgy), or which nucleate in the material from second-phase particles and eventually grow and coalescence leading to material failure (Tvergaard, 1990). In many cases, the size of the voids is much larger than that of the single-crystal grains, so that the porous material can be idealized as a fine-scale polycrystalline matrix containing large void inclusions. Up to now, most studies on porous materials were carried out in the context of two-phase material systems, with the simplifying assumption that the matrix surrounding the voids is homogeneous and isotropic (e.g., Gurson, 1977). However, there is ample experimental and numerical evidence showing that the initial texture and its evolution can induce strong anisotropy in the response of polycrystalline materials (e.g., Bache and Evans, 2001; Caré and Zaoui, 1996; Lebensohn et al., 2013), which, in turn, could significantly affect the void growth and coalescence.

Motivated by these observations, we propose to develop a finite-strain constitutive model for porous viscoplastic polycrystals containing large pores, while accounting for the coupled interactions between the porosity growth and the texture evolution

for the polycrystalline matrix. More specifically, we will make use of recently developed nonlinear homogenization techniques (Song and Ponte Castañeda, 2017b; Ponte Castañeda, 2015) to characterize the instantaneous macroscopic behavior of porous polycrystals given the current state of the microstructure, as well as the evolution of the microstructure at finite-strain deformations. We begin by briefly reviewing some key references on the application of homogenization approaches for porous materials with *isotropic* matrix. Ponte Castañeda (1991) made use of a variational (VAR) statement for the properties of a linear comparison composite (LCC), together with the standard (linear) Hashin-Shtrikman bounds for the LCC, to obtain corresponding bounds for the effective flow potential of porous isotropic materials (see also Willis, 1991 and Michel and Suquet, 1992 for derivations of equivalent bounds using other methods). Ponte Castañeda and Zaidman (1994) made use of the VAR method of Ponte Castañeda (1991) to develop a finite-strain constitutive model for porous viscoplastic materials, accounting for the evolution of the porosity and void shape under triaxial loading conditions. By making use of the linear estimates of Ponte Castañeda and Willis (1995), the model was progressively generalized to incorporate the void distribution effects (Kailasam et al., 1997), void rotations under shear loading conditions (Kailasam and Ponte Castañeda, 1997), as well as elasticity and strain hardening of the matrix (Kailasam et al., 2000; Aravas and Ponte Castañeda, 2004).

While the predictions of the VAR method are found to be quite accurate for deviatoric loading conditions, where the effects of void shape changes are significant, they are overly stiff for high-triaxiality loading conditions, especially for low porosities and high nonlinearities. In order to resolve this deficiency associated with the VAR model, Danas and Ponte Castañeda (2009a) developed an improved finite-strain constitutive model, making use of the more advanced second-order (SO) homogenization method of Ponte Castañeda (2002), along with an ad hoc modification, enforcing the agreement of the predictions of the SO model with the exact results of spherical/cylindrical shells for purely hydrostatic loadings. While the SO model provides estimates that are in good agreement with FEM results, it involves certain fitting parameters and is therefore *not* fully predictive. More recently, Agoras and Ponte

Castañeda (2014) developed a finite-strain model for porous materials under triaxial loadings, making sole use of the VAR approach of Ponte Castañeda (1991), albeit in an iterative fashion (Ponte Castañeda, 2012; Agoras and Ponte Castañeda, 2013). The iterated variational method also provides estimates that recover the exact results of spherical/cylindrical shells for purely hydrostatic loadings (as the number of iteration $I \to \infty$), but has the additional advantage of being entirely predictive, not requiring any fitting parameters. In practice, it can be shown (Agoras and Ponte Castañeda, 2013) that a relatively small number of iterations ($I \approx 5-10$) is sufficient to provide accurate estimates for the corresponding $I \to \infty$ limits, so that the IVAR method is still relatively easy to implement. The iterated variational homogenization model was further generalized by Song et al. (2015) to incorporate the effects of void rotations under general shear loading conditions with non-vanishing macroscopic spin. In particular, it was found that void rotations can dramatically enhance the susceptibility of the porous materials to shear localizations for simple shear loading conditions.

In this connection, it should be remarked that Gurson's approach has also been generalized to account for void shape effects (e.g., Gologanu et al., 1993; Madou and Leblond, 2012a), as well as for the plastic anisotropy of the matrix (e.g., Benzerga and Besson, 2001; Monchiet et al., 2006; Keralavarma and Benzerga, 2010). These works have been reviewed in detail by Benzerga and Leblond (2010) and Benzerga et al. (2016) and we will not provide further details here. However, it should be mentioned that the Gurson's approach is less general than the homogenization method in several aspects. First, to the best knowledge of the authors, it has not been possible to obtain consistent estimates for the average strain-rate and spin fields in the voids by means of Gurson's approach. Thus, it has been necessary to combine the Gurson's limit analysis estimates for the yield surfaces of porous materials with evolution laws for the shape and orientation of the voids derived from the homogenization approach (improved through numerical fitting to FEM simulations of confocal shells). Second, Gurson's approach is difficult to generalize for a multi-phase porous polycrystal, and it is so far unable to capture the effects of texture and its evolution for polycrystal

solids.

By contrast, homogenization theories are already available to estimate the macroscopic response of *fully dense* viscoplastic polycrystals in terms of their morphological and crystallographic texture. In particular, a new class of nonlinear homogenization methods, improving significantly on the "classical" theories (e.g., Hill, 1965; Hutchinson, 1976; Molinari et al., 1987; Lebensohn et al., 1993), were developed by Ponte Castañeda and coworkers. Like the above-mentioned homogenization methods for porous viscoplastic materials, these theories rely on the use of a linear comparison composite (LCC), whose microstructure is identical to that of the nonlinear polycrystal, but whose single-crystal behavior is identified with a certain linearization of the corresponding nonlinear response, guided by suitably designed variational principles. Among these, Nebozhyn et al. (2001) made use of the variational principle of deBotton and Ponte Castañeda (1995) (a generalization of the VAR method of Ponte Castañeda, 1991), together with the standard (linear) self-consistent estimates (Kröner, 1958; Willis, 1977) for the LCC, to obtain rigorous bounds of the self-consistent type for the effective flow stress of the nonlinear polycrystals. Improved bounds were obtained by Idiart (2011), making use of a more general variational principle of Idiart and Ponte Castañeda (2007a). However, this method requires to solve a more complicated optimization problem, and is therefore much harder to implement. Precisely because of the bounding status of the above estimates, they are expected to overestimate the effective flow stress of polycrystals. More accurate self-consistent estimates were developed by Liu and Ponte Castañeda (2004a), making use of a generalization of the SO method of Ponte Castañeda (2002). The SO self-consistent estimates have been found to be fairly accurate in several comparisons with full-field numerical simulations (e.g., Lebensohn et al., 2004; Lebensohn et al., 2007). However, the SO method has some undesired features, including the facts that the macroscopic constitutive relation and field statistics cannot be extracted directly from the LCC, and that it exhibits a duality gap (i.e., the estimates resulting from the primary and complementary variational statements are different). These deficiencies are due to the lack of fully stationarity of the variational principle with respect to the properties

of the LCC. In order to remedy this shortcoming, Ponte Castañeda (2015) recently proposed a refined fully optimized second-order (FOSO) variational approach, in such a way that the resulting estimates are allowed to be fully stationary, while retaining all the distinctive advantages of the earlier SO method of Liu and Ponte Castañeda (2004a). Very recently, Song and Ponte Castañeda (2017d) made use of the FOSO method to obtain estimates of the self-consistent type for the macroscopic behavior, as well as for the evolution of the microstructure for hexagonal polycrystals. Comparisons with available full-field numerical results show that the FOSO method of Ponte Castañeda (2015) provides the most accurate and reliable estimates among the various nonlinear self-consistent methods available to date.

While significant progress has been made in the modeling of the macroscopic behavior and microstructure evolution in fully dense polycrystals, far fewer models are available for porous polycrystals. Lebensohn et al. (2004) made use of the "affine" procedure of Masson et al. (2000), originally designed for solid polycrystals, to model the viscoplastic response of porous polycrystals containing *intergranular* voids (where the voids and crystal grains are of similar sizes). It was found that the anisotropy induced by texture evolution has important effects on the porosity growth and macroscopic response of these voided polycrystals. However, the model cannot handle purely hydrostatic loadings (Lebensohn et al., 2004), and it becomes necessary to introduce an ad hoc linearization procedure to artificially soften the response at high triaxialities. More recently, Lebensohn et al. (2011) made use of a generalization of the SO method of Liu and Ponte Castañeda (2004a) to obtain estimates for the effective flow potential of porous polycrystals containing intergranular voids. While the predictions of this method are in excellent agreement with numerical simulations for low triaxialities, the corresponding results at high triaxialities exhibit the same shortcoming of the earlier homogenization models for porous materials with isotropic matrix, and are unrealistically stiff, especially at low porosities.

In this context, it should be remarked that accurate homogenization models have been proposed to describe the macroscopic behavior of porous single crystals (e.g., Mbiakop et al., 2015a; Song and Ponte Castañeda, 2017a; 2017b; 2017c), making

use of recent advances in homogenization approaches. In particular, Song and Ponte Castañeda (2017a) employed the VAR method of deBotton and Ponte Castañeda (1995) to generate bounds for the effective flow potential of porous single crystals. Moreover, the iterated homogenization procedure of Agoras and Ponte Castañeda (2013) was used to "discretize" the properties of the matrix, thus obtaining tighter bounds at high triaxialities. Improved estimates for the effective flow potential of porous single crystals were recently obtained by Song and Ponte Castañeda (2017b, 2017c), making use of the more advanced FOSO method of Ponte Castañeda (2015) along with a generalization of the iterated homogenization method. In addition, these authors made use of consistent homogenization estimates for the strain-rate and spin fields in the phases to develop evolution laws for the microstructure, accounting for lattice rotation, as well as for changes in the size, shape and orientation of the voids. The iterated second-order (ISO) model was then used to investigate both the instantaneous and finite-strain macroscopic response of porous FCC and HCP single crystals, demonstrating a complex coupled interactions between the crystallographic anisotropy induced by the preferred slip directions, and the morphological anisotropy induced by the ellipsoidal geometry of the voids. In particular, the predictions of the model are found to be in good agreement with the full-field simulations of Srivastava and Needleman (2015) for porous FCC single crystals.

Motivated by the above considerations, in this chapter we develop a general finite-strain constitutive model for porous polycrystals consisting of large pores that are distributed in a fine-scale polycrystalline matrix, by means of a generalization of the ISO model of Song and Ponte Castañeda (2017b) for porous single crystals. The model provides estimates not only for the instantaneous response of the porous polycrystal for a given state of the microstructure, but also for the evolution of the pore geometry and matrix texture at finite-strain deformations. More specifically, the porous polycrystal is modeled as a *two-scale* composite, with a particulate structure at the larger length scale, and with a granular structure for the matrix at the smaller length scale. We make use of the recently developed FOSO method of Ponte Castañeda (2015), appropriately generalized for a two-scale composite, to characterize the instantaneous

macroscopic response of porous polycrystals. We will also make use of the iterated homogenization approach of Agoras and Ponte Castañeda (2013) to "discretize" the polycrystalline matrix to obtain improved results for the macroscopic response of porous polycrystals, especially at low porosities and high triaxialities. Furthermore, we make use of consistent homogenization estimates for the average strain rate and spin fields in the phases to develop consistent evolution laws for the two-scale substructure, as characterized by the porosity, void morphology, grain morphology, as well as the crystallographic texture of the polycrystal. In the next chapter, we will consider specific applications of the model for porous FCC and HCP polycrystals.

6.2 Background and formulation

6.2.1 Sub-structural characterization

In this work, we consider polycrystalline solids containing "large" voids, where the size of the voids is much larger than that of the single-crystal grains, while still much smaller than the size of specimen. The porous polycrystal can then be modeled as a *two-scale* composite material, whose sub-structural features are shown schematically in Fig. 6.1. Specifically, Fig. 6.1(a) shows—at the mesoscale—a representative volume element (RVE) Ω of the material, which consists of vacuous inclusions (phase 2) distributed *randomly* in a polycrystalline matrix (phase 1), occupying the sub-regions $\Omega^{(2)}$ and $\Omega^{(1)}$, respectively. On the other hand, Fig. 6.1(b) shows—at the microscale—an RVE Ω^* inside of the polycrystalline matrix $\Omega^{(1)}$, which is assumed to be a *random* aggregate of perfectly bonded single-crystal grains. For simplicity, we restrict our attention to a monolithic polycrystalline matrix, so that the grains differ from each other only in terms of crystallographic orientation, but not in composition. Moreover, we assume that the crystal orientations take on a set of N discrete values, and define phase r ($r = 1, ..., N$) to be given by all the grains with the same crystallographic orientation, and occupying the sub-region $\Omega^{(1,r)}$. In the following, we make use of the symbols $\langle\cdot\rangle$, $\langle\cdot\rangle^{(q)}$ ($q = 1, 2$) and $\langle\cdot\rangle^{(1,r)}$ ($r = 1, ..., N$) to denote

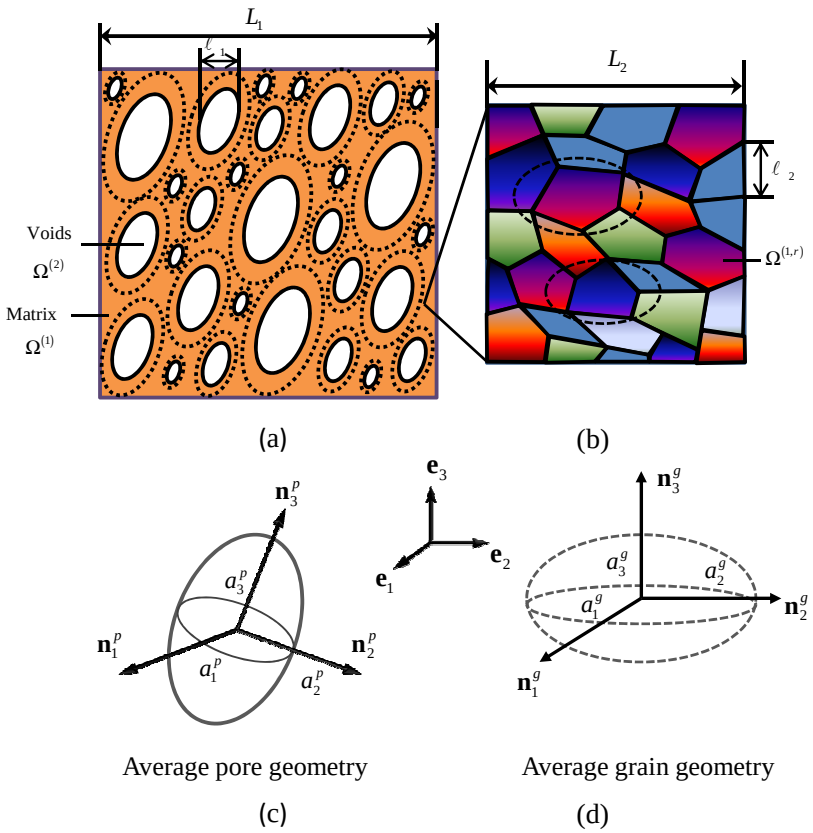

Figure 6.1: Schematic representation of a porous polycrystal consisting of aligned, ellipsoidal voids (solid lines) that are distributed with ellipsoidal symmetry (dotted lines) in a polycrystalline matrix, with the size of the voids much larger than that of the single-crystal grains. (a) Macroscopic RVE: porous polycrystals with a particulate meso-structure, (b) Mesoscopic RVE: polycrystalline matrix with a granular micro-structure, (c) Average pore geometry in the macroscopic RVE, (d) Average grain geometry in the mesoscopic RVE.

volume averages of fields over Ω, $\Omega^{(q)}$ and $\Omega^{(1,r)}$, respectively. Letting L_1, l_1, L_2, l_2 characterize respectively the size of the RVE Ω, the size of a typical void, the size of an RVE within the polycrystalline matrix and the size of a typical grain (see Fig. 6.1), we make use of the hypothesis of *separation of the length scales*, defined by

$$l_2 \ll L_2 < l_1 \ll L_1. \tag{6.1}$$

For convenience, the heterogeneity induced by the voids at the mesoscale scale will be referred to as the *meso-structure*, while that induced by the different phases of single-crystal grains at the microscale will be referred to as the *micro-structure*. It is

assumed that both the meso- and micro-structures of interest are *statistically uniform*, *ergodic* and possess *no long-range order* (Willis, 1981). It is further assumed that the meso-structure is *statistically independent* from the underlying micro-structure (Smyshlyaev and Willis, 1998).

The sub-structure of the two-scale porous polycrystals in Fig. 6.1 can be completely characterized by the indicator functions of the phases

$$\theta^{(q,r)}(\mathbf{x}) = \begin{cases} 1, & \text{if} \quad \mathbf{x} \in \Omega^{(q,r)} \\ 0, & \text{otherwise} \end{cases}, \tag{6.2}$$

where the first superscript $q = 1, 2$, while the second superscript $r = 1, ..., N$ if $q = 1$, and $r = 1$ if $q = 2$ (this is because the void phase $\Omega^{(2)}$ is homogeneous at both the meso- and micro-scale). It is remarked that the $\theta^{(q,r)}$ are two-scale functions, since they incorporate sub-structural information both over the microscale l_2 and the mesoscale l_1. A more precise description of the latter statement may be given by introducing a new spatial variable $\mathbf{y} = \mathbf{x}/\epsilon$, with ϵ being a small parameter, together with the following decomposition

$$\theta^{(q,r)}(\mathbf{x}) = \chi^{(q)}(\mathbf{x})\chi^{(q,r)}(\mathbf{y}). \tag{6.3}$$

Here the indicator functions $\chi^{(q)}(\mathbf{x})$ and $\chi^{(q,r)}(\mathbf{y})$ characterize respectively the meso-structure (Fig. 6.1(a)) and the micro-structure (Fig. 6.1(b)) of the two-scale composite, and are defined by

$$\chi^{(q)}(\mathbf{x}) = \begin{cases} 1, & \text{if} \quad \mathbf{x} \in \Omega^{(q)} \\ 0, & \text{otherwise,} \end{cases} \qquad \chi^{(q,r)}(\mathbf{y}) = \begin{cases} 1, & \text{if} \quad \mathbf{y} \in \Omega^{(q,r)} \\ 0, & \text{otherwise.} \end{cases} . \tag{6.4}$$

Note that the functions $\chi^{(q)}(\mathbf{x})$ and $\chi^{(q,r)}(\mathbf{y})$ are now single-scale functions, where the $\chi^{(q)}$ $(q = 1, 2)$ are defined over Ω and vary over l_1, while the $\chi^{(q,r)}$ $(q = 1, 2, r = 1, ..., N)$ are defined over $\Omega^{(q)}$ and vary over l_2.

In general, the sub-structure of the *random* porous polycrystal can be described by

means of the two-scale multi-point statistics, which are appropriate ensemble averages of the two-scale indicator functions $\theta^{(q,r)}(\mathbf{x})$ (see Agoras and Ponte Castañeda, 2011 for details). However, due to the assumption that the meso- and micro-structure of the porous polycrystal are statistically independent, the two-scale statistics of the composite may be conveniently expressed in terms of the corresponding mesoscopic multi-point statistics, i.e., $p^{(q)}(\mathbf{x})$, $p^{(pq)}(\mathbf{x},\mathbf{x}')$, etc., as well as the microscopic multi-point statistics, i.e., $p^{(q,r)}(\mathbf{y})$, $p^{(q,rs)}(\mathbf{y},\mathbf{y}')$, etc. Thus, we prescribe more precisely the meso- and micro-structure of the porous polycrystals in the following.

Meso-structure of the porous medium

At the meso-scale, the porous material is assumed to have a random, particulate meso-structure of the "ellipsoidal" type (Ponte Castañeda and Willis, 1995). As shown in Fig. 6.1(a), the pores (phase 2) are assumed to be of ellipsoidal shape (on *average*), and to be aligned, but distributed randomly in the matrix (phase 1), in such a fashion that the two-point statistics for the distribution of the centers of the pores are also "ellipsoidal", but of possibly different shape and orientation. These meso-structural features may be formally prescribed through the one-point statistics of the phases $p^{(q)}(\mathbf{x}) = \langle \chi^{(q)}(\mathbf{x}) \rangle = c^{(q)} = |\Omega^{(q)}|/|\Omega|$ $(q = 1, 2)$, along with two positive-definite, symmetric second-order tensors $\boldsymbol{Z}^p$ and $\boldsymbol{Z}^d$, defining the ellipsoidal shape of the pores and of the angular dependence of the two-point probability for the distribution of their centers. More specifically, the ellipsoidal pores occupy regions described by

$$\Omega^{(2)} = \{\mathbf{x} : |\boldsymbol{Z}^p \mathbf{x}| \leq 1\}, \tag{6.5}$$

and their centers are distributed with two-point probability functions

$$p^{(d)}(\mathbf{x},\mathbf{x}') = p^{(d)}(\mathbf{x}-\mathbf{x}') = p^{(d)}\left(\left|\boldsymbol{Z}^d(\mathbf{x}-\mathbf{x}')\right|\right). \tag{6.6}$$

Note that, in the above expressions, we have made use of the fact that the meso-structures are statistically uniform and ergodic, so that the one-point probabilities

are constants, the two-point probabilities depend only on the relative position $\mathbf{x}-\mathbf{x}'$, and the ensemble averages can be replaced by the corresponding volume averages. Note further that the effect of the void distribution on the macroscopic behavior of the porous polycrystals is only of second order in the volume fraction of the voids (porosity) and becomes less important at low to moderate porosities. For this reason, we further assume that the ellipsoidal shape and orientation of the distribution function are identical to the ellipsoidal shape and orientation of the voids, i.e., $\boldsymbol{Z}^p = \boldsymbol{Z}^d$ (Song et al., 2015; Song and Ponte Castañeda, 2017b). Here we define $f = c^{(2)}$ to be the volume fraction of the voids (or porosity), $w_1^p = a_3^p/a_1^p, w_2^p = a_3^p/a_2^p$ to be the two aspect ratios of the representative ellipsoids characterizing the shape and distribution of the voids (where a_1^p, a_2^p and a_3^p are the lengths of the three semi-axes of the ellipsoid), and $\mathbf{n}_1^p$, $\mathbf{n}_2^p$ and $\mathbf{n}_3^p$ to be unit vectors along the three principal directions of the representative ellipsoid (see Fig. 6.1(c)). Note that the principal directions of the voids can be more compactly denoted by a single rotation tensor $\mathbf{G}^p$, which relates the void axes $\mathbf{n}_i^p$ $(i = 1,2,3)$ and sample axes $\mathbf{e}_i$ $(i = 1,2,3)$ via the relation $\mathbf{n}_i^p = \left(\mathbf{G}^p\right)^{\mathrm{T}} \mathbf{e}_i$ $(i = 1,2,3)$.

Micro-structure of the polycrystalline matrix

At the micro-scale, the polycrystalline matrix occupying $\Omega^{(1)}$ is assumed to have a granular micro-structure (see Fig. 6.1(b)), where the N single-crystal phases are distributed with a prescribed orientation distribution function (ODF) and associated two-point statistics. The ODF determines the *crystallographic* texture, while the corresponding two-point statistics correlate with the *average* grain shape and serve to characterize approximately the *morphological texture*. The lattice orientations of the different single-crystal phases are assumed to take on a set of discrete values, as characterized by the rotation tensors $\mathbf{Q}^{(1,r)}$ $(r = 1,...,N)$, so that the lattice vectors $\mathbf{l}_i^{(1,r)}$ $(i = 1,2,3)$ for a given crystal orientation are related to the corresponding lattice vectors $\mathbf{l}_i$ $(i = 1,2,3)$ for a 'reference' single-crystal via $\mathbf{l}_i^{(1,r)} = \left(\mathbf{Q}^{(1,r)}\right)^T \mathbf{l}_i$ $(i = 1,2,3)$. Making use of the statistical uniformity and ergodicity of the micro-structure, the one-point probability of phase r can be identified with the corresponding volume fraction

of phase r, such that $p^{(1,r)}(\mathbf{y}) = \langle \chi^{(1,r)}(\mathbf{y}) \rangle^{(1)} = c^{(1,r)} = |\Omega^{(1,r)}|/|\Omega^{(1)}|$ $(r = 1, ..., N)$. In addition, the two-point probability function of finding simultaneously phase r at $\mathbf{y}$ and phase s at $\mathbf{y}'$ are assumed to exhibit "ellipsoidal" symmetry (Willis, 1977), as characterized by a second order tensor $\boldsymbol{Z}^g$, i.e.,

$$p^{(1,rs)}(\mathbf{y}, \mathbf{y}') = p^{(1,rs)}(\mathbf{y} - \mathbf{y}') = \langle \chi^{(1,r)} \chi^{(1,s)} \rangle^{(1)} = p^{(1,rs)} \left(|\boldsymbol{Z}^g (\mathbf{y} - \mathbf{y}')| \right). \tag{6.7}$$

The above assumption implies that, *on average*, all grains have the same ellipsoidal shape, as determined by the two aspect ratios $w_1^g = a_3^g/a_1^g, w_2^g = a_3^g/a_2^g$ (where a_1^g, a_2^g and a_3^g are the lengths of the three semi-axes of the grain ellipsoid), together with the three principal axes $\mathbf{n}_1^g$, $\mathbf{n}_2^g$ and $\mathbf{n}_3^g$ of the grains (see Fig. 6.1(d)). Similarly, the orientation of the grains can be described by a rotation tensor $\mathbf{G}^g$, which relates the grain axes $\mathbf{n}_i^g$ $(i = 1, 2, 3)$ to the sample axes $\mathbf{e}_i$ $(i = 1, 2, 3)$ via the relation $\mathbf{n}_i^g = \left(\mathbf{G}^g\right)^{\mathrm{T}} \mathbf{e}_i$ $(i = 1, 2, 3)$.

In this context, it should be remarked that, the above described one- and two-point probabilities associated with the meso- and micro-structures do *not* suffice to determine exactly the properties of the two-scale porous polycrystals. However, in this work we will make use of the estimates of the Ponte Castañeda and Willis (PCW) type (Ponte Castañeda and Willis, 1995) for the particulate meso-structure, together with the estimates of the self-consistent (SC) type (Hershey, 1954; Kröner, 1958; Willis, 1977) for the granular micro-structure, to obtain accurate estimates for the effective behavior of these two-scale composites. It is well known that the above estimates depend only on the one- and two-point statistics. Thus, for our purposes, the two-scale sub-structure of the porous polycrystals may be completely characterized by the set of sub-structural variables

$$\mathbf{s} \equiv \{f, w_1^p, w_2^p, \mathbf{G}^p; \mathbf{Q}^{(1,r)}, w_1^g, w_2^g, \mathbf{G}^g\}, \tag{6.8}$$

where the variables $\{f, w_1^p, w_2^p, \mathbf{G}^p\}$ describe the meso-structure of the composite, while the other variables $\{\mathbf{Q}^{(1,r)}, w_1^g, w_2^g, \mathbf{G}^g\}$ describe the micro-structure of the composite. Note that, in this work, the volume fraction $c^{(1,r)}$ of each single-crystal phase is taken to be fixed, due to the incompressibility of the single-crystal grains (this

is why we do not include $c^{(1,r)}$ in the sub-structural variables (6.8)). Thus, during finite-strain deformations, the evolution of the ODF for the polycrystalline matrix is characterized by the evolution of the rotation tensors $\mathbf{Q}^{(1,r)}$ $(r = 1, ..., N)$, but not $c^{(1,r)}$ $(r = 1, ..., N)$. However, it should be mentioned that there are other ways to describe the evolution of the ODF (see, e.g., Dawson and Marin, 1997).

6.2.2 Local material behavior

In this work, we mainly focus on the behavior of porous polycrystals under large plastic deformations and, thus, the elastic deformation of the single-crystal phases (which is typically very small) will be neglected. In addition, the single-crystal grains are assumed to deform by dislocation creep along well-defined crystallographic slip systems, and the constitutive response of the single-crystal grains will be taken to be viscoplastic, as can be described by

$$\boldsymbol{D} = \frac{\partial u^{(1,r)}}{\partial \boldsymbol{\sigma}}(\boldsymbol{\sigma}), \quad u^{(1,r)}(\boldsymbol{\sigma}) = \sum_{k=1}^{K} \phi_{(k)}^{(r)}(\tau_{(k)}^{(r)}). \tag{6.9}$$

Here $\boldsymbol{D}$ is the Eulerian strain rate, $\boldsymbol{\sigma}$ is the Cauchy stress, and $u^{(1,r)}$ is the stress potential for the rth single-crystal phase. The convex functions $\phi_{(k)}^{(r)}$ $(k = 1, \cdots, K)$ characterize the response of the K slip systems in the rth single-crystal phase with orientation $\mathbf{Q}^{(1,r)}$, and depend on the resolved shear (or Schmid) stresses

$$\tau_{(k)}^{(r)} = \boldsymbol{\sigma} \cdot \boldsymbol{\mu}_{(k)}^{(r)}, \quad \text{where} \quad \boldsymbol{\mu}_{(k)}^{(r)} = \frac{1}{2}\left(\boldsymbol{n}_{(k)}^{(r)} \otimes \boldsymbol{m}_{(k)}^{(r)} + \boldsymbol{m}_{(k)}^{(r)} \otimes \boldsymbol{n}_{(k)}^{(r)}\right). \tag{6.10}$$

In addition, the $\boldsymbol{\mu}_{(k)}^{(r)}$ are second-order tensors obtained from the symmetrized dyadic product of the unit vectors $\boldsymbol{n}_{(k)}^{(r)}$, normal to the slip plane, and $\boldsymbol{m}_{(k)}^{(r)}$, along the slip direction, for the kth system in a crystal with orientation $\mathbf{Q}^{(1,r)}$. Note that the Schmid tensors $\boldsymbol{\mu}_{(k)}^{(r)}$ for a monolithic polycrystalline matrix are related to the corresponding tensors $\boldsymbol{\mu}_{(k)}$ for a 'reference' crystal via $\boldsymbol{\mu}_{(k)}^{(r)} = \left(\mathbf{Q}^{(1,r)}\right)^{\mathrm{T}} \boldsymbol{\mu}_{(k)} \mathbf{Q}^{(1,r)}$. A commonly used

model for the slip potentials is given by the power-law form:

$$\phi_{(k)}^{(r)}(\tau) = \frac{\dot{\gamma}_0 \left(\tau_0\right)_{(k)}^{(r)}}{n+1} \left| \frac{\tau}{\left(\tau_0\right)_{(k)}^{(r)}} \right|^{n+1}, \tag{6.11}$$

where $n \geq 1$ is the creep exponent (or the inverse of the strain-rate sensitivity $m = 1/n$), $\left(\tau_0\right)_{(k)}^{(r)} > 0$ is the reference flow stress of the kth slip system, and $\dot{\gamma}_0$ is a reference strain rate. Note that the creep exponent n could, in general, be different for different slip systems, but, for simplicity, it will be taken here to be the same for all slip systems. In particular, the limits as n tends to 1 and ∞ are of special interest, since they correspond to linearly viscous and rigid–ideally plastic behavior.

On the other hand, the stress potential of the voids (phase 2 in the porous mesostructure) is such that $u^{(2)}(\boldsymbol{\sigma}) = 0$ if $\boldsymbol{\sigma}$ is identically zero, while $u^{(2)}(\boldsymbol{\sigma}) = \infty$ otherwise.

Given the local properties of each phase described above, the local constitutive relation between the Eulerian strain rate $\mathbf{D}$ and the Cauchy stress $\boldsymbol{\sigma}$ in the two-scale porous polycrystal is given by

$$\mathbf{D} = \frac{\partial u}{\partial \boldsymbol{\sigma}} \left(\mathbf{x}, \boldsymbol{\sigma}\right), \tag{6.12}$$

where $u(\mathbf{x}, \boldsymbol{\sigma})$ is the local stress potential of the composite, defined by

$$u(\mathbf{x}, \boldsymbol{\sigma}) = \chi^{(1)}(\mathbf{x}) \sum_{r=1}^{N} \chi^{(1,r)}(\mathbf{y}) u^{(1,r)}(\boldsymbol{\sigma}) + \chi^{(2)}(\mathbf{x}) u^{(2)}(\boldsymbol{\sigma}). \tag{6.13}$$

Note that in the above expression use has been made of the relation (6.3).

6.3 Instantaneous effective response

For a given fixed state of the two-scale sub-structure, the instantaneous effective response of the porous polycrystal, characterizing the relation between the average strain rate $\langle \mathbf{D} \rangle = \overline{\mathbf{D}}$ and the average stress $\langle \boldsymbol{\sigma} \rangle = \overline{\boldsymbol{\sigma}}$, may be written in the form (Hill, 1963)

$$\overline{\mathbf{D}} = \frac{\partial \widetilde{u}(\overline{\boldsymbol{\sigma}})}{\partial \overline{\boldsymbol{\sigma}}}, \tag{6.14}$$

where $\widetilde{u}$ is the effective stress potential for the porous polycrystal given by

$$\widetilde{u}(\overline{\boldsymbol{\sigma}}) = \min_{\boldsymbol{\sigma}\in\mathcal{S}(\overline{\boldsymbol{\sigma}})} \langle u(\mathbf{x},\boldsymbol{\sigma})\rangle = (1-f) \min_{\boldsymbol{\sigma}\in\mathcal{S}^{(1)}(\overline{\boldsymbol{\sigma}})} \langle u(\mathbf{x},\boldsymbol{\sigma})\rangle^{(1)}$$
$$= (1-f) \min_{\boldsymbol{\sigma}\in\mathcal{S}^{(1)}(\overline{\boldsymbol{\sigma}})} \sum_{r=1}^{N} c^{(1,r)} \langle u^{(1,r)}(\boldsymbol{\sigma})\rangle^{(1,r)}. \tag{6.15}$$

Here $\mathcal{S}(\overline{\boldsymbol{\sigma}})$ is the set of statically admissible stress fields, including all stress fields $\boldsymbol{\sigma}$ that are divergence free and satisfy the condition $\langle\boldsymbol{\sigma}\rangle = \overline{\boldsymbol{\sigma}}$, while $\mathcal{S}^{(1)}(\overline{\boldsymbol{\sigma}})$ denotes a subset of $\mathcal{S}(\overline{\boldsymbol{\sigma}})$, including all stress fields $\boldsymbol{\sigma}$ that are divergence free, lead to zero traction on the void surfaces, and satisfy the condition $\langle\boldsymbol{\sigma}\rangle^{(1)} = (1-f)^{-1}\overline{\boldsymbol{\sigma}}$. It should be emphasized that the effective stress potential (6.15) depends not only on the local properties of the phases, but also on the instantaneous state of the sub-structure of the composite, as characterized by the set of sub-structural variables (6.8).

Due to the nonlinear constitutive relation of the single-crystal phases and the random character of their distributions, the effective potential (6.15) can not be obtained exactly. In this work, we make use of the recently developed fully optimized second-order (FOSO) variational homogenization method (Ponte Castañeda, 2015), together with the iterated homogenization procedure (Agoras and Ponte Castañeda, 2013; Song and Ponte Castañeda, 2017b), to generate accurate estimates for the instantaneous response of the two-scale porous polycrystals. In the following, we first recall the main features of the FOSO method. The FOSO method is then used in an incremental fashion (Song and Ponte Castañeda, 2017b) to obtain improved estimates.

6.3.1 Fully optimized second-order variational estimates

The central idea of the FOSO method is to express the effective potential of a nonlinear composite in terms of that of a linear comparison composite (LCC), whose sub-structure is identical to that of the actual composite. In addition, the properties of the LCC have to be chosen optimally according to a suitably designed variational principle. For later use, we first describe the LCC involved in the FOSO method.

Here we consider a two-scale porous LCC with the same sub-structure as the nonlinear porous polycrystal (see Fig. 6.1), but with local stress potential given by

$$u_L(\mathbf{x},\boldsymbol{\sigma}) = \chi^{(1)}(\mathbf{x})\sum_{r=1}^{N}\chi^{(1,r)}(\mathbf{y})u_L^{(1,r)}(\boldsymbol{\sigma}) + \chi^{(2)}(\mathbf{x})u_L^{(2)}(\boldsymbol{\sigma}). \tag{6.16}$$

In this expression, the $u_L^{(1,r)}(\boldsymbol{\sigma})$ $(r = 1,...,N)$ are quadratic functions of the stress $\boldsymbol{\sigma}$, as given by

$$u_L^{(1,r)}(\boldsymbol{\sigma}) = \frac{1}{2}\boldsymbol{\sigma}\cdot\mathbb{M}^{(1,r)}\boldsymbol{\sigma} + \boldsymbol{\eta}^{(1,r)}\cdot\boldsymbol{\sigma}, \tag{6.17}$$

where $\mathbb{M}^{(1,r)}$ and $\boldsymbol{\eta}^{(1,r)}$ are the viscous compliance tensor and eigenstrain-rate tensor of the rth single-crystal phase in the LCC. They are defined by (Ponte Castañeda, 2015)

$$\mathbb{M}^{(1,r)} = \sum_{k=1}^{K}\frac{1}{2\mu_{(k)}^{(r)}}\boldsymbol{\mu}_{(k)}^{(r)}\otimes\boldsymbol{\mu}_{(k)}^{(r)}, \quad \text{and} \quad \boldsymbol{\eta}^{(1,r)} = \sum_{k=1}^{K}\eta_{(k)}^{(r)}\,\boldsymbol{\mu}_{(k)}^{(r)}, \tag{6.18}$$

where the scalars $\mu_{(k)}^{(r)}$ are the positive slip viscosities, while the $\eta_{(k)}^{(r)}$ are the slip eigenstrain rates $(k = 1,...,K)$. Similarly, the function $u_L^{(2)}(\boldsymbol{\sigma})$ is the stress potential for the vacuous phase in the LCC, and can be written in a form completely analogous to (6.17), but with the viscous compliance $\mathbb{M}^{(2)} \to \infty$ and the eigenstrain-rate tensor $\boldsymbol{\eta}^{(2)} = \mathbf{0}$. Note that the stress potential of the LCC described above is mathematically analogous to that of a thermoelastic composite. Note further that $\mu_{(k)}^{(r)}$ and $\eta_{(k)}^{(r)}$ are unknown a priori, and are to be determined by an optimization procedure to be described below.

The effective stress potential $\widetilde{u}_L$ of the LCC can then by obtained from the following two-scale homogenization problem

$$\widetilde{u}_L(\overline{\boldsymbol{\sigma}}) = \min_{\boldsymbol{\sigma}\in\mathcal{S}(\overline{\boldsymbol{\sigma}})}\langle u_L(\mathbf{x},\boldsymbol{\sigma})\rangle = (1-f)\min_{\boldsymbol{\sigma}\in\mathcal{S}^{(1)}(\overline{\boldsymbol{\sigma}})}\langle u_L(\mathbf{x},\boldsymbol{\sigma})\rangle^{(1)}. \tag{6.19}$$

Following the work of Agoras and Ponte Castañeda (2011), the stress potential (6.19) for the LCC may be determined by means of a two-step sequential homogenization procedure, decomposing the original two-scale problem into two single-scale problems for the associated meso- and micro-structures. In particular, at the micro-scale, we

make use of the estimates of the self-consistent (SC) type (Hershey, 1954; Kröner, 1958; Willis, 1977) to determine the effective behavior of the linear polycrystalline matrix. Then, at the meso-scale, we make use of the estimates of the Ponte Castañeda and Willis (PCW) type to obtain the macroscopic behavior of the porous LCC with the homogenized polycrystalline matrix. The final result of $\widetilde{u}_L$ can be expressed as

$$\widetilde{u}_L(\overline{\boldsymbol{\sigma}}) = \frac{1}{2}\overline{\boldsymbol{\sigma}} \cdot \widetilde{\mathbb{M}}\overline{\boldsymbol{\sigma}} + \widetilde{\boldsymbol{\eta}} \cdot \overline{\boldsymbol{\sigma}} + \frac{1}{2}\widetilde{g}, \tag{6.20}$$

where the effective viscous compliance tensor $\widetilde{\mathbb{M}}$, effective eigenstrain rate tensor $\widetilde{\boldsymbol{\eta}}$, and the effective energy at zero applied stress $\widetilde{g}$ in (6.20) are, respectively, given by expression (6.60), (6.61) and (6.63) in Appendix I. In these expressions, $\mathbb{M}^1$, $\boldsymbol{\eta}^{(1)}$ and $g^{(1)}$ are given by (6.55)-(6.58) in Appendix I, while $\mathbb{M}^{(2)} \to \infty$, $\boldsymbol{\eta}^{(2)} = \mathbf{0}$, $g^{(2)} = 0$, and $c^{(2)} = f$. Note that the effective properties of the porous LCC depend on the local properties (6.18), as well as on the sub-structural variables (6.8).

Following a similar development of Ponte Castañeda (2015), the FOSO estimates for the effective stress potential $\widetilde{u}$ (as defined by (6.15)) of the two-scale *nonlinear* porous polycrystal can be shown (see Appendix II) to be given by

$$\widetilde{u}^{\mathrm{SO}}(\overline{\boldsymbol{\sigma}}) = (1-f)\sum_{r=1}^{N} c^{(1,r)} \sum_{k=1}^{K} \left[\alpha_{(k)}^{(r)}\phi_{(k)}^{(r)}(\check{\tau}_{(k)}^{(r)}) + (1-\alpha_{(k)}^{(r)})\phi_{(k)}^{(r)}(\hat{\tau}_{(k)}^{(r)})\right], \tag{6.21}$$

where the $\alpha_{(k)}^{(r)}$ $(0 < \alpha_{(k)}^{(r)} < 1)$ are appropriately chosen 'weight factors', while $\check{\tau}_{(k)}^{(r)}$ and $\hat{\tau}_{(k)}^{(r)}$ are stress variables determined by the stationary conditions (6.88) and (6.89) in Appendix II. In particular, $\check{\tau}_{(k)}^{(r)}$ and $\hat{\tau}_{(k)}^{(r)}$ are chosen to be such that $\check{\tau}_{(k)}^{(r)} \le \hat{\tau}_{(k)}^{(r)}$, and can be obtained by solving the set of quadratic equations (6.88) and (6.89), so that

$$\check{\tau}_{(k)}^{(r)} = \overline{\tau}_{(k)}^{(r)} - \sqrt{\frac{1-\alpha_{(k)}^{(r)}}{\alpha_{(k)}^{(r)}}}\sqrt{\overline{\overline{\tau}}_{(k)}^{(r)} - \left(\overline{\tau}_{(k)}^{(r)}\right)^2} = \overline{\tau}_{(k)}^{(r)} - \sqrt{\frac{1-\alpha_{(k)}^{(r)}}{\alpha_{(k)}^{(r)}}}\mathrm{SD}^{(1,r)}\left(\tau_{(k)}^{(r)}\right), \tag{6.22}$$

and

$$\hat{\tau}_{(k)}^{(r)} = \overline{\tau}_{(k)}^{(r)} + \sqrt{\frac{\alpha_{(k)}^{(r)}}{1-\alpha_{(k)}^{(r)}}}\sqrt{\overline{\overline{\tau}}_{(k)}^{(r)} - \left(\overline{\tau}_{(k)}^{(r)}\right)^2} = \overline{\tau}_{(k)}^{(r)} + \sqrt{\frac{\alpha_{(k)}^{(r)}}{1-\alpha_{(k)}^{(r)}}}\mathrm{SD}^{(1,r)}\left(\tau_{(k)}^{(r)}\right). \tag{6.23}$$

Here

$$\begin{aligned} &\overline{\tau}_{(k)}^{(r)} = \overline{\boldsymbol{\sigma}}^{(1,r)} \cdot \boldsymbol{\mu}_{(k)}^{(r)}, \quad \overline{\overline{\tau}}_{(k)}^{(r)} = \boldsymbol{\mu}_{(k)}^{(r)} \cdot \langle \boldsymbol{\sigma} \otimes \boldsymbol{\sigma} \rangle^{(1,r)} \boldsymbol{\mu}_{(k)}^{(r)}, \quad \text{and} \\ &\mathrm{SD}^{(1,r)}\left(\tau_{(k)}^{(r)}\right) = \sqrt{\overline{\overline{\tau}}_{(k)}^{(r)} - \left(\overline{\tau}_{(k)}^{(r)}\right)^2} \end{aligned} \tag{6.24}$$

are the first moment, the second moment, and the standard deviation, respectively, of the resolved shear stress over slip system k in single-crystal phase r of the two-scale LCC. In the above expressions, $\overline{\boldsymbol{\sigma}}^{(1,r)}$ and $\langle \boldsymbol{\sigma} \otimes \boldsymbol{\sigma} \rangle^{(1,r)}$ are, respectively, the first and second moment of the stress field over the rth single-crystal phase in the LCC, as given by (6.78) and (6.80) in the Appendix I.

Making use of the stationary condition (6.87) in Appendix II, it follows that the local properties of the two-scale porous LCC, as determined by the slip viscosities $\mu_{(k)}^{(r)}$ and slip eigenstrain rates $\eta_{(k)}^{(r)}$ in (6.18), satisfy the 'generalized secant' condition

$$\frac{1}{2\mu_{(k)}^{(r)}} = \frac{\phi_{(k)}^{(r)\prime}(\hat{\tau}_{(k)}^{(r)}) - \phi_{(k)}^{(r)\prime}(\check{\tau}_{(k)}^{(r)})}{\hat{\tau}_{(k)}^{(r)} - \check{\tau}_{(k)}^{(r)}}, \quad \text{and} \quad \eta_{(k)}^{(r)} = \phi_{(k)}^{(r)\prime}(\check{\tau}_{(k)}^{(r)}) - \frac{1}{2\mu_{(k)}^{(r)}}\check{\tau}_{(k)}^{(r)}. \tag{6.25}$$

Expressions (6.22), (6.23) and (6.25) constitute a set of $4N \times K$ nonlinear algebraic equations for the variables $\hat{\tau}_{(k)}^{(r)}$, $\check{\tau}_{(k)}^{(r)}$, $\mu_{(k)}^{(r)}$ and $\eta_{(k)}^{(r)}$ ($r = 1, ..., N$, $k = 1, ..., K$). In general, these equations need to be solved numerically by means of an appropriate method, e.g., a fixed-point method.

Due to the fully stationarity of the FOSO estimate (6.21) with respect to the properties of the LCC (Ponte Castañeda, 2015), the macroscopic constitutive relation and the corresponding field statistics of the nonlinear porous polycrystals can be estimated directly from those in the LCC (Idiart and Ponte Castañeda, 2007c). Thus,

the macroscopic stress-strain rate relation for the nonlinear composite is given by

$$\overline{\mathbf{D}} = \frac{\partial \widetilde{u}^{\mathrm{SO}}}{\partial \overline{\boldsymbol{\sigma}}}(\overline{\boldsymbol{\sigma}}) = \frac{\partial \widetilde{u}_L}{\partial \overline{\boldsymbol{\sigma}}}(\overline{\boldsymbol{\sigma}}) = \widetilde{\mathbb{M}}\overline{\boldsymbol{\sigma}} + \widetilde{\boldsymbol{\eta}}. \tag{6.26}$$

Here $\widetilde{\mathbb{M}}$ and $\widetilde{\boldsymbol{\eta}}$ are, respectively, the effective compliance tensor and the effective eigenstrain-rate tensor of the two-scale LCC, as provided by (6.60) and (6.61) in Appendix I. It is important to note that, despite its appearance, the relation (6.26) is *nonlinear*, due to the nonlinear dependence of $\widetilde{\mathbb{M}}$ and $\widetilde{\boldsymbol{\eta}}$ on the applied stress $\overline{\boldsymbol{\sigma}}$.

In this context, it should be remarked that the results discussed in this section are valid for any choice of the weight factors $\alpha_{(k)}^{(r)}$ appearing in (6.21). Unfortunately, at this stage we do not have any mathematically or physically based prescription to select $\alpha_{(k)}^{(r)}$ in an optimal fashion, although recent work by Michel and Suquet (2017) suggests that the selection of the $\alpha_{(k)}^{(r)}$ could depend on higher moments of the stress field. For simplicity, we choose $\alpha_{(k)}^{(r)} = 1/2$ $(r = 1, ..., N;\ k = 1, ..., K)$, which is the most symmetric choice. However, it should be kept in mind that there may be other better choices for the values of $\alpha_{(k)}^{(r)}$, and this will be investigated in future work.

The average slip rates $\overline{\gamma}_{(k)}^{(r)}$ over slip system k in single-crystal phase r of the polycrystalline matrix, which are required to satisfy the condition

$$\overline{\mathbf{D}}^{(1,r)} = \sum_{k=1}^{K} \overline{\gamma}_{(k)}^{(r)} \boldsymbol{\mu}_{(k)}^{(r)}, \tag{6.27}$$

may also be estimated directly from the LCC, and are provided by (Song and Ponte Castañeda, 2017b)

$$\overline{\gamma}_{(k)}^{(r)} = \frac{1}{2\mu_{(k)}^{(r)}} \overline{\tau}_{(k)}^{(r)} + \eta_{(k)}^{(r)} = \alpha_{(k)}^{(r)} \phi_{(k)}^{(r)\prime}(\tilde{\tau}_{(k)}^{(r)}) + (1 - \alpha_{(k)}^{(r)}) \phi_{(k)}^{(r)\prime}(\hat{\tau}_{(k)}^{(r)}). \tag{6.28}$$

It should be emphasized that $\overline{\gamma}_{(k)}^{(r)} \neq \phi_{(k)}^{(r)\prime}(\overline{\tau}_{(k)}^{(r)})$, since the average of a nonlinear function is generally different from the function of the average (see, e.g., Fig. 3.2 in chapter 3).

At this point, it is remarked that the FOSO estimate (6.21) for $\widetilde{u}$ is a generalization of the variational (VAR) homogenization estimate of deBotton and Ponte Castañeda

(1995), which may be recovered from the FOSO estimate (6.21) by formally setting the slip eigenstrain rates $\eta_{(k)}^{(r)} = 0$ (and therefore $\boldsymbol{\eta}^{(1,r)} = \mathbf{0}$). In its final form, the VAR estimate for the effective stress potential $\widetilde{u}$ of the nonlinear porous polycrystal is given by

$$\widetilde{u}^{\mathrm{VAR}}(\overline{\boldsymbol{\sigma}}) = (1-f)\sum_{r=1}^{N} c^{(1,r)} \sum_{k=1}^{K} \phi_{(k)}^{(r)}(\hat{\tau}_{(k)}^{(r)}). \tag{6.29}$$

Here the stress variables $\hat{\tau}_{(k)}^{(r)}$ are given by

$$\hat{\tau}_{(k)}^{(r)} = \sqrt{\overline{\overline{\tau}}_{(k)}^{(r)}} = \sqrt{\boldsymbol{\mu}_{(k)}^{(r)} \cdot \langle \boldsymbol{\sigma} \otimes \boldsymbol{\sigma} \rangle^{(1,r)} \boldsymbol{\mu}_{(k)}^{(r)}}, \tag{6.30}$$

where the second moment $\langle \boldsymbol{\sigma} \otimes \boldsymbol{\sigma} \rangle^{(1,r)}$ may be obtained from equation (6.80) in Appendix I, with the eigenstrain rate tensor $\boldsymbol{\eta}^{(1,r)} = \mathbf{0}$. In turn, the slip viscosities $\mu_{(k)}^{(r)}$ in the two-scale LCC are given by the 'secant' conditions

$$\frac{1}{2\mu_{(k)}^{(r)}} = \frac{\phi_{(k)}^{(r)\prime}(\hat{\tau}_{(k)}^{(r)})}{\hat{\tau}_{(k)}^{(r)}}. \tag{6.31}$$

Note that the VAR estimates for the average slip rates $\overline{\gamma}_{(k)}^{(r)}$ over different slip systems can also be estimated directly from the LCC, i.e.,

$$\overline{\gamma}_{(k)}^{(r)} = \frac{\phi_{(k)}^{(r)\prime}(\hat{\tau}_{(k)}^{(r)})}{\hat{\tau}_{(k)}^{(r)}} \overline{\tau}_{(k)}^{(r)} \neq \phi_{(k)}^{(r)\prime}(\overline{\tau}_{(k)}^{(r)}). \tag{6.32}$$

The FOSO estimates (6.21) are known (Ponte Castañeda, 2015) to be exact to second order in the heterogeneity contrast, thus being more accurate then the VAR estimates (6.29), which are only exact to first order in the heterogeneity contrast. In fact, it can be shown that the VAR estimates provide rigorous lower bounds for all other estimates for the effective stress potential $\widetilde{u}$ (deBotton and Ponte Castañeda, 1995), and in particular, for the FOSO estimates (6.21), assuming that the same estimates are used for the LCC. While the FOSO estimates (6.21) are fairly accurate in most cases, they are found to be too strong for cases of low porosity, high nonlinearity, especially at high stress triaxialities. As already noted in the earlier context of porous

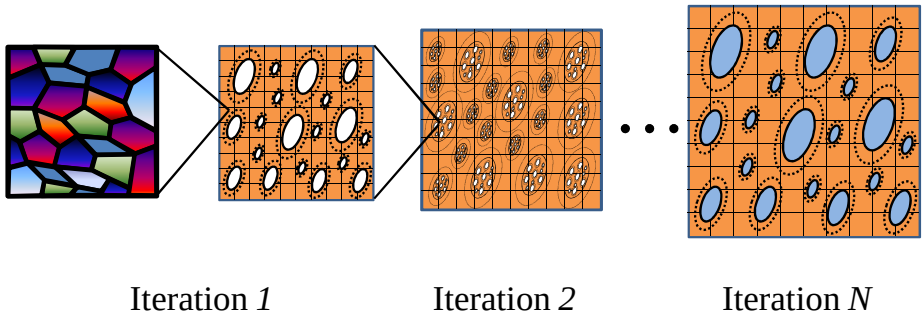

Figure 6.2: Schematic representation of the iterated homogenization procedure for a two-scale porous polycrystal consisting of aligned, ellipsoidal pores (solid lines) that are distributed with the same ellipsoidal symmetry (dotted lines) in a polycrystalline matrix. The size of the pores are much larger than the size of the single-crystal grains (see iteration 1), and the grids within the matrix phase schematically represents the anisotropy. Note that the homogenized polycrystalline matrix phase is the *same* for all iterations, and the size of the grains is much smaller than the size of the pores for all iterations.

isotropic materials (Agoras and Ponte Castañeda, 2011) and porous single crystals (Song and Ponte Castañeda, 2017a; 2017b; 2017c), this deficiency may be ascribed to the fact that the property of each single-crystal phase in the LCC is uniform (see (6.18)). However, it is possible to generate improved estimates by incorporating *non-uniform* properties for each single-crystal phase in the LCC, as will be seen below.

6.3.2 Iterated second-order method

Song and Ponte Castañeda (2017b) have recently used the FOSO approach of Ponte Castañeda (2015), together with the iterated homogenization procedure of Agoras and Ponte Castañeda (2011), to generate second-order variational estimates for the effective stress potential of porous viscoplastic single crystals. This iterated second-order (ISO) approach allows the use of *non-uniform* matrix properties for the LCC and, therefore, can provide improved estimates compared with the non-iterated FOSO method. In this work, we will employ a generalization of the ISO procedure to obtain improved estimates for the effective stress potential $\widetilde{u}$ of the two-scale, viscoplastic porous polycrystals. The crux of the ISO procedure is to reconstruct the porous substructure incrementally in a "self-similar" fashion (see Fig. 6.2). In the first iteration

($i = 1$), the pores are distributed in the polycrystalline matrix (the left most figure of Fig. 6.2) with a volume concentration of $c^{(2)}_{[1]} > f$, and with the shape and distribution of the pores characterized by the second-order tensor $\boldsymbol{Z}^p$ and $\boldsymbol{Z}^d$, respectively. At each subsequent iteration i, the composite material from the lower $i-1$ iteration level is distributed in the form of "composite inclusion" in the same polycrystalline matrix (including the same morphological and crystallographic texture) with a volume fraction $c^{(2)}_{[i]}$, and with inclusion and distribution shapes that are identical to the distribution shape of the pores at the first iteration (as described by $\boldsymbol{Z}^d$). This procedure is repeated I times until we reach the final, level-I composite with the desired porosity f, such that

$$f = \prod_{i=1}^{I} c^{(2)}_{[i]}, \tag{6.33}$$

where the $c^{(2)}_{[i]}$ $(i = 2, ..., I)$ are the volume fractions of the "composite inclusion" in the level-i composite, and I is the total number of iteration. With the above construction procedure, it can be shown (Agoras and Ponte Castañeda, 2013) that the resulting I-level composite still belongs to the class of random porous polycrystals defined in section 6.2.1, as characterized by the set of sub-structural variables (6.8). At this point, it should be remarked that, while the hierarchical structure of the I-level composite (with separation of the multiple length scales) is expected to have an effect on the macroscopic behavior relative to the original (non-iterated) sub-structure, it has been shown (Ponte Castañeda, 2012; Agoras and Ponte Castañeda, 2013) that the PCW estimates (depending only on the one- and two-point statistics) for the macroscopic behavior of *linearly viscous* porous materials are insensitive to the hierarchical nature of the sub-structure. Therefore, it will be assumed here that the same is true for the corresponding FOSO estimates of the PCW type for the nonlinear viscoplastic porous materials, keeping in mind that the iterated procedure is designed to better discretize the single-crystal phase in the matrix of the LCC. Note that because of separation of length scales, the size of the single-crystal grains in the polycrystalline matrix is always much smaller than the size of the inclusion phases for all iterations.

The effective properties of the porous polycrystals of interest may then be determined by sequentially homogenizing the above constructed I-level composite. At each iteration level $i = 1, ..., I$, the effective behavior of the composite may be obtained by means of the FOSO method (Ponte Castañeda, 2015). Thus, the ISO procedure involves, at each iteration level, an LCC with sub-structure identical to that of the corresponding nonlinear composite, but with a linear polycrystalline matrix and a linear (compressible) inclusion phase (where the size of the inclusions is much larger than that of the single-crystal grains in the matrix). In particular, the stress potential of the rth single-crystal phase in the polycrystalline matrix at the ith iteration is assumed to be of the form (6.17), but with the viscous compliance tensor and eigenstrain-rate tensor given by

$$\mathbb{M}_{[i]}^{(1,r)} = \sum_{k=1}^{K} \frac{1}{2\mu_{[i]}^{(r,k)}} \boldsymbol{\mu}_{(k)}^{(r)} \otimes \boldsymbol{\mu}_{(k)}^{(r)}, \quad \text{and} \quad \boldsymbol{\eta}_{[i]}^{(1,r)} = \sum_{k=1}^{K} \eta_{[i]}^{(r,k)} \ \boldsymbol{\mu}_{(k)}^{(r)}, \tag{6.34}$$

respectively. In the above expression, the label $[i]$ is used to denote the associated quantities in the i-level LCC, e.g., $\mu_{[i]}^{(r,k)}$ is the slip viscosity of slip system k in single-crystal phase r of the polycrystalline matrix at the level-i LCC, while $\eta_{[i]}^{(r,k)}$ is the corresponding slip eigenstrain rate. Furthermore, the effective behavior of each level LCC is computed by means of the two-step sequential homogenization procedure, along with the estimates of the SC and PCW type, as discussed in Appendix III.

Generalizing the estimate of Song and Ponte Castañeda (2017b) for porous single crystals, the ISO estimate for the effective stress potential $\widetilde{u}$ of the two-scale, viscoplastic porous polycrystal may be written as

$$\widetilde{u}^{\mathrm{ISO}}(\overline{\boldsymbol{\sigma}}) = \sum_{i=1}^{I} \left(1 - c_{[i]}^{(2)}\right) \left(\prod_{j=i+1}^{I} c_{[j]}^{(2)}\right) \times \left[\sum_{r=1}^{N} c^{(1,r)} \sum_{k=1}^{K} \left(\alpha_{(k)}^{(r)} \phi_{(k)}^{(r)}(\check{\tau}_{[i]}^{(r,k)}) + (1 - \alpha_{(k)}^{(r)}) \phi_{(k)}^{(r)}(\hat{\tau}_{[i]}^{(r,k)})\right)\right]. \tag{6.35}$$

Here the stress variables $\check{\tau}_{[i]}^{(r,k)}$ and $\hat{\tau}_{[i]}^{(r,k)}$ are given by expressions completely analogous

to (6.22) and (6.23), that is,

$$\check{\tau}_{[i]}^{(r,k)} = \overline{\tau}_{[i]}^{(r,k)} - \sqrt{\frac{1-\alpha_{(k)}^{(r)}}{\alpha_{(k)}^{(r)}}}\sqrt{\overline{\overline{\tau}}_{[i]}^{(r,k)} - \left(\overline{\tau}_{[i]}^{(r,k)}\right)^2} = \overline{\tau}_{[i]}^{(r,k)} - \sqrt{\frac{1-\alpha_{(k)}^{(r)}}{\alpha_{(k)}^{(r)}}}\mathrm{SD}_{[i]}^{(1,r)}\left(\tau_{[i]}^{(r,k)}\right) \quad (6.36)$$

and

$$\hat{\tau}_{[i]}^{(r,k)} = \overline{\tau}_{[i]}^{(r,k)} + \sqrt{\frac{\alpha_{(k)}^{(r)}}{1-\alpha_{(k)}^{(r)}}}\sqrt{\overline{\overline{\tau}}_{[i]}^{(r,k)} - \left(\overline{\tau}_{[i]}^{(r,k)}\right)^2} = \overline{\tau}_{[i]}^{(r,k)} + \sqrt{\frac{\alpha_{(k)}^{(r)}}{1-\alpha_{(k)}^{(r)}}}\mathrm{SD}_{[i]}^{(1,r)}\left(\tau_{[i]}^{(r,k)}\right), \quad (6.37)$$

where the weight factors $\alpha_{(k)}^{(r)}$ $(0 < \alpha_{(k)}^{(r)} < 1)$ will be set equal to $1/2$, for simplicity, while

$$\begin{aligned} &\overline{\tau}_{[i]}^{(r,k)} = \overline{\boldsymbol{\sigma}}_{[i]}^{(1,r)} \cdot \boldsymbol{\mu}_{(k)}^{(r)}, \quad \overline{\overline{\tau}}_{[i]}^{(r,k)} = \boldsymbol{\mu}_{(k)}^{(r)} \cdot \langle \boldsymbol{\sigma} \otimes \boldsymbol{\sigma} \rangle_{[i]}^{(1,r)} \boldsymbol{\mu}_{(k)}^{(r)}, \quad \text{and} \\ &\mathrm{SD}_{[i]}^{(1,r)}\left(\tau_{[i]}^{(r,k)}\right) = \sqrt{\overline{\overline{\tau}}_{[i]}^{(r,k)} - \left(\overline{\tau}_{[i]}^{(r,k)}\right)^2} \end{aligned} \quad (6.38)$$

are, respectively, the first moment, the second moment, and the standard deviation of the resolved shear stress over slip system k in single-crystal phase r in the polycrystalline matrix at the level-i LCC. In these expressions, $\overline{\boldsymbol{\sigma}}_{[i]}^{(1,r)}$ and $\langle \boldsymbol{\sigma} \otimes \boldsymbol{\sigma} \rangle_{[i]}^{(1,r)}$ are the first and second moments of the stress field, respectively, over single-crystal phase r in the polycrystalline matrix at the level-i LCC, as given by expression (6.111) and (6.112) in Appendix III.

In turn, the properties of the LCC must be specified such that the slip viscosities $\mu_{[i]}^{(r,k)}$ and slip eigenstrain rates $\eta_{[i]}^{(r,k)}$ of the rth single-crystal phase at level-i LCC satisfy the 'generalized secant' condition

$$\frac{1}{2\mu_{[i]}^{(r,k)}} = \frac{\phi_{(k)}^{(r)\prime}(\hat{\tau}_{[i]}^{(r,k)}) - \phi_{(k)}^{(r)\prime}(\check{\tau}_{[i]}^{(r,k)})}{\hat{\tau}_{[i]}^{(r,k)} - \check{\tau}_{[i]}^{(r,k)}}, \quad \text{and} \quad \eta_{[i]}^{(r,k)} = \phi_{(k)}^{(r)\prime}(\check{\tau}_{[i]}^{(r,k)}) - \frac{1}{2\mu_{[i]}^{(r,k)}}\check{\tau}_{[i]}^{(r,k)}. \quad (6.39)$$

Note that the ISO estimate (6.35) requires the solution of a set of $4K \times N \times I$ nonlinear algebraic equations, as given by (6.36), (6.37), and (6.39), for an equal amount of unknown quantities $\check{\tau}_{[i]}^{(r,k)}$, $\hat{\tau}_{[i]}^{(r,k)}$, $\mu_{[i]}^{(r,k)}$ and $\eta_{[i]}^{(r,k)}$ associated with each slip system

$(k = 1, ..., K)$, each single-crystal phase $(r = 1, ..., N)$, and each iteration $(i = 1, ..., I)$. While the above set of equations contain rather large number of unknowns, they can be efficiently solved by means of a simple fixed-point method. Further details on the computation of (6.35) are provided in Appendix IV.

As noted by Song and Ponte Castañeda (2017b), the ISO estimate (6.35) is also exact to second order in the heterogeneity contrast, retaining the distinguishing feature of the FOSO estimate (6.21). Moreover, due to the fully stationarity of the ISO estimates, the macroscopic behavior and field statistics of the nonlinear porous polycrystal can also be extracted directly from the LCC. However, as will be seen in Chapter 7, the ISO improves significantly over the FOSO for the cases of small porosity, large nonlinearity and large stress triaxiality, which are of crucial importance in practical applications. In general, the accuracy of the ISO improves progressively with increasing values of I, thus being optimal when $I \to \infty$ (Ponte Castañeda, 2012). However, the fast convergence of the ISO with increasing values of I allows the use of relatively small number of iterations ($I \sim 5-10$) to obtain very accurate results (Agoras and Ponte Castañeda, 2013). Therefore, $I = 10$ will be used in this work, which has been found to provide sufficiently accurate estimates for the effective behavior of the porous polycrystals (with error less than 1% relative to the corresponding limits as $I \to \infty$). Furthermore, it should be remarked that the specific values of the concentration variables $c_{[i]}^{(2)}$ $(i = 1, ..., I)$ in (6.33) will not significantly affect the accuracy of the ISO, given that the total number of iteration I is large enough. In this work, we choose $c_{[i]}^{(2)} = f^{1/I}$ $(i = 1, ..., I)$, for simplicity.

Making use of the fact that the macroscopic behavior of the nonlinear porous polycrystal can be estimated directly from the suitably chosen LCC, the effective constitutive relation of the nonlinear composite may be obtained via

$$\overline{\mathbf{D}} = \frac{\partial \widetilde{u}^{\mathrm{ISO}}}{\partial \overline{\boldsymbol{\sigma}}}(\overline{\boldsymbol{\sigma}}) = \widetilde{\mathbb{M}}_{[I]}\overline{\boldsymbol{\sigma}} + \widetilde{\boldsymbol{\eta}}_{[I]}, \tag{6.40}$$

where $\widetilde{\mathbb{M}}_{[I]}$ and $\widetilde{\boldsymbol{\eta}}_{[I]}$ are the effective viscous compliance tensor and effective eigenstrain rate tensor, respectively, of the final level-I LCC, as given by expression (6.90)

and (6.91) in Appendix III. It should be recalled that relation (6.40) is nonlinear, since $\widetilde{\mathbb{M}}_{[I]}$ and $\widetilde{\boldsymbol{\eta}}_{[I]}$ depend nonlinearly on the applied stress $\overline{\boldsymbol{\sigma}}$.

The average slip rate $\overline{\gamma}^{(r)}_{(k)}$ over each slip system k of the rth single-crystal phase in the polycrystalline matrix, as defined by (6.27), can also be estimated directly from those in the LCC. However, due to the non-uniform distribution of each single-crystal phase in the LCC, it is necessary to first compute the average slip rates over the single-crystal phase at each level LCC, and then compute the appropriate weighted averages to obtain the desired average slip rates over the single-crystal phase in the whole polycrystalline matrix. Following a development similar to that of Song and Ponte Castañeda (2017b), it can be shown (see Appendix III) that the average slip rate $\overline{\gamma}^{(r)}_{(k)}$ is given by

$$\overline{\gamma}^{(r)}_{(k)} = \frac{1}{1-f}\left[\alpha^{(r)}_{(k)}\sum_{i=1}^{I}\left(c^{m}_{[i]}\phi^{(r)\prime}_{(k)}(\check{\tau}^{(r,k)}_{[i]})\right) + \left(1-\alpha^{(r)}_{(k)}\right)\sum_{i=1}^{I}\left(c^{m}_{[i]}\phi^{(r)\prime}_{(k)}(\hat{\tau}^{(r,k)}_{[i]})\right)\right], \tag{6.41}$$

where the $c^{m}_{[i]}$ $(i = 1, ..., I)$ are the *total* volume fraction of the level-i polycrystalline matrix over the entire level-I composite, as given by equation (6.115) in Appendix III.

Finally, it should be remarked that a generalization for porous polycrystals of the iterated variational (IVAR) homogenization estimate (Song and Ponte Castañeda, 2017a) for porous single crystals may be obtained by formally setting $\eta^{(r,k)}_{[i]} = 0$ (and therefore $\boldsymbol{\eta}^{(1,r)}_{[i]} = \mathbf{0}$). In particular, the IVAR estimate for $\widetilde{u}$ is given by

$$\widetilde{u}^{\mathrm{IVAR}}(\overline{\boldsymbol{\sigma}}) = \sum_{i=1}^{I}\left(1-c^{(2)}_{[i]}\right)\left(\prod_{j=i+1}^{I}c^{(2)}_{[j]}\right)\left[\sum_{r=1}^{N}c^{(1,r)}\sum_{k=1}^{K}\phi^{(r)}_{(k)}(\hat{\tau}^{(r,k)}_{[i]})\right], \tag{6.42}$$

where the stress variables $\hat{\tau}^{(r,k)}_{[i]}$ depend on the second moment of the resolved shear stress over the rth single-crystal phase at the level-i LCC:

$$\hat{\tau}^{(r,k)}_{[i]} = \sqrt{\overline{\tau}^{(r,k)}_{[i]}} = \sqrt{\boldsymbol{\mu}^{(r)}_{(k)}\cdot\langle\boldsymbol{\sigma}\otimes\boldsymbol{\sigma}\rangle^{(1,r)}_{[i]}\boldsymbol{\mu}^{(r)}_{(k)}}. \tag{6.43}$$

Here the second moments $\langle\boldsymbol{\sigma}\otimes\boldsymbol{\sigma}\rangle^{(1,r)}_{[i]}$ are given by expression (6.112) in Appendix

III, with the eigenstrain rate tensor $\boldsymbol{\eta}_{[i]}^{(1,r)} = \mathbf{0}$. In turn, the slip viscosities $\mu_{(k)}^{(i,r)}$ are determined by the 'secant' conditions

$$\frac{1}{2\mu_{[i]}^{(r,k)}} = \frac{\phi_{(k)}^{(r)\prime}(\hat{\tau}_{[i]}^{(r,k)})}{\hat{\tau}_{[i]}^{(r,k)}}. \tag{6.44}$$

Note that the IVAR estimate (6.42) is also a rigorous lower bound for the effective stress potential $\widetilde{u}$ of the porous polycrystals. However, the IVAR bound is expected to be more accurate than the VAR bounds, especially at low porosity, high nonlinearity and high stress triaxiality (Agoras and Ponte Castañeda, 2013; Song and Ponte Castañeda, 2017a).

6.4 Evolution of the sub-structure

During a finite deformation process, the sub-structure of the porous polycrystals, as characterized by the sub-structural variables (6.8), evolves as a consequence of the finite changes in the geometry of the materials at large strains. In this section, we make use of standard kinematics, along with estimates for the average strain rate and spin fields in the pores and grains, to develop approximate evolution laws for the sub-structural variables (6.8). Making use of the hypothesis of separation of length scales (see (6.1)), and of the fact that the meso-structure is statistically independent from the micro-structure, the evolution of the sub-structural variables (6.8) may be determined separately for the meso- and micro-structure.

6.4.1 Porosity evolution

Due to the incompressibility of the polycrystalline matrix, the volume change of the porous polycrystal should equal the volume change of the pores. Therefore, the porosity evolution is governed by (Gurson, 1977)

$$\dot{f} = (1-f)\overline{D}_{kk}, \tag{6.45}$$

where it is recalled that $\overline{\mathbf{D}}$ is the macroscopic strain rate, as given by (6.40).

6.4.2 Pore morphology evolution

The evolution of the shape and orientation of the pores (and their distribution) depends on the local fields in a complex fashion, which are extremely difficult to determine exactly. However, in the context of a homogenization procedure, it is sufficient to obtain evolution laws for the *average* shape and orientation of the pores. Therefore, it is assumed (Ponte Castañeda and Zaidman, 1994; Kailasam and Ponte Castañeda, 1998; Aravas and Ponte Castañeda, 2004) that the average shape and orientation of the pores (and their distribution) evolve with the average strain rate $\overline{\mathbf{D}}^{(2)}$ and the average spin $\overline{\mathbf{W}}^{(2)}$ in the pores. Then, the average shape of the pores (and their distribution) remains ellipsoidal, but can change its aspect ratios and orientation during the deformation process. Making use of standard kinematical arguments for ellipsoids subjected to uniform deformations, we obtain the following evolution laws for the aspect ratios w_1^p and w_2^p:

$$\dot{w}_1^p = w_1^p \left(\overline{D}_{33}^{(2)'} - \overline{D}_{11}^{(2)'} \right), \quad \text{and} \quad \dot{w}_2^p = w_2^p \left(\overline{D}_{33}^{(2)'} - \overline{D}_{22}^{(2)'} \right). \tag{6.46}$$

Here the average strain rate $\overline{\mathbf{D}}^{(2)}$ can be consistently estimated by means of the ISO procedure, as provided by (6.104) with $i = 1$ ($\overline{\mathbf{D}}^{(2)} = \overline{\mathbf{D}}_{[1]}^{(2)}$) in Appendix III. Note that the primes in this section denote the tensor components relative to coordinate axes that are instantaneously aligned with the principal directions of the ellipsoidal voids.

On the other hand, the evolution of the principal directions of the pores, as characterized by the orthogonal tensor $\mathbf{G}^p$ in (6.8), is governed by

$$\dot{\mathbf{G}}^p = -\mathbf{G}^p \overline{\boldsymbol{\omega}}^p, \tag{6.47}$$

where $\overline{\boldsymbol{\omega}}^p$ is the spin of the Eulerian axes of the average deformation gradient of the

pores, with its non-zero components given by (Ogden, 1984)

$$\left[1-\frac{\left(w_t^p\right)^2}{\left(w_s^p\right)^2}\right]\overline{\omega}_{st}^{(2)'}=\left[1-\frac{\left(w_t^p\right)^2}{\left(w_s^p\right)^2}\right]\overline{W}_{st}^{(2)'}+\left[1+\frac{\left(w_t^p\right)^2}{\left(w_s^p\right)^2}\right]\overline{D}_{st}^{(2)'},\quad s,t=1,2,3,\quad s\neq t, \tag{6.48}$$

where $w_3^p = a_3^p/a_3^p = 1$, and $\overline{\mathbf{W}}^{(2)}$ denotes the average spin tensor in the pore phase, as provided by (6.109) with $i = 1$ ($\overline{\mathbf{W}}^{(2)} = \overline{\mathbf{W}}_{[1]}^{(2)}$) in Appendix III. It should be remarked that, when any two of the aspect ratios are equal, i.e., $w_s^p = w_t^p$ ($s \neq t$), the principal directions of the voids should be chosen in such a way that $\overline{D}_{st}^{(2)'} = 0$ and $\overline{\omega}_{st}^{(2)'} = \overline{W}_{st}^{(2)'}$.

At this point, it should be noted that the evolution equations (6.45)-(6.47) completely characterize the evolution of the porous meso-structure. We will next derive evolution laws for the granular micro-structure of the underlying polycrystalline matrix.

6.4.3 Grain morphology evolution

For the granular micro-structure of the polycrystal solids, it will be assumed that the *average* shape and orientation of the single-crystal grains are controlled by the average strain rate $\overline{\mathbf{D}}^{(1)}$ and spin $\overline{\mathbf{W}}^{(1)}$ in the polycrystalline matrix (Liu et al., 2005). This is the simplest hypothesis that is consistent with the preservation of the integrity of the composite—the grains are required to fill the entire space. Thus, the aspect ratios w_1^g and w_2^g for the ellipsoidal grains are governed by kinematical relations completely analogous to (6.46), that is,

$$\dot{w}_1^g = w_1^g\left(\overline{D}_{33}^{(1)'}-\overline{D}_{11}^{(1)'}\right),\quad \text{and}\quad \dot{w}_2^g = w_2^g\left(\overline{D}_{33}^{(1)'}-\overline{D}_{22}^{(1)'}\right), \tag{6.49}$$

where $\overline{\mathbf{D}}^{(1)}$ can be obtained by means of the global average condition $\overline{\mathbf{D}}^{(1)} = (1-f)^{-1}(\overline{\mathbf{D}} - f\overline{\mathbf{D}}^{(2)})$.

Similarly, the principal directions of the ellipsoidal grains, as described by the orthogonal tensor $\mathbf{G}^g$ in (6.8), are governed by a kinematical relation completely analogous to (6.47):

$$\dot{\mathbf{G}}^g = -\mathbf{G}^g\overline{\boldsymbol{\omega}}^m, \tag{6.50}$$

where $\overline{\boldsymbol{\omega}}^m$ denotes the spin of the Eulerian axes of the average deformation gradient of the polycrystalline matrix. In particular, the non-zero components of $\overline{\boldsymbol{\omega}}^m$ are given by expressions similar to (6.48), but with w_i^p $(i = 1, 2, 3)$, $\overline{\mathbf{D}}^{(2)}$ and $\overline{\mathbf{W}}^{(2)}$ replaced by w_i^g $(i = 1, 2, 3)$, $\overline{\mathbf{D}}^{(1)}$ and $\overline{\mathbf{W}}^{(1)}$, respectively. Here $\overline{\mathbf{W}}^{(1)}$ is the average spin in the polycrystalline matrix, which may be determined from the global average condition $\overline{\mathbf{W}}^{(1)} = (1 - f)^{-1}(\overline{\mathbf{W}} - f\overline{\mathbf{W}}^{(2)})$, with $\overline{\mathbf{W}}$ denoting the macroscopic spin, and $\overline{\mathbf{W}}^{(2)}$ given by (6.109) with $i = 1$.

6.4.4 Crystallographic texture evolution

The crystallographic orientation of the lattice inside of the rth single-crystal grain, as characterized by the rotation tensor $\mathbf{Q}^{(1,r)}$ in (6.8), is assumed to evolve—on average—with the average "elastic" spin in the rth single-crystal phase, i.e.,

$$\dot{\mathbf{Q}}^{(1,r)} = -\mathbf{Q}^{(1,r)}\overline{\boldsymbol{\omega}}_e^{(1,r)}. \tag{6.51}$$

Here the average "elastic" spin $\overline{\boldsymbol{\omega}}_e^{(1,r)}$ is given by the difference between the average "continuum" spin $\overline{\mathbf{W}}^{(1,r)}$ and the average "plastic" spin $\overline{\mathbf{W}}_{pl}^{(1,r)}$ in the single-crystal phases (Mandel, 1972), that is

$$\overline{\boldsymbol{\omega}}_e^{(1,r)} = \overline{\mathbf{W}}^{(1,r)} - \overline{\mathbf{W}}_{pl}^{(1,r)}. \tag{6.52}$$

Note that the average continuum spin $\overline{\mathbf{W}}^{(1,r)}$ is given by (6.118) in Appendix III, while the average plastic spin $\overline{\mathbf{W}}_{pl}^{(1,r)}$ can be written in terms of the average slip rates $\overline{\gamma}_{(k)}^{(r)}$ (see (6.41)) in the rth single-crystal phase:

$$\overline{\mathbf{W}}_{pl}^{(1,r)} = \frac{1}{2}\sum_{k=1}^{K}\overline{\gamma}_{(k)}^{(r)}\left(\mathbf{m}_{(k)}^{(r)} \otimes \mathbf{n}_{(k)}^{(r)} - \mathbf{n}_{(k)}^{(r)} \otimes \mathbf{m}_{(k)}^{(r)}\right). \tag{6.53}$$

In summary, the instantaneous macroscopic constitutive relation (6.40), together with the evolution equations (6.45)-(6.47) and (6.49)-(6.51), constitute a complete viscoplastic model—referred to here as the ISO model—for the finite-strain macro-

scopic response of the two-scale porous polycrystals. In this context, it should be remarked that, for a given sub-structural configuration characterized by (6.8), the effective constitutive response (6.40) is completely determined by the set of variables $\check{\tau}_{[i]}^{(r,k)}$, $\hat{\tau}_{[i]}^{(r,k)}$, $\mu_{[i]}^{(r,k)}$ and $\eta_{[i]}^{(r,k)}$ ($r = 1, ..., N$; $k = 1, ..., K$; $i = 1, ..., I$), which are obtained by solving the set of nonlinear equations (6.36), (6.37) and (6.39). Moreover, the evolution of the sub-structural variables (6.8) may be determined by straightforward numerical integration of the aforementioned evolution equations, by means of an appropriate integration scheme, e.g., the forward-Euler scheme (Liu, 2003; Danas and Ponte Castañeda, 2009a). It should be emphasized that, except for the ad hoc choice made for the weight factors $\alpha_{(k)}^{(r)}$, the ISO model is *fully predictive*, in the sense that it requires no fitting parameters to experimental results or numerical simulations, and applies to two-scale porous polycrystals with general ellipsoidal voids and grains (with possibly different ellipsoidal shape from that of the voids), general crystallographic texture, subjected to general loading conditions. Finally, note that the elasticity of the grains has been neglected in this work, but could be easily incorporated, at least approximately, as already done in the context of porous isotropic materials (e.g., Aravas and Ponte Castañeda, 2004).

6.5 Concluding remarks

In this chapter, we developed a novel finite-strain homogenization model for viscoplastic porous polycrystals consisting of large voids distributed in a fine-scale polycrystalline matrix, subjected to general three-dimensional loading conditions. The porous polycrystal is idealized as a random *two-scale* composite, which has a particulate meso-structure at the larger length scale, and a granular micro-structure for the matrix at the smaller length scale. The instantaneous macroscopic response of the porous polycrystal is determined by means of the fully optimized second-order (FOSO) homogenization procedure of Ponte Castañeda (2015), together with an appropriate generalization of the iterated homogenization approach of Agoras and Ponte Castañeda (2013). More specifically, the effective behavior of the nonlinear porous

polycrystal is estimated in terms of that of a linear comparison composite (LCC), with a two-scale sub-structure identical to that of the nonlinear composite of interest. The effective behavior of the two-scale LCC is determined sequentially through the combined use of the self-consistent estimates (Hershey, 1954; Willis, 1977) for the polycrystalline matrix, and the PCW estimates (Ponte Castañeda and Willis, 1995) for the porous composite. Moreover, the iterated homogenization procedure of Agoras and Ponte Castañeda (2013) is used to "discretize" the properties of the polycrystalline matrix to obtain significantly improved results at high triaxialities, especially for low porosities and high nonlinearities. Furthermore, consistent homogenization estimates for the average strain-rate and spin fields in the phases are used to establish evolution laws for the relevant sub-structural variables, accounting for the evolution of porosity, average shape and orientation of the pores, as well as the morphological and crystallographic texture of the underlying polycrystalline matrix. In its final form, the iterated second-order (ISO) homogenization model can be viewed as a standard internal-variable viscoplastic model, with the sub-structural variables playing the role of internal variables.

Compared to other models that have been developed in the literature for porous materials, the new ISO model has several distinctive features. First, to the best knowledge of the authors, the ISO model is the first constitutive model that accounts explicitly for the two-scale structure of the porous polycrystals. Most importantly, the model can consistently account for the combined effects of the evolution of pore geometry and matrix texture. Second, unlike the classical homogenization techniques, the ISO model makes use of a linearization scheme depending on the field fluctuations in the phases, which endows it the capability to handle strongly nonlinear effects and dilatational response in nominally incompressible materials due to the presence of pores. Third, the ISO model applies for porous polycrystals with general ellipsoidal voids and grains, general crystallographic anisotropy (e.g., cubic, hexagonal) and general material nonlinearities, which are subjected to general three-dimensional loading conditions. Fourth, except for the ad hoc choice made for the weight parameters $\alpha_{(k)}^{(r)}$, the ISO model is fully predictive in the sense that no fitting parameters or compli-

cated interpolations are required. Thus, given the local behavior of the constituents and the initial state of the sub-structure, the ISO model can provide estimates for the time-dependent, finite-strain macroscopic response of the porous polycrystals under general loading conditions. This constitutes one of the main advantages relative to other phenomenological models, which require recalibration/redevelopment for porous materials with different crystallography, void morphology, and constitutive properties (e.g., nonlinearity) of the matrix. However, the ISO model is still amenable to potential improvements by using other choices of the weight parameters $\alpha_{(k)}^{(r)}$. In fact, recent work of Michel and Suquet (2017) suggests that $\alpha_{(k)}^{(r)}$ could be related to higher moments of the stress field, and this could provide insight into developing mathematically or physically motivated prescriptions for $\alpha_{(k)}^{(r)}$. Finally, it should be remarked that, the ISO model can be implemented numerically into constitutive subroutines for general-purpose finite element codes, as has already been done for porous materials with isotropic matrix phases (Aravas and Ponte Castañeda, Aravas and Ponte Castañeda; Danas and Aravas, 2012). In the next chapter, we consider specific applications of the ISO model for porous viscoplastic FCC and HCP polycrystals.

6.6 Appendix I: Two-scale LCC in the FOSO method

This Appendix deals with the determination of the effective properties and field statistics of the two-scale linear comparison composite (LCC) involved in the FOSO procedure in section 6.3.1. As already stated, the homogenization problem for the two-scale LCC may be decomposed into two single-scale problems: (i) a micro-scale homogenization problem for the polycrystalline matrix (Fig. 6.1 (b)), and (ii) a meso-scale homogenization problem for the porous medium (with a homogenized matrix) (Fig. 6.1 (a)). As will be detailed further below, the effective behavior of the polycrystalline matrix is determined by means of the estimates of the self-consistent (SC) type (Hershey, 1954; Kröner, 1958;Willis, 1977), while that of the porous medium is

obtained by means of the estimates of the Ponte Castañeda and Willis (PCW) type (Ponte Castañeda and Willis, 1995). In general, it is necessary to first homogenize the polycrystalline matrix at the micro-scale, and then homogenize the porous medium at the meso-scale, as will be discussed below.

6.6.1 Homogenization at the micro-scale

Recalling that the viscous compliance tensor and eigenstrain rate tensor of the single-crystal phase are given by (6.18), the effective stress potential for the polycrystalline matrix may be written in the form (Willis, 1981)

$$u_L^{(1)}(\overline{\boldsymbol{\sigma}}^*) = \frac{1}{2}\overline{\boldsymbol{\sigma}}^* \cdot \mathbb{M}^{(1)}\overline{\boldsymbol{\sigma}}^* + \boldsymbol{\eta}^{(1)} \cdot \overline{\boldsymbol{\sigma}}^* + \frac{1}{2}g^{(1)}, \tag{6.54}$$

where $\overline{\boldsymbol{\sigma}}^*$ in (6.54) denotes the volume average of the stress field over the RVE Ω^* inside of the polycrystalline matrix (see Fig. 6.1(b)), and $\mathbb{M}^{(1)}$, $\boldsymbol{\eta}^{(1)}$, and $g^{(1)}$ are , respectively, the effective viscous compliance, effective eigenstrain rate and effective energy at zero applied stress of the polycrystal. They are given by

$$\begin{aligned} &\mathbb{M}^{(1)} = \sum_{r=1}^{N} c^{(1,r)}\mathbb{M}^{(1,r)}\mathbb{B}^{(1,r)}, \quad \boldsymbol{\eta}^{(1)} = \sum_{r=1}^{N} c^{(1,r)}\left(\mathbb{B}^{(1,r)}\right)^T\boldsymbol{\eta}^{(1,r)}, \quad \text{and} \\ &g^{(1)} = \sum_{r=1}^{N} c^{(1,r)}\boldsymbol{\eta}^{(1,r)} \cdot \mathbf{b}^{(1,r)}, \end{aligned} \tag{6.55}$$

where $\mathbb{B}^{(1,r)}$ and $\mathbf{b}^{(1,r)}$ are stress-concentration tensors for the rth single-crystal phase in the polycrystalline matrix. Note that in $(6.55)_3$ use has been made of the fact that the energy at zero stress $g^{(1,r)} = 0$ for all the single-crystal phases.

In particular, the SC estimates for the effective viscous compliance tensor $\mathbb{M}^{(1)}$ is given by the solution of the implicit equation

$$\mathbb{M}^{(1)} = \left\{\sum_{r=1}^{N} c^{(1,r)}\left[\mathbb{M}^{(1,r)} + \mathbb{M}^*\right]^{-1}\right\}^{-1} - \mathbb{M}^*, \tag{6.56}$$

where $\mathbb{M}^* = \left(\mathbb{Q}^{(1)}\right)^{-1} - \mathbb{M}^{(1)}$ is the constraint tensor, and $\mathbb{Q}^{(1)}$ is a fourth-order mi-

crostructural tensor given by

$$\mathbb{Q}^{(1)} = \mathbb{L}^{(1)} - \mathbb{L}^{(1)}\mathbb{P}^{(1)}\mathbb{L}^{(1)}, \quad \mathbb{P}^{(1)} = \frac{1}{4\pi \det(\boldsymbol{Z}^g)} \int_{|\boldsymbol{\zeta}|=1} \frac{\mathbb{H}^{(1)}}{|(\boldsymbol{Z}^g)^{-1}\boldsymbol{\zeta}|^3} dS,$$
$$H^{(1)}_{ijkl} = \left(\boldsymbol{K}^{(1)}\right)^{-1}_{ik} \zeta_j \zeta_l|_{(ij)(kl)}, \quad K^{(1)}_{ik} = L^{(1)}_{ijkl}\zeta_j\zeta_l, \tag{6.57}$$

with $\mathbb{L}^{(1)} = (\mathbb{M}^{(1)})^{-1}$, and with the parentheses in the subscripts of $(6.57)_3$ denoting symmetrization with respect to the corresponding indices. Recall that the second-order tensor $\boldsymbol{Z}^g$ in (6.57) characterizes the "shape" of the two-point probability functions, and correlates with the *average* shape of the single-crystal grains.

Furthermore, the SC estimates for the associated stress-concentration tensors are given by

$$\mathbb{B}^{(1,r)} = \left(\mathbb{M}^{(1,r)} + \mathbb{M}^*\right)^{-1}\left(\mathbb{Q}^{(1)}\right)^{-1}, \quad \text{and} \quad \mathbf{b}^{(1,r)} = \left(\mathbb{M}^{(1,r)} + \mathbb{M}^*\right)^{-1}\left(\boldsymbol{\eta}^{(1)} - \boldsymbol{\eta}^{(1,r)}\right). \tag{6.58}$$

6.6.2 Homogenization at the meso-scale

Having determined the effective properties of the polycrystalline matrix $\mathbb{M}^{(1)}$, $\boldsymbol{\eta}^{(1)}$ and $g^{(1)}$ by means of the micro-scale homogenization, the effective stress potential $\widetilde{u}_L$ for the porous LCC, as defined by (6.19), is given by expression (6.59) in section 6.3.1.

$$\widetilde{u}_L(\overline{\boldsymbol{\sigma}}) = \frac{1}{2}\overline{\boldsymbol{\sigma}} \cdot \widetilde{\mathbb{M}}\overline{\boldsymbol{\sigma}} + \widetilde{\boldsymbol{\eta}} \cdot \overline{\boldsymbol{\sigma}} + \frac{1}{2}\widetilde{g}, \tag{6.59}$$

where $\widetilde{\mathbb{M}}$, $\widetilde{\boldsymbol{\eta}}$ and $\widetilde{g}$ are, respectively, the effective viscous compliance, eigenstrain rate and energy at zero applied stress for the porous LCC. For later use, in this subsection we provide expressions that are valid for an LCC of a particulate microstructure with general *non-vacuous* inclusions.

The PCW estimates for the effective compliance tensor $\widetilde{\mathbb{M}}$ of the LCC is given by

$$\widetilde{\mathbb{M}} = \mathbb{M}^{(1)} + c^{(2)}\left[\left(\mathbb{M}^{(2)} - \mathbb{M}^{(1)}\right)^{-1} + (1 - c^{(2)})\mathbb{Q}\right]^{-1}, \tag{6.60}$$

where it is recalled that $c^{(2)}$ denotes the volume fraction of the inclusions, $\mathbb{M}^{(2)}$ is the viscous compliance tensor for the inclusions, and $\mathbb{Q}$ is a fourth-order microstructural tensor given by (6.57), with $\boldsymbol{Z}^g$ in $(6.57)_2$ replaced by $\boldsymbol{Z}^p$ characterizing the average shape of the pores and their distribution.

On the other hand, the effective eigen-strain rate tensor of the LCC is given by

$$\widetilde{\boldsymbol{\eta}} = \boldsymbol{\eta}^{(1)} + c^{(2)} \left(\mathbb{B}^{(2)}\right)^T \left(\boldsymbol{\eta}^{(2)} - \boldsymbol{\eta}^{(1)}\right), \tag{6.61}$$

where $\mathbb{B}^{(2)}$ is the corresponding stress-concentration tensor given by

$$\mathbb{B}^{(2)} = \left[\mathbb{I} + (1 - c^{(2)})\mathbb{Q}\left(\mathbb{M}^{(2)} - \mathbb{M}^{(1)}\right)\right]^{-1}, \tag{6.62}$$

with $\mathbb{I}$ being the fully symmetric fourth-order identity tensor, and $\boldsymbol{\eta}^{(2)}$ denoting the eigenstrain rate for the inclusions. Furthermore, the effective energy $\widetilde{g}$ of the LCC at zero applied stress is given by

$$\widetilde{g} = c^{(2)} \left[\left(\boldsymbol{\eta}^{(2)} - \boldsymbol{\eta}^{(1)}\right) \cdot \mathbf{b}^{(2)} + g^{(2)}\right] + (1 - c^{(2)}) g^{(1)}, \tag{6.63}$$

where $\mathbf{b}^{(2)}$ denotes the corresponding stress-concentration tensor provided by

$$\mathbf{b}^{(2)} = \left(1 - c^{(2)}\right) \mathbb{B}^{(2)} \mathbb{Q} \left(\boldsymbol{\eta}^{(1)} - \boldsymbol{\eta}^{(2)}\right), \tag{6.64}$$

and $g^{(2)}$ is the energy at zero stress for the inclusion phase.

At this point, it should be noted that the corresponding expressions for a porous LCC may be easily obtained by taking the appropriate limits as the inclusions become infinitely soft, and by taking the inclusion concentration to be the porosity. i.e., $\mathbb{M}^{(2)} \to \infty$, $\boldsymbol{\eta}^{(2)} = \mathbf{0}$, $g^{(2)} = 0$, and $c^{(2)} = f$ in (6.60)-(6.64).

6.6.3 Field statistics in the two-scale LCC

Having obtained the effective stress potential $\widetilde{u}_L$ (see (6.59)) of the two-scale LCC, we can compute the first and second moments of the stress field in the phases of the

LCC by taking the derivative of $\widetilde{u}_L$ with respect to the appropriate modulus tensor of the phases (see, e.g., Ponte Castañeda and Suquet, 1998). In this context, it is important to recall that the field statistics in the LCC can be used directly to estimate the corresponding quantities in the actual nonlinear composite.

First, we determine the field statistics in the matrix and inclusions at the meso-scale. Once again, the expressions provided below are valid for a two-scale LCC with general non-vacuous inclusions. The corresponding expressions for a porous LCC may be obtained by taking the appropriate limits as already discussed above. For a given macroscopic stress $\overline{\boldsymbol{\sigma}}$, the first moment, or the phase average, of the stress field over the matrix phase may be determined by

$$\overline{\boldsymbol{\sigma}}^{(1)} = \frac{1}{1-c^{(2)}}\frac{\partial \widetilde{u}_L}{\partial \boldsymbol{\eta}^{(1)}} = \mathbb{B}^{(1)}\overline{\boldsymbol{\sigma}} + \mathbf{b}^{(1)}, \tag{6.65}$$

where $\mathbb{B}^{(1)}$ and $\mathbf{b}^{(1)}$ are the associated stress-concentration tensors for the matrix phase at the meso-scale, and can be obtained by means of the global average conditions:

$$\mathbb{B}^{(1)} = \frac{1}{1-c^{(2)}}\left(\mathbb{I} - c^{(2)}\mathbb{B}^{(2)}\right), \quad \text{and} \quad \mathbf{b}^{(1)} = -\frac{c^{(2)}}{1-c^{(2)}}\mathbf{b}^{(2)}. \tag{6.66}$$

It is recalled that $\mathbb{B}^{(2)}$ and $\mathbf{b}^{(1)}$ are provided by equation (6.62) and (6.64), respectively. Moreover, the second moment of the stress field over the matrix phase may be computed via

$$\begin{aligned}\langle \boldsymbol{\sigma}\otimes\boldsymbol{\sigma}\rangle^{(1)} = \frac{2}{1-c^{(2)}}\frac{\partial \widetilde{u}_L}{\partial \mathbb{M}^{(1)}} =& \overline{\boldsymbol{\sigma}}^{(1)}\otimes\overline{\boldsymbol{\sigma}}^{(1)} - \frac{1}{c^{(2)}}\left(\overline{\boldsymbol{\sigma}}^{(1)} - \overline{\boldsymbol{\sigma}}\right)\otimes\left(\overline{\boldsymbol{\sigma}}^{(1)} - \overline{\boldsymbol{\sigma}}\right) - \\ & \frac{1}{c^{(2)}}\left[\mathbb{Q}^{-1}\left(\overline{\boldsymbol{\sigma}}^{(1)} - \overline{\boldsymbol{\sigma}}\right)\right]\cdot\frac{\partial \mathbb{Q}}{\partial \mathbb{M}^{(1)}}\left[\mathbb{Q}^{-1}\left(\overline{\boldsymbol{\sigma}}^{(1)} - \overline{\boldsymbol{\sigma}}\right)\right].\end{aligned} \tag{6.67}$$

Here $\partial\mathbb{Q}/\partial\mathbb{M}^{(1)}$ is an eighth-order tensor, the evaluation of which is detailed in Appendix 3 of Liu (2003). Note that the last term of (6.67) involves the summation over indices corresponding to the numerator of $\partial\mathbb{Q}/\partial\mathbb{M}^{(1)}$.

Similarly, it can be shown that the average strain rate $\overline{\mathbf{D}}^{(2)}$ in (6.67) in the inclu-

sion phase can be determined by means of

$$\overline{\mathbf{D}}^{(2)} = \mathbb{A}^{(2)}\overline{\mathbf{D}} + \mathbf{a}^{(2)}, \tag{6.68}$$

where $\mathbb{A}^{(2)}$ and $\mathbf{a}^{(2)}$ are the associated strain-rate concentration tensors given by

$$\mathbb{A}^{(2)} = \left\{c^{(2)}\mathbb{I} + \left(1-c^{(2)}\right)\left[\left(\mathbb{M}^{(1)} - \mathbb{M}^{(1)}\mathbb{Q}\mathbb{M}^{(1)}\right)\left(\mathbb{M}^{(2)}\right)^{-1} + \mathbb{M}^{(1)}\mathbb{Q}\right]\right\}^{-1}, \tag{6.69}$$

and

$$\mathbf{a}^{(2)} = -\left(1-c^{(2)}\right)\mathbb{A}^{(2)}\left(\mathbb{I} - \mathbb{M}^{(1)}\mathbb{Q}\right)\left[\boldsymbol{\eta}^{(1)} - \mathbb{M}^{(1)}\left(\mathbb{M}^{(2)}\right)^{-1}\boldsymbol{\eta}^{(2)}\right]. \tag{6.70}$$

Then, the average strain rate $\overline{\mathbf{D}}^{(1)}$ in the matrix phase may be obtained from the global average condition

$$\overline{\mathbf{D}}^{(1)} = \frac{1}{1-c^{(2)}}\left(\overline{\mathbf{D}} - c^{(2)}\overline{\mathbf{D}}^{(2)}\right). \tag{6.71}$$

Correspondingly, the PCW estimate for the average spin field over the inclusion phase is given by

$$\overline{\mathbf{W}}^{(2)} = \overline{\mathbf{W}} - \mathbb{C}^{(2)}\overline{\mathbf{D}} - \boldsymbol{\beta}^{(2)}, \tag{6.72}$$

where $\overline{\mathbf{W}}$ is the macroscopic spin field, while $\mathbb{C}^{(2)}$ and $\boldsymbol{\beta}^{(2)}$ are the associated spin-concentration tensors determined by

$$\mathbb{C}^{(2)} = \left(1-c^{(2)}\right)\mathbb{R}\left[\left(\mathbb{M}^{(2)}\right)^{-1} - \left(\mathbb{M}^{(1)}\right)^{-1}\right]\mathbb{A}^{(2)}, \tag{6.73}$$

and

$$\boldsymbol{\beta}^{(2)} = \left(1-c^{(2)}\right)\mathbb{R}\left\{\left[\left(\mathbb{M}^{(2)}\right)^{-1} - \left(\mathbb{M}^{(1)}\right)^{-1}\right]\mathbf{a}^{(2)} + \left(\mathbb{M}^{(1)}\right)^{-1}\boldsymbol{\eta}^{(1)} - \left(\mathbb{M}^{(2)}\right)^{-1}\boldsymbol{\eta}^{(2)}\right\}. \tag{6.74}$$

Here the fourth-order tensor $\mathbb{R}$ is given by

$$\mathbb{R} = \frac{1}{4\pi\det(\boldsymbol{Z}^p)}\int\limits_{|\boldsymbol{\zeta}|=1}\frac{\hat{\mathbb{H}}^{(1)}(\boldsymbol{\zeta})}{|(\boldsymbol{Z}^p)^{-1}\boldsymbol{\zeta}|^3}dS, \tag{6.75}$$

where $\hat{\mathbb{H}}^{(1)}(\boldsymbol{\zeta})$ is given by $(6.57)_3$, but with the symmetric parts with respect to the indices i and j replaced by the corresponding skew-symmetric parts. Then, it follows that the average spin in the polycrystalline matrix is given by the global average condition

$$\overline{\mathbf{W}}^{(1)} = \frac{1}{1-c^{(2)}}\left(\overline{\mathbf{W}} - c^{(2)}\overline{\mathbf{W}}^{(2)}\right). \tag{6.76}$$

Next, we determine the field statistics in each single-crystal phase r underlying the matrix phase at the micro-scale. Making use of a procedure similar to (6.65), the first moment of the stress field over the rth single-crystal phase is given by

$$\overline{\boldsymbol{\sigma}}^{(1,r)} = \frac{1}{(1-c^{(2)})\,c^{(1,r)}}\frac{\partial \widetilde{u}_L}{\partial \boldsymbol{\eta}^{(1,r)}} = \frac{1}{(1-c^{(2)})\,c^{(1,r)}}\left(\frac{\partial \widetilde{u}_L}{\partial \boldsymbol{\eta}^{(1)}}\frac{\partial \boldsymbol{\eta}^{(1)}}{\partial \boldsymbol{\eta}^{(1,r)}} + \frac{\partial \widetilde{u}_L}{\partial g^{(1)}}\frac{\partial g^{(1)}}{\partial \boldsymbol{\eta}^{(1,r)}}\right), \tag{6.77}$$

where the chain rule has been used in (6.77). Making use of expression (6.65), (6.55) and (6.63), it can be shown that $\overline{\boldsymbol{\sigma}}^{(1,r)}$ may be rewritten in a simpler form:

$$\overline{\boldsymbol{\sigma}}^{(1,r)} = \mathbb{B}^{(1,r)}\overline{\boldsymbol{\sigma}}^{(1)} + \mathbf{b}^{(1,r)}, \tag{6.78}$$

where $\overline{\boldsymbol{\sigma}}^{(1)}$ is the average stress field in the matrix phase (at the meso-scale) given by (6.65). Interestingly, the first moment $\overline{\boldsymbol{\sigma}}^{(1,r)}$ in the single-crystal phase, as given by (6.78), is identical to the first moment computed by assuming that the solid polycrystalline matrix is subjected to a mesoscopic stress $\overline{\boldsymbol{\sigma}}^{(1)}$.

Similarly, the corresponding second moment of the stress field over the rth single-crystal phase may be determined by

$$\begin{aligned}\langle \boldsymbol{\sigma}\otimes\boldsymbol{\sigma}\rangle^{(1,r)} &= \frac{2}{(1-c^{(2)})\,c^{(1,r)}}\frac{\partial \widetilde{u}_L}{\partial \mathbb{M}^{(1,r)}} \\ &= \frac{2}{(1-c^{(2)})\,c^{(1,r)}}\left(\frac{\partial \widetilde{u}_L}{\partial \mathbb{M}^{(1)}}\frac{\partial \mathbb{M}^{(1)}}{\partial \mathbb{M}^{(1,r)}} + \frac{\partial \widetilde{u}_L}{\partial \boldsymbol{\eta}^{(1)}}\frac{\partial \boldsymbol{\eta}^{(1)}}{\partial \mathbb{M}^{(1,r)}} + \frac{\partial \widetilde{u}_L}{\partial g^{(1)}}\frac{\partial g^{(1)}}{\partial \mathbb{M}^{(1,r)}}\right),\end{aligned} \tag{6.79}$$

where use has been made of the chain rule in (6.79). Making use of expression (6.67),

(6.65) and (6.63), it follows that $\langle \boldsymbol{\sigma} \otimes \boldsymbol{\sigma} \rangle^{(1,r)}$ in (6.79) may be rewritten as

$$\langle \boldsymbol{\sigma} \otimes \boldsymbol{\sigma} \rangle^{(1,r)} = \frac{1}{c^{(1,r)}} \left(\frac{\partial \mathbb{M}^{(1)}}{\partial \mathbb{M}^{(1,r)}} \cdot \langle \boldsymbol{\sigma} \otimes \boldsymbol{\sigma} \rangle^{(1)} + 2 \frac{\partial \boldsymbol{\eta}^{(1)}}{\partial \mathbb{M}^{(1,r)}} \cdot \overline{\boldsymbol{\sigma}}^{(1)} + \frac{\partial g^{(1)}}{\partial \mathbb{M}^{(1,r)}} \right), \tag{6.80}$$

where $\partial \mathbb{M}^{(1)} / \partial \mathbb{M}^{(1,r)}$, $\partial \boldsymbol{\eta}^{(1)} / \partial \mathbb{M}^{(1,r)}$, and $\partial g^{(1)} / \partial \mathbb{M}^{(1,r)}$ are eighth-, sixth- and fourth-order tensors, respectively, the determination of which is detailed in Appendix 3 of Liu (2003), and $\langle \boldsymbol{\sigma} \otimes \boldsymbol{\sigma} \rangle^{(1)}$ is the second moment of the stress field in the matrix phase at the meso-scale, as given by (6.67). In this context, it is important to remark that (6.80) is *different* from the second moment computed by assuming that the solid polycrystalline matrix is subjected to a mesoscopic stress $\overline{\boldsymbol{\sigma}}^{(1)}$. This is because $\langle \boldsymbol{\sigma} \otimes \boldsymbol{\sigma} \rangle^{(1)} \neq \overline{\boldsymbol{\sigma}}^{(1)} \otimes \overline{\boldsymbol{\sigma}}^{(1)}$, due to the field fluctuations in the matrix phase.

The average strain rate in the rth single-crystal phase may be estimated by using the *linear* constitutive relations of the single-crystal phases in the LCC, i.e.,

$$\overline{\mathbf{D}}^{(1,r)} = \mathbb{M}^{(1,r)} \overline{\boldsymbol{\sigma}}^{(1,r)} + \boldsymbol{\eta}^{(1,r)}. \tag{6.81}$$

Similarly, the corresponding average spin $\overline{\mathbf{W}}^{(1,r)}$ in the rth single-crystal phase is given by

$$\overline{\mathbf{W}}^{(1,r)} = \overline{\mathbf{W}}^{(1)} - \mathbb{R}^{(1)} \left(\mathbb{P}^{(1)} \right)^{-1} \left(\overline{\mathbf{D}}^{(1)} - \overline{\mathbf{D}}^{(1,r)} \right), \tag{6.82}$$

where $\mathbb{P}^{(1)}$ is a fourth-order microstructural tensor given by $(6.57)_2$, and $\mathbb{R}^{(1)}$ is given by expression (6.75), with $\boldsymbol{Z}^p$ in (6.75) replaced by $\boldsymbol{Z}^d$. Recall that $\overline{\mathbf{W}}^{(1)}$ and $\overline{\mathbf{D}}^{(1)}$ are given by (6.76) and (6.71), respectively.

6.7 Appendix II: FOSO estimates for the two-scale porous polycrystal

In this Appendix, we provide detailed derivations of the FOSO estimates for the effective stress potential $\widetilde{u}$ of the two-scale viscoplastic porous polycrystals.

Following Ponte Castañeda (2015), the local stress potential $u^{(1,r)}$ (see (6.9)) of the nonlinear porous polycrystal can be rewritten by means of a variational repre-

sentation, in terms of the local potential $u_L^{(1,r)}$ (see (6.17)) of the two-scale LCC, so that

$$u^{(1,r)}(\boldsymbol{\sigma}) = \underset{\substack{\mu_{(n)}^{(r)},\eta_{(n)}^{(r)} \\ n=1,\dots,K}}{\text{stat}} \left\{ u_L^{(1,r)}(\boldsymbol{\sigma}) - \sum_{k=1}^{K} V_{(k)}^{(1,r)}(\mu_{(k)}^{(r)},\eta_{(k)}^{(r)}) \right\}, \tag{6.83}$$

where the 'stat' denotes a stationary operation, and the $V_{(k)}^{(1,r)}(\mu_{(k)}^{(r)},\eta_{(k)}^{(r)})$ are error functions given by

$$V_{(k)}^{(1,r)}(\mu_{(k)}^{(r)},\eta_{(k)}^{(r)}) = \alpha_{(k)}^{(r)} \check{V}_{(k)}^{(1,r)}(\mu_{(k)}^{(r)},\eta_{(k)}^{(r)}) + (1-\alpha_{(k)}^{(r)}) \hat{V}_{(k)}^{(1,r)}(\mu_{(k)}^{(r)},\eta_{(k)}^{(r)}). \tag{6.84}$$

Here $\alpha_{(k)}^{(r)}$ $(0 < \alpha_{(k)}^{(r)} < 1)$ is a weight factor, and the functions $\check{V}_{(k)}^{(1,r)}$ and $\hat{V}_{(k)}^{(1,r)}$ are given by (Ponte Castañeda, 2015)

$$\begin{aligned}
\check{V}_{(k)}^{(1,r)}(\mu_{(k)}^{(r)},\eta_{(k)}^{(r)}) &= \underset{\check{\tau}_{(k)}^{(r)}}{\text{stat}} \left\{ \check{\tau}_{(k)}^{(r)}\eta_{(k)}^{(r)} + \frac{1}{4\mu_{(k)}^{(r)}}(\check{\tau}_{(k)}^{(r)})^2 - \phi_{(k)}^{(r)}(\check{\tau}_{(k)}^{(r)}) \right\}, \quad \text{and} \\
\hat{V}_{(k)}^{(1,r)}(\mu_{(k)}^{(r)},\eta_{(k)}^{(r)}) &= \underset{\hat{\tau}_{(k)}^{(r)}}{\text{stat}} \left\{ \hat{\tau}_{(k)}^{(r)}\eta_{(k)}^{(r)} + \frac{1}{4\mu_{(k)}^{(r)}}(\hat{\tau}_{(k)}^{(r)})^2 - \phi_{(k)}^{(r)}(\hat{\tau}_{(k)}^{(r)}) \right\}.
\end{aligned} \tag{6.85}$$

It should be emphasized here that $\check{V}_{(k)}^{(1,r)}$ and $\hat{V}_{(k)}^{(1,r)}$ are *different* functions in general, since they are evaluated at different stationary points $\check{\tau}_{(k)}^{(r)}$ and $\hat{\tau}_{(k)}^{(r)}$ (see Ponte Castañeda, 2015 for details).

Substituting expression (6.83) of $u^{(1,r)}$ into (6.15), and interchanging the order of the minimum and stationary operations, the effective stress potential $\widetilde{u}$ of the nonlinear porous polycrystal can be written as

$$\widetilde{u}(\overline{\boldsymbol{\sigma}}) = \underset{\substack{\mu_{(n)}^{(s)},\eta_{(n)}^{(s)} \\ s=1,\dots,N \\ n=1,\dots,K}}{\text{stat}} \left\{ \widetilde{u}_L(\overline{\boldsymbol{\sigma}}) - (1-f) \sum_{r=1}^{N} c^{(1,r)} \sum_{k=1}^{K} V_{(k)}^{(1,r)}(\mu_{(k)}^{(r)},\eta_{(k)}^{(r)}) \right\}, \tag{6.86}$$

where use have been made of expression (6.19) for $\widetilde{u}_L$. Note that the trial fields in the variational principle (6.86) are the slip viscosities $\mu_{(k)}^{(r)}$ and the slip eigenstrain rates $\eta_{(k)}^{(r)}$ for the LCC, which are *not* subjected to any differential constraints and have been chosen to be piecewise constants in (6.86). Note further that the conditions for

equilibrium and compatibility are enforced through the LCC.

Now, we spell out the stationary conditions associated with the variational estimate (6.86). In particular, the stationary conditions for the variables $\check{\tau}_{(k)}^{(r)}$ and $\hat{\tau}_{(k)}^{(r)}$, implicit in the definitions (6.85) for the functions $\check{V}_{(k)}^{(1,r)}$ and $\hat{V}_{(k)}^{(1,r)}$, are given by

$$\phi_{(k)}^{(r)\prime}(\hat{\tau}_{(k)}^{(r)}) - \frac{1}{2\mu_{(k)}^{(r)}}\hat{\tau}_{(k)}^{(r)} = \eta_{(k)}^{(r)} = \phi_{(k)}^{(r)\prime}(\check{\tau}_{(k)}^{(r)}) - \frac{1}{2\mu_{(k)}^{(r)}}\check{\tau}_{(k)}^{(r)}. \tag{6.87}$$

Next, we consider the stationary conditions for the variables $\eta_{(k)}^{(r)}$ and $\mu_{(k)}^{(r)}$. When taking derivative of the term $\widetilde{u}_L$ with respect to these variables, we make use of expression (6.18) and of the chain rule to write the derivatives with respect to $\eta_{(k)}^{(r)}$ and $\mu_{(k)}^{(r)}$, respectively, in terms of the first and second moments of the stress field in the LCC via expression (6.77) and (6.79). Then, it follows that the stationary condition with respect to $\eta_{(k)}^{(r)}$ are given by

$$\alpha_{(k)}^{(r)}\check{\tau}_{(k)}^{(r)} + (1-\alpha_{(k)}^{(r)})\hat{\tau}_{(k)}^{(r)} = \overline{\boldsymbol{\sigma}}^{(1,r)} \cdot \boldsymbol{\mu}_{(k)}^{(r)} = \overline{\tau}_{(k)}^{(r)}, \tag{6.88}$$

where $\overline{\boldsymbol{\sigma}}^{(1,r)}$ denotes the first moment of the stress field over the rth single-crystal phase in the LCC, as given by expression (6.78) in Appendix I, while $\overline{\tau}_{(k)}^{(r)}$ is the first moment of the resolved shear stress over slip system k in single-crystal phase r of the LCC. Similarly, the stationary conditions with respect to the slip viscosities $\mu_{(k)}^{(r)}$ are given by

$$\alpha_{(k)}^{(r)}\left(\check{\tau}_{(k)}^{(r)}\right)^2 + (1-\alpha_{(k)}^{(r)})\left(\hat{\tau}_{(k)}^{(r)}\right)^2 = \boldsymbol{\mu}_{(k)}^{(r)} \cdot \langle \boldsymbol{\sigma} \otimes \boldsymbol{\sigma} \rangle^{(1,r)} \boldsymbol{\mu}_{(k)}^{(r)} = \overline{\overline{\tau}}_{(k)}^{(r)}, \tag{6.89}$$

where $\langle \boldsymbol{\sigma} \otimes \boldsymbol{\sigma} \rangle^{(1,r)}$ denotes the second moment of the stress field over the rth single-crystal phase in the LCC, as given by expression (6.80) in Appendix I, while $\overline{\overline{\tau}}_{(k)}^{(r)}$ is the second moment of the resolved shear stress over slip system k in single-crystal phase r of the LCC.

Making use of the stationary conditions (6.88) and (6.89) in (6.86), it can be easily shown that the effective stress potential $\widetilde{u}$ may be rewritten in a simplified form given

by (6.21).

6.8 Appendix III: Expressions for the LCC in the ISO method

In this Appendix, we provide expressions for the macroscopic behavior and field statistics in the LCC involved in the ISO model for the two-scale porous polycrystals. These expressions provide generalizations of the corresponding expressions in the work of Song and Ponte Castañeda (2017b) for porous single crystals. Similar to the ISO procedure of Song and Ponte Castañeda (2017b), the sub-structure of the LCC in the present work is of the "self-similar" type (see Fig. 6.2), with the matrix phases possessing different properties at different iterations ($i = 1, ..., I$). However, in the present work the matrix phase at each iteration is a polycrystalline aggregate, which has a fine-scale granular micro-structure.

Given the local properties (6.34) of the single-crystal phases at each iteration, the effective behavior of the polycrystalline matrix may be obtained by means of the SC estimates, as already discussed in Appendix I. In particular, the effective viscous compliance tensor $\mathbb{M}^{(1)}_{[i]}$, effective eigenstrain rate $\boldsymbol{\eta}^{(1)}_{[i]}$, and effective energy at zero stress $g^{(1)}_{[i]}$ for the level-i polycrystalline matrix may be computed via equation (6.56), $(6.55)_2$ and $(6.55)_3$, respectively, with $\mathbb{M}^{(1,r)}$ and $\mathbb{M}^*$ in (6.56) replaced by the corresponding quantities $\mathbb{M}^{(1,r)}_{[i]}$ and $\mathbb{M}^*_{[i]}$ at the ith iteration. Moreover, the associated stress-concentration tensors $\mathbb{B}^{(1,r)}_{[i]}$ and $\mathbf{b}^{(1,r)}_{[i]}$ for the rth single-crystal phase at the ith iteration are given by equations completely analogous to (6.58), with the quantities $\boldsymbol{\eta}^{(1)}$, $\boldsymbol{\eta}^{(1,r)}$ and $\mathbb{Q}^{(1)}$ in (6.58) replaced by the corresponding quantities $\boldsymbol{\eta}^{(1)}_{[i]}$, $\boldsymbol{\eta}^{(1,r)}_{[i]}$ and $\mathbb{Q}^{(1)}_{[i]}$, respectively, at the ith iteration. Applying the above described procedure for each iteration level, we can obtain the *homogenized* properties for the polycrystalline matrix at each iteration ($i = 1, ..., I$), as well as the associated stress-concentration tensors.

Having obtained the effective properties of the polycrystalline matrix at each

iteration, the effective properties of the LCC may be determined by means of the PCW estimates (Ponte Castañeda and Willis, 1995) at each iteration, following the development of Song and Ponte Castañeda (2017b). Making use of equation (6.60) in Appendix I, the viscous compliance tensor $\widetilde{\mathbb{M}}_{[i]}$ of the level-i LCC is given by

$$\widetilde{\mathbb{M}}_{[i]} = \mathbb{M}^{(1)}_{[i]} + c^{(2)}_{[i]} \left[\left(\widetilde{\mathbb{M}}_{[i-1]} - \mathbb{M}^{(1)}_{[i]} \right)^{-1} + (1 - c^{(2)}_{[i]}) \mathbb{Q}_{[i]} \right]^{-1}, \qquad i = 1, ..., I, \tag{6.90}$$

where it is recalled that the $c^{(2)}_{[i]}$ $(i = 1, ..., I)$ are the volume fractions of the inclusion phase in the level-i LCC, which can be simply chosen as $c^{(2)}_{[i]} = f^{1/I}$ $(i = 1, .., I)$, and the $\mathbb{Q}_{[i]}$ $(i = 1, ..., I)$ are fourth-order microstructural tensors, depending on the matrix property $\mathbb{M}^{(1)}_{[i]}$ and pore morphology. It should be mentioned that $\widetilde{\mathbb{M}}_{[0]} \to \infty$ in (6.90), denoting the compliance tensor of the pores at the first iteration.

In addition, the effective eigenstrain-rate tensor $\widetilde{\boldsymbol{\eta}}_{[i]}$ of the level-i LCC is given by

$$\widetilde{\boldsymbol{\eta}}_{[i]} = \boldsymbol{\eta}^{(1)}_{[i]} + c^{(2)}_{[i]} \left(\mathbb{B}^{(2)}_{[i]} \right)^{T} \left(\widetilde{\boldsymbol{\eta}}_{[i-1]} - \boldsymbol{\eta}^{(1)}_{[i]} \right), \qquad i = 1, ..., I, \tag{6.91}$$

where the stress concentration tensor $\mathbb{B}^{(2)}_{[i]}$ for the inclusion phase is given by

$$\mathbb{B}^{(2)}_{[i]} = \left[\mathbb{I} + (1 - c^{(2)}_{[i]}) \mathbb{Q}_{[i]} \left(\widetilde{\mathbb{M}}_{[i-1]} - \mathbb{M}^{(1)}_{[i]} \right) \right]^{-1}, \quad i = 1, ..., I, \tag{6.92}$$

Note that $\widetilde{\boldsymbol{\eta}}_{[0]} = \mathbf{0}$ in (6.91), representing the eigenstrain-rate tensor of the pores at the first iteration. The effective energy $\widetilde{g}_{[i]}$ of the level-i LCC is then given by

$$\widetilde{g}_{[i]} = c^{(2)}_{[i]} \left[\left(\widetilde{\boldsymbol{\eta}}_{[i-1]} - \boldsymbol{\eta}^{(1)}_{[i]} \right) \cdot \mathbf{b}^{(2)}_{[i]} + \widetilde{g}_{[i-1]} \right] + (1 - c^{(2)}_{[i]}) g^{(1)}_{[i]}, \quad i = 1, ..., I, \tag{6.93}$$

where the stress-concentration tensor $\mathbf{b}^{(2)}_{[i]}$ is provided by

$$\mathbf{b}^{(2)}_{[i]} = \left(1 - c^{(2)}_{[i]} \right) \mathbb{B}^{(2)}_{[i]} \mathbb{Q}_{[i]} \left(\boldsymbol{\eta}^{(1)}_{[i]} - \widetilde{\boldsymbol{\eta}}_{[i-1]} \right), \quad i = 1, ..., I. \tag{6.94}$$

Now, letting $\overline{\boldsymbol{\sigma}}_{[i]} = \langle \boldsymbol{\sigma} \rangle_{[i]}$ denote the average stress field over the level-i LCC, and $\overline{\boldsymbol{\sigma}}^{(2)}_{[i]}$ denote the corresponding average stress field over the inclusion phase of the

level-i LCC, it follows that

$$\overline{\boldsymbol{\sigma}}_{[i]}^{(2)} = \mathbb{B}_{[i]}^{(2)}\overline{\boldsymbol{\sigma}}_{[i]} + \mathbf{b}_{[i]}^{(2)}, \quad i = 1, ..., I. \tag{6.95}$$

Now, making use of (6.95) recursively for $i = I, ..., 1$, along with the fact that

$$\overline{\boldsymbol{\sigma}}_{[I]} = \overline{\boldsymbol{\sigma}} \quad \text{and} \quad \overline{\boldsymbol{\sigma}}_{[i-1]} = \overline{\boldsymbol{\sigma}}_{[i]}^{(2)}, \quad i = I, ..., 2, \tag{6.96}$$

it can be shown that $\overline{\boldsymbol{\sigma}}_{[i]}^{(2)}$ may be expressed in terms of the macroscopic stress $\overline{\boldsymbol{\sigma}}$ and the stress-concentration tensors $\mathbb{B}_{[i]}^{(2)}$ and $\mathbf{b}_{[i]}^{(2)}$ (at different iterations) as

$$\overline{\boldsymbol{\sigma}}_{[i]}^{(2)} = \left[\prod_{j=i}^{I} \mathbb{B}_{[j]}^{(2)}\right]\overline{\boldsymbol{\sigma}} + \sum_{j=i+1}^{I}\left(\prod_{l=i}^{j-1} \mathbb{B}_{[l]}^{(2)}\right)\mathbf{b}_{[j]}^{(2)} + \mathbf{b}_{[i]}^{(2)}, \quad i = 1, ..., I. \tag{6.97}$$

Then, the effective stress potential of the level-i LCC is given by

$$\widetilde{u}_{L[i]}\left(\overline{\boldsymbol{\sigma}}_{[i]}\right) = \frac{1}{2}\overline{\boldsymbol{\sigma}}_{[i]} \cdot \widetilde{\mathbb{M}}_{[i]}\overline{\boldsymbol{\sigma}}_{[i]} + \widetilde{\boldsymbol{\eta}}_{[i]} \cdot \overline{\boldsymbol{\sigma}}_{[i]} + \frac{1}{2}\widetilde{g}_{[i]}, \quad i = 1, ..., N, \tag{6.98}$$

where $\overline{\boldsymbol{\sigma}}_{[i]}$ may be determined by equation (6.96) and (6.97), while $\widetilde{\mathbb{M}}_{[i]}$, $\widetilde{\boldsymbol{\eta}}_{[i]}$ and $g_{[i]}$ are given by expression (6.90), (6.91) and (6.93), respectively.

Making use of expression (6.67), the second moment of the stress field in the matrix phase of the level-i LCC is given by

$$\begin{aligned}\langle \boldsymbol{\sigma} \otimes \boldsymbol{\sigma} \rangle_{[i]}^{(1)} = \overline{\boldsymbol{\sigma}}_{[i]}^{(1)} \otimes \overline{\boldsymbol{\sigma}}_{[i]}^{(1)} - \frac{1}{c_{[i]}^{(2)}}\left(\overline{\boldsymbol{\sigma}}_{[i]}^{(1)} - \overline{\boldsymbol{\sigma}}_{[i]}\right) \otimes \left(\overline{\boldsymbol{\sigma}}_{[i]}^{(1)} - \overline{\boldsymbol{\sigma}}_{[i]}\right) - \\ \frac{1}{c_{[i]}^{(2)}}\left[\mathbb{Q}_{[i]}^{-1}\left(\overline{\boldsymbol{\sigma}}_{[i]}^{(1)} - \overline{\boldsymbol{\sigma}}_{[i]}\right)\right] \cdot \frac{\partial \mathbb{Q}_{[i]}}{\partial \mathbb{M}_{[i]}^{(1)}}\left[\mathbb{Q}_{[i]}^{-1}\left(\overline{\boldsymbol{\sigma}}_{[i]}^{(1)} - \overline{\boldsymbol{\sigma}}_{[i]}\right)\right], \quad i = 1, ..., N.\end{aligned} \tag{6.99}$$

Following a procedure similar to that used for computing $\overline{\boldsymbol{\sigma}}_{[i]}^{(2)}$, the average strain rate $\overline{\mathbf{D}}_{[i]}^{(2)}$ over the inclusion phase of the level-i LCC is given by

$$\overline{\mathbf{D}}_{[i]}^{(2)} = \mathbb{A}_{[i]}^{(2)}\overline{\mathbf{D}}_{[i]} + \mathbf{a}_{[i]}^{(2)}, \quad i = 1, ..., I, \tag{6.100}$$

where $\overline{\mathbf{D}}_{[i]} = \langle \mathbf{D} \rangle_{[i]}$ $(i = 1, ..., I)$ denotes the average strain-rate field over the level-i

LCC, and the $\mathbb{A}_{[i]}^{(2)}$ and $\mathbf{a}_{[i]}^{(2)}$ $(i = 1, ..., I)$ are the associated strain-rate concentration tensors provided by

$$\mathbb{A}_{[i]}^{(2)} = \left\{ c_{[i]}^{(2)} \mathbb{I} + (1 - c_{[i]}^{(2)}) \left[\left(\mathbb{M}_{[i]}^{(1)} - \mathbb{M}_{[i]}^{(1)} \mathbb{Q}_{[i]} \mathbb{M}_{[i]}^{(1)} \right) \widetilde{\mathbb{M}}_{[i-1]}^{-1} + \mathbb{M}_{[i]}^{(1)} \mathbb{Q}_{[i]} \right] \right\}^{-1}, \quad i = 1, ..., I, \tag{6.101}$$

and

$$\mathbf{a}_{[i]}^{(2)} = -\left(1 - c_{[i]}^{(2)}\right) \mathbb{A}_{[i]}^{(2)} \left(\mathbb{I} - \mathbb{M}_{[i]}^{(1)} \mathbb{Q}_{[i]} \right) \left(\boldsymbol{\eta}_{[i]}^{(1)} - \mathbb{M}_{[i]}^{(1)} \widetilde{\mathbb{M}}_{[i-1]}^{-1} \widetilde{\boldsymbol{\eta}}_{[i-1]} \right), \quad i = 1, ..., I. \tag{6.102}$$

Following a development completely analogous to that used above for the derivation of (6.97), and accounting for the relations

$$\overline{\mathbf{D}}_{[I]} = \overline{\mathbf{D}} \quad \text{and} \quad \overline{\mathbf{D}}_{[i-1]} = \overline{\mathbf{D}}_{[i]}^{(2)}, \quad i = I, ..., 2, \tag{6.103}$$

$\overline{\mathbf{D}}_{[i]}^{(2)}$ may be expressed by means of the macroscopic strain rate $\overline{\mathbf{D}}$ and the associated strain-rate concentration tensors $\mathbb{A}_{[i]}^{(2)}$ and $\mathbf{a}_{[i]}^{(2)}$ (at different iterations) as

$$\overline{\mathbf{D}}_{[i]}^{(2)} = \left[\prod_{j=i}^{I} \mathbb{A}_{[j]}^{(2)} \right] \overline{\mathbf{D}} + \sum_{j=i+1}^{I} \left(\prod_{l=i}^{j-1} \mathbb{A}_{[l]}^{(2)} \right) \mathbf{a}_{[j]}^{(2)} + \mathbf{a}_{[i]}^{(2)}, \quad i = 1, ..., I. \tag{6.104}$$

The average spin field over the inclusion phase of the level-i LCC can also be obtained by means of the PCW estimate

$$\overline{\mathbf{W}}_{[i]}^{(2)} = \overline{\mathbf{W}}_{[i]} - \mathbb{C}_{[i]}^{(2)} \overline{\mathbf{D}}_{[i]} - \boldsymbol{\beta}_{[i]}^{(2)}, \quad i = 1, ..., I, \tag{6.105}$$

where the $\overline{\mathbf{W}}_{[i]} = \langle \mathbf{W} \rangle_{[i]}$ $(i = 1, ..., I)$ are the average spin field over the level-i LCC, and the $\mathbb{C}_{[i]}^{(2)}$ and $\boldsymbol{\beta}_{[i]}^{(2)}$ $(i = 1, ..., I)$ are the associated spin-concentration tensors determined by

$$\mathbb{C}_{[i]}^{(2)} = \left(1 - c_{[i]}^{(2)}\right) \mathbb{R}_{[i]} \left[\widetilde{\mathbb{M}}_{[i-1]}^{-1} - \left(\mathbb{M}_{[i]}^{(1)} \right)^{-1} \right] \mathbb{A}_{[i]}^{(2)}, \quad i = 1, ..., I, \tag{6.106}$$

and

$$\boldsymbol{\beta}_{[i]}^{(2)} = \left(1 - c_{[i]}^{(2)}\right)\mathbb{R}_{[i]}\left\{\left[\widetilde{\mathbb{M}}_{[i-1]}^{-1} - \left(\mathbb{M}_{[i]}^{(1)}\right)^{-1}\right]\mathbf{a}_{[i]}^{(2)} + \left(\mathbb{M}_{[i]}^{(1)}\right)^{-1}\boldsymbol{\eta}_{[i]}^{(1)} - \widetilde{\mathbb{M}}_{[i-1]}^{-1}\widetilde{\boldsymbol{\eta}}_{[i-1]}\right\},$$
$$i = 1, ..., I. \tag{6.107}$$

Here the $\mathbb{R}_{[i]}$ $(i = 1, ..., N)$ are fourth-order microstructural tensors depending on the matrix compliance tensor $\mathbb{M}_{[i]}^{(1)}$ and the pore morphology, and are given by expressions similar to (6.75). Making use of (6.105) recursively for $i = I, ..., 1$, and accounting for the relations

$$\overline{\mathbf{W}}_{[I]} = \overline{\mathbf{W}} \quad \text{and} \quad \overline{\mathbf{W}}_{[i-1]} = \overline{\mathbf{W}}_{[i]}^{(2)}, \quad i = I, ..., 2, \tag{6.108}$$

$\overline{\mathbf{W}}_{[i]}^{(2)}$ may be written in the form

$$\overline{\mathbf{W}}_{[i]}^{(2)} = \overline{\mathbf{W}} - \left(\sum_{j=i}^{I}\mathbb{C}_{[j]}^{(2)}\overline{\mathbf{D}}_{[j]}\right) - \sum_{j=i}^{I}\boldsymbol{\beta}_{[j]}^{(2)}, \quad i = 1, ..., I, \tag{6.109}$$

where we recall that the $\overline{\mathbf{D}}_{[i]}$ $(i = 1, ..., N)$ are determined by (6.103) and (6.104). At this point, it should be noted that the average stress, strain-rate and spin fields over the pores of the LCC can be obtained from equation (6.97), (6.104) and (6.109), respectively, by setting $i = 1$ (i.e., $\overline{\boldsymbol{\sigma}}^{(2)} = \overline{\boldsymbol{\sigma}}_{[1]}^{(2)}$, $\overline{\mathbf{D}}^{(2)} = \overline{\mathbf{D}}_{[1]}^{(2)}$ and $\overline{\mathbf{W}}^{(2)} = \overline{\mathbf{W}}_{[1]}^{(2)}$).

Then, the average stress, strain-rate and spin fields over the matrix phase of the level-i LCC can be easily obtained from the global average conditions:

$$\overline{\boldsymbol{\sigma}}_{[i]}^{(1)} = \frac{1}{1 - c_{[i]}^{(2)}}\left(\overline{\boldsymbol{\sigma}}_{[i]} - c_{[i]}^{(2)}\overline{\boldsymbol{\sigma}}_{[i]}^{(2)}\right), \quad \overline{\mathbf{D}}_{[i]}^{(1)} = \frac{1}{1 - c_{[i]}^{(2)}}\left(\overline{\mathbf{D}}_{[i]} - c_{[i]}^{(2)}\overline{\mathbf{D}}_{[i]}^{(2)}\right),$$
$$\overline{\mathbf{W}}_{[i]}^{(1)} = \frac{1}{1 - c_{[i]}^{(2)}}\left(\overline{\mathbf{W}}_{[i]} - c_{[i]}^{(2)}\overline{\mathbf{W}}_{[i]}^{(2)}\right), \quad i = 1, ..., I. \tag{6.110}$$

At this stage, it is important to note that we have obtained the field statistics in the inclusion (phase 2) and matrix (phase 1) of the LCC at each iteration. Next, we determine, at each iteration, the field statistics in the single-crystal phases ($r = 1, ..., N$) underlying the polycrystalline matrix.

The first moment of the stress field in the rth single-crystal phase in the level-i

polycrystalline matrix can be determined by means of equation (6.78), i.e.,

$$\overline{\boldsymbol{\sigma}}_{[i]}^{(1,r)} = \mathbb{B}_{[i]}^{(1,r)}\overline{\boldsymbol{\sigma}}_{[i]}^{(1)} + \mathbf{b}_{[i]}^{(1,r)}. \tag{6.111}$$

As already discussed at the beginning of Appendix III, the stress-concentration tensors $\mathbb{B}_{[i]}^{(1,r)}$ and $\mathbf{b}_{[i]}^{(1,r)}$ in (6.111) for the rth single-crystal phase at the ith iteration are given by expressions similar to (6.58), with the quantities $\mathbb{M}^{(1)}$, $\boldsymbol{\eta}^{(1)}$, $\boldsymbol{\eta}^{(1,r)}$ and $\mathbb{Q}^{(1)}$ in (6.58) replaced by the corresponding quantities $\mathbb{M}_{[i]}^{(1)}$, $\boldsymbol{\eta}_{[i]}^{(1)}$, $\boldsymbol{\eta}_{[i]}^{(1,r)}$ and $\mathbb{Q}_{[i]}^{(1)}$, respectively, at the ith iteration. Similarly, the corresponding second moment of the stress field may be obtained by means of equation (6.80), i.e.,

$$\langle\boldsymbol{\sigma}\otimes\boldsymbol{\sigma}\rangle_{[i]}^{(1,r)} = \frac{1}{c_{[i]}^{(1,r)}}\left(\frac{\partial\mathbb{M}_{[i]}^{(1)}}{\partial\mathbb{M}_{[i]}^{(1,r)}}\cdot\langle\boldsymbol{\sigma}\otimes\boldsymbol{\sigma}\rangle_{[i]}^{(1)} + 2\frac{\partial\boldsymbol{\eta}_{[i]}^{(1)}}{\partial\mathbb{M}_{[i]}^{(1,r)}}\cdot\overline{\boldsymbol{\sigma}}_{[i]}^{(1)} + \frac{\partial g_{[i]}^{(1)}}{\partial\mathbb{M}_{[i]}^{(1,r)}}\right), \tag{6.112}$$

where it is recalled that $\langle\boldsymbol{\sigma}\otimes\boldsymbol{\sigma}\rangle_{[i]}^{(1)}$ is given by (6.99), and the computation of the derivatives in (6.112) has been discussed in detail in Appendix 3 of Liu (2003).

Making use of the linear constitutive relations of the single-crystal phases in the LCC, together with equation (6.34) and (6.36)-(6.39), the average strain rate over the rth single-crystal phase in the i-level polycrystalline matrix can be written as

$$\begin{aligned}\overline{\mathbf{D}}_{[i]}^{(1,r)} &= \mathbb{M}_{[i]}^{(1,r)}\overline{\boldsymbol{\sigma}}_{[i]}^{(1,r)} + \boldsymbol{\eta}_{[i]}^{(1,r)} = \sum_{k=1}^{K}\left(\frac{1}{2\mu_{[i]}^{(r,k)}}\overline{\tau}_{[i]}^{(r,k)} + \eta_{[i]}^{(r,k)}\right)\boldsymbol{\mu}_{(k)}^{(r)} \\ &= \sum_{k=1}^{K}\left[\alpha_{(k)}^{(r)}\phi_{(k)}^{(r)\prime}(\check{\tau}_{[i]}^{(r,k)}) + (1-\alpha_{(k)}^{(r)})\phi_{(k)}^{(r)\prime}(\hat{\tau}_{[i]}^{(r,k)})\right]\boldsymbol{\mu}_{(k)}^{(r)}.\end{aligned} \tag{6.113}$$

Then, the average strain-rate field over the rth single-crystal phase in the entire I-level LCC (with contributions from all iterations) can be straightforwardly obtained from the weighted average of $\overline{\mathbf{D}}_{[i]}^{(1,r)}$ in (6.113), i.e.,

$$\overline{\mathbf{D}}^{(1,r)} = \sum_{i=1}^{I}\frac{c_{[i]}^{m}}{1-f}\overline{\mathbf{D}}_{[i]}^{(1,r)}, \tag{6.114}$$

where the $c_{[i]}^{m}$ $(i = 1, ..., I)$ are the *total* volume fraction of the level-i polycrystalline

matrix over the entire level-I composite, as given by

$$c^m_{[i]} = \left(\prod_{j=i+1}^{I} c^{(2)}_{[j]}\right)\left(1 - c^{(2)}_{[i]}\right). \tag{6.115}$$

Making use of equation (6.113) and (6.114), it follows that the average slip rates $\overline{\gamma}^{(r)}_{(k)}$ over slip system k in single-crystal phase r, as defined in (6.27), are given by equation

$$\overline{\gamma}^{(r)}_{(k)} = \frac{1}{1-f}\left[\alpha^{(r)}_{(k)} \sum_{i=1}^{I}\left(c^m_{[i]}\phi^{(r)'}_{(k)}(\check{\tau}^{(r,k)}_{[i]})\right) + \left(1 - \alpha^{(r)}_{(k)}\right)\sum_{i=1}^{I}\left(c^m_{[i]}\phi^{(r)'}_{(k)}(\hat{\tau}^{(r,k)}_{[i]})\right)\right]. \tag{6.116}$$

The average spin field $\overline{\mathbf{W}}^{(1,r)}_{[i]}$ over the rth single-crystal phase in the level-i polycrystalline matrix is given by an expression similar to (6.82), that is,

$$\overline{\mathbf{W}}^{(1,r)}_{[i]} = \overline{\mathbf{W}}^{(1)}_{[i]} - \mathbb{R}^{(1)}_{[i]}\left(\mathbb{P}^{(1)}_{[i]}\right)^{-1}\left(\overline{\mathbf{D}}^{(1)}_{[i]} - \overline{\mathbf{D}}^{(1,r)}_{[i]}\right), \tag{6.117}$$

where $\mathbb{R}^{(1)}_{[i]}$ and $\mathbb{P}^{(1)}_{[i]}$ are fourth-order microstructural tensors depending on the matrix property $\mathbb{M}^{(1)}_{[i]}$ and the grain morphology, and are given by expressions similar to those for $\mathbb{R}^{(1)}$ and $\mathbb{P}^{(1)}$, respectively, in Appendix I. Recall that $\overline{\mathbf{W}}^{(1)}_{[i]}$ and $\overline{\mathbf{D}}^{(1)}_{[i]}$ are given by $(6.110)_3$ and $(6.110)_2$, respectively. Similarly, the average spin field over the rth single-crystal phase in the entire I-level LCC can be obtained from the weighted average of $\overline{\mathbf{W}}^{(1,r)}_{[i]}$ in (6.117), namely

$$\overline{\mathbf{W}}^{(1,r)} = \sum_{i=1}^{I} \frac{c^m_{[i]}}{1-f}\overline{\mathbf{W}}^{(1,r)}_{[i]}. \tag{6.118}$$

6.9 Appendix IV: Numerical Implementation of the ISO model

In this Appendix, we provide details on the numerical implementation of the ISO model. The ISO model consists of two main ingredients: (i) the determination of the instantaneous response of the porous polycrystal, as characterized by the effective stress potential (6.35), for given fixed values of the sub-structural variables (6.8), and

(ii) the prediction of the evolution of the sub-structural variables (6.8) in large deformations. For part (ii), the sub-structural variables (6.8) can be updated by means of straightforward numerical integration of the evolution laws (6.45)-(6.47), and (6.49)-(6.51). In this work, the explicit forward-Euler integration scheme is used, as adopted by Aravas and Ponte Castañeda (2004) and Danas and Ponte Castañeda (2009a) in the context of porous materials with isotropic matrix. Since the numerical integration of the evolution laws has been discussed thoroughly in the above references, we will not provide further details here for brevity. In the following, we will focus on part (i) of the ISO model.

As already mentioned in section 6.3.2, the computation of the ISO estimates (6.35) requires the solution of a set of $4 \times N \times K \times I$ nonlinear algebraic equations (6.36), (6.37) and (6.39) for the unknown variables $\check{\tau}_{[i]}^{(r,k)}$ $(N \times K \times I)$, $\hat{\tau}_{[i]}^{(r,k)}$ $(N \times K \times I)$, $\mu_{[i]}^{(r,k)}$ $(N \times K \times I)$ and $\eta_{[i]}^{(r,k)}$ $(N \times K \times I)$, where it is recalled that the first two sets of unknowns are stress variables depending on the first and second moments of the stress field in the LCC, while the last two sets of unknowns correspond to the properties (i.e., slip viscosities and slip eigenstrain rates) of the LCC. Here the stress variables $\check{\tau}_{[i]}^{(r,k)}$ and $\hat{\tau}_{[i]}^{(r,k)}$ are chosen to be the primary unknowns, while the slip viscosities $\mu_{[i]}^{(r,k)}$ and slip eigenstrain rates $\eta_{[i]}^{(r,k)}$ are taken to be functions of the primary unknowns, as given by (6.39). (Note that it is also possible to choose $\mu_{[i]}^{(r,k)}$ and $\eta_{[i]}^{(r,k)}$ to be the primary unknowns, but this choice is found to be numerically less stable.) Thus, the original problem is reduced to the solution of $2 \times N \times K \times I$ nonlinear algebraic equations, as given by (6.36) and (6.37), for an equal amount of primary unknowns $\check{\tau}_{[i]}^{(r,k)}$ and $\hat{\tau}_{[i]}^{(r,k)}$. The above equations can be efficiently solved by means of the *fixed-point method* as follows.

1. Given the macroscopic stress $\overline{\boldsymbol{\sigma}}$, the initial guesses for the primary unknowns $\check{\tau}_{[i]}^{(r,k)}$ and $\hat{\tau}_{[i]}^{(r,k)}$ $(i = 1, ..., I;\ r = 1, ..., N;\ k = 1, ..., K)$ are assumed. Here we use the symbols $\left(\check{\tau}_{[i]}^{(r,k)}\right)_j$ and $\left(\hat{\tau}_{[i]}^{(r,k)}\right)_j$ to denote the current guesses for the primary unknowns at the jth fixed-point loop, where $j = 1$ for the initial guesses.

2. With the current guesses $\left(\check{\tau}_{[i]}^{(r,k)}\right)_j$ and $\left(\hat{\tau}_{[i]}^{(r,k)}\right)_j$ for the primary unknowns, the

slip viscosities $\mu_{[i]}^{(r,k)}$ and slip eigenstrain rates $\eta_{[i]}^{(r,k)}$ ($i = 1, ..., I$; $r = 1, ..., N$; $k = 1, ..., K$) are determined by means of (6.39), and the viscous compliance tensor $\mathbb{M}_{[i]}^{(1,r)}$ and viscous eigenstrain rate tensor $\boldsymbol{\eta}_{[i]}^{(1,r)}$ ($i = 1, ..., I$; $r = 1, ..., N$) are computed by means of (6.34) for each single-crystal phase in the polycrystalline matrix at each iteration.

3. The effective viscous compliance tensor $\mathbb{M}_{[i]}^{(1)}$, effective eigenstrain rate tensor $\boldsymbol{\eta}_{[i]}^{(1)}$, effective energy at zero applied stress $g_{[i]}^{(1)}$, and the corresponding stress-concentration tensors $\mathbb{B}_{[i]}^{(1,r)}$ and $\mathbf{b}_{[i]}^{(1,r)}$ ($i = 1, ..., I$; $r = 1, ..., N$) are computed for the polycrystalline matrix at each iteration, by means of equation (6.55)-(6.58), where the quantities in (6.55)-(6.58) should be replaced by the corresponding quantities at the ith iteration, as already discussed at the beginning of Appendix III.

4. The derivatives of the effective properties of the polycrystalline matrix, $\frac{\partial \mathbb{M}_{[i]}^{(1)}}{\partial \mathbb{M}_{[i]}^{(1,r)}}$, $\frac{\partial \boldsymbol{\eta}_{[i]}^{(1)}}{\partial \mathbb{M}_{[i]}^{(1,r)}}$, and $\frac{\partial g_{[i]}^{(1)}}{\partial \mathbb{M}_{[i]}^{(1,r)}}$, are computed for each iteration and each single-crystal phase ($i = 1, ..., I$; $r = 1, ..., N$). Detailed formulations for computing these derivatives are provided in Appendix 3 of Liu (2003), and will not be repeated here for brevity.

5. The effective compliance tensor $\widetilde{\mathbb{M}}_{[i]}$, the effective eigenstrain rate tensor $\widetilde{\boldsymbol{\eta}}_{[i]}$, as well as the corresponding stress-concentration tensors $\mathbb{B}_{[i]}^{(2)}$ and $\mathbf{b}_{[i]}^{(2)}$ ($i = 1, ..., N$), for the LCC at each iteration are computed by means of equations (6.90)-(6.92) and (6.94).

6. The first and second moments of the stress field over the polycrystalline matrix (phase 1) at each iteration, $\overline{\boldsymbol{\sigma}}_{[i]}^{(1)}$ and $\langle \boldsymbol{\sigma} \otimes \boldsymbol{\sigma} \rangle_{[i]}^{(1)}$ ($i = 1, ..., I$), are computed by means of (6.96), (6.97), (6.99) and $(6.110)_1$.

7. The first and second moments of the stress field over the rth single-crystal phase in the polycrystalline matrix at each iteration, $\overline{\boldsymbol{\sigma}}_{[i]}^{(1,r)}$ and $\langle \boldsymbol{\sigma} \otimes \boldsymbol{\sigma} \rangle_{[i]}^{(1,r)}$ ($i = 1, ..., I$; $r = 1, ..., N$), are computed by means of equation (6.111) and (6.112),

respectively. Then, the first and second moments of the resolved shear stress $\overline{\tau}_{[i]}^{(r,k)}$ and $\overline{\overline{\tau}}_{[i]}^{(r,k)}$ $(i = 1, ..., I;\ r = 1, ..., N;\ k = 1, ..., K)$ are computed by means of equation (6.38).

8. The new estimations for the primary unknowns, $\left(\check{\tau}_{[i]}^{(r,k)}\right)_{\text{new}}$ and $\left(\hat{\tau}_{[i]}^{(r,k)}\right)_{\text{new}}$, are computed by means of (6.36) and (6.37), respectively.

9. The sum of the magnitudes of the relative errors between the new estimations and old guesses for the primary unknowns are computed. If the error is smaller than a prescribed tolerance (typically 10^{-8}), convergence is reached. If not, the guesses for the primary unknowns are updated by means of a 'partial' update scheme:

$$\begin{aligned}\left(\check{\tau}_{[i]}^{(r,k)}\right)_{j+1} &= (1-\beta)\left(\check{\tau}_{[i]}^{(r,k)}\right)_{j} + \beta\left(\check{\tau}_{[i]}^{(r,k)}\right)_{\text{new}},\\ \left(\hat{\tau}_{[i]}^{(r,k)}\right)_{j+1} &= (1-\beta)\left(\hat{\tau}_{[i]}^{(r,k)}\right)_{j} + \beta\left(\hat{\tau}_{[i]}^{(r,k)}\right)_{\text{new}},\end{aligned} \tag{6.119}$$

where β $(0 < \beta \leq 1)$ is a weight factor that controls the fraction of the solutions that are updated in each fixed-point loop. (Note that the standard fixed-point method corresponds to $\beta = 1$.) It should be emphasized that, for the cases of high nonlinearities, a relatively small value of β should be used in order to achieve smooth convergence. In this work, $\beta = 1/3$ is used for nonlinearities $n \leq 3$, while $\beta = 1/8$ is used for $n > 3$. Then, steps 2-9 are repeated until convergence is reached.

Finally, it should be remarked that the ISO model requires the computation of fourth-order microstructural tensors and their derivatives (e.g., $\mathbb{Q}_{[i]}$ and $\partial\mathbb{Q}_{[i]}/\partial\mathbb{M}_{[i]}^{(1)}$), whose components are two-dimensional integrals that need to be evaluated numerically in general. In this work, a two-dimensional Gaussian quadrature integration scheme is adopted to compute these integrals in spherical coordinate systems. In particular, when the polycrystalline matrix phase $\mathbb{M}_{[i]}^{(1)}$ is strongly anisotropic, or when the shape tensors $\boldsymbol{Z}^p$ or $\boldsymbol{Z}^d$ are very different from the identity tensor, a relatively large number of Gaussian points is required to guarantee the accuracy of these inte-

grals. In the next chapter, 200 Gaussian points are used for each integration direction, which are found to be sufficient to generate accurate results.

Chapter 7

Iterated second-order homogenization model for viscoplastic porous polycrystals with large voids: Applications

In chapter 6 of this work, a new homogenization model was developed for the macroscopic behavior of the two-scale porous polycrystals consisting of large pores distributed in a fine-scale polycrystalline matrix. In this chapter, the model is used to investigate both the instantaneous effective behavior and the finite-strain macroscopic response of porous FCC and HCP polycrystals for axisymmetric loading conditions. The stress triaxiality and Lode parameter are found to have significant effects on the evolution of the sub-structure, which in turn have important implications on the overall hardening/softening behavior of the porous polycrystal. The intrinsic effect of the texture evolution of the polycrystalline matrix is deduced by comparing with corresponding results for porous isotropic materials, and found to be significant. In particular, it is found that the macroscopic behavior of the porous polycrystal is controlled by porosity growth at high triaxialities, while it is controlled by texture evolution of the matrix at low triaxialities, with a sharp transition between the poros-

ity controlled regime and texture controlled regime.

7.1 Introduction

In chapter 6, we have proposed a finite-strain model for the macroscopic behavior of two-scale porous polycrystals containing large pores distributed in a fine-scale polycrystalline matrix. The model is based on the fully optimized second-order (FOSO) method of Ponte Castañeda (2015) used in incremental fashion (Agoras and Ponte Castañeda, 2013), and is referred to as the Iterated Second-order (ISO) model. The ISO model consists of two main ingredients: (i) the determination of the instantaneous response of the porous polycrystals for fixed values of the sub-structural variables, and (ii) the prediction of the evolution of the sub-structural variables at finite strains.

In this model, the sub-structural variables characterizing the two-scale structure of the porous polycrystals are given by the set

$$\mathbf{s} \equiv \{f, w_1^p, w_2^p, \mathbf{G}^p; \mathbf{Q}^{(1,r)}, w_1^g, w_2^g, \mathbf{G}^g\}. \tag{7.1}$$

Here f is the volume fraction of the pores (porosity), $w_1^p = a_3^p/a_1^p$, and $w_2^p = a_3^p/a_2^p$ are the two aspect ratios of the representative ellipsoids characterizing the shape (and distribution) of the pores (a_1^p, a_2^p and a_3^p are the lengths of the three semi-axes of the ellipsoid), $\mathbf{G}^p$ is a second-order rotation tensor characterizing the principal axes of the pores relative to the sample axes (see Fig. 6.1 in chapter 6). In addition, $\mathbf{Q}^{(1,r)}$ ($r = 1, ..., N$) is a rotation tensor describing the crystallographic orientation of the rth single-crystal phase in the polycrystalline matrix, $w_1^g = a_3^g/a_1^g$ and $w_2^g = a_3^g/a_2^g$ are two aspect ratios characterizing the average ellipsoidal shape of the crystal grains (a_1^g, a_2^g and a_3^g are the lengths of the three semi-axes of the grain ellipsoid), and $\mathbf{G}^g$ is a second-order rotation tensor describing the principal directions of the ellipsoidal grains relative to the sample axes. Among the above sub-structural variables (7.1), the first four variables (f, w_1^p, w_2^p, and $\mathbf{G}^p$) describe the porous meso-structure of the composite (see Fig. 6.1 (a) of chapter 6), while the remaining variables characterize

the underlying micro-structure of the polycrystalline matrix (see Fig. 6.1 (b) of chapter 6).

The ISO model makes use of the effective behavior of a suitably chosen two-scale linear comparison composite (LCC)—with sub-structure identical to that of the nonlinear porous polycrystal of interest—to estimate the effective behavior of the nonlinear composite. In particular, the two-scale homogenization problem for the LCC is decomposed into two single-scale problems for the associated meso- and micro-structure, so that the effective behavior of the LCC can be determined by means of a two-step sequential homogenization approach. At the micro-scale, the effective properties of the linear polycrystalline matrix are determined by means of the self-consistent estimates (Hershey, 1954; Kröner, 1958; Willis, 1977), while at the meso-scale, the effective properties of the porous LCC are obtained by means of the estimates of the Ponte Castañeda and Willis (1995) type. In addition, the iterated homogenization procedure of Agoras and Ponte Castañeda (2013) is used to "discretize" the polycrystalline matrix, in such a way that *non-uniform* properties of the polycrystalline matrix are used for the LCC, thereby generating improved estimates for the effective behavior of the nonlinear porous polycrystal, especially for low porosities and high stress triaxialities. Furthermore, consistent homogenization estimates for the strain-rate and spin fields in the pores and grains are used to develop evolution equations for the sub-structural variables (7.1), characterizing the evolution of the size, shape and orientation of the pores (at the meso-scale), as well as of the morphological and crystallographic texture of the polycrystalline matrix (at the micro-scale).

In this chapter, we consider specific applications of the ISO model for two different types of porous polycrystals, including the porous (high-symmetry) FCC polycrystals in section 7.2 and porous (low-symmetry) HCP polycrystals in section 7.3. In each section, we examine the instantaneous effective behavior of the porous polycrystals for fixed states of the sub-structure, as well as the finite-strain macroscopic response of the porous polycrystals with evolving sub-structures, under axisymmetric loading conditions for different stress triaxialities and Lode parameters. The effect of

the loading conditions on the sub-structure evolution, field statistics, and the overall hardening/softening behavior of the porous polycrystals is investigated in detail. In addition, the intrinsic effect of the texture evolution for the polycrystalline matrix is deduced by comparing with the corresponding results for the porous isotropic materials. Finally, some general conclusions will be drawn in section 7.4.

7.2 Applications to porous FCC polycrystals

In this section, we employ the ISO model to study the instantaneous effective properties and finite-strain response of porous FCC polycrystals. The corresponding results generated by the IVAR model will also be included for comparison purposes.

For FCC single crystals, the deformation takes place through slip on a set of four slip planes of the type $\{111\}$ along three slip directions (per plane) of the type $\langle 110\rangle$, which constitute the 12 octahedral slip systems. Of these, five are linearly independent, thus allowing arbitrary plastic deformation for the single-crystal grains. For simplicity, all slip systems are assumed to be non-hardening with the same reference flow stresses, i.e., $(\tau_0)_{(k)} = \tau_0$ $(k = 1, ..., 12)$. In addition, the reference strain rate $\dot{\gamma}_0$ and the creep exponent n are also assumed to be identical for all slip systems.

7.2.1 Instantaneous effective response

In this subsection, we make use of the ISO model to generate estimates for the instantaneous effective behavior of porous FCC polycrystals for fixed states of the sub-structure. For simplicity, the FCC polycrystalline matrix is taken here to be *untextured*, with "equiaxed" $(w_1^g = w_2^g = 1)$ single-crystal grains and *uniformly distributed* crystallographic orientations, such that the polycrystalline matrix exhibits an overall isotropic behavior.

For later use, we briefly recall the definition of *gauge surface* (Leblond et al., 1994). Given that the viscous exponent n is identical for all the available slip systems in the polycrystalline matrix, it can be shown (Ponte Castañeda and Suquet, 1998) that the effective stress potential $\widetilde{u}$ is a homogeneous function of degree $n+1$ on the

macroscopic stress $\overline{\boldsymbol{\sigma}}$, so that it can be expressed in the form

$$\widetilde{u}(\overline{\boldsymbol{\sigma}}) = \frac{\dot{\gamma}_0 \sigma_0}{n+1} \left(\frac{\Gamma(\overline{\boldsymbol{\sigma}})}{\sigma_0} \right)^{n+1}, \tag{7.2}$$

where σ_0 is a reference stress that will be defined later, and $\Gamma(\overline{\boldsymbol{\sigma}})$ is the gauge factor, which depends on the sub-structural variables (7.1) of the composite and on the material parameters n and $(\tau_0)_{(k)}$. Noting that $\Gamma(\overline{\boldsymbol{\sigma}})$ is homogeneous of degree one in $\overline{\boldsymbol{\sigma}}$, it can be easily shown that the normalized tensor

$$\overline{\boldsymbol{\Sigma}}(\overline{\boldsymbol{\sigma}}) = \frac{\overline{\boldsymbol{\sigma}}}{\Gamma(\overline{\boldsymbol{\sigma}})} \tag{7.3}$$

always lies on an equi-potential surface

$$\widetilde{u}(\overline{\boldsymbol{\Sigma}}) = \frac{\dot{\gamma}_0 \sigma_0^{-n}}{n+1}, \tag{7.4}$$

which is defined to be the *gauge surface*. Thus, we can determine the gauge surface by computing the effective stress potential $\widetilde{u}$ for $\overline{\boldsymbol{\sigma}}$ of an arbitrary magnitude, determining the corresponding gauge factor $\Gamma(\overline{\boldsymbol{\sigma}})$ from (7.2), and then normalizing $\overline{\boldsymbol{\sigma}}$ according to (7.3). Note that in the ideally plastic limit ($n \to \infty$), the gauge surface (7.4) tends to the standard yield surface. Note further that the normal to the gauge surface dictates the direction of the induced macroscopic plastic flow.

Noting that a porous untextured polycrystal is effectively a two-phase porous material with a homogeneous isotropic matrix, it is of interest to compare the new results with the corresponding results for a porous von Mises solid. For this purpose, we choose the reference flow stress σ_0 in (7.4) to be the effective flow stress $\tilde{\sigma}_0$ of the corresponding *untextured* fully dense polycrystal. Recall that the effective flow stress $\widetilde{\sigma}_0$ is defined by the relation

$$\widetilde{u}(\overline{\boldsymbol{\sigma}}) = \frac{\dot{\gamma}_0 \widetilde{\sigma}_0(L)}{n+1} \left(\frac{\overline{\sigma}_e}{\widetilde{\sigma}_0(L)} \right)^{n+1}, \tag{7.5}$$

where $\overline{\sigma}_e = \sqrt{3/2 \overline{\boldsymbol{\sigma}}' \cdot \overline{\boldsymbol{\sigma}}'}$ is the von Mises equivalent stress ($\overline{\boldsymbol{\sigma}}'$ is the deviatoric stress

tensor), and L ($-1 \le L \le 1$) is the Lode parameter defined by

$$L = \frac{2\overline{\sigma}_{II} - \overline{\sigma}_I - \overline{\sigma}_{III}}{\overline{\sigma}_I - \overline{\sigma}_{III}}, \tag{7.6}$$

where $\overline{\sigma}_I \ge \overline{\sigma}_{II} \ge \overline{\sigma}_{III}$ are the (ordered) principal stresses. Note that L is related to the third invariant of the macroscopic stress tensor, and characterizes the type of shear in the deviatoric space. In particular, $L = -1$ (or 1) corresponds to axisymmetric shear, with the maximum (or minimum) principal stress aligned with the symmetry axis, while $L = 0$ corresponds to simple shear. The symbol $\widetilde{\sigma}_0(L)$ in (7.5) is used to emphasize that the effective flow stress $\tilde{\sigma}_0$ is *not* a constant, but depends on the Lode parameter L (see, e.g., Ponte Castañeda and Suquet, 1998). In the following, the reference stress in (7.4) is taken to be $\sigma_0 = \widetilde{\sigma}_0(-1) = \widetilde{\sigma}_0(1)$, corresponding to the effective flow stress of the fully dense polycrystal under axisymmetric shear. For brevity, we will simply use $\widetilde{\sigma}_0^*$ to denote the above effective flow stress. In general, the exact results of $\widetilde{\sigma}_0^*$ are not available, and we will make use of the fully optimized second-order (FOSO) method of Ponte Castañeda (2015) to obtain estimates of the self-consistent type for $\widetilde{\sigma}_0^*$ (see below).

In this work, we confine our attention to *axisymmetric* loadings ($L = \pm 1$) with the symmetry axis aligned with $\mathbf{e}_3$, so that we can write the macroscopic stress tensor $\overline{\boldsymbol{\sigma}}$ as

$$\overline{\boldsymbol{\sigma}} = \overline{\sigma}_m \mathbf{I} + \overline{\sigma}_e \left(\frac{1}{3} L \mathbf{e}_1 \otimes \mathbf{e}_1 + \frac{1}{3} L \mathbf{e}_2 \otimes \mathbf{e}_2 - \frac{2}{3} L \mathbf{e}_3 \otimes \mathbf{e}_3 \right), \tag{7.7}$$

where $\overline{\sigma}_m = \mathrm{tr}(\overline{\boldsymbol{\sigma}})/3$ is the mean stress. Note that loading (7.7) with $L = -1$ corresponds to axisymmetric tension ($\overline{\sigma}_{11} = \overline{\sigma}_{22} \le \overline{\sigma}_{33}$), while loading (7.7) with $L = 1$ corresponds to axisymmetric compression ($\overline{\sigma}_{11} = \overline{\sigma}_{22} \ge \overline{\sigma}_{33}$). The corresponding normalized stress tensor $\overline{\boldsymbol{\Sigma}}$, as defined by (7.3), may be written in a form completely analogous to (7.7), with $\overline{\sigma}_m$ and $\overline{\sigma}_e$ replaced by the corresponding normalized quantities $\overline{\Sigma}_m$ and $\overline{\Sigma}_e$, respectively. Note that $\overline{\boldsymbol{\Sigma}}$ is proportional to $\overline{\boldsymbol{\sigma}}$, but has a generally different magnitude. We define the stress triaxiality to be

$$X_\Sigma = \overline{\Sigma}_m / \overline{\Sigma}_e = X_\sigma = \overline{\sigma}_m / \overline{\sigma}_e. \tag{7.8}$$

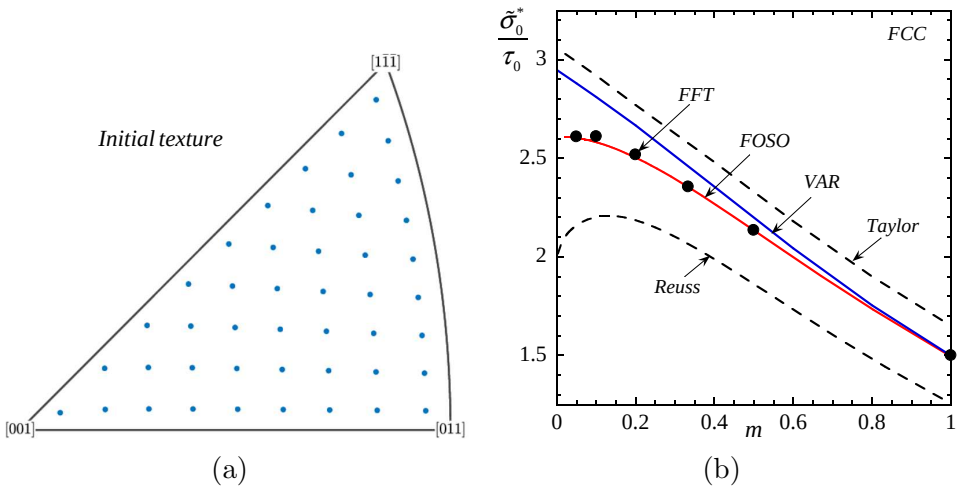

Figure 7.1: (a) Inverse pole figure of the isotropic texture of the FCC polycrystal (matrix), using 45 equally weighted and uniformly distributed orientations in a stereographic triangle. (b) Effective flow stress $\widetilde{\sigma}_0^*$, normalized by the slip stress τ_0, for untextured fully dense FCC polycrystals subjected to axisymmetric shear, as functions of the rate sensitivity $m = 1/n$.

At this point, it should be recalled that the ISO model requires solving a set of nonlinear equations with the total number of unknowns proportional to the total number of slip systems. For this reason, it is of great interest to use as few crystallographic orientations as possible to represent the texture of the polycrystalline matrix. Provided that the crystallographic texture of the polycrystalline matrix is isotropic, and that the loading condition (7.7) is axisymmetric, it is possible to consider a reduced number of orientations on a spherical triangle (Nebozhyn, 2000; Van Houtte and Aernoudt, 1976). In this work, we make use of 45 *equally weighted* orientations on an appropriate spherical triangle, as shown in the *inverse pole figure* in Fig. 7.1(a), where the loading axis $\mathbf{e}_3$ is plotted in terms of the local crystal axes of different single-crystal grains in the polycrystal. Therefore, various points in the spherical triangle of Fig. 7.1(a) denotes the direction of the loading axis $\mathbf{e}_3$ as seen from the local crystal axes. Moreover, equal-area projection is used in Fig. 7.1(a) and in all inverse pole figures shown in this chapter. Contributions from the orientations outside of this triangle are taken into account by proper symmetrization of the averages over the triangle (Nebozhyn, 2000), making use of the symmetry of the crystal and loading. Note that the above choice of crystallographic orientations has

been found to be sufficient to obtain accurate estimates for the effective flow stress and field statistics in untextured fully dense FCC polycrystals (e.g., Liu and Ponte Castañeda, 2004a).

Next, we make use of the FOSO method of Ponte Castañeda (2015) to compute the estimates of the self-consistent type for the effective flow stress $\widetilde{\sigma}_0^*$ for untextured FCC polycrystals, under axisymmetric shear stress (7.7) with $\overline{\sigma}_m = 0$. (Note that the results are the same for $L = -1$ and 1). Fig. 7.1(b) shows the FOSO estimates of $\widetilde{\sigma}_0^*$, normalized by the reference flow stress τ_0 for each slip system, for different rate-sensitivity exponents $m = 1/n$ ranging from 1 (linearly viscous) to 0 (ideally plastic limit). For comparison purposes, the corresponding results are also included for the Taylor upper bounds, Reuss lower bounds, variational (VAR) upper bounds of the self-consistent type (Nebozhyn et al., 2001), as well as the full-field FFT results (Lebensohn et al., 2007). The main observation in the context of Fig. 7.1(b) is that the FOSO estimates of the self-consistent type are in excellent agreement with the FFT results for the entire range of m. Moreover, the FOSO results lie between the VAR (and Taylor) upper bounds and Reuss lower bounds for all values of m. Although the VAR bounds are much tighter than the Taylor bounds, they still overestimate the FFT results, especially for low rate sensitivities. In particular, for $n = 5$ the VAR bounds are approximately 6% larger than the FOSO and FFT results. Given that we have full access to the FOSO self-consistent estimates, and that the FOSO estimates for the effective flow stress of solid polycrystals are in excellent agreement with numerical results available in the literature (see also Song and Ponte Castañeda, 2017d), we will make use of the FOSO method to compute the self-consistent estimates for the effective flow stress $\widetilde{\sigma}_0^*$ for all the isotropic solid polycrystals involved in this work.

In the following, we investigate the effective properties of porous FCC polycrystals by means of gauge surfaces, as defined by (7.4). More specifically, we present results for the gauge surfaces computed by means of the ISO and IVAR method developed in chapter 6. It should be recalled that both methods make use of the effective behavior of a linear comparison composite (LCC)—with the same two-scale sub-structure as

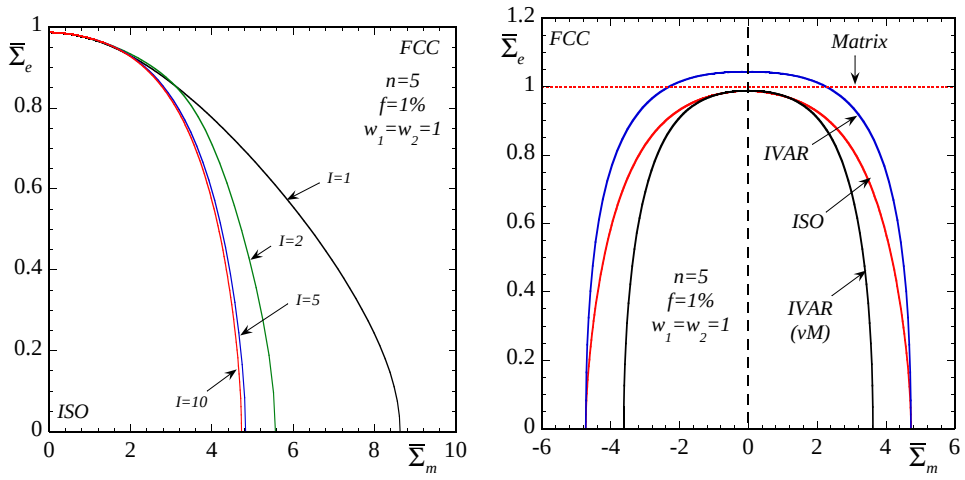

Figure 7.2: The $\overline{\Sigma}_m$-$\overline{\Sigma}_e$ cross sections of the ISO gauge surfaces for the porous untextured FCC polycrystals ($n = 5$) with porosity $f = 1\%$ and spherical pores ($w_1^p = w_2^p = 1$), subjected to axisymmetric loadings (7.7) with $L = -1$ ($\overline{\sigma}_{11} = \overline{\sigma}_{22} \leq \overline{\sigma}_{33}$). (a) The effect of the iteration number I on the ISO gauge surfaces, where different values of I are considered ($I = 1, 2, 5, 10$). (b) Comparison of the ISO and IVAR gauge surfaces for porous FCC polycrystals, where the corresponding results for a porous von Mises material are also included.

the nonlinear composite of interest—to estimate the effective behavior of the nonlinear porous polycrystal. The effective properties of the two-scale LCC are determined by means of a two-step sequential homogenization approach, where the self-consistent estimates are used to compute the effective response of the linear polycrystalline matrix at the micro-scale, and the PCW estimates (Ponte Castañeda and Willis, 1995) are used to compute the effective properties of the porous LCC at the meso-scale. Note that the properties of the LCC are unknown a priori, and need to be chosen in an optimal fashion according to suitably designed variational principles. In particular, the ISO method makes use of a 'generalized secant' linearization of the nonlinear response, incorporating dependence on both the first and second moments of the stress field in the LCC. On the other hand, the IVAR method makes use of a secant linearization of the nonlinear response, evaluated at the second moment of the stress field. Note that the IVAR estimates for the gauge surfaces are thought to provide outer bounds for the gauge surfaces of the porous polycrystals.

Fig. 7.2 shows the $\overline{\Sigma}_m$-$\overline{\Sigma}_e$ cross sections of the ISO gauge surfaces for a porous

untextured FCC polycrystal with a viscous exponent $n = 5$, porosity $f = 1\%$, and pore aspect ratios $w_1^p = w_2^p = 1$, subjected to axisymmetric loadings (7.7). The above considered porous polycrystal exhibits overall isotropic behavior and, thus, the corresponding gauge surface depends only on the three isotropic invariants of the normalized stress ($\overline{\Sigma}_m$, $\overline{\Sigma}_e$ and L). In general, the gauge surfaces are different for $L = 1$ and $L = -1$. However, it is straightforward to show that the gauge surfaces for $L = 1$ and $L = -1$ are symmetric with respect to the purely deviatoric axis $\overline{\Sigma}_m = 0$. Thus, we will only present results for $L = -1$, keeping in mind that the corresponding results for $L = 1$ may be obtained by flipping the results for $L = -1$ with respect to the deviatoric axis.

Fig. 7.2(a) shows the effect of the iteration number I on the ISO gauge surfaces for the porous FCC polycrystals. The main observation from Fig. 7.2(a) is that the ISO gauge surface becomes progressively tighter with increasing values of I for large triaxialities, tending to a certain limit at sufficiently large values of I. (The ISO gauge surface for $I > 10$ is practically indistinguishable to that for $I = 10$ and, thus, no additional results are shown.) The improvement over the non-iterated FOSO gauge surface ($I = 1$) is found to be quite significant: the hydrostatic strength for the ISO gauge surface with $I = 10$ is nearly half of that for the FOSO gauge surface. On the other hand, the ISO gauge surface is rather insensitive to the iteration number I for small triaxialities, indicating that the FOSO gauge surface ($I = 1$) is already quite accurate. Furthermore, the convergence of the ISO gauge surface with increasing values of I is very fast, so that a relatively small number of iterations ($I = 5 - 10$) is sufficient to achieve most of the improvement. Thus, *all the ISO results presented below for the porous FCC polycrystals are computed for* $I = 10$, which are found to be sufficiently accurate, with error expected to be less than 1% when compared with the corresponding $I \to \infty$ limits (computed numerically for very large values of I).

Fig. 7.2(b) shows the comparison between the ISO and IVAR gauge surfaces for the porous polycrystals. We also include the corresponding IVAR gauge surface (Agoras and Ponte Castañeda, 2013) for a porous von Mises solid with the isotropic matrix characterized by a stress potential completely analogous to (7.5), but with the

effective flow stress $\widetilde{\sigma}_0(L)$ in (7.5) replaced by a *constant* flow stress σ_0^{vM}. In particular, we choose $\sigma_0^{\mathrm{vM}} = \widetilde{\sigma}_0^*$, so that the gauge surface for a fully dense polycrystal or von Mises material is given by the straight line $\overline{\Sigma}_e = 1$. We observe from Fig. 7.2(b) that the ISO gauge surface for the porous polycrystal lies within the corresponding IVAR outer bound for all triaxialities, except for the purely hydrostatic loadings ($X_\Sigma \to \infty$), where the ISO gauge surface coincides with the IVAR bound. Moreover, we can see that the ISO gauge surface always lies within the corresponding gauge surface for the solid FCC polycrystal ($\overline{\Sigma}_e = 1$), as expected on physical grounds. By contrast, the IVAR gauge surface for the porous polycrystal exceeds the surface $\overline{\Sigma}_e = 1$ for the range of the triaxiality $0 \lesssim |X_\Sigma| \lesssim 3$, indicating that the IVAR estimate is too large. Furthermore, we observe that for $0 \lesssim |X_\Sigma| \lesssim 2$, the ISO gauge surface for the porous polycrystal is very similar to the IVAR gauge surface for the porous von Mises solid. However, for large magnitudes of the triaxiality, the ISO gauge surface are somewhat larger than the IVAR (von Mises) gauge surface.

In this connection, it is important to remark that the IVAR (von Mises) gauge surface has been found to be in very good agreement with the full-field, numerical results available in the literature for von Mises matrix materials at all triaxialities (e.g., Agoras and Ponte Castañeda, 2013). The fact that the hydrostatic strength of the porous untextured polycrystal is expected to be similar to that of the porous von Mises solid suggests that the ISO gauge surface in Fig. 7.2(b) may overestimate the effective behavior of the porous FCC polycrystal at high triaxialities. Finally, it should be noted that improved estimates may be obtained by means of the more general FOSO method of Ponte Castañeda (2016) used in an iterated fashion. This more general method involves one less approximation than the method of Ponte Castañeda (2015) for crystalline solids, and is expected to yield improved results, although at the expense of increased implementation complexities. Alternatively, improvements could also be made by using other, yet-to-be-developed choices for the weight factors $\alpha_{(k)}^{(r)}$ in the ISO model. At the very least, the weights could be used as fitting parameters to improve the results for hydrostatic loadings. However, for simplicity, we have chosen not to pursue this strategy in this first application of the method for porous

polycrystals.

7.2.2 Finite-strain macroscopic response

In this subsection, we explore the sub-structure evolution and the finite-strain macroscopic response for porous FCC polycrystals. In particular, we consider a porous FCC polycrystal with an initially random, isotropic distribution of spherical pores ($w_1^p = w_2^p = 1$) in porosity $f_0 = 1\%$. Moreover, the FCC polycrystalline matrix is taken to be initially untextured, with "equiaxed" grains ($w_1^g = w_2^g = 1$) and uniformly distributed crystallographic orientations (see Fig. 7.1(a)). Hardening of the crystal grains is neglected, so that $(\tau_0)_{(k)} = \tau_0$ ($k = 1, ..., 12$) throughout the deformation. In particular, the material parameters are taken to be $\tau_0 = 245$MPa, $\dot{\gamma}_0 = 1.53 \times 10^{-9}\text{s}^{-1}$ and $n = 5$, which are known to be appropriate for Ni-based single crystals (Srivastava and Needleman, 2015). We consider axisymmetric loadings of type (7.7), and $\overline{\boldsymbol{\sigma}}$ is taken to be *fixed* in time. In particular, we set $\overline{\sigma}_e = \tau_0 = 245$MPa, and prescribe the stress triaxiality by setting $\overline{\sigma}_m = X_\sigma \overline{\sigma}_e$. In this subsection, we restrict our attention to uniaxial loading conditions:

(i) Uniaxial tension ($X_\sigma = 1/3$ and $L = -1$), and

(ii) Uniaxial compression ($X_\sigma = -1/3$ and $L = 1$).

Due to the symmetry of the applied loadings and material, the average shapes of the pores and grains evolve from their initially spherical shapes to (generally different) spheroidal shapes ($w_1^p = w_2^p = w^p$, and $w_1^g = w_2^g = w^g$), while the principal axes of the pores and grains remain fixed during the deformation ($\mathbf{G}^p = \mathbf{G}^d = \mathbf{I}$), with the symmetry axes of the pores and grains always aligned with the loading axis $\mathbf{e}_3$. Moreover, the crystallographic texture of the polycrystalline matrix, as characterized by the rotation tensors $\mathbf{Q}^{(1,r)}$ in (7.1), also evolves during the deformation, leading to the development of possibly strong crystallographic anisotropy of the matrix. Furthermore, the resulting macroscopic strain rate $\overline{\mathbf{D}}$ can be shown to be axisymmetric, as given by $\overline{\mathbf{D}} = \overline{D}_p(\mathbf{e}_1 \otimes \mathbf{e}_1 + \mathbf{e}_2 \otimes \mathbf{e}_2) + \overline{D}_n \mathbf{e}_3 \otimes \mathbf{e}_3$, where $\overline{D}_n$ and $\overline{D}_p$ denote, respectively, the strain rate along and transverse to the loading axis $\mathbf{e}_3$. Then, the macroscopic

equivalent strain rate is given by

$$\overline{D}_e = \sqrt{\frac{2}{3}\overline{\mathbf{D}}' \cdot \overline{\mathbf{D}}'} = \frac{2}{3}\left|\overline{D}_n - \overline{D}_p\right|, \tag{7.9}$$

where $\overline{\mathbf{D}}'$ is the macroscopic deviatoric strain rate. For future reference, it is useful to introduce the time-like variable

$$\overline{E}_e = \int_0^t \overline{D}_e dt = \frac{2}{3}\int_0^t \left|\overline{D}_n - \overline{D}_p\right| dt, \tag{7.10}$$

where t denotes time.

Similarly, the macroscopic logarithmic (creep) strain $\overline{\mathbf{E}}^c$ is also axisymmetric, and is provided by

$$\overline{\mathbf{E}}^c = \overline{E}_p^c(\mathbf{e}_1 \otimes \mathbf{e}_1 + \mathbf{e}_2 \otimes \mathbf{e}_2) + \overline{E}_n^c \mathbf{e}_3 \otimes \mathbf{e}_3, \tag{7.11}$$

where $\overline{E}_n^c = \int_0^t \overline{D}_n dt$ and $\overline{E}_p^c = \int_0^t \overline{D}_p dt$ denote, respectively, the creep strain component along and transverse to the symmetry axis $\mathbf{e}_3$. The corresponding macroscopic equivalent strain is given by

$$\overline{E}_e^c = \frac{2}{3}\left|\overline{E}_n^c - \overline{E}_p^c\right| = \frac{2}{3}\left|\int_0^t (\overline{D}_n - \overline{D}_p) dt\right|. \tag{7.12}$$

Note that the macroscopic equivalent creep strain $\overline{E}_e^c$ may increase or decrease with time, while the time-like variable $\overline{E}_e$ is guaranteed to increase monotonically with time (unless $\overline{D}_n = \overline{D}_p$). In particular, when the sign of the term $\left(\overline{D}_n - \overline{D}_p\right)$ remains unchanged throughout the deformation, we have that $\overline{E}_e = \overline{E}_e^c$. In fact, this is found to be the case for most loading conditions considered in this work, except for certain high triaxiality loadings when $\left(\overline{D}_n - \overline{D}_p\right)$ can change sign at very large strains. For this reason, we make use of $\overline{E}_e$ as a time-like variable (and not $\overline{E}_e^c$).

For later use, it is pertinent to define the macroscopic equivalent strain rate $\overline{D}_e^0$ for the corresponding fully dense untextured polycrystal under axisymmetric shear, i.e.,

$$\overline{D}_e^0 = \dot{\gamma}_0 \left(\frac{\overline{\sigma}_e}{\widetilde{\sigma}_0^*}\right)^n, \tag{7.13}$$

where it is recalled that $\widetilde{\sigma}_0^*$ denotes the effective flow stress of the untextured fully dense solid polycrystal under axisymmetric shear, as estimated by the FOSO procedure.

As already mentioned, during the finite-strain deformation of a porous polycrystal, the porosity, pore morphology, as well as the underlying texture of the matrix can evolve (see Fig. 7.3(a)), resulting in contributions to the macroscopic response due to both the geometrical changes in the pores and the texture evolution of the matrix. For this reason, we also consider the case for a porous polycrystal with a *fixed isotropic texture* for the matrix, but still with evolving porosity and void morphology (see Fig. 7.3(b)). In this case, the porous polycrystal is effectively a two-phase porous material with a homogeneous isotropic matrix. Comparisons between the results for a porous polycrystal (Fig. 7.3(a)) and for a porous isotropic material (Fig. 7.3(b)) will allow us to assess the intrinsic effects of the texture evolution for the polycrystalline matrix, as opposed to the effect associated with porosity evolution.

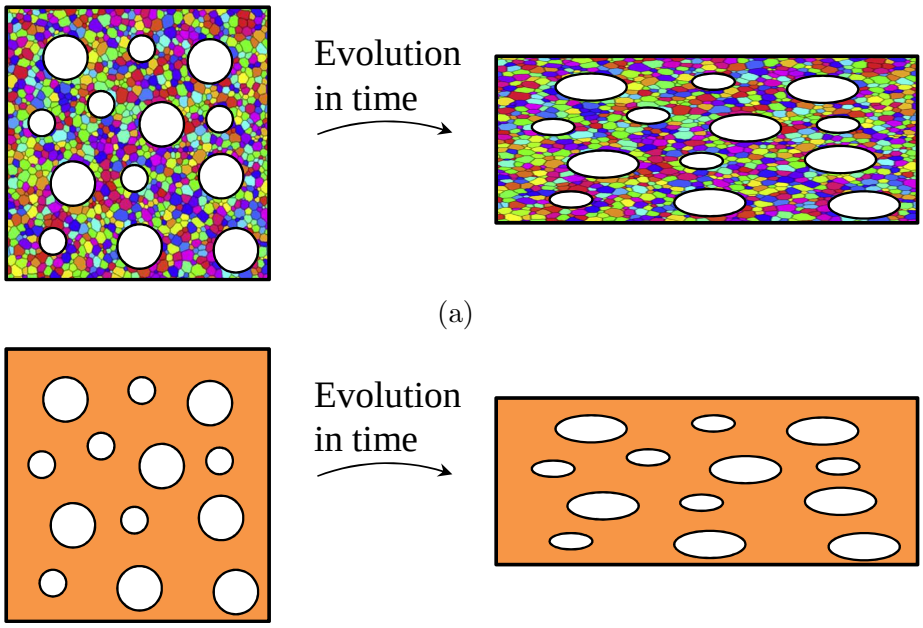

Figure 7.3: Schematic representation of (a) a porous polycrystal with changes in both the pore geometry and the underlying texture for the matrix, and (b) a porous polycrystal with changes in the pore geometry, but with a *fixed isotropic texture* for the matrix. The porous polycrystal in (b) is equivalent to a two-phase porous material with an isotropic matrix phase.

Uniaxial tension

Fig. 7.4 shows the ISO and IVAR results for the evolution of the sub-structure for porous FCC polycrystals subjected to uniaxial tension ($X_\sigma = 1/3$ and $L = -1$). The corresponding results for a porous isotropic material (without texture evolution for the matrix) are also included for comparison. Fig. 7.4(a) presents results for the normalized porosity f/f_0 versus the time-like variable $\overline{E}_e$. We observe from Fig. 7.4(a) that the ISO plot of f/f_0 for a porous FCC polycrystal increases with $\overline{E}_e$ with a progressively slower rate, and saturates at a finite value around 1.39 at sufficiently large strains. Moreover, the ISO results for a porous FCC polycrystal and for a porous isotropic material are initially very similar, but they deviate from each other at larger strains ($\overline{E}_e > 0.2$), with the former growing more rapidly than the latter. This could suggest that the FCC polycrystalline matrix becomes progressively harder to deform (see discussion of Fig. 7.5(a) below) and, as a consequence, more deformation has to be accommodated by the pores. The above observation also holds for the corresponding IVAR plots, with the only difference that the IVAR predictions for the porosity growth are much smaller than the ISO, as expected from the fact that the IVAR estimates for the macroscopic behavior of the porous medium are stronger than the corresponding ISO estimates for $X_\sigma = 1/3$ (see Fig. 7.2(b)).

Fig. 7.4(b) shows the corresponding results for the pore aspect ratio $w^p = w_1^p = w_2^p$, as well as for the grain aspect ratio $w^g = w_1^g = w_2^g$. It is observed that for the porous FCC polycrystal, the ISO results for both w^p and w^g start from one and increase monotonically with $\overline{E}_e$, with w^p growing more rapidly than w^g. This implies that the average shapes of the pores and grains evolve from their initially spherical shapes towards prolate spheroidal shapes. Given that the porosity approaches a finite value at large strains (Fig. 7.4(a)), the pores tend to become cylindrical with infinite aspect ratio. Moreover, the ISO plot of w^p for the porous FCC polycrystal is very similar to that for the porous isotropic material, with the former increasing slightly faster than the latter. This suggests that the texture evolution for the polycrystalline matrix has no significant effect on the pore shape changes. Of course, the ISO result for the

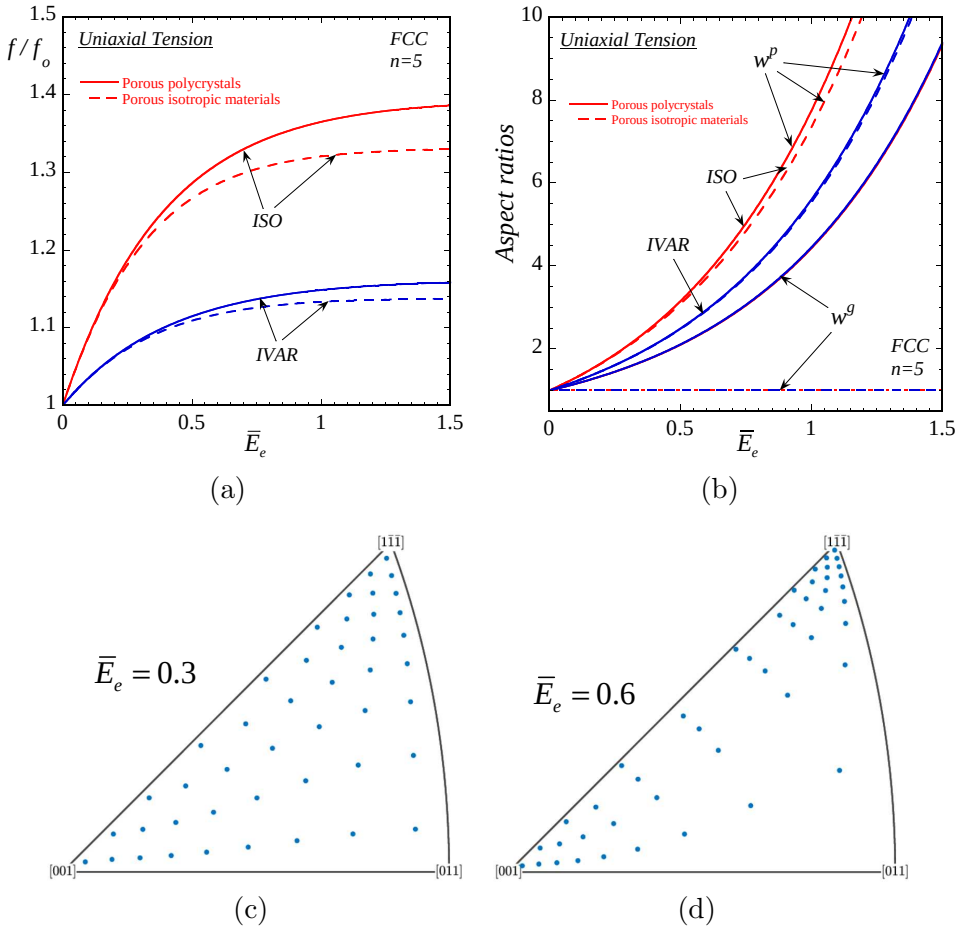

Figure 7.4: ISO results for porous FCC polycrystals with an initially isotropic distribution of spherical pores ($w_1^p = w_2^p = 1$) in $f_0 = 1\%$ porosity, subjected to uniaxial tension ($X_\sigma = 1/3$ and $L = -1$). The polycrystalline matrix is taken to be initially untextured, and the solid lines correspond to cases with texture evolution for the matrix (see Fig. 7.3(a)), while the dashed lines correspond to cases without texture evolution for the matrix (so that the matrix is always isotropic) (see Fig. 7.3(b)). Plots are shown for the (a) normalized porosity f/f_0, (b) pore aspect ratios $w^p = w_1^p = w_2^p$, and grain aspect ratios $w^g = w_1^g = w_2^g$, as functions of the time-like variable $\overline{E}_e$. (c) ISO results for the inverse pole figure of the FCC polycrystalline matrix at $\overline{E}_e = 0.3$, and (d) $\overline{E}_e = 0.6$. In (a) and (b), the corresponding IVAR results are also included for comparison.

grain aspect ratio w^d for the porous isotropic material remains constant throughout the deformation. The above observations are also true for the corresponding IVAR results. However, the IVAR plots for w^p grow more slowly than the ISO, as expected. Finally, it is interesting to note that the ISO and IVAR plots for the grain aspect ratio w^g of the porous polycrystal show almost identical predictions, with pores changing shape faster than the grains on average.

Fig. 7.4(c) and 7.4(d) show the ISO predictions for the crystallographic texture of the FCC polycrystalline matrix at $\overline{E}_e = 0.3$ and 0.6, respectively. We can see that the poles shift towards the $[1\bar{1}\bar{1}]$ and [001] directions, indicating the development of a bimodal texture, with the density for the poles being larger on the $[1\bar{1}\bar{1}]$ corner. In fact, the texture evolution for the FCC polycrystalline matrix is very similar to that for a fully dense polycrystal (not shown). As will be seen next, the evolution of the sub-structural variables shown in Fig. 7.4 has significant implications for the macroscopic response of the porous polycrystal.

Fig. 7.5 displays the corresponding ISO and IVAR results for the macroscopic response, as well as for the field fluctuations in the matrix phase of the porous FCC polycrystals. Fig. 7.5(a) presents results for the macroscopic equivalent strain rate $\overline{D}_e$ as a function of $\overline{E}_e$. These results are normalized by the FOSO estimate of $\overline{D}_e^0$ (see (7.13)), which is the macroscopic equivalent strain rate of an untextured fully dense FCC polycrystal. We also include, for comparison, the corresponding results for a porous isotropic material (dashed lines) and for a fully dense FCC polycrystal (dotted lines). Note that $\overline{D}_e/\overline{D}_e^0$ is a measure of the normalized effective viscous compliance for the composites and, hence, increasing $\overline{D}_e/\overline{D}_e^0$ implies softening, while decreasing $\overline{D}_e/\overline{D}_e^0$ implies hardening. In particular, we observe that the ISO plot for a solid FCC polycrystal decreases monotonically with $\overline{E}_e$, indicating a progressively hardening behavior of the material. Given that strain hardening for the crystal grains has been neglected, the hardening behavior can only be attributed to the texture evolution observed in Fig. 7.4(c) and 7.4(d). Moreover, the macroscopic behavior of the porous FCC polycrystal is found to be qualitatively similar to that of the fully dense polycrystal, but to be significantly different from that of the porous isotropic

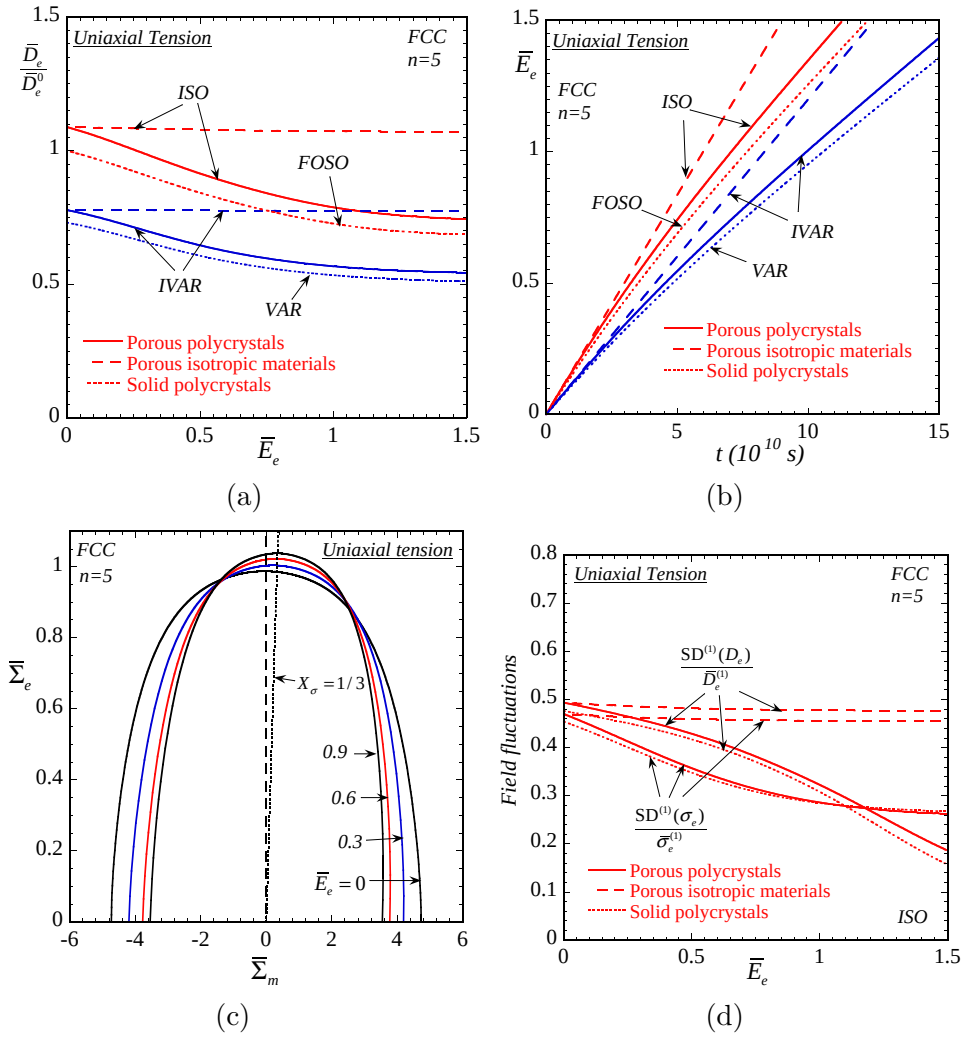

Figure 7.5: ISO results for porous FCC polycrystals with an initially isotropic distribution of spherical pores ($w_1^p = w_2^p = 1$) in $f_0 = 1\%$ porosity, subjected to uniaxial tension ($X_\sigma = 1/3$ and $L = -1$). The polycrystalline matrix is taken to be initially untextured, and the solid lines correspond to cases allowing texture evolution for the matrix, while the dashed lines correspond to cases allowing no texture evolution for the matrix (so that the matrix is always isotropic). Results are shown for (a) the normalized macroscopic equivalent strain rate $\overline{D}_e/\overline{D}_e^0$ as a function of $\overline{E}_e$, (b) the macroscopic equivalent creep strain $\overline{E}_e^c$ as a function of time, (c) the ISO gauge surfaces of the porous FCC polycrystal at different strain levels ($\overline{E}_e = 0$, 0.3, 0.6 and 0.9), and (d) the standard deviations of the von Mises stress $\mathrm{SD}^{(1)}(\sigma_e)$, and the equivalent strain rate $\mathrm{SD}^{(1)}(D_e)$ in the polycrystalline matrix, respectively, normalized by the average von Mises stress $\overline{\sigma}_e^{(1)}$ and equivalent strain rate $\overline{D}_e^{(1)}$ in the matrix, as functions of $\overline{E}_e$.

material (the latter exhibits only a very weak hardening behavior induced by the pore shape change). These observations strongly suggest that the overall behavior of the porous FCC polycrystal for this particular loading is controlled by the texture evolution of the matrix, and is largely unaffected by the porosity evolution and pore shape changes. The IVAR model leads to predictions that are qualitatively similar to the ISO estimates, but exhibiting higher nonlinear viscosity in quantitative terms. (Note that the IVAR results for $\overline{D}_e$ are also normalized by the FOSO estimates of $\overline{D}_e^0$.) In particular, the macroscopic behavior of the porous FCC polycrystal estimated by the IVAR model is even more stronger than that of a fully dense solid polycrystal estimated by the FOSO model, suggesting that the IVAR predictions are overly viscous and cannot be very accurate.

Fig. 7.5(b) gives the corresponding results for the macroscopic equivalent creep strain $\overline{E}_e^c$ as a function of time. It can be seen that the ISO plots for both the porous and fully dense FCC polycrystals increase monotonically in time with progressively decreasing slopes, consistent with the decreasing macroscopic strain rates observed in Fig. 7.5(a). As already discussed, this hardening behavior is due to the texture evolution for the FCC polycrystal (matrix). In contrast, the ISO plot for the porous isotropic material increases almost linearly in time with a faster rate, since the porosity evolution and pore shape change have no significant effects on the overall hardening or softening behavior of the material for this particular loading. The IVAR model yields qualitatively similar results, but underestimates the growth of $\overline{E}_e^c$, as expected.

Fig. 7.5(c) shows the evolution of the ISO gauge surfaces for the porous FCC polycrystal during uniaxial tension, for different strain levels ($\overline{E}_e$ = 0, 0.3, 0.6 and 0.9). It can be seen that the gauge surface expands along the uniaxial tension loading direction (X_Σ = 1/3) with increasing values of $\overline{E}_e$, indicating a hardening behavior of the material, consistent with the findings in Fig. 7.5(a). On the other hand, the gauge surface is found to contract with increasing $\overline{E}_e$ for large magnitudes of the triaxiality, implying a softening behavior. The above observations clearly demonstrate a distortional hardening (or softening) effect due to the evolution of the sub-structure.

In addition, it is expected that the porous polycrystal will gradually develop overall anisotropy as the deformation progresses. This effect could be shown by the evolution of other cross sections (e.g., the longitudinal shear versus the axisymmetric shear) of the gauge surfaces. However, such more general results are beyond the scope of this work, and will be pursued in future work.

Fig. 7.5(d) display the ISO results for the standard deviations of the von Mises stress ($\mathrm{SD}^{(1)}(\sigma_e)$) and equivalent strain rate ($\mathrm{SD}^{(1)}(D_e)$) in the polycrystalline matrix, as functions of $\overline{E}_e$. These results are normalized, respectively, by the average von Mises stress $\overline{\sigma}_e^{(1)}$ and equivalent strain rate $\overline{D}_e^{(1)}$ in the matrix. For comparison purposes, the corresponding results are also included for the porous isotropic material and fully dense FCC polycrystal. There are two sources giving rise to field fluctuations in the polycrystalline matrix : (i) the heterogeneity due to the presence of voids (at the meso-scale), and (ii) the heterogeneity induced by different orientations of the single-crystal grains in the matrix (at the micro-scale). We observe from Fig. 7.5(d) that both the stress and strain rate fluctuations in the polycrystalline matrix become progressively weaker with increasing $\overline{E}_e$. Moreover, they are rather similar to the field fluctuations in a fully dense FCC polycrystal, but are quite different from those in an isotropic matrix (being almost constants), suggesting that the field fluctuations are controlled by the texture evolution of the polycrystalline matrix, but not so much by the porosity evolution. This is consistent with the fact that the texture of the polycrystalline matrix evolves significantly (see Fig. 7.4(c) and 7.4(d)), while the porosity does not change significantly (see Fig. 7.4(a)).

Uniaxial compression

Fig. 7.6 presents ISO and IVAR plots for the sub-structure evolution of porous FCC polycrystals under uniaxial compression ($X_\sigma = -1/3$ and $L = 1$). We also include, for comparison, the corresponding results for a porous isotropic material. We observe from Fig. 7.6(a) and 7.6(b) that the ISO estimates for the normalized porosity f/f_0 and the pore aspect ratio $w^p = w_1^p = w_2^p$ decrease monotonically with $\overline{E}_e$ and tend to zero simultaneously at $\overline{E}_e \approx 0.5$. This implies that the initially spherical pores evolve

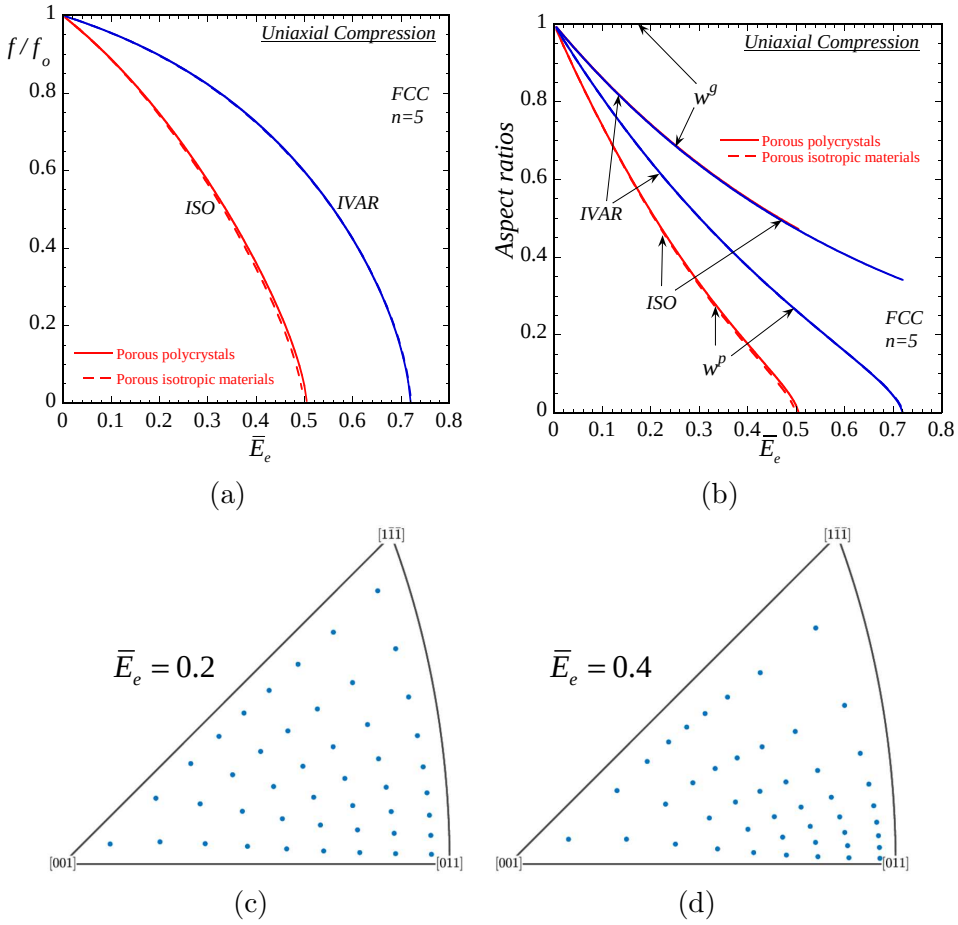

Figure 7.6: ISO results for porous FCC polycrystals with an initially isotropic distribution of spherical pores ($w_1^p = w_2^p = 1$) in $f_0 = 1\%$ porosity, subjected to uniaxial compression ($X_\sigma = -1/3$ and $L = 1$). The polycrystalline matrix is taken to be initially untextured, and the solid lines correspond to cases with texture evolution for the matrix, while the dashed lines correspond to cases without texture evolution for the matrix (so that the matrix is always isotropic). Plots are shown for the (a) normalized porosity f/f_0, (b) pore aspect ratios $w^p = w_1^p = w_2^p$, and grain aspect ratios $w^g = w_1^g = w_2^g$, as functions of the time-like variable $\overline{E}_e$. (c) ISO results for the inverse pole figure of the FCC polycrystalline matrix at $\overline{E}_e = 0.2$, and (d) $\overline{E}_e = 0.4$. In (a) and (b), the corresponding IVAR results are also included for comparison.

continuously towards oblate spheroidal ones, and finally collapse into penny-shaped micro-cracks. Moreover, we observe from Fig. 7.6(b) that the ISO results for the grain aspect ratio $w^g = w_1^g = w_2^g$ decrease with $\overline{E}_e$ in a slower rate, and terminate at a finite value when the porosity goes to zero. This means that the initially equiaxed grains tend to become flat, leading to the development of morphological anisotropy of the polycrystalline matrix. Furthermore, we can see from Fig. 7.6(a) and 7.6(b) that the ISO plots of f/f_0 and w^p are very similar for the porous FCC polycrystal and for the porous isotropic material, suggesting that the texture evolution of the polycrystalline matrix has *no* significant effect on the behavior of the voids for this specific loading condition. The above observations are also true for the corresponding IVAR plots, with the only difference that the IVAR plots of f/f_0 and w^p vary much more slowly with $\overline{E}_e$, leading to slower collapse of the voids.

Fig. 7.6(c) and 7.6(d) display the ISO results for the crystallographic texture of the FCC polycrystalline matrix at $\overline{E}_e = 0.2$ and 0.4, respectively. We observe that all the poles shift gradually towards the [011] corner with increasing values of $\overline{E}_e$, leading to a unimodal [011] texture. Moreover, it is found that the texture evolution for the polycrystalline matrix shown in Fig. 7.6(c) and 7.6(d) is, again, very similar to that for a fully dense FCC polycrystal (not shown). In this connection, it should be remarked that the evolution of the sub-structure for uniaxial compression (Fig. 7.6) is significantly different from that for uniaxial tension (Fig. 7.4), as expected on physical grounds.

Fig. 7.7 presents the ISO and IVAR results for the finite-strain macroscopic response, as well as for the field fluctuation of the porous FCC polycrystals subjected to uniaxial compression. For comparison purposes, we also include the corresponding results for a porous isotropic material (dashed lines) and for a fully dense FCC polycrystal (dotted lines). Fig. 7.7(a) display plots for the normalized macroscopic strain rate $\overline{D}_e/\overline{D}_e^0$ as a function of $\overline{E}_e$. We can see from Fig. 7.7(a) that $\overline{D}_e/\overline{D}_e^0$ for the fully dense FCC polycrystal does not change much with increasing values of $\overline{E}_e$, indicating that the developing [011] texture has no significant effects on the macroscopic behavior of the polycrystal. As a consequence, the ISO estimate for the

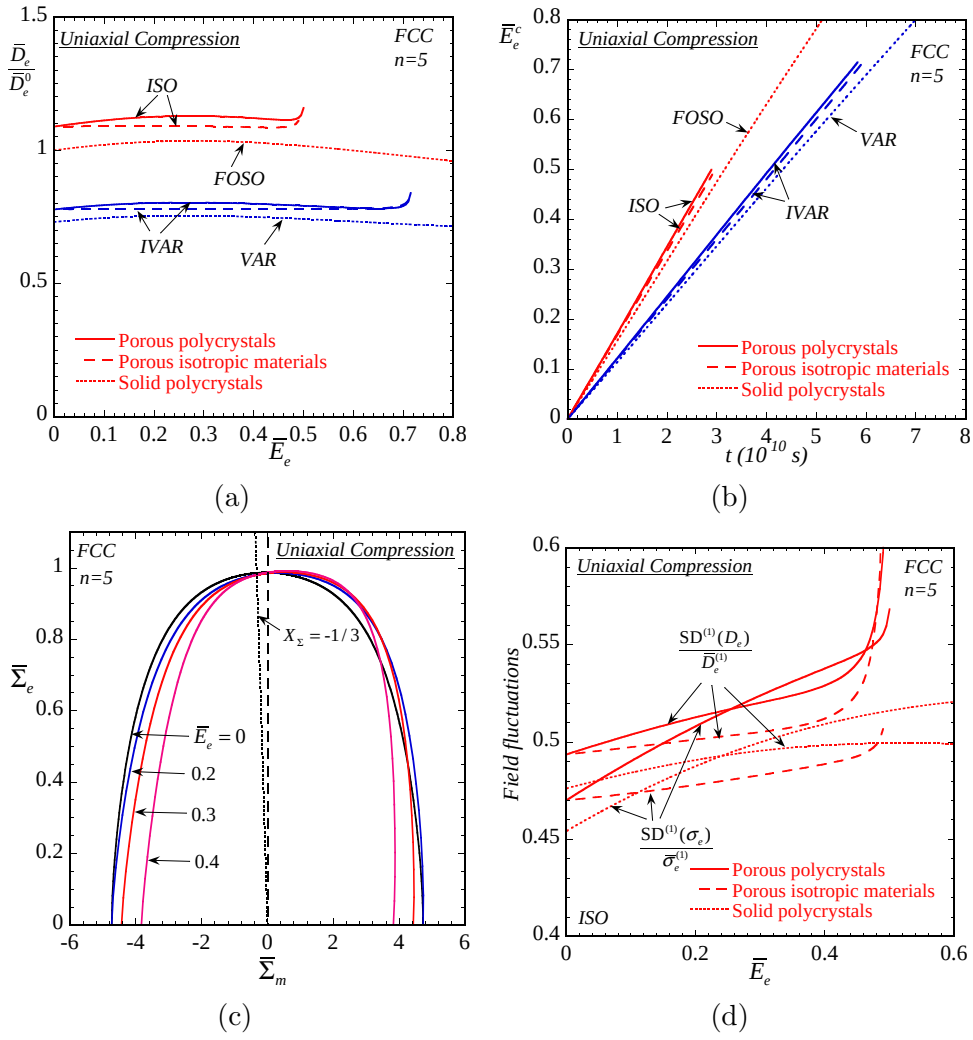

Figure 7.7: ISO results for porous FCC polycrystals with an initially isotropic distribution of spherical pores ($w_1^p = w_2^p = 1$) in $f_0 = 1\%$ porosity, subjected to uniaxial compression ($X_\sigma = -1/3$ and $L = 1$). The polycrystalline matrix is taken to be initially untextured, and the solid lines correspond to cases allowing texture evolution for the matrix, while the dashed lines correspond to cases allowing no texture evolution for the matrix (so that the matrix is always isotropic). Results are shown for (a) the normalized macroscopic equivalent strain rate $\overline{D}_e/\overline{D}_e^0$ as a function of $\overline{E}_e$, (b) the macroscopic equivalent creep strain $\overline{E}_e^c$ as a function of time, (c) the ISO gauge surfaces of the porous FCC polycrystal at different strain levels ($\overline{E}_e = 0$, 0.2, 0.3 and 0.4), and (d) the standard deviations of the von Mises stress $\mathrm{SD}^{(1)}(\sigma_e)$, and the equivalent strain rate $\mathrm{SD}^{(1)}(D_e)$ in the polycrystalline matrix, respectively, normalized by the average von Mises stress $\overline{\sigma}_e^{(1)}$ and equivalent strain rate $\overline{D}_e^{(1)}$ in the matrix, as functions of $\overline{E}_e$.

macroscopic response of the porous FCC polycrystal is very similar to that for the porous isotropic material, with the former being only slightly softer than the latter. This suggests that the simplifying assumption on the isotropy of the matrix could be a good approximation for this special loading condition. The above observations also hold for the corresponding IVAR results, but the IVAR predictions are much more viscous than the corresponding ISO predictions.

In this context, note that the $\overline{D}_e/\overline{D}_e^0$ curves for the porous medium exhibit abrupt upturns at the end of the deformation, indicating a strong softening behavior. As already discussed in detail in the previous work (e.g., Agoras and Ponte Castañeda, 2014; Song et al., 2015; Song and Ponte Castañeda, 2017c), this is induced by the sharp drop of the pore aspect ratio w^p prior to void closure (see Fig. 7.6(b)), which has a dramatic softening effect that controls the overall behavior of the porous medium. However, this result may *not* be physically relevant, since the softening occurs at very small aspect ratios ($w_p \approx 0.05$), where void surface contact may have already taken place (not captured by the ISO model), thus suppressing the softening effect due to void collapse (Hutchinson and Tvergaard, 2012). From now on, we will ignore this strong softening behavior prior to void collapse, unless otherwise noted. In any event, the behavior of the porous polycrystal is expected to be similar to that of a fully dense polycrystal after void closure, although the presence of already formed micro-cracks may be important for other loading conditions.

Fig. 7.7(b) presents plots for the macroscopic creep strain $\overline{E}_e^c$ versus time. We observe that the ISO plots for the porous FCC polycrystal and porous isotropic material stay very close to each other, and they increase almost linearly with time. This is in agreement with the fact that the corresponding macroscopic strain rates are rather similar and are almost constants throughout the deformation (see Fig. 7.7(a)). Furthermore, the ISO plots for the porous medium are also quite similar to that for a fully dense FCC polycrystal, due to the low porosity in the materials. The IVAR model yields qualitatively similar results, but it underestimates the growth of $\overline{E}_e^c$, as expected.

Fig. 7.7(c) shows the corresponding ISO gauge surfaces for the porous FCC poly-

crystal during uniaxial compression, for $\overline{E}_e$ = 0, 0.2, 0.3 and 0.4. We can see that the gauge surface does not evolve significantly along the uniaxial compression loading direction (X_Σ = −1/3), implying that the macroscopic response of the material does not change much for this particular loading direction, as already seen in Fig. 7.7(a). However, the gauge surface may extend or contract with increasing strain for other triaxialities, indicating strong distortional hardening or softening effects of the sub-structure evolution shown in Fig. 7.6.

Fig. 7.7(d) gives the ISO results for the normalized standard deviation of the von Mises stress ($\mathrm{SD}^{(1)}(\sigma_e)/\overline{\sigma}_e^{(1)}$) and equivalent strain rate ($\mathrm{SD}^{(1)}(D_e)/\overline{D}_e^{(1)}$) in the matrix of the porous polycrystal, as functions of $\overline{E}_e$. We also include, for comparison, the corresponding results for the porous isotropic material (dashed lines) and solid FCC polycrystal (dotted lines). We observe from Fig. 7.7(d) that both the stress and strain rate fluctuations in the polycrystalline matrix become stronger with increasing $\overline{E}_e$, which are significantly different from those for uniaxial tension (Fig. 7.5(d)). In particular, we observe that the field fluctuations in the polycrystalline matrix are qualitatively similar to those in the solid polycrystal for $0 \leq \overline{E}_e \lesssim 0.4$, while qualitatively similar to those in the porous isotropic material for larger strains. This suggests that the texture evolution of the matrix governs the field fluctuations at the beginning, while the geometrical changes in the pores take over at large strains.

In summary, the texture evolution for the polycrystalline matrix surrounding the voids can have significant effects on the macroscopic response, as well as on the field fluctuations of the porous polycrystal. In particular, for low triaxiality loading conditions (e.g., uniaxial tension), the macroscopic behavior of the porous polycrystal can be largely controlled by the texture evolution of the matrix, with porosity playing a minor role. However, as will be seen in the next section, for high triaxiality conditions, porosity evolution may assume a dominant role.

7.3 Applications to porous HCP polycrystals

In this section, we make use of the ISO model to investigate both the instantaneous and finite-strain behavior of porous HCP polycrystals. We consider HCP crystals with a c/a ratio of 1.59, a creep exponent n of 6.25, and a reference strain rate $\dot{\gamma}_0 = 0.001\text{s}^{-1}$. These parameters are known to be appropriate for commercially pure titanium at 750°C (Balasubramanian and Anand, 2002). The principal slip systems for these materials are taken to be (i) basal slip ($\{0001\}\langle 11\bar{2}0\rangle$), (ii) prismatic slip ($\{10\bar{1}0\}\langle 11\bar{2}0\rangle$), and (iii) first- ($\{10\bar{1}\bar{1}\}\langle 11\overline{2}3\rangle$) and second-order ($\{11\bar{2}2\}\langle 11\bar{2}3\rangle$) pyramidal-$\langle c+a\rangle$ slip. These three different families of slip systems will be denoted by labels A, B and C, respectively. Note that the three basal slips plus the three prismatic slips supply only four (two each) linearly independent slip systems, allowing no straining along the hexagonal crystal axis. However, the twelve first-order pyramidal slips and the six second-order pyramidal slips each contain sets of five linearly independent slip systems. In addition, the reference flow stresses $(\tau_0)_{(k)}$ $(k = 1, ..., 24)$ are taken to be identical for each family of slip systems, but generally different for different families of slip systems. Here we take the basal and prismatic slips to be the "soft" slip systems with identical reference flow stress $\tau_A = \tau_B$, while the first- and second-order pyramidal slips to be the "hard" slip systems with a reference flow stress τ_C. Then, we define a contrast parameter $M = \tau_C/\tau_A = \tau_C/\tau_B$ to describe the crystal anisotropy of the HCP crystals. In particular, $M = 10$ is used for titanium crystals (Balasubramanian and Anand, 2002). However, we will consider more general values of M to investigate the effect of the crystal anisotropy.

7.3.1 Instantaneous effective response

In this subsection, we use the ISO model to generate estimates for the instantaneous effective response of porous HCP polycrystals for fixed states of the microstructure, focusing on the effect of the crystal anisotropy (M), porosity, and the average pore shape.

The HCP polycrystalline matrix is assumed to be *untextured*, so that the single-

crystal grains are equiaxed (w_1^g = w_2^g = 1), and the crystallographic orientations are uniformly distributed. Moreover, the loading conditions are taken to be axisymmetric, as given by (7.7). As already mentioned, the ISO model requires solving sets of nonlinear algebraic equations with a number of unknowns proportional to the total number of available slip systems in the polycrystalline matrix. Therefore, it is of interest to use as few crystallographic orientations as possible. Taking advantage of the symmetry for the crystal and loadings (Van Houtte and Aernoudt, 1976; Kocks et al., 1998), it is possible to reduce the number of required orientatons (see, e.g., Nebozhyn, 2000). In particular, a set of 45 *equi-spaced* orientations on an appropriate spherical triangle (Liu and Ponte Castañeda, 2004b; Nebozhyn, 2000) is found to yield very good accuracy. Furthermore, we choose $\sigma_0 = \widetilde{\sigma}_0^*$ in (7.4), so that all the gauge surfaces shown below are normalized by the effective flow stress of the corresponding untextured fully dense HCP polycrystal under axisymmetric shear.

Fig. 7.8 shows the $\overline{\Sigma}_m$-$\overline{\Sigma}_e$ cross sections of the ISO gauge surfaces for the porous HCP polycrystals with untextured matrix, and for axisymmetric loading (7.7) with $L = -1$. As already discussed, the corresponding results for $L = 1$ can be obtained by flipping the results for $L = -1$ with respect to the deviatoric axis $\overline{\Sigma}_m = 0$. Fig. 7.8(a) shows the effect of the iteration number I on the ISO gauge surfaces for porous Ti polycrystals ($M = 10$) with porosity $f = 1\%$ and spherical pores ($w_1^p = w_2^p = 1$), where different iteration numbers are considered ($I = 1$, 2, 5 and 10). It can be seen from Fig. 7.8(a) that the behavior of the ISO gauge surface as a function of I for the porous Ti polycrystals is quite similar to that for the porous FCC polycrystals (see Fig. 7.2(a)), suggesting that the effect of the iteration number I is rather similar for both types of crystal symmetries (HCP and FCC). In particular, we observe from Fig. 7.8 that the ISO gauge surface becomes progressively tighter with increasing values of I for large triaxialities, converging to a certain limit for large values of I. However, the ISO gauge surface does not change significantly with increasing I for small triaxialities, in agreement with the fact that the FOSO gauge surface ($I = 1$) is already very accurate. As already mentioned, $I = 10$ is found to be sufficient to obtain accurate estimates (with error less than 1%) for the corresponding $I \to \infty$

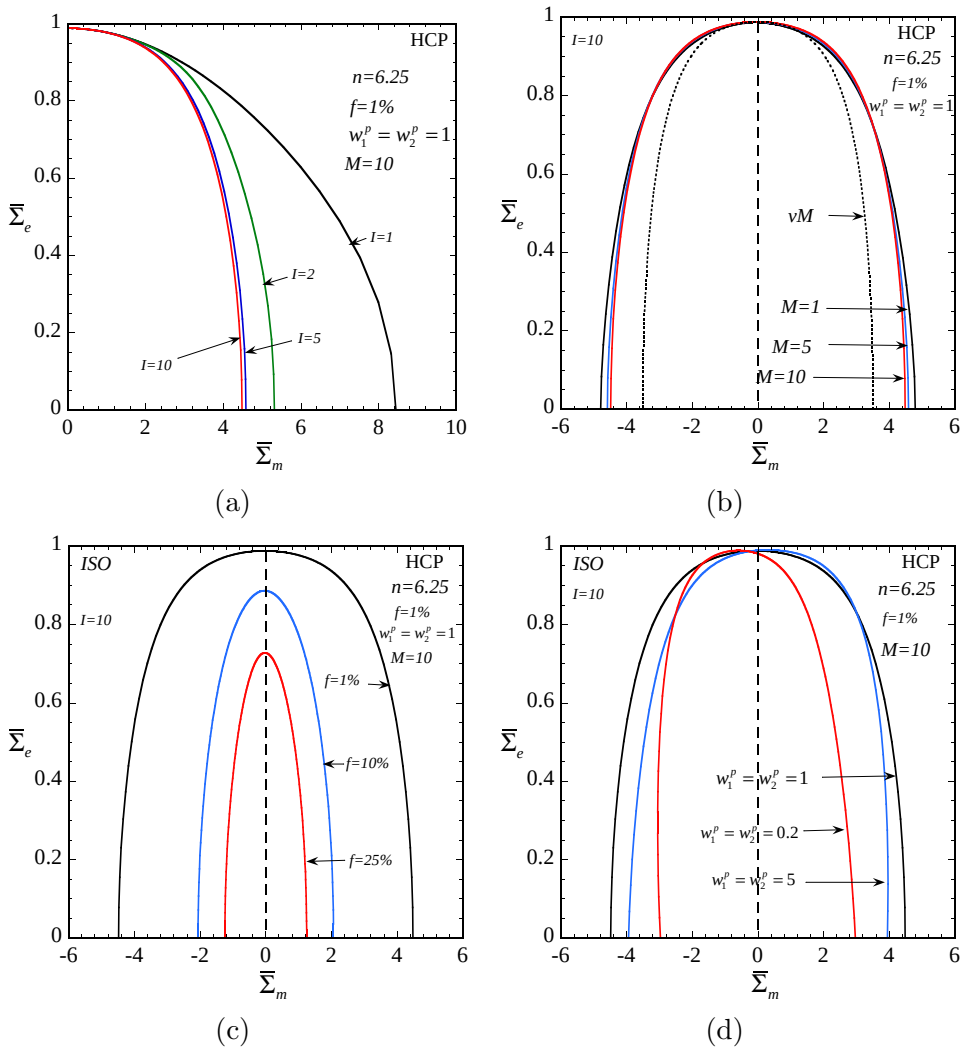

Figure 7.8: The $\overline{\Sigma}_m$-$\overline{\Sigma}_e$ cross sections of gauge surfaces for viscoplastic (n = 6.25) porous HCP polycrystals, subjected to loading conditions (7.7) with $L = -1$ ($\overline{\sigma}_{11} = \overline{\sigma}_{22} \leq \overline{\sigma}_{33}$). The effect of the (a) iteration number I, (b) crystal anisotropy ($M = \tau_C/\tau_A = \tau_C/\tau_B$), (c) porosity f, and (d) average pore shape, as described by the pore aspect ratios w_1^p and w_2^p, on the ISO gauge surfaces are shown.

limit. Therefore, *all the ISO results shown below for the porous HCP polycrystals will be computed for* $I = 10$.

Fig. 7.8(b) presents results for the ISO gauge surfaces of porous HCP polycrystals with porosity $f = 1\%$ and spherical pores ($w_1^p = w_2^p = 1$), but with different crystal anisotropies ($M = 1, 5, 10$). The corresponding IVAR gauge surface (Agoras and Ponte Castañeda, 2013) for a porous von Mises solid is also shown for comparison. It can be seen from Fig. 7.8(b) that the ISO gauge surfaces for the porous polycrystals are fairly independent of the crystal anisotropy M, as expected from the fact that the homogenized response for the untextured HCP polycrystalline matrix is isotropic, regardless of the values of M. Similar to the observations made in Fig. 7.2(b), for $0 \lesssim |X_\Sigma| \lesssim 2$ the ISO gauge surfaces for all values of M are in very good agreement with the IVAR (von Mises) results, while for large triaxialities ($|X_\Sigma| > 2$) the corresponding ISO gauge surfaces are somewhat stronger than the IVAR (von Mises) gauge surfaces.

Fig. 7.8(c) shows the effect of the porosity on the ISO gauge surfaces for porous Ti polycrystals ($M = 10$) with spherical pores ($w_1^p = w_2^p = 1$), where different values of the porosity ($f = 1\%$, 5% and 10%) are considered. We can see from Fig. 7.8(c) that as f increases, the ISO gauge surface becomes tighter for all values of X_Σ, indicating a softer response for the material, as expected. Moreover, the contraction of the ISO gauge surface with increasing values of f is found to be more significant at large triaxialities, thus leading to changes in the shape of the gauge surfaces. In particular, note the significant differences in the curvature of the ISO gauge surfaces near the deviatoric axis ($\overline{\Sigma}_m = 0$).

Fig. 7.8(d) shows the effect of the average pore shape on the ISO gauge surfaces for porous Ti polycrystals ($M = 10$) with a fixed porosity $f = 1\%$. More specifically, we compare the ISO gauge surfaces for porous Ti polycrystals with spherical pores ($w_1^p = w_2^p = 1$), prolate spheroidal pores ($w_1^p = w_2^p = 5$) and oblate spheroidal pores ($w_1^p = w_2^p = 0.2$). In addition, the symmetry axis of the pores is taken to be aligned with the symmetry axis of the loading $\mathbf{e}_3$. It is observed from Fig. 7.8(d) that changing the pore shape can induce significant changes in the size, shape and orientation of the gauge surfaces. In addition, the effect of the pore shape on the ISO gauge surfaces

exhibits a strong dependence on the stress triaxiality. For instance, changing the pore shape from spherical ($w_1^p = w_2^p = 1$) to prolate spheroidal ($w_1^p = w_2^p = 5$) leads to softer response of the material at purely hydrostatic loadings, while it leads to stronger response of the material for a certain range of low to moderate stress triaxialities. This fact suggests that the pore shape evolution could have a strong distortional hardening or softening effect on the macroscopic response of porous polycrystals.

7.3.2 Finite-strain macroscopic response

In this subsection, we use the ISO model to investigate the finite-strain macroscopic response of porous Ti polycrystals, focusing on the effect of the stress triaxiality and Lode parameter. Specifically, we consider a porous Ti polycrystal ($M = 10$) consisting of initially spherical pores distributed randomly and isotropically ($w_1^p = w_2^p = 1$) in a polycrystalline matrix, with an initial porosity $f_0 = 1\%$. The matrix is assumed to have initially isotropic morphological ($w_1^g = w_2^g = 1$) and crystallographic texture. For simplicity, strain hardening of the polycrystalline matrix is neglected, so that the reference flow stresses τ_A, τ_B, τ_C and the contrast parameter M for the crystal grains remain fixed throughout the deformation. We consider axisymmetric loadings (7.7) with $\overline{\boldsymbol{\sigma}}$ being *fixed* in time. In this subsection, we consider the following two cases:

(i) Axisymmetric tension with $L = -1$ ($\overline{\sigma}_{11} = \overline{\sigma}_{22} \leq \overline{\sigma}_{33}$), and

(ii) Axisymmetric compression with $L = 1$ ($\overline{\sigma}_{11} = \overline{\sigma}_{22} \geq \overline{\sigma}_{33}$).

For each case, we consider different values of the stress triaxiality. In particular, we set $\overline{\sigma}_e = \tau_A$, and prescribe the stress triaxiality by setting $\overline{\sigma}_m = X_\sigma \overline{\sigma}_e$. With the objective of studying the intrinsic effect of the texture evolution for the polycrystalline matrix, we also include the corresponding results for a porous isotropic material obtained by fixing the initially isotropic texture of the polycrystalline matrix (see Fig. 7.3(b)).

Axisymmetric tension

In Fig. 7.9, we investigate the effect of the stress triaxiality on the evolution of the sub-structure of porous Ti polycrystals, for axisymmetric loadings (7.7) with $L = -1$

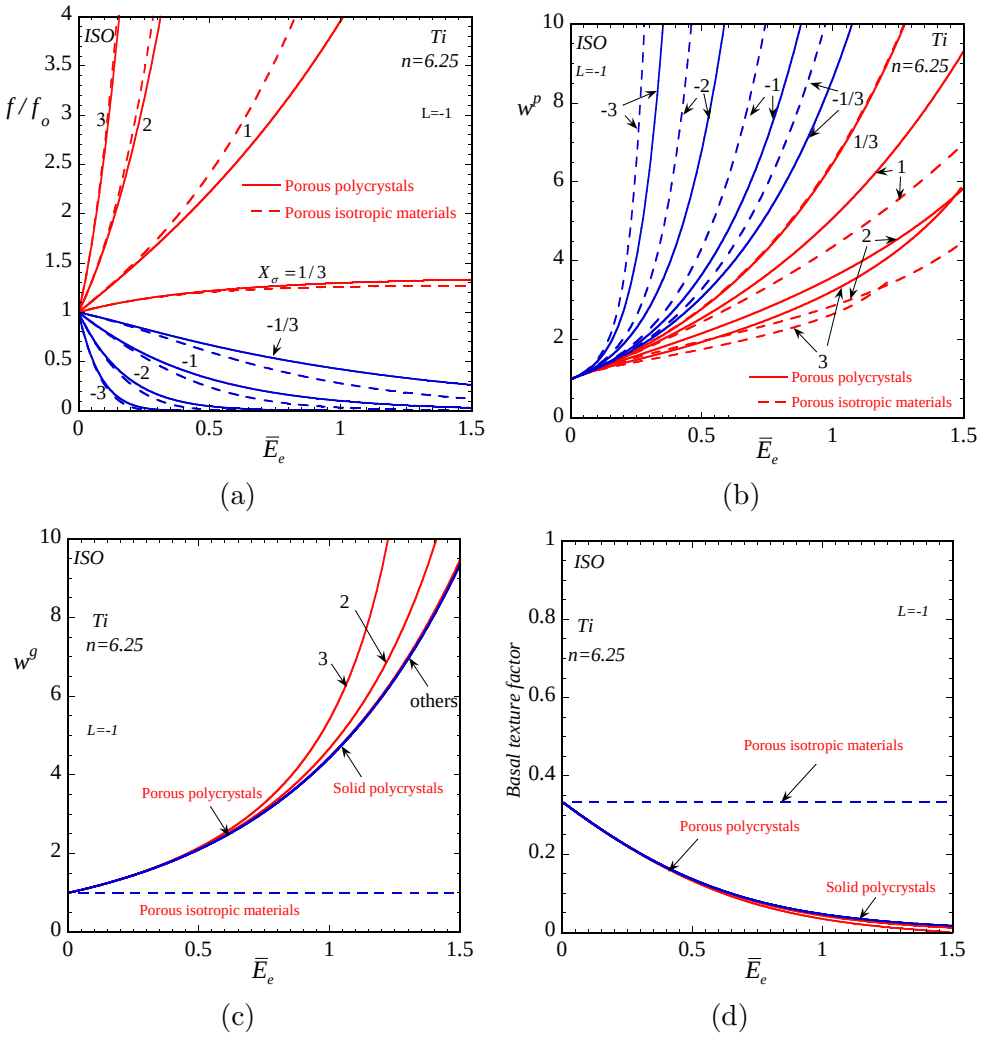

Figure 7.9: ISO results for porous Ti ($M = 10$) polycrystals with an initially isotropic distribution of spherical pores ($w_1^p = w_2^p = 1$) in $f_0 = 1\%$ porosity, subjected to axisymmetric loadings (7.7) with $L = -1$ ($\overline{\sigma}_{11} = \overline{\sigma}_{22} \leq \overline{\sigma}_{33}$) and various triaxialities X_σ. The polycrystalline matrix is taken to be initially untextured, and the solid lines correspond to cases with texture evolution for the matrix, while the dashed lines correspond to cases without texture evolution for the matrix (so that the matrix is always isotropic). Plots are shown for the evolution of the (a) normalized porosity f/f_0, (b) pore aspect ratios $w^p = w_1^p = w_2^p$, (c) grain aspect ratios $w^g = w_1^g = w_2^g$, and (d) basal texture factor along the loading axis $\mathbf{e}_3$, as functions of the time-like variable $\overline{E}_e$.

($\overline{\sigma}_{11} = \overline{\sigma}_{22} \leq \overline{\sigma}_{33}$). We also include, for comparison, the corresponding results for a porous isotropic material (dashed lines) and a fully dense Ti polycrystal (dotted lines). We consider eight values of X_σ ranging from −3 (strong compressive loadings) to 3 (strong tensile loadings), with the results for positive triaxialities ($X_\sigma > 0$) shown in red, and negative triaxialities ($X_\sigma < 0$) shown in blue. Fig. 7.9(a) shows the ISO plots for the normalized porosity f/f_0 as a function of $\overline{E}_e$. We can see that for large positive triaxialities ($X_\sigma = 3$, 2 and 1), the porosity increases monotonically with $\overline{E}_e$, while for negative triaxialities the porosity decreases continuously to zero leading to void collapse. For $X_\sigma = 1/3$ (uniaxial tension), f/f_0 initially increases with $\overline{E}_e$ and saturates at a finite value around 1.33, similar to the observation made for the porous FCC polycrystals in Fig. 7.4(a). As expected, f/f_0 grows faster for larger values of X_σ in the range $X_\sigma \geq 1$, while f/f_0 decreases faster for smaller values of X_σ in the range $X_\sigma \leq 1/3$. For a given value of X_σ, the f/f_0 plots for the porous polycrystal and for the porous isotropic material are qualitatively similar, but have some quantitative differences. In particular, the evolution of f/f_0 is found to be slightly slower for the porous polycrystal than for the porous isotropic material.

Fig. 7.9(b) displays the corresponding ISO results for the pore aspect ratio $w^p = w_1^p = w_2^p$. It is observed that w^p increases monotonically with $\overline{E}_e$ for all values of X_σ, indicating that the average pore shape deforms continuously from spherical to prolate spheroidal. Moreover, the growth of w^p is found to be faster for smaller values of X_σ. In particular, for $X_\sigma = -2$ and −3 the pore aspect ratio w^p tends to infinity when f/f_0 goes to zero (see Fig. 7.9(a)), indicating that the initially spherical pores collapse into infinitely thin needles. For given values of X_σ, the w^p plots for the porous polycrystals are, once again, qualitatively similar to those for the porous isotropic materials. In quantitative terms, the growth of w^p is found to be slower for the porous polycrystal than for the porous isotropic material for $X_\sigma < 1/3$, while the opposite is true for $X_\sigma > 1/3$.

Fig. 7.9(c) gives the corresponding ISO results for the grain aspect ratio $w^g = w_1^g = w_2^g$, characterizing the morphological texture of the polycrystalline matrix. We observe that when $X_\sigma \leq 1$, the w^g plots for the porous polycrystals are rather insen-

sitive to the stress triaxiality: they all start from one and increase progressively with $\overline{E}_e$, suggesting that the average grain shape evolves from spherical towards prolate spheroidal. Moreover, these curves are found to be very similar to the corresponding curve for a fully dense polycrystal. (Recall that results for the fully dense polycrystal are independent of the stress triaxiality, since the behavior of a fully dense polycrystal is insensitive to the hydrostatic pressure.) Therefore, the behavior of the w^g plots is quite different from that of the corresponding w^p plots, which exhibit a strong dependence on the stress triaxiality (see Fig. 7.9(b)). For $X_\sigma = 3$ and 2, while the w^g plots are initially similar to those for $X_\sigma \leq 1$, they increase more rapidly at larger values of $\overline{E}_e$. Of course, $w^g = 1$ for the porous isotropic material, since the morphological texture of the matrix is fixed during the deformation.

Fig. 7.9(d) presents results for the evolution of the crystallographic texture for the polycrystalline matrix. In particular, we use the *basal texture factor* (Lebensohn et al., 2007) along the axial loading direction $\mathbf{e}_3$ to characterize the evolving crystallographic texture. The basal texture factor is defined to be the weighted average of the projections of the $\langle c \rangle$-axes along the axial loading direction $\mathbf{e}_3$, i.e., $\langle \cos^2 \phi^{(r)} \rangle$, with $\phi^{(r)}$ denoting the angle between the $\langle c \rangle$-axes of the rth single-crystal grain and the loading axis $\mathbf{e}_3$. Note that the basal texture factor equals to one when the $\langle c \rangle$-axes of all the grains are aligned with the axial loading direction $\mathbf{e}_3$, while it equals to zero when the $\langle c \rangle$-axes of all the grains are perpendicular to the axial loading direction $\mathbf{e}_3$. We observe from Fig. 7.9(d) that for all values of X_σ, the basal texture factor starts from 1/3 (the value for an isotropic crystallographic texture) and decreases monotonically with $\overline{E}_e$, implying that the $\langle c \rangle$-axes of the single-crystal grains tend to become perpendicular to the loading axis $\mathbf{e}_3$. Moreover, it can be seen that the texture evolution of the polycrystalline matrix is fairly independent of the triaxiality, being rather similar to the texture evolution for a fully dense Ti polycrystal. According to the observations made in the context of Fig. 7.9(c) and 7.9(d), it can be deduced that the evolution of both the morphological and crystallographic texture of the polycrystalline matrix is fairly insensitive to the stress triaxiality for the cases considered here. Finally, it is noted that the basal texture factor remains a constant

1/3 for a porous isotropic material, since the crystallographic texture is fixed during the deformation process.

Fig. 7.10 shows the corresponding ISO results for the relative slip activities and macroscopic response of the porous Ti polycrystals. In particular, Fig. 7.10(a) gives results for the relative activities for the three different families of slip systems (basal, prismatic and pyramidal slips). The relative activity (RA) for a given slip mode (basal, prismatic, or pyramidal) is defined to be

$$RA_{mode} = \frac{\sum_{r=1}^{N} c^{(1,r)} \sum_{\text{mode}} |\overline{\gamma}_{(k)}^{(r)}|}{\sum_{r=1}^{N} c^{(1,r)} \sum_{k=1}^{K} |\overline{\gamma}_{(k)}^{(r)}|}, \tag{7.14}$$

where the numerator denotes the sum of the absolute values of the slip rates on all the slip systems that belong to a given slip mode, while the denominator denotes the sum over all the available slip systems. It can be seen from Fig. 7.10(a) that the activities for the soft systems (basal and prismatic) are much larger than that for the hard systems (pyramidal), indicating that most shear deformations in the polycrystalline matrix are accommodated by the soft slip systems, as expected on physical grounds. In addition, for all values of X_σ the prismatic activity increases progressively with strain, while the basal activity decreases with strain. The results for the relative activities for $X_\sigma = 3$ at large strains (beyond $\overline{E}_e \approx 1.42$) are not expected to be physically relevant, since they occur for very large porosities, and void coalescence may have already taken place leading to failure of the material. It is important to note that, the basal slips can *not* accommodate axisymmetric shear deformation when the $\langle c \rangle$-axis of the grain is aligned or perpendicular to the axial loading direction $\mathbf{e}_3$. Thus, as the $\langle c \rangle$-axes of the grains become progressively perpendicular to the $\mathbf{e}_3$ (see Fig. 7.9(d)), a large amount of grains that are initially favorably orientated for basal slips (e.g., grains with their $\langle c \rangle$-axes lying between the axial and transverse directions) become gradually less favorably oriented, leading to the overall reduction of the basal activity. Furthermore, it is interesting to note that the pyramidal activity is almost zero up to $\overline{E}_e \approx 0.5$, but it starts to increase with $\overline{E}_e$ at larger strains, indicating that the strain accommodation starts requiring the activation of the (10 times harder)

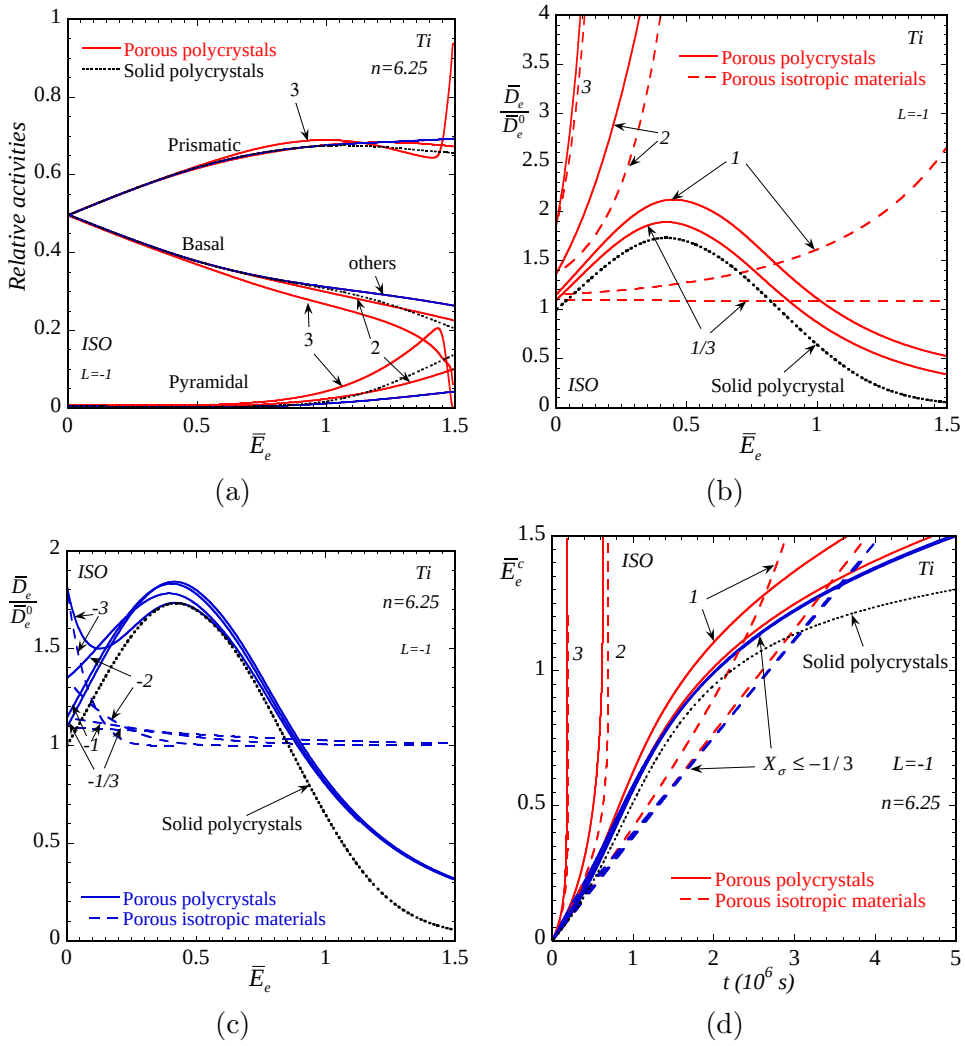

Figure 7.10: ISO results for porous Ti ($M = 10$) polycrystals with an initially isotropic distribution of spherical pores ($w_1^p = w_2^p = 1$) in $f_0 = 1\%$ porosity, subjected to axisymmetric loadings (7.7) with $L = -1$ ($\overline{\sigma}_{11} = \overline{\sigma}_{22} \leq \overline{\sigma}_{33}$) and various triaxialities X_σ. The polycrystalline matrix is taken to be initially untextured, and the solid lines correspond to cases with texture evolution for the matrix, while the dashed lines correspond to cases without texture evolution for the matrix (so that the matrix is always isotropic). Results are shown for (a) the relative activities for different families of slip systems, (b) the normalized macroscopic strain rate $\overline{D}_e/\overline{D}_e^0$ for positive triaxialities, and (c) the corresponding results in (b) for negative triaxialities, as functions of the time-like variable $\overline{E}_e$. Results are also shown for (d) the macroscopic creep strain $\overline{E}_e^c$ as a function of time t.

pyramidal slip systems. Finally, note that the slip activities for the polycrystalline matrix are qualitatively similar to those for the fully dense polycrystal (dotted lines), while the slip activities for the isotropic matrix are almost constants throughout the deformation (not shown for brevity).

Fig. 7.10(b) and 7.10(c) display results for the macroscopic equivalent strain rate $\overline{D}_e$, normalized by the equivalent strain rate $\overline{D}_e^0$ for the corresponding *untextured* Ti polycrystal (see (7.13)), as a function of $\overline{E}_e$. We also include, for comparison, the corresponding results for a porous isotropic material (dashed lines) and a solid polycrystal (dotted lines). The results for positive triaxialities are shown in Fig. 7.10(b), while the results for negative triaxialities are shown in Fig. 7.10(c). In particular, we observe from Fig. 7.10(b) that the $\overline{D}_e/\overline{D}_e^0$ plot for a fully dense polycrystal initially increases with $\overline{E}_e$ (softening) and then decreases with $\overline{E}_e$ (hardening), which is induced by the texture evolution observed in Fig. 7.9(c) and 7.9(d). In addition, we observe that for $X_\sigma = 3$ and 2, the $\overline{D}_e/\overline{D}_e^0$ plots for the porous polycrystal and porous isotropic material are fairly similar to each other (but are dramatically different from the corresponding plot for the solid polycrystal): they both increase very rapidly with $\overline{E}_e$ suggesting strong softening behaviors. This softening is clearly induced by the significant porosity growth observed in Fig. 7.9(a). Therefore, it can be deduced that for large positive triaxialities, the overall behavior of the porous polycrystal is controlled by porosity growth, with the texture evolution of the matrix playing a diminished role. On the other hand, for $X_\sigma \leq 1$ the macroscopic behavior of the porous polycrystal is quite different from that of the porous isotropic material (see Fig. 7.10(b) and 7.10(c)), although the evolution of the porosity and pore shape for these materials are very similar (see Fig. 7.9(a) and 7.9(b)). For instance, for $X_\sigma = 1$, $1/3$ and $-1/3$, the porous polycrystal exhibits a softening–hardening behavior largely consistent with that of the solid polycrystal, regardless of how the porosity and pore shape evolve, suggesting that the overall behavior of the porous polycrystal for small triaxialities is strongly controlled by the texture evolution of the matrix. Note that for $X_\sigma = -3$, the porous polycrystal exhibits a complex hardening–softening–hardening behavior. By referring to the corresponding plots for the porosity evolution (Fig. 7.9(a)), we can

deduce that the initial hardening is due to the significant porosity reduction, while the subsequent behavior—being almost identical to that of the solid polycrystal—is due to the texture evolution for the matrix. Finally, it is well worth emphasized that the transition between the texture controlled regime and the porosity controlled regime is very sharp and takes place between $X_\sigma = 1$ and 2.

Fig. 7.10(d) presents results for the macroscopic creep strain $\overline{E}_e^c$ as a function of time. It is observed that, for $X_\sigma = 3$ and 2, the plots of the $\overline{E}_e^c$ for both the porous polycrystals and porous isotropic materials are fairly similar: they all grow very rapidly in time with monotonically increasing rates, in agreement with the increasing macroscopic strain rate observed in Fig. 7.13(b). As already discussed, this strong softening behavior is due to the significant porosity growth, which would be expected to lead to final failure of the material by void coalescence. For $X_\sigma \leq 1$, the plots of $\overline{E}_e^c$ for the porous polycrystals have "S" shapes with non-monotonic changes in the slope, consistent with the non-monotonic behavior of the corresponding $\overline{D}_e/\overline{D}_e^0$ plots in Fig. 7.10(b) and 7.10(c). These curves are qualitatively similar to that for a fully dense Ti polycrystal, but are significantly different from the corresponding curves for the porous isotropic materials (with more or less uniform slopes), which again confirms that the macroscopic behavior of the porous polycrystal at low triaxialities is largely controlled by the texture evolution of the matrix.

Fig. 7.11 shows ISO plots for the standard deviations of the von Mises stress ($\mathrm{SD}^{(1)}(\sigma_e)$) and equivalent strain rate ($\mathrm{SD}^{(1)}(D_e)$) in the polycrystalline matrix, as functions of $\overline{E}_e$. They are normalized, respectively, by the average von Mises stress $\overline{\sigma}_e^{(1)}$ and equivalent strain rate $\overline{D}_e^{(1)}$ in the matrix. It can be seen from Fig. 7.11(a) that, for very large triaxialities ($X_\sigma = 3$ and 2), the stress fluctuations increase rapidly with $\overline{E}_e$. This is induced by the rapid porosity growth observed in Fig. 7.9(a), which leads to the presence of more heterogeneities (i.e., vacuous inclusions) in the polycrystalline matrix. However, for smaller triaxialities ($X_\sigma \leq 1$), the stress fluctuations in the matrix are fairly similar to that in a fully dense polycrystal. This is because the porosity remains fairly low in these cases (e.g., f is less than 7% for $X_\sigma = 1$, and f is even lower for other triaxialities), and the stress fluctuation is mainly governed

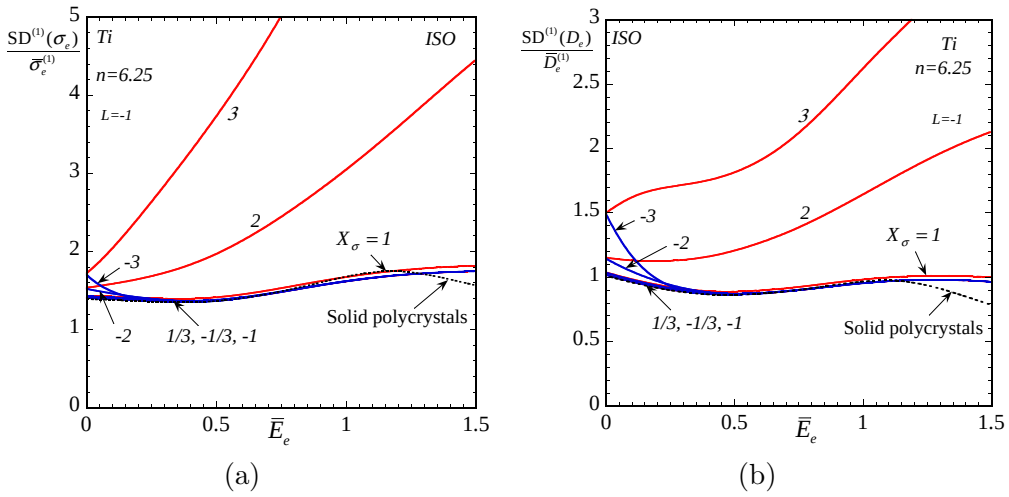

Figure 7.11: ISO results for porous Ti ($M = 10$) polycrystals with an initially isotropic distribution of spherical pores ($w_1^p = w_2^p = 1$) in $f_0 = 1\%$ porosity, subjected to axisymmetric loadings (7.7) with $L = -1$ ($\overline{\sigma}_{11} = \overline{\sigma}_{22} \leq \overline{\sigma}_{33}$) and various triaxialities X_σ. Results are shown for the standard deviation of (a) the von Mises stress $\mathrm{SD}^{(1)}(\sigma_e)$, and (b) the equivalent strain rate $\mathrm{SD}^{(1)}(D_e)$, normalized by the average von Mises stress $\overline{\sigma}_e^{(1)}$ and equivalent strain rate $\overline{D}_e^{(1)}$ in the matrix, respectively, as functions of the time-like variable $\overline{E}_e$.

by the underlying texture of the polycrystalline matrix. The above observations also hold for the strain rate fluctuations shown in Fig. 7.11(b), with the difference that the magnitudes of the strain rate fluctuations are somewhat smaller.

Axisymmetric compression

In Fig. 7.12, we examine the effect of the stress triaxiality X_σ on the evolution of the sub-structure of porous Ti polycrystals, for axisymmetric loadings (7.7) with $L = 1$ ($\overline{\sigma}_{11} = \overline{\sigma}_{22} \geq \overline{\sigma}_{33}$), and for different triaxialities. For comparison purposes, we also include the corresponding results for a porous isotropic material (in dashed lines) and a fully dense polycrystal (in dotted lines). Fig. 7.12(a) and 7.12(b) present ISO plots for the normalized porosity f/f_0 and pore aspect ratio $w^p = w_1^p = w_2^p$, respectively, as functions of $\overline{E}_e$. We observe from Fig. 7.12(a) that the general features of the f/f_0 plots are similar for $L = 1$ and for $L = -1$ (Fig. 7.9(a)). This suggests that the effect of the stress triaxiality on the porosity evolution is qualitatively similar for these loading conditions, where the porosity grows faster for larger triaxialities ($X_\sigma \geq 1$), while it

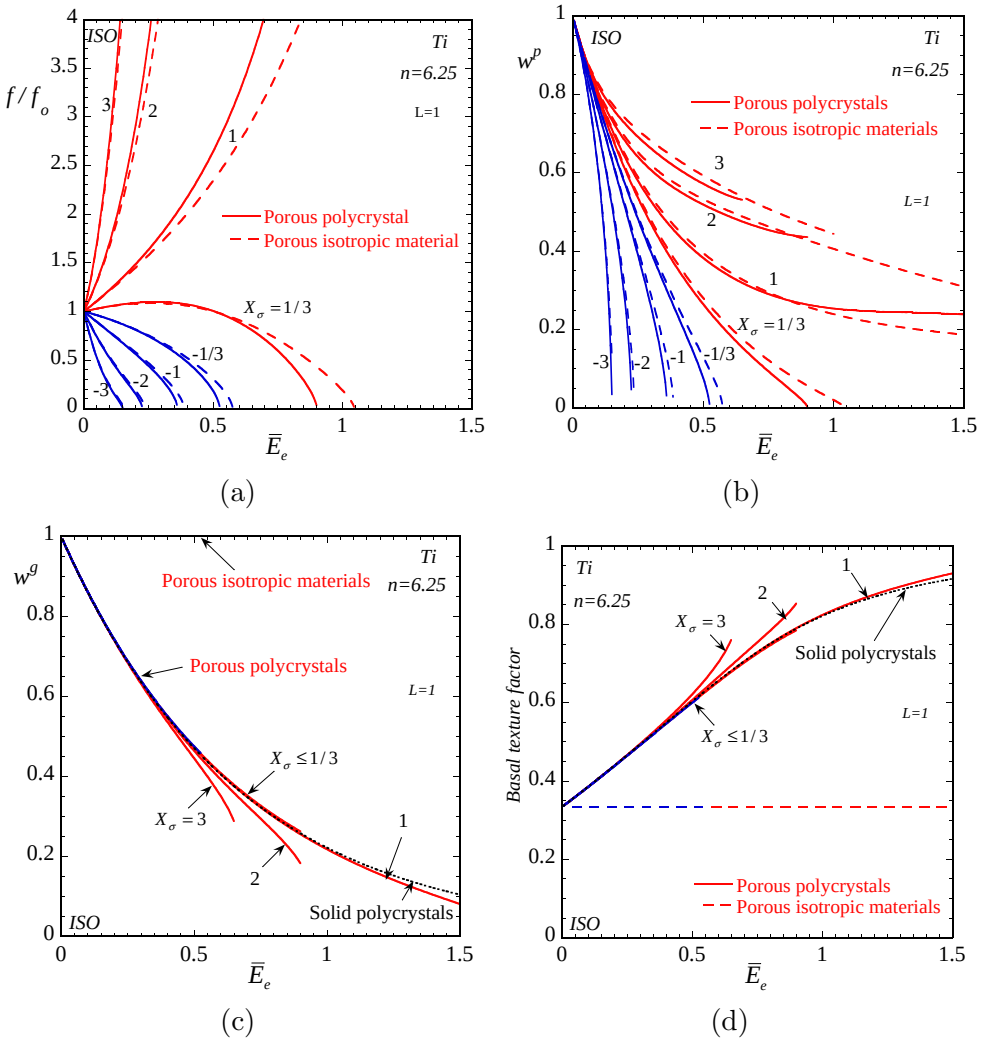

Figure 7.12: ISO results for porous Ti ($M = 10$) polycrystals with an initially isotropic distribution of spherical pores ($w_1^p = w_2^p = 1$) in $f_0 = 1\%$ porosity, subjected to axisymmetric loadings (7.7) with $L = 1$ ($\overline{\sigma}_{11} = \overline{\sigma}_{22} \geq \overline{\sigma}_{33}$) and various triaxialities X_σ. The polycrystalline matrix is taken to be initially untextured, and the solid lines correspond to cases with texture evolution for the matrix, while the dashed lines correspond to cases without texture evolution for the matrix (so that the matrix is always isotropic). Plots are shown for the evolution of the (a) normalized porosity f/f_0, (b) pore aspect ratios $w^p = w_1^p = w_2^p$, (c) grain aspect ratios $w^g = w_1^g = w_2^g$, and (d) basal texture factor along the loading axis $\mathbf{e}_3$, as functions of the time-like variable $\overline{E}_e$.

decreases faster for smaller triaxialities ($X_\sigma < 1/3$). However, for given negative triaxialities, the f/f_0 plots drop much more rapidly with $\overline{E}_e$ for $L = 1$ than for $L = -1$, indicating that voids are more prone to collapse for $L = 1$ than for $L = -1$. On the other hand, we observe from Fig. 7.12(b) that w^p decreases with $\overline{E}_e$ for all triaxialities, implying that the initially spherical pores evolve gradually towards oblate spheroidal pores. In addition, the pore shape evolution is found to be more rapid for low triaxialities, similar to the findings in Fig. 7.9(b). In particular, for $X_\sigma \leq 1/3$, w^p goes to zero at the same strain when f/f_0 goes to zero (see Fig. 7.12(a)), indicating that the initially spherical pores collapse into penny-shaped micro-cracks. Finally, note that the behavior of the pores for the porous polycrystals and for the porous isotropic materials are qualitatively similar, with slight quantitative differences.

Fig. 7.12(c) and 7.12(d) present the corresponding results for the evolution of the morphological and crystallographic texture, respectively, for the underlying polycrystalline matrix. The corresponding results for a fully dense polycrystal are also included in dotted lines for comparison. We observe from Fig. 7.12(c) that the grain aspect ratio $w^g = w_1^g = w_2^g$ starts from one and decreases monotonically with $\overline{E}_e$ for all values of X_σ, indicating that the initially equiaxed grains evolve progressively towards oblate spheroidal grains. On the other hand, the basal texture factor in Fig. 7.12(d) starts from 1/3 and increases monotonically with $\overline{E}_e$ for all triaxialities, which implies that the $\langle c \rangle$-axes of the grains tend to be aligned with the loading axis $\mathbf{e}_3$ forming strong basal textures. Therefore, the texture evolution for $L = 1$ is opposite to that for $L = -1$ (Fig. 7.9(c) and 7.9(d)), demonstrating a significant effect of the Lode parameter. Again, the texture evolution is found to be fairly insensitive to the triaxiality, and to be rather similar to that of a solid polycrystal, except for $X_\sigma = 3$ and 2, when the texture evolves more rapidly at large strains. For porous isotropic materials, both the grain aspect ratio and basal texture factor are constants, taking the value 1 and 1/3, respectively, since the texture of the matrix is fixed.

Fig. 7.13 shows the corresponding results for the relative activities and for the finite-strain effective behavior of the porous Ti polycrystal. Fig. 7.13(a) displays plots for the relative activities of the basal, prismatic and pyramidal slip systems.

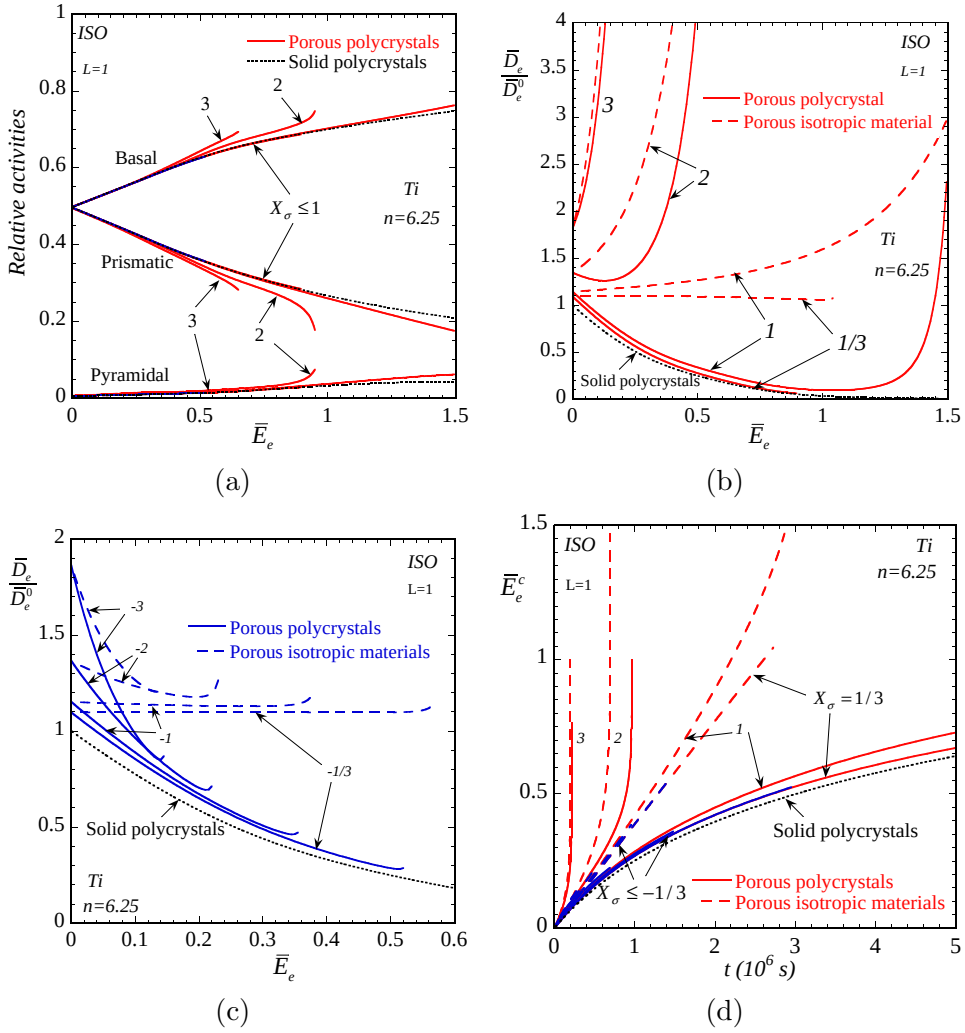

Figure 7.13: ISO results for porous Ti ($M = 10$) polycrystals with an initially isotropic distribution of spherical pores ($w_1^p = w_2^p = 1$) in $f_0 = 1\%$ porosity, subjected to axisymmetric loadings (7.7) with $L = 1$ ($\overline{\sigma}_{11} = \overline{\sigma}_{22} \geq \overline{\sigma}_{33}$) and various triaxialities X_σ. The polycrystalline matrix is taken to be initially untextured, and the solid lines correspond to cases with texture evolution for the matrix, while the dashed lines correspond to cases without texture evolution for the matrix (so that the matrix is always isotropic). Results are shown for (a) the relative activities for different families of slip systems, (b) the normalized macroscopic strain rate $\overline{D}_e/\overline{D}_e^0$ for positive triaxialities, and (c) the corresponding results in (b) for negative triaxialities, as functions of the time-like variable $\overline{E}_e$. Results are also shown for (d) the macroscopic creep strain $\overline{E}_e^c$ as a function of time t.

We observe from Fig. 7.13(a) that the evolution of the basal and prismatic activities for $L = 1$ is roughly opposite to that for $L = -1$ (Fig. 7.10(a)): the basal activity increases with $\overline{E}_e$, while the prismatic activity decreases with $\overline{E}_e$. Specifically, the basal slips are seen to contribute to more than 50% of the total shear deformations in the matrix throughout the deformation, which may lead to the development of strong basal textures, as already observed in Fig. 7.12(d). Note that as the $\langle c \rangle$-axes of the grains rotate towards the loading axis $\mathbf{e}_3$, a large amount of grains that are initially less favorably orientated for basal slips (e.g., grains with their $\langle c \rangle$-axes perpendicular to $\mathbf{e}_3$) become more favorably oriented to accommodate shear deformation through basal slips, thus resulting in the overall growth of the basal activity. Furthermore, we can see that the pyramidal activity increases with $\overline{E}_e$ for all triaxialities, indicating that more pyramidal slips are required to accommodate shear deformations in the matrix. Finally, note that the evolution of the relative activities for the porous polycrystal is very similar to that for a fully dense polycrystal, except for very large triaxialities ($X_\sigma = 3$ and 2), where the evolution of the relative activities is somewhat faster.

Fig. 7.13(b) and 7.13(c) present the corresponding ISO results for the normalized macroscopic equivalent strain rate $\overline{D}_e/\overline{D}_e^0$ for the porous polycrystals. The corresponding plots for a porous isotropic material (dashed lines) and for a fully dense Ti polycrystal (dotted lines) are also included for comparison. We can see from Fig. 7.13(b) that the $\overline{D}_e/\overline{D}_e^0$ plot for a solid polycrystal decreases monotonically with $\overline{E}_e$, suggesting a continuous hardening behavior (due to texture evolution), which is significantly different from the case for $L = -1$. For large positive values of the triaxiality ($X_\sigma = 3$ and 2), the porous polycrystal exhibits a strong softening behavior similar to that of the porous isotropic material. As already discussed, this behavior is induced by the significant porosity growth (see Fig. 7.12(a)), which has a strong softening effect that completely dominates the hardening effect of texture evolution. On the other hand, for $X_\sigma \leq 1$, the $\overline{D}_e/\overline{D}_e^0$ plot for a porous polycrystal exhibits a behavior largely consistent with that for a solid polycrystal, but dramatically different from that for a porous isotropic material. For instance, for $X_\sigma = 1$ the porous polycrystal exhibits an initial hardening behavior followed by a strong softening behavior at

very large strains. This clearly demonstrates the competition between the hardening mechanism provided by texture evolution and the softening mechanism provided by porosity growth. For $X_\sigma < 0$ (see Fig. 7.13(c)), while the $\overline{D}_e/\overline{D}_e^0$ curves for the porous polycrystal start from different values, depending on the triaxiality, they quickly tend to the corresponding plot for the fully dense polycrystal. This is because the porosity decreases in these cases and the behavior of the porous polycrystal becomes progressively closer to that of a fully dense polycrystal. Again, the macroscopic response of the porous polycrystal exhibits a sharp transition between the texture controlled regime and the porosity controlled regime, and the transition occurs between $X_\sigma = 1$ and 2.

Fig. 7.13(d) shows plots of the macroscopic equivalent creep strain $\overline{E}_e^c$ versus time. It is observed that for large positive triaxialities ($X_\sigma = 3$ and 2), the $\overline{E}_e^c$ plot for the porous polycrystal grows very rapidly with increasing slopes, exhibiting a behavior qualitatively similar to that of the porous isotropic material. On the other hand, for $X_\sigma \leq 1$ the $\overline{E}_e^c$ plots for the porous polycrystal increase in time with a progressively decreasing rate, exhibiting a behavior qualitatively similar to that of the solid polycrystal. These observations confirm the fact that porosity growth controls the macroscopic response of the porous polycrystal at high triaxialities, while the texture evolution of the matrix takes over at low triaxialities.

Fig. 7.14 presents the corresponding ISO plots for the standard deviations of the von Mises stress ($\mathrm{SD}^{(1)}(\sigma_e)$) and equivalent strain rate ($\mathrm{SD}^{(1)}(D_e)$) in the polycrystalline matrix, as functions of $\overline{E}_e$. They are normalized, respectively, by the average von Mises stress $\overline{\sigma}_e^{(1)}$ and equivalent strain rate $\overline{D}_e^{(1)}$ in the matrix. By comparing the stress fluctuations for $L = 1$ in Fig. 7.14(a) with those for $L = -1$ in Fig. 7.11(a), we can see that the general trends for $L = 1$ and -1 are very similar, but there are some differences. Most importantly, for $X_\sigma \leq 1/3$, the stress fluctuations become progressively weaker for $L = 1$, while they exhibit more complex (non-monotonic) behavior for $L = -1$. These discrepancies are mainly due to the significantly different texture evolutions in the matrix for $L = 1$ and -1 (see Fig. 7.12(d) and 7.9(d)). In addition, the stress fluctuations in the polycrystalline matrix at low triaxialities are found to

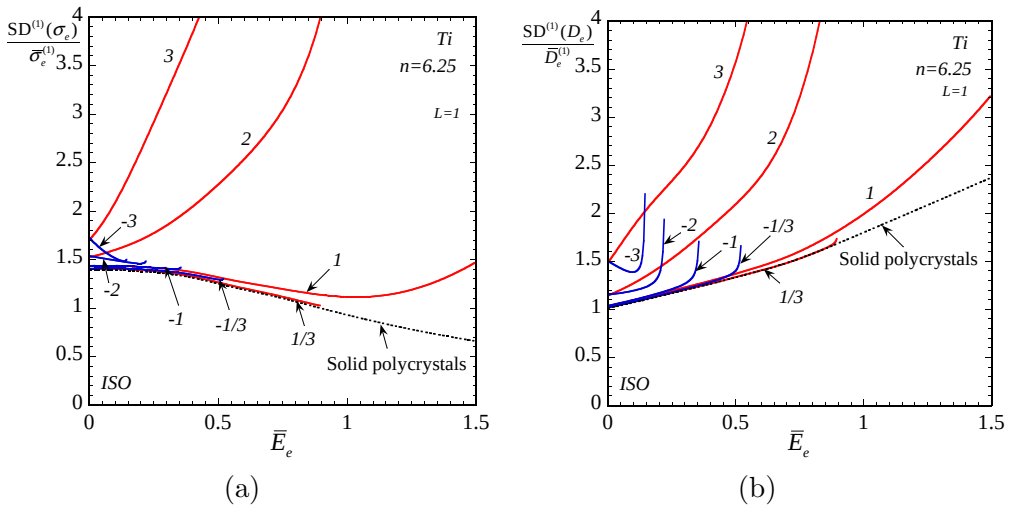

Figure 7.14: ISO results for porous Ti ($M = 10$) polycrystals with an initially isotropic distribution of spherical pores ($w_1^p = w_2^p = 1$) in $f_0 = 1\%$ porosity, subjected to axisymmetric loadings (7.7) with $L = 1$ ($\overline{\sigma}_{11} = \overline{\sigma}_{22} \geq \overline{\sigma}_{33}$) and various triaxialities X_σ. Results are shown for the standard deviation of (a) the von Mises stress $\mathrm{SD}^{(1)}(\sigma_e)$, and (b) the equivalent strain rate $\mathrm{SD}^{(1)}(D_e)$, normalized by the average von Mises stress $\overline{\sigma}_e^{(1)}$ and equivalent strain rate $\overline{D}_e^{(1)}$ in the matrix, respectively, as functions of the time-like variable $\overline{E}_e$.

be similar to those in the solid polycrystal, consistent with the fact that the porosity remains quite low for these cases and the fluctuations are largely determined by the underlying texture of the matrix. On the other hand, we can see from Fig. 7.14(b) that the strain rate fluctuations increase significantly with $\overline{E}_e$, suggesting stronger localizations of the deformation in the polycrystalline matrix. Note that for negative triaxialities, the strain rate fluctuations increase abruptly at the end of the deformation. As already mentioned, these results could be questioned on physical grounds, since they occur at very small pore aspect ratios ($w^p < 0.1$) prior to void collapse, where the contact of the void surface may have already taken place, thus changing the field distributions in the matrix.

7.4 Concluding remarks

In chapter 6, a finite-strain homogenization model was developed for the macroscopic response of two-scale porous polycrystals consisting of large pores distributed

randomly in a fine-scale polycrystalline matrix. The model is based on the fully optimized second-order (FOSO) homogenization method of Ponte Castañeda (2015), as well as on a generalization of the iterated homogenization procedure of Agoras and Ponte Castañeda (2013), and is referred to as the Iterated Second-Order (ISO) homogenization model. In particular, the ISO model developed in this work for porous polycrystals provides a generalization of the model of Song and Ponte Castañeda (2017b) for porous single crystals, by allowing the underlying matrix to have a fine-scale micro-structure consisting of single-crystal grains of different orientations.

In this chapter, the ISO model was used to generate estimates for both the instantaneous response and the evolution of the sub-structure for porous FCC and HCP polycrystals, subjected to axisymmetric loadings with different Lode parameters ($L = -1$ or 1) and stress triaxialities. The intrinsic effect of the texture evolution of the polycrystalline matrix was deduced by comparing with the corresponding results for porous isotropic materials, and found to be quite significant. More specifically, due to texture evolution the polycrystalline matrix may become progressively harder (or softer) to deform and, as a consequence, more (or less) deformation is accommodated by the pores. Similar observations have also been made by Lebensohn et al. (2004), although in the context of polycrystalline solids containing intergranular voids. Moreover, the texture evolution of the polycrystalline matrix was found to be fairly independent of the stress triaxiality, but to be quite sensitive to the Lode parameter. For instance, for porous HCP polycrystals the hexagonal axes of the crystal grains may tend to be perpendicular to, or aligned with, the axisymmetric loading axis, depending on the Lode parameter ($L = -1$ or 1). Thus, texture evolution can lead to strong crystallographic anisotropy of the polycrystalline matrix, which has important implications on the macroscopic response of the porous polycrystals. Furthermore, it was found that the porous polycrystal exhibits a behavior qualitatively similar to that of a fully dense polycrystal at low triaxialities, while it exhibits a strong softening behavior similar to that of a porous isotropic material at high triaxialities. These results strongly suggest that the overall hardening/softening behavior of the porous polycrystal is controlled by the texture evolution of the matrix at low

triaxialities, while it is controlled by porosity growth at high triaxialities, with a sharp transition from one regime to the other.

In summary, the results of this chapter help confirm the significant effect of the texture evolution of the matrix on the macroscopic response of porous materials, suggesting the need of accounting for the combined effects of porosity growth and texture evolution. Therefore, the capability of the ISO model to effectively handle the multi-scale nature of the porous polycrystals constitutes one of the distinctive advantages relative to other more empirical models. In addition, the ISO model is fully predictive—without the need of fitting parameters requiring recalibration for different material systems—and applies for a wide range of porous polycrystals with different crystallographic anisotropies, porosities, void morphologies and material nonlinearities. Having said this, the ISO model may still be susceptible to potential improvements, especially for high-triaxiality loadings. Improved results may be possible by means of other, yet-to-be-developed choices of the weight factors $\alpha_{(k)}^{(r)}$, and this will be pursued in future work.

Chapter 8

Closure

In this dissertation, a general nonlinear homogenization framework was developed for viscoplastic porous single crystals and porous polycrystals subjected to finite deformations. The framework has the ability to account for the instantaneous effective behavior of porous crystals for given fixed states of the microstructure, as described by the porosity, average pore morphology and the texture of the underlying matrix, as well as for the evolution of the microstructure at finite-strain deformations. The model is based on the recently developed fully optimized second-order homogenization approach of Ponte Castañeda (2015), and makes use of the effective behavior of a linear comparison composite (LCC)—with the same microstructure as the nonlinear composite of interest—to obtain the effective properties of the actual nonlinear composite. In particular, the above homogenization procedure is used in an iterative fashion (Agoras and Ponte Castañeda, 2013) to "discretize" the properties of the matrix in the LCC, thus generating significantly improved estimates, especially for high triaxialities and low porosities. , consistent homogenization estimates for the average strain rate and spin in the phases are used to develop evolution laws for the microstructural variables. In its final form, the model can be treated as a standard internal variable viscoplastic model, with microstructural variables serving as internal variables. The theoretical framework developed in this dissertation was used to generate estimates for the instantaneous macroscopic behavior and microstructure evolution for porous FCC and HCP single crystals and polycrystals. Next, we

summarize the main results in this dissertation.

In **Chapter 2**, a generalization of a recently developed iterated variational homogenization (IVH) method (Agoras and Ponte Castañeda, 2013) was used to obtain bounds for the effective flow potential of porous viscoplastic single crystals. The method was then implemented for low-symmetry, high-anisotropy porous HCP single crystals, such as porous ice, to investigate the macroscopic response of these materials under axisymmetric loading conditions. It was found that the overall size, shape and orientation of the macroscopic gauge surfaces exhibit a strong dependence on the instantaneous values of the porosity, void shape and crystal anisotropy, suggesting strong distortional hardening/softening effects in the macroscopic response of these materials under finite-strain loading conditions (leading to evolution of the microstructure). In addition, consistent IVH estimates for the average strain rate in the voids were computed to explore their implications for the evolution of the microstructure. Thus, it was found that strong crystal anisotropy may lead to fast porosity growth at low stress triaxiality and to significant void distortion rates at high stress triaxiality, which is in contrast to the corresponding results for porous isotropic materials. Furthermore, it was found that the dependence of the porosity growth and void distortion on the initial void shape is also strongly affected by the crystal anisotropy. In fact, the crystal anisotropy largely dominates over the effect of the void shape, leading to significantly different behaviors for porous ice and porous isotropic materials.

In **Chapter 3**, the fully optimized second-order (FOSO) variational method of Ponte Castañeda (2015), in combination with an appropriate generalization of the iterated homogenization procedure of Agoras and Ponte Castañeda (2013), was used to advance a finite-strain homogenization model for porous viscoplastic single crystals. The Iterated Second-order (ISO) homogenization model provides estimates that are exact to second order in the heterogeneity contrast for the instantaneous response of two-phase composite materials, and therefore improves on the IVH model developed in Chapter 2, which provides bounds that are only exact to first order in the heterogeneity contrast. Correspondingly, the ISO model also provides improved estimates

for the average strain rate and spin fields in the phases, thus leading to more accurate predictions for the evolution of the microstructure. In particular, the ISO model is the first model to consistently account for the evolution of both the "crystallographic" anisotropy induced by lattice rotation, as well as the "morphological" anisotropy induced by changes in size, shape and orientation of the voids. These distinguishing features are crucial for satisfying the overall objectivity requirements.

In **Chapter 4**, the ISO developed in Chapter 3 was used to generate estimates for both the instantaneous response and the evolution of the microstructure for porous viscoplastic FCC and HCP single crystals. The resulting estimates were found to be in quite good agreement with FEM results available from the literature (Srivastava and Needleman, 2012; 2015; Mbiakop et al., 2015b), demonstrating a remarkable predictive capability for the ISO model. Specifically, it was found that the effective instantaneous response of porous single crystals exhibits a strong dependence on the "crystallographic" anisotropy induced by the preferred orientation and constitutive properties of the active slip systems, as well as on the "morphological" anisotropy determined by the instantaneous values of the porosity and void shape. In addition, the intrinsic crystallographic anisotropy was found to have a significant effect on the dependence of the macroscopic response of the porous single crystals on the porosity and void morphology, indicating a complex, coupled interaction between the two different types of anisotropies. Furthermore, the evolution of the microstructure and the finite-strain response of porous crystals were found to be quite sensitive to the specific loading conditions, as characterized by the loading orientation, Lode angle and stress triaxiality. In particular, the ISO model revealed a significant effect of the crystallographic anisotropy on the evolution of the microstructure, which in turn has implications for the overall hardening (or softening)—and therefore also for shear localization—in these materials.

In **Chapter 5**, the FOSO method of Ponte Castañeda (2015) was used, for the first time, to obtain estimates of the self-consistent type for the finite-strain response and texture evolution of viscoplastic fully dense polycrystals. The FOSO model was first used to investigate the effective flow stress and field statistics of untextured HCP

polycrystals with varying degree of rate sensitivity and grain anisotropy. It was found that the FOSO estimates for the effective flow stress satisfy all known bounds, and show perfect agreement with the available FFT results. In particular, while the improvements over the earlier POSO estimates are only moderate for the effective flow stresses, they are rather significant for the field statistics, especially for low rate sensitivity and high grain anisotropy. The FOSO model was then employed to study the finite-strain response and texture evolution for initially isotropic HCP polycrystals, subjected to uniaxial compression. It was found that a strong basal texture develops as a result of the dominant basal slips. In addition, the HCP polycrystal was found to become strongly anisotropic, and to exhibit an overall softening-hardening behavior.

Chapter 6 was concerned with the development of a finite-strain homogenization model for the macroscopic response of viscoplastic porous polycrystals consisting of large pores embedded in a fine-scale polycrystalline matrix. The porous polycrystal was modeled as a two-scale composite, which has a porous meso-structure at the larger length scale, and a granular structure for the underlying matrix at the smaller length scale. The instantaneous response of the porous polycrystal for a fixed state of the sub-structure was determined by means of a generalization of the ISO homogenization method developed in Chapter 3. The method makes use of a linear comparison composite (LCC) with the same sub-structure as the actual nonlinear composite, but whose local properties are chosen optimally via a suitably designed variational principle. The effective properties of the resulting two-scale LCC were determined by means of a sequential homogenization procedure, involving the self-consistent estimates for the effective behavior of the polycrystalline matrix, and the Hashin-Shtrikman type estimates for the effective behavior of the porous composite. Additionally, consistent homogenization estimates for the average strain rate and spin fields in the phases were used to develop evolution laws for the sub-structural variables, accounting for the evolution of porosity, pore and grain morphology, as well as the crystallographic texture of the matrix. The model is quite general, and applies to two-scale porous polycrystals with general ellipsoidal pores and grains, general crystallographic texture and general crystal anisotropy, which are subjected to general three-dimensional

loading conditions.

In **Chapter 7** , the ISO model developed in Chapter 6 for porous polycrystals was used to generate estimates for both the instantaneous response and the evolution of the sub-structure for porous FCC and HCP polycrystals, subjected to axisymmetric loadings with different Lode parameters ($L = -1$ or 1) and stress triaxialities. The intrinsic effect of the texture evolution of the polycrystalline matrix was deduced by comparing with the corresponding results for porous isotropic materials, and found to be quite significant. More specifically, due to texture evolution the polycrystalline matrix may become progressively harder (or softer) to deform and, as a consequence, more (or less) deformation is accommodated by the pores. Similar observations have also been made by Lebensohn et al. (2004), although in the context of polycrystalline solids containing intergranular voids. Moreover, the texture evolution of the polycrystalline matrix was found to be fairly independent of the stress triaxiality, but to be quite sensitive to the Lode parameter. For instance, for porous HCP polycrystals the hexagonal axes of the crystal grains may tend to be perpendicular to, or aligned with, the axisymmetric loading axis, depending on the Lode parameter ($L = -1$ or 1). Thus, texture evolution can lead to strong crystallographic anisotropy of the polycrystalline matrix, which has important implications on the macroscopic response of the porous polycrystals. Furthermore, it was found that the porous polycrystal exhibits a behavior qualitatively similar to that of a fully dense polycrystal at low triaxialities, while it exhibits a strong softening behavior similar to that of a porous isotropic material at high triaxialities. These results strongly suggest that the overall hardening/softening behavior of the porous polycrystal is controlled by the texture evolution of the matrix at low triaxialities, while it is controlled by porosity growth at high triaxialities.

In summary, the results in this dissertation helped confirm the significant effect of the anisotropy of the matrix—either due to the local crystallography in single crystals or to the texture of polycrystals—on the overall constitutive response of porous single crystals and porous polycrystals, suggesting an additional level of complexity in the modeling of such materials. Due to its ability to deal with broad classes of materials with different crystallographic anisotropies, material nonlinearities, porosities and

void morphologies—without the need for fitting parameters requiring recalibration for different material systems—the ISO homogenization model provides a powerful tool for effectively handling the effect of porosity in viscoplastic single crystals and polycrystals.

Although significant progress has been made in modeling the behavior of porous single crystals and porous polycrystals, much remains to be done along these lines. First, the ISO model developed in this work is still amenable to potential improvements, especially for hydrostatic loading conditions, by means of other choices of the weight parameters $\alpha_{(k)}^{(r)}$ involved in the ISO model. In this regard, it is worth mentioning the recent work of Michel and Suquet (2017), which suggests that $\alpha_{(k)}^{(r)}$ could be related to higher-order moments of the stress field. This could be helpful in developing mathematically or physically motivated prescriptions for choosing $\alpha_{(k)}^{(r)}$ in an optimal fashion. At the very least, the weights $\alpha_{(k)}^{(r)}$ could be used as fitting parameters to improve the results for hydrostatic loadings. Second, at this stage, the ISO model only applies for porous polycrystals containing large pores, with the pore size much larger than the grain size. In reality, the voids present in polycrystalline solids may have different sizes relative to the grain size. For this reason, a further generalization of the ISO method to model the behavior of polycrystalline solids containing voids with different sizes is of great interest. Third, the main deformation mechanism in this work is taken to be dislocation creep of the single-crystal phases. The effects of other important mechanisms, such as twinning, dislocation climb, grain boundary sliding and dynamic recrystallization, should be considered in future work. Fourth, the effect of infinitesimal elasticity that was neglected in this work should be pursued in future work. This would allow us to further account for elastic distortions of the single-crystal phases, as well as to deal with cyclic loading conditions, where the effect of elastic unloading is crucial. Moreover, this will allow the model to be implemented into constitutive subroutines in commercial FEM codes (e.g., ABAQUS). Fifth, this work assumes that all crystals with the same initial orientation rotate together as one unit (phase), as governed by the *average* elastic spin over all grains in that phase. This assumption is similar to that made by most mean-field theories and,

as a consequence, the orientation of crystals in a given phase remain uniform throughout the deformation. However, the stress, strain rate and spin fields inside the grains can exhibit significant fluctuations, especially for low rate sensitivity and high grain anisotropy. Therefore, the above assumption could be too simplistic, and improved evolution laws making use of additional field-fluctuation information—being already available in the current homogenization model—should be pursued in future work.

Appendix

Appendix A

The evolution of pore shape and orientation in plastically deforming metals: implications for macroscopic response and shear localization

A constitutive model is proposed for the macroscopic response of porous plastic metals at finite strains. Besides taking into account the porosity evolution, which leads to pressure sensitivity and dilatant response, the model can also account for changes in the average shape and orientation of the pores by means of suitable microstructural variables which play the role of internal variables and serve to characterize the evolving anisotropy of the material. In particular, the model is used to determine the evolution of the average shape and orientation of the voids under simple shear loading, as well as to explore the concomitant implications for the macroscopic response and shear localization. The intrinsic effect of the void rotations is deduced from comparisons with corresponding results for pure shear loading (where the voids change shape, but undergo no rotation on average), and found to be significant. In addition, more

general loading conditions, involving combined tension and shear, are considered, and the effect of the stress triaxiality is investigated. It is found that there is an abrupt transition in the localization strain at a certain value of the triaxiality of about 0.3, with the localization strain dropping sharply both as the triaxiality increases, or decreases from this value. Furthermore, the results suggest that void rotations can dramatically enhance the susceptibility of the material to shear localization for a certain range of triaxiality values (between, approximately, 0.3 and 0.8).

A.1 Introduction

Ductile metals are known to contain random distributions of micro-voids, which are produced either as a consequence of the forming process itself (e.g., HIPPing and forging), or which nucleate in the material from second-phase particles and eventually grow and coalesce leading to material failure (Tvergaard, 1990; Benzerga and Leblond, 2010). When such porous materials are subjected to finite strains, the size, shape and orientation of the voids, as well as the positions of the voids relative to each other, evolve with the deformation. This work is concerned with the use of certain recently developed homogenization approaches (Agoras and Ponte Castañeda, 2013; Agoras and Ponte Castañeda, 2014) to describe the instantaneous macroscopic response of porous viscoplastic (including rigid plastic in the rate-insensitive limit) materials given the current state of the microstructure, as well as the evolution of the microstructure with the deformation, and its implications for failure through shear localization. In the present work, however, we focus on loading conditions involving macroscopic shear strains and leading to significant void rotations (as well as changes in porosity and void shape).

It should be emphasized that over the years there have been several other approaches that have been proposed to model the behavior of porous ductile materials. Gurson (1977) made use of limit analysis for a spherical shell to propose an isotropic, pressure-sensitive plasticity model accounting for dilatant behavior. This model has been shown to be accurate for nearly hydrostatic loading conditions (i.e., for high

stress triaxialities), but less so for deviatoric loadings and, in particular, cannot account for void shape and orientation changes leading to anisotropy development for such loadings. Yamamoto (1978) considered the effects of compressibility and porosity evolution on theoretical predictions for shear localization in porous media, and found that localization is facilitated by increasing triaxiality. In particular, these Gurson model prediction indicate that the material should become more resistant to failure by shear localization at low to vanishingly low stress triaxialities. However, this is in contradiction with recent experimental observations (Bao and Wierzbicki, 2004; Barsoum and Faleskog, 2007), which suggest that lower triaxialities tend to facilitate failure by shear localization at sufficiently low triaxialities. Motivated by these experimental results, Nahshon and Hutchinson (2008) have recently proposed a phenomenological modification of the constitutive model of Gurson (1977), consisting in a reinterpretation of the porosity evolution law as an isotropic damage evolution law to empirically account for the effects of the third invariant of the loading (Lode angle) on the material response at low triaxialities. By introducing suitable parameters and fitting them to appropriate experimental data, this approach has been successful in modeling certain features of material failure at low triaxialities (Xue et al., 2013). On the other hand, the homogenization models of interest in this work aim to be entirely predictive, by introducing suitable microstructural variables directly accounting for the changes in shape and orientation of the voids, and the associated changes in the overall anisotropy and instantaneous hardening of the material. While capturing this level of detail is certainly more challenging, the potential gains in terms of predictive capabilities could justify the added computational cost, which would still be much smaller than that required for full-field numerical simulations.

Additional approaches include micro-mechanical approaches attempting to generalize the work of Gurson (1977) by considering more general spheroidal and ellipsoidal void shapes (Gologanu et al., 1993; Madou and Leblond, 2012a). The advantage of these approaches is that they give accurate predictions for high-triaxiality loading conditions, but they are less general than the homogenization approaches, in particular, because it has not been possible to derive corresponding evolution equations

for the void rotation by means of these analyses. In this sense, the homogenization approaches to be developed in this work are more general since they provide consistent estimates for the average strain rate and vorticity in the voids, which can in turn be used to generate self-consistent evolution equations for the average void shape and rotation (Ponte Castañeda and Zaidman, 1994; Kailasam and Ponte Castañeda, 1998). Recently, Madou and Leblond (2013a) and Madou et al. (2013b) have proposed a combined approach making use of the Gurson limit analysis approach to obtain accurate estimates for the yield surface at high triaxialities, and of the homogenization approach of Ponte Castañeda and Zaidman (1994) and Kailasam and Ponte Castañeda (1998), improved through numerical fitting to finite-element simulations of confocal shells, to model the evolution of the void shape and rotation in the porous materials at low triaxialities.

A third approach is to make use of full-field numerical simulations, such as the ones recently carried out by Srivastava and Needleman (2013) and Tvergaard (2012; 2014), building on earlier work (e.g., Needleman, 1972; Tvergaard, 1981). These simulations typically assume periodicity of the microstructure so that the numerical calculation can be restricted to a unit cell of the microstructure. While this approach is expected to be more accurate than the approximate homogenization models of interest in this work, the assumption of periodicity of the microstructure is a limiting factor, the microstructures of actual porous metals normally being random. Furthermore, the numerical results for periodic distributions of voids show great sensitivity to the microstructural parameters, suggesting that accounting for the randomness of the porosity distribution may be crucial. In this sense, the homogenization estimates to be discussed below offer the capability of accounting for the random distribution of the voids by means of the two-point correlation functions for their centers, as well as changes in the average shape and orientation of the voids.

The first homogenization estimates accounting for the overall compressibility in the instantaneous response of porous viscoplastic solids were given by Ponte Castañeda and Willis (1988), making use of the nonlinear Hashin-Shtrikman-type variational approach of Talbot and Willis (1985). Improved estimates were obtained by Ponte

Castañeda (1991) making use of a new variational approach for a linear comparison composite (LCC) (see also Willis, 1991, and Michel and Suquet, 1992 for derivations of these estimates by other methods). Ponte Castañeda and Zaidman (1994) made use of the LCC variational homogenization method of Ponte Castañeda (1991) to advance constitutive models for porous viscoplastic solids accounting for the evolution of the microstructure (i.e., porosity and average void shape) under finite-strain loading conditions. In that work, the changes in pore shape were found to have a significant effect on the macroscopic response of the material at low stress triaxialities. In particular, it was shown that shear localization could take place at low triaxialities by void collapse—something that could not be accounted for by the Gurson model. By making use of the linear estimates of Ponte Castañeda and Willis (1995), this model was generalized to account for void-distribution effects (Kailasam et al., 1997), void rotations under general non-vanishing spin loadings (Kailasam and Ponte Castañeda, 1997), as well as strain-hardening and elasticity for the matrix phase (Kailasam et al., 2000; Aravas and Ponte Castañeda, 2004). The numerical implementation of these models in general purpose finite-element codes (e.g., ABAQUS) was considered by Aravas and Ponte Castañeda (2004).

While the predictions generated by these variational models have been found to be quite good for deviatoric loadings, where void shape changes are dominant, they become progressively less accurate with increasing stress triaxiality, especially for low porosities and high material nonlinearities (see Ponte Castañeda and Suquet, 1998 for more details). For this reason, several attempts have been made to obtain improved homogenization estimates for porous viscoplastic materials. In particular, building on the earlier work by Danas et al. (2008), Danas and Ponte Castañeda (2009a, 2009b) proposed an improved constitutive model for porous materials with evolving microstructures. The model was derived by making use of the more sophisticated "second-order" LCC procedure of Ponte Castañeda (2002), together with an ad hoc interpolation/extrapolation scheme, enforcing the exact agreement of the second-order model with the Gurson model for the special case of spherical/cylindrical voids subjected to purely hydrostatic loadings. The second-order model was found to deliver

fairly accurate results for the macroscopic response in several comparisons with FEM and other exact results. The model was also found to predict the development of shear localization instabilities due to void collapse at small stress triaxialities (Danas and Ponte Castañeda, 2012), although some of the predictions may need to be corrected to account for the possibility of contact of the void faces (Hutchinson and Tvergaard, 2012). In addition, it should be mentioned that Idiart (2008) has developed estimates based on sequentially layered microstructures, which have the distinguishing feature of reproducing exactly the hydrostatic point for spherical shells.

In this work, we will pursue an alternative approach that is based entirely on the variational linear comparison homogenization procedure—albeit used in a novel incremental fashion (Ponte Castañeda, 2012). This approach can account for the expected *non-uniformity* of the properties of the matrix phase in the porous LCC—and leads to results that are also in complete agreement with the predictions of the Gurson approach for high triaxialities. Thus, Agoras and Ponte Castañeda (2013) have developed an incremental procedure for generating constitutive models for porous viscoplastic materials consisting of random "ellipsoidal" distributions of ellipsoidal voids, where the shape and orientation of the voids may be different from that of their distribution. The method makes use of the work of Agoras and Ponte Castañeda (2011) to provide estimates for a finite number N of iterations of the macroscopic viscoplastic stress potential for porous materials with given, fixed microstructure. When the number of iterations is $N = 1$, the method recovers exactly the predictions of the earlier variational linear comparison method (Ponte Castañeda, 1991), and leads to progressively more accurate estimates as the number of iterations N is increased, especially for high triaxialities. In the limit as $N \to \infty$ the iterated estimates of Agoras and Ponte Castañeda (2013) recover identically those of Ponte Castañeda (2012), when the shape of the pores and the distribution are identical, and therefore they also recover the well-known exact result for purely hydrostatic loadings of the composite-sphere assemblage (Leblond et al., 1994) and the infinite-rank sequentially laminated microstructures (Idiart, 2008). In practice, however, it can be shown that a small number of iterations ($N \simeq 5 - 10$) is sufficient to generate accurate results,

which implies that the new iterated estimates are also relatively easy to compute. In recent work, Agoras and Ponte Castañeda (2014) have made use of the iterated variational procedure of Agoras and Ponte Castañeda (2013) to obtain consistent evolution equations for the average void shape under general triaxial, finite-strain loading conditions. In the present work, we propose to consider more general loading conditions incorporating the effects of void rotations due to shear-type loadings. This will be accomplished following similar developments in the context of the earlier variational procedure by Kailasam and Ponte Castañeda (1998) (see also Aravas and Ponte Castañeda, 2004), which make use of consistent homogenization estimates for the average strain-rate and vorticity in the porous phase to generate evolution equations for the void orientation, as well as the porosity and average shape of the pores. To bring out the significant effect of the pore shape and orientation, some results will be shown for the effective yield surfaces of porous plastic materials with various values of the pore aspect ratios and orientation angles. In addition, we will consider simple shear loading and investigate the effect of void rotations by comparisons with pure shear loadings, which result in void shape changes, but not in void rotations. Then, the model will be used to investigate the effect of the stress triaxiality on the macroscopic response and possible development of shear band instabilities in rigid-plastic porous materials with power-law strain hardening that are subjected to combined shear and tension under plane strain conditions. Our focus will be on the effect of the evolution of the pore orientation (and shape) on the anisotropic response and failure of the porous materials.

A.2 The iterated variational linear comparison homogenization model

In this section, we summarize the basic variables and equations of the Iterated Variational linear comparison Homogenization model developed by Agoras and Ponte Castañeda (2013, 2014), which we will henceforth refer to as the IVH model for

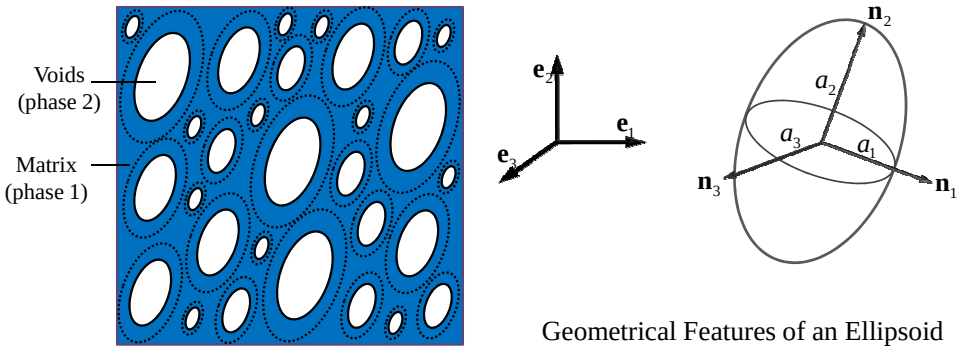

Figure A.1: Schematic representation of a porous metal consisting of aligned, ellipsoidal voids (solid lines) that are distributed with the same ellipsoidal symmetry (dotted lines) in a metal matrix.

short. We first introduce the internal variables of the IVH model, which characterize the hardening of the matrix (metal), porosity, shape and orientation of the voids. Next, we provide the macroscopic constitutive relation of the rigid-plastic porous metals and evolution laws for the above-mentioned internal variables. At last, expressions for the overall hardening rate are derived. For simplicity, elastic strains will be neglected in this work. However, it is straightforward to include such strains approximately, as was done, for example, by Aravas and Ponte Castañeda (2004).

A.2.1 Internal variables

The porous material is made up of two phases. The matrix material (phase 1) is isotropic, incompressible and rigid-plastic, and obeys the von Mises yield criterion:

$$\Phi(\boldsymbol{\sigma}) = \sigma_e^2 - \sigma_y^2 = 0, \tag{A.1}$$

where $\sigma_e = \sqrt{\frac{3}{2}\boldsymbol{\sigma}_d \cdot \boldsymbol{\sigma}_d}$ is the equivalent stress ($\boldsymbol{\sigma}_d$ is the stress deviator tensor) and σ_y is the yield stress under uniaxial tension. In addition, isotropic hardening of the matrix is assumed so that σ_y is a function of the accumulated plastic strain ε_M^p, such that

$$\sigma_y\left(\varepsilon_M^p\right) = \sigma_0\left(1 + \frac{\varepsilon_M^p}{\varepsilon_0}\right)^M, \tag{A.2}$$

where σ_0 is the initial tensile yield stress, ε_0 is the reference yield strain, and M is the strain hardening exponent of the matrix.

As shown in Fig. A.1, the voids (phase 2) are assumed to be of ellipsoidal shape (on average), and to be aligned, but distributed randomly in the matrix with a two-point correlation function for their centers characterized by "ellipsoidal" symmetry (Willis, 1977; Ponte Castañeda and Willis, 1995). In this work, for simplicity (Agoras and Ponte Castañeda, 2014), it is further assumed that the ellipsoidal shape and orientation of the distribution (i.e., the dashed ellipsoids in Fig.A.1) is identical to the ellipsoidal shape and orientation of the voids (i.e., the solid ellipsoids in Fig.A.1). However, it should be emphasized that, in general, the ellipsoid characterizing the distribution can be different from the ellipsoid characterizing the voids (Ponte Castañeda and Willis, 1995; Agoras and Ponte Castañeda, 2013).

According to the above hypothesis, the porous metal can be completely described by the set of internal variables defined by

$$\mathbf{s} \equiv \{\varepsilon_M^p, f, w_1, w_2, \mathbf{n}_1, \mathbf{n}_2, \mathbf{n}_3\}, \tag{A.3}$$

where ε_M^p characterizes the hardening of the matrix through equation (A.2), f is the volume fraction of the voids (porosity), $w_1 = a_3/a_1, w_2 = a_3/a_2$ are two aspect ratios characterizing the shape of the voids and distribution (a_1, a_2 and a_3 are respectively the lengths of the three semi-axes of the ellipsoid), and $\mathbf{n}_1$, $\mathbf{n}_2$ and $\mathbf{n}_3$ are unit vectors along the three principal directions of the ellipsoid. It is remarked here that, among the above-defined internal variables (A.3), ε_M^p describes a property of matrix phase, while the others (f, w_1, w_2, $\mathbf{n}_1$, $\mathbf{n}_2$, $\mathbf{n}_3$) characterize the microstructure of the porous metal. In addition, under the assumption that the ellipsoid characterizing the shape and orientation of the voids coincides with that of the distribution, the porous metal exhibits orthotropic behavior, with the axes of orthotropy coinciding with the principal directions of the voids. Note that these axes generally rotate with the deformation.

A.2.2 Macroscopic constitutive behavior

The macroscopic constitutive relation of the porous material is given by the iterated variational homogenization (IVH) estimate of Agoras and Ponte Castañeda (2013), which makes use of the effective properties of an appropriately chosen "linear comparison composite" (LCC), to estimate the effective behavior of the nonlinear porous material of interest. The key idea of the IVH is to construct the porous microstructure iteratively in a self-similar fashion, such that a more accurate description of the local fields in the porous metal can be achieved through appropriate statistics (i.e., second moments). In addition, the effective behavior of the LCC is computed iteratively by means of the estimates of Ponte Castañeda and Willis (1995) (to be referred to here as PCW estimates). As detailed in Agoras and Ponte Castañeda (2014), the effective yield surface of the porous material is given by

$$\widetilde{\Phi}^{IVH}(\overline{\boldsymbol{\sigma}};\mathbf{s}) = \left(\overline{\overline{\sigma}}_e^{(1)}(\overline{\boldsymbol{\sigma}};\mathbf{s})\right)^2 - \sigma_y^2 = 0, \tag{A.4}$$

where $\widetilde{\Phi}^{IVH}$ is the effective yield function, and $\overline{\overline{\sigma}}_e^{(1)}$ denotes the square root of the second moment of the equivalent stress field over the matrix phase, depending on both the macroscopic stress $\overline{\boldsymbol{\sigma}}$ and internal variables $\mathbf{s}$. For given $\overline{\boldsymbol{\sigma}}$ and $\mathbf{s}$, the determination of $\overline{\overline{\sigma}}_e^{(1)}$ in (A.4) requires the solution of a system of N nonlinear equations

$$\overline{\overline{\sigma}}_e^{(1)} = \left[\mathcal{F}_{[i]}\left(r_{[2]},...,r_{[N]}\right)\right]^{1/2}, \quad i = 1,...,N, \tag{A.5}$$

where the functions $\mathcal{F}_{[i]}\left(r_{[2]},...,r_{[N]}\right)$ are defined by expressions (A.29) in the Appendix, the variables $r_{[i]} > 0 \quad (i = 2,..,N)$ correspond to the remaining $N-1$ unknowns (see Agoras and Ponte Castañeda, 2014 for their physical meaning), and N is the number of iterations used in IVH. It should be mentioned here that the accuracy of the IVH improves progressively with increasing N. However, the fast convergence of the IVH with increasing values of N (Agoras and Ponte Castañeda, 2013) allows the use of relatively small numbers of iterations N to get accurate results, and hence, $N = 10$ is used in this work, which can be shown to give sufficient accurate predictions.

In particular, when porous materials consisting of initially spherical voids distributed isotropically in the matrix ($w_1 = w_2 = 1$) are subjected to purely hydrostatic loading condition $\overline{\boldsymbol{\sigma}} = \overline{\sigma}_m \mathbf{I}$, where $\overline{\sigma}_m = \mathrm{tr}\overline{\boldsymbol{\sigma}}/3$ and $\mathbf{I}$ is the second-order identity tensor, the solution to the system of equations (A.5) can be shown to be given by

$$\overline{\overline{\sigma}}_e^{(1)} = \frac{3}{2}\left(\sum_{j=1}^{N}\frac{1-c_{[j]}^{(2)}}{\sqrt{c_{[j]}^{(2)}}}\right)^{-1} |\,\overline{\sigma}_m\,|, \quad r_{[i]} = \left(\sqrt{\frac{c_{[i]}^{(2)}}{c_{[1]}^{(2)}}}\prod_{k=1}^{i-1} c_{[k]}^{(2)}\right)^{-1}, \quad i = 2,...,N. \tag{A.6}$$

where the $c_{[i]}^{(2)} > 0 \quad (i = 1,...,N)$ are incremental volume fractions in the IVH model, which are required to satisfy the condition $f = \prod_{i=1}^{N} c_{[i]}^{(2)}$. It should be noted here that the specific values of $c_{[i]}^{(2)} \quad (i = 1,...,N)$ will not significantly affect the accuracy of the IVH (Agoras and Ponte Castañeda, 2014) and they can be simply chosen as $c_{[i]}^{(2)} = f^{1/N} \quad (i = 1,...,N)$. For general microstructures and applied loadings, the system of equations (A.5) has to be solved numerically by means of an appropriate method, e.g., the Newton-Raphson method, where the above solution (A.6) can be used as an initial guess.

The macroscopic constitutive behavior of the porous metal is governed by the normality rule:

$$\overline{\mathbf{D}} = \dot{\lambda}\mathbf{N}, \quad \mathbf{N} \equiv \frac{\partial\widetilde{\Phi}^{IVH}}{\partial\overline{\boldsymbol{\sigma}}} = 2\overline{\overline{\sigma}}_e^{(1)}\frac{\partial\overline{\overline{\sigma}}_e^{(1)}}{\partial\overline{\boldsymbol{\sigma}}}, \tag{A.7}$$

where $\overline{\mathbf{D}}$ is the macroscopic Eulerian strain-rate tensor, $\dot{\lambda} \geq 0$ is the plastic multiplier, which can be determined from the "consistency condition," as will be discussed in section A.2.4, and $\mathbf{N}$ is the normal to the yield surface. For the effective yield function $\widetilde{\Phi}$ defined by relation (A.4) and (A.5), it can be shown (Agoras and Ponte Castañeda, 2014) that

$$\mathbf{N} = \frac{3}{\gamma}\widehat{\mathbb{M}}_{[N]}^{PCW}(r_{[j]})\,\overline{\boldsymbol{\sigma}}, \quad \text{with} \quad \gamma \equiv f\frac{1-c_{[1]}^{(2)}}{c_{[1]}^{(2)}} + \sum_{i=2}^{N}(1-c_{[i]}^{(2)})\left(\prod_{j=i+1}^{N} c_{[j]}^{(2)}\right)\frac{1}{r_{[i]}}, \tag{A.8}$$

where $\widehat{\mathbb{M}}_{[N]}^{PCW}(r_{[j]})$ is the normalized viscous compliance tensor given by expression (A.28) in the Appendix.

A.2.3 Evolution of the internal variables

When the porous metals undergo finite-strain deformation, the internal variables defined in (A.3) evolve, and in turn, affect the instantaneous effective constitutive relation of the materials. In this subsection, evolution equations for the internal variables defined in (A.3), characterizing both the hardening of matrix and the microstructure of the porous metals, are developed.

The evolution law for the accumulated plastic strain ε_M^p is given by (Gurson, 1977)

$$\dot{\varepsilon}_M^p = \dot{\lambda}\frac{\overline{\boldsymbol{\sigma}}\cdot\mathbf{N}}{(1-f)\sigma_y}, \tag{A.9}$$

where use is made of the condition that the macroscopic plastic work, $\overline{\boldsymbol{\sigma}}\cdot\overline{\mathbf{D}} = \dot{\lambda}\overline{\boldsymbol{\sigma}}\cdot\mathbf{N}$, is equal to the microscopic plastic work in the matrix phase, $(1-f)\sigma_y\dot{\varepsilon}_M^p$. It is recalled here that the tensile yield stress σ_y depends on the accumulated plastic strain ε_M^p through relation (A.2).

Considering the incompressibility of the matrix phase, the change in volume of the porous material equals the change in volume of the voids, and the evolution law for the porosity f takes the form (Gurson, 1977)

$$\dot{f} = (1-f)\overline{D}_{kk}, \tag{A.10}$$

where it is recalled that $\overline{\mathbf{D}}$ is the macroscopic Eulerian strain-rate tensor. Note that this expression can also be consistently derived from the variational homogenization methods (Ponte Castañeda and Zaidman, 1994).

The evolution of the shape and orientation of the voids (and distribution) depends on the local fields in a very complicated fashion, which is in practice, extremely difficult to determine exactly. However, for the purpose of homogenization, it is sufficient to know how the average shape and orientation of the voids (and distribution) evolve. Following the work of Ponte Castañeda and Zaidman (1994), Kailasam and Ponte Castañeda (1997, 1998) and Aravas and Ponte Castañeda (2004), it is assumed that the shape of the voids and distribution remain ellipsoidal during the deformation pro-

cess, but change their aspect ratios and orientations. More specifically, it is assumed that, on the average, the voids (and distribution) change their shape and orientation with the average strain-rate and spin field in the voids. Making use of these assumptions and of standard kinematical arguments for evolution of ellipsoid under uniform field, it follows that the evolution law of the aspect ratios $w_\alpha \quad (\alpha = 1, 2)$ is given by

$$\dot{w}_\alpha = w_\alpha \left(\mathbf{n}_3 \otimes \mathbf{n}_3 - \mathbf{n}_\alpha \otimes \mathbf{n}_\alpha \right) \cdot \overline{\mathbf{D}}^{(2)}, \qquad \alpha = 1, 2, \tag{A.11}$$

where $\overline{\mathbf{D}}^{(2)} = \mathbb{A}^{(2)} \overline{\mathbf{D}}$ is the average strain-rate tensor in the void phase, $\mathbb{A}^{(2)}$ is the strain-rate concentration tensor determined by expressions (A.31) and (A.32) in the Appendix.

Correspondingly, the following evolution equations are obtained for the unit vectors $\mathbf{n}_\alpha$ $(i = 1, 2, 3)$ along the three principal directions of the voids, namely

$$\dot{\mathbf{n}}_\alpha = \overline{\boldsymbol{\omega}} \mathbf{n}_\alpha, \qquad \alpha = 1, 2, 3, \tag{A.12}$$

where $\overline{\boldsymbol{\omega}}$ is an anti-symmetric tensor. Since the principal directions of the voids coincide with the Eulerian axes of the average deformation gradient of the voids, $\overline{\boldsymbol{\omega}}$ is determined by the well-known kinematical relation (e.g., Ogden, 1984)

$$\overline{\boldsymbol{\omega}} = \overline{\mathbf{W}}^{(2)} + \frac{1}{2} \sum_{\substack{\alpha,\beta=1 \\ \alpha \neq \beta \\ w_\alpha \neq w_\beta}}^{3} \frac{w_\alpha^2 + w_\beta^2}{w_\alpha^2 - w_\beta^2} \left[\left(\mathbf{n}_\alpha \otimes \mathbf{n}_\beta + \mathbf{n}_\beta \otimes \mathbf{n}_\alpha \right) \cdot \overline{\mathbf{D}}^{(2)} \right] \mathbf{n}_\alpha \otimes \mathbf{n}_\beta, \tag{A.13}$$

where $w_3 = a_3/a_3 = 1$, and $\overline{\mathbf{W}}^{(2)}$ is the average spin tensor of the voids. The tensor $\overline{\mathbf{W}}^{(2)}$ can be determined consistently from the IVH procedure in terms of the macroscopic strain-rate $\overline{\mathbf{D}}$ and macroscopic spin $\overline{\mathbf{W}}$, by means of expression (3.83), along with (A.34) and (A.35), as shown in the Appendix. For cases in which at least two aspect ratios are identical, special care needs to be taken, and this will be discussed later in this section.

For later use, we also provide the expression for the Jaumann derivative $\overset{\triangledown}{\mathbf{n}}_\alpha$ of the

orientation vectors, namely

$$\overset{\triangledown}{\mathbf{n}}_\alpha = \dot{\mathbf{n}}_\alpha - \overline{\mathbf{W}}\mathbf{n}_\alpha = \left(\overline{\boldsymbol{\omega}} - \overline{\mathbf{W}}\right)\mathbf{n}_\alpha, \qquad \alpha = 1,2,3. \tag{A.14}$$

The above equation may be rewritten in terms of the plastic spin $\overline{\mathbf{W}}^p = \overline{\mathbf{W}} - \overline{\boldsymbol{\omega}}$ (Dafalias, 1985; Aravas and Ponte Castañeda , 2004), representing the spin of the continuum relative to the microstructure, in the form

$$\overset{\triangledown}{\mathbf{n}}_\alpha = -\overline{\mathbf{W}}^p\mathbf{n}_\alpha, \qquad \alpha = 1,2,3. \tag{A.15}$$

Making use of expression (A.13) and (3.83), the plastic spin $\overline{\mathbf{W}}^p$ can be given explicitly by expression (A.36) in the Appendix.

It should be noted that when at least two of the aspect ratios are the same, certain components of $\overline{\mathbf{W}}^p$ become indeterminate. For example, when $w_1 = w_3$, the porous metal becomes transversely isotropic about the $\mathbf{n}_2$ direction, which leaves $\overline{W}^p_{13}$ indeterminate. Since $\overline{W}^p_{13}$ then becomes inconsequential, it can be set equal to zero. In other words, $\overline{\omega}_{13} = \overline{W}_{13}$ in this case. In addition, for spherical voids where $w_1 = w_2 = w_3$, the porous metal becomes isotropic, and similarly, we can set $\overline{\mathbf{W}}^p = \mathbf{0}$ and $\overline{\boldsymbol{\omega}} = \overline{\mathbf{W}}$.

With the evolution laws for the internal variables provided above, the porous medium remains orthotropic throughout the deformation process, although the axes of orthotropy can rotate in general. However, it should be recalled here that separate evolution laws for the shape and orientation of the voids and distribution can be considered (Kailasam et al., 1997; Kailasam, 1998). However, this will not be pursued in this work, since the effect of distribution is not expected to be significant for porous materials at low to moderate porosities.

A.2.4 The consistency condition and macroscopic hardening rate

The consistency condition is given by

$$\dot{\widetilde{\Phi}}^{IVH}(\overline{\boldsymbol{\sigma}};\mathbf{s}) = \frac{\partial\widetilde{\Phi}^{IVH}}{\partial\overline{\boldsymbol{\sigma}}}\cdot\overset{\triangledown}{\overline{\boldsymbol{\sigma}}} + \frac{\partial\widetilde{\Phi}^{IVH}}{\partial\varepsilon^{p}_{M}}\dot{\varepsilon}^{p}_{M} + \frac{\partial\widetilde{\Phi}^{IVH}}{\partial f}\dot{f} + \sum_{\alpha=1}^{2}\frac{\partial\widetilde{\Phi}^{IVH}}{\partial w_{\alpha}}\dot{w}_{\alpha} + \sum_{\alpha=1}^{3}\frac{\partial\widetilde{\Phi}^{IVH}}{\partial\mathbf{n}_{\alpha}}\cdot\overset{\triangledown}{\mathbf{n}}_{\alpha} = 0, \tag{A.16}$$

where $\overset{\triangledown}{\overline{\boldsymbol{\sigma}}} = \dot{\overline{\boldsymbol{\sigma}}} - \overline{\mathbf{W}}\overline{\boldsymbol{\sigma}} + \overline{\boldsymbol{\sigma}}\overline{\mathbf{W}}$ is the Jaumann derivative of the macroscopic stress tensor. In connection with (A.16), we recall that $\dot{\varepsilon}^{p}_{M}$, $\dot{f}$, $\dot{w}_{\alpha}$ and $\overset{\triangledown}{\mathbf{n}}_{\alpha}$ are given by the associated evolution laws (*A*.9), (*A*.10), (*A*.11) and (*A*.15) respectively. Making use of these evolution laws, the consistency condition (*A*.16) may be rewritten as

$$\mathbf{N}\cdot\overset{\triangledown}{\overline{\boldsymbol{\sigma}}} - \dot{\lambda}H_{J} = 0, \tag{A.17}$$

where $\dot{\lambda}$ is the plastic multiplier and H_J is the macroscopic Jaumann hardening rate of the porous metal, given by

$$H_{J} = H_{\varepsilon} + H_{f} + H_{w} + H_{\mathbf{n}}, \tag{A.18}$$

with

$$\begin{aligned} H_{\varepsilon} &= \frac{2\overline{\boldsymbol{\sigma}}\cdot\mathbf{N}}{1-f}\frac{d\sigma_{y}}{d\varepsilon^{p}_{M}}, \qquad H_{f} = -(1-f)N_{kk}\frac{\partial\widetilde{\Phi}^{IVH}}{\partial f}, \\ H_{w} &= -\sum_{\alpha=1}^{2}\left[(\mathbf{n}_{3}\otimes\mathbf{n}_{3} - \mathbf{n}_{\alpha}\otimes\mathbf{n}_{\alpha})\cdot\mathbb{A}^{(2)}\mathbf{N}\right]\frac{\partial\widetilde{\Phi}^{IVH}}{\partial w_{\alpha}}, \\ H_{\mathbf{n}} &= \overline{\boldsymbol{\Omega}}^{p}\cdot\sum_{\alpha=1}^{3}\left(\frac{\partial\widetilde{\Phi}^{IVH}}{\partial\mathbf{n}_{\alpha}}\otimes\mathbf{n}_{\alpha}\right), \end{aligned} \tag{A.19}$$

where $\overline{\boldsymbol{\Omega}}^{p}$ is given by expression (A.38) in the Appendix.

Making use of the consistency condition (A.17), the plastic flow rule (A.7) may

be rewritten in standard form as

$$\overline{\mathbf{D}} = \frac{\mathbf{N} \cdot \overset{\triangledown}{\boldsymbol{\sigma}}}{H_J} \mathbf{N}, \tag{A.20}$$

where it is recalled that $\mathbf{N}$ is given by (A.8), and H_J is given by expressions (A.18) and (A.19).

In conclusion, the plastic flow rule (A.20), combined with the yield criterion (A.4) and evolution laws (A.9), (A.10), (A.11) and (A.15), constitute a (complete) internal variable plasticity model, referred to here, for brevity, as the IVH model. It should be emphasized that the model incorporates the effect of void rotation, which then can be applied for general loading conditions including those involving simple shears. Under given loading conditions for the rigid-plastic porous metal, the IVH model has to be implemented incrementally, and the key ingredients of the procedure are: (1) the computation of the instantaneous response of the material at the end of each increment, and (2) the update of the internal variables (A.3) through the integration of the evolution laws. Here, we will adopt the backward Euler method proposed in the work of Aravas and Ponte Castañeda (2004) for the integration of the IVH model. At last, it should be emphasized that the IVH model is fully predictive, as it does not involve any fitting parameters. In other words, given the constitutive properties of the ductile matrix material and the initial values of the microstructural variables, the model provides estimates for the time-dependent, anisotropic response of the porous plastic metal.

In the next sections, we consider several applications of the IVH model. First, we provide results for the instantaneous macroscopic properties of porous materials subjected to combined shear and hydrostatic stress, with the goal of investigating the various effects of porosity, void shape and void orientation on the macroscopic yield surface of porous materials with prescribed (fixed) microstructures. Additional results for the effect of the porosity and pore shape (but not void orientation) for other types of loading conditions, as well as comparisons with other models and numerical results, have been given by Agoras and Ponte Castañeda (2013). Next,

we will consider the time-dependent response of the porous material under *simple shear* loading, investigating the evolution of the void shape and orientation and its implications for the macroscopic response and shear localization. The results will be compared to the earlier results of Agoras and Ponte Castañeda (2014) for *pure shear* loading, where void rotations are not expected, in particular, to assess the effect of void rotations under simple shear conditions. Finally, we will consider more general loading conditions involving combined shear and tension under plane strain conditions to investigate the effect of stress triaxiality on the macroscopic response of the porous materials, as well as implications for shear localization.

A.3 Instantaneous response: Macroscopic yield surfaces for combined shear and hydrostatic loading

In this section, we investigate the predictions of the IVH model for the instantaneous macroscopic response of porous metals, focusing on the effect of the microstructural variables, and especially on the effect of the void rotation. For simplicity, we restrict our considerations on microstructural configurations such that the principal axis $\mathbf{n}_2$ of the voids is always fixed and aligned with the corresponding laboratory axis $\mathbf{e}_2$, so that the average void orientation is completely characterized by the angle θ formed by the microstructural vector $\mathbf{n}_1$ and the laboratory axis $\mathbf{e}_1$, as shown in Fig. A.2. In this case, the microstructural variables reduce to the porosity, f, the two aspect ratios characterizing the ellipsoidal shape of the voids (and their distribution), $w_1 = a_3/a_1$ and $w_2 = a_3/a_2$, as well as the average orientation angle of the voids, θ.

We examine the effect of the microstructural variables on the yield surface of a porous metal for loading conditions of the type

$$\overline{\boldsymbol{\sigma}} = \overline{\sigma}_m \mathbf{I} + \overline{\sigma}_{13} \left(\mathbf{e}_1 \otimes \mathbf{e}_3 + \mathbf{e}_3 \otimes \mathbf{e}_1 \right), \tag{A.21}$$

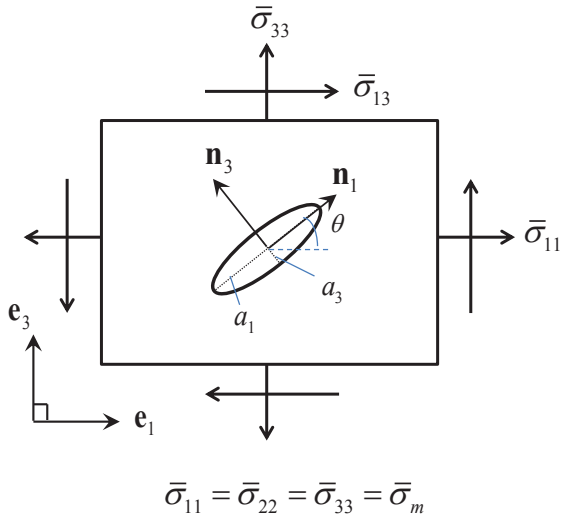

Figure A.2: Schematic representation (on the plane $\mathbf{e}_1$-$\mathbf{e}_3$) of the stress states and the associated pore average shape and orientation considered in the results of Fig. A.3.

combining hydrostatic stress $\overline{\sigma}_m$ and shear stress $\overline{\sigma}_{13} = \pm\overline{\sigma}_e/\sqrt{3}$ (see also Fig. A.2), where $\overline{\sigma}_e$ is the macroscopic equivalent stress.

Figure A.3(a) shows $\overline{\sigma}_m - \overline{\sigma}_{13}$ cross sections of the yield surfaces for $f = 1\%, 3\%$ and 10% porosity, with the pore average shape taken in all cases to be ellipsoidal with aspect ratios $w_1 = 0.1$ and $w_2 = 0.2$, and orientation angle $\theta = 0$. The main observation from Fig. A.3(a) is that increasing the porosity f leads to the reduction of the yield surface (especially at high stress triaxialities) and, thus, to softer behavior, as expected. In addition, note that the yield surfaces tend to become flat for low triaxialities (near the shear stress axis), especially for low porosities. This strongly nonlinear behavior is a well-known feature of porous plasticity.

On the other hand, Fig. A.3(b) shows $\overline{\sigma}_m - \overline{\sigma}_{13}$ cross sections of the yield surfaces of materials with fixed porosity $f = 10\%$ and orientation angle $\theta = 0$ for three different types of pore shape: an oblate pore shape with aspect ratios $w_1 = w_2 = 0.2$, a prolate pore shape with $w_1 = w_2 = 5$, and a more general, ellipsoidal pore shape with $w_1 = 0.2$ and $w_2 = 5$. In general, we observe from Fig. A.3(b) that changing the pore shape (i.e., changing the aspect ratios w_1 and w_2) has the effect of changing both the size and the shape of the yield surface, although *not* its orientation, which in turn implies that the pore shape may have *anisotropic* hardening or softening effects. In particular, we

observe that the material with oblate pores ($w_1 = w_2 = 0.2$) is quite softer than that with prolate pores ($w_1 = w_2 = 5$) for all combinations of shear $\overline{\sigma}_{13}$ and hydrostatic stress $\overline{\sigma}_m$. Note that the differences between these two yield curves are of the same order as those between the yield curves for porosities $f = 1\%$ and $f = 3\%$ or for porosities $f = 3\%$ and $f = 10\%$ in Fig. A.3(a), indicating that the effect of the pore shape may be accordingly of the same order as that of the porosity and, therefore, quite significant. The material with more general, ellipsoidal pores ($w_1 = 0.2$ and $w_2 = 5$) is softer than the other two under hydrostatic loading $\overline{\sigma}_m$ and harder than the other two under pure shear loading $\overline{\sigma}_{13}$, suggesting that the void shape change may have a strong hardening or a strong softening effect, depending on the loading direction.

Finally, Figs. A.3(c) and A.3(d) examine the effect of the pore orientation angle θ on the $\overline{\sigma}_m - \overline{\sigma}_{13}$ cross section of the yield surface of a porous metal with $f = 10\%$ porosity. More specifically, Fig. A.3(c) compares yield curves for orientation angles $\theta = 0, \pi/4$ and $\pi/6$ of ellipsoidal pores with aspect ratios $w_1 = 0.1$ and $w_2 = 0.2$, while Fig. A.3(d) compares yield curves for orientation angles $\theta = 0, \pi/4$ and $-\pi/4$ of oblate pores with aspect ratios $w_1 = w_2 = 0.2$. In the context of these results, it should be remarked that the yield stress of the material under purely hydrostatic loading $\overline{\sigma}_m$ is independent of the angle θ, as a result of the isotropic character of this loading. Note that the symmetry of the yield curves for $\theta = \pi/4$ and $\theta = -\pi/4$ about the axes $\overline{\sigma}_m = 0$ and $\overline{\sigma}_{13} = 0$ (see Fig. A.3(d)) reflects the corresponding symmetry of the applied loading with respect to the orientations $\theta = \pi/4$ and $\theta = -\pi/4$. In addition, it is observed that changes in the orientation of the pores result in changes not only in the size and shape of the yield surface, as in Figs. A.3(a) and A.3(b), but also in its orientation. The rotation of the yield surface induced by the corresponding rotation of the voids, as observed in Figs. A.3(c) and A.3(d), has important implications on the plastic anisotropy, as well as on the overall hardening/softening of the material. Note, for instance, that when the porous material is subjected to pure hydrostatic tension (or compression) $\overline{\sigma}_m$ the direction of the induced plastic flow, as defined by the normal $\mathbf{N}$ to the yield curves in Figs. A.3(c) and A.3(d), may vary substantially,

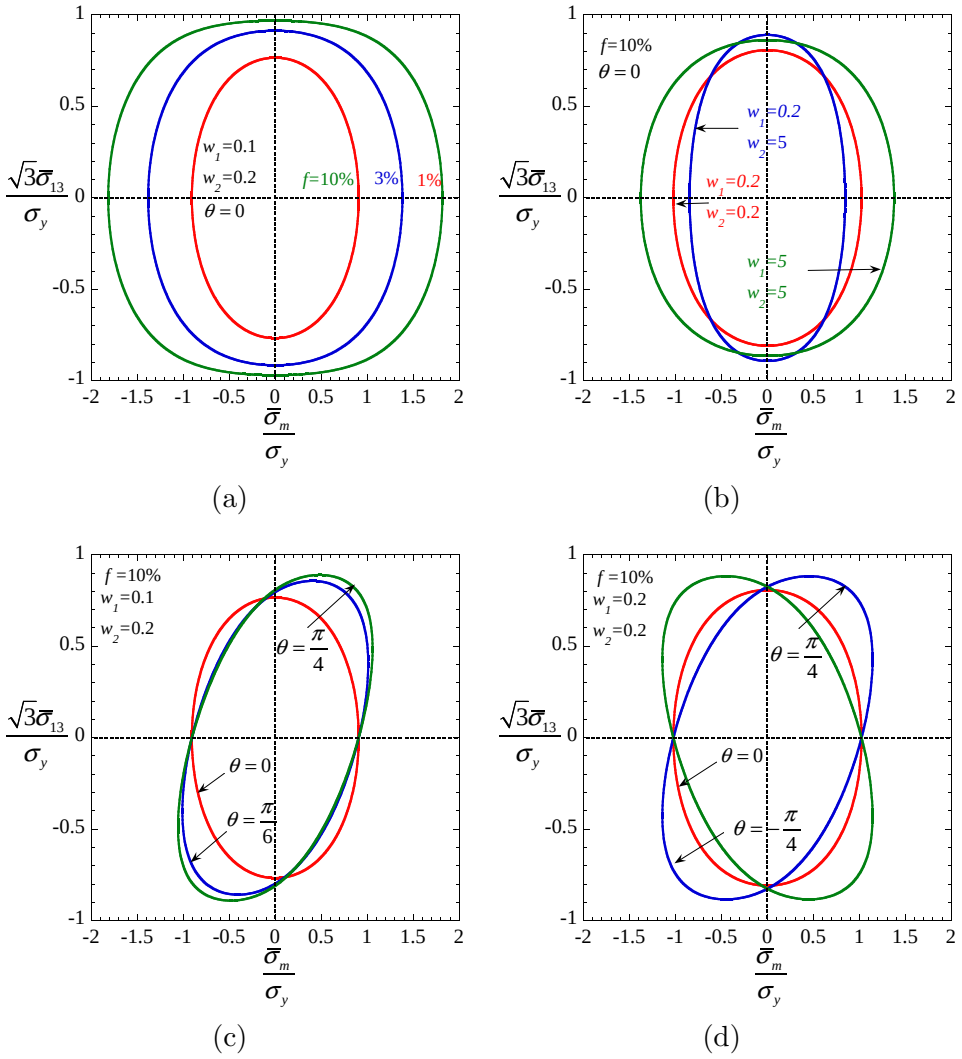

Figure A.3: The effect of the (a) porosity f, (b) pore average shape, as defined by the aspect ratios w_1 and w_2, (c) and (d) pore average orientation, as defined by the angle θ (Fig. A.2), on the yield surface of a porous material subjected to a mean stress $\overline{\sigma}_m$ combined with a shear stress $\overline{\sigma}_{13}$ (see Fig. A.2). In each case, yield curves on the plane $\overline{\sigma}_m - \overline{\sigma}_{13}$ are shown for different values of the variable the effect of which is being considered.

depending on the orientation of the voids, e.g., while for $\theta = 0$ the plastic flow is purely dilatational, for $\theta = \pi/4$ the plastic flow involves both a dilatational and a substantial shear component. An analogous conclusion can be drawn for the case that a pure shear stress $\overline{\sigma}_{13}$ is applied. Furthermore, we observe that the hydrostatic stress $\overline{\sigma}_m$ required to produce (instantaneously) simple shear deformation of the material, i.e., plastic flow parallel to the $\overline{\sigma}_{13}$ axis, is zero when the orientation of the voids is parallel to the direction of the applied shear ($\theta = 0$), but it reaches a value which is comparable to the corresponding shear stress $\overline{\sigma}_{13}$ when the voids are inclined at an angle $\theta = \pi/4, \pi/6$ or $-\pi/4$ with respect to the direction of the applied shear deformation.

A.4 Finite-strain response under plane strain conditions: Microstructure evolution, macroscopic stress-strain behavior and localization

In this section, we consider porous materials consisting of initially spherical voids distributed randomly and isotropically ($w_1 = w_2 = 1$) in a rigid-plastic matrix, with a yield stress σ_y characterized by the isotropic strain hardening relation (A.2), where $\varepsilon_0 = 0.001$ and $M = 0.1$. This material is subjected to plane strain loading conditions, prescribed by the affine velocity field $\mathbf{v} = \overline{\mathbf{L}}\mathbf{x}$, where $\overline{\mathbf{L}}$ is the velocity gradient tensor and $\mathbf{x}$ stands for the points on the boundary of the specimen. The components of $\overline{\mathbf{L}}$ are independent of $\mathbf{x}$, but not necessarily fixed in time, so that special conditions such as fixed stress triaxiality during the loading may be enforced when the components of $\overline{\mathbf{L}}$ are allowed to evolve in time. Specifically, letting $\overline{L}_{ij}$ denote the components of $\overline{\mathbf{L}}$ relative to a fixed coordinate system $\mathbf{e}_i$, two different cases corresponding to non-symmetric and symmetric $\overline{\mathbf{L}}$, respectively, are considered, as shown schematically in Figs. A.4(a) and A.4(b):

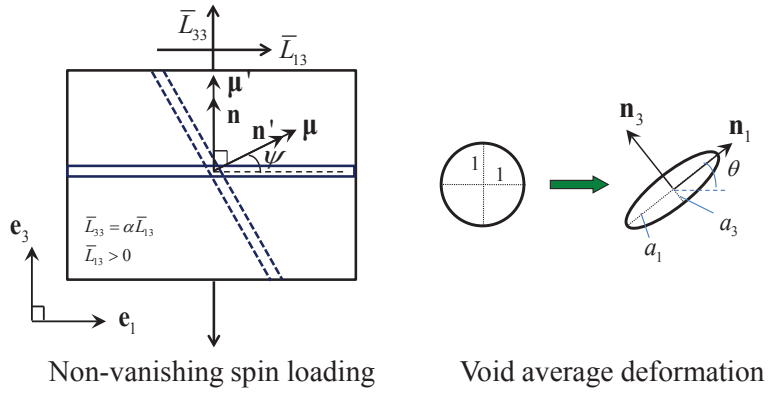

(a)

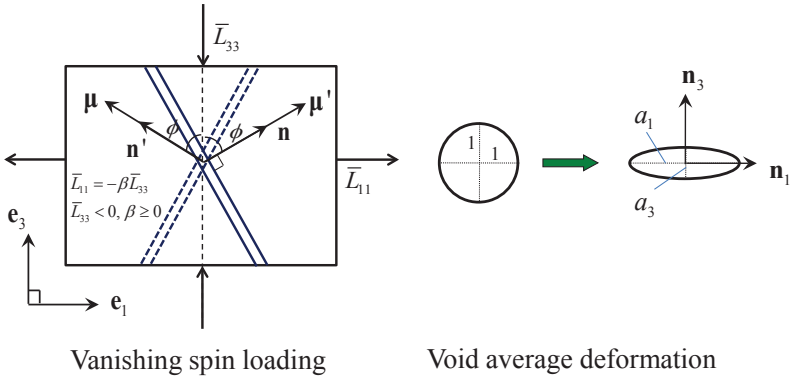

(b)

Figure A.4: Schematic representation of the (a) non-vanishing spin and (b) vanishing spin, plane strain loading conditions, defined by (A.22) and (A.23), respectively, along with the associated in-plane, average deformation of a representative void (sphere to ellipsoid). The void shape and orientation in the deformed state are defined by the associated aspect ratios $w_1 = a_3/a_1$ and $w_2 = a_3/a_2$, and the orientation angle θ, respectively. The geometrical features of the localization band that may develop at a certain critical strain are also shown.

- *Non-vanishing spin shear.*

$$\overline{L} = \begin{pmatrix} 0 & 0 & 1 \\ 0 & 0 & 0 \\ 0 & 0 & \alpha \end{pmatrix}, \quad \overline{D} = \begin{pmatrix} 0 & 0 & \frac{1}{2} \\ 0 & 0 & 0 \\ \frac{1}{2} & 0 & \alpha \end{pmatrix}, \quad \overline{W} = \begin{pmatrix} 0 & 0 & \frac{1}{2} \\ 0 & 0 & 0 \\ -\frac{1}{2} & 0 & 0 \end{pmatrix}, \quad \text{with} \quad \alpha \in \mathbb{R}, \tag{A.22}$$

and

- *Vanishing-spin shear.*

$$\overline{L} = \begin{pmatrix} \beta & 0 & 0 \\ 0 & 0 & 0 \\ 0 & 0 & -1 \end{pmatrix}, \quad \overline{D} = \begin{pmatrix} \beta & 0 & 0 \\ 0 & 0 & 0 \\ 0 & 0 & -1 \end{pmatrix}, \quad \overline{W} = \begin{pmatrix} 0 & 0 & 0 \\ 0 & 0 & 0 \\ 0 & 0 & 0 \end{pmatrix}, \quad \text{with} \quad \beta \geq 0. \tag{A.23}$$

Note that a loading of the type (A.22) is a combination of uniaxial straining with shear, while a loading of the type (A.23) corresponds to bi-axial straining. In general, a loading of the type (A.22) is expected to affect not only the porosity f and the average void (ellipsoidal) shape, as defined by the aspect ratios $w_1 = a_3/a_1$ and $w_2 = a_3/a_2$, but also the average void orientation in the $\mathbf{e}_1 - \mathbf{e}_3$ plane, as defined by the angle θ in Fig. A.4(a). On the other hand, a loading of the type (A.23) affects the porosity and the average void shape, but *not* the void orientation, i.e., under the loading conditions (A.23) the void orientation vectors $\mathbf{n}_i$ coincide with the fixed vectors $\mathbf{e}_i$ throughout the deformation (see Fig. A.4(b)).

For future reference, it is convenient to also introduce the macroscopic equivalent strain $\overline{E}_e = \int_0^t \overline{D}_e dt$, where t denotes the time variable, and $\overline{D}_e = \sqrt{\frac{2}{3}\overline{\mathbf{D}}_d \cdot \overline{\mathbf{D}}_d}$ is the equivalent strain-rate (with $\overline{\mathbf{D}}_d$ denoting the strain-rate deviator tensor). In particular, for the case of the non-vanishing spin loading (A.22),

$$\overline{D}_e = \frac{2}{3}\left(\overline{D}_{33}^2 + 3\overline{D}_{13}^2\right)^{1/2}, \tag{A.24}$$

while for the case of the vanishing-spin loading (A.23),

$$\overline{D}_e = \frac{2}{3}\left(\overline{D}_{11}^2 - \overline{D}_{11}\overline{D}_{33} + \overline{D}_{33}^2\right)^{1/2}. \tag{A.25}$$

As we have seen in the previous section, the variations of the various microstructural variables (f, w_1, w_2 and θ) during the deformation process may each have hardening or softening effects, the competition or synergy among which determines the overall hardening or softening of the macroscopic response of the material. As a consequence, there may be a certain critical strain during the loading process at which the softening effects may prevail over the hardening effects and, thus, the porous material may become unstable. In this work, we will consider specifically *macroscopic*, or *material* instabilities, which are characterized by localization of the plastic deformation within a thin band (or loss of strong ellipticity). As given by Rice (1977), the critical conditions for strain localization in rigid-plastic solids are:
(i) the normal $\mathbf{N}$ to the yield surface must be of the form

$$\mathbf{N} = \frac{1}{2}(\boldsymbol{\mu}\otimes\mathbf{n} + \mathbf{n}\otimes\boldsymbol{\mu}), \tag{A.26}$$

where $\mathbf{n}$ denotes the unit normal to the plane of the localization band and $\boldsymbol{\mu}$ is a suitably determined vector, and
(ii) the Jaumann hardening modulus H_J must be equal to the following critical value

$$H_{cr} = \frac{1}{2}|\boldsymbol{\mu}|^2(\overline{\sigma}_{\mu\mu} - \overline{\sigma}_{nn}), \tag{A.27}$$

where $\overline{\sigma}_{\mu\mu}$ and $\overline{\sigma}_{nn}$ are the normal stresses in the directions of $\boldsymbol{\mu}$ and $\mathbf{n}$, respectively.

Note that condition (A.26) is equivalent to requiring the localization plane to be a non-deforming plane. It can be easily shown that under the plane strain loading conditions (A.22) or (A.23) there exist two non-deforming planes (interchange the role of $\mathbf{n}$ and $\boldsymbol{\mu}$ in (A.26)), both of which are parallel to the constrained direction $\mathbf{e}_2$. For the non-vanishing spin loading (A.22), one of these planes has normal $\mathbf{e}_3$ and the other has normal oriented at an angle $\psi = \tan^{-1}\alpha$ with respect to $\mathbf{e}_1$ (see Fig. A.4(a)). On

the other hand, for the vanishing-spin loading (A.23), the two non-deforming planes are symmetrical relative to the directions $\mathbf{e}_1$ and $\mathbf{e}_3$, with their normals forming equal angles $\phi = \tan^{-1}\sqrt{\beta}$ with the direction $\mathbf{e}_3$ (see Fig. A.4(b)). Note also that the vector $\boldsymbol{\mu}$ may be easily obtained in terms of $\mathbf{n}$ and $\mathbf{N}$ by solving the linear equation (A.26), given that the normal $\mathbf{N}$ to the yield surface may be readily determined by means of the IVH estimate (A.8) for any given microstructural configuration and stress state during a loading of the type (A.22) or (A.23). It can also be shown that the vectors $\mathbf{n}$ and $\boldsymbol{\mu}$ are symmetrical with respect to the principal directions of $\mathbf{N}$ on the plane $\mathbf{n} - \boldsymbol{\mu}$, which in the case of the vanishing spin loading (A.23) coincide with the fixed directions $\mathbf{e}_1$ and $\mathbf{e}_3$. An implication of the latter result is that $\overline{\sigma}_{\mu\mu} = \overline{\sigma}_{nn}$ (since $\overline{\boldsymbol{\sigma}}$ is co-axial with $\mathbf{N}$) and, therefore, the critical condition (A.27) reduces to $H_{cr} = 0$ for the case of the vanishing-spin loading (A.23). Moreover, it should be mentioned that for vanishing-spin loading (A.23), the critical condition $H_{cr} = 0$ is reached on the two possible localization planes simultaneously, due to symmetry. However, for non-vanishing spin loading (A.22), the critical condition (A.27) on the two possible localization planes are not met at the same time. In fact, for the loading (A.22) considered in this work, it is found that the localization condition is always first met on the plane with unit normal $\mathbf{e}_3$, which is parallel to the shear loading plane. For this reason, only the critical conditions corresponding to this plane are shown in the following results for non-vanishing spin loading (A.22).

It should also be recalled that the predictions of the IVH model for vanishing-spin loadings (A.23), with β chosen to be constant throughout any given deformation history (fixed strain triaxiality) have been discussed in detail in Agoras and Ponte Castañeda (2014). In the present work, we focus on the predictions of the IVH model for the non-vanishing spin loading (A.22). In order to highlight the effect of void rotations, however, we will compare the new IVH results for non-vanishing spin loadings (A.22) with corresponding IVH results for vanishing-spin loadings (A.23). More specifically, in subsection A.4.1, we consider the special cases $\alpha = 0$ in (A.22) and $\beta = 1$ in (A.23), corresponding to simple and pure shear deformation, respectively. In subsection A.4.2 we also consider plane strain loadings of the type (A.22) and

(A.23), where the parameters α and β are computed such that the stress triaxiality $X_\sigma \equiv \overline{\sigma}_m/\overline{\sigma}_e$ is held fixed to a prescribed value throughout the deformation. Note that, constitutive models of the Gurson type, which account for the porosity but not for the shape and orientation of the voids, can *not* discriminate between the non-vanishing spin and vanishing-spin type of loadings considered in this work.

In addition, it should be remarked that for all results discussed in the following subsections the critical conditions for strain localization ($H_J = H_{cr}$) are labelled with *filled circles*. At this point, we recall that for the non-vanishing spin loading (A.22), the critical condition is first reached on the plane parallel to the shear loading plane and, for this reason, only the critical conditions corresponding to this plane are marked in the following results. Although shown for completeness, it should be emphasized that any IVH results beyond the filled circles may not be physically relevant, since a post-bifurcation study (which is beyond the scope of the present work) would be needed after the onset of localization. Furthermore, it should be recalled that under conditions of void collapse, i.e., when the aspect ratios w_1 and w_2 assume very small (or very large) values, the hypothesis adopted in the context of the IVH model that the pore shape remains ellipsoidal may become questionable on physical grounds, given that contact of the void surfaces is expected to take place prior to the complete void closure (Hutchinson and Tvergaard, 2012). For this reason, and given that for the loading conditions considered here we always have $w_1 \leq w_2 \leq 1$, conditions of considerably distorted pore shapes corresponding to the (arbitrarily chosen) aspect ratio $w_1 = 0.1$ are marked in the plots by *open squares*.

A.4.1 Simple and pure shear loading

It should be remarked that both simple shear deformation and pure shear deformation are isochoric loadings ($\overline{D}_{kk} = 0$) and, therefore, do *not* alter the porosity f in the material. The main difference between these loadings is that, while *simple shear* induces the evolution of both the average void shape and orientation, *pure shear* produces changes in the void shape, but *not* in the void orientation.

Figure A.5 shows plots of the predictions of the IVH model for the internal vari-

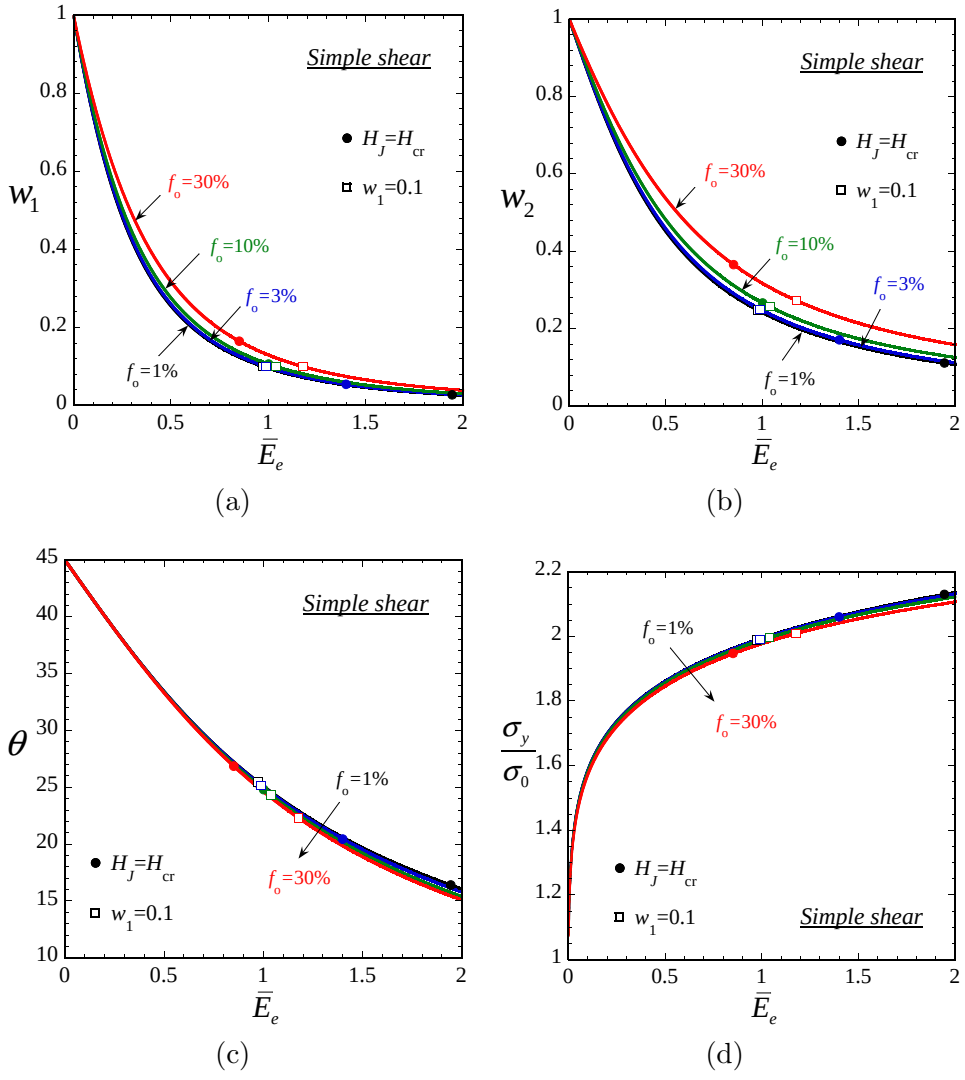

Figure A.5: IVH results for *simple shear* deformation of initially isotropic porous materials with porosities $f = 1\%, 3\%, 10\%$ and 30% ($f = f_0$ =fixed). Plots are shown for the evolution of the void aspect ratios (a) $w_1 = a_3/a_1$ and (b) $w_2 = a_3/a_2$, (c) void orientation angle θ, (d) yield stress σ_y of the matrix.

ables, as functions of the applied strain $\overline{E}_e$ under *simple shear* deformation, for initial porosities $f_0 = 1\%, 3\%, 10\%$ and 30% ($f = f_0$ =fixed). We observe that the aspect ratios w_1 (Fig. A.5(a)) and w_2 (Fig. A.5(b)) decrease monotonically with increasing strain $\overline{E}_e$ and tend to zero as $\overline{E}_e \to \infty$, indicating that the average void shape deforms continuously from spherical ($w_1 = w_2 = 1$) to flat ($w_1, w_2 \to 0$), while the average orientation of the voids (Fig. A.5(c)), as defined by the angle θ (see Fig. A.2), undergoes a continuous, clockwise rotation towards the horizontal axis. As expected, the yield stress of the matrix σ_y (Fig. A.5(d)) increases monotonically with increasing strain $\overline{E}_e$ with a rate that is initially very large, but then slows down as $\overline{E}_e$ continues to increase. Note further that the value of the porosity f_0 does not have a significant effect on the evolution of the internal variables.

Fig. A.6 shows the corresponding plots for the macroscopic response of the porous materials under simple shear deformation. From the results of Fig. A.6(a) for the macroscopic shear stress $\overline{\sigma}_{13}$, we observe that the porous metal exhibits a softer behavior for larger values of the porosity f_0 (note, for example, that $\overline{\sigma}_{13}$ is substantially smaller for $f_0 = 30\%$ than for $f_0 = 1\%$ porosity), as expected on physical grounds. In addition, we observe that, for any given f, $\overline{\sigma}_{13}$ increases initially with increasing $\overline{E}_e$ up to a certain critical strain, depending on f, at which it reaches a maximum (marked by a dot), and then drops continuously with further increases in $\overline{E}_e$. The aforementioned critical strain corresponds to the situation where the Jaumann hardening modulus H_J in Fig. A.6(c) reaches the critical value H_{cr}, implying the localization of the plastic deformation in a *shear band*, parallel to the shear plane of the loading (see Fig. A.4(a)). The initial hardening regime in the stress-strain response of Fig. A.6(a) is a consequence of the corresponding strain hardening of the matrix (Fig. A.5(d)), while the subsequent softening regime is induced by the anisotropic evolution of the microstructure (Figs. A.5(a)-A.5(c)), since the porosity f does not change during the loading. From the results of Fig. A.6(a), we also observe that the onset of localization occurs at smaller strains for higher values of the porosity f, indicating that the softening effect of the anisotropic evolution of the microstructure may be stronger for higher porosities.

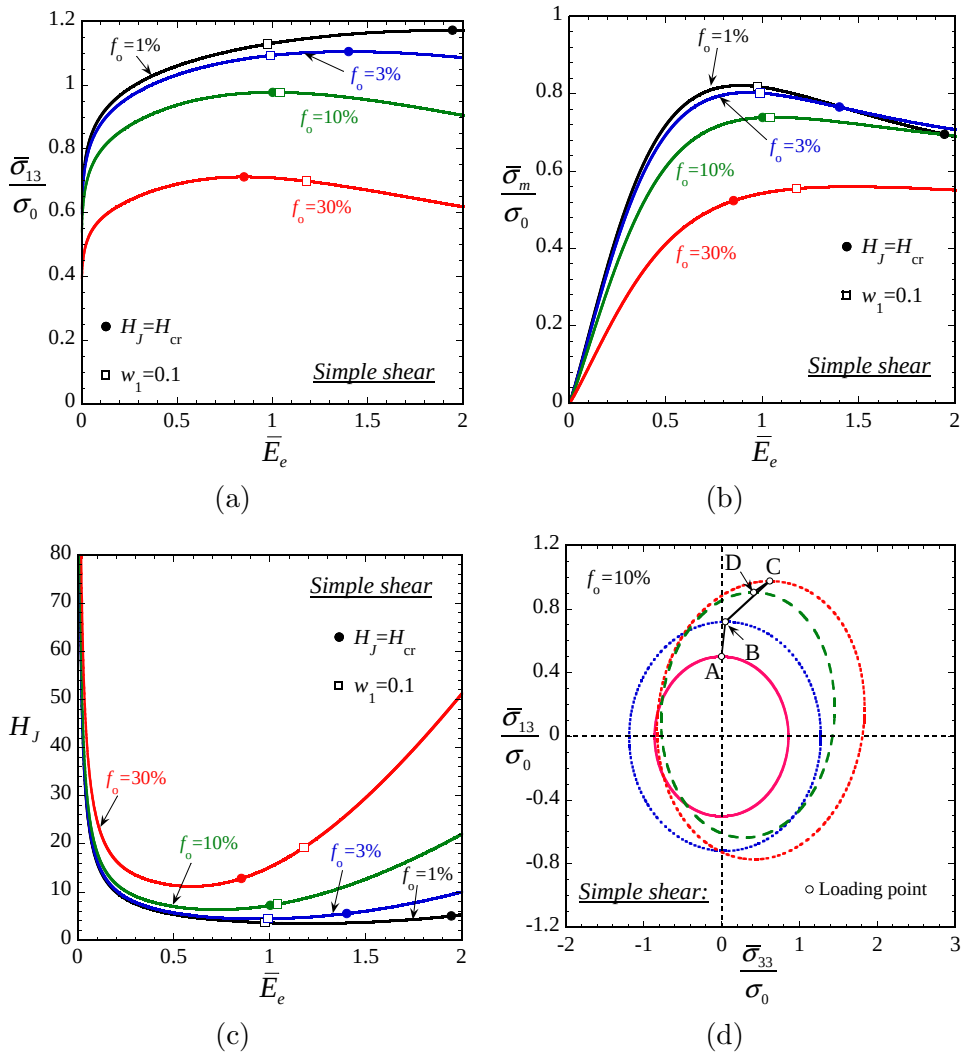

Figure A.6: IVH results for *simple shear* deformation of initially isotropic porous materials with porosities $f = 1\%, 3\%, 10\%$ and 30% ($f = f_0$ =fixed). Plots are shown for the evolution of (a) average shear stress $\overline{\sigma}_{13}$, (b) average mean stress $\overline{\sigma}_m$ and (c) macroscopic Jaumann hardening rate H_J. (d) The actual stress state (loading point) and associated $\overline{\sigma}_{13}-\overline{\sigma}_{33}$ cross section of the yield surface for the material with $f = 10\%$ porosity are shown at the strain levels: (A) $\overline{E}_e = 0$, (B) $\overline{E}_e = 0.037$, (C) $\overline{E}_e = 1.095$ and (D) $\overline{E}_e = 1.999$; the remaining non-zero (fixed) stress components on the yield curves shown are: (A) $\overline{\sigma}_{11} = 0$ and $\overline{\sigma}_{22} = 0$, (B) $\overline{\sigma}_{11} = 0.051\sigma_0$ and $\overline{\sigma}_{22} = 0.047\sigma_0$, (C) $\overline{\sigma}_{11} = 0.876\sigma_0$ and $\overline{\sigma}_{22} = 0.722\sigma_0$, and (D) $\overline{\sigma}_{11} = 0.981\sigma_0$ and $\overline{\sigma}_{22} = 0.680\sigma_0$.

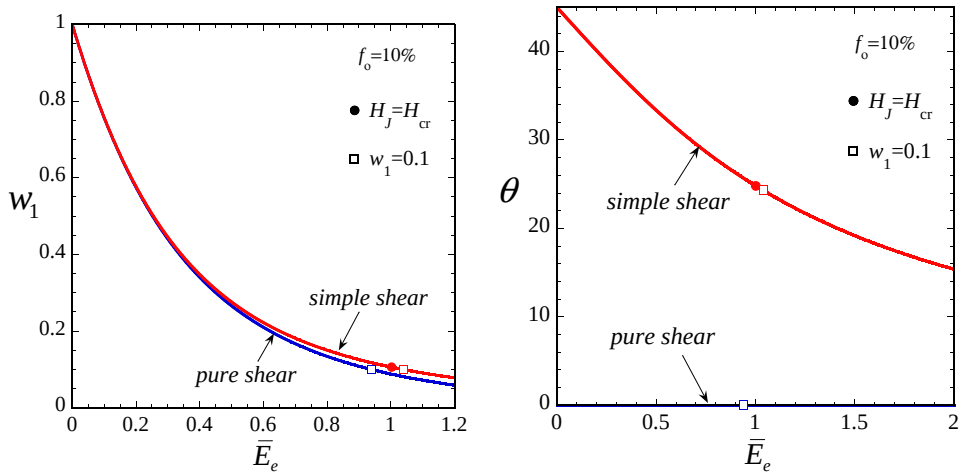

Figure A.7: Comparison of IVH results for *simple shear* deformation of an initially isotropic porous material with $f = 10\%$ porosity with corresponding results for *pure shear* deformation. Plots are shown for the evolution of the (a) void aspect ratio w_1, (b) void orientation angle θ.

The main observation from the results of Fig. A.6(b) is that the average mean stress $\overline{\sigma}_m$ produced in the porous material by the applied simple shear deformation reaches unexpectedly large values. In particular, for any given porosity f, we observe that $\overline{\sigma}_m$ is initially zero, but increases monotonically up to a certain strain level and then drops continuously with increasing strain. Note that, for each value of f, the maximum value of the mean stress $\overline{\sigma}_m$ is comparable with the corresponding maximum shear stress $\overline{\sigma}_{13}$, although $\overline{\sigma}_m < \overline{\sigma}_{13}$ (see Figs. A.6(a) and A.6(b)).

Fig. A.6(d) shows additional results for the evolution of the stress state (loading point) in the material with $f = 10\%$ porosity. In particular, this figure shows plots of the $\overline{\sigma}_{13} - \overline{\sigma}_{33}$ cross section of the yield surface, including the loading point, under the (fixed) conditions: (A) $\overline{E}_e = 0$, $\overline{\sigma}_{11} = 0$ and $\overline{\sigma}_{22} = 0$, (B) $\overline{E}_e = 0.037$, $\overline{\sigma}_{11} = 0.051\sigma_0$ and $\overline{\sigma}_{22} = 0.047\sigma_0$, (C) $\overline{E}_e = 1.095$, $\overline{\sigma}_{11} = 0.876\sigma_0$ and $\overline{\sigma}_{22} = 0.722\sigma_0$, and (D) $\overline{E}_e = 1.999$, $\overline{\sigma}_{11} = 0.981\sigma_0$ and $\overline{\sigma}_{22} = 0.680\sigma_0$. From these results, we observe that the yield surface expands from $\overline{E}_e = 0$ to $\overline{E}_e = 1.03$ and contracts from $\overline{E}_e = 1.03$ to $\overline{E}_e = 1.999$, reflecting accordingly the effect due to the strain hardening of the matrix as well as the hardening and softening effects of the anisotropic evolution of the microstructure (Figs. A.5(a)-A.5(c)) on the macroscopic response of the material (Figs. A.6(a) and

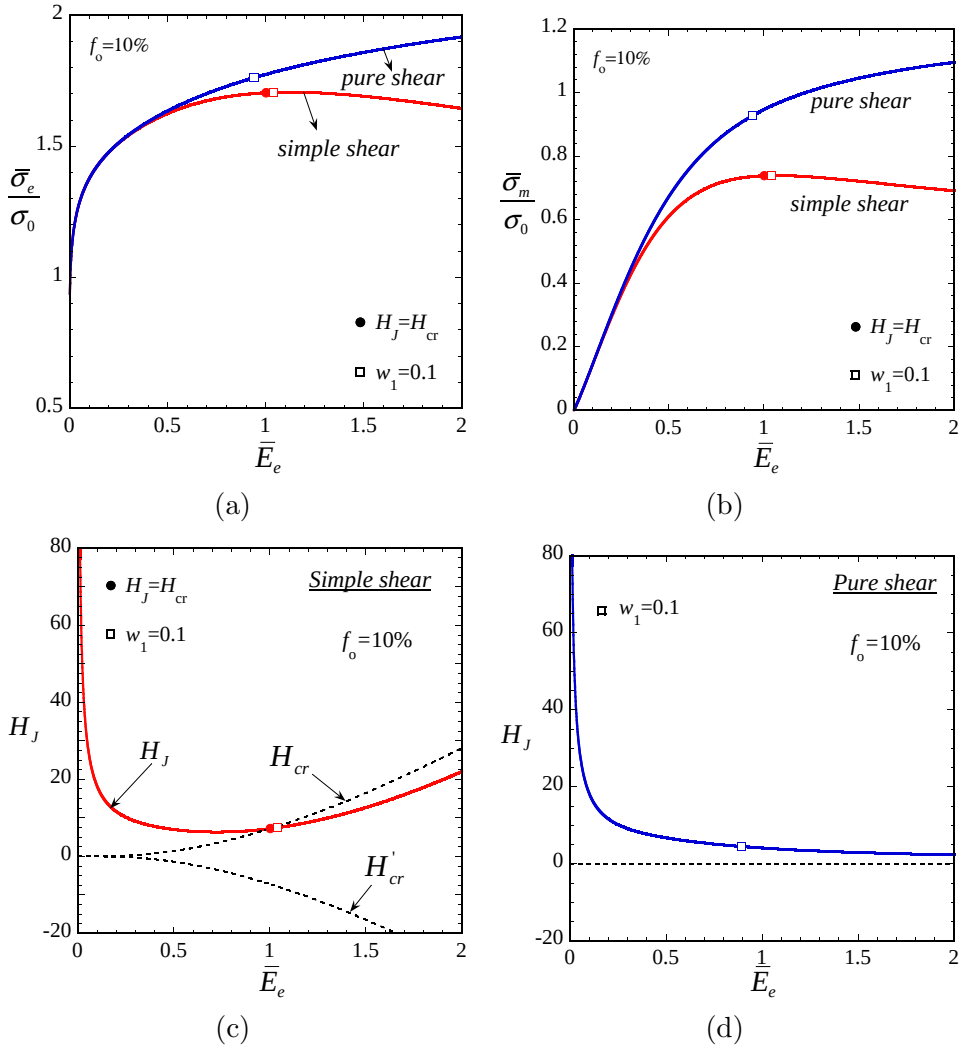

Figure A.8: Comparison of IVH results for *simple shear* deformation of an initially isotropic porous material with f = 10% porosity with corresponding results for *pure shear* deformation. Plots are shown for the evolution of the (a) average equivalent stress $\overline{\sigma}_e$, (b) average mean stress $\overline{\sigma}_m$, and macroscopic Jaumann hardening rate H_J for (c) simple shear and (d) pure shear.

A.6(b)). In addition, we observe that the yield surface rotates and translates along both the $\overline{\sigma}_{13}$ and the $\overline{\sigma}_{33}$ axis (as well as along the axes $\overline{\sigma}_{11}$ and $\overline{\sigma}_{22}$) with increasing strain, which in turn lead to the gradual development of large hydrostatic stresses $\overline{\sigma}_m$ during the simple shear deformation of the material (notice the shift of the loading point with increasing $\overline{E}_e$), as observed in Fig. A.6(b).

Figure A.7 and A.8 compare the response of a porous material with f = 10% porosity under *simple* and *pure shear* deformations. The results of Fig. A.7(a) for w_1 show that the evolution of the pore shape under simple shear is very similar with that under pure shear, with w_1 being only slightly larger in the former than in the latter case. Similar observations apply for the void aspect ratio w_2 and, thus, we omit the corresponding plot. On the other hand, from Fig. A.7(b) we observe that the void rotation is substantially different for the two types of loading, since the void orientation angle θ changes substantially under simple shear, while it remains fixed (aligned with the loading axes) under pure shear. It is also noted for completeness that the evolution of the yield stress of the matrix σ_y for pure shear is very similar with that for simple shear (Fig. A.5(d)) and, for this reason, the corresponding comparison for σ_y is also omitted. More interestingly, we observe from Figs. A.8(a) and A.8(b) that the stress-strain response of the porous material is almost identical for the two types of loading up to $\overline{E}_e \approx 0.3$. At larger strains, the two curves deviate from each other, with the stress-strain curve for pure shear increasing continuously with increasing $\overline{E}_e$ and the curve for simple shear exhibiting a softening behavior after a certain strain level. Accordingly, Fig. A.8(d) shows that under pure shear the critical condition ($H_J = 0$) for strain localization is never met, while Fig. A.8(c) shows that under simple shear the associated critical condition ($H_J = H_{cr}$) is satisfied at a given strain, at which the material behavior localizes into a shear band. The above observations indicate that the rotation of the voids (on average) has a strong softening effect at large enough strains which ultimately leads to the development of instabilities in the macroscopic behavior of the material.

A.4.2 Plane-strain loading at fixed stress triaxiality X_σ

Figure A.9-A.11 show plots of the IVH estimates for the evolution of the internal and macroscopic variables, as a function of the macroscopic equivalent strain $\overline{E}_e$, for the non-vanishing spin (continuous curves) and vanishing-spin (dotted curves) loading conditions (A.22) and (A.23), respectively. In these plots, the values of α and β are allowed to change with the deformation such that the stress triaxiality X_σ remains fixed throughout the loading process. Results are shown for an initially isotropic distribution of spherical voids with initial porosity $f_0 = 10\%$, subjected to stress triaxialities $X_\sigma = -1, -0.1, 0.1, 0.3, 0.6, 1$. Since the evolution of σ_y for the loading conditions considered here is similar to that discussed earlier for simple shear deformation (Fig. A.5(d)), the corresponding plots are omitted for brevity.

High triaxiality ($X_\sigma = 1$). When the porous material is subjected to the relatively large stress triaxiality $X_\sigma = 1$, under either non-vanishing spin or vanishing-spin loading conditions, we observe that the porosity f (Fig. A.9(a)) grows continuously and very rapidly with increasing strain $\overline{E}_e$, indicating accordingly a strong softening of the material. The changes on the average shape and orientation of the voids with increasing $\overline{E}_e$, as defined by the evolution of the microstructural variables w_1 (Fig. A.9(b)), w_2 (Fig. A.9(c)) and θ (Fig. A.9(d)), are not significant, when compared with the evolution of the porosity f. In addition, comparing the results for the evolution of the microstructure under non-vanishing spin (continuous curves) and vanishing-spin (dotted curves) loading, we infer that void rotation has practically no effect on the evolution of the porosity (Fig. A.9(a)), although it has some effect at large enough strains on the pore shape change (Figs. A.9(b) and A.9(c)).

From the results of Figs. A.10(a) and A.10(c) for the non-vanishing spin loading, we observe that at the early stages of the deformation the macroscopic response of the material exhibits hardening, which is due to the strain hardening of the matrix phase. However, as can be seen from Fig. A.11(a), the macroscopic hardening modulus H_J drops rather quickly, and at some critical value of the strain, it reaches the appropriate critical value H_{cr}, indicating the onset of strain localization. Subsequently,

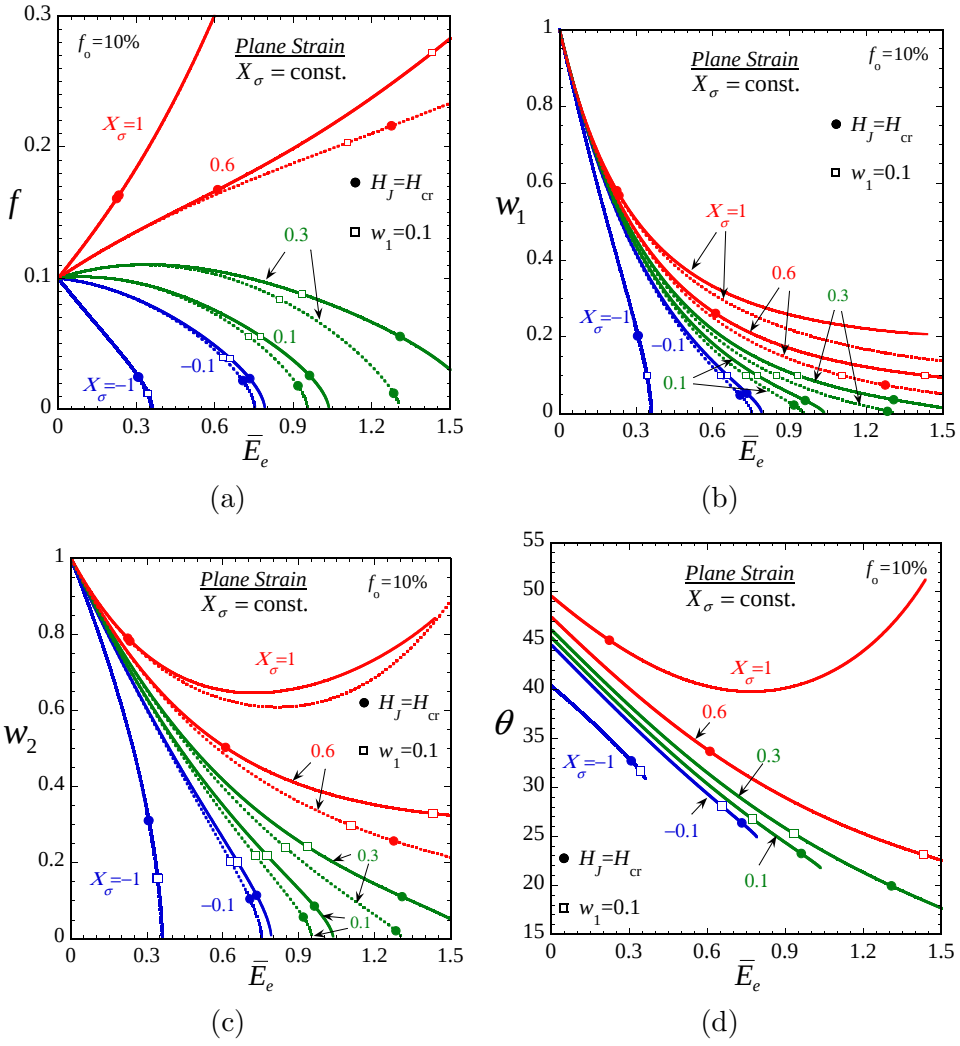

Figure A.9: IVH results for an initially isotropic porous material with $f_0 = 10\%$ initial porosity subjected to plane strain loading with fixed stress triaxiality X_σ. The evolution of the associated internal variables is shown as a function of the macroscopic equivalent strain $\overline{E}_e$ for the cases of non-vanishing spin loadings (continuous curves) and vanishing-spin loadings (dotted curves). (a) Porosity f for both cases. Void aspect ratios (b) $w_1 \equiv a_3/a_1$ and (c) $w_2 \equiv a_3/a_2$, also for both cases. (d) Void orientation angle θ for non-vanishing spin loadings.

the material exhibits continuous softening and the shear and normal components of the stress drop (see Figs. A.10(a) and A.10(c)). Furthermore, we observe that the evolution of the stress-strain curves (Figs. A.10(a) and A.10(c)) and of the hardening modulus (Fig. A.11(a)) for the non-vanishing spin loading are almost identical with the corresponding results for the vanishing-spin loading (Figs. A.10(b), A.10(d) and A.11(b)), which is consistent with our earlier observation that void rotation has a negligible effect on the evolution of the porosity (Fig. A.9(a)). The above observations indicate that, under either non-vanishing spin or vanishing-spin conditions, for the loading case $X_\sigma = 1$ the macroscopic response of the material is dominated by the softening effect due to the growth of the porosity, while the effects of the pore shape and orientation are negligible.

Moderate triaxiality ($X_\sigma = 0.6$). From the results for $X_\sigma = 0.6$, under either non-vanishing spin or vanishing-spin conditions, we observe that the porosity f (Fig. A.9(a)) grows once again, but with a smaller growth rate than for the case $X_\sigma = 1$. Thus, the evolution of the porosity acts again as a softening mechanism, but this time has a weaker effect. The void aspect ratio w_1 (Fig. A.9(b)) decreases gradually with increasing strain $\overline{E}_e$, as for the case $X_\sigma = 1$, but at a faster rate. On the other hand, the evolution of both w_2 (Fig. A.9(c)) and θ (Fig. A.9(d)) is significantly different for $X_\sigma = 0.6$ than for $X_\sigma = 1$, with w_2 and θ evolving faster and reaching smaller values in the present case. Comparing the evolution of the microstructural variables f, w_1 and w_2 for non-vanishing spin and vanishing-spin loadings (with $X_\sigma = 0.6$), it may be inferred that void rotation has the effect of accelerating void growth (Fig. A.9(a)) and decelerating the void shape change (Figs. A.9(b) and A.9(c)).

From the results of Figs. A.10(a) and A.10(c), we observe that the initial hardening regime of the macroscopic response for the case $X_\sigma = 0.6$ extends for larger strains than that for $X_\sigma = 1$, while from Fig. A.11(a) we observe that the drop of the hardening modulus H_J is slower for $X_\sigma = 0.6$ and, accordingly, the onset of strain localization occurs at a larger strain. Note that both these observations are consistent with our earlier observation that the softening effect due to the porosity growth is

weaker for $X_\sigma = 0.6$ than for $X_\sigma = 1$ (see Figs. A.9(a)). Quite interestingly, we observe from Fig. A.11(b) that the critical strain at the onset of localization for the case of the vanishing-spin loading is more than twice that for the case of the non-vanishing spin loading (see Fig. A.11(a)). Similar to the case of simple shear loading discussed in subsection A.4.1, this observation for $X_\sigma = 0.6$ suggests that void rotation may have a dramatic destabilizing effect on the macroscopic response of the material. In addition, it should be remarked that, for the non-vanishing spin conditions, localization takes place while the void shape is still quite rounded (the average aspect ratio w_1 reaching a value of 0.1 at nearly twice the critical strain). On the other hand, for the vanishing-spin conditions, the localization condition is met much later when the void shape is already quite flat and contact of the void faces may have already taken place. This suggests that shear localization may indeed be more physically relevant for non-vanishing spin conditions, where void rotations are significant, than for vanishing-spin conditions, where void rotations are not expected.

Small triaxiality ($X_\sigma = 0.3$). The evolution of the porosity f (Fig. A.9(a)) for $X_\sigma = 0.3$ is substantially different from that for the cases $X_\sigma = 0.6$ and $X_\sigma = 1$, discussed above. In particular, for $X_\sigma = 0.3$, we observe that the porosity f increases slightly up to a certain strain and then decreases continuously and tends to zero with increasing $\overline{E}_e$, indicating that the porosity evolution plays the role of a hardening mechanism in this case. Furthermore, we observe that the aspect ratios w_1 and w_2 (Figs. A.9(b) and A.9(c)) decrease faster for $X_\sigma = 0.3$ than for $X_\sigma = 0.6$ and go to zero at the same strain that f goes to zero, indicating a tendency of the voids to *collapse to micro-cracks*. In addition, we observe that the rotation of the voids, as defined by the evolution of the angle θ (Fig. A.9(d)), is only slightly faster for $X_\sigma = 0.3$ than for $X_\sigma = 0.6$. Comparing the evolution of the porosity f (Fig. A.9(a)) and aspect ratios w_1 (Fig. A.9(b)) and w_2 (Fig. A.9(c)) under non-vanishing spin and vanishing-spin loading, we observe that void rotation has the effect of decelerating the void collapse rate, i.e., the variables f, w_1 and w_2 go to zero at a larger strain for the non-vanishing spin loading.

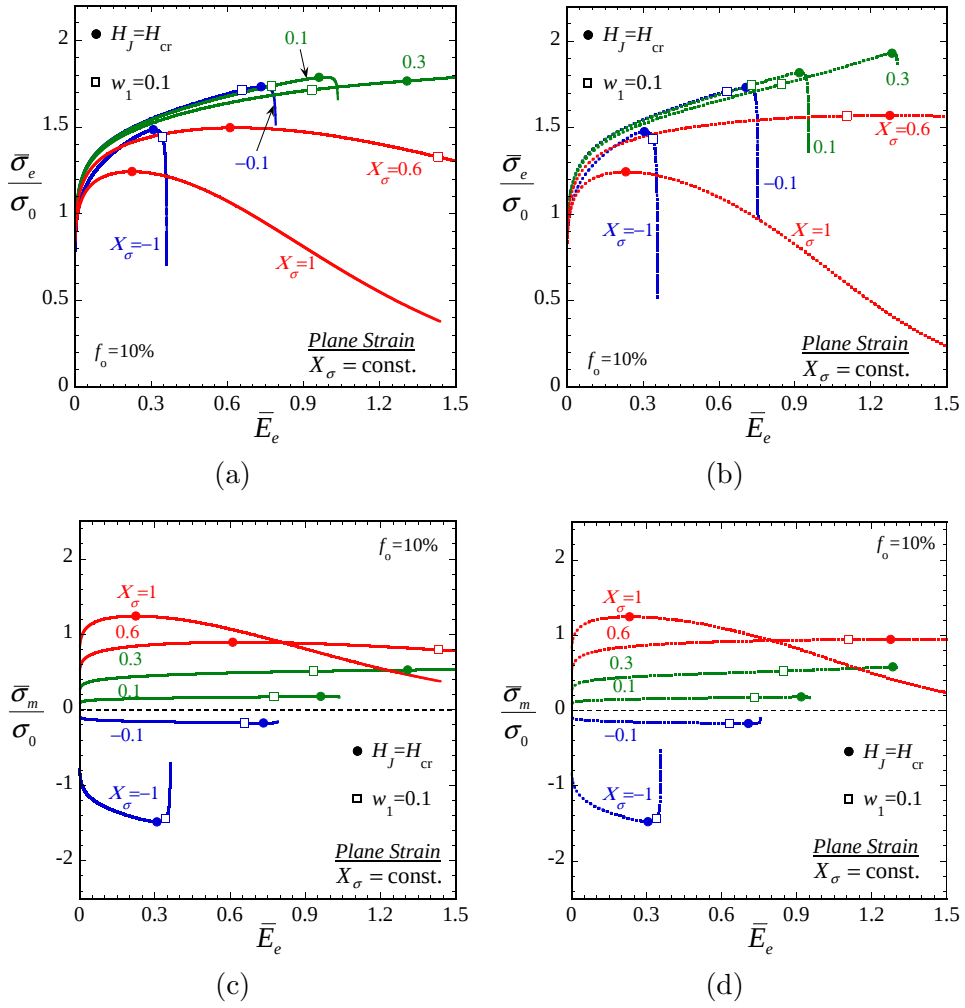

Figure A.10: IVH results for an initially isotropic porous material with f_0 = 10% initial porosity subjected to plane strain loading with fixed stress triaxiality X_σ. The evolution of the associated macroscopic variables is shown as a function of the macroscopic equivalent strain $\overline{E}_e$ for the cases of non-vanishing spin loadings (continuous curves) and vanishing-spin loadings (dotted curves). Average equivalent stress $\overline{\sigma}_e$ for (a) non-vanishing spin loadings and (b) vanishing-spin loadings. Average mean stress $\overline{\sigma}_m$ for (c) non-vanishing spin loadings and (d) vanishing-spin loadings.

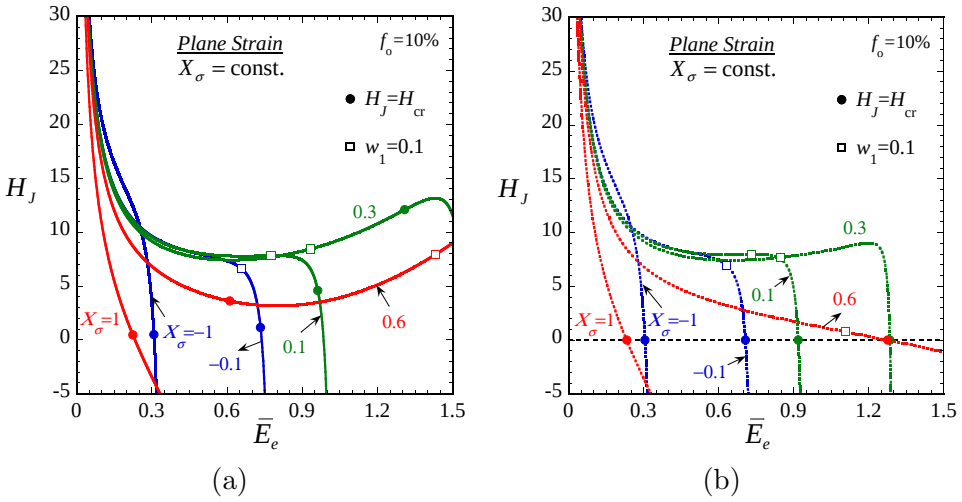

Figure A.11: IVH results for an initially isotropic porous material with $f_0 = 10\%$ initial porosity subjected to plane strain loading with fixed stress triaxiality X_σ. Results are shown for the macroscopic Jaumann hardening modulus H_J for (a) non-vanishing spin and (b) vanishing-spin loadings.

The macroscopic stress-strain curves in Fig. A.10(a) show that the material response is harder for $X_\sigma = 0.3$ than for $X_\sigma = 0.6$, which is consistent with the fact that the evolution of the porosity (Fig. A.9(a)) acts as a hardening mechanism (at large enough strains) in the former case and as a softening mechanism in the latter. In addition, comparing the stress-strain curves for non-vanishing spin loading (Figs. A.10(a) and A.10(c)) with the corresponding curves for vanishing-spin loading (Figs. A.10(b) and A.10(d)), we observe that the macroscopic behavior of the porous metal is slightly softer for the former than for the later type of loading, which is consistent with the fact that the slower reduction of the porosity in the former case (see Fig. A.9(a)) leads to a weaker hardening behavior of the material.

The most remarkable feature of the results shown in Fig. A.11 for $X_\sigma = 0.3$, for both the non-vanishing spin and the vanishing-spin loading, is that the macroscopic behavior of the material becomes unstable at sufficiently large strains, despite the hardening induced by the reduction of the porosity (Fig. A.9(a)). As argued by Agoras and Ponte Castañeda (2014) in the context of vanishing-spin loading conditions with fixed strain triaxiality, the basic mechanism responsible for this instability is the collapse of the voids, which has a softening effect that at the critical strain becomes

sufficiently strong to overcome the corresponding hardening effects due to the reduction of the porosity and the strain hardening of the matrix phase. Note that for the non-vanishing spin loading the instability occurs at a slightly larger strain than for the vanishing-spin loading, suggesting that for the loading case $X_\sigma = 0.3$ void rotation may have a (weak) hardening effect, which is consistent with the fact that the void collapse rate for the non-vanishing spin loading is slower (i.e., the aspect ratios w_1 and w_2 in Figs. A.9(b) and A.9(c) decrease with slower rates) than for the vanishing-spin loading.

In contrast with the loading cases $X_\sigma = 0.6$ and $X_\sigma = 1$, we observe that for $X_\sigma = 0.3$ the onset of strain localization takes place for relatively small aspect ratios (e.g., under the non-vanishing spin loading, $w_1 \approx 0.05$ and $w_2 \approx 0.1$). As already mentioned, the relevance of this prediction could be questioned on the basis of the fact that void surface contact is expected to take place earlier and to have a hardening effect that could ultimately prevent strain localization (Hutchinson and Tvergaard, 2012). In this connection, it should be remarked that the recent (unit cell) numerical analysis by Tvergaard (2014) on the development of shear localization instabilities in elastic-plastic porous materials has shown that void surface contact delays the onset of localization, but it does *not* completely eliminate it. Although quantitative comparisons of the predictions of the IVH model with results from the latter work can *not* be made due to differences in the microstructural features and loading conditions considered, it is interesting to remark that, at least for the case of the non-vanishing spin loading, the predictions of the IVH model for relatively small stress triaxialities (e.g., $X_\sigma = 0.3$) are qualitatively consistent with the corresponding numerical results of Tvergaard (2014) for shear localization, as well as for the propensity of the voids to collapse to micro-cracks, which in the context of the IVH model provides the required softening mechanism for strain localization.

Very small and negative triaxialities ($X_\sigma = 0.1, -0.1, -1$). The evolution of the internal and macroscopic variables in Fig. A.9-A.11 for the stress triaxialities $X_\sigma = 0.1, -0.1$ and -1 is qualitatively similar with that for the loading case $X_\sigma = 0.3$, discussed above.

Note, however, that for smaller values of X_σ the voids collapse to micro-cracks faster, i.e., the variables f (Fig. A.9(a)), w_1 (Fig. A.9(b)) and w_2 (Fig. A.9(c)) drop to zero faster with decreasing values of X_σ (for $X_\sigma \leq 0.3$). As a result, void closure ($f = 0$) occurs at smaller strains, while the softening effect due to void collapse becomes stronger for smaller values of X_σ, thus leading to instabilities at smaller strains. The differences between the results for the non-vanishing spin (continuous curves) and vanishing-spin (dotted curves) loading, for any given variable in Fig. A.9-A.11, decrease with decreasing X_σ and for $X_\sigma = -1$ there are practically no differences for the two types of loading, suggesting that void rotations play no role on the macroscopic response of the porous materials at these levels of triaxiality.

A.4.3 Failure curves

We conclude this section with a discussion of the effect of the stress triaxiality on the ductile failure of porous materials, as defined by the onset of macroscopic strain localization. To this end, Fig. A.12 shows plots of the critical equivalent strain $\overline{E}_e^{cr}$ at the onset of localization as a function of the applied stress triaxiality X_σ. Fig. A.12(a) presents results for the non-vanishing spin loading (A.22), with fixed X_σ, for $f_0 = 1\%, 10\%$ and 30% initial porosity, while Fig. A.12(b) compares the failure curve for $f_0 = 10\%$ of Fig. A.12(a) with corresponding results for the vanishing-spin loading (A.23) with fixed X_σ. The dashed portion of each failure curve in Fig. A.12 corresponds to instabilities occurring for void aspect ratios $w_1^{cr} < 0.1$ ($w_2^{cr} > w_1^{cr}$). In this connection, we recall that under loading conditions leading to the collapse ($w_1, w_2 \to 0$) of the voids, partial contact of the opposite faces of the voids is expected to take place prior to complete void closure (Hutchinson and Tvergaard, 2012) and, thus, the approximation that the void shape remains ellipsoidal is expected to become invalid for sufficiently small values of the void aspect ratios. It should be emphasized, however, that the ellipsoidal pore-shape assumption adopted by the IVH model refers *not* to the shape of any individual void but to the shape of the voids *on average*. Thus, it could be argued that partial contact of opposite faces in any given void is equivalent to splitting the void into two (or more) voids, the average shape of which

may still be (approximately) described by a characteristic ellipsoid. For this reason, it is plausible that the average ellipsoidal-shape assumption may still be physically relevant even after contact of the void faces has occurred in individual voids. In other words, despite the fact that the IVH model does *not* account for void surface contact, the instabilities of Fig. A.12 for $w_1^{cr} < 0.1$ may still be physically relevant.

From the results of Fig. A.12(a), we observe that the failure curves exhibit a maximum at a certain value X_σ^* of the stress triaxiality X_σ, which for porosities $f_0 = 10\%$ and 30% is $X_\sigma^* \approx 0.3$ and for $f_0 = 1\%$ is $X_\sigma^* \approx 0.4$. For any given f_0, we observe that the material becomes progressively more unstable (i.e., the critical strain $\overline{E}_e^{cr}$ becomes smaller) with either increasing or decreasing X_σ from $X_\sigma = X_\sigma^*$. This behavior may be understood to be a consequence of the fact that the effect of the underlying softening mechanisms that are responsible for failure become progressivey stronger with either increasing or decreasing X_σ from $X_\sigma = X_\sigma^*$. In this connection, we recall from the results of the previous subsection for $f_0 = 10\%$ that the dominant failure mechanism in the range of stress triaxialities $X_\sigma < 0.3$ is void collapse, while in the range $X_\sigma > 1$ it is void growth. Thus, it would appear that void rotations can also have a significant effect for intermediate values of X_σ.

The failure curves of Fig. A.12(b) for non-vanishing spin and vanishing-spin loadings are very similar for stress triaxialities in the regions $X_\sigma < 0.3$ and $X_\sigma > 1$, suggesting accordingly that the effect of void rotation is relatively weak for loadings with $X_\sigma < 0.3$ or $X_\sigma > 1$. On the other hand, for values $0.3 \lesssim X_\sigma \lesssim 1$ we observe that the failure curves of Fig. A.12(b) are substantially different, indicating that the effect of void rotation is rather significant in this intermediate range. In particular, note that for the vanishing-spin loading the critical strain $\overline{E}_e^{cr} \to \infty$ as $X_\sigma \to 0.5$, while for the non-vanishing spin loading $\overline{E}_e^{cr} \approx 0.8$ for $X_\sigma = 0.5$.

Finally, it should be recalled in the context of Fig. A.12 that, for any given f_0, there is a region of stress triaxialities within which strain localization occurs for substantially distorted pore shapes, i.e., for pore shapes characterized by an aspect ratio $w_1^{cr} < 0.1$ (see dashed portions of the curves in Fig. A.12). The main conclusions concerning the instabilities in this range of stress triaxialities, as discussed above, could

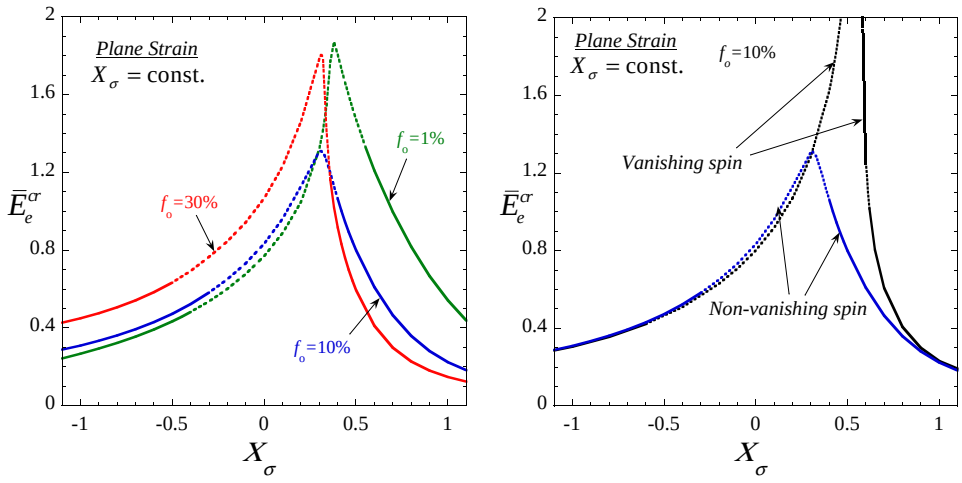

Figure A.12: (a) The critical strain $\overline{E}_e^{cr}$ at the onset of macroscopic localization in initially isotropic porous materials subjected to non-vanishing spin loading of the type (A.22) with fixed stress triaxiality X_σ, is plotted as a function of X_σ, for f_0 = $1\%, 10\%$ and 30%. (b) The failure curve of Part (a) for f_0 = 10% is compared with corresponding results for vanishing-spin loading of the type (A.23) with fixed X_σ. The dashed portion of each failure curve corresponds to instabilities occurring at a void aspect ratio $w_1 < 0.1$.

be affected quantitatively by the fact that contact of the void surfaces is expected to take place before the onset of localization. However, at least for non-vanishing spin loadings, the recent work by Tvergaard (2014) suggests that contact of the void surfaces does not change the propensity of the material to localize, although such void surface contact may delay the onset of localization, relative to the predictions of the IVH model (which ignores contact of the void surfaces).

A.5 Concluding remarks

In this paper, we have extended the constitutive model of Agoras and Ponte Castañeda (2013, 2014) for porous rigid-plastic materials to account for void rotations under general finite-deformation loading conditions. The model makes use of the iterated variational linear comparison homogenization (IVH) method developed by Ponte Castañeda (2012) to characterize the instantaneous macroscopic response of porous metals by means of yield surfaces depending on the current values of the porosity, the

average shape and orientation of the pores, as well as the shape and orientation of the distribution function for the centers of the pores. In addition, consistently derived homogenization estimates for the average strain-rate and vorticity in the pores are used to derive corresponding evolution equations for the porosity, average shape and orientation of the voids (and their distribution). In its final form, the IVH model can be regarded as a standard "internal variable" plasticity model, where the evolution of the microstructural variables accounts for "geometrical" contributions to the overall hardening/softening of the porous material, adding to the usual "constitutive" contributions already accounted for through the evolution of the yield stress in the solid matrix material.

The model was first applied to investigate the macroscopic response of initially isotropic rigid-plastic porous metals under *simple shear* loading. It was found that significant stress triaxialities develop in the material as a result of a strong in-plane anisotropy that is induced by the change in the pore average shape from spherical to flat ellipsoids. This finding is in qualitatively agreement with earlier results of Kailasam and Ponte Castañeda (1997) and Danas and Ponte Castañeda (2009a), but quite different from the prediction of Gurson-type models, where the material is assumed to remain isotropic, so that no normal stresses (or stress triaxiality) can develop under *simple shear* loading. In addition, strain localization was predicted to take place in a shear band parallel to the shear plane of the loading. By means of suitable comparisons with the corresponding results for *pure shear* loading—where the voids undergo no rotation on average and no shear localization occurs—we deduced that the rotation of the voids for simple shear loading conditions has a strong softening effect, which tends to dramatically enhance the susceptibility of the material to fail by shear localization. In this context, it is crucial to note that the average rotation of the voids is a consequence of non-vanishing macroscopic spin associated with *simple shear* loading conditions, since the vanishing-spin conditions associated with *pure shear* loading for initially isotropic distributions of spherical voids would produce no void rotations on average.

Next, the macroscopic response of the porous metal was investigated for com-

bined plane strain tension and shear with prescribed, fixed stress triaxiality X_σ. It was found that the stress triaxiality has a strong effect on the evolution of the porosity and average shape of the pores, which has a very significant effect on both the shear and normal components of the macroscopic stress, leading to the development of shear localization at sufficiently large strains. In particular, consistent with earlier observations (Agoras and Ponte Castañeda, 2014), the main failure mechanism is found to be void growth at large stress triaxialities ($X_\sigma \gtrsim 1$) and void collapse at small stress triaxialities ($X_\sigma \lesssim 0.3$), such that the localization strain decreases both with increasing triaxialities at the larger triaxialities, and with decreasing triaxialities at the lower triaxialities. For these ranges of triaxialities, voids rotations were found to have no significant effects on the macroscopic hardening of the material and therefore no implications for shear localization. On the other hand, for intermediate values of X_σ ($0.3 \lesssim X_\sigma \lesssim 1$), it was found that void rotations tend to destabilize the macroscopic response of the porous materials leading to much lower localization strains than when void rotations are not present (as in biaxial straining of the material). This stronger susceptibility to failure by shear localization for shearing loading conditions (i.e., with non-vanishing spin) would appear to be consistent with recent finite element simulation results (Tvergaard, 2014) for porous plastic media with periodic microstructures (although great care should be exercised when comparing instability results for random and periodic microstructures, due to the great sensitivity of these results to the initial distribution of the pores as determined, for example, by the shape of the unit cell in the periodic context). In this context, it is also important to recall that the IVH model does not take into account the possible contact of void surfaces (Hutchinson and Tvergaard, 2012) at sufficiently low stress triaxialities. However, while contact of the void faces is expected to have a hardening effect on the macroscopic response, which may indeed slow down the possible development of shear localization instabilities, the finite element results of Tvergaard (2014) show that at least for shear loading conditions contact of the void faces is not enough to completely stop the development of shear bands. In this sense, our results are at the very least qualitatively consistent with the FEM results in that porous materials

are predicted to be more susceptible to failure by shear localization for "shearing" loading conditions leading to non-vanishing spins of the voids than for "axial" loading conditions where no void rotations are expected.

This observation translates into an additional level of complexity in modeling the macroscopic response of porous plastic materials. While experimental results have shown that the stress triaxiality does not suffice to characterize the failure of porous metals at low stress triaxialities, and other measures such as the Lode parameter must be introduced, the observations of the previous paragraph strongly suggest that even the triaxiality and the Lode parameter may not be enough to completely describe failure of porous metals in the low to moderate stress triaxiality regime. Indeed, the results of this work strongly suggest that the macroscopic spin, or vorticity can have strong implications for shear localization at intermediate values of the triaxiality. In turn this suggests that to really be able to model and predict failure of porous plastic materials it may be necessary to implement a more microscopic point of view, since these failure mechanisms may ultimately be controlled by microscopic features such as the evolution of the average size, shape and orientation of the voids. While macroscopic stress measures such as the triaxiality and the Lode parameter certainly have implications for failure on porous ductile materials, their effects are only indirect—through the corresponding effects on the evolution of the microstructure. In this sense, it would appear that it may be necessary to directly account for such microstructural evolution effects, something that could only be accomplished with more sophisticated constitutive models accounting for additional microstructural variables beyond the porosity. It is precisely for these reasons that homogenization models, such as the one developed in the context of this work, have a distinct advantage, since they allow the direct incorporation of appropriate statistical variables, such as the average void shape and orientation, suitably describing the state and anisotropic evolution of the porous microstructure. In addition, these homogenization models can be generalized in a seamless fashion to account for additional microstructural features, such as crystallographic texture, whose evolution is known to be crucial in modeling the response of certain low-symmetry materials, such as magnesium and

polar ice. Thus, the techniques developed in this work could be generalized to model the combined effect of porosity and crystallographic texture in porous low-symmetry polycrystals, building on recent work by Lebensohn et al. (2011) making use of less sophisticated homogenization methods to determine macroscopic yield surfaces of porous polycrystals.

A.6 Appendix: Detailed expressions for the model

In this Appendix, we provide the required detailed expressions for the IVH model, referring to Agoras and Ponte Castañeda (2013) and Agoras and Ponte Castañeda (2014) for their derivations. In this context, it is important to recall that these expressions are obtained by means of the (PCW) estimates of Ponte Castañeda and Willis (1995) for the LCC at each iteration step. In addition, use is made of the results of Idiart and Ponte Castañeda (2007c) to relate the averages and second moments of the fields in the matrix and vacuous phases of the LCC to the corresponding quantities in the actual nonlinear porous material.

We begin by recalling that the normalized effective viscous compliance tensors $\widehat{\mathbb{M}}_{[i]}^{PCW}$ of the i-level LCC is given by

$$\begin{aligned}
\widehat{\mathbb{M}}_{[1]}^{PCW} &= \mathbb{K} + c_{[1]}^{(2)}\left[\hat{\mathbb{Q}}^{(p)} - c_{[1]}^{(2)}\hat{\mathbb{Q}}^{(d)}\right]^{-1},\\
\widehat{\mathbb{M}}_{[i]}^{PCW} &= r_{[i]}^{-1}\mathbb{K} + r_{[i]}^{-1}c_{[i]}^{(2)}\left[\left(r_{[i]}\,\widehat{\mathbb{M}}_{[i-1]}^{PCW} - \mathbb{K}\right)^{-1} + (1-c_{[i]}^{(2)})\hat{\mathbb{Q}}^{(d)}\right]^{-1}\\
&\equiv \widehat{\mathbb{M}}_{[i]}^{PCW}(r_{[2]},...,r_{[i]}), \qquad i = 2,...,N,
\end{aligned} \tag{A.28}$$

where $\mathbb{K}$ is the fourth-order identity tensor in the deviatoric space, the variables $c_{[i]}^{(2)}$ $(i = 1,...,N)$ are incremental volume fractions, the variables $r_{[i]}$ $(i = 2,...,N)$ are normalized shear moduli in the LCC (see Agoras and Ponte Castañeda, 2014 for details), $\hat{\mathbb{Q}}^{(p)}$ and $\hat{\mathbb{Q}}^{(d)}$ are the fourth-order microstructural tensors, accounting for the shape and orientation of the pores and their distribution, respectively. In this Appendix, it is assumed for generality that the shape and orientation of the pores and distribution may be different. However, in the body of the paper, and in all the results

presented therein, it has been assumed that the shape and orientation of the pores are identical to those of their distribution, and hence that $\hat{\mathbb{Q}}^{(p)} = \hat{\mathbb{Q}}^{(d)} = \hat{\mathbb{Q}}(w_\alpha, \mathbf{n}_i)$. In general, these microstructural tensors have to be computed numerically, as shown in the work of Aravas and Ponte Castañeda (2004).

For the rigid plastic porous metal, the second moment of the equivalent stress field over the matrix phase $\left(\overline{\overline{\sigma}}_e^{(1)}\right)^2$ can be shown to satisfy the relations (Agoras and Ponte Castañeda, 2014)

$$\begin{aligned}
\left(\overline{\overline{\sigma}}_e^{(1)}\right)^2 &= \frac{3}{2}\frac{1}{1-c_{[1]}^{(2)}}\overline{\boldsymbol{\sigma}}\cdot\left[\prod_{j=2}^{N}\mathbb{B}_{[j]}^{(2)}\right]^T\widehat{\mathbb{M}}_{[1]}^{PCW}\left[\prod_{j=2}^{N}\mathbb{B}_{[j]}^{(2)}\right]\overline{\boldsymbol{\sigma}} \equiv \mathcal{F}_{[1]}(r_{[2]},...,r_{[N]}),\\
\left(\overline{\overline{\sigma}}_e^{(1)}\right)^2 &= \frac{3}{2}\frac{r_{[i]}}{1-c_{[i]}^{(2)}}\overline{\boldsymbol{\sigma}}\cdot\left[\prod_{j=i+1}^{N}\mathbb{B}_{[j]}^{(2)}\right]^T\left[\widehat{\mathbb{M}}_{[i]}^{PCW}-c_{[i]}^{(2)}(\mathbb{B}_{[i]}^{(2)})^T\widehat{\mathbb{M}}_{[i-1]}^{PCW}\mathbb{B}_{[i]}^{(2)}\right]\left[\prod_{j=i+1}^{N}\mathbb{B}_{[j]}^{(2)}\right]\overline{\boldsymbol{\sigma}}\\
&\equiv \mathcal{F}_{[i]}(r_{[2]},...,r_{[N]}), \qquad i=2,...,N,
\end{aligned} \tag{A.29}$$

where the corresponding stress concentration tensors are provided by

$$\mathbb{B}_{[i]}^{(2)} = \left[\mathbb{I}+(1-c_{[i]}^{(2)})\hat{\mathbb{Q}}^{(d)}\left(r_{[i]}\,\widehat{\mathbb{M}}_{[i-1]}^{PCW}-\mathbb{K}\right)\right]^{-1} \equiv \mathbb{B}_{[i]}^{(2)}(r_{[2]},...,r_{[i]}), \qquad i=2,...,N. \tag{A.30}$$

In this last expression, $\mathbb{I}$ is the fully symmetric, fourth-order identity tensor. As mentioned in section A.2.2, for given applied loading $\overline{\boldsymbol{\sigma}}$ and internal variables $\mathbf{s}$ of the porous metal, the N unknowns $\overline{\overline{\sigma}}_e^{(1)}$ and $r_{[i]}$ $(i=2,...,N)$ can be fully determined from the system of N nonlinear equations (A.29).

The iterated estimates of the PCW type for the average strain-rate in the voids is given by $\overline{\mathbf{D}}^{(2)} = \mathbb{A}^{(2)}\overline{\mathbf{D}}$, where $\mathbb{A}^{(2)}$ is the associated strain-rate concentration tensor, determined by (Agoras and Ponte Castañeda, 2013; Agoras and Ponte Castañeda, 2014)

$$\mathbb{A}^{(2)} = \prod_{i=1}^{N}\mathbb{A}_{[i]}^{(2)} \equiv \mathbb{A}^{(2)}(r_{[2]},...,r_{[N]}), \tag{A.31}$$

with

$$\begin{aligned}
\mathbb{A}_{[1]}^{(2)} &= \left[c_{[1]}^{(2)}\mathbb{I} + \mathbb{K}\left(\hat{\mathbb{Q}}^{(p)} - c_{[1]}^{(2)}\hat{\mathbb{Q}}^{(d)}\right)\right]^{-1}, \\
\mathbb{A}_{[i]}^{(2)} &= \left[c_{[i]}^{(2)}\mathbb{I} + (1 - c_{[i]}^{(2)})\left[\left(\mathbb{K} - \mathbb{K}\hat{\mathbb{Q}}^{(d)}\mathbb{K}\right)\left(r_{[i]}\,\widehat{\mathbb{M}}_{[i-1]}^{PCW}\right)^{-1} + \mathbb{K}\hat{\mathbb{Q}}^{(d)}\right]\right]^{-1} \\
&\equiv \mathbb{A}_{[i]}^{(2)}(r_{[2]}, ..., r_{[i]}), \qquad i = 2, ..., N.
\end{aligned} \tag{A.32}$$

It should be noted that $\mathbb{A}_{[1]}^{(2)}$, which corresponds to the strain-rate concentration tensor at the first level LCC, depends on the shape and orientation of both the pores and distribution, through the microstructural tensors $\hat{\mathbb{Q}}^{(p)}$ and $\hat{\mathbb{Q}}^{(d)}$; however, the other strain-rate concentration tensors $\mathbb{A}_{[i]}^{(2)}$ $(i = 2, ..., N)$, which correspond to higher level LCCs, only depend on the shape and orientation of the pore distribution, through the tensor $\hat{\mathbb{Q}}^{(d)}$.

Similarly, the average spin tensor of the voids can be obtained iteratively from the corresponding estimates of the PCW type for the LCC at each increment, and is given by

$$\overline{\mathbf{W}}^{(2)} = \overline{\mathbf{W}} - \mathbb{C}^{(2)}\overline{\mathbf{D}}, \tag{A.33}$$

where $\mathbb{C}^{(2)}$ is the associated spin concentration tensor in the voids, determined by

$$\mathbb{C}^{(2)} = \sum_{i=1}^{N}\left[\mathbb{C}_{[i]}^{(2)}\left(\prod_{j=i+1}^{N}\mathbb{A}_{[j]}^{(2)}\right)\right], \tag{A.34}$$

with

$$\begin{aligned}
\mathbb{C}_{[1]}^{(2)} &= -\left(\mathbf{\Pi}^{(p)} - c_{[1]}^{(2)}\mathbf{\Pi}^{(d)}\right)\mathbb{A}_{[1]}^{(2)}, \\
\mathbb{C}_{[i]}^{(2)} &= (1 - c_{[i]}^{(2)})\mathbf{\Pi}^{(d)}\left[\mathbb{K}\left(r_{[i]}\widehat{\mathbb{M}}_{[i-1]}^{PCW}\right)^{-1} - \mathbb{I}\right]\mathbb{A}_{[i]}^{(2)} \\
&\equiv \mathbb{C}_{[i]}^{(2)}(r_{[2]}, ..., r_{[i]}), \qquad i = 2, ..., N.
\end{aligned} \tag{A.35}$$

Note that $\mathbf{\Pi}^{(p)}$ and $\mathbf{\Pi}^{(d)}$ are the fourth-order Eshelby microstructural tensors, which correspond to the rotation of pores and their distribution, respectively. In the present work, where the shape and orientation of the pores are identical to that of their

distribution, $\mathbf{\Pi}^{(p)} = \mathbf{\Pi}^{(d)} = \mathbf{\Pi}(w_\alpha, \mathbf{n}_i)$. The tensor $\mathbf{\Pi}$ can be computed numerically following the procedure developed by Aravas and Ponte Castañeda (2004). Similar to the strain-rate concentration tensor, the spin concentration tensor $\mathbb{C}^{(2)}_{[1]}$ corresponding to the first-level LCC, depends on the shape and orientation of both the pores and distribution; the other spin concentration tensors $\mathbb{C}^{(2)}_{[i]}$ $(i = 2, ..., N)$ corresponding to higher-level LCCs, depend only on the shape and orientation of the pore distribution.

Given the above expressions (3.83), (A.34), (A.35), along with relation (A.13), the plastic spin $\overline{\mathbf{W}}^p = \overline{\mathbf{W}} - \overline{\boldsymbol{\omega}}$ can be given by

$$\begin{aligned}\overline{\mathbf{W}}^p = &-\frac{1}{2}\sum_{\substack{\alpha,\beta=1\\ \alpha\neq\beta\\ w_\alpha\neq w_\beta}}^{3}\frac{w_\alpha^2+w_\beta^2}{w_\alpha^2-w_\beta^2}\left[(\mathbf{n}_\alpha\otimes\mathbf{n}_\beta+\mathbf{n}_\beta\otimes\mathbf{n}_\alpha)\cdot\left(\prod_{i=1}^{N}\mathbb{A}^{(2)}_{[i]}\right)\overline{\mathbf{D}}\right]\mathbf{n}_\alpha\otimes\mathbf{n}_\beta\\ &+\sum_{i=1}^{N}\left[\mathbb{C}^{(2)}_{[i]}\left(\prod_{j=i+1}^{N}\mathbb{A}^{(2)}_{[j]}\right)\right]\overline{\mathbf{D}}.\end{aligned} \tag{A.36}$$

Consistent with the work of Aravas and Ponte Castañeda (2004), the plastic spin may then be rewritten as

$$\overline{\mathbf{W}}^p = \dot{\lambda}\overline{\mathbf{\Omega}}^p, \tag{A.37}$$

where $\overline{\mathbf{\Omega}}^p$ is given by

$$\begin{aligned}\overline{\mathbf{\Omega}}^p = &-\frac{1}{2}\sum_{\substack{\alpha,\beta=1\\ \alpha\neq\beta\\ w_\alpha\neq w_\beta}}^{3}\frac{w_\alpha^2+w_\beta^2}{w_\alpha^2-w_\beta^2}\left[(\mathbf{n}_\alpha\otimes\mathbf{n}_\beta+\mathbf{n}_\beta\otimes\mathbf{n}_\alpha)\cdot\left(\prod_{i=1}^{N}\mathbb{A}^{(2)}_{[i]}\right)\mathbf{N}\right]\mathbf{n}_\alpha\otimes\mathbf{n}_\beta\\ &+\sum_{i=1}^{N}\left[\mathbb{C}^{(2)}_{[i]}\left(\prod_{j=i+1}^{N}\mathbb{A}^{(2)}_{[j]}\right)\right]\mathbf{N}.\end{aligned} \tag{A.38}$$

Bibliography

Agoras, M., Ponte Castañeda, P., 2011. Homogenization estimates for multi-scale nonlinear composites. Eur. J. Mech. A/Solids. 30, 828–843.

Agoras, M., Ponte Castañeda, P., 2013. Iterated linear comparison bounds for viscoplastic porous materials with "ellipsoidal" microstructures. J. Mech. Phys. Solids. 61, 701–725.

Agoras, M., Ponte Castañeda, P., 2014. Anisotropic finite-strain models for porous viscoplastic materials with microstructure evolution. Int. J. Solids Struct. 51, 981–1002.

Aravas, N., Ponte Castañeda, P., 2004. Numerical methods for porous metals with deformation-induced anisotropy. Comput. Methods Appl. Mech. Engrg. 193, 3767–3805.

Bache, M.R., Evans, W.J., 2001. Impact of texture on mechanical properties in an advanced titanium alloy. Mater. Sci. Eng. A 319-321 409-414.

Balasubramanian, S., Anand, L., 2002. Plasticity of initially textured hexagonal polycrystals at high homologous temperatures: application to titanium. Acta. Mater. 50, 133-148.

Bao, Y., Wierzbicki, T., 2004. On fracture locus in the equivalent strain and stress triaxiality space. Int. J. Mech. Sciences 46, 81–98.

Barsoum, I., Faleskog, J., 2007. Rupture mechanisms in combined tension and shear—Experiments. Int. J. Solids Struct. 44, 1768–1786.

Benzerga, A., Besson, J., 2001. Ductile Failure Modeling. Eur. J. Mech. A/Solids 20, 397-434.

Benzerga, A.A., Leblond, J-B., 2010. Ductile fracture by void growth to coalescence. Adv. Appl. Mech. 44, 169-305.

Benzerga, A., Leblond, J.B., Needleman, A. and Tvergaard, V., 2016. Ductile Failure Modeling. Int. J. Fract. 201, 29-80.

Bilger, N., Auslender, F., Bornert, M., Michel, J.-C., Moulinec, H., Suquet, P., Zaoui, A., 2005. Effect of a nonuniform distribution of voids on the plastic response of voided materials: a computational and statistical analysis. Int. J. Solids Struct. 42, 517–538.

Boehlert, C.J., Chen, Z., Gutirrez-Urrutia, I., Llorca, J. and Prez-Prado, M.T., 2012. In situ analysis of the tensile and tensile-creep deformation mechanisms in rolled AZ31. Acta. Mater. 60, 1889-1904.

Bunge, H.J., Esling, C. (Eds.), 1982. Quantitative texture analysis. Deutsche Gesellschaft für Metallkunde.

Caré, S., Zaoui, A., 1996. Cavitation at triple nodes in -zirconium polycrystals. Acta. Mater. 44, 1323-1336.

Castelnau, O., Canova, G.R., Lebensohn, R.A., Duval, P., 1997. Modelling viscoplastic behavior of anisotropic polycrystalline ice with a self-consistent approach. Acta. Mater. 45, 4823-4834.

Castelnau, O., Duval, P., Lebensohn, R.A. and Canova, G.R., 1996. Viscoplastic modeling of texture development in polycrystalline ice with a selfconsistent approach: Comparison with bound estimates. J. Geophys. Res. 101, 13851-13868.

Chauve, T., Montagnat, M., Piazolo, S., Journaux, B., Wheeler, J., Barou, F., Mainprice, D. and Tommasi, A., 2017. Non-basal dislocations should be accounted for in simulating ice mass flow. Earth Planet. Sci. Lett. 473, 247-255.

Crépin, J., Bretheau, T., Caldemaison., D. , 1996. Cavity growth and rupture of β-treated zirconium: A crystallographic model. Acta. Mater. 44, 4927–4935.

Dafalias, Y.F.., 1985. The plastic spin. J.. Appl. Mech. 52, 865871.

Danas, K., Aravas, N., 2012. Numerical modeling of elasto-plastic porous materials with void shape effects at finite deformations. Composites Part B 43, 2544-2559.

Danas, K., Idiart, M.I., Ponte Castañeda, P., 2008. A homogenization-based constitutive model for isotropic viscoplastic porous media. Int. J. Solids Struct. 45, 3392-3409.

Danas, K., Ponte Castañeda, P., 2009a. A finite-strain model for anisotropic viscoplastic porous media: I—Theory. Eur. J. Mech. A/Solids 28, 387–401.

Danas, K., Ponte Castañeda, P., 2009b. A finite-strain model for anisotropic viscoplastic porous media: II—Applications. Eur. J. Mech. A/Solids 28, 402–416.

Danas, K., Ponte Castañeda, P., 2012. Influence of the Lode parameter and the stress triaxiality on the failure of elasto-plastic porous materials. Int. J. Solids Struct. 49, 1325–1342.

Dawson, P.R., Marin, E.B., 1997. Computational mechanics for metal deformation processes using polycrystal plasticity. Adv. Appl. Mech. 34, 77–169.

deBotton, G., Ponte Castañeda, P., 1995. Variational estimates for the creep behavior of polycrystals. Proc. R. Soc. Lond. A 448, 121–142.

Dendievel, R., Bonnet, G., Willis, J.R., 1991. Bounds for the creep behaviour of polycrystalline materials. In Inelastic deformation of composite materials. Springer, New York, 175–192.

Duval, P., Ashby, M.F., Anderman, I., 1983. Rate-controlling processes in the creep of polycrystalline ice. J. Phys. Chem. 87, 4066–4074.

Fritzen, F., Forest, S., Bohlke, T., Kondo, D., Kanit, T., 2012. Computational homogenization of elasto-plastic porous metals. Int. J. Plasticity 29, 102–119.

Gan, Y.X., Kysar, J.W., Morse, T.L., 2006. Cylindrical void in a rigid-ideally plastic single crystal II: Experiments and simulations. Int. J. Plasticity 22 39–72.

Gologanu, M., Leblond, J.-B., Devaux, J., 1993. Approximate models for ductile metals containing non-spherical voids – case of axisymmetric prolate ellipsoidal cavities. J. Mech. Phys. Solids 41, 1723–1754.

Gurson, A. L., 1977. Continuum theory of ductile rupture by void nucleation and growth. J. Engng. Mater. Technol. 99, 2–15.

Ha, S., Kim, K., 2010. Void growth and coalescence in fcc single crystals. Int. J. Mech. Sci. 52, 863–873.

Han, X., Besson, J., Forest, S., Tanguy, B. and Bugat, S., 2013. A yield function for single crystals containing voids. Int. J. Solids Struct. 50, 2115–2131.

Hershey, A.V., 1954. The elasticity of an isotropic aggregate of anisotropic cubic crystals. J. Appl. Mech. 21, 236-240.

Hill, R., 1948. A theory of the yielding and plastic flow of anisotropic metals. Proc. R. Soc. Lond. A 193, 281-297.

Hill, R., 1963. Elastic properties of reinforced solids: some theoretical principles. J. Mech. Phys. Solids 11, 357-372.

Hill, R., 1965. Continuum micro-mechanics of elastoplastic polycrystals. J. Mech. Phys. Solids 13, 89-101.

Hori, M., Nemat-Nasser, S., 1988. Mechanics of void growth and void collapse in crystals. Mechanics of Materials. Mech. Mater. 7, 1–13.

Hutchinson, J.W., 1976. Bounds and self-consistent estimates for creep of polycrystalline materials. Proc. R. Soc. Lond. A 348, 101-127.

Hutchinson, J. W., Tvergaard, V., 2012. Comment on "Influence of the Lode parameter and the stress triaxiality on the failure of elasto-plastic porous materials" by K. Danas and P. Ponte Castañeda. Int. J. Solids Struct. 49, 3484–3485.

Idiart, M.I., 2008. Modeling the macroscopic behavior of two-phase nonlinear composites by infinite-rank laminates. J. Mech. Phys. Solids 56, 2599–2617.

Idiart, M. I., 2011. Bounding the plastic strength of polycrystalline solids by linear-comparison homogenization methods. Proc. R. Soc. Lond. A 468, 1136–1153.

Idiart, M. I., Ponte Castañeda, P, 2007a. Variational linear comparison bounds for nonlinear composites with anisotropic phases. I. General results. Proc. R. Soc. Lond. A 463, 907-924.

Idiart, M. I., Ponte Castañeda, P, 2007b. Variational linear comparison bounds for nonlinear composites with anisotropic phases. II. Crystalline materials. Proc. R. Soc. Lond. A 463, 925–943.

Idiart, M. I., Ponte Castañeda, P, 2007c. Field statistics in nonlinear composites. I. Theory. Proc. R. Soc. Lond. A 463, 183–202.

Kailasam, M., Aravas, N., Ponte Castañeda, P., 2000. Porous metals with developing anisotropy: Constitutive models, computational issues and applications to deformation processing. Computer Modeling in Engineering and Sciences 1, 105–118.

Kailasam, M., Ponte Castañeda, P., 1997. The evolution of anisotropy in porous materials and its implications for shear localization. *IUTAM Symposium on Mechanics of Granular and Porous Materials*, N.A. Fleck and A.C.F. Cocks, Eds., Kluwer Academic Publishers, 365–376.

Kailasam, M., Ponte Castañeda, P., Willis, J. R., 1997. The effect of particle size, shape, distribution and their evolution on the constitutive response of nonlinearly viscous composites. I. Theory. Phil. Trans. R. Soc. Lond. A 355, 1835–1852.

Kailasam, M., 1998. A general constitutive theory for particulate composites and porous materials with evolving microstructures, Ph.D. thesis, University of Pennsylvania, 1998.

Kailasam, M., Ponte Castañeda, P., 1998. A general constitutive theory for linear and nonlinear particulate media with microstructure evolution. J. Mech. Phys. Solids 46, 427–465.

Keralavarma, S.M., Benzerga, A., 2010. A constitutive model for plastically anisotropic solids with non-spherical voids. J. Mech. Phys. Solids 58, 874-901.

Kocks, U.F., Tomé, C.N., Wenk, H.R., 1998. Texture and Anisotropy Cambridge University Press.

Kröner, E., 1958. Berechnung der elastischen Konstanten des Vielkristalls aus den Konstanten des Einkristalls. Z. Physik 151, 504–518.

Kysar, J.W., Gan, Y.X., Mendez-Arzuza, G., 2005. Cylindrical void in a rigid-ideally plastic single crystal. Part I: Anisotropic slip line theory solution for face-centered cubic crystals. Int. J. Plasticity 21, 1481-1520.

Laws, N., 1973. On the thermostatics of composite materials. J. Mech. Phys. Solids 21, 9-17.

Lebensohn, R.A., Escobedo, J.P., Cerreta, E.K., Dennis-Koller, D., Bronkhorst, C.A., Bingert, J.F., 2013. Modeling void growth in polycrystalline materials. Acta Mater. 61(18), pp.6918-6932.

Lebensohn, R.A., Idiart, M.I., Ponte Castañeda, P. Vincent, P.-G., 2011. Dilatational viscoplasticity of polycrystalline solids with intergranular cavities. Phil. Mag. 91, 3038–3067.

Lebensohn, R.A., Liu, Y., Ponte Castañeda, 2004. On the accuracy of the self-consistent approximation for polycrystals: comparison with full-field numerical simulations. Acta Mater. 52(18), 5347-5361.

Lebensohn, R.A., Solas, D., Canova, G., Brechet, Y., 1996. Modelling damage of Al-Zn-Mg alloys. Acta. Mater. 44(1), 315-325.

Lebensohn, R.A., Tomé, C.N., 1993. A self-consistent anisotropic approach for the simulation of plastic deformation and texture development of polycrystals: application to zirconium alloys. Acta Metall. Mater. 41, 2611-2624.

Lebensohn, R.A., Tomé, C.N., Maudlin, P.J., 2004. A selfconsistent formulation for the prediction of the anisotropic behavior of viscoplastic polycrystals with voids. J. Mech. Phys. Solids 52, 249-278.

Lebensohn, R.A., Tomé, C.N., Ponte Castañeda, 2007. Self-consistent modeling of the mechanical behaviour of viscoplastic polycrystals incorporating intragranular field fluctuations. Phil. Mag. 87, 4287-4322.

Lebensohn, R.A., Tomé, C.N. and Maudlin, P.J., 2004. A selfconsistent formulation for the prediction of the anisotropic behavior of viscoplastic polycrystals with voids. J. Mech. Phys. Solids 52, 249-278.

Leblond, J-B., Perrin, G., Suquet, P., 1994. Exact results and approximate models for porous viscoplastic solids. Int. J. Plasticity 10, 213–235.

Ling, C., Besson, J., Forest, S., Tanguy, B., Latourte, F. and Bosso, E., 2016. An elastoviscoplastic model for porous single crystals at finite strains and its assessment based on unit cell simulations. Int. J. Plasticity 84, 58–87.

Liu, Y., 2003. Macroscopic behavior, field fluctuations and texture evolution in viscoplastic polycrystals. Ph.D. thesis, University of Pennsylvania.

Liu, Y., Ponte Castañeda, P. 2004a. Second-order theory for the effective behavior and field fluctuations in viscoplastic polycrystals. J. Mech. Phys. Solids 52, 467-495.

Liu, Y., Ponte Castañeda, P. 2004b. Homogenization estimates for the average behavior and field fluctuations in cubic and hexagonal viscoplastic polycrystals. J. Mech. Phys. Solids 52, 1175-1211.

Liu, Y., Gilormini, P., Ponte Castañeda, P. 2003. Variational self-consistent estimates for texture evolution in viscoplastic polycrystals. Acta. Mater. 51(18), 5425-5437.

Liu, Y., Gilormini, P., Ponte Castañeda, P. 2005. Homogenization estimates for texture evolution in halite. Tectonophysics. Tectonophysics 406(3), 179-195.

Madou, K., Leblond, J-B., 2012a. A Gurson-type criterion for porous ductile solids containing arbitrary ellipsoidal voids—I: Limit-analysis of some representative cell. J. Mech. Phys. Solids 60, 1020–1036.

Madou, K., Leblond, J-B., 2013a. Numerical studies of porous ductile materials containing arbitrary ellipsoidal voids - I: Yield surfaces of representative cells. Eur. J. Mech. A/Solids 42, 480–489.

Madou, K., Leblond, J-B., Morin, L., 2013b. Numerical studies of porous ductile materials containing arbitrary ellipsoidal voids - II: Evolution of the length and orientation of the void axes. Eur. J. Mech. A/Solids 42, 490–507.

Mandel Jean, 1972. Plasticité et viscoplasticité. CISM Udine Courses and Lectures vol. 97. Springer-Verlag, New-York.

Masson, R., Bornert, M., Suquet, P., Zaoui, A., 2000. An affine formulation for the prediction of the effective properties of nonlinear composites and polycrystals. J. Mech. Phys. Solids 48, 1203-1227.

Mbiakop, A., Constantinescu, A., Danas, K., 2015. A model for porous single crystals with cylindrical voids of elliptical cross-section. Int. J. Solids Struct. 64, 100-119.

Mbiakop, A., Constantinescu, A., Danas, K., 2015. An analytical model for porous single crystals with ellipsoidal voids. J. Mech. Phys. Solids 84, 436–467.

Michel, J.C., Suquet, P., 1992. The constitutive law of nonlinear viscous and porous materials. J. Mech. Phys. Solids 40, 783 – 812.

Michel, J.C., Suquet, P., 2017. Effective potentials in nonlinear polycrystals and quadrature formulae. Proc. R. Soc. A 473, 20170213.

Molinari, A., Canova, G.R., Ahzi, S., 1987. A self-consistent approach of the large deformation polycrystal viscoplasticity. Acta Metall. Mater. 35, 2983–2994.

Monchiet, V., Gruescu, C., Charkaluk, E., Kondo, D., 2006. Approximate yield criteria for anisotropic metals with prolate or oblate voids. C R Mecanique 334,431-439.

Morin, L., Leblond, J.B., Kondo, D., 2015. A Gurson-type criterion for plastically anisotropic solids containing arbitrary ellipsoidal voids. Int. J. Solids Struct. 77, 86–101.

Nahshon, K., Hutchinson, J. W., 2008. Modification of the Gurson model for shear failure. Eur. J. Mechanics A/Solids 27, 1–17.

Nebozhyn, M. V., 2000. Variational self-consistent estimates for the effective behavior of viscoplastic polycrystals. Ph.D. Thesis. University of Pennsylvania. U.S.A.

Nebozhyn, M. V., Gilormini, P., Ponte Castañeda, P., 2001. Variational self-consistent estimates for cubic viscoplastic polycrystals: the effects of grain anisotropy and shape. J. Mech. Phys. Solids 49, 313–340.

Needleman, A., 1972. Void growth in an elastic-plastic medium. Journal of Applied Mechanics 39, 964-970.

Ogden, 1984. Non-linear elastic deformations. Halsted Press, New York 128-130.

O'regan, T.L., Quinn, D.F., Howe, M.A., McHugh, P.E., 1997. Void growth simulations in single crystals. Comput. Mech. 20, 115–121.

Paux, J., Morin, L., Brenner, R., Kondo, D., 2015. An approximate yield criterion for porous single crystals. Eur. J. Mech. A-Solid 51, 1–10.

Ponte Castañeda, P., 1991. The effective mechanical properties of nonlinear isotropic composites. J. Mech. Phys. Solids 39, 45–71.

Ponte Castañeda, P., 1999. Nonlinear polycrystals with microstructure evolution. In Proceedings of the 9th International Symposium. Continuum Models and Discrete Systems. World Scientific Publishing Co. pp.22-28.

Ponte Castañeda, P., 2002. Second-order homogenization estimates for nonlinear composites incorporating field fluctuations. I – Theory. J. Mech. Phys. Solids 50, 737–757.

Ponte Castañeda, P., 2012. Bounds for nonlinear composites via iterated homogenization. J. Mech. Phys. Solids 60, 1583–1604.

Ponte Castañeda, P., 2015. Fully optimized second-order variational estimates for the macroscopic response and field statistics in viscoplastic crystalline composites. Proc. R. Soc. A 471, 20150665.

Ponte Castañeda, P., 2016. Stationary variational estimates for the effective response and field fluctuations in nonlinear composites. J. Mech. Phys. Solids 96, 660-682.

Ponte Castañeda, P., Suquet, P., 1998. Nonlinear composites. Adv. Appl. Mech. 34, 171–302.

Ponte Castañeda, P., Willis, J. R., 1988. On the overall properties of nonlinearly viscous composites. Proc. R. Soc. Lond. A 416, 217–244.

Ponte Castañeda, P., Willis, J. R., 1995. The effect of spatial distribution on the effective behavior of composite materials and cracked media. J. Mech. Phys. Solids 43, 1919–1951.

Ponte Castañeda, P., Zaidman, M., 1994. Constitutive models for porous materials with evolving microstructures. J. Mech. Phys. Solids 42, 1459–1497.

Reuss, A., 1929. Calculation of the flow limits of mixed crystals on the basis of the plasticity of monocrystals. Z. Angew. Math. Mech. 9, 49-58.

Rice, J.R., 1977. The localization of plastic deformation. Proceedings of the 14th International Congress of Theoretical and Applied Mechanics, North-Holland Publishing Company, pp. 207–220.

Saby, M., Bernacki, M., Roux, E., Bouchard, P.O., 2013. Three-dimensional analysis of real void closure at the meso-scale during hot metal forming processes. Comput. Mater. Sci. 77, 194-201.

Schacht, T., Untermann, N., Steck, E., 2003. The influence of crystallographic orientation on the deformation behaviour of single crystals containing microvoids. Int. J. Plasticity 19, 1605–1626.

Schulson, E.M. and Duval, P., 2009. Creep and fracture of ice. Cambridge University Press. Vol. 432.

Shen, H., Oppenheimer, S.M., Dunand, D.C., Brinson, L.C., 2006. Numerical modeling of pore size and distribution in foamed titanium. Mech. Mater. 38, 933-944.

Shokr, M., Sinha, N., 2015. Sea ice: physics and remote sensing. John Wiley and Sons.

Siemes, H., 1974. Anwendung der Taylor-Theorie auf die Regelung von kubischen Mineralen. Z. Angew. Math. Mech. 43, 149-157.

Smyshlyaev, V.P., Willis, J.R., 1998. A non-localvariational approach to the elastic energy minimalization of martensitic polycrystals. Proc. R. Soc. London A 454, 1573-1613.

Song, D., Agoras, M., Ponte Castañeda, P., 2015. The evolution of pore shape and orientation in plastically deforming metals: Implications for macroscopic response and shear localization. Mech. Mater. 90, 47–68.

Song, D., Ponte Castañeda, P., 2017a. Macroscopic response of strongly anisotropic porous viscoplastic single crystals and applications to ice. Extreme Mech. Lett. 10, 41–49.

Song, D., Ponte Castañeda, P., 2017b. A finite-strain homogenization model for viscoplastic porous single crystals: I– Theory. J. Mech. Phys. Solids 107, 560–579.

Song, D., Ponte Castañeda, P., 2017c. A finite-strain homogenization model for viscoplastic porous single crystals: II– Applications. J. Mech. Phys. Solids 107, 580–602.

Song, D., Ponte Castañeda, P., 2017d. Fully optimized second-order homogenization estimates for the effective behavior and texture evolution of viscoplastic polycrystals. In preparation

Song, D., Ponte Castañeda, P., 2017e. A finite-strain multiscale homogenization model for viscoplastic porous polycrystals with large voids: I– Theory. In preparation

Song, D., Ponte Castañeda, P., 2017f. A finite-strain multiscale homogenization model for viscoplastic porous polycrystals with large voids: II– Applications. In preparation

Srivastava, A., Gopagoni, S., Needleman, A., Seetharaman, V., Staroselsky, A., Banerjee, R., 2012. Effect of specimen thickness on the creep response of a Ni-based single-crystal superalloy. Acta. Mater. 60, 5697–5711.

Srivastava, A., Needleman, A., 2012. Porosity evolution in a creeping single crystal. Modelling Simul. Mater. Sci. Eng. 20, p.035010.

Srivastava, A., Needleman, A., 2013. Void growth versus void collapse in a creeping single crystal. J. Mech. Phys. Solids 61, 1169-1184.

Srivastava, A., Needleman, A., 2015. Effect of crystal orientation on porosity evolution in a creeping single crystal. Mech. Mater. 90, 10–29.

Suquet, P., 1992. On bounds for the overall potential of power law materials containing voids with an arbitrary shape. Mechanics Research Communications 19, 51–58.

Talbot, D.R.S.., Willis, J. R., 1985. Variational principles for inhomogeneous nonlinear media. I.M.A. J. appl. Math. 35, 39–54.

Taylor, G.I., 1938. Plastic strain in metals. J. Inst. Metals. 62, 307-324.

Tvergaard, V., 1981. Influence of voids on shear band instabilities under plane strain conditions. Int. J. Fracture 17, 389–407.

Tvergaard, V., 1990. Material failure by void growth. Adv. Appl. Mech. 27, 83–151.

Tvergaard, V., 2012. Effect of stress-state and spacing on voids in a shear-field. International Journal of Solids and Structures 49, 3047–3054..

Tvergaard, V., 2014. Bifurcation into a localized mode from non-uniform periodic deformations around a periodic pattern of voids. J. Mech. Phys. Solids 69, 112–122.

Tvergaard, V., 2015. Study of localization in a void-sheet under stress states near pure shear. Int. J. Solids Struct. 75-76, 134–142.

Van Houtte, P., Aernoudt, E., 1976. Considerations on the crystal and the strain symmetry in the calculation of deformation textures with the Taylor theory. Mater. Sci. Eng. 23, 11-22.

Willis, J. R., 1977. Bounds and self-consistent estimates for the overall moduli of anisotropic composites. J. Mech. Phys. Solids 25, 185–202.

Willis, J. R., 1981. Variational and related methods for the overall properties of composites. Adv. Appl. Mech. 21, 1-78.

Willis, J. R., 1983. *The overall response of composite materials*, ASME J. Appl. Mech. 50, 1202–1209.

Willis, J.R., 1991. On methods for bounding the overall properties of nonlinear composites. J. Mech. Phys. Solids 39, 73–86.

Xue, Z,. Faleskog, J., Hutchinson, J. W., 2013. Tension-torsion fracture experiments Part II: Simulations with the extended Gurson model and a ductile fracture criterion based on plastic strain. Int. J. Solids Struct. 50, 4258–4269.

Yamamoto, H., 1978. Conditions for shear localization in the ductile fracture of void containing materials. Int. J. Fract. 14, 347-365.

Yerra, S.K., Tekog, C., Scheyvaerts, F., Delannay, L., Van Houtte, P., Pardoen, T., 2010. Void growth and coalescence in single crystals. Int. J. Solids Struct. 47, 1016–1029.